# COMPUTATIONAL AERODYNAMICS OF ORDERED VORTEX FLOWS

H. W. M. HOEIJMAKERS

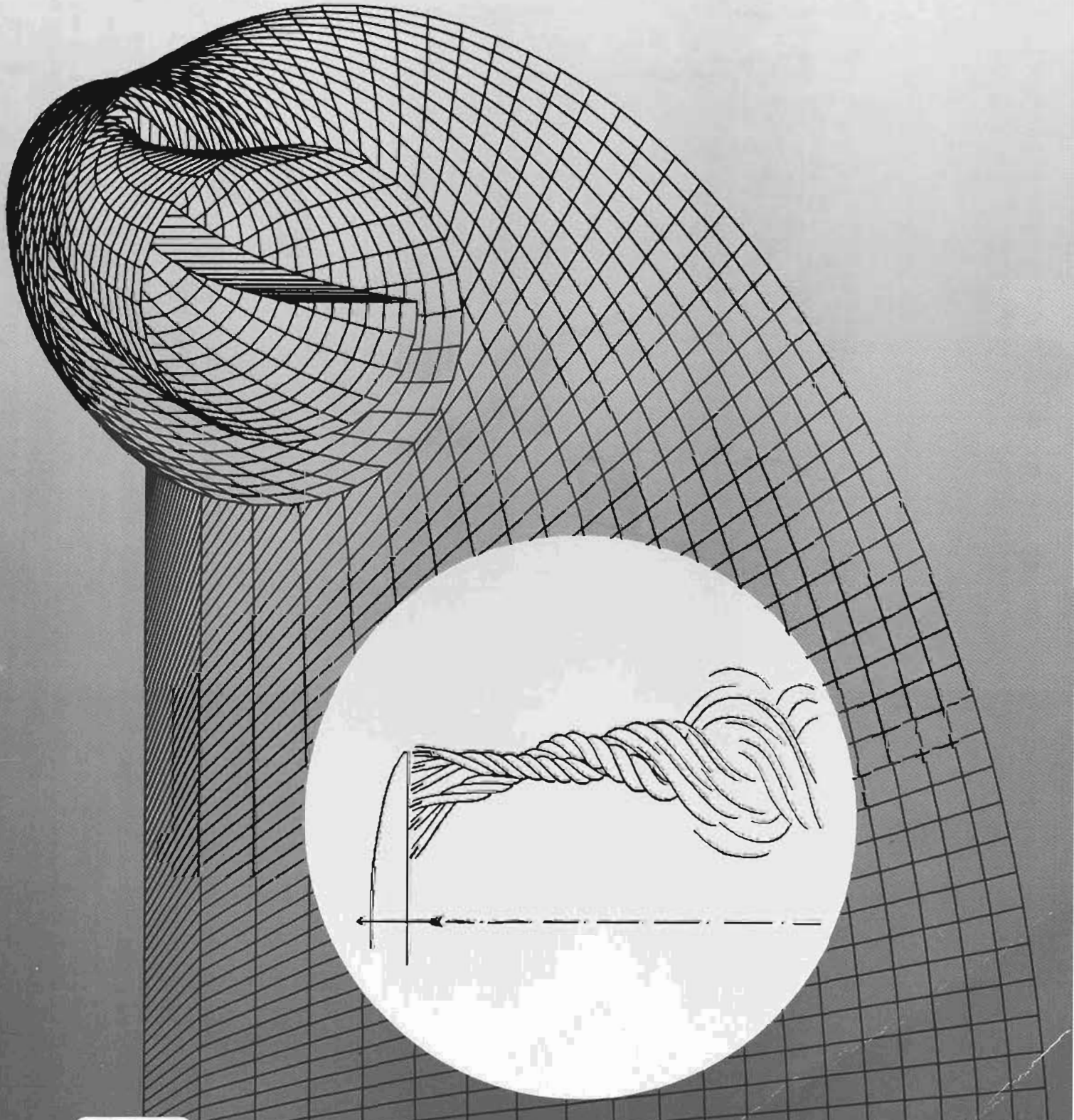

TR diss
1729

469923
317 9128
TR diss 1729



# COMPUTATIONAL AERODYNAMICS OF ORDERED VORTEX FLOWS

**PROEFSCHRIFT**

ter verkrijging van de graad van doctor
aan de Technische Universiteit Delft,
op gezag van de Rector Magnificus,
Prof. drs. P. A. Schenck,
in het openbaar te verdedigen
ten overstaan van een commissie
door het College van Dekanen
daartoe aangewezen,
op dinsdag 30 mei 1989
te 14.00 uur.

door

HENDRIK WILLEM MARIE HOEIJMAKERS

Vliegtuigbouwkundig Ingenieur
geboren te Sevenum

TR diss
1729

Dit proefschrift is goedgekeurd door de promotoren:
Prof. dr. ir. J. L. van Ingen
en
Prof. dr. ir. P. Wesseling

*Aan: Mijn ouders,*
*Truus, Marieke, Bart-Jan*

ACKNOWLEDGEMENTS

The author is indebted to a number of persons and institutes for their cooperation and support during the course of the research described in this thesis:
- The Directors of the Nationaal Lucht- en Ruimtevaartlaboratorium (National Aerospace Laboratory NLR) for the opportunity to present the results of this research work in the form of a thesis.
- The Scientific Research Division of the Directorate of Materiel of the Royal Netherlands Air Force, RNLAF, which supported parts of the investigations.
- Ir. N.G. Verhaagen of the Department of Aerospace Engineering of the Technical University Delft for a very stimulating co-operation on vortex flow aerodynamics.
- Ir. B. Bennekers and Ir. W. Vaatstra, both formerly of the Informatics Division of NLR, for their contribution in the development of the computer programs.
- A number of (now former) students that contributed to the subject during their practical training period at NLR: C.M. van Beek, R.F. Kerting Olivier, D. Winkelaar, T.M. Boerema, M.L.M. Buffat, S.H.J. Naarding, R. van Manen and L.M.C. Ferro.
- The fellow vortex-flow aerodynamicists at NLR and elsewhere for the many stimulating discussions on the subject.
- The persons at NLR that contributed to the production process of this thesis, especially: Monique Ekelschot for the typing and Randy Wijngaarde for the preparation of most of the illustrations.

COVER
Design: J.T.A.M. Groos
Sub-figure taken from "Aerodynamics" by F.W. Lanchester (1907).
With permission of Constable & Company, London

# STELLINGEN

bij het proefschrift

# COMPUTATIONAL AERODYNAMICS OF ORDERED VORTEX FLOWS

door

**H. W. M. Hoeijmakers**

30 mei 1989

1. Dat de predictie van "vortex breakdown" met behulp van een rekenmethode gebaseerd op slender-body theorie voor de voorrandwervel ingebed in een vooraf berekende buitenstroming, zoals gepoogd door Luckring, geen goede correlatie oplevert met experimentele gegevens had kunnen worden voorzien. (J.M. Luckring: Theory for the Core of a Three-Dimensional Leading-Edge Vortex, AIAA Paper 85-0108).

2. Lijnwervels zijn dusdanig singuliere elementen dat het gebruik ervan als discrete representatie van wervelvlakken dient te worden afgeraden en wel in een mate die omgekeerd evenredig is met de complexiteit van deze discretisering.

3. Om voor deltavleugels met voorrandwervels een bevredigende correlatie tussen berekende en gemeten drukverdelingen te verkrijgen, is het noodzakelijk de effecten van secundaire loslating in rekening te brengen. (Hoofdstuk 8 van dit proefschrift).

4. De grote verscheidenheid aan stromingsverschijnselen die optreden in de compressibele stroming om een eenvoudige configuratie als de delta- of dubbeldeltavleugel maakt deze configuratie tot een relevant testgeval voor het valideren van aërodynamische rekenmethoden. Dit heeft als consequentie dat verder gedetailleerd experimenteel stromingsonderzoek aan dergelijke vleugels noodzakelijk is.
(Proceedings of the Symposium on the International Transonic Vortex Flow Experiment on Euler Code Validation, Stockholm, 1986).

5. Hoewel de gelineariseerde supersone stroming een eenvoudiger karakter heeft dan de gelineariseerde subsone stroming, vraagt het toepassen van een panelenmethode, voor één en dezelfde configuratie, meer zorgvuldigheid in het geval van een supersone dan in het geval van een subsone aanstroming.

6. De vergelijking $u_x u_y - u = 0$ met $u = 0$ voor $y = 0$, heeft behalve de oplossingen $u = 0$ en $u = y(x + a)$ met $a$ een constante, zeer waarschijnlijk nog andere oplossingen.

7. Het is noodzakelijk dat een aërodynamisch rekenprogramma de gebruiker, liefst bij herhaling, waarschuwt in het geval dat: de bereikte oplossing niet voldoet aan vooraf gestelde nauwkeurigheidscriteria; standaard "fixes" zijn toegepast, etc.

8. De stroming om twee-dimensionale "automobielen" of "treinen" vertoont, zelfs wanneer gesimuleerd met een rekenmethode gebaseerd op een geavanceerd wiskundig model, onvoldoende overeenkomst met de stroming om werkelijke automobielen of treinen om als leidraad te kunnen dienen bij het ontwerp van deze voertuigen.

9. Het houden van een "kick-off" bijeenkomst, bijvoorbeeld aan het begin van het jaar, met een door een "executive" uitgesproken overzicht over de afgelopen periode en de verwachtingen voor de komende periode bevordert de betrokkenheid van de individuele werknemer met zijn/haar organisatie, bedrijf of ander werkverband en zou daarom vanzelfsprekend moeten zijn.

10. Het lezen van meer dan één biografie over een bepaald persoon geeft naast een vergroot inzicht in die persoon ook inzicht in de voorkeuren van de biografen.
    1. *Der fliegende Holländer; Das Leben des Fliegers und Flugzeug*-konstrukteurs A.H.G. Fokker, door A.H.G. Fokker en Bruce Gould. Vertaald in het Duits en bewerkt door Carl Hanns Pollog, Rascher & Cie A.-G. Verlag, Zürich, 1933.
    2. Fokker: The Creative Years, door A.R. Weyl, Putnam, 1965.

11. Duo- (en erger) banen in het basisonderwijs zijn niet bevorderlijk voor de kwaliteit van dat onderwijs.

12. Het roken aan boord van vliegtuigen moet geheel verboden worden.

SUMMARY

The physical aspects, the mathematical modeling, the development and application of computational methods for the simulation of vortical flows are described. The high-Reynolds number vortex flows considered are assumed to be steady, sub-critical and such that the structure of the flow is well-ordered and consists of thin shear layers and slender vortex cores embedded in otherwise irrotational flow.

The applications considered are vortex wakes and the flow about three-dimensional (slender) configurations with the flow separating from known separation lines, mostly the sharp leading edges.

CONTENTS

PART ONE: PHYSICAL ASPECTS AND MATHEMATICAL MODELING OF ORDERED VORTEX FLOWS


| | | Page |
|---|---|---|
| 1 | INTRODUCTION | 3 |
| | 1.1 Background | 3 |
| | 1.2 Purpose and outline of thesis | 4 |
| 2 | FEATURES OF ORDERED VORTEX FLOWS | 5 |
| | 2.1 Vortex wakes - Weak interaction | 5 |
| | 2.2 Leading-edge vortex flow - Strong interaction | 5 |
| | 2.3 Separation from smooth slender bodies - Strong interaction | 8 |
| 3 | MATHEMATICAL MODELING OF ORDERED VORTEX FLOWS | 9 |
| | 3.1 General discussion | 9 |
| | 3.2 High-Reynolds number flow model | 9 |
| | 3.3 Governing equations, fundamental properties of the flow | 11 |
| | 3.4 Vortex sheets and vortex filaments | 15 |
| | 3.4.1 Vortex sheets | 15 |
| | 3.4.2 Vortex filaments | 16 |
| | 3.5 Potential flow | 19 |
| | 3.6 Rolled-up vortex core model | 21 |
| | 3.6.1 Vortex-filament/feeding-sheet model | 21 |
| | 3.6.2 Remarks on possible more accurate core models | 22 |
| | 3.7 Boundary conditions for potential-flow model | 23 |
| 4 | FURTHER ASPECTS OF SLENDER, NARROW VORTEX CORES | 27 |
| | 4.1 Introduction | 27 |
| | 4.2 Vortex cores as regions with distributed vorticity | 27 |
| | 4.2.1 Solution of Euler equations | 27 |
| | 4.2.2 Velocity field induced by vortex core | 30 |
| | 4.3 Vortex core as an infinitely long, tightly wound vortex sheet | 33 |
| | 4.3.1 Formulation of the problem | 33 |
| | 4.3.2 Asymptotic solution | 35 |
| | 4.4 Vortex filament/feeding sheet model | 37 |
| | 4.4.1 Induced velocity field | 37 |
| | 4.4.2 Matching of velocity fields | 38 |
| | 4.4.3 The entrainment of a vortex core | 39 |
| | 4.5 Numerical example | 42 |
| 5 | POTENTIAL FLOW FORMULATIONS USED IN PRESENT STUDY | 43 |
| | 5.1 Three-dimensional flow with free vortex sheets | 43 |
| | 5.1.1 Integral representation for the solution | 43 |
| | 5.1.2 Description of the geometry | 45 |
| | 5.1.3 Nonlinearity of the problem | 45 |
| | 5.2 Quasi-two-dimensional description in cross-flow planes - Approximation for slender configurations and slowly varying vortex wakes | 46 |
| | 5.2.1 Description of the cross-flow-plane geometry | 46 |
| | 5.2.2 Expansion of the integral representation | 47 |
| | 5.2.3 Expansion of the boundary conditions | 51 |
| | 5.2.4 Special case: conical flow | 53 |
| | 5.3 Two-dimensional time-dependent analogy - Trefftz plane analysis for vortex wakes | 53 |
| | 5.3.1 Time-dependent analogy | 53 |
| | 5.3.2 Expression for the velocity in the Trefftz plane | 55 |
| | 5.3.3 Is the initial-value problem well-posed? | 55 |

Page

PART TWO: COMPUTATIONAL METHODS FOR ORDERED VORTEX FLOW


6 SUMMARY OF EXISTING COMPUTATIONAL METHODS 59
6.1 Methods for computing vortex wakes 59
6.2 Methods for computing leading-edge vortex flows 62
6.3 Methods for computing vortex flows associated with smooth-surface separation 64
6.4 Methods developed in the present study 65

7 METHOD FOR QUASI TWO-DIMENSIONAL VORTEX-WAKE ROLL-UP 67
7.1 Introduction 67
7.2 Two-dimensional second-order panel method 67
7.2.1 General aspects 67
7.2.2 Small-curvature expansion 68
7.2.3 Numerical scheme 70
7.3 Treatment of highly rolled-up regions 71
7.3.1 Single-branched spirals 71
7.3.2 Double-branched spirals 72
7.4 Rediscretization 73
7.5 Computational procedure 73
7.6 Invariants of the motion 74
7.7 Examples of application 78
7.7.1 Elliptically loaded wing 78
7.7.2 Ring wing 83
7.7.3 Wing with deployed part-span flap 85
7.7.4 Delta wing with leading-edge vortex separation 89
7.8 Assessment of inherent smoothing properties of present method - Periodic vortex sheet 92
7.8.1 Introduction 92
7.8.2 Computation of the velocity field 92
7.8.3 Linear growth of normal modes 93
7.8.4 Nonlinear growth of normal modes 93

8 METHOD FOR QUASI TWO-DIMENSIONAL VORTEX FLOW ABOUT SLENDER CONFIGURATIONS 95
8.1 Introduction 95
8.2 Treatment of streamwise derivatives 96
8.2.1 Velocity potential 96
8.2.2 Velocity field 97
8.2.3 Boundary conditions 98
8.3 Two-dimensional second-order panel method 100
8.3.1 Velocity potential due to doublet distribution 100
8.3.2 Cross-flow plane velocity due to doublet distribution 100
8.3.3 Streamwise velocity due to doublet distribution 100
8.3.4 Velocity potential due to source distribution 101
8.3.5 Cross-flow plane velocity due to source distribution 101
8.3.6 Streamwise velocity due to source distribution 101
8.3.7 Influence of a panel on itself 101
8.3.8 *Numerical scheme - aerodynamic influence coefficients* 101
8.4 Application of boundary and auxiliary conditions 103
8.4.1 Lifting surface segment $C_w$ 103
8.4.2 Wing segment $C_w$ with composite source/doublet distribution 105
8.4.3 Vortex sheet segment $C_v$ 107
8.4.4 Kutta condition 109
8.5 Solution of system of nonlinear equations 109
8.5.1 System of equations 109
8.5.2 Newton's method 110
8.5.3 Initial guess for starting iteration procedure 115
8.6 Examples of application 115
8.6.1 Thin, unit-aspect-ratio delta wing 115
8.6.2 Influence of length of vortex sheet 117
8.6.3 Convergence of the numerical scheme 117
8.6.4 Iterative solution procedure 117
8.6.5 Effect of entrainment on the solution 117
8.6.6 Solution for unit-aspect-ratio delta wing at angles of attack between 2.5 and 40 deg 119
8.6.7 Solution at very low incidence 119
8.6.8 Side-slipping delta wing 120
8.6.9 Bi-convex delta wing 121
8.6.10 Investigation of the vortex core 121
8.6.11 Comparison with Smith's solution 123
8.6.12 Comparison with experimental data 124
8.6.13 An attempt to model secondary separation 125
8.6.14 Separated flow from a slender circular cone 126
8.6.15 Double-delta wing 128
8.6.16 Strake-wing configuration 129

Page

9 METHOD FOR THREE-DIMENSIONAL LEADING-EDGE VORTEX FLOW ABOUT THIN WINGS 131
9.1 Introduction 131
9.2 Transformation to a rectangular computational domain 132
9.3 Second-order panel method 134
9.3.1 Preliminaries 134
9.3.2 Small-curvature expansion for the surface integrals 135
9.3.3 Small-curvature expansion for the far-wake integrals 136
9.3.4 Small-curvature expansion for the feeding-sheet integrals 137
9.3.5 Small-curvature expansion contribution of vortex 137
9.3.6 Numerical integration 138
9.3.7 Numerical scheme - doublet distribution 140
9.3.8 Numerical scheme - geometry 142
9.4 Implementation of boundary and auxiliary conditions 144
9.4.1 Conditions on a wing panel 144
9.4.2 Conditions on a vortex-sheet panel 144
9.4.3 Conditions on a vortex-core segment 144
9.4.4 Implied conditions 145
9.5 Solution of system of nonlinear equations 145
9.5.1 Quasi-Newton method 146
9.5.2 Derivation of Jacobian matrix 146
9.5.3 Initial guess for iteration procedure 149
9.6 Examples of application 151
9.6.1 Basic test case: Unit-aspect ratio delta wing at 20 deg incidence 151
9.6.2 Influence of the length of the leading-edge vortex sheet 151
9.6.3 Influence of the length of the near wake 153
9.6.4 Convergence of the numerical scheme 153
9.6.5 Three-dimensional character of the solution 155
9.6.6 Convergence history of iterative solution procedure 155
9.6.7 Solution for the 76-deg swept delta wing at angles of attack between 10 and 40 deg 157
9.6.8 Solution for delta wings of different angle of sweep 159
9.6.9 Comparison with experiment 159
9.6.10 Comparison with results of an Euler code 160

10 CONCLUDING REMARKS 161

REFERENCES 163

LIST OF SYMBOLS 167

TABLES 1-3: List of various integrals employed in present study 169

APPENDIX A: Equivalence between the velocity induced by a doublet distribution and that induced by a surface vorticity distribution 171
APPENDIX B: Solution of Euler equations for slender axi-symmetric vortex core 173
APPENDIX C: Linear analysis of Kelvin-Helmholtz instability 175
APPENDIX D: Derivation of $\bar{E}_1$, $\bar{E}_2$, $\bar{E}_3$, $\bar{E}_4$ and $\bar{E}_5$ 177
APPENDIX E: Derivative with respect to $G_\ell$ of $\bar{E}_1$, $\bar{E}_2$ and $\bar{E}_3$ 179
APPENDIX F: Computation of $\bar{E}_{10}$, $\bar{E}^c_{10}$, $\bar{E}_{01}$, $\bar{E}^c_{01}$, $\bar{E}_{20}$, $\bar{E}_{11}$ and $\bar{E}_{02}$ 185
APPENDIX G: Solution of four diagonal block matrix equation 195

CURRICULUM VITAE 197

SAMENVATTING (Summary in Dutch) 199

# PART ONE
# PHYSICAL ASPECTS AND MATHEMATICAL MODELING OF ORDERED VORTEX FLOWS

# 1 INTRODUCTION

## 1.1 Background

In aircraft aerodynamics flows involving free shear (vortex) layers and vortex cores, generally called vortex flows, play an important role. At the high Reynolds numbers pertinent to the aerodynamics of aircraft free shear layers form whenever the air flows around a body with a sharp edge (Prandtl-1922). The properties of the (thin) shear layer are determined by the condition, the so-called Kutta condition, that the velocity is finite at the edge and that the vorticity is convected away from it. Furthermore, away from the edge the shear layer usually tends to roll up into vortex core(s), in which sooner or later most of the vorticity becomes concentrated. The resulting vortical flow structure is often well-ordered, steady and persistent. On an aircraft configuration the flow may separate before the edge is reached, i.e. separate from locations on the smooth surface, also resulting in a vortical flow pattern. Contrary to the case of separation from an (aerodynamically) sharp edge, in the case of smooth-body separation the location of flow separation depends on Reynolds number, angle of attack, etc. and is a priori unknown.

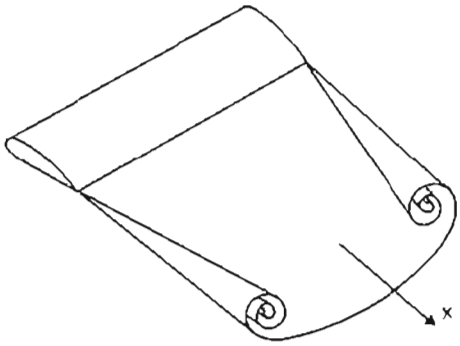


Fig. 1.1a Weak interaction; trailing vortex wake

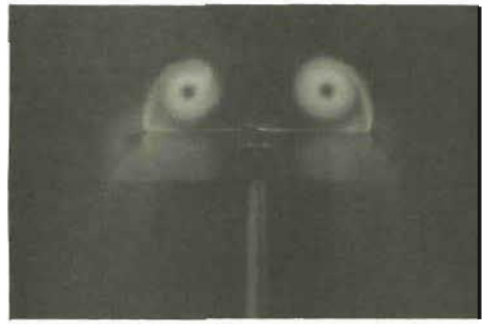

FROM: VERHAAGEN– 1983

Fig. 1.1b Strong interaction; leading-edge vortex flow

Two types of vortex flow can be distinguished, vortex flow where there is a weak and vortex flow where there is a strong interaction of the rotational flow region(s) with the flow over the surface of the configuration. One possible measure of the interaction is the relative magnitude of the contribution due to the vorticity to the velocity at the surface of the configuration. For example, the vortex flow associated with the vortex wake that forms when the flow leaves the surface of a wing at its trailing edge (Fig. 1.1a) is usually a weak-interaction type of vortex flow. In this case the rotational flow is directed away from the shedding edge and away from the surface where it was generated, the vorticity vector being directed approximately perpendicular to the shedding edge. For weak-interaction vortex flow the lift increases approximately linearly with incidence, at least until viscous flow effects become significant.

Strong-interaction vortex flow can occur when the flow separates at the side edge of a low-aspect-ratio wing or at the highly swept leading edge of a slender wing (Fig. 1.1b) and also when the flow separates from the smooth surface of the configuration. In these cases the vorticity vector is approximately parallel to the shedding edge (or separation line). A strong interaction also takes place when the vortex wake of one component of the configuration closely approaches other components of the aircraft. Examples are the interaction of the wake of the wing with the flow about the tail surfaces and the flow about "closely-coupled" canard-wing configurations (Fig. 1.1c). In the case of strong interaction the rotational flow region(s) are close to the surface of the configuration and often remain in the near proximity of the shedding edge. The local surface velocity and pressure distribution and the overall characteristics of the configuration are affected considerably, in some cases favourably in other cases unfavourably. For strong-interaction vortex flow typically the lift increases nonlinearly with incidence, often up to high incidences where ultimately the ordered vortex-flow pattern breaks down.

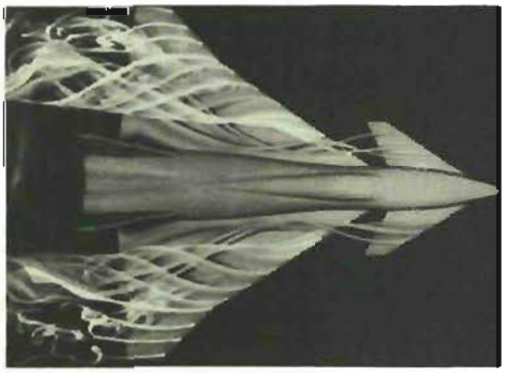

Fig. 1.1c Strong interaction; closely-coupled canard-wing

FROM: VERHAAGEN– 1983

Fig. 1.2 Double-delta (idealisation of strake-wing) vortex flow

The analysis of aerodynamic vortex flow and its computation is a subject that continues to receive a great deal of attention.
In the early days of aerodynamic wing theory the trailing wake of a wing of finite span at low incidence was an important subject. The main reason being that the velocity field associated with the wake is related to the induced drag (drag due to lift, sometimes also called "vortex drag") of the wing, which has no counterpart in two-dimensional airfoil theory. In contemporary computational aerodynamics the interest in vortex flow has been aroused because of the favourable effects induced by leading-edge vortex flow on highly swept wing and strake-wing (Fig. 1.2) configurations at high incidence, where it results in a substantial increase of the lift. This is of great practical importance for configurations with these wings with their, according to classical wing theory, relatively small lift slope.

There exists an extensive literature on various aspects of aerodynamical vortex flow. However, predicting the behaviour of trailing wakes is still considered a difficult task, while strong-interaction vortex flows like leading-edge vortex flow pose an even greater problem.
Since the attached-flow theories commonly used in present-day design procedures are inadequate to predict the high-angle-of-attack characteristics of configurations utilizing vortex flow, the design of such configurations has been almost entirely empirical. In these circumstances the resulting aircraft geometry is inevitably the result of laborious and costly cut-and-try type of wind tunnel investigations, including measurement of detailed surface pressure distributions and flow visualization. In spite of this the resulting designs have proven to be quite successful in "harnessing" the vortices, thereby enlarging the flight envelope considerably.
However, if the vortex lift capabilities of slender-wing, strake-wing, canard-wing and even more exotic configurations, that for their characteristics rely on ordered, controllable vortex flow, are to be fully utilized a detailed knowledge and adequate mathematical modeling of this type of flow is required. It is in this area that computational methods can make a major contribution. This contribution consists in a better understanding of vortex flow behaviour and in reducing the number of candidate configurations considered for extensive wind-tunnel testing, or even suggesting improved designs, through computer simulation. If the theoretical tools are capable of predicting not only the overall forces and moments, spanwise loadings, etc. but also the detailed surface velocity and pressure distribution they will be of great help to the aircraft designer. Also the possibility to analyze in detail the flow field will help significantly to gain insight in vortical flow structures.

## 1.2 Purpose and outline of thesis

The purpose of the present study is to contribute to an increased understanding and utilization of vortical type of aerodynamic flows through the development, validation and application of numerical methods for the prediction of the detailed aerodynamic characteristics of aircraft configurations with vortex flow. Both cases with weak and with strong interaction vortex flow will be considered. Validation will take place through comparison with results of other theoretical methods and with available experimental data.

In this study we consider steady flow at high Reynolds number. Although transonic vortex flow is of great practical importance, the present study is restricted to equally important vortex flows that occur at low speed, i.e. during take-off, landing and manoeuvering. It avoids the added complexity of another nonlinear flow phenomenon: shock waves, and the complex interaction of vortex flow and shock waves. Furthermore, as long as the flow remains sub-critical, we may assume linearized compressible flow, or as assumed here: incompressible flow.

This thesis is divided into two parts. In the first part, consisting of chapters 1 through 5, the physical aspects of ordered vortex flows, their mathematical modeling and some general properties of this type of flow are described. The physics of a number of important weak and strong-interaction vortex flows is described in chapter 2. In chapter 3 various aspects of the mathematical modeling of (ordered) vortex flows are described, including some well-known fundamental results. The discussion in this chapter leads to the adoption of a potential flow model with embedded compact regions of rotational flow, namely vortex sheets and vortex cores. The effect of vortex cores on the flow outside the core itself can be accounted for by a relatively simple model involving a vortex filament and "feeding" sheets, which is also described in chapter 3. In chapter 4 further aspects of vortex cores are considered in some more detail, specifically for the simplified case of isolated slender vortex cores. For this type of vortex core some extensions of analysis results found in the literature are obtained. This analysis facilitates a closer look at the vorticity components inside the vortex core and at the flow field inside as well as outside the vortex core. It is shown that in the vortex core the circumferential velocity component is converted into an axial velocity component, resulting in a swirling jet-like type of flow which entrains fluid into the core. By matching of the external flow fields an improved core model is derived that accounts for the above mentioned entrainment of a vortex core.
In chapter 5 the mathematical model for the three-dimensional flow about configurations with vortex flow is summarized and the method of solution by integral representations is described. The fully 3D potential flow problem, nonlinear in terms of its boundary conditions, is a difficult problem. However, for vortex wakes and for the flow about slender configurations further simplifying assumptions can be made that lead to a quasi-2D problem, or rather a sequence of quasi-2D problems, which is still nonlinear, but less demanding in working out the details of a solution procedure. In this chapter the quasi-2D formulation of the problem is obtained from the one for the fully 3D case, providing direct insight in the approximations involved.

The second part, consisting of chapters 6 through 10, covers computational methods for the determination of the aerodynamic characteristics of aircraft configurations with ordered vortex flows. Chapter 6 starts with an inventory of existing computational methods. This inventory indicates the weak and strong points of the existing methods and also where improved computational methods are required.
The main contribution of the present investigation is the development of panel methods for solving the (nonlinear) problem of potential flow with free vortex sheets and vortex cores. The methods developed and their applications are discussed in increasing order of complexity, namely starting with the two quasi-2D formulations and ending with the 3D one. These methods are:

- Chapter 7: method for computing vortex sheet motion in two dimensions, i.e. the quasi-2D problem as formulated within the framework of the two-dimensional unsteady analogy of three-dimensional (weak-interaction) vortex wakes.

- Chapter 8: method for computing, within the framework of the slender-body approximation, the quasi-2D (strong-interaction) vortex flow about more or less arbitrarily shaped slender wings and bodies, with free vortex sheets starting from prescribed and fixed lines of separation.

- Chapter 9: method for computing the fully 3D (strong-interaction) vortex flow about infinitesimally thin, slender wings with a leading-edge vortex sheet attached all along its leading edge. The 3D-flow method is further restricted to isolated wing configurations in (port/starboard side) symmetric flow.

Finally, chapter 10 contains the main conclusions of the present study and some recommendations for further research.

The present study has been carried out by the author while employed at NLR. Some of the results presented here have been published earlier in NLR reports or articles in journals, see the references in chapter 11.

## 2 FEATURES OF ORDERED VORTEX FLOWS

In this chapter the physical features of a number of vortex flows are described in more detail. In all cases we will deal exclusively with flows that will be termed ordered vortex flows. Ordered vortex flows are flows with a topologically well-defined, steady and stable flow pattern, which is maintained within a sizable range of flight parameters (incidence, sideslip, Reynolds number, Mach number, etc.). This implies that most cases considered here are vortex flows associated with "controlled" flow separation, i.e. flow separating at aerodynamically sharp edges.

We will consider incompressible flow only. The motivation for this is that most vortex flow interactions occur at low speed, for vortex wakes during take-off and landing and for leading- and side-edge vortex flow also during manoeuvres. Furthermore, for slender wings there is experimental evidence that the influence of Mach number on the characteristic features of the flow is small as long as the component of the free stream Mach number normal to the leading edge ($M_\infty \cos\Lambda$) is less than 0.7, e.g. see Stanbrook & Squire-1964, Miller & Wood - 1983.

### 2.1 Vortex wakes - Weak interaction

At the trailing edge of a wing of finite span at incidence the velocity on the lower wing surface and the velocity on the upper wing surface are equal in magnitude but different in direction. This three-dimensional flow effect, caused by the air tending to flow around the wing tip from the lower ("pressure") side to the upper ("suction") side of the wing, results in the shedding of vorticity and the formation of the vortex wake. In the vortex wake the vortex lines are approximately directed in free-stream direction, i.e. away from the trailing edge, and they are not located near the surface of the generating wing, resulting in a "weak interaction" between the surface pressure distribution and vortex wake.

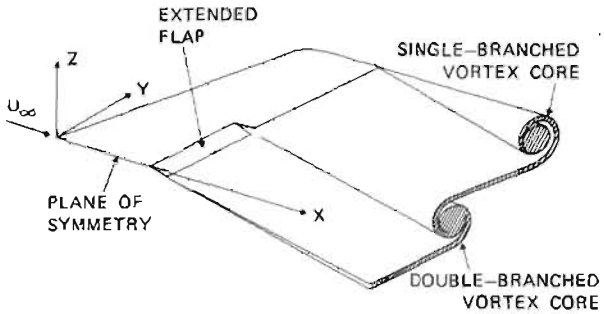


Fig. 2.1 Downstream development of a vortex wake

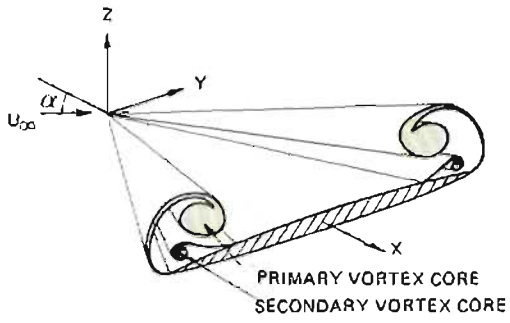


Fig. 2.2 Vortex flow about delta wing

If the Reynolds number is large, convection is much larger than diffusion and the vorticity remains within a thin free shear layer. Due to the velocity induced by the vorticity contained within the layer, the layer tends to roll up into vortex cores. This rolling-up may occur in various ways. The most well-known is the tip vortex. It is the single-branched vortex that forms at the free edge of a shear layer (Fig. 1.1a). In case the trailing wake contains vorticity of both signs, vorticity of each sign will roll-up into separate vortices. Examples of this are the wake of a highly swept wing and the wake of a wing with deployed part-span flaps. Such wakes contain both single-branched (at the edges) and double-branched vortex cores. Even if the shed vorticity is of one sign one or more double-branched vortices may be formed (see Fig. 2.1). Where these centers of roll-up develop is not always a priori evident. For a single straight trailing edge the local extrema of the trailing vorticity (inflection points in the spanwise loading) act often as a center of roll-up, but for more complex shapes of the trailing vortex system the situation is less clear.

In downstream direction vorticity from the shear layer is continuously fed into the vortex core(s), resulting into a growth of the vortex core(s), both in strength and usually also in cross-sectional dimension. The stretching of the shear layer associated with the roll-up process counteracts the effect of viscous diffusion, so that quite often one observes that the shear layer remains relatively thin up to several spans downstream of the trailing edge.

Further downstream of the configuration the roll-up process will be completed, most of the vorticity residing within a limited number of vortex cores (e.g. the trailing vortex pair). The concentration of vorticity into these relatively compact regions of rotational flow is probably responsible for their surprisingly stable and persistent character. The strong and persistent trailing vortex system of large transport aircraft has proven to present a possible hazard for other air traffic, which has resulted in stringent rules imposed at present on air traffic involving large aircraft.

Still further downstream, cores with vorticity of the same or opposite sign, if close enough to each other, start to merge, accompanied by viscous diffusion and decay. Alternatively, complicated longitudinal instabilities may be triggered before the merging or decay process has started, resulting in a somewhat earlier break-up of the trailing vortex system.

### 2.2 Leading-edge vortex flow - Strong interaction

The low speed high-angle-of-attack flow about low-aspect-ratio highly swept wings with leading-edge vortex separation has been described extensively in the literature. Based primarily on experimental investigations by amongst others Legendre-1952, Earnshaw-1962, Wentz & McMahon-1966, Fink & Taylor-1967 and Hummel-1979 the topology of the high-Reynolds number flow about these wings is well-established. At moderate to high angles of attack the flow separates at the leading edge, resulting in a free shear layer emanating from the edge (Fig. 2.2).

Under influence of the vorticity contained in it, the free shear layer rolls up in a spiral fashion to form a relatively compact single-branched core with distributed vorticity, the so-called leading-edge vortex. The presence of this core in the proximity of the wing surface affects the pressure distribution on the wing to a large extent, the predominant effect being a low pressure region underneath the position of the vortex core (Fig. 2.3). It is this low-pressure region that is mainly responsible for the increment in the lift due to the vortex flow, the so-called vortex lift. As the angle of attack is decreased, or equivalently the leading-edge sweep is decreased, the vortex system becomes weaker, smaller and closer to the wing surface resulting in a suction peak that is lower and narrower, i.e. sharper. It has been observed in experiments that the adverse pressure gradient in the region just outboard of the lateral position of the center of the leading-

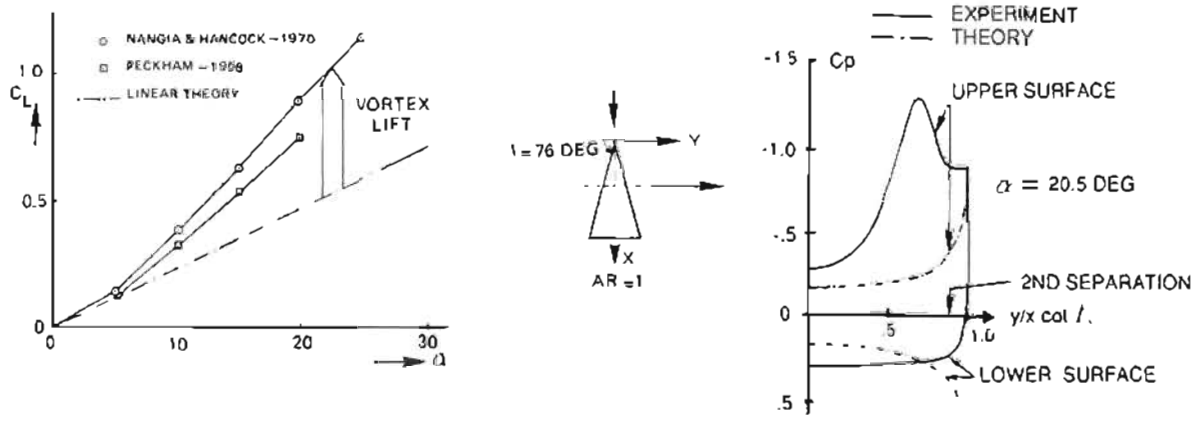


Fig. 2.3 Pressure distribution and lift coefficient on a slender delta wing

edge vortex core causes a so-called secondary separation. The free shear layer emanating smoothly at the line of secondary separation rolls up in a vortex core also, its vorticity being of opposite sign compared to that of the vorticity within the leading-edge vortex core. The extent of the effect of secondary separation on the surface pressure distribution has been observed to depend strongly on whether the boundary layer is laminar or turbulent. It appears that secondary separation effects are largest for the laminar case. Generally for both laminar and turbulent flow they become relatively more important for cases with narrow suction peaks, i.e. for wings with low leading-edge sweep and at small incidence.

Viewed in downstream direction, the leading-edge vortex is continually being fed with vorticity shed at the leading edge which is transported through the free shear layer to the vortex core, so that the latter is increasing in strength as well as in cross-sectional dimension. Downstream of the trailing edge, i.e. in the wake, the free shear layer continues to feed vorticity into the leading-edge vortex core. In the wake the vorticity of sign opposite to that within the leading-edge vortex core, which is shed along almost all of the trailing edge between the plane of symmetry and the wing tip, starts to roll up in a double-branched, so-called trailing-edge vortex core. This two-vortex system, mushroom shaped, has first been observed experimentally by Maltby-1962 and more recently by Hummel-1979 and Verhaagen-1983.

As a result of the strong interaction of the leading-edge vortex core and the flow above the slender wing large "vortex-lift" increments are produced. It has been observed that depending on the leading-edge sweep a stable vortex-flow pattern can persist up to incidences as high as 25 to 35 deg.

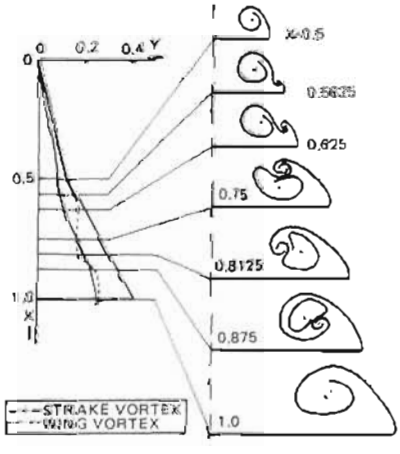


Fig. 2.4 Vortex flow about double-delta wing

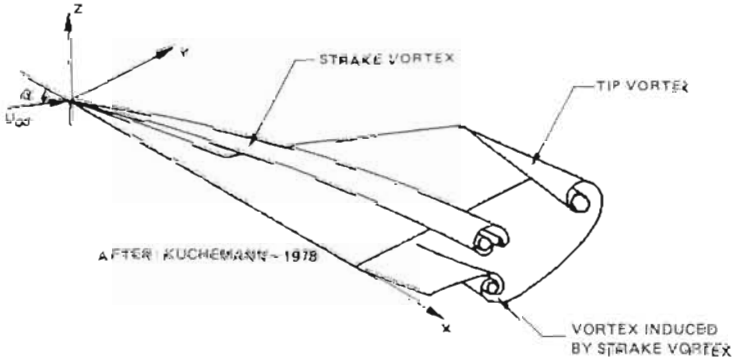


Fig. 2.5 Conceptual view strake-wing vortex flow

For wings with low or moderate leading-edge sweep favourable vortex flow effects can be invoked by adding a relatively small, highly swept leading-edge extension, commonly named "strake". The vortex flow above strake-wing configurations is more complex than the delta-wing vortex flow. Investigations by amongst others Wentz & McMahon-1966, Lamar & Luckring-1979, Brennenstuhl & Hummel-1982 have provided valuable insight into the vortex layer structure above strake-wing configurations. Verhaagen-1983, employing a laser light-sheet flow visualization technique (see Fig. 1.2), has acquired additional valuable topological information. Thompson-1985 has also provided such information from water-tunnel studies. From these investigations it follows that above a strake-wing configuration the (single-branched) leading-edge vortex, originating at the leading edge of the strake continues above the wing. The vortex modifies the wing flow field considerably inducing in addition to the favourable effects on the strake itself, favourable effects on the main wing as well. In case of sufficiently (depending on leading-edge sharpness, etc.) swept wing leading edges and at high angle of attack the flow separates also at the wing leading edge. The shear layer emanating from the wing leading edge forms the downstream continuation of the shear layer emanating from the strake leading edge (Fig. 2.4). In this single shear layer a double-branched vortex develops. This so-called wing vortex starts right at the kink in the leading edge and viewed in downstream direction, travels along the shear layer, looping around the (single-branched) strake vortex. At some point downstream of the kink the two cores (with distributed vorticity of the same sign) merge into one core.

At smaller sweep angles and at lower incidences the flow does not separate at the wing leading edge. In this case the flow picture is not yet competely clear. Mostly it is assumed that the shear layer detaches (from the leading edge) at the kink (as proposed by Küchemann-1978, p. 254) resulting in the flow pattern sketched in Fig. 2.5. Here the main difficulty lies downstream of the kink in the "free end" of the shear layer from the strake leading edge. Except under very special conditions "free ends" of shear layers tend to roll up into vortex cores. In Küchemann's view this results into another vortex with vorticity of sign opposite to that in the strake vortex. It might also be hypothesized that downstream of the kink the strake leading-edge shear layer continues as a shear layer that is attached to the wing upper surface, now emanating from some separation (?) line (see also the discussion in Smith-1983).
In the high-angle-of-attack case the shear layer presumably contains vorticity of one sign only. The vorticity in the shear about layer between the core of the strake vortex and the core of the wing vortex is either swept towards the strake vortex or towards the wing vortex. Consequently this connecting shear layer will decrease in strength in a continuous manner. It can be envisioned that at intermediate wing leading-edge sweeps and at intermediate values of the incidence the weak shear layer will "collapse" onto the wing upper surface (Fig. 2.6), i.e. coalesce with the wing boundary layer. If the wing sweep (or angle of attack) is reduced still further the wing vortex system degenerates to a leading edge separation bubble. The latter will eventually be completely engulfed by the wing boundary layer, i.e. the flow may be considered as attached flow. Note that in Fig. 2.4-2.6 secondary flow separations, which complicate the matter even more, have been omitted. Clearly more detailed investigation will be needed to clarify the precise details of the flow structure for the case of strake-wing configurations.

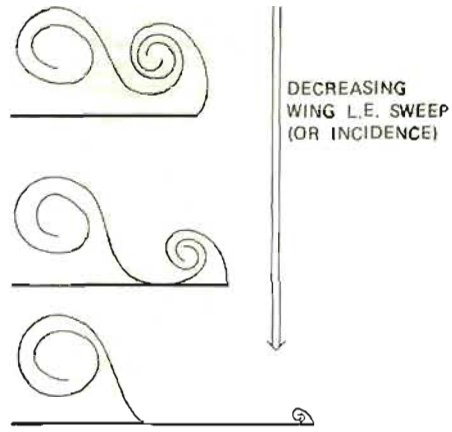


Fig. 2.6 Possible vortex flow pattern about strake-wing configuration; downstream of link

A limit to the favourable effects induced by the vortex flow is reached when large-scale vortex breakdown occurs above the wing. Vortex breakdown manifests itself as an abrupt increase in the cross-sectional area of the vortex core, a decrease in the magnitude of axial and circumferential velocity components and in an increase in the turbulence level in the vortex core. However, the overall strong circulatory flow pattern does not disappear. The mechanism underlying vortex breakdown is still unclear (e.g. Hall-1972), however, it does appear to depend rather weakly on Reynolds number. The latter may suggest that in essence it is an inviscid flow phenomenon. It has been observed that with increasing angle of attack vortex breakdown progresses in upstream direction and that it occurs in regions where there is an increase in the pressure along the core (e.g. Erickson-1982). Part of the increase in core dimension may possibly be explained as the response of the inviscid outer part of the rotational core to a pressure rise.
For the case of simple delta wings the angle of attack at which vortex breakdown reaches the trailing edge depends strongly on the sweep of the leading edge (see Fig. 2.7). For double-delta wings and strake-wing configurations such a simple correlation can not be obtained. At the higher incidences vortex breakdown is often accompanied by an asymmetric flow pattern. For simple delta wings asymmetric flow patterns without vortex breakdown have been observed for leading-edge sweep angles in excess of 80 degrees (Fig. 2.7). Although maintaining a well-organised vortex flow above the wing up to large angles of attack is one of the prime considerations in strake-wing design, the phenomenon of vortex breakdown is not addressed further in this study.

Recently Gad-el-Hak & Blackwelder-1985 and Payne et al.-1986, have obtained results of low-speed experimental studies that indicate that the leading-edge shear layer is not really a smooth layer, but consists of a sequence of small vortices travelling along the layer towards the vortex core. Whether this thin shear-layer type of instability observed at low-Reynolds number and laminar flow conditions is a true characteristic of leading-edge vortex layers or possibly was induced by vibrations of the model or flow unsteadiness, is not yet clear.
Recently Verhaagen & van Manen-1987 found that also at higher speeds the leading-edge shear layer might consist of small-scale vortical flow structures (see Fig. 2.8). It is not clear what effect the small-scale structures have on the time-averaged structure of the shear layer and on the vortex core.
However, in the present study we will assume that the flow is steady and that free shear layers may be considered as steady regions with continuous rotational flow without small-scale sub-structures.

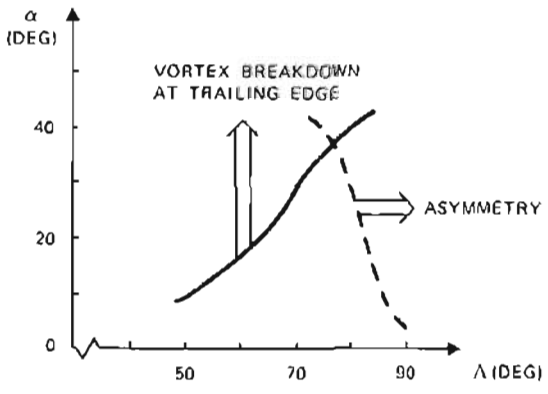


Fig. 2.7 Vortex breakdown and vortex asymmetry for delta wing

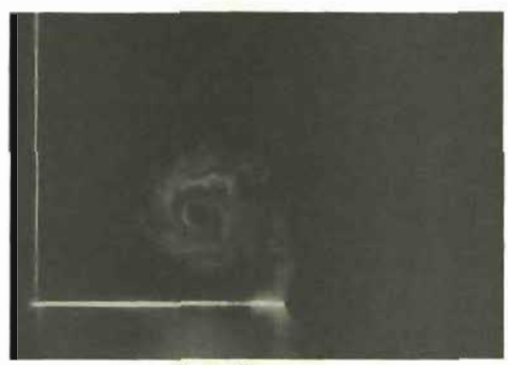


Fig. 2.8 Sub-scale structure in leading-edge vortex layer, Verhaagen & van Manen - 1986

2.3 Separation from smooth slender bodies - Strong interaction

A very fascinating flow problem is the vortex flow associated with flow separation from smooth slender bodies, such as aircraft forebodies and especially elongated missile configurations (e.g. Peake & Tobak-1980, Skow & Erickson-1982). At low incidences the flow separates symmetrically, resulting in a symmetric flow pattern (Fig. 2.9). At higher incidences the flow may still separate nearly symmetrically (or be forced to do so), however the flow may also lock into an asymmetric flow pattern or even alternate occasionally and without apparent reason between two different asymmetric patterns (e.g. Ericsson & Reding 1981). The asymmetric flow pattern is accompanied by lateral forces of the same order of magnitude as the normal force. Especially in the case of the alternating pattern guidance and control problems may result.

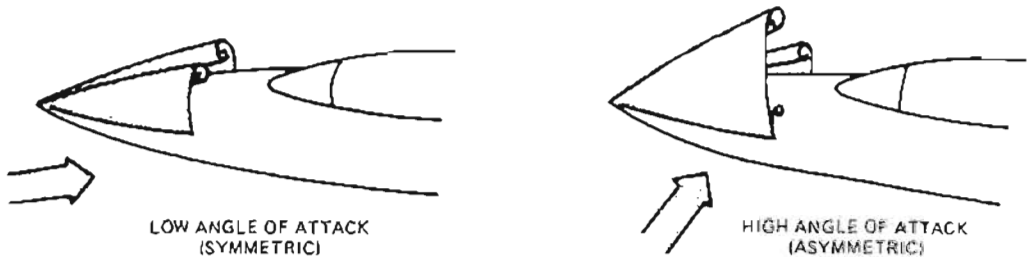


Fig. 2.9 Forebody vortex flow patterns

The asymmetry may be related to:

(i) an asymmetry in the position of the lines of separation, e.g. the one on the starboard side starting closer to the nose than the one located on the port side;
(ii) an asymmetry in the location of point of separation in the cross-flow plane;
(iii) the existence of asymmetric flow solutions at nominally symmetric conditions (i.e. symmetric configuration at zero side slip, symmetric separation lines).

Especially the latter possibility, also conceivable in case of separation from sharp edges, is quite interesting from the computational point of view; the (nonlinear) flow problem has more than one solution. The main difference between vortex flow involving sharp edges and vortex flow associated with separation from smooth slender bodies (and also the secondary separation on slender wings) is that determining the location of the line(s) of separation forms an essential part of the problem. The latter undoubtedly involves a strongly coupled interaction of the inviscid outer flow with the boundary layer on the body (e.g. Fiddes-1980, who considered slender-body vortex flow). An extensive analysis has not yet been carried out for secondary separation on wings with leading-edge vortices. In the present work this viscid-inviscid coupling will not be considered, i.e. it will be assumed that the location of the line(s) of separation is known a priori from geometric considerations (sharp edges) or from experimental investigation.

## 3 MATHEMATICAL MODELING OF ORDERED VORTEX FLOWS

### 3.1 General discussion

The characteristic feature of vortex flow is the presence of free shear layers and the development of vortex cores. In addition, especially in the case of "strong-interaction" vortex flows such as leading-edge vortex flow, the position and strength of the shear layers and the cores have a significant effect on the surface pressure distribution. This is quite different from the traditional case of attached flow, where often it may be assumed that the precise position of the wake affects the wing pressure distribution only slightly, justifying a convenient fixed choice of its position.

For the present type of flow, as is in general the case in aerodynamics, the Reynolds-averaged Navier-Stokes equations model essentially all flow details. However, additional (empirical) equations are needed to model the turbulence in an appropriate manner; in this case for a rather complicated flow. Furthermore, the computer resources required for numerically solving the three-dimensional flow equations on a mesh that is sufficiently fine to resolve the boundary layers and free shear layers, as well as the vortex cores are still quite excessive.

For most high-Reynolds-number vortex flows considered here, viscous effects are confined to thin boundary layers, thin free shear layers emanating from fixed edges and centers of vortex cores. Hence the global flow features are relatively independent of Reynolds number. This implies that the Euler equations, which allow for convection of rotational flow at arbitrary locations in 3D space, provide an adequate approximation of the equations of motion. On a local scale, specifically at points where the flow separates and vorticity is shed into the flow field, some kind of model for viscous-flow dominated features will be required. Although the computer requirements of Euler codes can be met by the current generation of supercomputers, routine practical application of these codes is only just emerging.

As will be argued in the next section, in our present case the vortical flow regions occupy only small portions (thin or narrow) of the 3D space with otherwise irrotational flow. Then the flow may be modelled as a potential flow with embedded vortical flow regions, i.e. vortex layers or sheets and vortex cores.

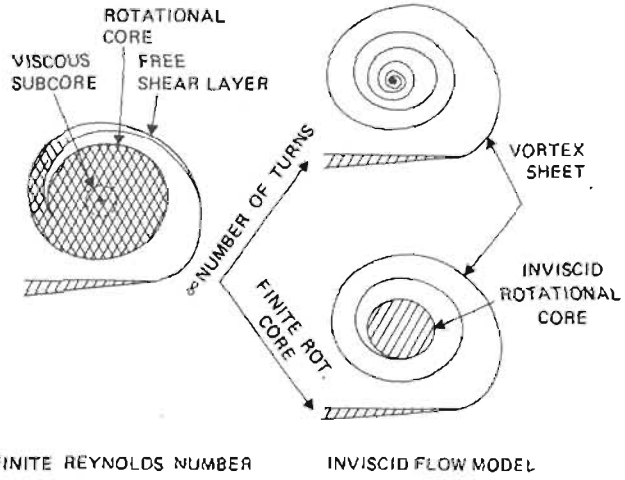


Fig. 3.1 Models of leading-edge vortex core

Now the vortical flow regions are "fitted" into the flow, i.e. are treated explicitly as such in the solution procedure. Here "fitting" means that starting from some a priori assumed position and vorticity distribution of the vortex system both position and vorticity distribution are adjusted until the governing equations and the boundary conditions are fully satisfied. "Fitting" methods differ from methods that solve the Navier-Stokes or Euler equations where the vortical flow regions are "captured" implicitly as part of the solution, i.e. they may, at least in principle, appear everywhere in the flow field.

That one has to fit the vortical flow regions is a clear disadvantage of the potential-flow model because now one has to decide a priori on the presence of vortical flow regions. Furthermore, the flow field topology should be well-defined and known in advance.
In return, the computer requirements of potential-flow methods are relatively modest.

### 3.2 High-Reynolds number flow model

In the case of attached flow there exists a more or less well-established asymptotic analysis for the flow at high Reynolds numbers, which leads to the classical potential-flow + boundary-layer type of mathematical model. Unfortunately, a complete asymptotic analysis is not available for the present type of flow. This implies that some of the simplifications, which inevitably have to be introduced in order to obtain a model that is manageable on presently available computer facilities, are necessarily based on heuristic arguments and experimental observations.

In this section arguments are presented that lead to the mathematical model used in the computational method developed in the present study.

In the regions adjacent to the surface of the configuration (i.e. in the boundary layer) and in the free shear layers viscous forces are of the same order of magnitude as the inertial and pressure forces. In the case of laminar flow the thickness of these layers is of the order of $\sqrt{(\nu\tau)}$, where $\tau$ is the time elapsed since the fluid in the layer was first subject to viscous action. The time $\tau$ is proportional to $s/U_\infty$, where $s$ is the path length along the streamline that emanates from the shedding edge. This results in a shear-layer thickness of order $L\sqrt{(s/L)}/\sqrt{Re}$, where $L$ is a characteristic length of the configuration. For the boundary-layer $s$ will be of order $L$ at most, hence the thickness of the layer is of order $L/\sqrt{Re}$. The Reynolds number is typically $10^6$-$10^7$, so that the boundary layer is thin and in first approximation may be neglected. For the free shear layer $s$ will also be of order $L$, but as it rolls up the thickness of the layer may become of the same order as its distance to other parts of the free shear layer and hence may not be neglected everywhere.

The discussion presented here is based on the assumption of laminar flow. Most rolling-up free shear layers, even in the laboratory, are turbulent, i.e. the fluid motion is irregular and the rate of diffusion is greater than in the case of laminar flow. However, for the initial roll-up processes considered here the most important feature of the shear layer is its vorticity content and its ability to form cores of rotational flow. For the latter the precise rate of diffusion is not important and arguments based on laminar flow will be quantitatively correct and can be used to construct the present high-Reynolds-number flow model.

In the following we discuss the rolling-up shear layer for the case of large but finite Reynolds number.

For the leading-edge vortex where the vortex lines are more or less parallel to the shedding edge, it is observed that (see Fig. 3.1):

(i) Near the edge s is of the order of L and the shear layer thickness is negligible. For the limiting case of infinite Reynolds number the shear layer is modelled as a vortex sheet, i.e. a layer of infinitesimal thickness containing the vorticity shed at the edge.

(ii) At locations where the shear layer rolls up $s \to \infty$ and the thickness of the layer, however small, will at some s become of the same order of magnitude as the distance between subsequent loops of the spiraling layer. In this region a distinct shear layer can no longer be observed. Viscous diffusion will smear out the velocity and vorticity gradients within the partly overlapping loops of the shear layer (e.g. Maskell-1962, Guiraud & Zeytounian-1977, 1979). Subsequently, distinct traces of the shear layer can no longer be observed and a region with a continuous distribution of vorticity is formed. In this vortex core viscous forces can be ignored again, except for a region near the center of the core where the velocity gradients are large. In the latter region, the so-called viscous subcore, the full Navier-Stokes equations must be used, while in the inviscid part of the core the flow is governed by the Euler equations.

For the limiting case of inviscid flow, two possible models can be envisaged. The first one emerges if we just consider the shear layer: for $Re \to \infty$ its thickness vanishes and the core consists of a tightly wound spiral vortex sheet of infinite angular extent (Fig. 3.1). In the second model the point of view is the already formed core: for $Re \to \infty$ the viscous subcore vanishes, and a core of inviscid rotational flow results with the vortex sheet feeding into it (see Fig. 3.1). Both models represent an inviscid core of rotational flow of finite extent.

In the case of a spiral vortex sheet of infinite extent the flow is potential flow everywhere, with a discontinuity in potential across the vortex sheet. In case of the inviscid rotational core the flow is potential flow with vortex sheets and with an embedded region with rotational flow. In Chapter 4 further details of both inviscid vortex core models will be considered.

From a computational point of view both core models present difficulties. Because an infinite sheet cannot be handled, the vortex sheet model requires an asymptotic solution for its innermost part to be matched to the outer part.
The continuous vorticity model poses a problem because the extent of the core is unknown, the core is free-floating in space, the inner rotational flow solution must be matched to the outer potential flow solution and also because it may be expected that in this inviscid model the velocity and vorticity will be singularly behaved at the center of the core. What core model is to be preferred depends on whether one is interested in the flow field inside or outside the vortex core flow.
For the flow inside the core the distributed vorticity core model with its continuous velocity field will better represent (finite Re) reality. For the outer flow field both models will be equivalent and in section 3.6 a simple representation of either core model will be introduced.

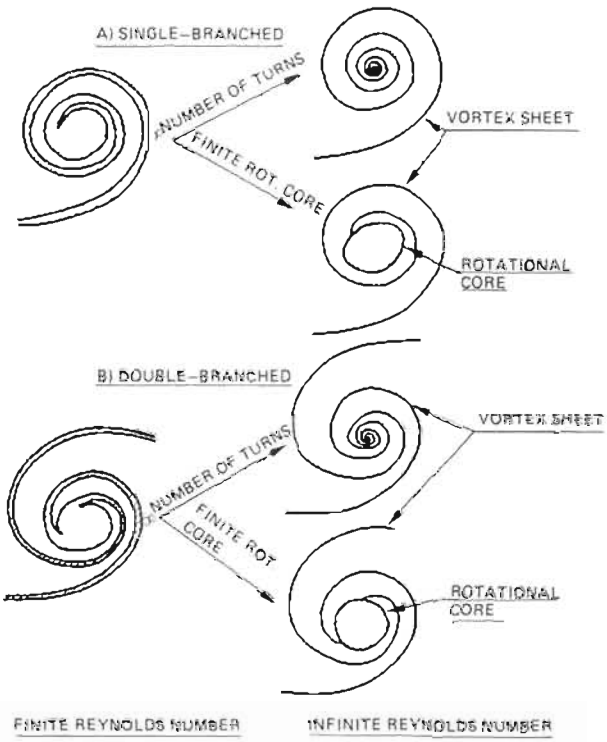


Fig. 3.2 Models of wake vortex cores

For the rolling-up wake shear layer, with its vortex lines more or less perpendicular to the shedding edge, a similar discussion can be held as given above for the leading-edge vortex. This implies that, at least during the initial roll-up process, the flow may be considered to be potential flow again, with embedded vortex sheets and vortex cores. The vortex sheets model the thin shear layers, while the vortex cores (single-branched and double-branched) represent the rolled-up regions (see Fig. 3.2).

Further downstream of the wing, the roll-up process will be completed and most vorticity will be contained within the cores. At this stage, depending on the distance between the cores, interaction between and merging of cores with vorticity of the same or of opposite sign may occur. At a still later stage this will be accompanied by viscous diffusion and decay. Alternatively, complicated longitudinal instabilities may be triggered before the merging or decay process has started, resulting in a break-up of the vortex system. These later stages of development will not be discussed here, instead the reader is referred to e.g. Steger & Kutler-1977 and Bilanin et al.-1977.

3.3 Governing equations, fundamental properties of the flow

Incompressible (laminar) viscous flow is governed by the equation for the conservation of mass and the Navier-Stokes equations of conservation of momentum, i.e.

$$\bar{\nabla}.\bar{u} = 0 \tag{3.1a}$$

$$\frac{D\bar{u}}{D\tau} = -\frac{1}{\rho}\bar{\nabla}p + \nu\nabla^2\bar{u} \tag{3.1b}$$

respectively, where $\frac{D}{D\tau} = \frac{\partial}{\partial\tau} + (\bar{u}.\bar{\nabla})$ denotes the total derivative with respect to time $\tau$. Introduction of the vorticity vector $\bar{\omega}$ as

$$\bar{\omega} = \bar{\nabla} \times \bar{u} \tag{3.2a}$$

and taking the curl of Eq. (3.1b) results in the so-called vorticity transport equation

$$\frac{D\bar{\omega}}{D\tau} = (\bar{\omega}.\bar{\nabla})\bar{u} + \nu\nabla^2\bar{\omega} \tag{3.2b}$$

For two-dimensional flows, here defined as flows that are identical in all y-z planes, the vorticity vector has only one component, i.e. $\bar{\omega} = \omega\bar{e}_x$. Introduction of the stream function $\psi$ as $\bar{u} = -\bar{e}_x \times \bar{\nabla}\psi$, results in the so-called vorticity/stream function formulation of the Navier-Stokes equations in two dimensions:

$$\nabla^2\psi = -\omega \tag{3.3a}$$

$$\frac{D\omega}{D\tau} = \nu\nabla^2\omega \tag{3.3b}$$

Note that in two dimensions there is no counterpart for the three-dimensional vorticity stretching term $(\bar{\omega}.\bar{\nabla})\bar{u}$. Therefore a two-dimensional flow model does not necessarily contain all the essential features of three-dimensional flow.

In the following we introduce a few useful quantities for rotational flow.

*Vortex lines are defined as curves which at each point* are tangential to $\bar{\omega}$.

Next consider the family of vortex lines that pass through a given reducible*) closed curve $\partial S$. The surface formed by these vortex lines is a so-called vortex tube, which may be thought of as the surface generated when simultaneously all points of the curve $\partial S$ are moved through space along vortex lines (Fig. 3.3).

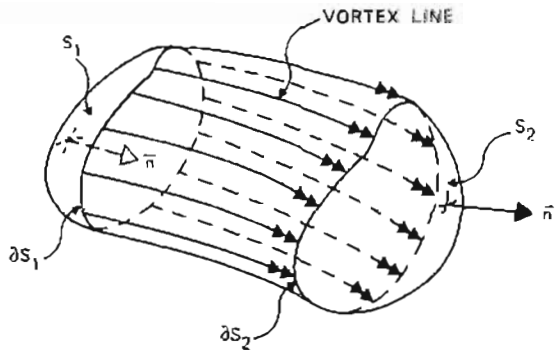


Fig. 3.3 Vortex tube

The flux of vorticity across any surface S bounded by $\partial S$ is

$$\iint_S \bar{\omega}.\bar{n}\,dS \tag{3.4a}$$

where $\bar{n}$ is the normal to the surface S. This quantity has the same value for any S, as long as the bounding curve $\partial S$ is closed and lies on the same vortex tube. This can be shown by considering the divergence theorem for a portion of the vortex tube closed off by the surfaces $S_1$ and $S_2$, like shown in Fig. 3.3:

$$\iiint_V \bar{\nabla}.\bar{\omega}\,dV = \iint_{S_1} \bar{\omega}.\bar{n}\,dS - \iint_{S_2} \bar{\omega}.\bar{n}\,dS \tag{3.4b}$$

where there is no contribution from the surface of the vortex tube and $\bar{n}$ on $S_1$ has the same sense relative to the vortex tube as $\bar{n}$ on $S_2$.

Since $\bar{\nabla}.\bar{\omega} = \bar{\nabla}.\bar{\nabla}\times\bar{u} \equiv 0$ the volume integral in Eq. (3.4b) vanishes, which proves that the flux of vorticity, also termed the strength of the vortex tube is independent of the choice of S.

A vortex tube could enclose a volume with distributed vorticity, i.e. a vortex core. Also, a vortex tube with an infinitesimal cross-section has a constant strength, equal to its area multiplied by the local value of $|\bar{\omega}|$ (which may tend to infinity), all along its length. That the strength is constant implies that in an unbounded flow field a vortex tube cannot begin or end in the interior of the flow field other than at a solid surface.

Applying Stoke's theorem to Eq. (3.4a) results in

$$\iint_S \bar{\omega}.\bar{n}\,dS = \int_{\partial S} \bar{u}.d\bar{\ell} = \Gamma \tag{3.4c}$$

where $d\bar{\ell}$ is an element of the closed curve $\partial S$ bounding S. In Eq. (3.4c) $\Gamma$ denotes the circulation round $\partial S$, which is evidently equal to the flux of vorticity through $\partial S$, which is also the strength of the vortex tube.

*) A reducible closed curve is a curve that by continuous deformation can be reduced to a point, without passing outside the fluid.

One could also consider the circulation around another closed curve denoted by C, not necessarily lying on a vortex tube, specifically one that is convected with the flow field. In general the circulation then will change with time

$$\Gamma(\tau) = \int_{C(\tau)} \bar{u}.d\bar{\ell} \tag{3.4d}$$

Differentiation with respect to time $\tau$, then results in e.g. Batchelor-1970:

$$\frac{d\Gamma}{d\tau} = \int_C \frac{D\bar{u}}{D\tau}.d\bar{\ell} + \int_C \bar{u}.\{(d\bar{\ell}.\bar{\nabla})\bar{u}\} \tag{3.4e}$$

where the first term is due to the rate of change of the velocity vector and the second term due to the rate of change of the element $\delta\bar{\ell}$ of C.
Substitution of Eq. (3.1b) in the first term and noting that the integrand of the second term equals $d\bar{\ell}.\bar{\nabla}|\bar{u}|^2/2$ gives

$$\frac{d\Gamma}{d\tau} = \nu\int_C (\nabla^2\bar{u}).d\bar{\ell} + \int_C d\bar{\ell}.\bar{\nabla}(\tfrac{1}{2}|\bar{u}|^2 + \frac{p}{\rho}) \tag{3.4f}$$

The second term in Eq. (3.4f) vanishes upon application of Stoke's theorem, while the integrand of the first term can be expressed in terms of the vorticity field, using $\bar{\nabla}\times(\bar{\nabla}\times\bar{u}) = -\nabla^2\bar{u} + \bar{\nabla}(\bar{\nabla}.\bar{u}) = -\nabla^2\bar{u}$, as

$$\frac{d\Gamma}{d\tau} = -\nu\int_C (\bar{\nabla}\times\bar{\omega}).d\bar{\ell} \tag{3.4g}$$

This shows that the circulation around the closed curve C, moving with the fluid, can only change through viscous diffusion.

For the high Reynolds number, fully developed, flow considered here it may be assumed that, in regions away from the surface of the configuration, the high-gradient regions in the free shear layers and vortex cores, closed regions with separated flow etc., the viscous forces are much smaller than the inertial and pressure forces. Hence there the Navier-Stokes equations (3.1b) reduce to the Euler equations, so that the governing equations become:

$$\bar{\nabla}.\bar{u} = 0 \tag{3.5a}$$

$$\frac{D\bar{u}}{D\tau} = -\frac{1}{\rho}\bar{\nabla}p \tag{3.5b}$$

while the vorticity transport equation (3.2b) reduces to

$$\frac{D\bar{\omega}}{D\tau} = (\bar{\omega}.\bar{\nabla})\bar{u} \tag{3.5c}$$

From the vorticity/stream function formulation for two-dimensional inviscid flow, i.e.

$$\nabla^2\Psi = -\omega \tag{3.6a}$$

$$\frac{D\omega}{D\tau} = 0 \tag{3.6b}$$

it follows then that in two dimensions $\omega$ is convected with the fluid as a conserved quantity.

Now it follows immediately from Eq. (3.4g) that in inviscid flow the circulation round any closed curve C moving with the flow, is constant in time. This is Kelvin's circulation theorem.

It implies that the flux of vorticity across any surface S bounded by C is also constant in time. Hence in an (incompressible) inviscid flow a vortex tube, identified at some initial point in time, moves with the flow and its strength does not change in time, as has been put forward by Helmholtz (± 1860). By contracting the cross-section of the vortex tube to zero, we obtain a vortex line, which also moves with the flow.

An important consequence of Kelvin's circulation theorem is that if the inviscid flow is irrotational at some initial time, it will remain irrotational at all subsequent times. What is then the source of vorticity in the cases discussed in the preceding chapter?
To answer this question, consider the fictitious case of the motion of an object through a fluid that is inviscid up to a certain time and viscous thereafter. The initial irrotational flow is determined completely by the condition of zero normal velocity at the solid surface. In general this inviscid irrotational flow will have a non-zero tangential component at the boundary. As the viscosity is turned on, the no-slip condition, which has to be applied irrespective of the smallness of the viscosity, then implies that the vorticity is infinite in an infinitesimally thin layer next to the solid surface. Of course, due to the viscous effects vorticity will diffuse away from the wall (a distance of the order of the boundary layer thickness) and at the same time it will be convected in downstream direction, along the surface, onto the wake and ultimately to infinity downstream. So the source of the vorticity is the solid surface, the mechanism being the no-slip condition at the surface.

When there is no boundary-layer separation the vorticity generated at the surface and directed along the surface at right angles to the flow direction is confined to a thin layer along the solid surface and to a thin wake which carries the vorticity downstream. So in the limit of infinite Reynolds number the flow is inviscid and irrotational everywhere, except at the body surface itself and at the infinitesimally thin wake. In this limit the flow velocity abruptly changes its direction across the wake surface.

In the case of two-dimensional flow the wake surface is degenerated because the pressure and consequently the velocity is continuous across it (see Fig. 3.4). So in effect the wake carries (cross-stream) vorticity of both signs, the net effect of which vanishes as the Reynolds number tends to infinity and the wake becomes a sheet. This implies that the irrotational flow can be determined without considering the singular wake surface.

This is quite different in the case of three-dimensional flow. Here the wake also convects a streamwise component of the vorticity which remains in the case of vanishing viscosity. This streamwise component of the vorticity is generated at the trailing edge where the upper and lower surface velocity have the same magnitude, but in general have a different direction (see Fig. 3.4). In the determination of the inviscid irrotational flow field now one has to consider the sheet that remains when the Reynolds number becomes infinite.

In the remainder of this section we consider some further results for inviscid flow with distributed vorticity. In the next section results are given for the special cases that the vorticity is confined to an infinitesimally thin layer or to a filament.

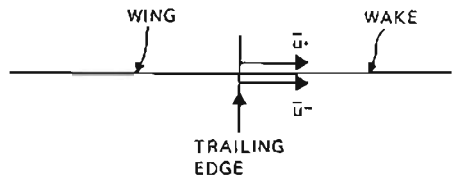


a) TWO - DIMENSIONAL $\bar{u}^- = \bar{u}^+$

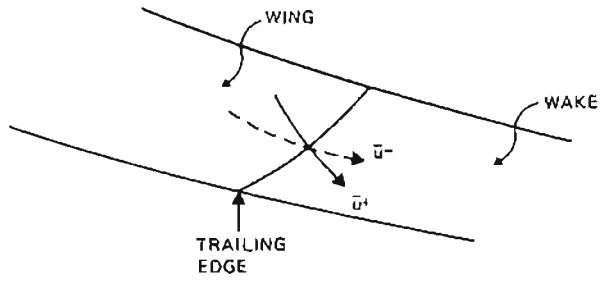


b) THREE - DIMENSIONAL $|\bar{u}^+| = |\bar{u}^-|$

Fig. 3.4 Two- and three-dimensional wakes

From the definition of the vorticity vector, Eq. (3.2a), one obtains, using the continuity equation $\bar{\nabla}.\bar{u} = 0$:

$$\nabla^2\bar{u} = -\bar{\nabla}\times\bar{\omega} \tag{3.7a}$$

This formulation of the flow field in terms of $\bar{u}$ and $\bar{\omega}$ permits, through fundamental solutions of Eq. (3.7a), the velocity field $\bar{u}$ to be expressed in terms of the vorticity distribution $\bar{\omega}$ and a velocity potential $\phi$, satisfying Eq. (3.7a) and the continuity equation, as follows:

$$\bar{u}(\bar{x}_o) = \bar{\nabla}\phi + \bar{u}_\omega(\bar{x}_o) \tag{3.7b}$$

with

$$\bar{u}_\omega(\bar{x}_o) = \frac{1}{4\pi}\iiint_V \bar{\omega}(\bar{x})\times\frac{\bar{r}}{|\bar{r}|^3}dV(\bar{x}) \tag{3.7c}$$

where $\bar{r} = \bar{x}_o - \bar{x}$, the volume integral is over the whole 3D space and $\phi$ satisfies Laplace's equation

$$\nabla^2\phi = 0 \tag{3.7d}$$

We will also consider the problem in a quasi-2D framework, so next some results for the limiting case of 2D flow are presented.

In two dimensions, taken here as the y-z plane, $\bar{\omega} = \omega\bar{e}_x$, $\bar{r} = (x_o - x)\bar{e}_x + \bar{R}$, so that upon carrying out the x-integration from $-\infty$ to $\infty$ (see Table 1.2-3) one finds:

$$\bar{U}(\bar{X}_o) = \bar{\nabla}\phi + \bar{U}_\omega(\bar{X}_o) \tag{3.8a}$$

with

$$\bar{U}_\omega(\bar{X}_o) = \frac{\bar{e}_x}{2\pi}\times\iint_S \omega(\bar{X})\frac{\bar{R}}{|\bar{R}|^2}dS(\bar{X}) \tag{3.8b}$$

where $\bar{U} = (0,V,W)$, $\bar{X} = (0,Y,Z)$ and $\bar{R} = \bar{X}_o - \bar{X}$ and $\phi$ satisfies the two-dimensional Laplace equation. In Eq. (3.8) and in the remainder of this study 2D quantities are indicated by capital symbols.

In case the vorticity $\omega$ is constant over the core region S, using Stoke's theorem, Eq. (3.8b) can be reduced to a contour integral, i.e.

$$\bar{U}_\omega(\bar{X}_o) = -\frac{\omega}{2\pi}\oint_{\partial S} \ln|\bar{R}|\,d\bar{\ell} \tag{3.8c}$$

where $\partial S$ denotes the perimeter of S and $d\bar{\ell}$ is an infinitesimal element of the curve $\partial S$. This latter formulation that just requires the position of the contour of the vortex core forms the basis of the so-called contour dynamics approach to the study of the interaction of several compact regions with uniform nonzero vorticity in an otherwise irrotational flow field, in two dimensions.

The velocity field induced by the distributed vorticity is linear in terms of the vorticity vector. So different vorticity distributions may be superposed. In the following we consider some simple distributions which could by combined to yield more complex vorticity distributions.

A first example is the 2D vortex layer of constant strength and constant width 2h, see Fig. 3.5a. The velocity field follows directly from Eq. (3.8b) as:

$$V(Y_o,Z_o) = -\omega h \quad \text{for} \quad Z_o > \delta$$
$$= -\omega Z_o \quad \text{for} \quad \delta > Z_o > -\delta$$
$$= \omega h \quad \text{for} \quad -\delta > Z_o$$

while $W(Y_o,Z_o) = 0$, i.e. the velocity is tangential to the layer. It is continuous, constant above and below the layer and linear across the layer.

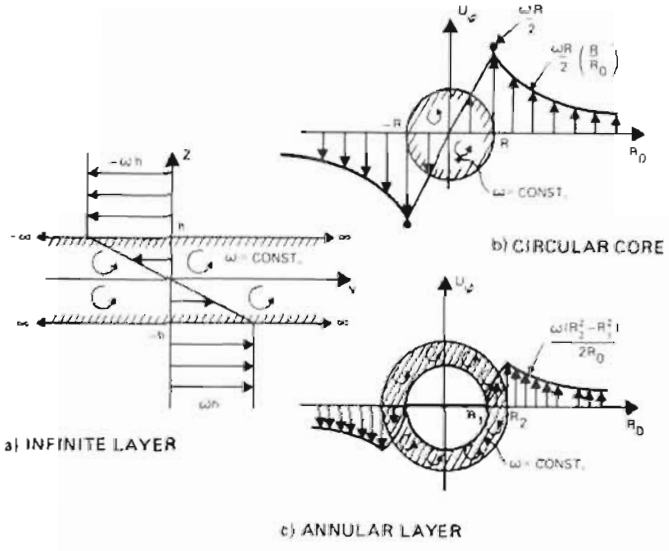


Fig. 3.5 Velocity field induced by regions with constant vorticity in 2D flow

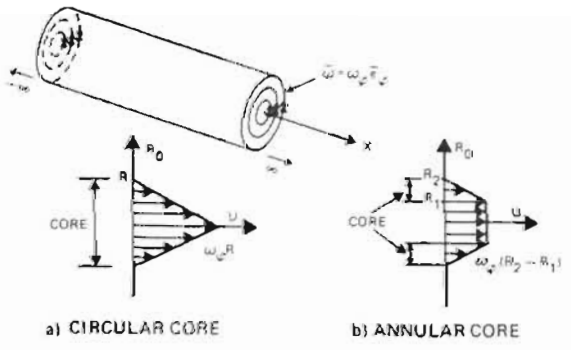


Fig. 3.6 Velocity field induced by infinitely long vortex core with circular cross section and constant circumferential vorticity

As a second example consider the velocity induced by a circular region with uniform vorticity $\omega$. The axi-symmetric velocity field follows from Eq. (3.8c) (see also Table 2.7-9) as:

$$U_\varphi(R_o) = \frac{\omega}{4R_o}\{R_o^2 + R^2 - |R_o^2 - R^2|\}$$

where $U_\varphi(R_o)$ denotes the circumferential velocity component and R is the radius of the circular vortex core. It follows then that

$$U_\varphi(R_o) = \frac{\Gamma}{2\pi R_o} \quad \text{for} \quad R_o > R$$
$$= \frac{\Gamma}{2\pi R}\left(\frac{R_o}{R}\right) \quad \text{for} \quad R_o < R$$

where $\Gamma = \pi R^2\omega$ is the circulation of the core. This velocity field is sketched in Fig. 3.5b. For $R_o > R$ it is identical to the velocity field induced by a vortex at the origin, for $R_o < R$ it corresponds to solid-body rotation. From the solution for the circular core one obtains the solution for a annular core by combining the solution for $R = R_1$ with the one for $R = R_2$. The result is given in Fig. 3.5c, showing the familiar $\Gamma/2\pi R_o$ result for $R_o > R_2$, stagnant flow for $R^2 < R_1$ and a nonlinear variation across the layer.

As a final example consider the core extending from $x = -\infty$ to $+\infty$, with constant circular cross-section and constant circumferential vorticity $\omega_\varphi$. Starting from Eq. (1.7c) it follows that for a infinitely long core with constant cross section S and with $\bar\omega$ independent of x the velocity at the point $\bar X_o$, in any plane perpendicular to the core, can be expressed as (a generalisation of Eq. (3.8b)):

$$\bar U_\omega(\bar X_o) = \frac{1}{2\pi}\int_S \bar\omega(\bar X) \times \frac{\bar R}{|\bar R|^2} dS \qquad (3.8d)$$

with $\bar R = \bar X_o - \bar X$. It then follows that for a circular core with $\bar\omega = \omega_\varphi \bar e_r$ where $\omega_\varphi$ is constant, the velocity only has a component $u(R_o)$ along the core with (see Fig. 3.6)

$$u(R_o) = 0 \quad \text{for} \quad R_o > R$$
$$= \omega_\varphi(R - R_o) \quad \text{for} \quad R_o < R$$

where R is radius of the core. This shows that the velocity outside the core is zero and inside the core increases linearly towards a maximum at the axis. Now it is also easy to imagine what the velocity field is due to an annular region with constant circumferential vorticity, namely a knotted pyramid type of axial velocity distribution, i.e. a jet-like flow.

Given the velocity field, the pressure is obtained directly from Bernoulli's theorem. This theorem states that in isentropic steady flow

$$H = \tfrac{1}{2}|\bar{u}|^2 + \frac{p}{\rho} + E \tag{3.9a}$$

is constant along a streamline ($\frac{DH}{Dt} = 0$). In the case of isentropic incompressible flow assumed here, the internal energy E is also constant along the streamlines.
In order to get the spatial variation of H, we use the vector identity $\bar{\nabla}(\tfrac{1}{2}\bar{u}.\bar{u}) = (\bar{u}.\bar{\nabla})\bar{u} + \bar{u}\times(\bar{\nabla}\times\bar{u})$ to (rewrite) the momentum equation, Eq. (3.5b), for steady flow as:

$$\bar{\nabla}(\tfrac{1}{2}\bar{u}.\bar{u}) + \frac{1}{\rho}\bar{\nabla}p = \bar{u}\times\bar{\omega} \tag{3.9b}$$

so that combining Eqs. (3.9a and b) one finds Crocco's theorem

$$\bar{\nabla}H = \bar{u}\times\bar{\omega} \tag{3.9c}$$

This shows that H is also constant along vortex lines and uniform in the case of irrotational flow. In the latter case the pressure coefficient can be expressed as

$$C_p = \frac{p-p_\infty}{\frac{1}{2}\rho U_\infty^2} = 1 - \frac{|\bar{u}|^2}{U_\infty^2} \tag{3.9d}$$

## 3.4 Vortex sheets and vortex filaments

There are limiting cases where the extent of the region containing vorticity becomes small in one or two directions. The first one considered here corresponds to vortex sheets, the second one to vortex filaments.

### 3.4.1 Vortex sheets

For vortex sheets the spatial vorticity distribution is defined by

$$\bar{\omega}(\bar{x}) = \bar{\gamma}(\bar{\bar{x}}(s,t))\,\delta[\,|\bar{x} - \bar{\bar{x}}(s,t)|\,] \tag{3.10a}$$

where $\bar{\bar{x}}(s,t)$ is the position in space of the vortex sheet, expressed in terms of an (s,t) curvi-linear surface coordinate system (see Fig. 3.7a); $\bar{\gamma}$ is the surface vorticity, which is tangential to the surface $\bar{\bar{x}}(s,t)$ and $\delta$ is the Dirac delta function. Substitution of $\bar{\omega}$ into Eq. (3.7c), followed by integration in normal direction, yields:

$$\bar{u}_\gamma(\bar{x}_o) = \frac{1}{4\pi}\iint_{S_v}\bar{\gamma}\times\frac{\bar{r}}{|\bar{r}|^3}dS \tag{3.10b}$$

where $S_v$ denotes the vortex sheet $\bar{x} = \bar{\bar{x}}(s,t)$ and $\bar{r} = \bar{x}_o - \bar{\bar{x}}(s,t)$. In terms of the curvi-linear coordinates the surface element dS is defined as

$$dS = |\frac{\partial\bar{\bar{x}}}{\partial s}\times\frac{\partial\bar{\bar{x}}}{\partial t}|\,ds\,dt \tag{3.10c}$$

The surface vorticity distribution $\bar{\gamma}$ is not completely arbitrary, it should, like the spatial vorticity $\bar{\omega}$, satisfy the condition implied by Kelvin & Helmholtz's vortex laws, namely that vortex lines do not begin or end in the fluid, i.e. form closed loops, are closed at infinity, start or end at a solid surface.

In two dimensions, here the y-z plane, the surface vorticity is directed along the x-axis, $\bar{\gamma}(s,t) = \gamma(t)\bar{e}_x$, so that it follows from from Eq. (3.10b), or directly from Eq. (3.8b) that:

$$\bar{U}_\gamma(\bar{x}_o) = \frac{\bar{e}_x}{2\pi}\times\int_{C_v}\gamma(t)\frac{\bar{R}}{|\bar{R}|^2}dC \tag{3.10d}$$

where $\bar{R} = \bar{X}_o - \bar{X}(t)$, $C_v$ denotes the trace of the vortex sheet, given by $\bar{X} = \bar{X}(t)$ (see Fig. 3.7b), while t denotes a parameter along $C_v$. The contour element dC is defined as

$$dC = |\frac{\partial\bar{X}}{\partial t}|\,dt \tag{3.10e}$$

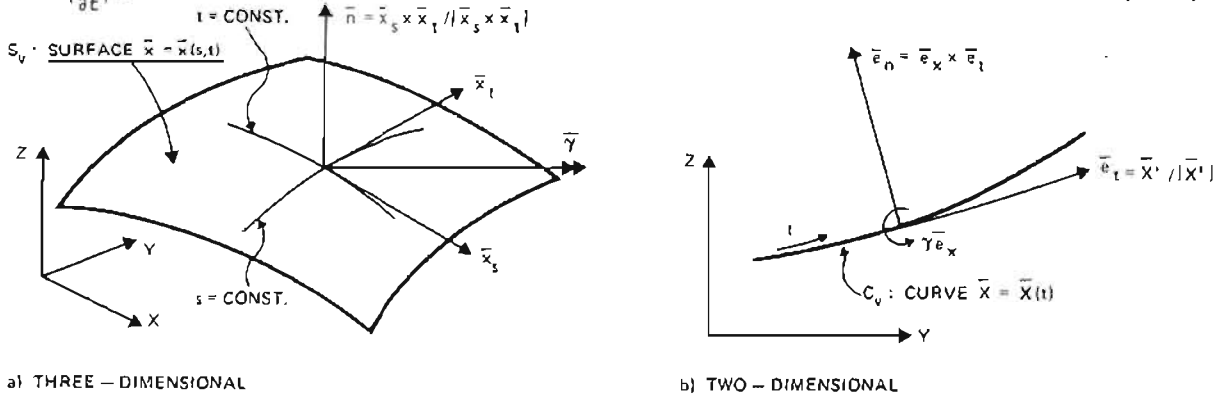


a) THREE – DIMENSIONAL

b) TWO – DIMENSIONAL

Fig. 3.7 Two- and three-dimensional vortex sheets

In 3D the velocity field induced by the vortex sheet is finite everywhere, except possibly at the boundary $\partial S_\gamma$ of $S_\gamma$ (only if $\bar\gamma(s,t) \neq 0$ at $\partial S_\gamma$). When the point $\bar x_o$ crosses the vortex sheet the velocity remains finite, although the tangential component is discontinuous. This discontinuity as $\bar x_o$ tends to $\bar x(s,t)$, is found by splitting $S_\gamma$ into two separate regions, a small area $S'_\gamma$ around $\bar x(s,t)$ in which $\bar x(s,t)$ and $\bar\gamma(s,t)$ may be expanded locally, and the remainder $S_\gamma - S'_\gamma$ of the area of integration. The contribution die to the latter area of integration is continuous, the one due to the integration over $S'_\gamma$ is discontinuous. The discontinuity can be expressed as

$$\Delta\bar u_\gamma(\bar x(s,t)) = \lim_{\varepsilon\to 0}\,[\bar u_\gamma(\bar x(s,t) + \varepsilon\bar n) - \bar u_\gamma(\bar x(s,t) - \varepsilon\bar n)]$$

$$= \bar\gamma(s,t) \times \bar n \qquad (3.11a)$$

where $\bar n$ is the unit normal to the vortex sheet $\bar x = \bar x(s,t)$ (see Fig. 3.5a), i.e.

$$\bar n = \left(\frac{\partial\bar x}{\partial s} \times \frac{\partial\bar x}{\partial t}\right) \Big/ \left|\frac{\partial\bar x}{\partial s} \times \frac{\partial\bar x}{\partial t}\right| \qquad (3.11b)$$

The discontinuous contribution in $\bar u_\gamma$ at $\bar x(s,t)$ is tangential to the vortex sheet and is perpendicular to the direction of $\bar\gamma$.

In two dimensions one finds a similar result, either directly from Eq. (3.11a) or from Eq. (3.10d) through the same type of process as described above for the 3D case. The discontinuity can be expressed as

$$\Delta\bar U_\gamma(\bar X(t)) = \lim_{\varepsilon\to 0}\,[\bar U_\gamma(\bar X(t) + \varepsilon\bar n) - \bar U_\gamma(\bar X(t) - \varepsilon\bar n)]$$

$$= \gamma(t)\bar e_x \times \bar e_n = -\gamma(t)\bar e_t \qquad (3.11c)$$

where $\bar e_n$ is the unit normal to the vortex sheet $\bar X = \bar X(t)$ (see Fig. 3.5b), i.e.

$$\bar e_n = \bar e_x \times \bar e_t \qquad (3.11d)$$

with $\bar e_t$ the unit tangential vector to $C_\nu$;

$$\bar e_t = \bar X' / |\bar X'| \qquad (3.11e)$$

where the prime denotes differentiation with respect to the parameter t.

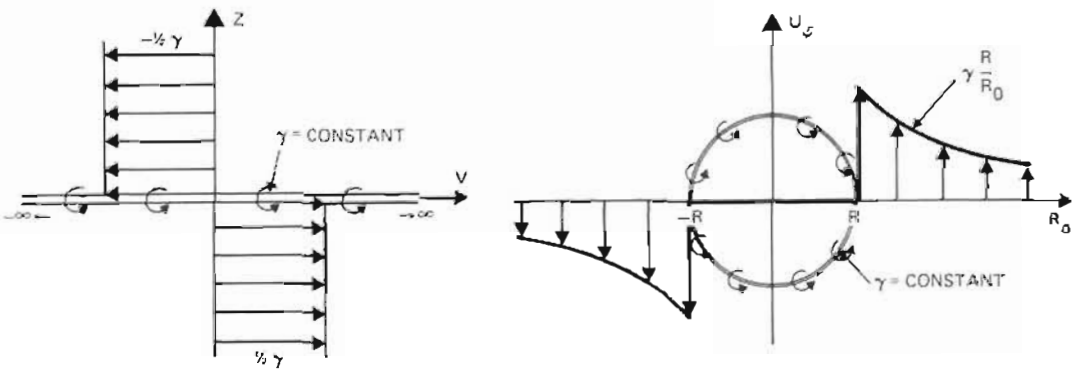


a) INFINITE VORTEX SHEET b) CIRCULAR VORTEX SHEET

Fig. 3.8 Velocity field induced by vortex sheets of constant strength in 2D flow

As a first example consider the 2D planar vortex sheet of constant strength, extending from $x = -\infty$ to $x = \infty$. The induced velocity follows directly from Eq. (3.10d) as:

$$V(Y_o, Z_o) = -\tfrac{1}{2}\gamma \quad \text{for } Z_o > 0$$

$$\tfrac{1}{2}\gamma \quad \text{for } Z_o < 0$$

while $W(Y_o, Z_o) = 0$. This velocity field, uniform below and above the vortex sheet, with a jump of magnitude $\gamma$ across the sheet is sketched in Fig. 3.8a. Comparison with Fig. 3.5a, nicely demonstrates how the vortex sheet with its discontinuous velocity field evolves as the limiting case of a infinitesimally thin vortex layer with a continuous velocity field.

Another example is the 2D circular vortex sheet of constant strength, the limiting case of the annular layer considered earlier, see Fig. 3.5c. The axisymmetric velocity field induced by the circular constant vortex sheet follows from Eq. (3.10d) as

$$U_\varphi(R_o) = \frac{\Gamma}{2\pi R_o} \quad \text{for } R_o > R$$

$$= 0 \quad \text{for } R_o < R$$

where $\Gamma = 2\pi R\gamma$ is the circulation of the core. This velocity field is sketched in Fig. 3.8b. For $R_o > R$ the velocity field is identical to that of a vortex of strength $\Gamma$ at the origin, inside the circular sheet the velocity is zero.

As a final example consider the cylindrical vortex sheet sketched in Fig. 3.9. Its vorticity distribution $\bar{\gamma}$ is independent of x, so that it follows from Eq. (3.10b) that

$$\bar{U}_\gamma(\bar{X}_o) = \frac{1}{2\pi}\int\int_{C_v} \bar{\gamma}\times\frac{\bar{R}}{|\bar{R}|^2}dC \qquad (3.11f)$$

In case $\bar{\gamma}$ has a constant circumferential component only it then follows that the velocity is directed along the x-axis and

$$u(R_o) = 0 \quad \text{for } R_o > R$$
$$= \gamma \quad \text{for } R_o < R$$

i.e. it resembles jet flow, see Fig. 3.9. The present case is the limiting case of the annular core considered in Fig. 3.6b.

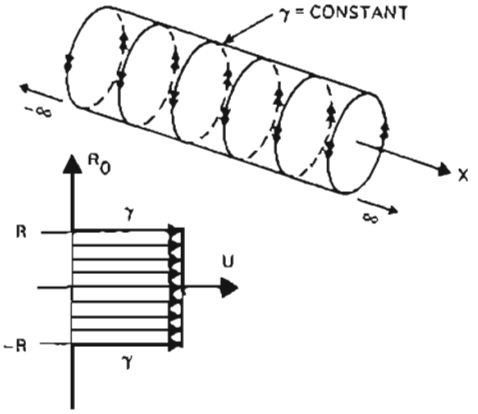


Fig. 3.9 Velocity induced by infinitely long cylindrical vortex sheet with constant circumferential vorticity

3.4.2 Vortex filaments

For a vortex filament, a region of vorticity contracting to a single curve, the vorticity distribution can be expressed as

$$\bar{\omega}(\bar{x}) = \Gamma(s)\{\frac{\delta[\,|\bar{x}-\bar{x}_v(s)|\,]}{|\bar{x}-\bar{x}_v(s)|}\}\{\frac{\bar{x}_v'}{|\bar{x}_v'|}\} \qquad (3.12a)$$

$\bar{x}_v(s)$ is the position in space of the filament (see Fig. 3.10a), expressed in terms of some coordinate s along the filament; $\Gamma(s)$ is the strength (= circulation) of the filament; $\bar{x}_v'/|\bar{x}_v'|$ is the unit vector along the filament, while $\bar{\omega}(\bar{x})$ is necessarily tangential to the filament; primes denote differentiation with respect to s. The velocity induced by the filament follows from Eq. (3.7c) as:

$$\bar{u}_v(\bar{x}_o) = \frac{1}{4\pi}\int_{C_f}\Gamma(s)(\bar{x}_v'ds)\times\frac{\bar{r}_v}{|\bar{r}_v|^3} \qquad (3.12b)$$

where $C_f$ denotes the filament $\bar{x} = \bar{x}_v(s)$ and $\bar{r}_v = \bar{x}_o - \bar{x}_v(s)$. Eq. (3.12b) corresponds with the law of Biot & Savart in electromagnetic theory and is often so referred to in aerodynamics as well.
The vortex filament may be a (curved) line vortex free-floating in 3D space, or be connected to a vortex sheet. In the latter case the strength of the vortex may increase because vortex lines can feed into the the vortex, while in the first case the strength of the line vortex will remain constant.

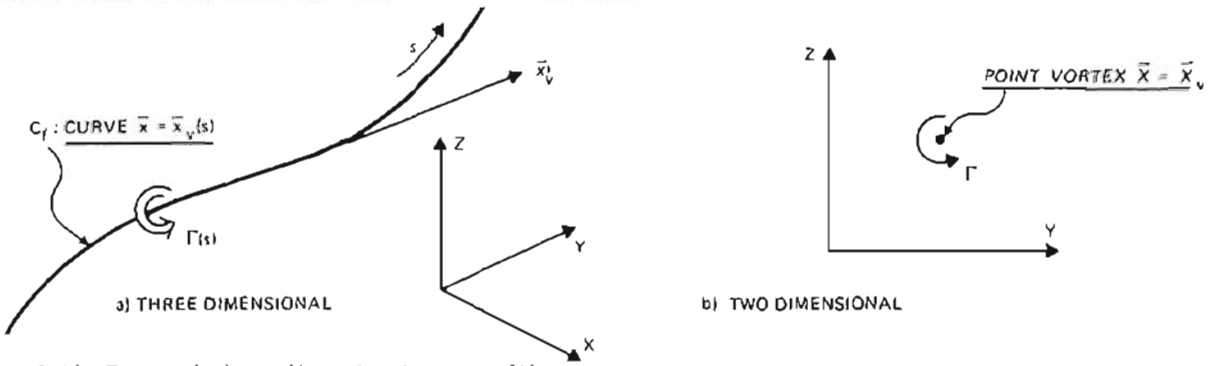


Fig. 3.10 Two- and three-dimensional vortex filaments

The two-dimensional counterpart of the vortex filament is the point vortex (see Fig. 3.10b) for which Eq. (3.12b) reduces to

$$\bar{U}_v(\bar{X}_o) = \frac{\Gamma}{2\pi}\frac{\bar{e}_x \times \bar{R}_v}{|\bar{R}_v|^2} \qquad (3.12c)$$

where $\bar{R}_v = \bar{X}_o - \bar{X}_v$ and $\bar{X}_v$ denote the position of the point vortex in the cross-flow plane.
The velocity induced by a vortex filament becomes unbounded when the point $\bar{x}_o$ approaches the filament. The behaviour of the velocity field can be found for $\bar{x}_o = \bar{x}_v(s^*) + \bar{d}$, where $\bar{d}$ is perpendicular to $\bar{x}_v'(s^*)$ and $|\bar{d}| \to 0$, by substituting into Eq. (3.12b) and expansion of $\Gamma(s)$ and $\bar{x}_v(s)$ about $s=s^*$. Then the following expression results for the "self-induced" velocity:

$$\bar{u}_v(\bar{x}_v(s^*)+\bar{d}) = \frac{\Gamma}{2\pi}\frac{\bar{x}_v' \times \bar{d}}{|\bar{x}_v'||\bar{d}|^2}$$

$$+ \frac{\Gamma}{4\pi}\frac{\bar{x}_v' \times \bar{x}_v''}{|\bar{x}_v'|^3}\ln(L/|\bar{d}|) + O(1), \text{ for } |\bar{d}| \to 0 \qquad (3.13a)$$

where the O(1) term includes another term with $\bar{x}_v''$ and the integration along the section of $C_f$ not near $\bar{x}_v(s^*)$. In above expression L is a characteristic length scale along the filament and all quantities are to be evaluated at $s=s^*$. The first term in Eq. (3.13a) tends to infinity like $1/|\bar{d}|$. Considering the filament as the limit R→0 of the circular vortex core of Fig. 3.5b, it is seen that this term is zero right at the filament.
The second term in Eq. (3.13a) depends on the curvature of the filament. If the filament is curved, the self-induced velocity becomes unbounded logarithmically. This implies that the filament can only be used as an outer-flow model for a curved finite-area vortex core if the internal structure of the core has been considered.

TABLE 3.1
Expressions for velocity field induced by rotational flow regions

| | 3D | 2D |
|---|---|---|
| Finite domain with distributed vorticity | $\bar{u}_\omega(\bar{x}_o) = \frac{1}{4\pi}\iiint_V \bar{\omega}(\bar{x}) \times \frac{\bar{r}}{\lvert\bar{r}\rvert^3} dV(\bar{x})$ <br> $\bar{r} = \bar{x}_o - \bar{x}$ (3.7c) | $\bar{U}_\omega(\bar{X}_o) = \frac{\bar{e}_x}{2\pi} \times \iint_S \omega(\bar{X}) \frac{\bar{R}}{\lvert\bar{R}\rvert^2} dS(\bar{X})$ <br> $\bar{R} = \bar{X}_o - \bar{X}$ (3.8b) |
| Vortex sheet | $\bar{u}_\gamma(\bar{x}_o) = \frac{1}{4\pi}\iint_{S_v} \bar{\gamma}(s,t) \times \frac{\bar{r}}{\lvert\bar{r}\rvert^3} dS(\bar{x})$ (3.10b) <br> $\Delta\bar{u}_\gamma(\bar{x}(s,t)) = \bar{\gamma}(s,t) \times \bar{n}$ (3.11a) <br> $\bar{r} = \bar{x}_o - \bar{x}(s,t)$ <br> $\bar{n} = (\bar{x}_s \times \bar{x}_t)/\lvert\bar{x}_s \times \bar{x}_t\rvert$ | $\bar{U}_\gamma(\bar{X}_o) = \frac{\bar{e}_x}{2\pi} \times \int_{C_v} \gamma(t) \frac{\bar{R}}{\lvert\bar{R}\rvert^2} dC(\bar{X})$ (3.10d) <br> $\Delta\bar{U}_\gamma(\bar{X}(t)) = -\gamma(t)\bar{e}_t$ (3.11c) <br> $\bar{R} = \bar{X}_o - \bar{X}(s,t)$ <br> $\bar{e}_t = \bar{X}'/\lvert\bar{X}'\rvert$ |
| Vortex filament | $\bar{u}_v(\bar{x}_o) = \frac{1}{4\pi}\int_{C_f} \Gamma(s)(\bar{x}_v' ds) \times \frac{\bar{r}_v}{\lvert\bar{r}_v\rvert^3}$ (3.12b) <br> $\bar{r}_v = \bar{x}_o - \bar{x}_v(s)$ | $\bar{U}_v(\bar{X}_o) = \frac{\Gamma}{2\pi} \frac{\bar{e}_x \times \bar{R}_v}{\lvert\bar{R}_v\rvert^2}$ (3.12c) <br> $\bar{R}_v = \bar{X}_o - \bar{X}_v(s)$ |

In the case of two-dimensional flow the vortex filament is straight and Eq. (3.13a) reduces to

$$\bar{U}_v(\bar{X}_v+\bar{D}) = \frac{\Gamma}{2\pi} \frac{\bar{e}_x \times \bar{D}}{\lvert\bar{D}\rvert^2} \quad , \text{for } |\bar{D}| \to 0 \tag{3.13b}$$

where $\bar{X}_v+\bar{D}$ is the position of a point near the vortex. So here the velocity tends to infinity like $1/|\bar{D}|$, but the self-induced velocity is zero.

In the present study we deal with vortices that have a nonzero cross-sectional area and are mildly curved only. Vortex filament are used as idealizations of finite-area vortex cores. This justifies that in case we evaluate the velocity at the filament (for the conditions to be applied on the vortex core) the self-induced velocity is omitted.

However, the second term in Eq. (3.13a) forms the starting point for the so-called Localized Induction Approximation (LIA) method. In this approach the motion in three dimensions of a thin vortex core is computed by convecting it with the velocity as expressed in the second term of Eq. (3.13a). In the method the time used to integrate the velocity in time is scaled appropriately with a quantity involving $\ln(|\bar{d}|/L)$. Since Eq. (3.13a) just represents the self-induced velocity, it has to be assumed that at all times other filaments or other parts of the same filament do not approach the point $\bar{x} = \bar{x}_v(s)$ too closely, since their contribution does involve a term like the first term in Eq. (3.13a) that becomes dominant and may not be neglected anymore.
A special example is the ring vortex of radius R, where the self-induced velocity, of magnitude $(\Gamma/4\pi R)\ln(R/|\bar{d}|)$, is normal to the plane of the ring, i.e. the ring is not distorted as it is convected through the fluid.

Table 3.1 provides an overview of the expressions for the velocity field induced by rotational flow regions of finite and infinitesimal extent as employed in the present study.

## 3.5 Potential flow

The potential-flow part in the general expression for the velocity, Eq. (3.7b), can be split into the contribution due to the velocity field at infinity (the undisturbed flow) and the velocity field due to the presence of solid bodies in the flowfield. The latter can be simulated by distributions of sources and doublets, i.e. elementary solutions of Laplace's equation Eq. (3.7d), on the surface of the solid geometry.

Denoting the surface by $S_w$ and assuming that it is specified as $\bar{x} = \bar{x}(s,t)$, i.e. in terms of curvilinear surface coordinates, one can write:

$$\phi(\bar{x}_o) = \bar{U}_\infty \cdot \bar{x}_o + \varphi_q(\bar{x}_o) + \varphi_\mu(\bar{x}_o) \tag{3.14a}$$

with

$$\varphi_q(\bar{x}_o) = -\frac{1}{4\pi}\iint_{S_w} q(s,t)\frac{dS}{|\bar{r}|} \tag{3.14b}$$

$$\varphi_\mu(\bar{x}_o) = \frac{1}{4\pi}\iint_{S_w} \mu(s,t)\frac{\bar{n}\cdot\bar{r}}{|\bar{r}|^3}dS \tag{3.14c}$$

where $q(s,t)$ and $\mu(s,t)$ are the source and doublet distribution, respectively, $\bar{n}$ is the unit normal defined in Eq. (3.11b) (see also Fig. 3.5a), $dS$ is the surface element defined in Eq. (3.10c) and $\bar{r} = \bar{x}_o - \bar{x}(s,t)$. All expressions for the potential and velocity due to source and doublet distributions are summarized in table 3.2.

TABLE 3.2
Expressions for the potential and velocity due to source and doublet distribution

| | 3D | 2D |
|---|---|---|
| Source distribution | $\varphi_q(\bar{x}_o) = \frac{-1}{4\pi}\iint_{S_w} q(s,t)\frac{dS(\bar{x})}{|\bar{r}|}$ (3.14b) | $\phi_q(\bar{X}_o) = \frac{1}{2\pi}\int_{C_w} q(t)\,\ell n(\frac{\lvert\bar{R}\rvert}{s_o})dC(\bar{X})$ (3.16a) |
| | $\Delta\varphi_q(\bar{x}(s,t)) = 0$ (3.14d) | $\Delta\phi_q(\bar{X}(s,t)) = 0$ (3.14d) |
| | $\bar{u}_q(\bar{x}_o) = \frac{1}{4\pi}\iint_{S_w} q(s,t)\frac{\bar{r}}{\lvert\bar{r}\rvert^3}dS(\bar{x})$ (3.15b) | $\bar{U}_q(\bar{x}_o) = \frac{1}{2\pi}\int_{C_w} q(t)\frac{\bar{R}}{\lvert\bar{R}\rvert^2}dC(\bar{X})$ (3.17a) |
| | $\Delta\bar{u}_q(\bar{x}(s,t)) = q(s,t)\bar{n}$ (3.15f) | $\Delta\bar{U}_q(\bar{X}(t)) = q(t)\bar{e}_n$ (3.17e) |
| Doublet distribution | $\varphi_\mu(\bar{x}_o) = \frac{1}{4\pi}\iint_{S_w} \mu(s,t)\frac{\bar{n}\cdot\bar{r}}{\lvert\bar{r}\rvert^3}dS(\bar{x})$ (3.14c) | $\phi_\mu(\bar{X}_o) = \frac{1}{2\pi}\int_{C_w} \mu(t)\frac{\bar{e}_n\cdot\bar{R}}{\lvert\bar{R}\rvert^2}dC(\bar{X})$ (3.16b) |
| | $\Delta\varphi_\mu(\bar{x}(s,t)) = \mu(s,t)$ (3.14d) | $\Delta\phi_\mu(\bar{X}_o) = \mu(t)$ (3.14d) |
| | $\bar{u}_\mu(\bar{x}_o) = \frac{1}{4\pi}\iint_{S_w}(\bar{n}\times\bar{\nabla}\mu)\times\frac{\bar{r}}{\lvert\bar{r}\rvert^3}dS(\bar{x})$ $-\frac{1}{4\pi}\int_{\partial S_w}\mu(\bar{x})\,d\bar{\ell}(\bar{x})\times\frac{\bar{r}_v}{\lvert\bar{r}_v\rvert^3}$ (3.15c) | $\bar{U}_\mu(\bar{X}_o) = -\frac{\bar{e}_x}{2\pi}\times\int_{C_w}\mu'(t)\frac{\bar{R}}{\lvert\bar{R}\rvert^2}dt$ $+\frac{1}{2\pi}\left[\mu(t)\frac{\bar{e}_x\times\bar{R}_v}{\lvert\bar{R}_v\rvert^2}\right]_{t=t_o}^{t=t_e}$ (3.17c) |
| | $\Delta\bar{u}_\mu(\bar{x}(s,t)) = \bar{\nabla}\mu$ (3.15f) | $\Delta\bar{U}_\mu(\bar{X}(t)) = \frac{\mu'(t)}{\lvert\bar{X}'(t)\rvert}\bar{e}_t$ (3.17e) |
| | $S_w$: $\bar{x}=\bar{x}(s,t)$<br>$\bar{r} = \bar{x}_o - \bar{x}(s,t)$<br>$\bar{n} = (\bar{x}_s \times \bar{x}_t)/\lvert\bar{x}_s \times \bar{x}_t\rvert$ | $C_w$: $\bar{X}=\bar{X}(t)$<br>$\bar{R} = \bar{X}_o - \bar{X}(t)$<br>$\bar{e}_n = \bar{e}_x \times \bar{e}_t$ , $\bar{e}_t = \bar{X}'/\lvert\bar{X}'\rvert$ |

Across the surface $S_w$ the velocity potential is discontinuous. The expression for the behaviour of $\varphi_q$ and $\varphi_\mu$ for points near $S_w$ itself can be found by setting $\bar{x}_o = \bar{x}(s^*,t^*)+\varepsilon\bar{n}$ and expansion of the integrals for small $\varepsilon$.
The result is:

$$\Delta\phi(\bar{x}(s,t)) = \lim_{\varepsilon\to 0}\left[\phi(\bar{x}(s,t)+\varepsilon\bar{n}) - \phi(\bar{x}(s,t)-\varepsilon\bar{n})\right] \tag{3.14d}$$

$$= \mu(s,t)$$

which shows that only the doublet distribution contributes in the jump across the surface $S_w$.

The velocity field corresponding to the potential given in Eq. (3.14) is:

$$\bar{\nabla}\phi(\bar{x}_o) = \bar{U}_\infty + \bar{u}_q(\bar{x}_o) + \bar{u}_\mu(\bar{x}_o) \tag{3.15a}$$

with

$$\bar{u}_q(\bar{x}_o) = \frac{1}{4\pi}\iint_{S_w} q(s,t)\frac{\bar{r}}{|\bar{r}|^3}dS \tag{3.15b}$$

$$\bar{u}_\mu(\bar{x}_o) = \frac{1}{4\pi}\iint_{S_w} (\bar{n}\times\bar{\nabla}\mu)\times\frac{\bar{r}}{|\bar{r}|^3}dS - \frac{1}{4\pi}\int_{\partial S_w} \mu\frac{d\bar{\ell}\times\bar{r}}{|\bar{r}|^3} \tag{3.15c}$$

In Eq. (3.15c) we expressed the velocity due to the doublet distribution in terms of (see Fig. 3.11):

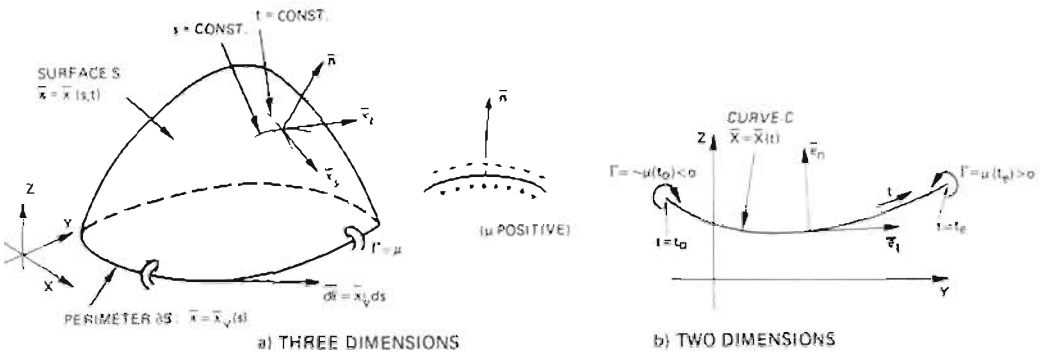


Fig. 3.11 Doublet distribution

- a surface integral over $S_w$ that can be recognized as the velocity due to a surface vorticity distribution of strength (see Eq. (3.10b)):

$$\bar{\gamma} = \bar{n}\times\bar{\nabla}\mu$$

$$= \left(\frac{\partial\mu}{\partial s}\frac{\partial\bar{x}}{\partial t} - \frac{\partial\mu}{\partial t}\frac{\partial\bar{x}}{\partial s}\right)/\left|\frac{\partial\bar{x}}{\partial s}\times\frac{\partial\bar{x}}{\partial t}\right| , \tag{3.15d}$$

- a line integral along the perimeter $\partial S_w$ of $S_w$ that can be recognized as the velocity due to a line vortex along $\partial S_w$ of strength, see Eq. (3.12b):

$$\Gamma = -\mu(\bar{x}(s,t)\in\partial S_w) \tag{3.15e}$$

In case the surface $S_w$ is a closed surface or in case the doublet distribution is zero on $\partial S_w$ this integral can be omitted.

This equivalence between the velocity field induced by a doublet distribution and the one induced by a surface vorticity distribution is worked out in Appendix A.

The important point to note here is that expressing the surface vorticity distribution, which is a vector, in terms of the gradient of a scalar, i.e. the doublet distribution, automatically ensures that Kelvin's & Helmholtz's vortex laws are satisfied. In this respect also note that vortex lines are either closed in themselves, or are closed through the line vortex along the perimeter $\partial S_w$.

For this reason we prefer to express the flow field induced by the vortex sheets $S_v$ and filaments $C_f$, Eqs. (3.10b) and (3.12b) respectively, in terms of a doublet distribution on $S_v$. This means that we have potential flow everywhere, except right at the vortex sheet where the velocity potential is discontinuous and right at the line vortex where the velocity potential is not defined. Both the vortex sheet and the vortex filament constitute regions of rotational flow of infinitesimal extent, embedded in potential flow.

Across the surface of the singularity distribution the velocity is discontinuous. It is found by the limiting process used before that the jump in the velocity can be expressed as:

$$\Delta\{\bar{\nabla}\phi(\bar{x}(s,t))\} = q(s,t)\bar{n} + \bar{\nabla}\mu(s,t) \tag{3.15f}$$

where we used that $\bar{\nabla}\mu$ is tangential to the surface, i.e. $(\bar{n}\times\bar{\nabla}\mu)\times\bar{n} = \bar{\nabla}\mu$.

In the present notation it is easily derived from Eq. (3.15d) that:

$$\bar{\nabla}\mu = \bar{\gamma}\times\bar{n}$$

$$= \left\{\frac{\partial\mu}{\partial s}\frac{\partial\bar{x}}{\partial t}\times\left(\frac{\partial\bar{x}}{\partial s}\times\frac{\partial\bar{x}}{\partial t}\right) - \frac{\partial\mu}{\partial t}\frac{\partial\bar{x}}{\partial s}\times\left(\frac{\partial\bar{x}}{\partial s}\times\frac{\partial\bar{x}}{\partial t}\right)\right\}/\left|\frac{\partial\bar{x}}{\partial s}\times\frac{\partial\bar{x}}{\partial t}\right|^2 \tag{3.15g}$$

In two-dimensional flow $q(s,t) = q(t)$, $\mu(s,t) = \mu(t)$ and $\bar{x}(s,t) = s\bar{e}_x + \bar{X}(t)$, while s runs from $-\infty$ to $\infty$. Upon substitution of this in the expressions for the velocity induced by the singularity distribution in 3D, carrying out the integration with respect to s, one finds that at the point $\bar{x}_o = s_o\bar{e}_x + \bar{X}_o$ the velocity potential induced by the source distribution becomes (see also table 3.2):

$$\phi_q(\bar{X}_o) = \frac{1}{2\pi}\int_{C_w} q(t)\ln\left(\frac{|\bar{R}|}{s_o}\right)dC$$

$$- \frac{1}{2\pi}\ln\left(\frac{2s_\infty}{s_o}\right)\int_{C_w} q(t)dC \tag{3.16a}$$

where $C_w$ is the 2D counterpart of $S_w$ and $s_\infty$ tends to infinity.
In Eq. (3.16a) $\bar{R} = \bar{X}_o - \bar{X}(t)$, the contour element dC is defined in Eq. (3.10e) and t is a parameter along $C_w$. From Eq. (3.16a) it is concluded that in case the integrated source strength equals zero the perturbation velocity potential remains bounded at infinity.

The velocity potential due to a doublet distribution in 2D follows in a similar manner from Eq. (3.14c) as:

$$\varphi_\mu(\bar{X}_o) = \frac{1}{2\pi}\int_{C_w} \mu(t)\frac{\bar{e}_n\cdot\bar{R}}{|\bar{R}|^2}dC \tag{3.16b}$$

where the unit normal vector $\bar{e}_n$ is defined as given in Eqs. (3.11d and e) and shown in Fig. 3.5, i.e.

$$\bar{e}_n = \bar{e}_x \times \bar{X}'/|\bar{X}'| \tag{3.16c}$$

Across the singularity distribution the velocity potential is discontinuous, as already indicated in Eq. (3.14d).

In two dimensions the contributions in the velocity induced by the singularity distribution become:

$$\bar{U}_q(\bar{X}_o) = \frac{1}{2\pi}\int_{C_w} q(t)\frac{\bar{R}}{|\bar{R}|^2}dC \tag{3.17a}$$

for the source distribution and

$$\bar{U}_\mu(\bar{X}_o) = \frac{\bar{e}_x}{2\pi}\times\left(-\int_{C_w}\mu'(t)\frac{\bar{R}}{|\bar{R}|^2}dt + \left[\mu(t)\frac{\bar{R}}{|\bar{R}|^2}\right]\Bigg|_{t=t_o}^{t=t_e}\right) \tag{3.17b}$$

for the doublet distribution. Note that the latter is again expressed in terms of the surface vorticity (see also Fig. 3.7b):

$$\bar{\gamma} = -\mu'(t)\bar{e}_x/|\bar{X}'| \tag{3.17c}$$

and the vortices at the beginning and end of the curve $C_w$, i.e.

$$\Gamma = -\mu(t_o) \text{ and } \Gamma = \mu(t_e) \tag{3.17d}$$

at $t=t_o$ and $t=t_e$, respectively.

The jump in the velocity across $C_w$ follows from Eq. (3.15f) as

$$\Delta\{\bar{\nabla}\phi(\bar{X}(t))\} = q(t)\bar{e}_n + \mu'(t)\bar{e}_t/|\bar{X}'| \tag{3.17e}$$

## 3.6 Rolled-up vortex core model

### 3.6.1 Vortex-filament/feeding-sheet model

In section 3.2 it has been argued that the vortex core that appears in the type of flows considered in the present study, is either a tightly wound vortex sheet of infinite extent or a finite-area region with rotational flow fed by a vortex sheet (see Figs. 3.1 and 3.2). Both these models pose difficulties computationally and in the following a further approximation is described.

For the purpose of computing the flow at the surface of the configuration $S_w$ or the vortex sheet $S_v$ outside its highly rolled-up portions representing vortex cores, resolution of the details within the vortex core is not needed. All that is required is a representation of the effect of the vortex core on the "outer flow". Referring to Figs. 3.1 and 3.2 a suitable approximation is to replace the inner portion of the vortex core, i.e. the rotational flow region or alternatively the tightly wound part of the spiral vortex sheet, by a vortex filament containing all the vorticity of the replaced portion. The approximate model is made complete by connecting the isolated vortex filament to the remainder of the vortex sheet by a so-called feeding sheet. The latter enables vorticity to be transported from the outer vortex sheet to the vortex filament and vice versa which consequently changes in strength. The above model applies both to single-branched and to double-branched cores (see Fig. 3.12).

The vortex core model we search for has, away from the vortex core, the same velocity field as the vortex core it represents. In the vortex core, the vorticity has three components, a component along the axis, a circumferential component and a radial component. In the model the vortex filament accounts for the axial component of the vorticity, the feeding sheet carries the radial component of the vorticity. The circumferential component of the vorticity is not accounted for. The examples of cylindrical vortex cores presented in sections 3.3 and 3.4 (see Figs. 3.6 and 3.9) indicate that for the cylindrical case the circumferential component of the vorticity contributes to the inner flow field only. However, it will be shown in the next chapter, where we consider in detail asymptotic solutions for isolated quasi-cylindrically growing vortex cores as leading-edge vortex cores, that for these cores the circumferential vorticity component induces in the outer flow field a radial (inflow) component of the velocity.

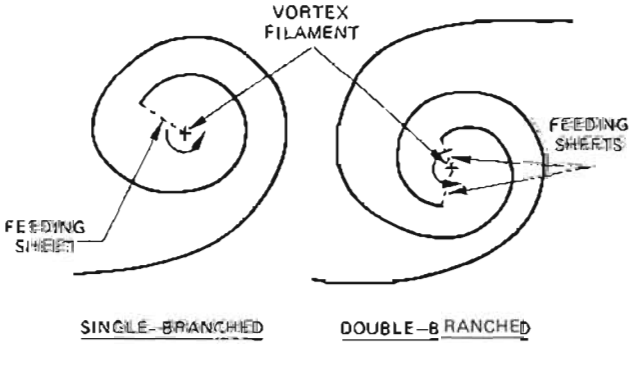


Fig. 3.12 Vortex filament/feeding sheet(s) vortex core model

In the present model of the vortex core this "entrainment" is accounted for by combining the vortex filament with a sink. While the circulation (and position) of the vortex filament follows from the outer flow the sink strength follows from the solution for the flow within the vortex core.

The simple single-branched vortex filament/feeding sheet model (without entrainment) has been used by Smith-1968 for the case of slender wing leading-edge vortices and by Pullin-1978 in his (numerical) study of similarity solutions for rolled-up vortex sheets. The double-branched vortex filament/feeding sheets model has been used by Pullin & Phillips-1981 for an investigation into the generalization of Kaden's problem of the roll-up of a semi-infinite vortex sheet to the roll-up of double-infinite vortex sheets.

We close this section by considering the doublet distribution that represents the rolled-up vortex core model just described.

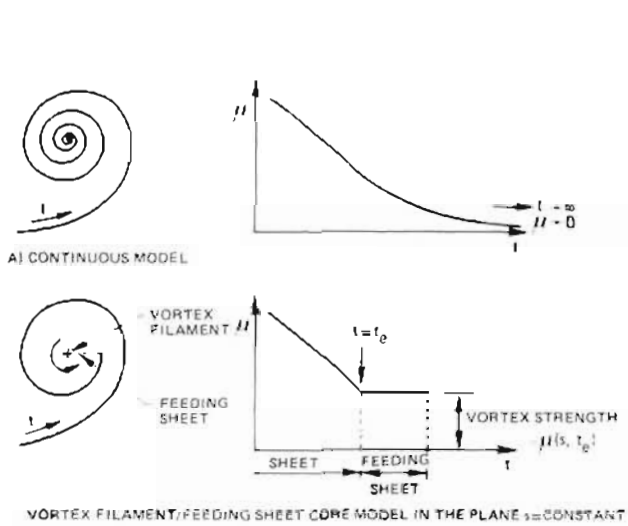


Fig. 3.13 Single-branched vortex core

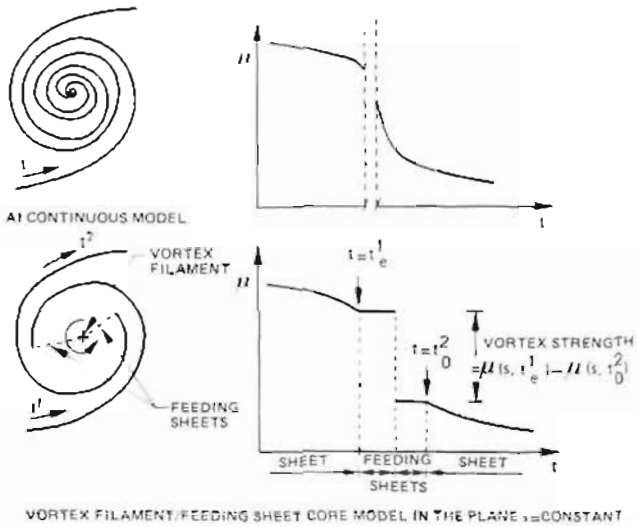


Fig. 3.14 Double-branched vortex core

The situation for the single-branched vortex core is sketched in Fig. 3.13. In the case of the infinitely long vortex sheet the doublet distribution will tend to zero with the parameter (here t) along the vortex sheet. The filament replaces the inner portion of the spiral. This leaves us with the finite-length vortex sheet, a feeding sheet of constant doublet strength (in the cross-flow plane s = constant) and a discontinuity in the doublet strength at the position of the vortex filament.

For a double-branched rolled-up vortex core a similar model applies, see Fig. 3.14. Replacing the inner part, with the high curvatures and gradients of the doublet distribution, by the vortex filament gives rise to two feeding sheets, each connecting the vortex to one edge of the cut vortex sheet. On the feeding sheets the doublet distribution is constant (in t-direction), the magnitude of the discontinuity equals the strength of the filament. A consequence of the model is that the surface vorticity on the feeding sheet is directed along the trace of the feeding sheet in the cross-flow plane s = constant. In general the vortex lines will have an abrupt change in direction as they move from the vortex sheet onto the feeding sheet. Also of course the model represents the axial component (i.e. the filament) and the radial component (i.e. the feeding sheet), but not the circumferential component of the surface vorticity. As indicated earlier and as we will see in detail in Chapter 4 the latter component is responsible for the entrainment of the vortex core.

3.6.2 Remarks on possible more accurate core models

The vortex filament/feeding sheet(s) model provides a relatively simple model for approximately axisymmetric vortex cores. In the presence of nearby wings or other parts of the rolling-up shear layers the vortex cores will have a more or less oval overall appearance. This implies that several loops of the outer vortex sheet are required before the above model will be a valid approximation. Since the asymptotic solutions for the inner part of the spiral vortex sheet as derived by amongst others Mangler & Weber-1967 and Gudrand & Zeytounian-1977, although providing a better approximation of the inner flow field, are also based on the assumption of near-axisymmetry, they do not resolve this problem. The same remark applies to the continuous rotational core model examined by Hall-1961, as well as the core models with a prescribed vorticity distribution as described by Leonard-1980, 1985.

A more advanced model is to use the rotational-core model as already depicted in Figs. 3.1 and 3.2. Whereas the overall size and circulation of the core will be determined by the outer flow, the vorticity distribution inside the core and also the entrainment will follow from solving Euler's equations (Eq. 3.5) inside the core. Such a physically more relevant approach could reduce the length of the outer sheet required, at the expense of having to solve (simultaneously) the Euler equations in the (relatively small) core. Huberson-1980 has implemented such a model for the case of two-dimensional time-dependent vortex wake roll-up. It also appears likely that the contour dynamics approach (see Eq. 3.8a) to handle compact regions of distributed vorticity in otherwise irrotational flow can be utilized to arrive at an improved modeling of vortex cores.

If vortex breakdown, or at least its inception, is an inviscid rotational flow phenomenon, as a number of investigators have suggested, the continuous rotational core model has the potential to simulate this as well. However, this has not yet been demonstrated, and it continues to be a point of dispute.

In spite of the clear advantages of using a more sophisticated vortex core model, in this study we will employ the computationally simpler isolated-filament/feeding-sheet(s) model. This implies that we intend to emphasize the interaction of the (compact) vortical flow regions with the flow about nearby solid surfaces and are less concerned with the flow inside the (compact) vortical flow regions themselves.

3.7 Boundary conditions for potential-flow model

The arguments presented in the preceding sections lead to a potential-flow model as depicted in Fig. 3.15 for the two examples we concentrate on in the present study. The model consists of a solid surface $S_w$ with thickness or without thickness, $S_w$ being a lifting body in the first case and a lifting surface in the latter case. Attached to prescribed and fixed (separation) lines on $S_w$ are free vortex sheets $S_v$ whose shape and position have to be determined as part of the solution. Vortex cores are embedded in the vortex sheets. Each vortex core, whether single or double-branched, is modeled by a vortex filament $C_f$ which is connected to the vortex sheet by a feeding sheet $S_F$.

$$\Phi_{xx} + \Phi_{yy} + \Phi_{zz} = 0$$

$S_W$ : $\bar{U}.\bar{n} = 0$

$S_V$ : $\bar{U}.\bar{n} = 0$, $\bar{\gamma} \times \bar{n}.\bar{U} = 0$

$\partial S_W$ : KUTTA CONDITION

CORE : FORCE FREE

$X \to -\infty$: $\bar{u} \to \bar{U}_\infty$

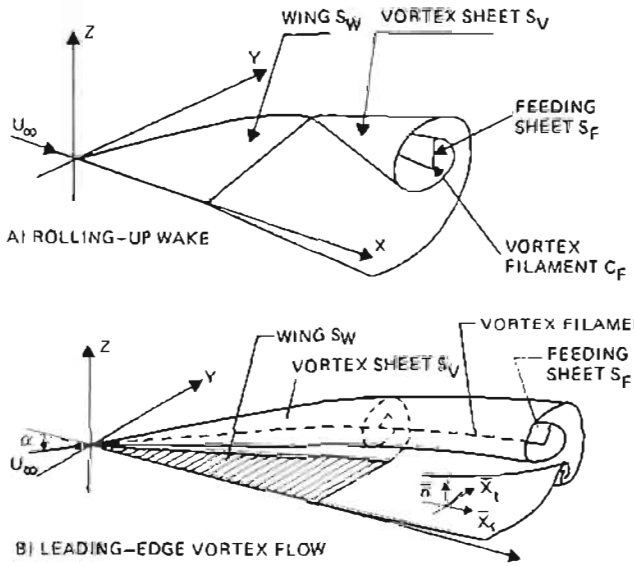


Fig. 3.15 Potential flow model of flow about configurations with vortex flow

In the following we discuss the boundary conditions to be imposed on the model.

(i) Solid surfaces $S_w$

In the present study we consider the steady flow about steady configurations only. The condition that the solid surface $S_w$ is a stream surface then is

$$\bar{u}.\bar{n} = 0, \text{ for } \bar{x} = \bar{x}(s,t)^+ \text{ on } S_w \tag{3.18a}$$

where $\bar{x}(s,t)^+$ denotes that the Neumann condition is to be imposed on the side of $S_w$ that is wetted by the flow. Writing $\bar{u}$ as the sum of the various contributions

$$\bar{u} = \bar{U}_\infty + \bar{u}_q + \bar{u}_\mu \tag{3.18b}$$

where $\bar{U}_\infty$ is the free-stream velocity, $\bar{u}_q$ the velocity induced by the source distribution on $S_w$ and $\bar{u}_\mu$ is the velocity due to the doublet distribution on $S_w$, $S_v$ and $S_F$ one obtains:

$$\tfrac{1}{2}q + \bar{u}^P_\mu.\bar{n} = -\bar{U}_\infty.\bar{n}, \text{ for } \bar{x} = \bar{x}(s,t)^+ \text{ on } S_w \tag{3.18c}$$

where $\bar{u}^P_\mu$ denotes the Principle Value of $\bar{u}_\mu$, i.e. the average across $\bar{x}(s,t)$. The stream surface condition Eq. (3.18c) is the only condition that applies on $S_w$, which means the q and $\mu$ cannot be chosen independently. There a several possible choices, some of which are described below.

On a configuration that is infinitesimally thin (i.e. is a lifting surface) $q = 0$ and one solves for $\mu$. On such a lifting surface the effect of wing thickness can be accounted for in a linear fashion by expanding Eq. (3.18c) around the mean wing surface. It then follows that q can be solved for directly, it is found to be proportional to the streamwise component of the gradient of the thickness distribution.

On a lifting configuration with thickness some form of doublet distribution is required, not necessarily on the surface $S_w$ of the configuration itself. In the literature (e.g. Sytsma et al.-1977) a variety of combinations of $\mu$ and q, embodied in current panel methods for solving the potential flow about airplane configurations, can be found. Examples are $q = 0$ with $\mu$ as unknown; q as unknown with $\mu$ specified, both q and $\mu$ as unknown with their values on upper and lower (wing) surface chosen identically, etc.

For thick, closed configurations there is an attractive alternative in which the Neumann condition, i.e. Eq. (3.18a), for the flow on the wetted side of the surface is converted into a Dirichlet condition for the flow in the physically non-relevant interior of the configuration. An example, see Fig. 3.16, is the formulation where the perturbation potential $\varphi$ at $\bar{x} = \bar{x}(s,t)^-$ is set equal to zero, i.e. with Eq. (3.14d):

$$-\tfrac{1}{2}\mu + \varphi^P = 0, \text{ for } \bar{x} = \bar{x}(s,t)^- \text{ on } S_w \tag{3.18d}$$

where $\varphi^P$ is the Principal Value of velocity potential induced by q and $\mu$ and $\bar{x}(s,t)^-$ denotes that the

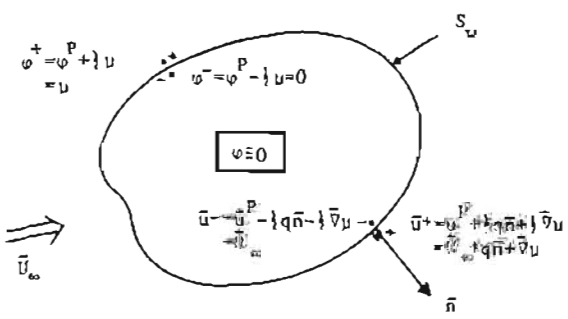


Fig. 3.16 Dirichlet condition on solid closed surface

Dirichlet condition is to be imposed on the side of $S_w$ not wetted by the flow. The str distribution is obtained by noting that Eq. (3.18d) implies that $\varphi$ is zero everywhere i enclosed by $S_w$. This also means that the normal derivative of $\varphi$ is zero at $\bar{x}(s,t)^-$, i.e.

$$-\tfrac{1}{2}q + \bar{u}^p.\bar{n} = 0, \text{ for } \bar{x} = \bar{x}(s,t)^- \text{ on } S_w$$

so that it follows directly from Eq. (3.18c) that the strength of the source distribution the external Neumann condition becomes:

$$q = -\bar{U}_\infty.\bar{n}$$

The velocity on the external side then is obtained by noting that Eq. (3.18d) implies that th potential on the external side $\bar{x}(s,t)^+$, $\varphi = \tfrac{1}{2}\mu + \varphi^-$ is equal to $\mu$. Since the perturbation velc interior is zero everywhere it follows from Eq. (3.15f) that:

$$\bar{u}(\bar{x}) = \bar{U}_\infty + q\bar{n} + \bar{\nabla}\mu, \text{ for } \bar{x} = \bar{x}(s,t)^+ \text{ on } S_w$$

*which does not involve any integral over the singularity distributions, while its normal compone* indeed as follows from Eq. (3.18f).

(ii) Vortex sheets $S_v$

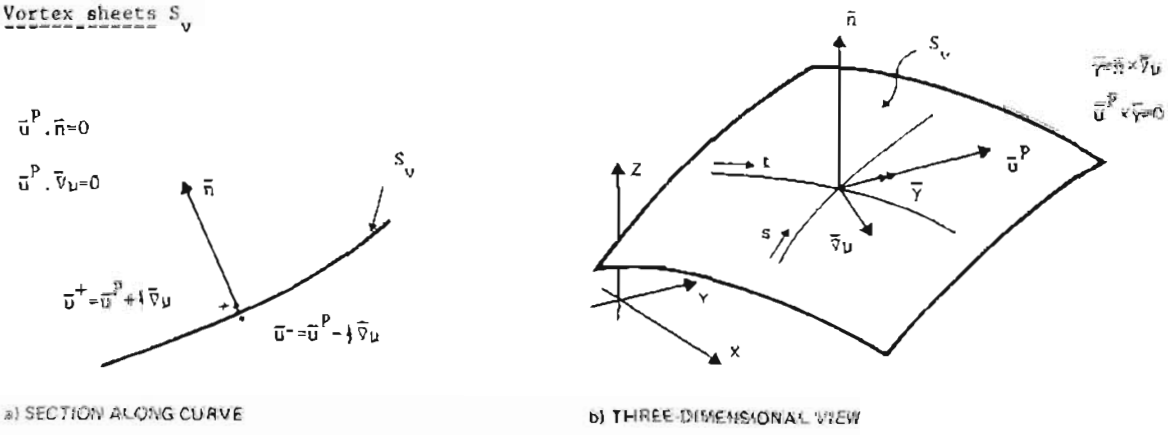


Fig. 3.17 Boundary conditions on a vortex sheet

Vortex sheets $S_v$ carry a doublet distribution only and two boundary conditions apply. The first one is that it is a streamsurface, i.e. using Eq. (3.15f) we find, with $\bar{n}.\bar{\nabla}\mu = 0$, that on both sides of $S_v$ the stream-surface condition is satisfied if:

$$\bar{u}^p.\bar{n} = 0, \text{ for } \bar{x} = \bar{x}(s,t) \text{ on } S_v, \tag{3.19a}$$

see Fig. 3.17a.

The second condition is that vortex sheets are non-solid surfaces and cannot support a pressure difference. The pressure coefficient follows from Bernoulli's equation given in Eq. (3.9).
The pressure difference across $S_v$ can then be expressed as

$$\Delta C_p = \tfrac{1}{2}(\bar{u}(\bar{x}(s,t)^+) + \bar{u}(\bar{x}(s,t)^-)).(\bar{u}(\bar{x}(s,t)^+) - \bar{u}(\bar{x}(s,t)^-)) = 0 \text{ on } S_v \tag{3.19b}$$

Substitution of Eq. (3.15f) then yields (see Fig. 3.12a):

$$\bar{u}^p(\bar{x}(s,t)).\bar{\nabla}\mu = 0 \text{ on } S_v \tag{3.19c}$$

where $\bar{u}^p(\bar{x}(s,t))$ is the total average velocity across $S_v$, i.e. the one including the contributions due to the free stream, the singularity distribution(s) on the solid surface $S_w$ and the doublet distribution on $S_v$.

Using the definition of the surface vorticity in terms of the gradient of the doublet distribution given in Eq. (3.15d), it follows that

$$\begin{aligned}\bar{u}^p \times \bar{\gamma} &= \bar{u}^p \times (\bar{n}\times\bar{\nabla}\mu) \\ &= (\bar{u}^p.\bar{\nabla}\mu)\bar{n} - (\bar{u}^p.\bar{n})\bar{\nabla}\mu = 0,\end{aligned} \tag{3.19d}$$

using Eqs. (3.19a and c). Thus on free vortex sheets the surface vorticity vector $\bar{\gamma}$ is parallel to the average velocity $\bar{u}^p$ (see Fig. 3.17b).

*In classical wing aerodynamics it is assumed that the trailing wake surface does not roll up, is flat and is* parallel to $\bar{U}_\infty$, thereby accepting that neither the normal-velocity boundary condition nor the zero-pressure-jump condition will be satisfied on $S_v$.
In this approximation we have that on the wake $\bar{\gamma}$ is parallel $\bar{U}_\infty$, which does satisfy Eq. (3.19c) to first order. Furthermore it implies that $\mu$ is constant in the direction of $\bar{U}_\infty$. The constant equals the value of the doublet distribution at the trailing edge. This treatment of the wake as a rigid vortex sheet, employed in current potential flow methods, leads to the linear problem of solving for the doublet distribution $\mu$ on $S_w$ by imposing the normal-velocity condition Eq. (3.18i) on $S_w$.

For the case of leading-edge vortex flow and wings with deployed flaps (and slats) the above rigid wake assumption is no longer accurate. The problem of the (linear potential) flow about configurations with free vortex sheets is non-linear in terms of the boundary conditions, this with respect to the unknown distributions but in particular with respect to the unknown location of the vortex sheet $S_v$. The solution of this nonlinear flow problem in the fully three-dimensional framework presents a formidable task. This forms the motivation to consider still further approximations leading to simpler problems in a less complete framework than the three-dimensional one. This will be pursued in Chapter 5.

(iii) Vortex cores $C_f + S_F$

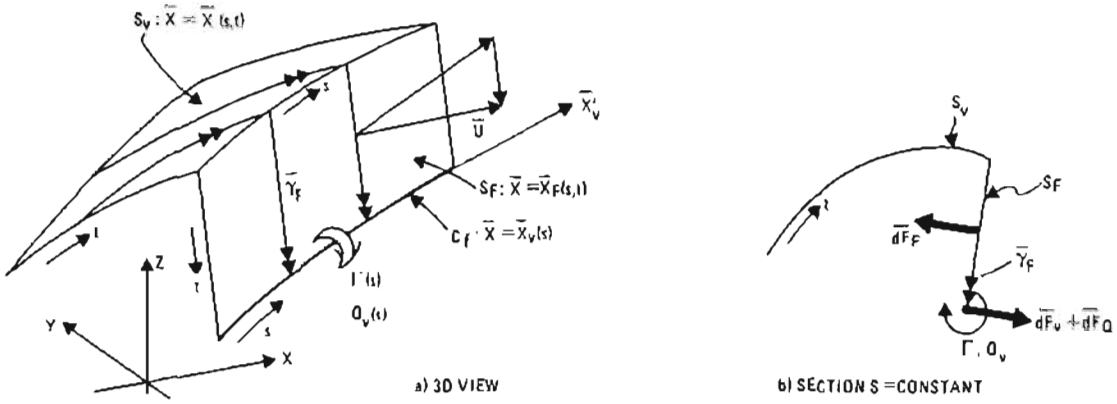


Fig. 3.18 Conditions on the vortex core

The appropriate condition on the vortex core model (Figs. 3.12-3.14) is arrived at by arguing that the tightly rolled-up vortex sheet it is replacing is force free along its entire, infinite, length, so that the model should sustain no net force either. This implies that for the model of the single-branched vortex core the force on the vortex filament exactly cancels the one on the feeding sheet. For single-branched leading-edge vortices this condition has first been derived by Brown & Michael-1954 and used by Smith-1968 and many others. Here it is extended to the case of a double-branched vortex as the condition that the force on the vortex filament cancels the ones on the two feeding sheets, see also Chapter 8. The condition on the core model is expressed as

$$\bar{F}_v(s) + \bar{F}_Q(s) + \bar{F}_F(s) = 0, \text{ for all } s.$$

Here the force $d\bar{F}_v$ on a segment $d\bar{l}_v$ of the vortex filament $C_f$ can be expressed as (see Fig. 3.18)

$$d\bar{F}_v(s) = \rho_\infty \Gamma(s)\{\bar{u}(\bar{x}_v(s)) \times \bar{x}'_v(s)\}ds \tag{3.20a}$$

where $s$ is a parameter (arclength) along the filament positioned at $\bar{x} = \bar{x}_v(s)$, $\Gamma(s)$ is the strength of the vortex, $\rho_\infty$ is the density and $\bar{u}(\bar{x}_v(s))$ is the velocity at the vortex. Here it is argued that for the present types of application the vortex filament represents the inner portion of a core that is mildly curved only, while also its effective radius is large. This implies that the self-induced velocity, given in Eq. (3.13a) may be ignored.

The contribution in the force due to the source strength associated with the entrainment (section 3.6.1) of the vortex core can be expressed as

$$d\bar{F}_Q = \rho_\infty Q_v(s)\bar{u}(\bar{x}_v(s))|\bar{x}'_v(s)|ds \tag{3.20b}$$

where $Q_v(s)$ is the negative of the entrainment of the vortex core.

The force $d\bar{F}_F$ on a segment of the feeding sheet $S_F$ connected to the filament element $d\bar{l}_v(s)$ can be expressed as (see Fig. 3.18):

$$d\bar{F}_F(s) = -\rho_\infty \bar{\gamma}_F(s) \times \{\int_t \bar{u}(\bar{x}_F(s,t))\left|\frac{\partial}{\partial s}\bar{x}_F(s,t) \times \frac{\partial}{\partial t}\bar{x}_F(s,t)\right| dt\}ds \tag{3.20c}$$

where $\bar{\gamma}_F(s)$ is the vorticity distribution on the feeding sheet located at $\bar{x} = \bar{x}_F(s,t)$, $t$ is a parameter along the feeding sheet, $\bar{u}(\bar{x}_F(s,t))$ is the velocity on the feeding sheet and the integration is along the feeding sheet.

Since the velocity will have a large component along the vortex core the force on the feeding sheet will be approximately perpendicular to the feeding sheet. This force is to be cancelled by the one on the vortex filament, which as a consequence must be in a velocity field which has two components, one along the filament and one component in the feeding sheet directed towards the vortex (see Fig. 3.18 and section 9.4.3).

(iv) Far field

Far from the configuration and its regions with vortical flow the flow is uniform, i.e.

$$\bar{u} \to \bar{U}_\infty = U_\infty(\bar{e}_x \cos\alpha\cos\beta + \bar{e}_y \sin\beta + \bar{e}_z \sin\alpha\cos\beta) \text{ for } |\bar{x}| \to \infty \tag{3.21}$$

This condition should be satisfied everywhere where $|\bar{x}| \to \infty$, except in the so-called Trefftz plane (the plane $x = +\infty$) where the downwash induced by the trace of the (rolled-up or unrolled) vortex wake can be related to the induced drag of the wing. In Eq. (3.21) $\alpha$ and $\beta$ denote the angle of attack and angle of side slip, respectively.
The formulation of the solution of the flow problem in terms of surface singularity distribution automatically satisfies the far field conditions; the perturbation velocity vanishes at infinity.

(v) Kutta condition

At sharp edges of the configuration, where the flow is forced to separate, conditions are imposed that guarantee that the potential flow leaves the surface $S_w$ in a "smooth" manner, i.e. without causing an infinite velocity at the edge and such that at the edge the pressure on lower and upper surface is equal.

There are several ways in which this condition has been implemented in computational methods. Examples are:
- In 2D: after conformal mapping the edge into a smooth part of the contour, which yields the mapping singular at the edge, impose the condition that in the computational plane the first derivative of the complex potential is zero at the edge, resulting in a finite velocity at the edge in the physical plane.
- In case the geometry of the wake is given apply the stream-surface condition, Eq. (3.19a), at a point just downstream of the edge on the assumed wake position.
- Specify that just upstream of the edge the pressure on upper and lower surface are equal, i.e. apply Eq. (3.19b) at the edge. In 2D this yields a linear equation. In 3D in the rigid-wake approximation this yields a (mildly) nonlinear equation to be added to the set of otherwise linear equations resulting from the stream-surface condition, Eq. (3.18), on $S_w$.

In the present study, where both position and strength of the free vortex sheets will be solved for, the Kutta condition is applied by imposing the two vortex sheet conditions, Eq. 3.19a and c, up to the edge where the vortex sheet $S_v$ joins the solid geometry $S_w$.

(vi) Symmetry

In most cases the configuration and the oncoming flow will have the plane y=0 as plane of symmetry. In that case the singularity distribution on starboard (y>0) and port (y<0) side are identical, and one just needs to solve for the unknown singularity distributions on the starboard-side. Of course the port side has to be accounted for, which is conveniently done be noting that if $\bar{u}^S(\bar{x})$ is the velocity at $\bar{x}$ due to a singularity distribution on the starboard side, the contribution due to the distribution on the (mirror-image) port side equals $[S]\bar{u}^S([S]\bar{x})$, where

$$S = \begin{pmatrix} 1 & 0 & 0 \\ 0 & -1 & 0 \\ 0 & 0 & 1 \end{pmatrix} \tag{3.22a}$$

is the so-called symmetry matrix. This implies that in case of symmetry one just needs to consider the distributions on the starboard-side geometry and that the contribution due to the complete configuration is

$$\bar{u}(\bar{x}) = \bar{u}^S(\bar{x}) + [S]\bar{u}^S([S]\bar{x}) \tag{3.22b}$$

A similar expression is valid for the perturbation velocity potential, i.e.

$$\varphi(\bar{x}) = \varphi^S(\bar{x}) + \varphi^S([S]\bar{x}) \tag{3.22c}$$

where $\varphi^S(\bar{x})$ denotes the contribution due to the starboard side singularity distribution.

# 4 FURTHER ASPECTS OF SLENDER, NARROW VORTEX CORES

## 4.1 Introduction

In the preceding chapter we derived a potential flow model in which a vortex core is represented by a vortex-filament/feeding-sheet combination. The presentation of the true vortex core by the vortex filament/feeding-sheet combination is based on the premise that at points not too close to the vortex core the velocity field due to vortex-filament/feeding-sheet combination matches the one due to the true vortex. The velocity field due to the true vortex follows from the vorticity distribution inside the vortex core, see Eq. (3.7c). This immediately implies that we require the flow solution inside the vortex core itself.

The vortex cores pertinent to the present study are vortex cores of a cross- sectional dimension small relative to a typical length scale along the axis of the vortex core, i.e. vortex cores that may be characterized as slender (slowly varying in axial direction, quasi-cylindrical) and narrow. In this chapter an approximate analysis of such cores is considered. For simplicity the analysis will be carried out on the core in isolation, i.e. in an uniform flow field. The two points of view discussed in section 3.2 will be considered (see Fig. 3.1): one in which the vortex core is a region with a continuous vorticity distribution (section 4.2) and one in which the vortex core consists of a tightly wound spiral vortex sheet (section 4.3). In section 4.4 the details of the matching of inner and outer flow fields, is considered and the final section provides a numerical example of comparison of the velocity fields due to distributed vorticity, rolled-up vortex sheet and vortex-filament core.

## 4.2 Vortex cores as regions with distributed vorticity

### 4.2.1 Solution of Euler equations

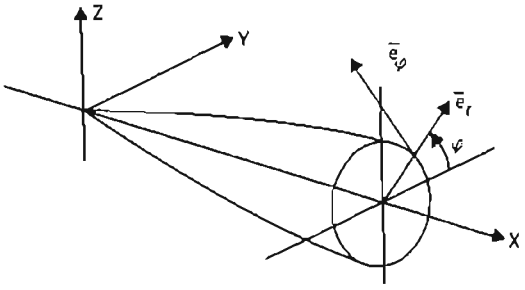


Fig. 4.1 Slender narrow core with distributed vorticity

Consider the slender, narrow region with rotational flow depicted in Fig. 4.1. The geometry and the flow are assumed to be axially symmetric. Denoting the radius of the cross-section of the core in the plane x = constant by $r_e(x)$, the velocity and pressure can be expressed as functions of $r/r_e(x)$ and x. The continuity and Euler equations for axi-symmetric incompressible flow in cylindrical coordinates are (Chapter 3):

$$\frac{\partial}{\partial x}u_x + \frac{1}{r}u_r + \frac{\partial}{\partial r}u_r = 0 \tag{4.1}$$

and

$$u_x \frac{\partial}{\partial x}u_x + u_r \frac{\partial}{\partial r}u_x + \frac{1}{\rho}\frac{\partial}{\partial x}p = 0 \tag{4.2a}$$

$$u_x \frac{\partial}{\partial x}u_r + u_r \frac{\partial}{\partial r}u_r - \frac{1}{r}u_\varphi^2 + \frac{1}{\rho}\frac{\partial}{\partial r}p = 0 \tag{4.2b}$$

$$u_x \frac{\partial}{\partial x}u_\varphi + u_r \frac{\partial}{\partial r}u_\varphi + \frac{1}{r}u_r u_\varphi = 0 \tag{4.2c}$$

respectively. Defining $\Theta = r/r_e(x)$ and noting that for any function $f = f(\Theta,x)$ the first derivatives with respect to r and x become

$$\frac{\partial f}{\partial r} = \frac{1}{r_e}\frac{\partial f}{\partial \Theta} \quad \text{and} \quad \frac{\partial f}{\partial x} = -\Theta\frac{r_e'}{r_e}\frac{\partial f}{\partial \Theta} + \frac{\partial f}{\partial x}$$

respectively, one finds from Eqs. (4.1) and (4.2) without approximation:

$$-\Theta\frac{\partial}{\partial\Theta}(r_e'u_x - \frac{1}{\Theta}u_r) + \frac{2}{\Theta}u_r + r_e\frac{\partial}{\partial x}u_x = 0 \tag{4.3}$$

$$-\Theta(r_e'u_x - \frac{1}{\Theta}u_r)\frac{\partial}{\partial\Theta}u_x - r_e'(\frac{\Theta}{\rho}\frac{\partial p}{\partial\Theta}) + r_e(u_x\frac{\partial}{\partial x}u_x + \frac{1}{\rho}\frac{\partial p}{\partial x}) = 0 \tag{4.4a}$$

$$-\Theta(r_e'u_x - \frac{1}{\Theta}u_r)\frac{\partial}{\partial\Theta}u_r - \frac{1}{\Theta}u_\varphi^2 + \frac{1}{\rho}\frac{\partial p}{\partial\Theta} + r_e u_x\frac{\partial}{\partial x}u_r = 0 \tag{4.4b}$$

$$-\Theta(r_e'u_x - \frac{1}{\Theta}u_r)\frac{\partial}{\partial\Theta}u_\varphi + \frac{1}{\Theta}u_r u_\varphi + r_e u_x\frac{\partial}{\partial x}u_\varphi = 0 \tag{4.4c}$$

These equations are subject to the boundary conditions that at the axis of the core the radial velocity component vanishes, i.e.

$$u_r = 0 \quad \text{for } \Theta = 0, \tag{4.5a}$$

and that at the edge of the vortex core the axial and circumferential component of the velocity and the pressure are given, i.e. follow from the matching with the outer flow. Here we specify

$$u_x = U_e(x),\ u_\varphi = V_e(x),\ p = P_e(x), \text{ for } \Theta = 1 \tag{4.5b}$$

In the following we will solve Eqs. (4.3)-(4.4) subject to the above boundary conditions under the assumption that the product of the core radius $r_e$ with the variation in x-direction of $u_x$, $u_r$, $u_\varphi$ and p may be neglected, i.e. the terms already marked in Eqs. (4.3)-(4.4). This assumption is always met for the case of conical flow where the velocity components and the pressure are constant in x-direction and depend on $\theta$ only. For flows that are not conical the solution will be valid for slender, narrow vortex cores.

The solution of Eqs. (4.3) and (4.4a-c), subject to the boundary conditions at the center of the core and at the edge of the core, i.e. Eq. (4.5a) and Eq. (4.5b), respectively, is derived in Appendix B in closed form as:

$$u_x = U_e\{1 - \alpha \ell n \frac{G(\theta)}{G(1)}\} \tag{4.6a}$$

$$u_r = -U_e \alpha G(\theta) \tag{4.6b}$$

$$u_\varphi = V_e[1 + (U_e\alpha/V_e)^2\{\frac{G(\theta)}{\theta r'_e} - \frac{G(1)}{r'_e} - \ell n\frac{G(\theta)}{G(1)}\}]^{\frac{1}{2}} \tag{4.6c}$$

$$\frac{p}{\rho} = \frac{p_e}{\rho} + V_c^2 r \ell n\frac{G(\theta)}{G(1)} + \frac{1}{2}(U_e\alpha/V_e)^2\{\frac{G(\theta)}{\theta r'_e} - \frac{G(1)}{r'_e} + G(1)^2 \ell n\frac{G(\theta)}{G(1)} - (\ell n\frac{G(\theta)}{G(1)})^2\}] \tag{4.6d}$$

where

$$G(\theta) = \frac{\{1 + (\theta r'_e)^2\}^{\frac{1}{2}} - 1}{\theta r'_e} \quad \text{and} \quad \alpha = \frac{\{1 + 4(V_e/U_e)^2 G(1)/r'_e\}^{\frac{1}{2}} - 1}{2G(1)/r'_e} \tag{4.6e}$$

This solution, for the case of conical flow the exact solution of the full Euler equations and for the more general case the exact solution of the approximate Euler equations, shows that at the center of the core $u_x$, $u_\varphi$ and p tend to infinity as $\ell n\theta$ for $\theta \to 0$. This clearly indicates that the inviscid solution will be invalid right at the center of the core. It is of interest to consider the total enthalpy of the solution:

$$\begin{aligned} H &= \frac{p}{\rho} + \frac{1}{2}(u_x^2 + u_r^2 + u_\varphi^2) \\ &= \frac{p_e}{\rho} + \frac{1}{2}[U_e^2 + V_e^2\{1 + (U_e\alpha/V_e)^2 G(1)^2\}] \\ &= H_e \end{aligned} \tag{4.7}$$

which turns out to be independent of $\theta$, i.e. constant within the cross-section of the vortex core, equal to the value at the edge of the vortex core. It then follows from Crocco's theorem, Eq. (3.9c), that the vortex lines and streamlines are parallel.

The vorticity distribution within the core, needed later to derive the velocity field outside the core, is obtained, in cylindrical coordinates, from Eq. (3.2a) as:

$$\begin{aligned} \bar{\omega} &= \bar{\nabla}\times\bar{u} \\ &= \frac{1}{r}\frac{\partial}{\partial r}(ru_\varphi)\bar{e}_x - \frac{\partial}{\partial x}u_\varphi\bar{e}_r + (\frac{\partial}{\partial x}u_r - \frac{\partial}{\partial r}u_x)\bar{e}_\varphi \\ &= \frac{1}{r_e}(\frac{1}{\theta}u_\varphi + \frac{\partial}{\partial\theta}u_\varphi)\bar{e}_x + (\theta r'_e\frac{\partial}{\partial\theta}u_\varphi - r_e\cancel{\frac{\partial}{\partial x}u_\varphi})\bar{e}_r - (\theta r'_e\frac{\partial}{\partial\theta}u_r + \frac{\partial}{\partial\theta}u_x - r_e\cancel{\frac{\partial}{\partial x}u_r})\bar{e}_\varphi \end{aligned} \tag{4.8}$$

Substitution of the velocity components given in Eqs. (4.6a-c) yields, within the quasi-cylindrical approximation in the general case and exact in the case of conical flow:

$$\omega_x = (\frac{V_e}{\theta r_e})[\frac{\{1 - (U_e\alpha/V_e)^2(\frac{G(1)}{r'_e} + \ell n\frac{G(\theta)}{G(1)})\}}{\{1 + (U_e\alpha/V_e)^2(\frac{G(\theta)}{\theta r'_e} - \frac{G(1)}{r'_e} - \ell n\frac{G(\theta)}{G(1)})\}^{\frac{1}{2}}}] \tag{4.9a}$$

$$\omega_r = -(\frac{V_e}{\theta r_e})(U_e\alpha/V_e)^2[\frac{G(\theta)}{\{1 + (U_e\alpha/V_e)^2(\frac{G(\theta)}{\theta r'_e} - \frac{G(1)}{r'_e} - \ell n\frac{G(\theta)}{G(1)})\}^{\frac{1}{2}}}] \tag{4.9b}$$

$$\omega_\varphi = (\frac{V_e}{\theta r_e})(\frac{U_e\alpha}{V_e}) \tag{4.9c}$$

From Eqs. (4.9a-c) it is clear that $\omega_x \sim \frac{1}{\theta}(-\ell n\theta)^{\frac{1}{2}}$, $\omega_\varphi \sim \frac{1}{\theta}$, $\omega_r \sim 0$ for $\theta \to 0$, i.e. as the core center is approached.

Using Eqs. (4.6a-c) and Eqs. (4.9a-c) it can be verified directly that the present solution indeed satisfies $\bar{u}\times\bar{\omega} = 0$, a direct verification of the result that followed from H = constant and Crocco's theorem.

The expressions derived above become somewhat simpler when expanding the expressions for $r'_e << 1$, i.e. slender conical, or in general slender and narrow vortex cores. It then follows neglecting terms of order $(r'_e)^2$;

$$u_x = U_e(1 - \hat{a}\ell n\theta) \tag{4.10a}$$

$$u_r = -\tfrac{1}{2}U_e\hat{a}(\theta r'_e) \tag{4.10b}$$

$$u_\varphi = V_e(1 - (U_e\hat{a}/V_e)^2\ell n\theta)^{\frac{1}{2}} \tag{4.10c}$$

$$p = P_e + \rho V_e^2\{\ell n\theta - \tfrac{1}{4}(U_e\alpha/V_e)^2(\ell n\theta)^2\} \tag{4.10d}$$

where

$$\hat{a} = \{1 + 2(V_e/U_e)^2\}^{\frac{1}{2}} - 1 \tag{4.10e}$$

These expressions have been derived earlier by Stewartson & Hall-1963, for the case of a slender conical vortex core, for which $r_e = Kx$, with $K<<1$.

In the solution for the flow inside the axi-symmetric slender and narrow core with distributed vorticity, given in Eqs. (4.10) and (4.11), there are two parameters on which the solution depends: the "swirl parameter" $V_e/U_e$ and the (local) slope of the core $r'_e$. Note that the latter only occurs in the radial velocity component, the radial velocity component going linearly to zero for $r'_e \to 0$.

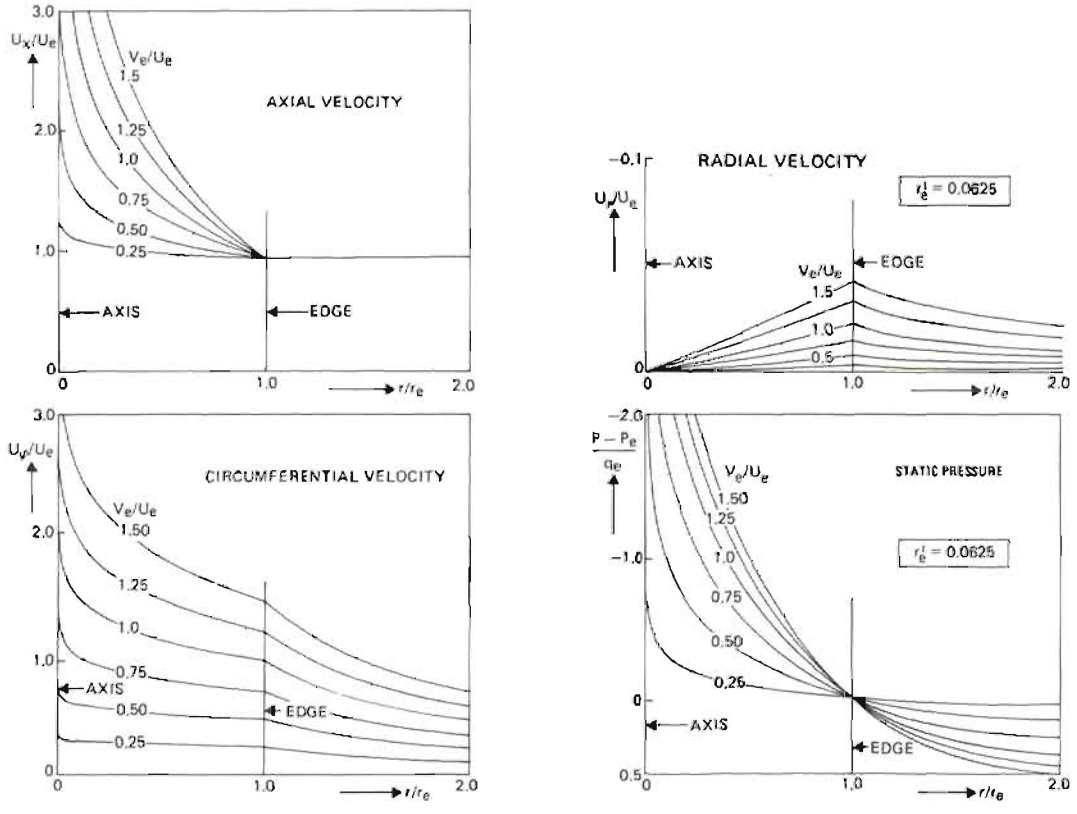


Fig. 4.2 Euler solution for various values of the swirl parameter

In Fig. 4.2 the solution is plotted for a number of values of the swirl parameter and for a value of $r'_e$ of 0.0625 (as estimated from Verhaagen-1983 for a 76-deg swept delta wing at 20 deg incidence for which $V_e/U_e \approx 1.0$). In Fig. 4.2 both the solutions inside and outside the core are plotted, the former will be discussed here, the latter in the next subsection. At the axis, $\theta = 0$, the axial velocity, circumferential velocity and pressure tend to infinity logarithmically. The example shown demonstrates that the singular behaviour is weak and results in an unrealistic solution in a relative small region in the immediate neighbourhood of the axis only. This suggests that since this is the only region with large velocity gradients, viscous effects will be confined to a small subcore indeed.

Denoting the order of magnitude of $r'_e$ by $\varepsilon$ it follows from Eqs. (4.10a-c) that

$$u_x = O(1)$$

$$u_r = O(\varepsilon) \tag{4.11}$$

$$u_\varphi = O(1)$$

In terms of $\varepsilon$ the radial velocity component is one order of magnitude smaller than the other two velocity components, which are order unity. The static pressure distribution $(p-P_e)/\tfrac{1}{2}\rho U_e^2(1 + (V_e/U_e)^2 + \tfrac{1}{4}(\hat{a}r'_e)^2\}$ decreases very rapidly to low values near the axis of the core, indicating that in this region compressibility effects will be important as well.
The velocity and pressure distribution of the Euler solution are, except right at the axis, qualitatively similar to the ones observed in experiment (e.g. Verhaagen & Kruisbrink-1985).

The components of the vorticity vector will be used in the next subsection to find the velocity field induced by the vortex core. In the present approximation of slender (conical or narrow) vortex cores, the vorticity components follow directly from Eqs. (4.9a-c) as:

$$\omega_x = (\frac{V_e}{\Theta r_e})[\frac{(U_e\hat{a}/V_e)^2(1 - \hat{a}\ell n\Theta)}{\hat{a}(1 - (U_e\hat{a}/V_e)^2\ell n\Theta)^{\frac{1}{2}}}] \tag{4.12a}$$

$$\omega_r = -\frac{1}{2}(\frac{V_e}{\Theta r_e})(U_e\hat{a}/V_e)^2[\frac{\Theta r_e'}{(1 - (U_e\hat{a}/V_e)^2\ell n\Theta)^{\frac{1}{2}}}] \tag{4.12b}$$

$$\omega_\varphi = (\frac{V_e}{\Theta r_e})(\frac{U_e\hat{a}}{V_e}) \tag{4.12c}$$

Denoting again the order of magnitude estimates of $r_e'$ by $\varepsilon$ and that of $r_e$ by $x\varepsilon$, it follows from Eqs. (4.12) that:

$$\begin{aligned}\omega_x &= O(1/x\varepsilon)\\ \omega_r &= O(1/x)\\ \omega_\varphi &= O(1/x\varepsilon)\end{aligned} \tag{4.13}$$

These order of magnitude estimates and the ones of Eq. (4.11), indicate that the radial component of both velocity and vorticity are one order of magnitude smaller than the corresponding other two components, but also that the circumferential component of the vorticity has the same order of magnitude as the axial component.

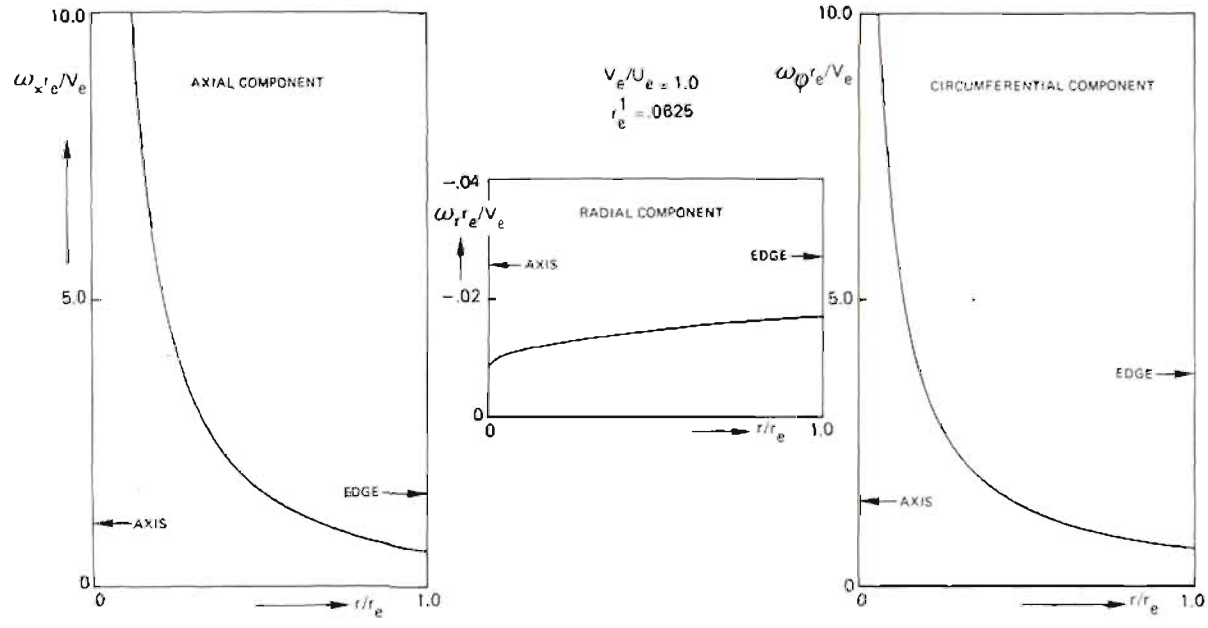


*Fig. 4.3 Vorticity distribution inside slender axi-symmetric vortex core*

The three components of the vorticity, made dimensionless by multiplication with (cross-sectional area)/(½ circulation) = $r_e/V_e$, are plotted in Fig. 4.3 for the typical condition of unit swirl parameter and $r_e' = 0.0625$. Near the center of the core the axial component $\omega_x$ behaves like $\sqrt{(-\ell n\Theta)}/\Theta$, $\omega_r$ like $1/\sqrt{(-\ell n\Theta)}$ and $\omega_\varphi$ like $1/\Theta$. Note that the radial component of the vorticity is quite small compared to the other two components. Near the edge of the vortex core the vorticity vector is nonzero, though the velocity is continuous at the edge (see Fig. 4.2). At the edge of the core $\omega_x/\omega_\varphi = U_e/V_e$ inside the core the circumferential vorticity is converted into axial vorticity, and near the axis $\omega_x/\omega_\varphi \sim \sqrt{(-\ell n\Theta)}$. The velocity distribution inside the vortex core has exactly the same behaviour, i.e. $u_x/u_\varphi \to U_e/V_e$ as $\Theta \to 1$ and $u_x/u_\varphi \to \sqrt{(-\ell n\Theta)}$ for $\Theta \to 0$: the circumferential velocity component is converted into the axial velocity component.

4.2.2 Velocity field induced by vortex core

The solution obtained in the preceding subsection applies to the flow inside the vortex core. Our primary interest is in the flow field outside the core and specifically to find a model for the vortex core that simulates its external flow field. With the vorticity distribution found in Eqs. (4.12a-c) the velocity field induced by the vortex core is given by, see Eq. (3.7c)

$$\bar{u}(\bar{x}_o) = \frac{1}{4\pi}\int\int\int_V \bar{\omega}(\bar{x})\times\frac{\bar{r}}{|\bar{r}|^3}dV(\bar{x}) \tag{4.14}$$

where $\bar{r} = \bar{x}_o - \bar{x}$.

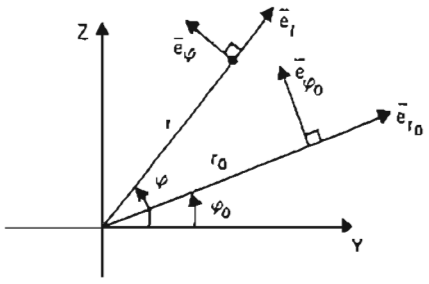


Fig. 4.4 Nomenclature for derivation of velocity induced by vortex core

In the following we write

$$\bar{\omega}(\bar{x}) = (\frac{1}{\Theta r_e})\bar{\Omega}(\Theta;x) \tag{4.15a}$$

with, see Fig. 4.4:

$$\bar{\Omega}(\Theta;x) = \xi\bar{e}_x + \eta\bar{e}_r + \zeta\bar{e}_\varphi \tag{4.15b}$$

where $\xi$, $\eta$ and $\zeta$ follow from Eqs. (4.12a-c) by multiplication with $\Theta r_e$.

Furthermore we decompose all vector quantities by one component in x-direction and two in the plane x = constant, see Fig. 4.4.

Writing

$$\bar{x}_o = x_o\bar{e}_x + \bar{X}_o \tag{4.15c}$$

$$\bar{x} = x\bar{e}_x + \bar{X}(\Theta,\varphi;x) \tag{4.15d}$$

and with

$$dV(\bar{x}) = rdrdxd\varphi = \Theta r_e^2 d\Theta dx d\psi \tag{4.15e}$$

the velocity induced by the rotational flow region becomes

$$\bar{u}(\bar{x}_o) = \frac{1}{4\pi}\int_{\Theta=0}^{1} d\Theta \int_{\varphi=0}^{2\pi} d\varphi \int_{x=0}^{\infty} r_e\bar{\Omega}(\Theta;x)\times\frac{(x_o-x)\bar{e}_x+\bar{X}_o-\bar{X}}{\{(x_o-x)^2+|\bar{X}_o-\bar{X}|^2\}^{3/2}}dx \tag{4.16}$$

The integration with respect to x can be carried out upon approximating the geometry and the vorticity distribution as:

$$\bar{\Omega}(;x) \approx \bar{\Omega}(\Theta;x_o) + (x-x_o)\bar{\Omega}_x(\Theta;x_o)$$

$$\bar{X}(\Theta,\varphi;x) \approx \bar{X}(\Theta,\varphi;x_o) + (x-x_o)\bar{X}_x(\Theta,\varphi;x_o)$$

$$r_e(x) \approx r_e(x_o) + (x-x_o)r_e'(x_o)$$

where the subscript x denotes (partial) differentiation with respect to x.
Denoting quantities in the plane $x=x_o$ with superscript o, one obtains:

$$\bar{u}(\bar{x}_o) \approx \frac{1}{4\pi}\int_{\Theta=0}^{1} d\Theta \int_{\varphi=0}^{2\pi} d\varphi\{\bar{\Omega}^o\times(\bar{R}I_0^1+\bar{S}I_1^1)r_e(x_o) - (r_e'(x_o)\bar{\Omega}^o+r_e(x_o)\bar{\Omega}_x^o)\times(\bar{R}I_1^1+\bar{S}I_2^1)\} \tag{4.17a}$$

where $\bar{R} = \bar{X}_o - \bar{X}^o$ (4.17b)

$$\bar{S} = \bar{e}_x + \bar{X}_x^o \tag{4.17c}$$

$$I_k^1 = \lim_{x_\infty\to\infty}\left(\int_{x=0}^{x_\infty}\frac{(x_o-x)^k dx}{|\bar{R}+(x_o-x)\bar{S}|^3}\right) \tag{4.17d}$$

The integrals defined in Eq. (4.17d) are worked out in Tables 3.4-6.

The above approximation is called the "tangent-cone" approximation, because it is exact for the conical case. Note that the above approach preserves the singular behaviour of the integrand in Eq. (4.16), while it is assumed that since for $|x_o-x|\gg 1$ the integrand decreases as $1/|x_o-x|^2$, the error associated with the linear approximation of $\bar{\Omega}(\Theta;x)$, $\bar{X}(\Theta,\varphi;x)$ and $r_e(x)$ is negligible.

Using the results of Tables 3.4-6 we get

$$\bar{u}(\bar{x}_o) = \frac{1}{4\pi}\int_{\Theta=0}^{1} d\Theta \int_{\varphi=0}^{2\pi}\{\bar{\Omega}^o\times(2\frac{\bar{R}}{|\bar{R}|^2} - 2\bar{e}_x\frac{\bar{X}_x^o\cdot\bar{R}}{|\bar{R}|^2} - \frac{\bar{e}_x}{x_o})r_e(x_o)$$

$$-(r_e'(x_o)\bar{\Omega}^o+r_e(x_o)\bar{\Omega}_x^o)\times\bar{e}_x(-2+2\ln\frac{x_\infty}{x_o} - \ln\frac{|\bar{R}|^2}{x_o^2})\}d\varphi$$

$$+O(\varepsilon^2) \tag{4.18}$$

with $\varepsilon$ denoting the order of magnitude of $r_e'$.

In order to carry out the integration with respect to $\varphi$ we write (see Fig. 4.4)

$$\bar{X} = \theta r_e \bar{e}_r$$

$$= \theta r_e(\cos\delta \bar{e}_r^o + \sin\delta \bar{e}_\varphi^o), \text{ with } \delta = \varphi - \varphi_o \tag{4.19a}$$

so that

$$\bar{R} = \bar{X}_o - \bar{X}^o$$

$$= (r_o - \theta r_e(x_o)\cos\delta)\bar{e}_r^o - \theta r_e(x_o)\sin\delta \bar{e}_\varphi^o \tag{4.19b}$$

and also

$$\bar{\Omega} = \xi \bar{e}_x + (\eta\cos\delta - \zeta\sin\delta)\bar{e}_r^o + (\eta\sin\delta + \zeta\cos\delta)\bar{e}_\varphi^o \tag{4.19c}$$

Substitution of Eqs. (4.19a-c) into Eq. (4.18), followed by integration with respect to $\varphi$ (using Table 2.1-9) results in:

$$\begin{aligned}\bar{u}(\bar{x}_o) = \frac{1}{2\pi}\int_{\theta=0}^{1} d\theta \Big[ & \bar{e}_x \Big\{ \zeta^o \frac{\pi}{\theta}\Big(1 - \frac{r_o^2 - \theta^2 r_e(x_o)^2}{|r_o^2 - \theta^2 r_e(x_o)^2|}\Big)\Big\} \\ & + \bar{e}_r^o\Big[-\zeta^o r_e'(x_o)\frac{\pi\theta r_e(x_o)}{r_o}\Big(1 + \frac{r_o^2 - \theta^2 r_e(x_o)^2}{|r_o^2 - \theta^2 r_e(x_o)^2|}\Big) \\ & \quad - \zeta_x^o \frac{\pi}{2\theta r_o}\big(r_o^2 + \theta^2 r_e(x_o)^2 - |r_o^2 - \theta^2 r_e(x_o)^2|\big)\Big) \\ & + \bar{e}_\varphi^o\Big\{ \zeta^o \frac{\pi r_e(x_o)}{r_o}\Big(1 + \frac{r_o^2 - \theta^2 r_e(x_o)^2}{|r_o^2 - \theta^2 r_e(x_o)^2|}\Big) \\ & \quad + \eta^o r_e'(x_o)\frac{\pi\theta r_e(x_o)}{r_o}\Big(1 + \frac{r_o^2 - \theta^2 r_e(x_o)^2}{|r_o^2 - \theta^2 r_e(x_o)^2|}\Big) \\ & \quad + \eta_x^o \frac{\pi}{2\theta r_o}\big(r_o^2 + \theta^2 r_e(x_o)^2 - |r_o^2 - \theta^2 r_e(x_o)^2|\big)\Big\}\Big] + O(\varepsilon^2)\end{aligned} \tag{4.20}$$

For points $\bar{x}_o$ outside the rotational flow region, i.e. for $r_o > r_e(x_o)$, we find:

$$\begin{aligned}\bar{u}(\bar{x}_o) = \frac{1}{2\pi}\int_{\theta=0}^{1} d\theta \Big[ & \bar{e}_r^o\Big(-\frac{\pi\theta}{r_o}\frac{\partial}{\partial x}(r_e^2\zeta)\Big|_{x=x_o}\Big) \\ & + \bar{e}_\varphi^o\Big[\frac{2\pi r_e(x_o)}{r_o}\zeta^o + \frac{\pi\theta}{r_o}\frac{\partial}{\partial x}(r_e^2\eta)\Big|_{x=x_o}\Big)\Big] + \ldots\end{aligned} \tag{4.21a}$$

The above expression shows that the radial inflow is caused by the circumferential component of the vorticity ($\omega_\varphi = \theta r_e \zeta$). The radial inflow becomes zero for a cylindrical vortex core with constant $U_e$ and $V_e$, in agreement with the examples discussed in Chapter 3.

The circumferential velocity is due to the axial component of the vorticity while also the radial component of the vorticity contributes a term small of higher order to the circumferential velocity. Note that for the case of the cylindrical core with constant $U_e$ and $V_e$ the contribution due to the radial vorticity component drops out, and we recover the simple example given in Chapter 3.

Employing Eqs. (4.12a-c) we can integrate with respect to $\theta$ in Eq. (4.21a), resulting in

$$\begin{aligned}\bar{u}(\bar{x}_o) = & -\frac{\bar{e}_r^o}{4r_o}\Big(\frac{d}{dx}(r_e^2 U_e \hat{\alpha})\Big|_{x=x_o}\Big) \\ & + \frac{\bar{e}_\varphi^o}{2\pi r_o}\Big(2\pi r_e V_e\Big|_{x=x_o}\Big) + \ldots, \quad \text{for } r_o > r_e(x_o)\end{aligned} \tag{4.21b}$$

This outer velocity distribution has been included in Fig. 4.2. It shows that the velocity is continuous across the edge of the core. The two components in Eq. (4.21b) have a $1/r_o$ behaviour, similar to the components of the velocity induced by a vortex and source located at the axis.

For a point inside the vortex core $r_o < r_e(x_o)$ we should recover the expressions given in Eq. (4.10). We find using Eq. (4.21a):

$$\bar{u}(\bar{x}_o) = \frac{1}{2\pi}\int_{\theta=0}^{\theta_o} d\theta\{\bar{e}_r^o\{-\frac{\pi\theta}{r_o}\frac{\partial}{\partial x}(r_e^2\zeta)\Big|_{x=x_o}\}$$

$$+ \bar{e}_\varphi^o\{\frac{2\pi r_e(x_o)}{r_o}\zeta^o + \frac{\pi\theta}{r_o}\frac{\partial}{\partial x}(r_e^2\eta)\Big|_{x=x_o}\}\}$$

$$+ \frac{1}{2\pi}\int_{\theta=\theta_o}^{1} d\theta\{\bar{e}_x\{\frac{2\pi}{\theta}\zeta^o\} - \bar{e}_r^o\{\frac{\pi r_o}{\theta}\zeta_x^o\} + \bar{e}_\varphi^o\{\frac{\pi r_o}{\theta}\eta_x^o\}\}+ \ldots \qquad (4.22a)$$

where $\theta_o = r_o/r_e(x_o)$. The above expression shows that the contribution due to the vorticity in the inner core region ($r < r_o$) has the same form as Eq. (4.21a). It also shows that the axial velocity is caused by the circumferential vorticity $\zeta$ in the outer core region ($r > r_o$), as was the case in the example of cylindrical cores discussed in the preceding chapter.

Integrating in Eq. (4.22a) with respect to $\theta$, neglecting terms of higher order, results in

$$\bar{u}(\bar{x}_o) = \bar{e}_x U_e\{-\tilde{a}\ell n\theta_o\}$$

$$- \frac{\bar{e}_r^o}{4}\frac{\theta_o}{r_e(x_o)}\{\frac{d}{dx}(r_e^2 U_e\hat{a})\Big|_{x=x_o}\}$$

$$+ \bar{e}_\varphi^o V_e\{1 - (U_e\hat{a}/V_e)^2\ell n\theta_o\}^{\frac{1}{2}} + \ldots, \quad \text{for } r_o < r_e(x_o) \qquad (4.22b)$$

which upon adding the axial free stream component $U_e\bar{e}_x$ is indeed equivalent to the velocity given in Eq. (4.10).

## 4.3 Vortex core as an infinitely long, tightly wound vortex sheet

### 4.3.1 Formulation of the problem

As argued in Chapter 3 a vortex core can also be considered as an infinitely long tightly wound vortex sheet (see Fig. 4.5). Between the turns of the sheet the flow is potential flow, while the potential is discontinuous across the sheet.

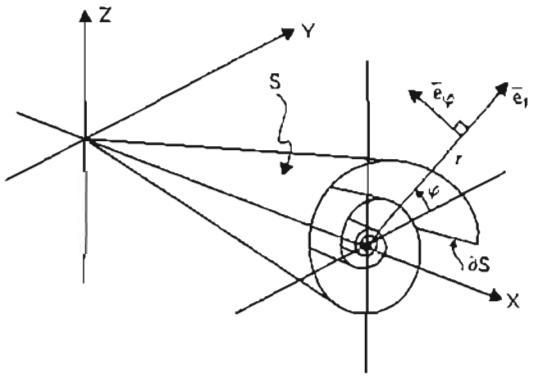


Fig. 4.5 Vortex core as a tightly wound spiral vortex sheet

The geometry of the vortex sheet and its doublet distribution is defined by

$$\bar{x} = x\bar{e}_x + \bar{X}(\theta;x) \qquad (4.23a)$$

and

$$\mu = \mu(\theta;x) \qquad (4.23b)$$

respectively, where $\theta = r/r_e(x)$. Here $r = r_e(x)$ denotes a suitably chosen reference point on the vortex sheet. The sheet itself is defined as

$$\varphi = \varphi_s(\theta;x) \qquad (4.23c)$$

so that in polar coordinates a point on the sheet can be expressed as

$$\bar{x} = x\bar{e}_x + \theta r_e\bar{e}_r$$

$$= x\bar{e}_x + \theta r_e\{\cos\varphi_s(\theta)\bar{e}_y + \sin\varphi_s(\theta)\bar{e}_z\}$$

The velocity induced by the vortex sheet is given in Eq. (3.15c) as

$$\bar{u}(\bar{x}_o) = \frac{1}{4\pi}\int_S \bar{\gamma}(\bar{x})\times\frac{\bar{r}}{|\bar{r}|^3}dS(\bar{x}) - \frac{1}{4\pi}\int_{\partial S}\mu(\bar{x})\frac{d\bar{\ell}(\bar{x})\times\bar{r}}{|\bar{r}|^3} \qquad (4.24a)$$

where $\bar{r} = \bar{x}_o - \bar{x}$ and

$$\bar{\gamma} = \bar{n}\times\bar{\nabla}\mu \qquad (4.26b)$$

For the present purposes it will be assumed that the outer edge of the vortex sheet is matched to the outer vortex sheet, so that the second term in Eq. (4.24a) may be omitted.

As for the case of the distributed vorticity we consider a "tangent-cone" approximation of Eq. (4.24a) by approximating the geometry and the doublet distribution as

$$\bar{X}(\theta;x) = \bar{X}(\theta;x_o) + (x-x_o)\bar{X}_x(\theta;x_o) \qquad (4.25a)$$

$$\mu(\theta;x) = \mu(\theta;x_o) + (x-x_o)\mu_x(\theta;x_o) \qquad (4.25b)$$

where the subscript x denotes differentiation with respect to x.

Now we find for the unit vector normal to the vortex sheet, using Eqs. (4.23a) and (4.25):

$$\bar{n} = (\bar{X}_x \times \bar{X}_\theta)/|\bar{X}_x \times \bar{X}_\theta|$$

$$\approx (\bar{e}_x \times \bar{X}^o_\theta + \bar{X}^o_x \times \bar{X}^o_\theta)/|\bar{X}^o_\theta|$$

where the superscript o denotes the value at $x=x_o$.

The surface vorticity vector on the sheet is

$$\bar{\gamma} = (-\bar{x}_x u_\theta + \bar{x}_\theta u_x)/|\bar{x}_x \times \bar{x}_\theta|$$

$$\approx (-\bar{e}_x u^o_\theta - \bar{X}^o_x u^o_\theta + \bar{X}^o_\theta u^o_x)/|\bar{X}^o_\theta|$$

The surface element dS is

$$dS = |\bar{x}_x \times \bar{x}_\theta| dx d\theta$$

$$\approx |\bar{X}^o_\theta| dx d\theta$$

so that the velocity induced by the vortex sheet can be expressed as

$$\bar{u}(\bar{x}_o) \approx \frac{1}{4\pi} \int_{\theta=0}^{1} \{-\bar{e}_x u^o_\theta + (-\bar{X}^o_x u^o_\theta + \bar{X}^o_\theta u^o_x)\} \times \{(\bar{e}_x + \bar{X}^o_x) I^1_1 + (\bar{X}_o - \bar{X}^o) I^1_0\} d\theta \qquad (4.26)$$

where $I^1_k$ follows from table 3.4-6 with $\bar{S} = \bar{X}^o_x$ and $\bar{R} = \bar{X}_o - \bar{X}^o$. Substitution into Eq. (4.26) and expansion with respect to $\varepsilon$, the order of magnitude of $r'_e$, yields:

$$\bar{u}(\bar{x}_o) \approx -\frac{1}{4\pi} \bar{e}_x \times \int_{\theta=0}^{1} u^o_\theta \frac{\bar{R}}{|\bar{R}|^2} d\theta$$

$$+ \frac{1}{2\pi} \bar{e}_x \{ \int_{\theta=0}^{1} u^o_\theta \bar{X}^o_x \cdot \frac{\bar{e}_x \times \bar{R}}{|\bar{R}|^2} d\theta - \bar{e}_x \cdot \int_{\theta=0}^{1} u^o_x \frac{\bar{R}}{|\bar{R}|^2} \times \bar{X}^o_\theta d\theta \} + O(\varepsilon^2) \qquad (4.27)$$

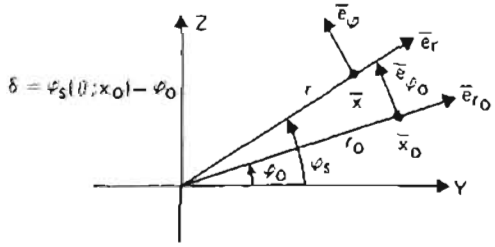


Fig. 4.6 Coordinate system for integration with respect to $\theta$

Now we write, see Fig. 4.6:

$$\bar{R} = \bar{X}_o - \bar{X}^o$$

$$= r_o \bar{e}^o_r - \theta r_e(x_o)(\cos\delta \bar{e}^{-o}_r + \sin\delta \bar{e}^{-o}_\varphi) \qquad (4.28)$$

so that one obtains from Eq. (4.27):

$$\bar{u}(\bar{x}_o) = \bar{e}_x u_x(r_o,\varphi;x) + \bar{e}^o_r u_r(r_o,\varphi;x) + \bar{e}^o_\varphi u_\varphi(r_o,\varphi;x) + O(\varepsilon^2) \qquad (4.29a)$$

where

$$u_x = \frac{r'_e r_o}{2\pi} \int_{\theta=0}^{1} u^o_\theta \left( \frac{\theta \sin\delta d\theta}{r_o^2 + \theta^2 r_e^2 - 2\theta r_e r_o \cos\theta} \right)$$

$$- \frac{r_e}{2\pi} \int_{\theta=0}^{1} u^o_x \left( \frac{r_o \frac{d}{d\theta}(\theta\sin\delta) - r_e \theta^2 \frac{d}{d\theta^2}\sin\delta}{r_o^2 + \theta^2 r_e^2 - 2\theta r_e r_o \cos\delta} d\theta \right) \quad <= O(\varepsilon) \qquad (4.29b)$$

$$u_r = -\frac{r_e}{2\pi} \int_{\theta=0}^{1} u^o_\theta \left( \frac{\theta \sin\delta d\theta}{r_o^2 + \theta^2 r_e^2 - 2\theta r_e r_o \cos\delta} \right) \quad <= O(1) \qquad (4.29c)$$

$$u_\varphi = -\frac{1}{2\pi} \int_{\theta=0}^{1} u^o_\theta \left( \frac{(r_o - r^o_e \theta \cos\delta) d\theta}{r_o^2 + \theta^2 r_e^2 - 2\theta r_e r_o \cos\delta} \right) \quad <= O(1) \qquad (4.29d)$$

The boundary conditions on the vortex sheet, discussed in Chapter 3, are the normal-velocity boundary condition, Eq. (3.19a)

$$\bar{u}^p \cdot \bar{n} = 0$$

and the condition that the (static) pressure is continuous across the vortex sheet. This zero-pressure-jump condition can be expressed as the condition, Eq. (3.19d):

$$(\bar{\gamma} \times \bar{n}) \cdot \bar{u}^p = 0$$

where $\bar{u}^p$ is the average velocity across the sheet.

Using $\bar{X}(\theta;x) = \theta r_e(\cos\delta\bar{e}_r^o + \sin\delta\bar{e}_\varphi^o)$, $\delta = \varphi-\varphi_s(\theta;x)$ the unit normal can be expressed as

$$\bar{n} = (\bar{e}_x r'_e\theta^2\varphi_{s_\theta} - \bar{e}_r^o\theta\varphi_{s_\theta} + \bar{e}_\varphi^o)/(1+\theta^2\varphi_{s_\theta}^2)^{\frac{1}{2}}, \text{ for } \varphi = \varphi_s(\theta;x)$$

The surface vorticity vector then, can be written as

$$\bar{\gamma} = (-\bar{e}_x\mu_\theta + \bar{e}_r^o(-\theta r'_e\mu_\theta+r_e\mu_x) + \bar{e}_\varphi^o r_e\theta\varphi_{s_\theta}\mu_x)/r_e(1+\theta^2\varphi_{s_\theta}^2)^{\frac{1}{2}}, \text{ for } \varphi = \varphi_s(\theta;x)$$

so that, to the required order of magnitude

$$\bar{\gamma}\times\bar{n} = [\bar{e}_x\{-\theta r'_e\mu_\theta+r_e(1+\theta^2\varphi_{s_\theta}^2)\mu_x) + \bar{e}_r^o\mu_\theta + \bar{e}_\varphi^o\theta\varphi_{s_\theta}\mu_\theta]/(1+\theta^2\varphi_{s_\theta}^2)$$

where we assumed that $\theta\varphi_{s_\theta}$ remains finite for $\theta\to 0$, $\varphi_s(\theta;x)\to\infty$.

Substitution of above expressions in the normal-velocity boundary condition gives

$$-\theta\varphi_{s_\theta}u_r(r_e\theta,\varphi_s(\theta);x) + u_\varphi(r_e\theta,\varphi_s(\theta);x) + Ur'_e\theta^2\varphi_{s_\theta} + O(\varepsilon^2) = 0 \tag{4.30a}$$

while for the pressure boundary condition one finds

$$\mu_\theta u_r^p(r_e\theta,\varphi_s(\theta);x) + \theta\varphi_{s_\theta}\mu_\theta u_\varphi^p(r_e\theta,\varphi_s(\theta);x) + U(-\theta r'_e\mu_\theta+r_e(1+\theta^2\varphi_{s_\theta}^2)\mu_x) + O(\varepsilon^2) = 0 \tag{4.30b}$$

where we added to the velocity induced by the vortex core itself the free-stream component $U\bar{e}_x$.

Solving for $u_r$ and $u_\varphi$ from Eqs. (4.30a and b) results in

$$u_r(r_e\theta,\varphi_s(\theta);x) = U(r'_e\theta - r_e\mu_x/\mu_\theta) \tag{4.31a}$$

$$u_\varphi(r_e\theta,\varphi_s(\theta);x) = -Ur'_e\theta\varphi_{s_\theta}\mu_x/\mu_\theta \tag{4.31b}$$

for $\theta\in[0,\theta_e]$, where it follows from Eqs.(4.29c and d) that

$$u_r(r,\varphi;x) = \frac{-r_e}{2\pi}\int_{\xi=0}^{1}\mu_\xi\left(\frac{\xi\sin\delta d\xi}{r^2+\xi^2r_e^2-2\xi r_e r\cos\delta}\right) \tag{4.31c}$$

$$u_\varphi(r,\varphi;x) = \frac{-1}{2\pi}\int_{\xi=0}^{1}\mu_\xi\left(\frac{(r-r_e\xi\cos\delta)d\xi}{r^2+\xi^2r_e^2-2\xi r_e r\cos\delta}\right) \tag{4.31d}$$

with $\delta = \varphi_s(\xi;x)-\varphi$.

The system of equations Eqs. (4.31a and b) consists of two coupled integro-differential equations for the two unknown functions $\mu(\theta;x)$ and $\varphi_s(\theta;x)$, to be solved for at each station x.

4.3.2 Asymptotic solution

Mangler & Weber-1967 have derived an asymptotic solution for a narrow conical vortex core. Adapting their solution for the present case of quasi-cylindrical narrow vortex cores, results in

$$\mu(\theta;x) = 2\pi V_e r_e\theta(1-(U_e\hat{\alpha}/V_e)^2\ln\theta)^{\frac{1}{2}} \tag{4.32a}$$

for the doublet distribution and in

$$\frac{\partial}{\partial\theta}\varphi_s(\theta;x) = -\left(\frac{U_e\hat{\alpha}}{V_e}\right)\frac{1}{\theta^2r'_e\{1-(U_e\hat{\alpha}/V_e)^2\ln\theta\}^{\frac{1}{2}}} \tag{4.32b}$$

for the shape of the vortex sheet, where $\varphi\in[\varphi_s(\theta;x)-2\pi,\varphi_s(\theta;x)]$. This asymptotic solution is for the typical case of unit swirl parameter and $r'_e = 0.0625$, plotted in Fig. 4.7.

The geometrical shape of the vortex sheet solution is presented in Fig. 4.7a. It indicates that as the axis of the core is approached the vortex sheet (10 turns computed) becomes nearly circular and that the gap between consecutive loops of the vortex sheet diminishes rapidly.

The doublet distribution and its derivative with respect to $\varphi$ along the vortex sheet are presented in Figs. 4.7b and c, respectively. It shows that both the doublet strength and its derivative with respect to $\varphi$ decrease rapidly with increasing $\varphi$. It also indicates that the inner loops of the vortex sheet, which are nearly circular, carry an almost constant doublet distribution.

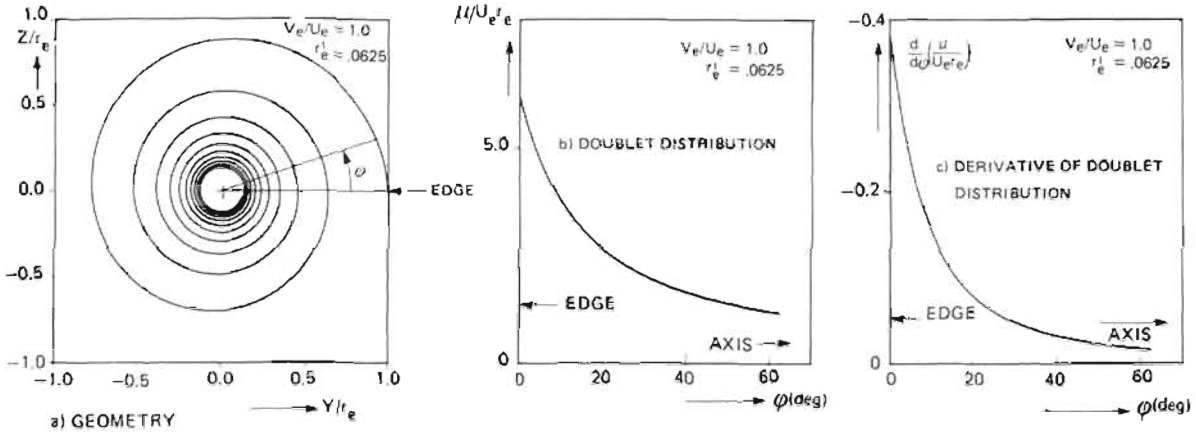


Fig. 4.7 Asymptotic solution for rolled-up vortex sheet core

The velocity field associated with the asymptotic solution can be expressed as:

$$U + u_x = U_e(1-\hat{\alpha}\ell n\theta) - \theta r_e' V_e\{1 - (U_e\hat{\alpha}/V_e)^2\ell n\theta\}^{\frac{1}{2}}(\varphi_s(\theta;x)-\varphi-\pi) + \ldots \tag{4.33a}$$

$$u_r = -\tfrac{1}{2}U_e\hat{\alpha}(\theta r_e') - (\theta r_e')^2 V_e(\frac{\hat{\alpha}+1}{\hat{\alpha}}-\ell n\theta)\{1 - (U_e\hat{\alpha}/V_e)^2\ell n\theta\}^{\frac{1}{2}}(\varphi_s(\theta;x)-\varphi-\pi)+ \ldots \tag{4.33b}$$

$$u_\varphi = V_e\{1 - (U_e\hat{\alpha}/V_e)^2\ell n\theta\}^{\frac{1}{2}} + \theta r_e' U_e(1-\hat{\alpha}\ell n\theta)(\varphi_s(\theta;x)-\varphi-\pi) + \ldots \tag{4.33c}$$

where $\varphi_s(\theta;x)$ follows from Eq. (4.32b).

These three components of the velocity are plotted in Fig. 4.8, again for the typical case considered earlier: unit swirl parameter, $r_e' = 0.0625$. The first term in the velocity field given in Eqs. 4.33a-c is axially symmetric and identical to the one found for the vortex core with distributed vorticity. Eqs. 4.10a-c plotted in Fig. 4.2. The second term in Eqs. (4.33a-c), one order of magnitude smaller than the first term, is the term that accounts for the jump in the velocity components across the vortex sheet. Also this non-axisymmetric part of the velocity field remains finite as the axis ($\theta=0$) is approached, i.e. it tends to zero like $\theta\sqrt{(\ell n\theta)}$, $\theta^2(\ell n\theta)^2$ and $\theta\ell n\theta$ for the axial, radial and circumferential component, respectively.

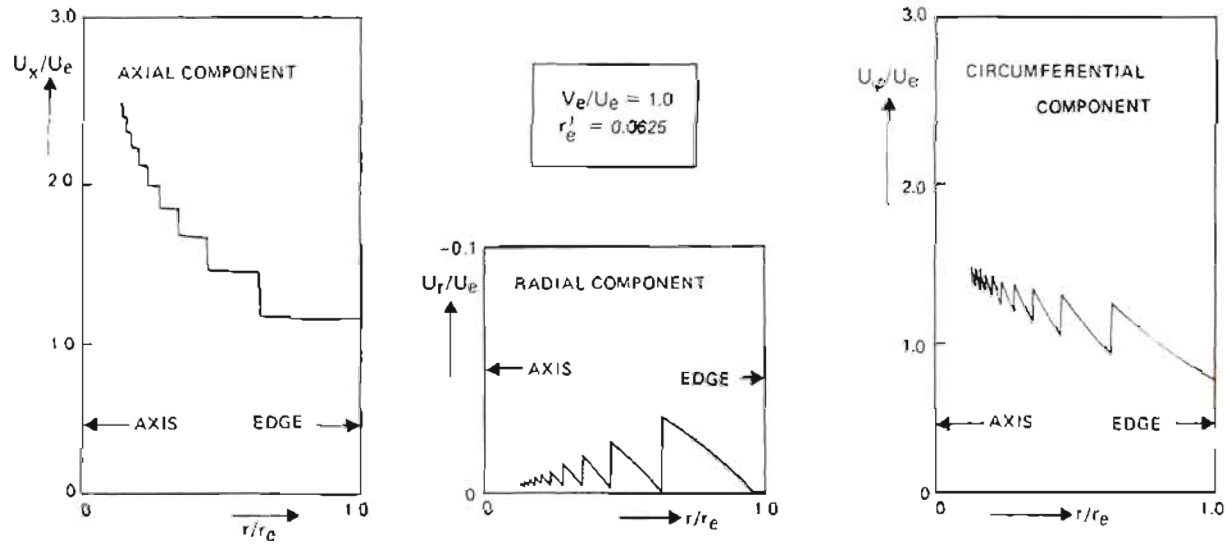


Fig. 4.8 Velocity distribution in rolled-up sheet core

It can be verified by substitution that the above asymptotic solution, valid near the center of the vortex core, i.e. for $\theta\to 0$, does indeed satisfy the normal velocity as well as the pressure-jump condition, as expressed in Eqs. (4.30a) and (4.30b) respectively.

It must be emphasized though that the above solution is just one possible solution and perhaps not the only one. However, solving the coupled and nonlinear integro- differential equations in closed form will be probably impossible. A numerical solution procedure to solve this set of equations has not been pursued in this study either, so here we only consider the above solution in more detail.

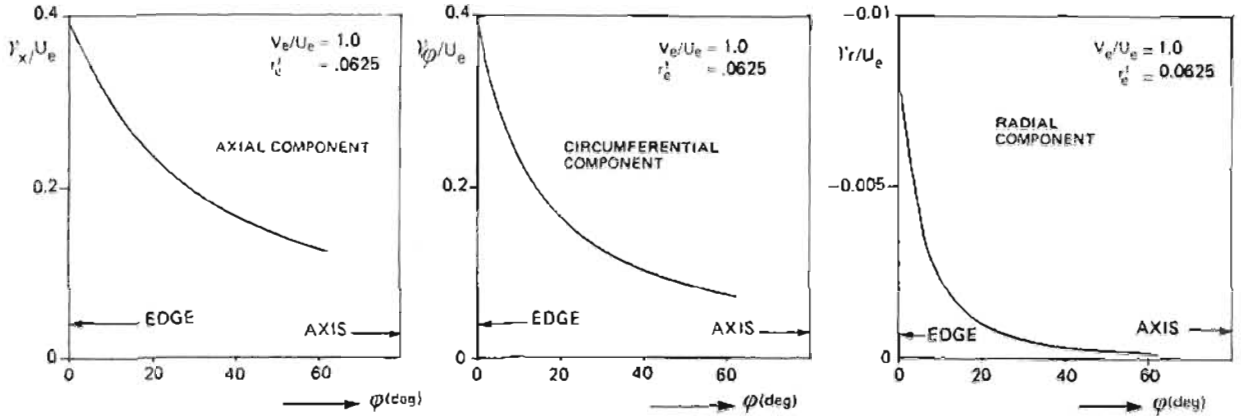


Fig. 4.9 Components of vorticity vector of asymptotic vortex sheet solution

The surface vorticity distribution on the vortex sheet follows from the above solution as

$$\bar{\gamma} = \gamma_x \bar{e}_x + \gamma_r \bar{e}_r + \gamma_\varphi \bar{e}_\varphi$$

where

$$\gamma_x = -U_e\{\frac{d}{d\theta}(\frac{\mu}{U_e r_e})\}/\{1 + \theta^2(\frac{d\varphi_s}{d\theta})^2\}^{\frac{1}{2}}$$

$$\gamma_r = -r'_e\{\theta\frac{d}{d\theta}(\frac{\mu}{U_e r_e}) - \frac{\mu}{U_e r_e}\}/\{1 + \theta^2(\frac{d\varphi_s}{d\theta})^2\}^{\frac{1}{2}} \qquad (4.34)$$

$$\gamma_\varphi = \theta r'_e \frac{d\varphi_s}{d\theta}(\frac{\mu}{U_e r_e})/\{1 + \theta^2(\frac{d\varphi_s}{d\theta})^2\}^{\frac{1}{2}}$$

Note that the $\gamma_\varphi/\gamma_x$ is identical to both $u_\varphi/u_x$ and $\omega_\varphi/\omega_x$. This quotient tends to zero for $\theta \to 0$ (and $\varphi \to \infty$), showing that in the vortex core the circumferential vorticity and velocity is converted into axial vorticity and velocity, respectively.

The components of the surface vorticity on the vortex sheet are plotted in Fig. 4.9. It shows that the radial component of the vortex sheet vorticity is quite small, that the axial and circumferential component have about the same value at the edge ($\varphi$=0) and that the axial component decreases at a slower rate than the circumferential component. The latter indicates as noted above that the vortex sheet vorticity is gradually turning in axial direction.

## 4.4 Vortex filament/feeding-sheet model

### 4.4.1 Induced velocity field

The vortex-filament/feeding-sheet model, introduced by Brown & Michael-1954, is used in the present study to simulate the outer flow field, given in Eq. 4.21b and included in Fig. 4.2, due to the vortex core. The model used for the purpose of this chapter is depicted in Fig. 4.10.

In the model the innermost turns of the spiralling vortex core are replaced by a line vortex (filament) of strength $\Gamma(x)$ which is connected to the outer part of the spiralling sheet by a so-called feeding sheet.

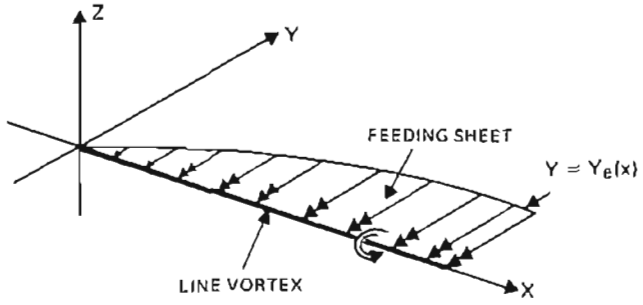


Fig. 4.10 Isolated vortex/feeding sheet vortex core model

The strength of the feeding sheet is $\frac{d\Gamma}{dx}$, i.e. it carries the vorticity that feeds into the vortex and increases the strength of the vortex filament. The velocity field induced by this model is:

$$\bar{u}(\bar{x}_o) = -\frac{1}{4\pi}\int_{x=0}^{\infty}\Gamma(x)\frac{\bar{r}}{|\bar{r}|^3}\times\bar{e}_x dx + \frac{1}{4\pi}\int_{x=0}^{\infty}\frac{d\Gamma}{dx}\left(\int_{y=0}^{y_e(x)}\frac{\bar{r}}{|\bar{r}|^3}\times\bar{e}_y dy\right)dx \qquad (4.35)$$

$$= \bar{u}_v(\bar{x}_o) + \bar{u}_\gamma(\bar{x}_o)$$

where $\bar{r} = \bar{x}_o - \bar{x}$.

We consider the first term (denoted by $\bar{u}_v$) of Eq. (4.35), the velocity induced by the line vortex first. Writing

$$\bar{x}_o = x_o\bar{e}_x + (y_o\bar{e}_y + z_o\bar{e}_z) = x_o\bar{e}_x + \bar{X}_o$$

$$\bar{x} = x\bar{e}_x$$

and, in the narrow-core quasi-cylindrical approximation, for the strength of the vortex

$$\Gamma(x) = \Gamma(x_o) + (x-x_o)\Gamma'(x_o) + \ldots$$

one obtains:

$$\bar{u}_v(\bar{x}_o) = \frac{-1}{4\pi}\int_{x=0}^{\infty}\Gamma(x)\frac{\bar{r}\times\bar{e}_x}{|\bar{r}|^3}\,dx$$

$$= \frac{-1}{4\pi}[(\bar{X}_o\times\bar{e}_x)\{\Gamma(x_o)I_o^1 - \Gamma'(x_o)I_1^1\} + \ldots]$$

where $I_0^1$ and $I_1^1$ follow (with $\bar{R}\equiv\bar{X}_o$ , $\bar{S}\equiv 0$) from Table 3.4-5, so that in the quasi-cylindrical approximation one obtains with $\Gamma = O(\varepsilon x)$:

$$\bar{u}_v(\bar{x}_o) = -\frac{1}{2\pi}\Gamma(x_o)\frac{\bar{X}_o\times\bar{e}_x}{|\bar{X}_o|^2} + O(\varepsilon^2) \qquad (4.36)$$

This circumferential term is of order 1 and represents the velocity induced by a discrete vortex situated in the cross-flow plane.

The second term (denoted by $\bar{u}_\gamma$) in Eq. (4.35), the one due to the doublet distribution on the feeding sheet, is worked out in a similar fashion. The feeding sheet is given as

$$\bar{x} = x\bar{e}_x + y\bar{e}_y$$

where $x\in[0,\infty]$ and $y\in[0,y_e(x)]$. For the narrow quasi-cylindrical vortex cores we consider here one has that

$$y_e(x) = y_e(x_o) + (x-x_o)y_e'(x_o) + \ldots$$

Substitution into the second term of Eq. (4.35), changing the integration variables from $(x,y)$ to $(\xi=x,\eta=y/y_e(x))$, we obtain:

$$\bar{u}_\gamma(\bar{x}_o) = \frac{1}{4\pi}\Gamma'(x_o)\int_{\eta=0}^{1}[y_e(x_o)\{\bar{e}_z I_1^1 + \bar{X}_o\times\bar{e}_y I_0^1\}$$

$$- y_e'(x_o)\{\bar{e}_z I_2^1 + \bar{X}_o\times\bar{e}_y I_1^1\}]d\eta + \ldots$$

Substitution of the expressions for $I_k^1$ of Table 3.4-6 and expansion with respect to $\varepsilon$ yields:

$$\bar{u}_\gamma(\bar{x}_o) = \frac{1}{2\pi}\Gamma'(x_o)y_e(x_o)(\bar{X}_o\times\bar{e}_y\int_{\eta=0}^{1}(\frac{d\eta}{|\bar{X}_o-y_e(x_o)\eta\bar{e}_y|^2}) + O(\varepsilon^2,\varepsilon^2\ln\varepsilon)$$

Carrying out the integration with respect to $\eta$ finally gives:

$$\bar{u}_\gamma(\bar{x}_o) = \frac{-1}{2\pi}\Gamma'(x_o)\{\tan^{-1}\frac{y_o}{z_o} - \tan^{-1}\frac{y_o-y_e(x_o)}{z_o}\}\bar{e}_x + O(\varepsilon^2,\varepsilon^2\ln\varepsilon) \qquad (4.37)$$

This velocity is directed in axial direction, order of magnitude $\varepsilon$. For $|\bar{x}_o| > y_e(x_o)$ this contribution is continuous. In the matching of the cross-flow plane velocity fields it plays no role.

*4.4.2 Matching of velocity fields*

Comparing the cross-flow plane velocity field due to the vortex-filament/feeding sheet model, given in Eq. (4.36), with the one due to the distributed vorticity core, given in Eq. (4.21b), shows that in order to match, the circumferential component of the velocity the vortex strength should equal

$$\Gamma(x) = 2\pi r_e V_e \qquad (4.38)$$

In order to also match the radial component we have to introduce in the vortex/feeding sheet model, besides the line vortex, a line source. The velocity field induced by a source distribution of strength $Q_v(x)$ is

$$\bar{u}_Q(x_o) = \frac{1}{4\pi}\int_{x=0}^{\infty}Q_v(x)\frac{\bar{r}}{|\bar{r}|^3}dx \qquad (4.39)$$

with $\bar{r} = \bar{x}_o-\bar{x}$.

In the narrow-core quasi-cylindrical approximation we write for $Q_v(x)$, similar to $\Gamma(x)$:

$$Q_v(x) = Q_v(x_o) + (x-x_o)Q_v'(x_o) + \ldots$$

Upon substitution into Eq. (4.39) one finds:

$$\bar{u}_Q(\bar{x}_o) = \frac{1}{4\pi}Q_v(x_o)\{\bar{e}_x I_1^1 + \bar{X}_o I_o^1\}$$

$$- \frac{1}{4\pi}Q_v'(x_o)\{\bar{e}_x I_2^1 + \bar{X}_o I_1^1\} + \ldots$$

where $I_k^1$ follows from Table 3.4-5, with $\bar{S} \equiv 0$ and $\bar{R} = \bar{X}_o$. Upon substitution and expansion for small $|\bar{X}_o| = O(x_o\varepsilon)$, one obtains with $Q_v = O(x_o\varepsilon^2)$:

$$\bar{u}_Q(\bar{x}_o) = \frac{1}{2\pi}Q_v(\bar{x}_o)\frac{\bar{X}_o}{|\bar{X}_o|^2} + O(\varepsilon^3, \varepsilon^2 l n \varepsilon) \tag{4.40}$$

This term is of order $\varepsilon$ and directed in radial direction.

Now matching the radial component of Eq. (4.21b) with Eq. (4.40) results in a source strength of magnitude

$$Q_v(x) = -\frac{\pi}{2}\frac{d}{dx}(r_e^2 U_e \Omega) \tag{4.41}$$

which is indeed $O(\varepsilon^2 x)$, i.e. one order of magnitude smaller than the circulation $\Gamma(x)$ of the vortex core.

It is therefore concluded that in order to have a consistent narrow-core quasi-cylindrical approximation the vortex core is to be modeled by a line vortex in combination with a line sink, the first one representing the circulation and the second one, one order of magnitude smaller, representing the "entrainment" of the vortex core.

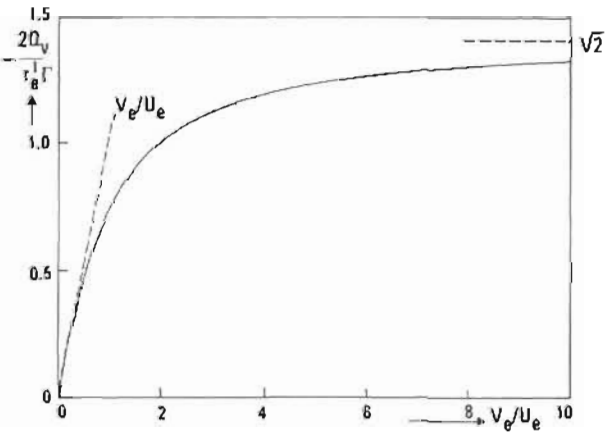


Fig. 4.11 Entrainment factor versus swirl

Assuming that the variation with x of $U_e$ and $V_e$ is of smaller order of magnitude than the variation with x of $r_e(x)$ then results in

$$\Gamma(x) = 2\pi r_e V_e \tag{4.42a}$$

$$Q_v(x) = -\pi r_e r_e' U_e\{(1 + 2(V_e/U_e)^2)^{\frac{1}{2}} - 1\} \tag{4.42b}$$

so that

$$\frac{Q_v}{\Gamma} = -\frac{1}{2}r_e' \frac{(1 + 2(V_e/U_e)^2)^{\frac{1}{2}} - 1}{V_e/U_e} \tag{4.42c}$$

depends on the local slope of the diameter of the core $r_e'$ and further solely on the swirl parameter $V_e/U_e$.

In Fig. 4.11 we plot the entrainment factor $Q_v/\Gamma$ divided by $-\frac{1}{2}r_e'$. It shows that the entrainment factor behaves like

$$\frac{Q_v}{\Gamma} = -\frac{1}{\sqrt{2}}r_e' \qquad \text{for } \frac{V_e}{U_e} \to \infty \tag{4.43a}$$

and

$$\frac{Q_v}{\Gamma} = -\frac{1}{2}r_e'\left(\frac{V_e}{U_e}\right) \qquad \text{for } \frac{V_e}{U_e} \to 0 \tag{4.43b}$$

The first linear relationship between entrainment and circulation has been used in our early attempts to account for the entrainment effects of vortex cores. The second, quadratic relationship may be useful for low-swirl vortex cores. Fig. 4.11 also indicates that for practical values of the swirl (i.e. near unity) the full expression, Eq. (4.42c), has to be used, as we will do in the present study.

It is also clear that for swirl parameters near 1 the entrainment will be small because $r_e'$, the semi-vertex angle of the vortex core, is small. For a sharp-edged delta wing the diameter of a vortex core is typically of the order of 30%-50% of the wing semi-span, i.e. $r_e' \sim 0.15\cot\Lambda - 0.25\cot\Lambda$. Furthermore, in the computational model $r_e$ is the length, in the cross-flow plane, of the feeding sheet which decreases as the length of the vortex sheet is increased. This implies that as the length of the vortex sheet is increased an increasing fraction of the entrainment is already accounted for by the rolled-up vortex sheet, leaving less to be modeled by the sink at the vortex axis. In the second part of this study we will investigate the influence of the modeling of the "residual" entrainment as a sink in some detail.

4.4.3 The entrainment of a vortex core

In the preceding section we found the entrainment via the matching of the velocity fields of the distributed vorticity core and the vortex-filament/feeding-sheet model. In this section we try to get some more insight in the physical meaning of this property associated with vortex cores that grow in strength along their axis.

It followed from the matching of the outer velocity field due to a distributed vorticity core and the one due to a vortex/source along the axis of the core that the vortex strength equals

$$\Gamma(x) = 2\pi r_e V_e$$

and the source strength is

$$Q_v(x) = -\frac{\pi}{2}\frac{d}{dx}(r_e^2 U_e \hat{\alpha})$$

Using the expression for the radial velocity component $u_r$ given in Eq. (4.10b) results in (see also Eq. (4.42b)

$$Q_v(x) = 2\pi r_e u_r(\theta=1;x)$$

$$= \int_{\partial S_{core}} \bar{u}.\bar{e}_n^c ds \qquad (4.44)$$

where $\partial S_{core}$ denotes the closed contour of the vortex core intersection with the plane x = const. and it is assumed that $\frac{d}{dx}U_e$ is negligibly small.
Note that $\bar{e}_n^c$ is the unit normal to $\partial S_{core}$ in the cross-flow plane, not the true normal to the 3D surface bounding the vortex core, see Fig. 4.12.

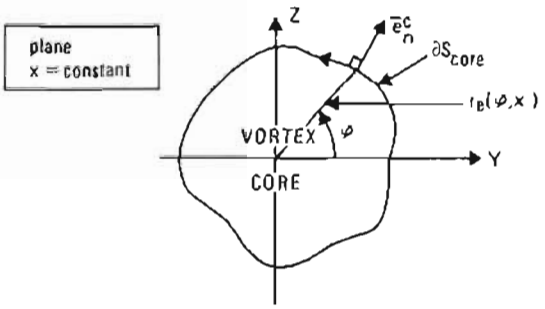


Fig. 4.12 Cross-section of vortex core

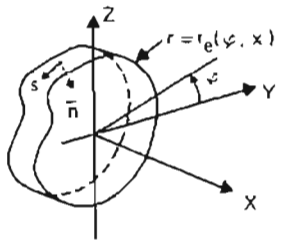


Fig. 4.13 Cross-section slice of vortex core

The source strength $Q_v$ can be expressed in terms of the axial mass transport by considering the conservation of mass for a slice of the vortex core. In the following we consider this for a slender vortex core of arbitrary cross-section, see Fig. 4.13.

The axial mass transport is

$$M(x) = \rho \iint_{\mathbb{S}_{core}} (\bar{u}.\bar{e}_x) dS \qquad (4.45)$$

where $\mathbb{S}_{core}$ is the cross-section of the core at x. Conservation of mass gives:

$$M(x+dx) = M(x) + \rho \int_x^{x+dx} dx \left( \int_{\partial S_{core}} \bar{u}.\bar{n} dS \right) \qquad (4.46a)$$

where $\partial S_{core}$ is the perimeter of the core cross-section and $\bar{n}$ the normal on the surface bounding the vortex core. This leads to

$$\frac{dM}{dx} = \rho \int_{\partial S_{core}} \bar{u}.\bar{n} ds \qquad (4.46b)$$

A point on the surface bounding the vortex core may be expressed as

$$\bar{x} = \bar{x}(x,\varphi)$$

$$= x\bar{e}_x + r_e(x,\varphi)\bar{e}_r$$

$$= x\bar{e}_x + (r_e\cos\varphi)\bar{e}_y + (r_e\sin\varphi)\bar{e}_z$$

so that

$$\bar{x}_x = \bar{e}_x + r_e'\bar{e}_r$$

$$\bar{x}_\varphi = (r_e\cos\varphi)_\varphi \bar{e}_y + (r_e\sin\varphi)_\varphi \bar{e}_z$$

and

$$\bar{x}_x \times \bar{x}_\varphi = r_e' r_e \bar{e}_x - (r_e\sin\varphi)_\varphi \bar{e}_y + (r_e\cos\varphi)_\varphi \bar{e}_z$$

while the normal vector $\bar{n} = (\bar{x}_x \times \bar{x}_\varphi)/|\bar{x}_x \times \bar{x}_\varphi|$ becomes:

$$\bar{n} = \{r_e' r_e \bar{e}_x - (r_e\sin\varphi)_\varphi \bar{e}_y + (r_e\cos\varphi)_\varphi \bar{e}_z\}/(r_e^2(1+r_e'^2) + r_{e_\varphi}^2)^{\frac{1}{2}}$$

Splitting into cross-flow plane quantities and axial quantities leads with

$$\bar{e}_n^c = \{(r_e\sin\varphi)_\varphi \bar{e}_y - (r_e\cos\varphi)_\varphi \bar{e}_z\}/(r_e^2 + r_{e_\varphi}^2)^{\frac{1}{2}}$$

and

$$ds = (r_e^2 + r_{e_\varphi}^2)^{\frac{1}{2}} d\varphi$$

to

$$\frac{dM}{dx} = -\rho \int_{\varphi=0}^{2\pi} (\bar{u}.\bar{e}_n^c) \frac{r_e^2 + r_{e_\varphi}^2}{[r_e^2(1+r_e'^2)+r_{e_\varphi}^2]^{\frac{1}{2}}} d\varphi + \rho \int_{\varphi=0}^{2\pi} (\bar{u}.\bar{e}_x) r_e' r_e \frac{(r_e^2 + r_{e_\varphi}^2)^{\frac{1}{2}}}{[r_e^2(1+r_e'^2)+r_{e_\varphi}^2]^{\frac{1}{2}}} d\varphi \tag{4.47}$$

where $\bar{u}$ is the velocity at the edge of the vortex core, i.e. $\bar{u} = \bar{u}(\Theta=1;x)$.

For <u>slender</u> cores, one may neglect $r_e'^2$, which results in

$$\frac{dM}{dx} = -\rho \int_{\varphi=0}^{2\pi} (\bar{u}.\bar{e}_n^c)(r_e^2 + r_{e_\varphi}^2)^{\frac{1}{2}} d\varphi + \rho \int_{\varphi=0}^{2\pi} (\bar{u}.\bar{e}_x) r_e' r_e d\varphi$$

$$= -\rho \int_{\partial S_{core}} (\bar{u}.\bar{e}_n^c) dS + \rho \int_{\varphi=0}^{2\pi} (\bar{u}.\bar{e}_x) \left(\frac{d}{dx} \int_{r=0}^{r_e} r dr\right) d\varphi \tag{4.48a}$$

Assuming that along the edge of the core the variation with $\varphi$ of $(\bar{u}.\bar{e}_x)$ is of higher order, one finally obtains

$$\frac{dM}{dx} = -\rho \int_{\partial S_{core}} (\bar{u}.\bar{e}_n^c) ds + \rho (\bar{u}.\bar{e}_x)_e \left(\frac{d}{dx} S_{core}\right) \tag{4.48b}$$

The first term in Eq. (4.48b) is recognized as minus the source strength $Q_v$ divided by the density $\rho$, see Eq. (4.44), leading to

$$Q_v(x) = -\frac{1}{\rho}\frac{dM}{dx} + (\bar{u}.\bar{e}_x)_e \left(\frac{d}{dx} S_{core}\right) \tag{4.49}$$

where $M(x)$ is defined in Eq. (4.45).

An alternative expression is obtained from Eq. (4.48a) by assuming that the variation with x of $(\bar{u}.\bar{e}_x)_e$ is small, resulting in

$$Q_v(x) = -\frac{1}{\rho}\frac{dM}{dx} + \frac{d}{dx} \int_{\varphi=0}^{2\pi} \left\{ \int_{r=0}^{r_e} (\bar{u}.\bar{e}_x)_e r dr \right) d\varphi$$

$$= -\frac{d}{dx}\left[ \int_{\varphi=0}^{2\pi} d\varphi \left[ \int_{r=0}^{r_e} \bar{e}_x.(\bar{u}(r,\varphi) - \bar{u}(r_e,\varphi)) r dr \right) d\varphi \right] \tag{4.50}$$

which indicates that the entrainment equals the gradient with respect to x of the increment in the axial volume transport.

In conical flow the velocity components are constant on rays through the apex, while the geometry scales linearly with the distance x from the apex. Taking Kx as scaling factor then results in, using Eq. (4.49):

$$Q_v(x) = 2K^2 x' - \iint_{S_{core}} [\bar{e}_x.\bar{u}(\xi,\eta) d\xi d\eta + (\bar{e}_x.\bar{u}_e) \iint_{S_{core}} d\xi d\eta] \tag{4.51}$$

where $\xi = y/Kx$ and $\eta = z/Kx$ and the term inside the brackets is independent of the cross-flow plane considered.

4.5 Numerical example

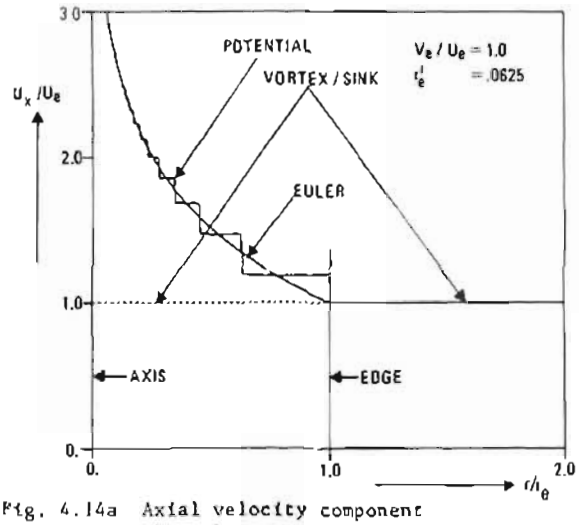


Fig. 4.14a Axial velocity component through vortex core

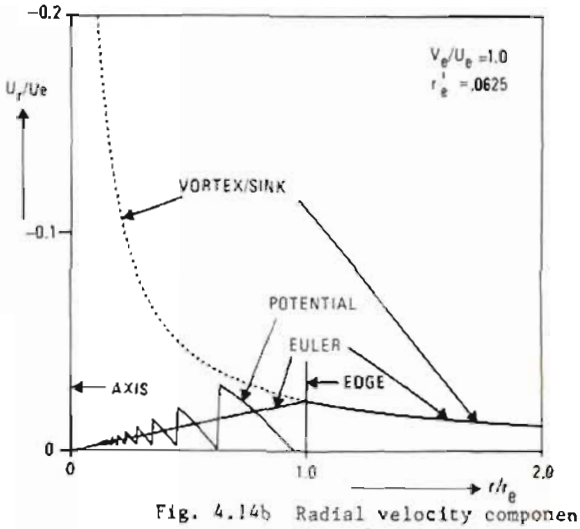


Fig. 4.14b Radial velocity component through vortex core

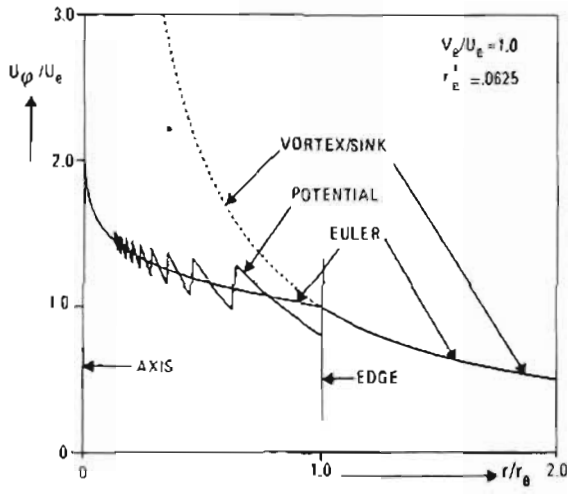


Fig. 4.14c Circumferential velocity component through vortex core

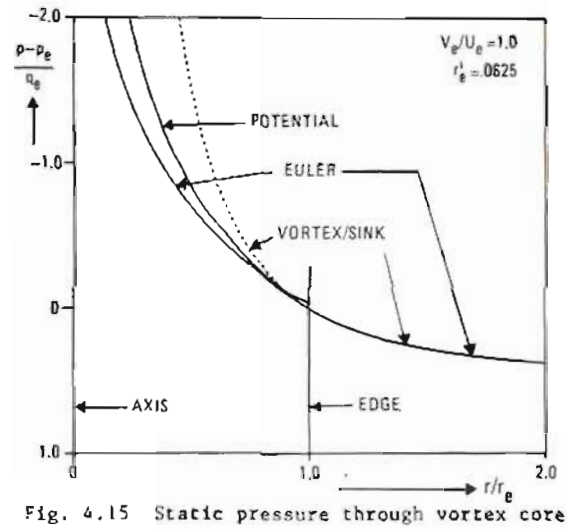


Fig. 4.15 Static pressure through vortex core

The expressions derived for the velocity components depend on the swirl parameter $V_e/U_e$, while the radial component also depends (linearly) on $r'_e$.

In this section we consider the numerically evaluated characteristics of a vortex core with swirl parameter $V_e/U_e$ of 1.0, a value found in experiments for the leading-edge vortex core above a 76-deg swept delta wing at 20 deg incidence. The parameter $r'_e$, the slope of the radius of the vortex core, corresponding to this case is 0.0625.

Figs. 4.14a-c show the distribution of the velocity components through the vortex core for the three models considered in this chapter. The figures show the solution for the distributed vorticity core, i.e. Eqs. (4.10a-c) or Eq. (4.22b) for $\theta = r/r_e \leq 1$ and Eq. (4.21b) for $r/r_e > 1$, the vortex sheet solution, i.e. Eqs. (4.33a-c) and the vortex/sink solution, which matches the Euler solution for $\theta > 1$ and formally does not apply for $\theta < 1$.

At the axis, $\theta=0$, the axial velocity component of the Euler solution tends to infinity like $-\ln\theta$. The axisymmetric part of the potential solution with the rolled-up vortex sheet has the same behaviour while the non-axisymmetric part, which jumps across the vortex sheet, tends to zero like $\theta\sqrt{(-\ln\theta)}$. The vortex/sink solution (the feeding sheet has been left out here) has no contribution in axial direction, it is just a model employed to simulate the external velocity field, not the internal one!

The radial velocity component (Fig. 4.14b) is one order of magnitude smaller than the axial or circumferential velocity component. The Euler solution is linear in $\theta$ inside the core and varies like $1/\theta$ for $\theta > 1$, i.e. outside the vortex core it matches the vortex/sink solution. The non-axisymmetric part of the vortex sheet solution jumps across the vortex sheet and behaves like $\theta^2(-\ln\theta)\sqrt{(-\ln\theta)}$ for $\theta\to 0$.

The circumferential velocity component (Fig. 4.14c) of the Euler solution varies like $\sqrt{(-\ln\theta)}$ for $\theta\to 0$, the non-axisymmetric part of the vortex sheet solution is discontinuous across the vortex sheet and behaves like $\theta(-\ln\theta)$ for $\theta\to 0$.

The velocity distribution of the Euler solution is qualitatively similar to the one observed in experiment. However, in the immediate neighborhood of the axis, where the computed velocity is (weakly) singular, viscous effects and probably compressibility effects will influence the velocity distribution to a large extent.

The static pressure distribution $(p-P_e)/q_e$, with $q_e = \frac{1}{2}\rho\{1+(V_e/U_e)^2+(\frac{1}{2}\hat{\alpha}r')^2\}$, is presented in Fig. 4.14d. The static pressure coefficient decreases very rapidly to very low values near the axis of the core, i.e. for $\theta\to 0$. At $\theta=1$ the pressure coefficient of the Euler solution smoothly joins the one due to the vortex/sink. Note that, indeed, for the asymptotic vortex-sheet solution the static pressure is continuous across the vortex sheet.

At $\theta=1$ the static pressure $(p-P_e)/q_e = 1 - |\bar{u}|^2/\{U_e^2+(\frac{1}{2}\hat{\alpha}r')^2U_e^2+V_e^2\}$ is, a follows from Eq. 4.33, order $(r')^2$, a term we should have omitted, formally speaking.

## 5 POTENTIAL FLOW FORMULATIONS USED IN PRESENT STUDY

In this chapter the general formulation to solve the potential flow problem at hand is discussed. We begin with the formulation of a method for the three-dimensional flow about general configurations with free vortex sheets. Solving this nonlinear 3D flow problem is a formidable task, which is the motivation to introduce approximations that reduce the fully 3D problem to a sequence of quasi-2D problems. Two formulations in a more simple, but approximate, quasi-2D framework will be discussed:

- the formulation based on the slender-body type of approximation
- the two-dimensional time-dependent analogy.

The computational method for the fully 3D problem, described in the second part of this thesis, will be suited for relatively simple configurations only, namely for thin (starboard-port side) symmetric, low-aspect-ratio wings with a vortex sheet connected all along its leading and trailing edge. The computational methods developed for the solving the problem in the less extensive quasi-2D frameworks will be more general. For the slender-body type of approximation the method to be described will be applicable to slender configurations with quite general cross-sections with multiple vortex sheets.
The method employing the 2D time-dependent approach will be suited for vortex wakes of general topology. In the present study we do not consider the 3D wake roll-up problem, where usually the interaction of the free vortex sheets with the flow near the wing is not as strong as for leading-edge vortex flow. However, the general formulation for the 3D problem, presented in the first section of this chapter can equally be applied to 3D vortex wakes.

The formulation in the quasi-2D frameworks will be derived here from the fully 3D framework, providing an insight in the validity of the various approximations.

### 5.1 Three-dimensional flow with free vortex sheets

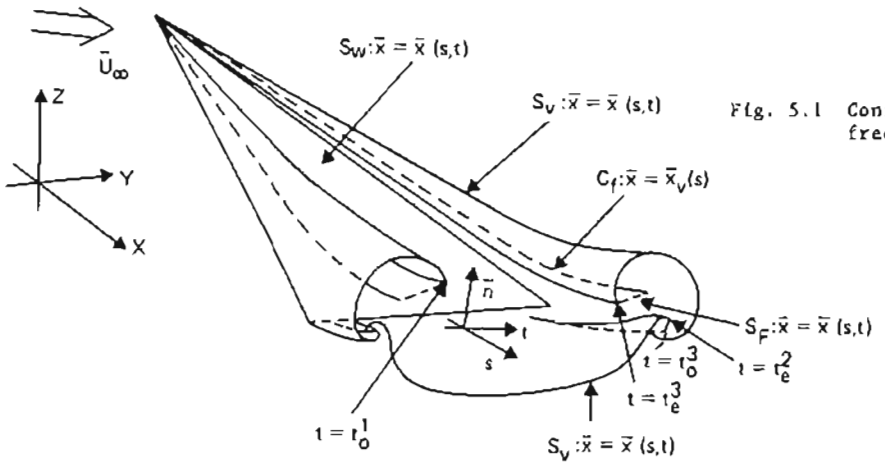


Fig. 5.1 Configuration with free vortex sheet

#### 5.1.1 Integral representation for the solution

In Chapter 3 it has been derived that the velocity potential and the velocity field can be expressed as the sum of the contributions due to (see Fig. 5.1):

- the free stream $\bar{U}_\infty$
- a source distribution $q$ on the solid surfaces $S_W$
- a doublet distribution $\mu$ on the solid surfaces $S_W$ and on the free vortex sheets and wakes $S_V$.

Here any rolled-up portion of the free vortex sheets, representing a vortex core, is modeled by a vortex-filament/feeding-sheet combination. The strength of the vortex filament $C_f$ and the doublet distribution on the feeding sheet $S_F$ are expressed in terms of the doublet distribution on the unrolled part of the vortex sheet (see Figs 3.13 and 3.14). The entrainment of the vortex core is accounted for through a source distribution on $C_f$.

In the following we summarize the expressions for the velocity and potential as derived in Chapter 3. The velocity potential $\Phi$ at $\bar{x}_o$ is expressed as, see Eq. (3.14):

$$\Phi(\bar{x}_o) = \bar{U}_\infty \cdot \bar{x}_o + \varphi_q(\bar{x}_o) + \varphi_\mu(\bar{x}_o) + \varphi_Q(\bar{x}_o) \tag{5.1a}$$

with

$$\varphi_q(\bar{x}_o) = -\frac{1}{4\pi}\iint_{S_W} q(s,t)\frac{dS}{|\bar{r}|} \tag{5.1b}$$

$$\varphi_\mu(\bar{x}_o) = \frac{1}{4\pi}\iint_{S_{W+V+F}} \mu(s,t)\frac{\bar{n}\cdot\bar{r}}{|\bar{r}|^3}dS \tag{5.1c}$$

$$\varphi_Q(\bar{x}_o) = -\frac{1}{4\pi}\int_{C_f} Q_V(s)\frac{|d\bar{\ell}|}{|\bar{r}_V|} \tag{5.1d}$$

where $\bar{r} = \bar{x}_o - \bar{x}(s,t)$, $\bar{r}_V = \bar{x}_o - \bar{x}_V(s)$ and $d\bar{\ell} = \bar{x}_V'(s)ds$. The geometry of and the source and doublet distribution on $S_W$, $S_V$ and $S_F$ are expressed in terms of curvi-linear surface coordinates $s$ and $t$. The unit normal $\bar{n}$ (see Fig. 5.1) and the surface element $dS$ are expressed in terms of the geometry $\bar{x} = \bar{x}(s,t)$, see Eq. (3.11b) and Eq. (3.10c) respectively.

The source strength $Q_v$, which represents the entrainment of the vortex core, follows from the relation Eq. (4.42b):

$$Q_v(s) = -\pi r_e r'_e U_e [(1 + 2(V_e/U_e)^2)^{\frac{1}{2}} - 1] \tag{5.1e}$$

where we approximate $U_e$ and $V_e$ by

$$U_e = U_\infty$$

$$V_e = \Gamma(s)/2\pi r_e$$

respectively, while $r_e(s)$ is taken as the length of the feeding sheet and $\Gamma(s)$ is the strength of the vortex core.

Across the singularity distribution the velocity potential is discontinuous, see Eq. (3.14d):

$$\Delta\phi(\bar{x}(s,t)) = \phi(\bar{x}(s,t)^+) - \phi(\bar{x}(s,t)^-) = \mu(s,t) \tag{5.1f}$$

The velocity vector $\bar{u}$ at $\bar{x}_o$ is expressed as, see Eq. (3.15):

$$\bar{u}(\bar{x}_o) = \bar{U}_\infty + \bar{u}_q(\bar{x}_o) + \bar{u}_\mu(\bar{x}_o) + \bar{u}_Q(\bar{x}_o) \tag{5.2a}$$

with

$$\bar{u}_q(\bar{x}_o) = \frac{1}{4\pi}\iint_{S_w} q(s,t)\frac{\bar{r}}{|\bar{r}|^3}dS \tag{5.2b}$$

$$\bar{u}_\mu(\bar{x}_o) = \frac{1}{4\pi}\iint_{S_{w+v+F}} \bar{\gamma}(s,t)\times\frac{\bar{r}}{|\bar{r}|^3}dS - \frac{1}{4\pi}\int_{C_f}[\mu(s,t_o^i)-\mu(s,t_e^{i-1})]\frac{d\bar{\ell}\times\bar{r}_v}{|\bar{r}_v|^3} \tag{5.2c}$$

$$\bar{u}_Q(\bar{x}_o) = \frac{1}{4\pi}\int_{C_f} Q_v(s)\frac{\bar{r}_v}{|\bar{r}_v|^3}|d\bar{\ell}| \tag{5.2d}$$

where $\bar{r} = \bar{x}_o - \bar{x}(s,t)$. Furthermore, the vortex filament term contains $\bar{r}_v = \bar{x}_o - \bar{x}_v(s)$ and the line element $d\bar{\ell} = \bar{x}'_v ds$, while the term inside the square brackets equals the strength of the vortex filament (see also Fig. 5.1).

The surface vorticity $\bar{\gamma}$, appearing in Eq. (5.2c), is defined in terms of the gradient of the doublet distribution, i.e.

$$\bar{\gamma} = \bar{n} \times \bar{\nabla}\mu \tag{5.2d}$$

which in Eq. (3.15d) is expressed in terms of $\frac{\partial\mu}{\partial s}$ and $\frac{\partial\mu}{\partial t}$.

Across the surface singularity distribution the velocity is discontinuous, see Eqs. (3.15f and g):

$$\Delta\bar{u}(\bar{x}(s,t)) = \bar{u}(\bar{x}(s,t)^+) - \bar{u}(\bar{x}(s,t)^-) = q(s,t)\bar{n} + \bar{\gamma}\times\bar{n} \tag{5.2e}$$

The integrals in Eqs. (5.1) and (5.2) include the contribution of each individual patch of the solid surface, each portion of the vortex sheet and all feeding sheets and vortex filaments. As indicated in Fig. 5.1 the topology of the free vortex sheets is assumed to be such that a vortex sheet is either connected to a solid surface (at a prescribed and fixed position) or to a feeding sheet (one branch of a vortex core). A vortex filament is fed by one or two feeding sheets for the case of a single or double-branched vortex core, respectively.

When evaluating the surface integrals in Eqs. (5.2b and c) computing time can be saved by noting that there is a correspondence between the velocity $\bar{u}_q(\bar{x}_o;q)$ induced at $\bar{x}_o$ by a source distribution $q$ and the velocity $\bar{u}_\gamma(\bar{x}_o;\bar{\gamma})$ induced by a surface vorticity distribution $\bar{\gamma}$. The correspondence can be expressed as

$$\begin{aligned}\bar{u}_\gamma(\bar{x}_o;\bar{\gamma}) &= \bar{e}_x \times \bar{u}_q(\bar{x}_o;q=\bar{e}_x\cdot\bar{\gamma}) \\ &+ \bar{e}_y \times \bar{u}_q(\bar{x}_o;q=\bar{e}_y\cdot\bar{\gamma}) \\ &+ \bar{e}_z \times \bar{u}_q(\bar{x}_o;q=\bar{e}_z\cdot\bar{\gamma})\end{aligned} \tag{5.3}$$

In some cases the source distribution cannot be used to simulate the flow. An example is the case of the infinitesimally thin wing, where the normal component of the velocity is zero on both sides of $S_w$, i.e. does not have the discontinuity inherently associated with a sources distribution of nonzero strength, see Eq. 5.2e.

In the case of a thick configuration a source distribution is not required when employing the Neumann boundary condition. However, as shown in section 3.7, the use of the Dirichlet condition requires the specific choice of the strength of the source distribution as $q = -\bar{U}_\infty\cdot\bar{n}$.

5.1.2 Description of the geometry

In the present study the surface $S_w$ of the configuration, $S_v$ of the vortex sheets and $S_F$ of the feeding sheets are expressed in terms of curvi-linear surface coordinates s and t in the form $\bar{x} = \bar{x}(s,t)$. Here s is usually chosen to be in direction of the x-coordinate, while t is chosen as a parameter along the section of the configuration with a cross-flow plane. The introduction of these surface coordinates, in contrast with the description of the surface in the form $z = z(x,y)$, avoids possible problems with $z(x,y)$ becoming multiple-valued, resulting in infinite derivatives, etc. as can easily become the case for the freely rolling-up vortex sheets (see Fig. 5.1).

In terms of the curvi-linear surface coordinates, the vectors $\bar{x}_s$ and $\bar{x}_t$ are directed along the curves t = constant and s = constant, respectively (see Fig. 3.5a). The unit vector $\bar{n}$ normal to the surface is thus proportional to $\bar{x}_s \times \bar{x}_t$, as already given in Eq. (3.11b), i.e.:

$$\bar{n} = (\bar{x}_s \times \bar{x}_t)/|\bar{x}_s \times \bar{x}_t| \tag{5.4a}$$

The s and t coordinate lines are not necessarily orthogonal, but never parallel. The surface element dS becomes:

$$dS = |\bar{x}_s \times \bar{x}_t| ds dt \tag{5.4b}$$

The geometry of the feeding sheets consists of straight-line segments connecting the edge $\bar{x} = \bar{x}(s,t_e)$ of the vortex sheet with the vortex filament at $\bar{x} = \bar{x}_v(s)$. So that the feeding sheet can be described as:

$$\begin{aligned} \bar{x} &= \bar{x}_p(s,t) \\ &= \bar{x}(s,t_e) + t(\bar{x}_v(s) - \bar{x}(s,t_e)), \text{ for } t \in [0,1] \end{aligned} \tag{5.4c}$$

Finally, the line element $d\bar{\ell}$ along the vortex filament becomes in terms of the parameter s along the filament:

$$d\bar{\ell} = \bar{x}_v' ds \tag{5.4d}$$

In the present study the s and t surface parameters are chosen in a for the specific geometry suitable way. For instance, for $S_w$ and $S_v$ the t parameter (Fig. 5.1) is mostly chosen as the scaled arc length along the curves s = constant. By choosing the scale factor equal to the total arc length along that same curve, $t \in [0,1]$ for each curve s = constant. By scaling s in a similar fashion (each portion of) the surface is mapped onto a rectangular domain in the (s,t) plane, which is convenient for setting up the discretization used in the computational method.

5.1.3 Nonlinearity of the problem

The problem of the flow about configurations with free vortex sheets is nonlinear in terms of the boundary conditions. The boundary conditions, derived in section 3.7, that are not already satisfied implicitly by formulating the solution in terms of surface singularity distributions, are summarized here:

(i) The solid surfaces $S_w$ are stream surfaces, i.e.:

$$\bar{u}.\bar{n} = 0 \quad \text{for } \bar{x} = \bar{x}(s,t)^+ \text{ on } S_w \tag{5.5a}$$

i.e. on that side of the surface wetted by the flow. For infinitesimally thin configurations q = 0, for thick configurations there is still a choice. For thick configurations there is the alternative of satisfying the Dirichlet condition for the internal flow (see section 3.7), i.e.

$$-\tfrac{1}{2}\mu + \varphi^P = 0 \quad \text{for } x = \bar{x}(s,t)^- \text{ on } S_w \tag{5.5b}$$

where $\varphi^P$ is the Principal Value of the perturbation potential, while simultaneously the source distribution follows from:

$$q = -\bar{U}_\infty.\bar{n} \tag{5.5c}$$

Condition (5.5a) or (5.5b and c) can be thought of as the condition that determines the strength of the singularity distribution on $S_w$.

(ii) The vortex sheets $S_v$ are stream surfaces, i.e.:

$$\bar{u}^P.\bar{n} = 0 \quad \text{for } \bar{x} = \bar{x}(s,t) \text{ on } S_v \tag{5.6a}$$

where $\bar{u}^P$ is the Principal Value of the velocity field, here $\bar{u}^P(\bar{x}(s,t)) = \frac{1}{2}(\bar{u}(\bar{x}(s,t)^+) + \bar{u}(\bar{x}(s,t)^-))$. The second condition that applies on $S_v$ is that the pressure is continuous across $S_v$, which can be expressed as, see Eqs. (3.19c and d):

$$\bar{u}^P \times \bar{\gamma}.\bar{n} = 0 \quad \text{for } \bar{x} = \bar{x}(s,t) \text{ on } S_v \tag{5.6b}$$

The two conditions (5.6a) and (5.6b) are the conditions that determine the doublet distribution $\mu(s,t)$ and the position $\bar{x}(s,t)$ of the vortex sheets $S_v$.

(iii) The vortex-filament/feeding-sheets combination $C_f + S_F$ is force free, i.e.

$$d\bar{F}_v + d\bar{F}_F + d\bar{F}_Q = 0 \quad \text{for } \bar{x} = \bar{x}_v(s) \text{ on } C_f \tag{5.7}$$

where in case of a double-branched vortex $d\bar{F}_F$ is the force on both feeding sheets. This condition determines the position $\bar{x}_v(s)$ of the vortex filament $C_f$.
The second condition that applies here is the entrainment relation which expresses $Q_v$ in terms of the velocity at the edge of the core and the length of the feeding sheet, see Eq. 5.1e.

The far-field boundary condition is satisfied automatically by the integral representation. The Kutta condition at $\partial S_w$ will be enforced by requiring continuity of the doublet distribution at the edges of $S_w$ and satisfying the conditions on $S_v$.

The boundary-value problem at hand is highly nonlinear because of the unknown position of the vortex sheets and filaments as they appear in the integral representation for the velocity field, e.g. Eqs. (5.1) and (5.2).
The solution of this nonlinear flow problem in the fully three-dimensional framework presents a formidable task. This forms the primary motivation to consider still further approximations leading to a simpler problem in a less extensive framework than the three-dimensional one. A second motivation is that the solution procedure for the nonlinear problem will be an iterative procedure that requires an initial guess sufficiently close to the ultimate solution of the nonlinear problem. The results of the quasi-2D flow method will help in constructing a suitable initial guess for the 3D flow method.
A possible third reason might be that in some cases the computationally less expensive quasi-2D flow method will give the investigator sufficient insight into the flow problem at hand and a fully 3D flow simulation is not required.

## 5.2 Quasi-two-dimensional description in cross-flow planes - Approximation for slender configurations and slowly varying vortex wakes

The geometry of configurations with leading-edge vortex flow and also the geometry of the vortex wake trailing behind the trailing edge of airplane configurations may be such that the flow quantities vary much less in streamwise direction than in cross-flow planes. This suggests the use of the slender-body approximation, in which derivatives in streamwise direction are one order of magnitude smaller than the derivatives in cross-flow planes.
In the slender-body framework it is assumed that for cases with lift the geometry extends to infinity downstream, i.e. from $s=0$ to $s=s_\infty=\infty$. This implies that a trailing edge cannot be accommodated in this framework. Another unpleasant feature of the approximation is that, for instance in subsonic leading-edge vortex flow it does not apply right at the apex of the configuration. Consequently one has to assume that this local violation of the underlying assumptions is not important for the solution in cross-flow planes downstream of the apex. A similar difficulty arises for the case of wake vortex flow, there at the trailing edge of the configuration.

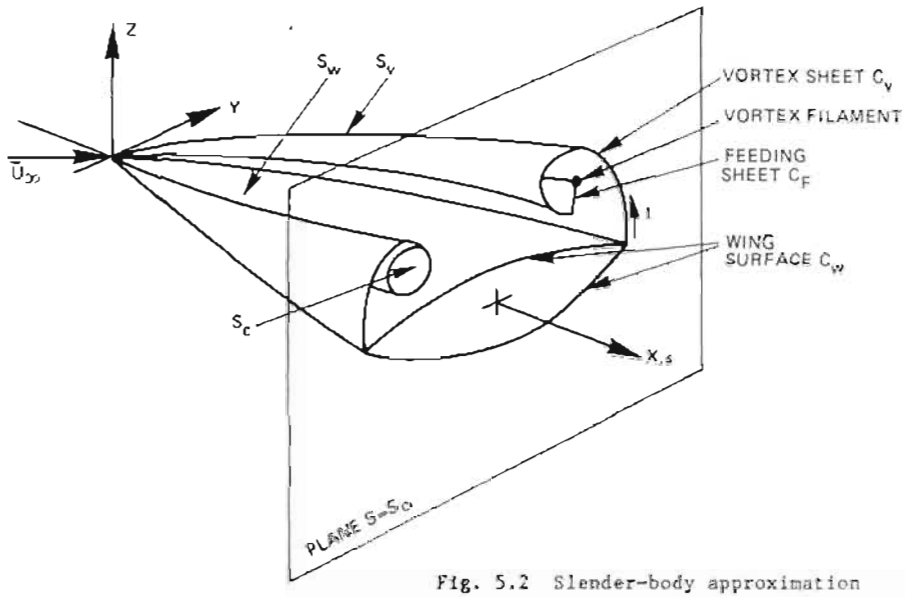


Fig. 5.2 Slender-body approximation

### 5.2.1 Description of the cross-flow plane geometry

In this section we will derive the expressions within the slender-body framework by expanding the expressions for 3D flow for slow variations in x-direction. To this aim we introduce the notation in which a particular plane *) $x = s =$ constant is considered (see Fig. 5.2). Vectors are decomposed into one component in x-direction and two components in the plane $x =$ constant. Quantities within a cross-flow plane are represented by capitals. For instance, the position of a point in the cross-flow plane $x = s$ is expressed as

$$\bar{x} = s\bar{e}_x + \bar{X} \tag{5.8a}$$

where it is assumed that $s=0$ corresponds with the first cross-section (e.g. apex) of the configuration and it is implied that $\bar{e}_x.\bar{X} \equiv 0$.

In particular we will consider the source and doublet distribution on $S_w$ and $S_v$. In the slender-body approximation the surfaces $S_w$ and $S_v$ are expressed as

$$\bar{x} = s\bar{e}_x + \bar{X}(t;s) \tag{5.8b}$$

where it is implied that $\bar{e}_x.\bar{X}(t;s) \equiv 0$. In a similar fashion we write for the doublet and source distribution

$$\mu = \mu(t;s) \tag{5.8c}$$

and

$$q = q(t;s) \tag{5.8d}$$

respectively.

*) In the present study we use cross-flow planes, i.e. planes perpendicular to the x-axis of the configuration. However, the quasi-cylindrical approximation could also be formulated using arbitrary 3D surfaces $s =$ constant instead of simple planes.

In the notation (t;s) s indicates the cross-flow plane considered and t the parameter along the intersection of the geometry with the plane x=s. In the following we denote differentiation with respect to s by the subscript s and differentiation with respect to t by a prime.

In the slender-body approximation it is assumed that $|\bar{X}'|$, $\mu'/U_\infty$, $q'/U_\infty$, etc. are all of order unity, while $|\bar{X}_s|$, $\mu_s/U_\infty$, $q_s/U_\infty$, etc. are all of order $\varepsilon$. Without loss of generality we can take $U_\infty$ equal to unity and omit it from the analysis. However, to keep track of the proper dimension of all quantities we choose to retain $U_\infty$ in all of the expressions that follow, taking $U_\infty=1$ in the order of magnitude estimates. In the present study it is assumed that the slenderness parameter $\varepsilon$ is small and that $\varepsilon\to 0$ as the vertex angle (or span/s) is reduced to zero.

Substitution of Eq. (5.8b) into the expression for the surface normal $\bar{n}$, Eq. (5.4a), then yields to order $\varepsilon^2$:

$$\bar{n} = \bar{e}_n - (\bar{X}_s.\bar{e}_n)\bar{e}_x + O(\varepsilon^2) \tag{5.9a}$$

where $\bar{e}_n$ is the unit normal to the trace of the surface in the cross-flow plane defined, as in the 2D case, in Eq. (3.11d), i.e.

$$\bar{e}_n = \bar{e}_x \times \bar{e}_t \tag{5.9b}$$

with

$$\bar{e}_t = \bar{X}'/|\bar{X}'| \tag{5.9c}$$

the unit vector tangential to the trace of the surface in the plane s = constant (see Fig. 5.3). Eq. (5.9a) expresses that the true 3D normal is tilted order $\varepsilon$ out of the cross-flow plane s = constant.

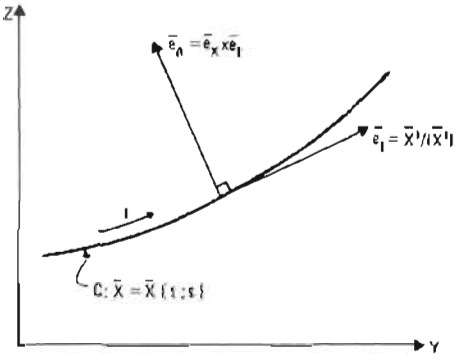


Fig. 5.3 Trace C of surface S in plane s=constant

The surface element dS, defined in Eq. (5.4a) can be expressed as

$$dS = |\bar{X}'|dsdt\{1 + O(\varepsilon^2)\} \tag{5.9d}$$

In the framework of the slender-body approximation the position of the vortex filament is expressed as

$$\bar{x} = s\bar{e}_x + \bar{X}_v(s) \tag{5.9e}$$

where $|\bar{X}_v|$ is of order $\varepsilon$. The line element of the vortex filament then can be expressed as

$$d\bar{\ell} = (\bar{e}_x + \bar{X}_{v_s})ds \tag{5.9f}$$

Also the description of the feeding sheet, Eq. (5.4c), can be expanded as

$$\bar{x} = s\bar{e}_x + \bar{X}(t_e;s) + t(\bar{X}_v(s) - \bar{X}(t_e;s)) \tag{5.9g}$$

Similarly one finds for the surface vorticity $\bar{\gamma}$, in Eq. (3.15d) expressed in terms of derivatives of $\mu$:

$$\bar{\gamma} = -(\mu'\bar{e}_x + \mu'\bar{X}_s - \mu_s\bar{X}')/|\bar{X}'| + O(\varepsilon^2) \tag{5.10}$$

In this expression the first term, the streamwise component of the vorticity, is of order unity. The second and third terms are components of the vorticity in the cross-flow plane itself, both small of order $\varepsilon$.

5.2.2 Expansion of the integral representation

In order to expand the surface integrals in Eqs. (5.1) and (5.2) the so-called tangent-cone approximation, already introduced in section 4.2.2 is used. In this approach it is assumed that, for the purpose of calculating the integral expressions in the plane, $s=s_o$, the geometry is conical, extending from $s=0$ to $s=\infty$, the slope of the cone being equal to the local streamwise slope, i.e.

$$\bar{X}(t;s) = \bar{X}(t;s_o) + (s-s_o)\bar{X}_s(t;s_o) \tag{5.11a}$$

$$\bar{X}_v(s) = \bar{X}_v(s_o) + (s-s_o)\bar{X}_{v_s}(s_o) \tag{5.11b}$$

Also for the singularity distributions we write

$$\mu(t;s) = \mu(t;s_o) + (s-s_o)\mu_s(t;s_o) \tag{5.11c}$$

$$q(t;s) = q(t;s_o) + (s-s_o)q_s(t;s_o) \tag{5.11d}$$

$$Q_v(s) = Q_v(s_o) + (s-s_o)Q_{v_s}(s_o) \tag{5.11e}$$

This approximation, consistent with the slender-body approximation, implies that the configuration does not deviate much from a conical configuration, which can be expressed as

$$|\bar{X}(t;s)/s - \bar{X}(t;s_o)/s_o| \ll 1, \text{ for all } s$$

Furthermore the plane $s=s_o$ must not be too close to the apex ($s=0$) or trailing-edge of the configuration or to any discontinuities in the streamwise slope of the configuration.
In the present quasi-2D framework we aim at developing expressions for the velocity potential and velocity such that for points near the configuration, i.e. for $\bar{X}_o \sim O(\varepsilon s_o)$, the velocity can be evaluated to $O(\varepsilon^2)$.

The velocity potential and velocity induced in the plane $s=s_o$ by the surface singularity distributions is obtained by substitution of Eqs. (5.8-11) in Eqs. (5.1-2), followed by integration with respect to s from 0 to $\infty$ and expansion in terms of $\varepsilon$.

The velocity potential induced at $\bar{x}_o = s_o\bar{e}_x + \bar{X}(s_o)$ by the source distribution becomes, retaining only the linear terms in $(s-s_o)$:

$$\varphi_q(\bar{x}_o) = -\frac{1}{4\pi}\int_{C_w} q I_o^o dC(t;s_o)$$

$$+\frac{1}{4\pi}\int_{C_w}\left(q_s + \frac{\bar{X}'\cdot\bar{X}'_s}{|\bar{X}'|^2}q\right)I_1^o dC(t;s_o) \qquad (5.12a)$$

with

$$I_k^o = \lim_{s_\infty\to\infty}\left[\int_{s_\infty}^{0}\frac{(s_o-s)^k ds}{|\bar{R}+(s_o-s)(\bar{e}_x+\bar{X}_s)|}\right] \qquad (5.12b)$$

where $dC = |\bar{X}'(t;s)|dt$, $\bar{R} = \bar{X}(s)-\bar{X}(t;s_o)$ and all further quantities are evaluated in the cross-flow plane $s=s_o$, e.g. $q = q(t;s_o)$, etc. The $I_k^o$ integrals are evaluated, to order $\varepsilon^2$, in Table 3.1-3. Substitution of $I_k^o$ into Eq. (5.12c) results in:

$$\varphi_q(\bar{x}_o) = \frac{1}{2\pi}\int_{C_w} q(t;s)\ln\left(\frac{|\bar{R}|}{s_o}\right)dC(t;s_o)$$

$$-\frac{1}{4\pi}Q(s_o)\ln(4s_\infty/s_o)$$

$$+\frac{1}{4\pi}Q_s(s_o)(2s_o-s_\infty) + O(s_o\varepsilon^3, s_o\varepsilon^2\ln\varepsilon) = \Phi_q(\bar{X}(s_o)) \qquad (5.12c)$$

where

$$Q(s_o) = \int_{C_w} q(t;s_o)dC(t;s_o) \qquad (5.12d)$$

is the total source strength in the cross-flow plane. It will be shown later that $Q(s_o) = O(s_o\varepsilon^2)$. This implies that in the present approximation just the first term, which is of order $\varepsilon s_o\ln\varepsilon$, is to be retained, all other terms contributing $O(\varepsilon^2)$ in the velocity. Note that the velocity potential $\Phi_q$ as derived for the 2D case, Eq. 3.16a, follows from Eq. (5.12c) assuming two-dimensionality, i.e. $q=q(t)$, etc. so that $Q$ = constant and adding the term resulting from the integration from $-s_\infty$ to 0.

The velocity potential induced at $\bar{x}_o = s_o\bar{e}_x + \bar{X}(s_o)$ by the doublet distribution becomes, retaining only the linear terms in $(s-s_o)$ in Eq. (5.1c) upon substitution of Eqs. 5.9a and 5.11:

$$\varphi_\mu(\bar{x}_o) = \frac{1}{4\pi}\int_{C_{w+v+F}}\mu(\bar{e}_n\cdot\bar{R})I_o^1 dC(t;s_o)$$

$$-\frac{1}{4\pi}\int_{C_{w+v+F}}\left\{\mu\frac{\bar{e}_x\times\bar{X}'_s}{|\bar{X}'|}\cdot\bar{R} + \mu_s(\bar{e}_n\cdot\bar{R})\right\}I_1^1 dC(t;s_o) \qquad (5.13a)$$

where $I_1^1$ is defined in Eq. (5.12b) and evaluated in Table 3.4-6. Substitution of the expressions for $I_o^1$ and $I_1^1$ and further expansion yields:

$$\varphi_\mu(\bar{x}_o) = \frac{1}{2\pi}\int_{C_{w+v+F}}\mu(t;s_o)\frac{\bar{e}_n\cdot\bar{R}}{|\bar{R}|^2}dC(t;s_o)$$

$$+ O(\varepsilon^3 s_o) = \Phi_\mu(\bar{X}(s_o)) \qquad (5.13b)$$

which is exactly $\Phi_\mu$, as derived for the 2D case, see Eq. (3.16b). On the feeding sheet $C_F$ the doublet distribution $\mu$ = constant, i.e. it acts as a cut in the quasi-2D flow domain (see Fig. 5.4). The integration over $C_F$, given as for instance $\bar{X} = \bar{X}(t_e;s_o) + t(\bar{X}_v(s_o)-\bar{X}(t_e;s_o))$ for $t\in[0,1]$, can be carried out in closed form:

$$\varphi_\mu^F(\bar{x}_o) = -\frac{\mu(t_e;s_o)}{2\pi}\left[\tan^{-1}\frac{\bar{R}_v\cdot\bar{L}}{\bar{R}_v\cdot\bar{e}_x\times\bar{L}_e} - \tan^{-1}\frac{\bar{R}_e\cdot\bar{L}_e}{\bar{R}_e\cdot\bar{e}_x\times\bar{L}_e}\right] \qquad (5.13c)$$

where $\bar{R}_v = \bar{X}(s_o)-\bar{X}_v(s_o)$, $\bar{R}_e = \bar{X}(s_o)-\bar{X}(t_e;s_o)$ and $\bar{L}_e = \bar{X}_v(s_o)-\bar{X}(t_e;s_o)$. A similar expression can be derived for the contribution in $\varphi(\bar{x}_o)$ due to the feeding sheet connecting the vortex filament with the edge $t=t_o$ (see Fig. 5.4), i.e. this feeding sheet is described by $\bar{X} = \bar{X}_v(s_o) + t(\bar{X}(t_o;s_o) - \bar{X}_v(s_o))$ for $t\in[0,1]$, and

$$\varphi_\mu^F(\bar{x}_o) = -\frac{\mu(t_o;s_o)}{2\pi}\left[\tan^{-1}\frac{\bar{R}_o\cdot\bar{L}_o}{\bar{R}_o\cdot\bar{e}_x\times\bar{L}_o} - \tan^{-1}\frac{\bar{R}_v\cdot\bar{L}_o}{\bar{R}_v\cdot\bar{e}_x\times\bar{L}_o}\right] \qquad (5.13d)$$

where $\bar{R}_o = \bar{X}(s_o)-\bar{X}(t_o;s_o)$, and $\bar{L}_o = \bar{X}(t_o;s_o) - \bar{X}_v(s_o)$.

Finally, the contribution due to the source distribution $Q_v(s)$ at the position of the vortex filament, given in Eq. (5.1d), can be expanded as

$$\varphi_Q(\bar{x}_o) = \frac{-1}{4\pi}Q_v(s_o)I_o^o$$

$$+ \frac{1}{4\pi}Q_{v_s}(s_o)I_1^o \qquad (5.14a)$$

from which it follows that, using the results of Table 3.1-3

$$\varphi_Q(\bar{x}_o) = \frac{1}{2\pi}Q_v(s_o)\ln\left(\frac{|\bar{R}_v|}{s_o}\right)$$

$$- \frac{1}{4\pi}Q_v(s_o)\ln(4s_\infty/s_o)$$

$$+ \frac{1}{4\pi}Q_{v_s}(s_o)(2s_o-s_\infty)$$

$$+ O(s_o\varepsilon^3, s_o\varepsilon^3\ln\varepsilon) \qquad (5.14b)$$

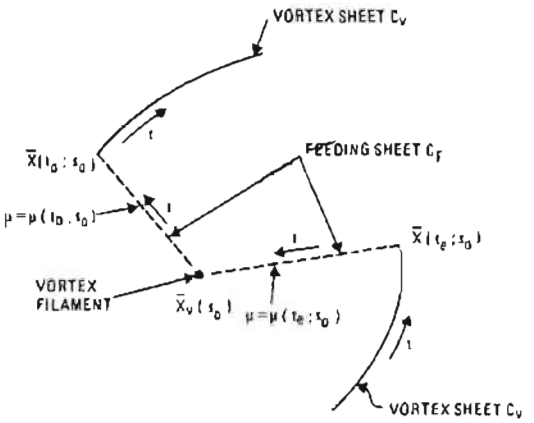


Fig. 5.4 Vortex core in a cross-flow plane

It follows from Eq. (5.1e) that $Q_v$ is of $O(s_o\varepsilon^2)$ so that only the first term contributes a term of $O(\varepsilon)$ in the velocity, the other two give rise to contributions of $O(\varepsilon^2)$ in the x-component of the induced velocity.

The contribution of the source and doublet distribution to the velocity field can be found in a similar fashion. From Eq. (5.2b) one finds that within the framework of the slender-body approximation the contribution due to the source distribution becomes

$$\bar{u}_q(\bar{x}_o) = \frac{1}{4\pi}\int_{C_w} q\bar{R}I_o^1 dC(t;s_o)$$

$$+ \frac{1}{4\pi}\int_{C_w}(q(\bar{e}_x+\bar{X}_s') - (q_s+q\frac{\bar{X}'\cdot\bar{X}_s'}{|\bar{X}'|^2})\bar{R})I_1^1 dC(t;s_o) \qquad (5.15a)$$

Substitution of $I_o^1$ and $I_1^1$ from table 3.1-6 and expansion with respect to $\varepsilon$ yields

$$\bar{u}_q(\bar{x}_o) = \bar{U}_q(\bar{X}(s_o);s_o) + u_q(\bar{X}(s_o);s_o)\bar{e}_x \qquad (5.15b)$$

with

$$\bar{U}_q(\bar{X}(s_o);s_o) = \frac{1}{2\pi}\int_{C_w} q(t;s_o)\frac{\bar{R}}{|\bar{R}|^2}dC(t;s_o) + O(\varepsilon^2) \qquad (5.15c)$$

and

$$u_q(\bar{X}(s_o);s_o) = \frac{-1}{2\pi}\int_{C_w} q(t;s_o)\bar{X}_s'(t;s_o)\cdot\frac{\bar{R}}{|\bar{R}|^2}dC(t;s_o)$$

$$- \frac{1}{2\pi s_o}Q(s_o) + O(\varepsilon^2) \qquad (5.15d)$$

The components of $\bar{u}_q(\bar{x}_o)$ in the plane $s=s_o$, which are of order unity, are exactly the ones in 2D. The component in x-direction, which is of order $\varepsilon$, has no counterpart in 2D flow and is caused by the circumstance that the source distribution on the line $t$ = constant is inclined with respect to the x-axis. The second term in Eq. (5.15d) is proportional to $Q(s_o)$, the total source strength in the cross-flow plane, which will be dropped upon having proved that Q is of order $\varepsilon^2 s_o$.

The contribution $\bar{u}_\mu$ due to the doublet distribution is given in Eq. (5.2c). Consider first the first term, i.e. the one due to the surface vorticity distribution $\bar{\gamma}$ on the configuration, vortex sheets and feeding sheets, denoted here by $\bar{u}_\gamma$. Using the expression for $\gamma$ given Eq. (5.10). The tangent-cone approximation results in

$$\bar{u}_\gamma(\bar{x}_o) = -\frac{\bar{e}_x}{4\pi}\times\{\int_{C_{w+v+F}}\mu'\bar{R}I_o^1 dt$$

$$+ \int_{C_{w+v+F}}(\mu_s\bar{X}'-\mu_s'\bar{R})I_1^1 dt\}$$

$$- \frac{1}{4\pi}\{\int_{C_{w+v+F}}(\mu'\bar{X}_s-\mu_s\bar{X}')\times\bar{R}I_o^1 dt$$

$$+ \int_{C_{w+v+F}}\{\mu_s\bar{X}_s'-\mu_s'\bar{X}_s)\times\bar{R} - \mu_s\bar{X}'\times\bar{X}_s\}I_1^1 dt\} \qquad (5.16a)$$

Substitution of $I_o^1$ and $I_1^1$ of table 3.1-6 and expansion with respect to $\varepsilon$ yields

$$\bar{u}_\gamma(\bar{x}_o) = \bar{U}_\gamma(\bar{X}(s_o);s_o) + u_\gamma(\bar{X}(s_o);s_o)\bar{e}_x \tag{5.16b}$$

with

$$\bar{U}_\gamma(\bar{X}(s_o);s_o) = -\frac{\bar{e}_x}{2\pi} \times \int_{C_{w+v+F}} \mu'(t;s_o)\frac{\bar{R}}{|\bar{R}|^2}dt + O(\varepsilon^2) \tag{5.16c}$$

$$u_\gamma(\bar{X}(s_o);s_o) = -\frac{\bar{e}_x}{2\pi} \cdot \int_{C_{w+v+F}} \mu'(t;s_o)\bar{X}_s(t;s_o)\times\frac{\bar{R}}{|\bar{R}|^2}dt$$

$$+ \frac{1}{2\pi}\int_{C_{w+v+F}} u_s(t;s_o)\frac{\bar{e}_n\cdot\bar{R}}{|\bar{R}|^2}dC(t;s_o) + O(\varepsilon^2) \tag{5.16d}$$

Note that $\bar{U}_\gamma$ is of order unity and is identical to the velocity induced by a 2D vortex sheet of strength $-\mu'(t;s_o)\bar{e}_x$, see Eq. (3.10d). The component of the velocity in x-direction $u_\gamma$ is of order $\varepsilon$.

Next we consider the second term, here denoted by $\bar{u}_v$, in Eq. (5.2c) which is due to the vortex filament. Using Eq. (5.11) we then find up to linear terms in $(s-s_o)$:

$$\bar{u}_v(\bar{x}_o) = -\frac{1}{4\pi}[\mu(t_e^{i-1};s_o)-\mu(t_o^i;s_o)]\bar{R}_v\times(\bar{e}_x+\bar{X}_{v_s}(s_o))I_o^1$$

$$+ \frac{1}{4\pi}[\mu_s(t_e^{i-1};s_o)-\mu_s(t_o^i;s_o)]\bar{R}_v\times(\bar{e}_x + \bar{X}_{v_s}(s_o))I_1^1 \tag{5.17a}$$

where $\bar{R}_v = \bar{X}(s_o) - \bar{X}_v(s_o)$. Substitution of $I_o^1$ and $I_1^1$ of table 3.1-6 then leads to

$$\bar{u}_v(\bar{x}_o) = \bar{U}_v(\bar{X}(s_o);s_o) + u_v(\bar{X}(s_o);s_o)\bar{e}_x \tag{5.17b}$$

with

$$\bar{U}_v(\bar{X}(s_o);s_o) = \frac{1}{2\pi}[\mu(t_e^{i-1};s_o)-\mu(t_o^i;s_o)]\frac{\bar{e}_x\times\bar{R}_v}{|\bar{R}_v|^2} + O(\varepsilon^2) \tag{5.17c}$$

and

$$u_v(\bar{X}(s_o);s_o) = \frac{\bar{e}_x}{2\pi}\cdot[\mu(t_e^{i-1};s_o)-\mu(t_o^i;s_o)]\bar{X}_{v_s}\times\frac{\bar{R}_v}{|\bar{R}_v|^2} + O(\varepsilon^2) \tag{5.17d}$$

Here $\bar{U}_v$, which is of order unity, is identical to the velocity induced by a vortex in 2D flow of strength equal to the discontinuity in the doublet distribution at the vortex, see Eq. (3.12c). The axial component of the velocity is of order $\varepsilon$.

In the cross-flow plane $\mu$ is constant along the feeding sheet. This implies that in Eq. (5.16c) and in the first integral appearing in Eq. (5.16a) the integration along $C_F$ vanishes, as indicated. The second term in Eq. (5.16d) can be evaluated in closed form, i.e. for the feeding sheet connecting $\bar{X}(t_e;s_o)$ to $\bar{X}_v(s_o)$ (see Fig. 5.4) one finds:

$$\bar{u}_\gamma^F(\bar{X}(s_o);s_o) = -\frac{\bar{e}_x}{2\pi}\mu_s(t_e;s_o)\{\tan^{-1}\frac{\bar{R}_v\cdot\bar{L}_e}{\bar{R}_v\cdot\bar{e}_x\times\bar{L}_e} - \tan^{-1}\frac{\bar{R}_e\cdot\bar{L}_e}{\bar{R}_e\cdot\bar{e}_x\times\bar{L}_e}\} \tag{5.18a}$$

where $\bar{R}_v$, $\bar{R}_e$ and $\bar{L}_e$ are defined following Eq. (5.13c). Similarly one finds for the contribution due to the feeding sheet that connects the vortex at $\bar{X}_v(s_o)$ to the $\bar{X}(t_o;s_o)$ (see Fig. 5.4):

$$\bar{u}_\gamma^F(\bar{X}(s_o);s_o) = -\frac{\bar{e}_x}{2\pi}\mu_s(t_o;s_o)\{\tan^{-1}\frac{\bar{R}_o\cdot\bar{L}_o}{\bar{R}_o\cdot\bar{e}_x\times\bar{L}_o} - \tan^{-1}\frac{\bar{R}_v\cdot\bar{L}_o}{\bar{R}_v\cdot\bar{e}_x\times\bar{L}_o}\} \tag{5.18b}$$

with $\bar{R}_o$ and $\bar{L}_o$ defined following Eq. (5.13d).

Finally, consider the contribution due to the source distribution $Q_v$ located on the vortex filament, Eq. (5.2d). Expansion yields

$$\bar{u}_Q(\bar{x}_o) = \frac{1}{4\pi}Q_v\{(\bar{e}_x+\bar{X}_v')I_1^1 + \bar{R}_v I_o^1\}$$

$$- \frac{1}{4\pi}Q_{v_s}\bar{R}I_1^1 \tag{5.19a}$$

from which one deduces, using table 3.4-6:

$$\bar{u}_Q(\bar{x}_o) = \frac{1}{2\pi}Q_v(s_o)\frac{\bar{R}_v}{|\bar{R}_v|^2} + O(\varepsilon^2, \varepsilon^2\ell n\varepsilon) \tag{5.19b}$$

The jumps in the velocity and velocity potential are also to be considered. Within the framework of the present quasi-2D flow, it follows immediately from Eq. (5.1d) that

$$\Delta\phi(\bar{X}(t;s_o)) = \phi(\bar{X}(t;s_o)^+) - \phi(\bar{X}(t;s_o)^-)$$
$$= \mu(t;s_o) \qquad (5.20a)$$

The jump in the velocity, for the 3D case given in Eq. (5.2e) becomes upon expansion in terms of $\varepsilon$:

$$\Delta\bar{u}(\bar{X}(t;s_o)) = \bar{u}(\bar{X}(t;s_o)^+) - \bar{u}(\bar{X}(t;s_o)^-)$$
$$= q(t;s_o)(\bar{e}_n - (\bar{X}_s(t;s_o).\bar{e}_n)\bar{e}_x)$$
$$+ \mu'(t;s_o)(\bar{e}_t - (\bar{X}_s(t;s_o).\bar{e}_t)\bar{e}_x)/|\bar{X}'(t;s_o)|$$
$$+ \mu_s(t;s_o)\bar{e}_x$$
$$+ O(\varepsilon^2) \qquad (5.20b)$$

where the two components in the cross-flow plane are of order unity and the one in x-direction is of order $\varepsilon$.

Inspecting the expressions derived for the velocity and the velocity potential induced in the cross-flow plane $x=s_o$ by the singularity distributions on the slender geometry one notes that (with $Q = O(\varepsilon^2)$) both $\phi(\bar{X}(s_o))$ and $\bar{u}(\bar{X}(s_o))$ are identical to the corresponding quantities in 2D flow and do not contain any derivative with respect to the parameter $s_o$. However, streamwise derivatives do occur in the expressions found for $u(\bar{X}(s_o))$, the component of the velocity in x-direction, i.e. Eqs. (5.15d), (5.16d) and (5.20b). Also of course, the streamwise derivatives will appear in the boundary conditions that apply for the present quasi-2D problem in the cross flow plane. These will be considered next.

5.2.3 Expansion of the boundary conditions

In the quasi-2D flow approximation the boundary conditions, Eqs. (5.5)-(5.7), are expanded in terms of $\varepsilon$ as well. In the cross-flow plane $x=s_o$ the velocity at the point $\bar{x}_o = s_o\bar{e}_x + \bar{X}_o$, with $\bar{X}_o = \bar{X}(s_o)$, is written as

$$\bar{u}(\bar{x}_o) = (U_\infty\cos\alpha\cos\beta + u(\bar{X}_o;s_o))\bar{e}_x + \bar{V}_\infty + \bar{U}(\bar{X}_o;s_o) + O(\varepsilon^2) \qquad (5.21a)$$

where

$$u(\bar{X}_o;s_o) = u_q(\bar{X}_o;s_o) + u_\mu(\bar{X}_o;s_o) \qquad + O(\varepsilon) \qquad (5.21b)$$

$$\bar{V}_\infty = \sin\beta\,\bar{e}_y + \sin\alpha\cos\beta\,\bar{e}_z \qquad + O(1) \qquad (5.21c)$$

$$\bar{U}(\bar{X}_o;s_o) = \bar{U}_q(\bar{X}_o;s_o) + \bar{U}_\mu(\bar{X}_o;s_o) + \qquad + O(1)$$
$$+ \bar{U}_Q(\bar{X}_o;s_o) + O(\varepsilon) \qquad (5.21d)$$

In Eq. (5.21) $\bar{U}_\mu$ and $u_\mu$ are the sums $\bar{U}_\chi + \bar{U}_\gamma$ and $u_\chi + u_\gamma$, respectively. In Eq. (5.21) we also indicated the leading order of magnitude of each term. This with the order of magnitude of $U_\infty\cos\alpha\cos\beta$, which is O(1), will be used to expand the boundary conditions to consistent order of approximation.

(i) Neumann boundary condition, Eqs. (5.5a) and (5.6a) on $C_{w+v}$

$$(\bar{V}_\infty + \bar{U}(\bar{X}(t;s_o)) - U_\infty\cos\alpha\cos\beta\bar{X}_s(t;s_o)).\bar{e}_n + O(\varepsilon^2) = 0 \qquad (5.22a)$$

which is to be applied for all points on the free vortex sheets $C_v$ and all points on the solid surfaces $C_w$, but not on the feeding sheets $C_f$. Note that the $\bar{X}_s$-term in Eq. (5.22a) accounts for the three-dimensionality of the present problem, it slightly (order $\varepsilon$) tilts the velocity vector out of the cross-flow plane. For configurations with thickness the second term acts as a source term in the quasi-2D flow, as follows from integration of Eq. (5.22a) along the contour $C_w$, which yields

$$Q(s_o) = \int_{C_w+v+f} (\bar{V}_\infty + \bar{U}(\bar{X}(t;s_o))).\bar{e}_n\,dC(t;s_o)$$
$$= U_\infty\cos\alpha\cos\beta\left[\int_{C_w} \bar{X}_s(t;s_o).\bar{e}_n\,dC(t;s_o)\right]$$
$$= U_\infty\cos\alpha\cos\beta\,\frac{dA}{ds}(s_o) \qquad (5.22b)$$

where A is the cross-sectional area of the configuration. It follows immediately that this source strength, or net outflow required to simulate the variation with s of the cross-sectional area of the configuration has order of magnitude $O(s_o\varepsilon^2)$, a fact that has been used several times in the preceding section.

(ii) Dirichlet boundary condition, Eqs. (5.5b and c) on $C_w$

The perturbation velocity potential $\phi = \phi_q + \phi_\mu + \phi_Q$ at points $\bar{X}(t;s_o)^-$ is set equal to zero, i.e.

$$-\tfrac{1}{2}\mu(t;s_o) + \Phi^P(\bar{X}(t;s_o)) + O(s_o\varepsilon^3) = 0 \qquad (5.23a)$$

for all points $\bar{X}(t;s_o)$ on closed contours $C_w$. Note that $\Phi^P$ denotes the Cauchy Principal Value part of $\phi_q + \phi_\mu + \phi_Q$. The strength of the source distribution, given in Eq. (5.5c) becomes:

$$q(t;s_o) = -(\bar{V}_\infty - U_\infty\cos\alpha\cos\beta\bar{X}_s(t;s_o)).\bar{e}_n + O(\varepsilon^2) \qquad (5.23b)$$

The velocity on the side of $C_w$ wetted by the external flow then follows from Eq. (3.18g) as

$$\bar{u}(\bar{X}(t;s_o)) = \bar{U}_\infty + q(t;s_o)\{\bar{e}_n - (\bar{X}_s(t;s_o).\bar{e}_n)\bar{e}_x\} + \mu'(t;s_o)\{\bar{e}_t - (\bar{X}_s(t;s_o).\bar{e}_t)\bar{e}_x\}/|\bar{X}'(t;s_o)| + u_s(t;s_o)\bar{e}_x + O(\varepsilon^2) \tag{5.23c}$$

(iii) Pressure jump condition across $C_v$, Eq. (5.6b)

$$\frac{\mu'(t;s_o)}{|\bar{X}'(t;s_o)|}\{\bar{V}_\infty + \bar{U}^p(\bar{X}(t;s_o)) - U_\infty \cos\alpha\cos\beta\bar{X}_s(t;s_o)\}.\bar{e}_t + U_\infty\cos\alpha\cos\beta u_s(t;s_o) + O(\varepsilon^2) = 0 \tag{5.24}$$

for all points on the vortex sheets $C_v$.
In Eq. (5.24) $\bar{U}^p(\bar{X}(t;s_o))$ is the Cauchy-Principal Value of $\bar{U}_q + \bar{U}_\mu + \bar{U}_Q$.

In purely 2D flow all terms in Eq. (5.24) are zero, except the first one. Therefore then Eq. (5.24) degenerates to the familiar condition that in 2D flow the doublet distribution is constant on free vortex sheets (e.g. the wake downstream of an airfoil). In the present quasi-2D case the second term, proportional to $\mu'$, admits a nonzero $\mu'$, while still, to the required order of magnitude, the pressure is continuous across the vortex sheet.

(iv) Zero-net-force condition on vortex core model, Eq. (5.7)
The force on the vortex filament, given in Eq. (3.20a), can be expanded as follows:

$$d\bar{F}_v(s_o) = \rho_\infty\mu(t_e;s_o)\{\bar{V}_\infty + \bar{U}(\bar{X}_v(s_o)) - U_\infty\cos\alpha\cos\beta\bar{X}_{v_s}(s_o)\}\times\bar{e}_x ds + O(s_o\varepsilon^3) \tag{5.25a}$$

In a similar fashion the contribution in the resultant force on the model due to the entrainment $(-Q_v)$ is expanded as, see Eq. (3.20b):

$$d\bar{F}_Q(s_o) = \rho_\infty Q_v(s_o)\{\bar{V}_\infty + \bar{U}(\bar{X}_v(s_o)) + U_\infty\cos\alpha\cos\beta\bar{e}_x\} + O(s_o\varepsilon^3) \tag{5.25b}$$

The force on the feeding sheet $C_F$, connecting $\bar{X}(t_e;s_o)$ to $\bar{X}_v(s_o)$ and carrying the constant doublet distribution $\mu(t_e;s_o)$ becomes, see Eq. (3.20c):

$$d\bar{F}_F(s_o) = -\rho_\infty\mu_s(t_e;s_o)U_\infty\cos\alpha\cos\beta\{\bar{X}_v(s_o) - \bar{X}(t_e;s_o)\}\times\bar{e}_x ds + O(s_o\varepsilon^3) \tag{5.25c}$$

Similarly one finds for the feeding sheet connecting $\bar{X}_v(s_o)$ to $\bar{X}(t_o;s_o)$ and carrying the constant doublet distribution $\mu(t_o;s_o)$:

$$d\bar{F}_F(s_o) = -\rho_\infty\mu_s(t_o;s_o)U_\infty\cos\alpha\cos\beta\{\bar{X}(t_o;s_o) - \bar{X}_v(s_o)\}\times\bar{e}_x ds + O(s_o\varepsilon^3) \tag{5.25d}$$

Combining Eqs. (5.25a-d) results in the condition on the vortex core:

$$\begin{aligned}\rho_\infty\bar{e}_x\times[&\mu(t_e;s_o)\{\bar{V}_\infty + \bar{U}(\bar{X}_v(s_o)) - U_\infty\cos\alpha\cos\beta\bar{X}_{v_s}(s_o)\}\\ &-\mu(t_o;s_o)\{\bar{V}_\infty + \bar{U}(\bar{X}_v(s_o)) - U_\infty\cos\alpha\cos\beta\bar{X}_{v_s}(s_o)\}\\ &- u_s(t_e;s_o)\{\bar{X}_v(s_o) - \bar{X}(t_e;s_o)\}U_\infty\cos\alpha\cos\beta\\ &+ u_s(t_o;s_o)\{\bar{X}_v(s_o) - \bar{X}(t_o;s_o)\}U_\infty\cos\alpha\cos\beta\\ &- Q_v(s_o)\bar{e}_x\times\{\bar{V}_\infty + \bar{U}(\bar{X}_v(s_o))\}] + O(s_o\varepsilon^3) = 0\end{aligned} \tag{5.25e}$$

where the 2nd and 4th terms are to be omitted in the case of a single-branched vortex core. Note that the zero-net-force condition is a vector with two components, both in the cross-flow plane.

The axial velocity component $u(\bar{X}_o;s_o)$ does not appear in the cross-flow plane boundary conditions. However, once we have obtained the solution this component is needed for the computation of the pressure as becomes clear from the expansion of the expression for the pressure coefficient, Eq. (3.9d), to consistent order, i.e. using Eq. (5.21a):

$$C_p = -[|\bar{U}(\bar{X}_o;s_o)|^2 + 2\bar{U}(\bar{X}_o;s_o).\bar{V}_\infty + 2u(\bar{X}_o;s_o)U_\infty\cos\alpha\cos\beta]/U_\infty^2 + O(\varepsilon^2) \tag{5.26}$$

In the slender-body framework the boundary conditions in the cross-flow plane may be regarded as a set of ordinary differential equations in terms of $s$ for $\bar{X}(t;s)$, $\bar{X}_v(s)$, $\mu(t;s)$ and $q(t;s)$. This suggests that a numerical marching procedure is possible. In order to start such a procedure one needs the solution at an initial station. Such an initial station could be the apex of the configuration where $\bar{X}(t;0) = \bar{X}_v(0) = \mu(t;0) = 0$. Another possibility is to use the given solution at some other station. The latter includes the *case of the flow about a low-aspect-ratio rectangular wing with the flow separating from the side-edges*, for which

$$\bar{X}(t;0) = \frac{b}{2}t\bar{e}_y,\quad \bar{X}_v(0) = \frac{b}{2}\bar{e}_y,\quad \mu(t;0) = 0.$$

5.2.4 Special case: conical flow

In case of a conical configuration the derivative with respect to s of the geometric quantities is identical for each cross-flow plane. This implies that the boundary conditions are identical for each cross-flow plane as well, thus reducing the problem to just one 2D problem. The resulting flow field is conical, i.e. it is a flow field in which the velocity components (and consequently the pressure) are constant on straigth lines (rays) through the apex.

Observation of the flow over the forward 70% of slender conical configurations such as delta wings and cones suggests that the flow is indeed conical as far as the flow topology (shape of surface streamlines, etc.) is concerned.
It has been amply demonstrated in the literature that in subsonic flow about delta wings and cones the pressure distribution varies along a ray from the apex, especially near the apex and naturally near the trailing edge. But in regions away from the apex and the trailing edge the flow is of slender-body type and approximately conical. Only in (inviscid) supersonic flow strict conical flow occurs on conical geometries.

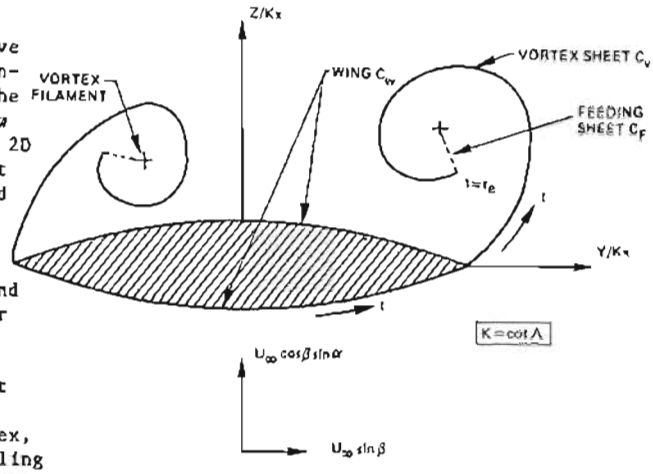


Fig. 5.5 Conical flow problem

In the present study we will treat the flow about slender conical configurations using the formulation described in sections 5.2.1-3 for slender configurations. In the application it will turn out that for a conical configuration the solution in every cross-flow plane scales linearly with s, i.e. with K = cotΛ (Fig. 5.5):

$$\bar{X}(t;s) = Ks\bar{X}(t),\ \bar{X}_v(s) = Ks\bar{X}_v \tag{5.27a}$$

for $C_{W+V+F}$ and $C_f$ respectively, while the singularity distributions satisfy

$$\mu(t;s) = Ks\mu(t) \tag{5.27b}$$

$$q(t;s) = q(t) \tag{5.27c}$$

Substitution of Eqs. (5.27a-c) in the boundary conditions, Eqs. (5.22)-(5.25) learns that for conical configurations in zero side slip ($\beta$=0) the conditions depend on one parameter only. This parameter, the so-called conical similarity parameter, is defined as

$$A = \frac{\tan\alpha}{\cot\Lambda} = \frac{\tan\alpha}{K} \tag{5.28}$$

Similarity implies that the solution obtained for a particular combination of incidence $\alpha$ and sweep $\Lambda$ is also the solution for any other combination of $\alpha$ and $\Lambda$ with the same value of $\Lambda$.

In the case of a conical configuration in side slip, substitution of Eqs. (5.27a-c) into the boundary conditions yields equations that depend on two parameters, the conical parameter A defined above and the additional parameter

$$B = \frac{\tan\beta}{\sin\alpha} \tag{5.29}$$

Thus for cases with $\alpha$, $\beta$ and K such that both A and B are the same, the solution will be the same.

5.3 Two-Dimensional time-dependent analogy - Trefftz-plane analysis for vortex wakes

For transport type aircraft in cruise condition the precise shape of the wake has in general only a small effect on the lift and on the pressure distribution on the wing. In most current computational methods for transport type aircraft it is therefore general practice to assume a rigid wake of some suitable shape. The boundary conditions on the wake are satisfied in some degenerate form only. Some other, more advanced methods, "relax" this rigid wake in an iterative procedure in order to satisfy the boundary conditions set forth in section 5.1. However, it has been demonstrated that the differences between the pressure distribution computed assuming a rigid wake and the one computed with a "relaxed" wake are confined to the trailing edge and tip regions. This suggests that in order to include boundary-layer corrections, for which the pressure at the trailing edge is rather important, the more accurate description of the wake in these regions is necessary. This is also true for transport type aircraft in landing or take-off configuration, for fighter aircraft with their low-aspect-ratio wings and for missiles, where in general there is a stronger interaction. For the case of leading-edge vortex flow we will consider the wake vortex sheet in the fully 3D framework. However, for the sometimes complex wakes downstream of more general configurations a quasi-2D formulation will be used. The motivation is that quite often it is observed that the trailing wake downstream of an aircraft configuration is only mildly curved in streamwise direction and that the variations in the flow variables are much larger in cross-flow planes than in streamwise direction. This observation leads to an approximation to the fully 3D problem, the so-called 2D unsteady analogy, which will be discussed next.

5.3.1 Time-dependent analogy

Under the assumption that the wake is slowly changing in x-direction the problem of determining the steady vortex wake in 3D space can be solved in an approximate manner. To this aim the problem, formulated in the framework of the slender-body approximation, is reformulated as a time-dependent problem. This is accomplished by replacing the streamwise coordinate s by $\tau U_\infty \cos\alpha\cos\beta$, where $\tau$ is a time-like coordinate. Then the boundary conditions on the vortex sheet, Eqs. (5.22a) and (5.24) transform into:

$$\{\bar{V}_\infty + \bar{U}(\bar{X}(t;\tau)) - \frac{d\bar{X}}{d\tau}(t;\tau)\}.\bar{e}_n + O(\varepsilon^2) = 0 \tag{5.30a}$$

and

$$\frac{\mu'(t;\tau)}{|\bar{X}'(t;\tau)|}\{\bar{V}_\infty + \bar{U}(\bar{X}(t;\tau)) - \frac{d\bar{X}}{d\tau}(t;\tau)\}.\bar{e}_t + \frac{d\mu}{d\tau}(t;\tau) + O(\varepsilon^2) = 0 \tag{5.30b}$$

respectively, where $\varepsilon$ denotes the order of magnitude of $\tilde{X}$ which is assumed to be small. In the case of vortex wake roll-up, i.e. in the absence of any solid surfaces $C_W$ that generate new vorticity, the two-dimensional time-dependent analogy follows as the solution of Eqs. 5.30a and b:

$$\frac{d\bar{X}}{d\tau}(t;\tau) = \bar{V}_\infty + \bar{U}(\bar{X}(t;\tau)) \tag{5.31a}$$

$$\frac{d\mu}{d\tau}(t;\tau) = 0 \tag{5.31b}$$

for all points on $C_V$ and $\bar{U}$ denotes the velocity due to the vortex sheet(s), i.e. $U = \bar{U}_\mu$. Here it is assumed that $Q_V$, the entrainment of vortex cores may be neglected altogether.
In a similar fashion it then follows from the condition on the vortex core model, Eq. (5.25d), that

$$\frac{d}{d\tau}\bar{X}_v(\tau) = \bar{V}_\infty + \bar{U}(\bar{X}_v(\tau)) \tag{5.32a}$$

$$\frac{d\mu}{d\tau}(t_e;\tau) = 0 \quad \text{and} \quad \frac{d\mu}{d\tau}(t_o;\tau) = 0 \tag{5.32b}$$

Effectively we have now a two-dimensional unsteady problem for the motion of the vortex wake in the cross-flow plane (the so-called Trefftz plane) as it is convected by its self-induced velocity.

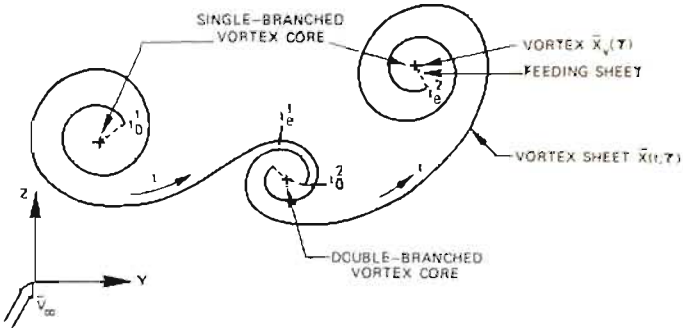


Fig. 5.6 Two-dimensional time-dependent analogy in the Trefftz plane

The analogy corresponds to the situation in which, in classical finite-wing aerodynamics with planar trailing wakes directed along $\bar{U}_\infty$, at $\tau = 0$ the solid geometry $S_W$ is removed instantaneously, leaving the planar trailing wake subject to its self-induced velocity field. The latter is in first approximation the velocity field induced by a planar wake extending from $x = -\infty$ to $\infty$, corresponding to a 2D situation in the cross-flow plane (see Fig. 5.6).

The time-dependent analogy is an initial-value problem describing the motion of the vortex sheet in two dimensions. The initial conditions of the problem are the shape of the trailing (or shedding) edge of the wing, i.e. $\bar{X}(t;0)$, and the distribution of the streamwise component of the vorticity at this edge.

The vorticity distribution at $\tau = 0$ is proportional to the spanwise derivative of the circulation distribution on the configuration. The latter is equivalent to the doublet distribution as defined here, i.e.:

$$\mu(y;0) = U_\infty \frac{c(y)c_\ell(y)}{2} \tag{5.33}$$

where $c_\ell(y)$ and $c(y)$ are the local lift coefficient and local chord, respectively.
More generally, the two-dimensional time-dependent analogy can be applied starting at the station downstream of the configuration where the interaction of the wake with the solid surface of the configuration has become sufficiently small and both shape and strength of the vortex wake are known from a computational method for 3D flow, or experiment.

The main limitation of the analogy is that the interaction of the rolling-up wake with nearby parts of the solid geometry, including the one that generated the wake, cannot be accounted for. Nevertheless, the unsteady analogy is a valuable approach to obtain a first insight in the topology of the rolling-up wake. It could also be used as pre-processor that generates the first guess for a method solving the fully three-dimensional problem.

The initial phase of the "evolution" of a vortex wake is characterized by the formation of vortex cores. It should be emphasized here that vortex sheet very rarely terminate as a free unrolled end. Generally at $\tau = 0$ the doublet distribution is already such that the free end rolls up immediately. This certainly includes the cases where $\mu(t;0)$ is singular, like at the position where at $\tau=0^-$ the wing tip was located.
In general, after some finite time the initially smooth vortex sheet may locally begin to deform more rapidly than elsewhere, possibly starting from singularities in vorticity strength and curvature, resulting in regions with vortex sheet roll-up. For these conditions it seems justified to model the rather compactly rolled-up regions by the vortex filament/ feeding sheet(s) model (see Fig. 5.6). Now we have a vortex sheet which is broken-up into piecewise continuous parts and two continuous portions of the vortex sheet are connected to each other through a double-branched vortex core.

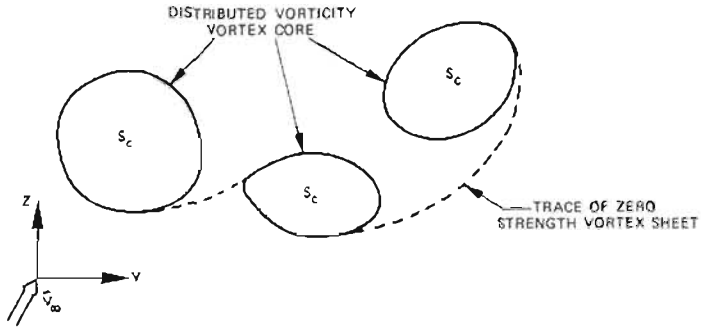


Fig. 5.7 Distributed vorticity model in the Trefftz plane for fully rolled-up wakes

After the wake has developed for a long time, all the vortex cores will have formed. These cores then contain most of the vorticity. At this stage of the roll-up process viscous effects are important in relatively small regions of large velocity gradients only, e.g. in the very center of vortex cores. Under these circumstances the pure vortex-sheet model of Fig. 5.6 may still describe the flow accurately. However, the vortical flow regions, represented in the vortex sheet model by a locally weak but highly stretched and tightly rolled-up vortex sheet, may more conveniently be described by a distributed vorticity model, for instance employing the stream function vorticity formulation of Eqs. (3.6a and b).

At this final stage of the inviscid roll-up process, which is beyond the scope of the present study, nearly all vorticity resides within the cores and the strength of the vortex sheets may be neglected (Fig. 5.7).

Subsequently the finite regions of rotational flow will continue to interact, viscous effects will become increasingly important and vortex cores may merge and finally diffuse completely.

5.3.2 Expression for the velocity in the Trefftz plane

The velocity induced at $\bar{X}_o$ in the Trefftz plane follows from section 5.2.2, Eqs. (5.16) and (5.17), all further terms being neglected, as

$$\bar{U}(\bar{X}_o;\tau) = \bar{V}_\infty + \bar{U}_\mu(\bar{X}_o;\tau) \tag{5.34a}$$

where $\bar{V}_\infty$ is defined in Eq. (5.21c), $\bar{U}_\mu$ in Eqs. (5.15) and (5.17):

$$\bar{V}_\infty = U_\infty \sin\beta \bar{e}_y + U_\infty \sin\alpha\cos\beta \bar{e}_z \tag{5.34b}$$

$$\bar{U}_\mu(\bar{X}_o;\tau) = -\frac{\bar{e}_x}{2\pi}\times\left(\int_{C_v}\frac{\partial\mu}{\partial t}(t;\tau)\frac{\bar{R}}{|\bar{R}|^2}dt - \frac{\bar{R}_v}{|\bar{R}_v|^2}[\mu(t;\tau)]\Big|_{t=t_o^i}^{t=t_e^{i-1}}\right) \tag{5.34c}$$

where $\bar{R} = \bar{X}_o - \bar{X}(t;\tau)$ and $\bar{R}_v = \bar{X}_o - \bar{X}_v(\tau)$.

In the present approximation the streamwise velocity component is $U_\infty \cos\alpha\cos\beta$ and constant. It is furthermore implied, see Eq. (5.32b), that the feeding sheets do not carry vorticity, they may be considered as cuts across which the velocity potential is discontinuous.

In Eq. (5.34) it is assumed that $\mu(t;\tau)$ and $\bar{X}(t;\tau)$ are piecewise continuous in t, i.e. that the vortex sheets $C_v$ can be broken up into segments consisting of a vortex sheet and connected to its edges possibly a vortex-filament/feeding-sheet vortex core model (see Fig. 5.6).

The velocity $\bar{U}(\bar{X}_o;\tau)$ as given in Eq. (5.34) satisfies Laplace's equation in the cross-flow plane, that is everywhere, except right at the vortex sheet and vortex core, while $\mu$ is convected as a conserved quantity, see Eqs. (5.31b) and (5.32b). The latter implies that, as frequently found in the literature, one could equally well have chosen $\mu$ instead of t as the independent parameter. In the present study t is preferred, avoiding the complexities associated with nonmonitonically varying $\mu$ along $C_v$.

5.3.3 Is the initial value problem well-posed?

It must be noted here that the matter of existence and uniqueness of solutions of the present continuous initial-value problem has not yet been fully resolved (e.g. Moore-1979). It can be shown, see Appendix C, that a flat doubly-infinite (periodic) vortex sheet of uniform strength $\gamma = \frac{\partial\mu}{\partial t}(t;0)$ = constant is unstable to small sinusoidal disturbances of any wave length $\lambda$, the so called Kelvin-Helmholtz instability (e.g. v.d. Vooren-1980). The (linear) growth rate of the disturbance is $\pi\gamma/\lambda$, i.e. the disturbance with smallest wave length grows fastest. It is to be expected that stretching of the sheet will reduce this catastrophic growth rate. However, since on the scale of vanishing wave length a non-uniform and curved vortex sheet may be considered as locally uniform and flat, the phenomenon of Kelvin-Helmholtz instability will undoubtedly play an important role in the motion of two-dimensional vortex sheets.

Aside from the Kelvin-Helmholtz instability there is the possibility that, during the later stages of the evolution of an instability wave, non-smooth solutions develop in finite time. It is expected that this non-analytical behaviour occurs locally only, namely right at the center of a rolled-up portion of the vortex sheet which we will remove anyway and replace by the vortex core model discussed earlier.

Furthermore, in the present study we consider the vortex sheet as a model of a thin shear layer. For a straight shear layer with uniform vorticity and thickness, it has been shown by Rayleigh-1896 that waves with a wave length less than about 5 times the shear layer thickness are not amplified. Longer waves do get amplified (but at a correspondingly smaller rate), while the maximum growth rate occurs at a wave length of about 8 times the shear layer thickness. This implies that, in order to predict through vortex sheet motion, the evolution of vortex layers with features several times their thickness, the numerical procedure must have sufficient smoothing to suppress the most unstable modes.

# PART TWO

## COMPUTATIONAL METHODS FOR ORDERED VORTEX FLOWS

| | | METHOD | |
|---|---|---|---|
| TYPE | FLOW MODEL | WEAK INTERACTION | STRONG INTERACTION |
| RIGID VORTEX | 3-D | CLASSICAL WING THEORY<br>VORTEX LATTICE METHOD | -<br>VORTEX LATTICE METHOD ($\alpha/2$)<br>SUCTION ANALOGY |
| | | PANEL METHOD<br>F.D. METHOD FULL-POT.FLOW | -<br>- |
| FITTED VORTEX | 3-D | VORTEX LATTICE METHOD<br>VORTEX SHEET METHOD | VORTEX LATTICE METHOD<br>VORTEX SHEET METHOD |
| | S-B<br>(+ CONICAL) | -<br>-<br>- | CONF. MAPPING METHOD<br>DISCRETE VORTEX METHOD<br>VORTEX SHEET METHOD |
| | 2-D-T | DISCRETE VORTEX METHOD<br>CLOUD-IN-CELL METHOD<br>VORTEX SHEET METHOD | -<br>-<br>- |
| CAPTURED VORTEX | 3-D | -<br>EULER F.D. METHOD<br>- | VORTICAL PRACTICLE METHOD<br>EULER F.D. METHOD<br>NAVIER-STOKES F.D. METHOD |
| | 2-D-T | CONTOUR DYNAMICS<br>FINITE-CORE METHOD<br>NAVIER-STOKES F.D. METHOD | -<br>-<br>- |

3-D : Three-dimensional flow
S-B : Slender body or slender wing approximation
2-D-T : Two-dimensional time-dependent analogy
F.D. : Finite difference or finite volume
[ ] Method developed in present study

Table 6.1 Classification of computational vortex flow methods

## 6 SUMMARY OF EXISTING COMPUTATIONAL METHODS

In this chapter an inventory is presented of existing computational methods for configurations with vortex flow. In the discussion we will follows a more or less chronological path through the literature, starting with the most simplified methods and ending with the more sophisticated ones. Methods for trailing wakes (weak interaction) have the longest history. These methods often have been extended in a quite natural way to cases with strong interaction vortex flow such as leading-edge vortex flow and the vortex flow resulting from separation from smooth bodies.

As indicated in Table 6.1 three types of method can be distinguished in the literature:

(i) Methods that, like classical wing theory, assume a wake of some rigid, suitably chosen, shape and account for strong interaction vortex flow effects through an empirical approach. These potential flow methods may be linear or nonlinear in term of the velocity potential, but are linear in terms of the boundary conditions.

(ii) Methods that explicitly fit vortex-flow regions in otherwise irrotational flow. These methods require, a priori, the topology of the vortex flow, but the precise location and strength of the vortex sheets and cores are determined as part of the solution. These potential flow methods are nonlinear in terms of the boundary conditions.

(iii) Methods that implicitly capture the vorticity in the vortex layers and cores as part of the solution of a nonlinear flow model that admits vorticity everywhere in space. No a priori knowledge of the vortex flow topology is required other than for reasons of minimizing discretization errors.

For the latter two types of method solving the flow problem in three dimensions presents a formidable task. This has been the motivation to consider the problem in the approximate, simplified, framework of quasi-two-dimensional flow. In the literature two such simplifications have been used, which have been discussed here in chapter 5 and are summarized below:

(i) The Slender-Body or slender-wing Approximation.
It is assumed that variations in streamwise direction are much smaller than those in the cross-flow plane. A further simplification is obtained when in addition it is assumed that the variation in streamwise direction is linear (geometry and velocity potential, i.e. velocity and pressure constant on rays from the apex): often referred to as flow with conical similarity.

(ii) The two-dimensional time-dependent analogy.
Variations in streamwise direction are assumed to be slow and any solid surfaces from which new vorticity is shed are assumed to be absent. This implies that one studies the convection (and diffusion) of regions of vorticity, e.g. wakes, generated at an upstream solid surface, or in the analogy at an earlier time.

As discussed in chapter 5 the 2D time-dependent analogy may be considered as a special case of the slender-body-approximation.

Each type of method has its merits and its typical domain of application which depends on the degree of detail required (preliminary design versus detailed analysis), computer resources available, desired ease of use, etc.
Recent reviews of methods for the computation of vortical type of flows, that provide additional background and more detailed descriptions of the various methods, have been presented by Saffman & Baker-1979, Smith-1980, Leonard-1980 and by the present author (1984).
In the next section we discuss existing computational methods for weak-interaction vortex flow (vortex wakes), followed by a discussion of computational methods for strong-interaction vortex flow.

### 6.1 Methods for computing vortex wakes

Rigid-wake assumption

In classical wing theory it is assumed that the wake of a wing of finite span may be represented as a vortex sheet embedded in potential flow. For lightly-loaded wings it may be assumed that taking the vortex sheet flat and undistorted, situated in the same plane for all incidences, has negligible effect on the flow on the wing surface itself. This avoids the difficult problem of determining the location of the trailing vortex sheet as part of the solution. This rigid-wake assumption, which renders the problem linear, is to good approximation valid for the lightly-loaded large-aspect-ratio wings of current transport aircraft configurations in cruise condition. This assumption is still used in most present-day vortex lattice and panel methods for linearized potential flow (e.g. Sytsma et al.-1977) and also in current finite-difference methods for transonic potential-flow (e.g. Holst et al.-1982). In both types of method it is common practice to assume a rigid wake of some suitably chosen shape with the vortex lines running along prescribed curves, while the boundary conditions on the wake, derived earlier in section 3.7, are not imposed explicitly but instead assumed to be satisfied to first order. In comparison of computed and measured pressure distributions the discrepancy caused by assuming some suitable position of the wake and not satisfying the full boundary conditions will be most evident in the region near the trailing edge and near the wing tip.

Wake relaxation - Fitted vortex methods

In the case of the interaction of the vortex wake with the flow about another nearby component of the configuration (e.g. tail plane, deployed flap, etc.) the precise location and roll-up of the wake becomes important; there is a stronger interaction and its effect can no longer be neglected. In general this is also true for the low-aspect-ratio (highly-loaded) wings of fighter aircraft and missile configurations.
In these cases the rigid wake model is no longer adequate, the wake will have to be "relaxed" and its actual shape and location have to be determined as part of the solution.
The necessity of wake relaxation was already recognized over fifty years ago, but in this pre-computer era little progress could be made in solving the full three-dimensional problem. However, sufficiently far downstream of the trailing edge the problem of determining the location of the three-dimensional steady vortex sheet is simplified by considering the sheet two-dimensional in the cross-flow (Trefftz) plane and unsteady by replacing the streamwise coordinate x by $U_\infty \tau$, where $U_\infty$ is the streamwise velocity of the wing and where $\tau$ has the dimension of time. In this time-dependent analogy (see section 5.3) the problem is reduced to an initial-value problem describing the motion of the vortex sheet in subsequent cross-flow planes. Kaden-1931 obtained a similarity solution for the spiral roll-up that occurs at the edge of a semi-infinite vortex sheet. Later Westwater-1935 obtained a numerical solution for the evolution of a vortex sheet of finite span. In Westwater's approach the continuous sheet is represented by an assembly of discrete vortices. Employing this discrete-vortex method (see Fig. 6.1) the evolution of the vortex sheet behind an elliptically loaded wing was computed "by hand", using only 20 vortices and carrying out 33 time steps, resulting in a plausible

looking roll-up. Following the advent of powerful computers Westwater's case was reconsidered, e.g. by Moore-1974, using more vortices and more accurate time-integration schemes than Westwater. However, these attempts have not been succesful: it appears that, due to the inaccurate representation of the velocity field at points near the vortex sheet, the discrete-vortex approach inevitably leads to chaotic motion in the region of the tip vortex or near other centers of roll-up, ruining the calculation. Despite various attempts to regularize the solution a reliable discrete-vortex method for tracking vortex sheet motion has not evolved thusfar. Also the "cloud-in-cell" method (e.g. Baker-1979), in which the velocity field is obtained by solving for the streamfunction due to the continuous vorticity distribution obtained by distributing the discrete vortices on an underlying computational grid, has its problems.

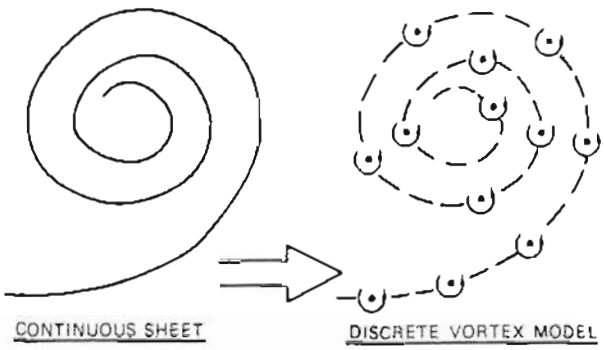


Fig. 6.1 Discrete-vortex method in plane $x=U_\infty t$

It appears that there is a fundamental difference between a continuous vortex sheet and an assembly of discrete vortices. In case the latter is used as a discretization of the former one has to ascertain that the spatial discretization error associated with the approximation remains bounded for all $t$.

To illustrate the difficulties associated with the discrete-vortex approximation we consider the velocity field induced by a straight vortex sheet segment of length 2a and of uniform strength $\gamma$ positioned along the y-axis. It follows from Eq. (3.10d) that the velocity induced at the point $\bar{X} = (Y,Z)$ is

$$\bar{U}(\bar{X}) = \frac{\gamma}{2\pi}\left[\bar{e}_y\left(\tan^{-1}\frac{Y-a}{Z} - \tan^{-1}\frac{Y+a}{Z}\right) - \bar{e}_z\left(\frac{1}{2}\ln\frac{(Y-a)^2+Z^2}{(Y+a)^2+Z^2}\right)\right] \tag{6.1a}$$

which for $a \to \infty$, the semi-infinite vortex sheet, becomes the velocity field

$$\bar{U}(\bar{X}) = -\frac{1}{2}\{\gamma\ \mathrm{sign}(Z)\}\bar{e}_y \tag{6.1b}$$

as already considered in Chapter 3, see Fig. 3.8a. The velocity field for $a = 2$ is depicted in Fig. 6.2a (for $Z > 0$ only). This velocity field is discontinuous across $Z = 0$ and very nearly uniform in the region considered in Fig. 6.2a. The discrete-vortex approximation is

$$\bar{U}(\bar{X}) = \frac{1}{2\pi}\left(\frac{2a\gamma}{N}\right)\sum_{i=1}^{N}\frac{-\bar{e}_y Z + \bar{e}_z(Y-Y_i)}{(Y-Y_i)^2+Z^2} \tag{6.2}$$

with $Y_i = -a + a(2i-1)/N$. The velocity field for N=8 is plotted in Fig. 6.2b. It shows that the velocity is singular at the vortices, resulting in errors becoming unbounded for $Z = 0$. For larger $Z$, of the order of distance $2a/N$ between the vortices, the error decreases rapidly. This is also illustrated in Figs. 6.2c and d which show the error contours in the vertical and horizontal component of the velocity, respectively.

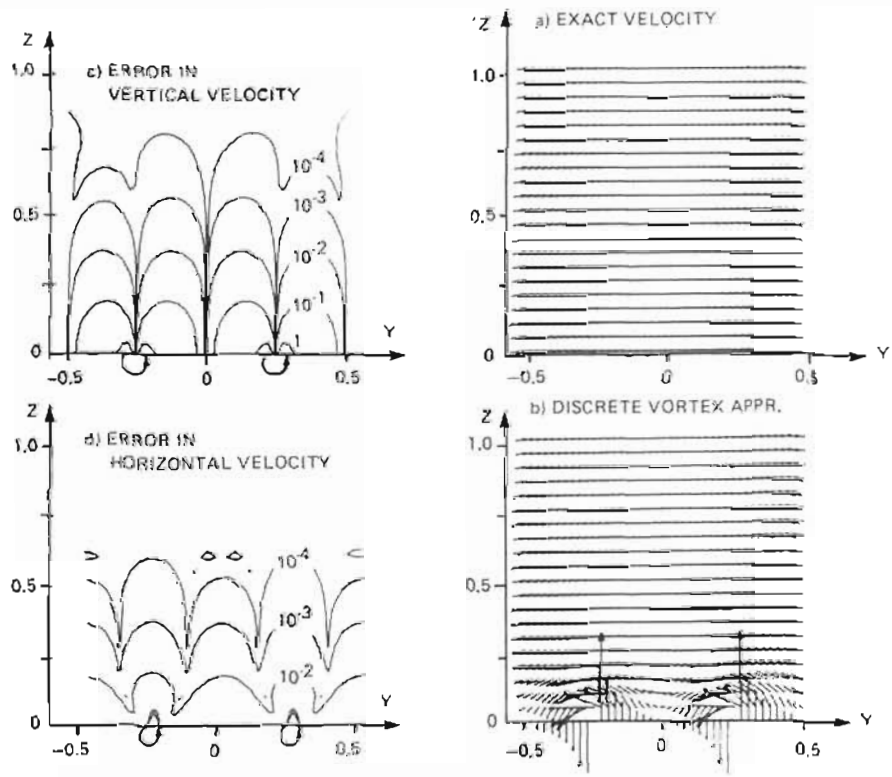


Fig. 6.2 Discrete vortex approximation with 8 vortices of vortex sheet segment $y \in [-2,2]$ of unit strength

Since the evolution of unsteady two-dimensional vortex sheets is of fundamental importance in understanding the large-scale behaviour of two- and three-dimensional shear layers in a variety of fluid-mechanical applications, the lack of reliable methods for its computation is rather unfortunate. In chapter 7 of the present study an accurate and reliable method, based on treating the vortex sheet as a continuous surface rather than as an assembly of points, will be developed.

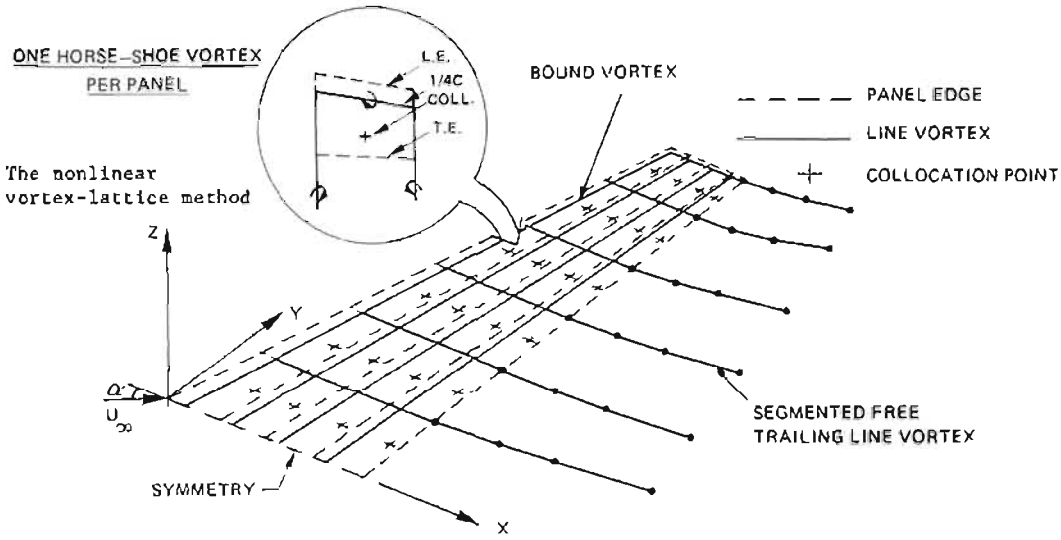


Fig. 6.3 The nonlinear vortex-lattice method

In the late sixties and early seventies it became possible to compute the detailed linear potential flow about three-dimensional configurations, though still with the classical rigid-wake assumption. In this same period the first attempts were made to compute three-dimensional wake roll-up. Mostly the vortex-lattice method was used to simulate the wing flow field (see Fig. 6.3). In the (non-linear) vortex-lattice method the "free" vortex filaments trailing from the "bound" vortices, that represent the wing, are relaxed in an iterative procedure. In this procedure the strength of the individual (horse-shoe) vortices, for a given position of the wake, is determined by imposing the zero-normal-velocity boundary condition, Eq. (3.18a), at a set of discrete points on the wing, the so-called collocation points. Subsequently a new position of the segmented "free" vortices is determined by imposing the boundary condition, Eqs. (3.19a-b), on the wake. As derived in section 3.7 these conditions are satisfied when the vortex lines, i.e. here the vortex filaments, are aligned with the local velocity vector, i.e. the free-stream velocity plus the velocity induced by all the horse-shoe vortices of given strength. Next the strength is updated by imposing with the new shape of the wake, the wing boundary conditions, etc. It is found that this nested iterative procedure usually fails when somewhere the wake approaches the configuration too closely and the interaction becomes too strong.

For the relatively small numbers of elements used in all applications reported thusfar (e.g. Butter & Hancock-1971, Rehbach-1971, Hedman-1973, Maskew-1973) a poorly resolved but realistic looking wake roll-up could be obtained. However, increasing the number of elements usually results in numerical problems (chaotic motion, etc.) similar to the problems encountered when using its two-dimensional counterpart of this method, namely the discrete-vortex method. In the current panel methods the aircraft configuration is represented more accurately than in the vortex-lattice method. However, the wake is again represented by discrete line vortices, often forming the continuation of the lift generating vortex lattice or vortex sheet on the wing camber surface. There have been some attempts to allow the wake to move (e.g. Labrujère & de Vries-1974, Jepps-1978) but as is the case in the vortex-lattice method the numerical results depend strongly on the details of the discretization and refining the panel scheme often results in the numerical problems indicated above.
In the advanced panel methods, at present in development at various institutes, not only the configuration but also the wake is represented more accurately. The latter is modeled as a continuous vortex sheet. Provided rolled-up regions (vortex cores) are modeled properly it may be expected that in the near future these advanced panel methods will be employed to obtain more reliable and consistent numerical wake roll-up procedures for three-dimensional flow.

Vortex wakes - captured vortex methods

In the vortex sheet approach the topology of the vortex wake has to be known a priori, i.e. one has to have some insight in the shape of the wake to be computed, including whether or not rolled-up regions will form. For most practical configurations the topology of the wake, to be "fitted" in the solution, is known or may possibly be derived from preliminary computations using the time-dependent analogy. However, in more complex cases this may present a problem. In these cases a method is required that "captures" the rolling-up vortex sheet as part of the solution. Quite recently it has been recognized that, even without much special measures, finite-difference methods that solve Euler's and Navier-Stokes' equations are capable of capturing rotational flow regions, i.e. vortex sheets and (thin) vortex layers, respectively (e.g. Rizzi-1982, Chattot et al.-1982). Although the published results of such three-dimensional-flow methods clearly need to be improved upon, they do indicate the great promise this approach holds.

In the framework of the two-dimensional unsteady analogy there have been earlier attempts to compute weak-interaction vortex flow solving Euler's and Navier-Stoke's equations by finite-difference methods. In these approaches vortex cores should evolve from initially thin layers in a natural way. This has been demonstrated by Weston & Liu-1982 employing a rather efficient method for solving Navier-Stokes' equations.
Zabusky-1979 considered the problem of the interaction between isolated regions with distributed but constant vorticity, simulating the final stages of inviscid wake roll-up.
In Zabusky's approach the velocity induced by a uniform rotational flow region is transformed in a line integral along the contour of the region, as shown in Chapter 3. Subsequently the position of the contour is followed as it moves with the fluid. Although the vorticity distribution of vortex cores produced by the roll-up of a vortex layer is expected to be far from uniform, this so-called method of "contour dynamics" may be useful for studying the final stages of inviscid roll-up.
Huberson-1980 considers a hybrid-type of method in which the unwound part of vortex sheet is modeled by discrete vortices and the rolled-up region as a finite core in which Euler's equations are solved by a finite-difference method.

## 6.2 Methods for computing leading-edge vortex flows

In this section we discuss methods for the strong-interaction vortex flow associated with the flow separating from the side edge and leading edge of a wing.

### Rigid-wake assumption

As early as 1939 Bollay considered the flow about rectangular wings of vanishing aspect ratio with flow separation along the side edges. Bollay's model is a vortex lattice (Fig. 6.3) of just one strip, where in addition the variation in chordwise direction of the circulation is prescribed as a mode function the magnitude of which is solved for. All the trailing legs of the lattice leave the wing at the side edge at some prescribed angle and extend from the edge to infinity downstream in the vertical plane through the side edge, neglecting the roll-up. The two unknowns of the problem, the strength of the "bound" vortex lattice and the shedding angle are solved for by imposing the normal velocity condition on the wing in the mean only and by imposing at the side-edge the (Helmholtz) alignment condition, also in the mean. It turns out that the so found angle at which the line vortices leave the wing is approximately $\alpha/2$, independent of the aspect ratio. This simple result is used throughout the literature to approximately model separation from side edges of wings of more general planform (e.g. Gersten-1961). It provides a reasonable agreement of computed and measured normal force without having to determine the position of the trailing vortices. However, due to the neglect of the roll-up the local pressure distribution is not well predicted.

The most widely used method for predicting the characteristics of configurations employing leading-edge vortex flow is the so-called "Polhamus suction analogy", Polhamus-1966. The analogy is based on the *conjecture that the vortex lift effect can be predicted* utilizing the edge suction forces. In classical lifting surface theory (e.g. Ward-1955) the velocity goes to infinity at all edges except the trailing edges, resulting in a finite suction force at leading and side edges.

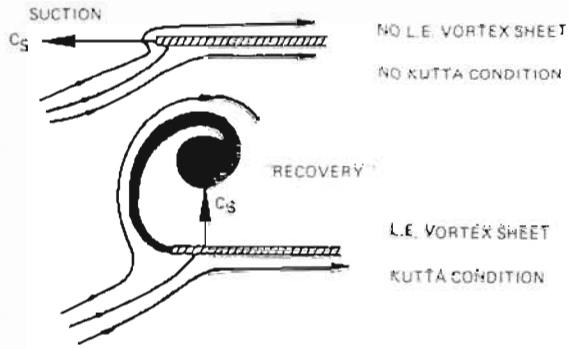


Fig. 6.4 Polhamus's leading-edge suction analogy

This force acts normal to the leading edge and lies in the plane of the wing, (partly) counteracting the drag force. The magnitude of the suction force depends on the amplitude of the singularity in the loading at the edge. On a three-dimensional wing the normal force, found from integration of the net pressure distribution, and the suction force combine to yield the correct lift, side force and induced drag of the wing. When the flow separates at the edge the suction force is lost. The analogy is based on the conjecture that in the latter case the suction force is recovered as a force rotated through 90 deg to act in the direction normal to the wing surface (Fig. 6.4). This implies that the aerodynamic forces and moments on configurations with vortex flow can be computed by utilizing any conventional linear attached flow method, without the necessity of having to solve a complex nonlinear problem. The magnitude of the suction force then follows from the behaviour of the loading near the edge. The suction analogy has been applied to a variety of cases, both in subsonic and in supersonic flow. In general the correlation of computed forces, and to a lesser extent moments, with experimental data is surprisingly good, but no theoretical explanation appears to have been given. However, the major drawback of the methods that use the suction analogy is that the pressure and velocity distribution cannot be predicted and that more complex situations, e.g. the interaction of a canard vortex with a wing, strake-wing vortex flow, vortex breakdown, etc. require the development of new empirical concepts.

With a vortex-lattice method as attached-flow solver Lamar and his co-workers (e.g. Lamar-1980) have developed the method towards a very useful engineering tool both for analysis and for design of quite general configurations, including strake-wing configurations.

### Fitted-vortex methods

Configurations that develop leading-edge vortex flow are in general slender, in the sense that in the streamwise direction variations in geometry and in the flow are much smaller than those in the cross-flow plane. In that case the full three-dimensional problem can be reduced to a quasi two-dimensional problem in successive cross-flow planes. If in addition the geometry is conical, i.e. a delta wing or a cone the flow is conical as well and only one cross-flow plane problem needs to be considered. The methods employing the slender-body approximation to conical configurations were the first to be applied with success to the computation of the flow about wings with leading-edge vortex flow. In the early fifties, Legendre-1952 and Brown & Michael-1954, devised an approximate model in this framework in which all vorticity shed at the leading edge is assumed to be concentrated in one isolated vortex (see Fig. 6.5). In order to allow for the growth in the strength of the vortex, the vortex is connected to the leading edge by a so-called feeding sheet. This feeding sheet carries the component of the vorticity parallel to the cross-flow plane and to first approximation contributes to the streamwise velocity component only. The condition imposed on the isolated vortex/feeding sheet combination is that it sustains no net force, i.e. the condition discussed in section 3.7 under (iii).

The flow problem (for zero side-slip) is solved employing a conformal mapping technique. This reduces the problem to within for those days solvable dimensions of having to determine the solution of a system of three nonlinear algebraic equations for the strength and position of the vortex. The conditions imposed were the zero-net-force condition (two components) on the vortex system and the Kutta condition at the leading edge. Later Maggler & Smith-1959 improved upon this early model by by including in the transformed plane a simple representation for a vortex sheet of finite extent, which in particular has a large effect on the Kutta condition. The resulting system of the order of 10 nonlinear equations was solved by laborious desk-machine computation. The next step was Smith's model (Smith-1968) in which the sheet of finite extent is fully accounted for (see Fig. 6.6). In the cross-flow plane the sheet is discretized in elements, each carrying an element-wise constant streamwise vorticity distribution. The unknown parameters in the description of the geometry of the sheet and its streamwise vorticity distribution are solved for by imposing at discrete points on the sheet the vortex-sheet boundary conditions (see section 3.7) that a vortex sheet is a stream surface and that the pressure is continuous across it. The resulting system of the order of 50 nonlinear equations is solved by a (nested) iterative procedure employing a digital computer. Results of Smith's vortex sheet method compare quite satisfactorily with experimental (turbulent) flow data.

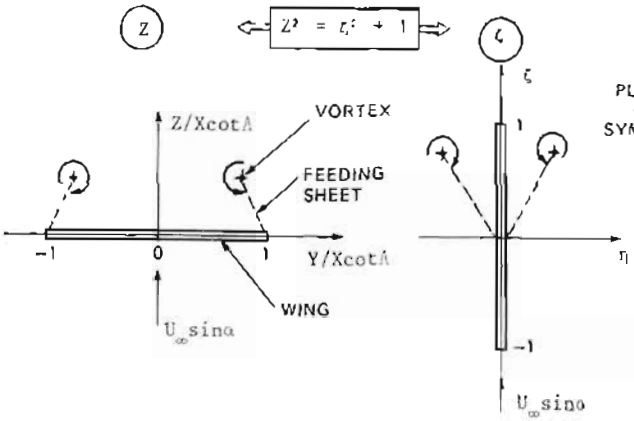


Fig. 6.5 Model of Brown & Michael for slender delta wing with leading-edge vortex separation

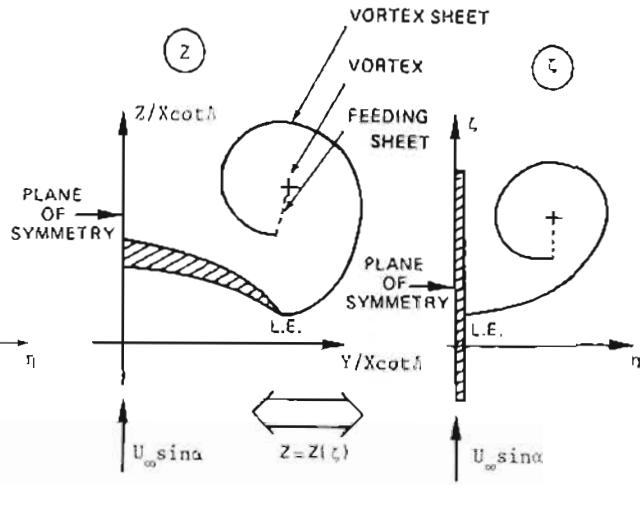


Fig. 6.6 The model of Smith for slender delta wing with leading-edge vortex separation

The above slender-body-approximation methods have also been extended to the case of slender wings with curved leading edges or chordwise camber. Using the conformal mapping technique Smith-1959 advanced Brown & Michael's model to plane wings with curved leading edges. Sacks-et.al.-1967 treated wing-body combinations employing a discrete vortex representation for the leading-edge vortex sheet. Although the vortex sheet appears chaotic the predicted forces compare reasonably well with experimental data. Clark-1976 has extended Smith's method to non-conical planforms. He found that the method was unable to deal with cases where second centers of roll-up, i.e. double-branched vortices, began to develop. Quite recently Peace-1983 developed an improved discrete-vortex method employing among other things the sub-vortex technique and a new vortex shedding model. The method has been applied to various slender wings, including strake-wing configurations; for the latter both the strake and the double-branched wing vortex (see Fig. 2.4) were computed. This demonstrated that discrete-vortex methods, though prone to numerical problems requiring careful tuning of the discretization, have the flexibility to cope with the vortex flow about more complex geometries.
Rao & Maskew-1982 employ an improved discrete-vortex method in the physical plane to compute the flow about general slender planforms, including wings with thickness. They also demonstrate that, before the vortex system becomes disordered, more than one center of roll-up can be computed by the discrete vortex technique.

In chapter 8 of the present study we will develop a slender-body-approximation method based on discretizing the vortex sheet more accurately using the panel method.

In the framework of three-dimensional flow the non-linear vortex-lattice method has attracted considerable attention (e.g. Belotserkovskii-1968, Rehbach-1973, Kandil et al.-1976, Schröder-1978, Rusak et al.-1983). In the non-linear vortex lattice method, the trailing line vortices are relaxed to assume the local flow direction. In regions of large variations, as usually occur in cases with vortex flow from leading and side edges, considerable numerical problems are encountered which become worse when more vortices are employed.
From a perusal of published results of nonlinear vortex-lattice methods, it must be concluded that, although forces and moments can be predicted reasonably well, representing a vortex sheet by discrete vortex filaments is apparently a too crude and too singularly behaved (see section 3.4.2) approximation. Luckring-1986 reaches a similar conclusion.

In the panel-method approach developed by Johnson et al.-1980, vortex sheets are represented more accurately by a piecewise continuous doublet distribution on flat panels. The vortex sheet emanating from the leading edge is allowed to attain a position and strength such that the boundary conditions (zero normal velocity and continuous pressure) on the vortex sheet are satisfied. The wake downstream of the trailing edge is a surface that is a smooth continuation of the wing and leading-edge vortex sheet; i.e. the geometry of this vortex sheet is fixed. The strength of the wake follows from imposing the condition that the pressure is continuous across the sheet, while the normal-velocity condition is not imposed (see also Nangia & Hancock-1970 who applied a similar model for an extension to three-dimensions of the simpler Brown & Michael model).
The main difficulty in the vortex sheet method is that one has to solve for both strength and geometry of the vortex sheet, i.e. one imposes boundary conditions that are of mixed analysis (the normal velocity condition)/design (the pressure condition) type. Constructing a numerically stable scheme, i.e. expressing the panelwise representations for geometry and doublet distribution in terms of unknown parameters to be solved for, has proven to be difficult. Finally it was found that a scheme derived from a least-squares fit involving parameters associated with the representations on 16 neighbouring panels provided sufficient stability for most cases. In general the (mostly with a rather coarse panel scheme) computed forces and moments are in satisfactory agreement with experimental data, while pressure distributions are often unsufficiently resolved to reveal the details in the distribution in the region underneath the vortical flow region.
In the present study (chapter 9) a panel method will be developed for the threedimensional flow problem that has a freely-moving near wake and a numerical approach that differs from the one of Johnson's method.

Captured-vortex methods

One of the first applications of a finite-volume method for solving Euler's equations to slender delta wings was reported by Eriksson & Rizzi-1981. It emerged that in this time-marching method (from rest to steady flow) a vortical flow was generated without explicitly imposing a Kutta type of condition at the leading edge. Comparing the computed results with experimental data and also with results from panel method computations suggest that due to the relatively coarse mesh used in these early applications, the amount of vorticity contained in the vortical flow region is too small and the vorticity is spread too much. As a result the computed upper surface suction peaks are lower than computed by a panel method, even lower than measured in experiment. A further anomaly is the appearance of a second, spike-like, suction peak right at the leading-edge, whether rounded or sharp. This indicates that the flow turns around the edge before it separates at a location on the upper wing surface slightly inboard of the leading edge.

In later applications (Hitzel & Schmidt-1984, Rizzi-1984), the spike-like suction peak is not so dominantly present, while studies on the influence of mesh density (Rizzi-1984) reveal a rather large influence of mesh density and lay-out on computed pressure distributions.

The treatment of flow separation at "aerodynamically sharp" edges in methods solving Euler's equations is a major issue. When inviscid flow turns around the edge it will expand to the limit of vacuum pressure. However, viscous flow will separate at the edge before the inviscid expansion limit is reached. This suggests that truly simulating high-Reynolds number flow using Euler's equations requires some kind of modeling (Kutta conditions). This is common practice in Euler methods for supersonic flow employing a space-marching solution technique, but not so in the more recent Euler methods that use a time marching solution technique.

Two reasons have been put forward for the inviscid separation phenomenon occuring in the latter type of method:

(i) During the time marching process, from rest to steady state, shock waves appear at the leading-edge which produce vorticity due to total pressure losses, resulting in the formation of the leading-edge vortex (Eriksson & Rizzi-1981, Hitzel & Schmidt-1984).

(ii) Separation occurs because of viscous-like terms due to (explicit and/or implicit) dissipative terms in the numerical scheme, e.g. shock-capturing algorithm, terms or procedures added for stability, surface boundary conditions, etc. (Raj-1984, Newsome-1985).

Raj-1984 reports that for the low Mach number cases he studied (using Jameson's FLO-57) the flow remainded subcritical throughout the evolution to steady state and still a vortical type of flow emerged. In a careful study by Newsome-1985 for the case of supersonic flow about a delta wing with subsonic (not infinitely sharp) leading edges two Euler solutions evolved, one for a relatively coarse mesh with and one for a fine mesh without leading-edge vortex separation. The latter solution, with the explicit dissipative terms turned off at the edge involves a cross-flow shock, on its downstream side accompanied by a small region of distributed vorticity, similar to solutions found earlier using shock-fitting. Following the time-accurate transient solutions it was observed that the coarsegrid solution evolved from one with a cross-flow shock to one with leading-edge vortex separation. The above investigations strongly suggest that in the time-marching Euler methods numerical and artificial dissipation are responsible for the flow separating at the leading edge.

It has been claimed that the finite-volume methods for solving Euler's equations also simulate vortex breakdown and secondary vortex separation. Vortex breakdown, at least its onset, has been reported to depend only weakly on Reynolds number so there may be some possibility that it can be modeled by Euler's equations. However, experimental data have shown that secondary-vortex separation does depend on Reynolds number and quite strongly on whether the boundary layer is laminar or turbulent, so it appears that as far as secondary separation is concerned observed similarities in the computational results are spurious numerical effects associated with the particular discretization used.

This indicates that also in captured vortex methods some a priori knowledge about the flow field topology is required in order to set up a mesh that is sufficiently fine in regions of vorticity production and to avoid excessive spreading of the vortical flow region(s).

The Euler methods used in above investigations are designed for transonic and supersonic flow and the convergence to steady state deteriorates badly for decreasing Mach numbers. In the Euler equations for incompressible flow this difficulty is avoided by using the artificial compressibility concept (Rizzi-1985), also used for solving the Navier-Stokes equations for incompressible flow.

Another method, due to Rehbach (Rehbach-1978, Morchoisne-1986) does not require the construction of a spatial mesh. In the (incompressible flow) method the velocity field is expressed as the contribution due to the "bound" wingsurface vorticity (approximated by the vortex-lattice method) and the contribution due to free floating "vorticity-carrying particles" The latter simulate the spatial vorticity distribution. The approach followed is a time-dependent one; starting from rest, the vortical particles are traced. At each time step the strength of the "bound" vortices is determined by satisfying, for a given spatial vorticity distribution, the normal velocity boundary condition on the wing. Subsequently, from predetermined separation lines, here sharp edges, new vortical particles are shed into the flow field. The strength of the new vortices is derived from Kutta-condition type considerations.

The vortical particles already in the flow field are convected with the local velocity, while the rate of change of the total amount of vorticity contained in any particle is obtained from an integral form of the vorticity transport equation. In this grid-free method for solving Euler's equations for incompressible flow vorticity is produced at predetermined locations only, but the vortex shedding mechanism used in the numerical model may have a considerable effect on the computed flow. In the Lagrangian type of approach of the vorticity transport equation excessive spreading of vorticity is avoided. A drawback of this method is that in order to obtain sufficiently detailed pressure distributions the number of vortical particles has to be quite large, resulting in considerable computational cost.

Krause, Shi & Hartwich-1983 developed a finite-difference method to solve the incompressible viscous flow about a delta wing of unit aspect ratio at 15 degrees incidence. It is found that in the numerical simulation the influence of the Reynolds number on the development of the leading-edge vortex is negligible. It is also indicated that the effect the truncation errors associated with the finite-difference scheme for inviscid flow already introduce an (artificial) vorticity production term in otherwise irrotational flow. Fujii & Kutler-1983, also using a finite-difference method, solve the Reynolds-averaged thin-layer Navier-Stokes equations for compressible flow about thick rounded and blunted delta-wings and strake-wing configurations. At the leading edge pressure spikes occur similar to those that show up in the results of finite-difference methods for solving Euler's equations. These again indicate that the flow is attached at the leading edge and separates a short distance inboard of the leading edge. In general this results in a weaker vortex than in case the flow separates at the edge. Although laminar flow was assumed, there is no sign of any secondary separation so dominantly present in laminar-flow experiments.

It should be noted that the methods for solving Euler's equations or the Navier-Stokes equations are relatively expensive. These methods require the processing speed of modern vector computers as the CRAY-XMP, CYBER 205 and NEC SX-2.

6.3 Methods for computing vortex flows associated with smooth-surface separation

Provided the separation lines are specified (e.g. known from experiment) and highly swept, the same types of computational method can be employed for computing the vortex flow associated with separation from a smooth surface as for computing vortex flow associated with separation at a sharp edge.

Although there have been some, not very successful, attempts to compute the flow about slender wings with both leading-edge and secondary separation, most emphasis in investigations concerning smooth-surface separation has been on slender-body vortex flows. Especially in missile aerodynamics a number of advanced engineering type methods have been developed, employing the ($\alpha$/2) rigid wake or fitted-vortex approach. The latter will be considered here in more detail.

The most simple method is due to Bryson-1959 (see Fig. 6.7), who considered the problem of the separated flow about slender bodies within the framework of slender-body theory. His method can be regarded as an adaptation of the Brown & Michael model of the flow about a slender delta wing or Smith's (-1959) model of the flow about more general slender wings. In this method all vorticity is concentrated into one isolated vortex. The unknowns of the problem are the position and strength of the vortex, solved for by imposing the Kutta condition (stagnation of the velocity in the cross-flow plane) at the point of separation and the condition that the vortex/feeding sheet combination sustains no net force. Bryson considered the symmetric situation only, reducing the problem further to one of 3 nonlinear algebraic equations for as many unknowns. Dyer, Fiddes & Smith-1981 considered the more general situation of Fig. 6.7, resulting in 6 nonlinear equations for as many unknowns. They succeeded in computing an unsymmetric solution for the position and strength of the vortices. Comparison with experimental data showed that this solution resulted in about the right order of magnitude of the side force.

In the framework of slender-body theory the discrete-vortex method can also be applied to the case of separation from a smooth surface. Angelucci-1971 obtains reasonable results using this approach for a cone with given location of the separation line. Wardlaw-1974 treats the unsymmetric flow past bodies of revolution, resulting in a flow pattern resembling a vortex street. There have been attempts to compute the line of separation tentatively (assuming a weak coupling) employing a simple criterion for boundary layer separation (Deffenbaugh & Koerner-1977) or a three-dimensional boundary-layer method (Botnan-1981), some with results of acceptable engineering accuracy.
The common feature of the above discrete vortex/vortex lattice methods is that a considerable degree of empiricism is required, especially with respect to the vortex shedding mechanism/Kutta condition.

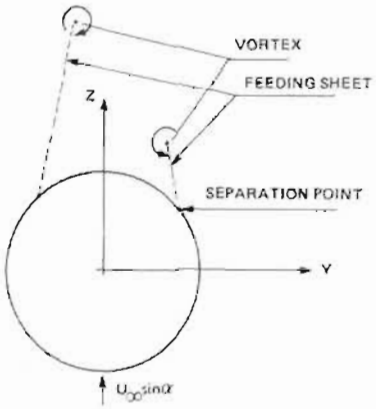


Fig. 6.7 Bryson's cross-flow plane method

The uncertainties connected with the shedding mechanism/Kutta condition are absent when a vortex sheet is used to simulate the flow. Fiddes-1980 employs the vortex sheet method for computing the symmetric separated flow past slender elliptic cones at incidence. The discretization, similar to Smith's-1968, is carried out in a transformed plane, in which the vortex sheet near the point of separation is regular. The position of the separation line is determined in an iterative fashion, using a laminar boundary-layer method and a triple-deck model for the viscous-inviscid interaction.
Fiddes & Smith-1982 extend the inviscid part of their vortex sheet method to the case of the unsymmetric separated flow past slender circular cones. It is demonstrated that for symmetric flow conditions and location of separation lines one symmetric solution and one (mirror-imaged) pair of unsymmetric solutions exist. The side force associated with the asymmetric solutions is of the same order of magnitude as the normal force, just like found in experiment.

The methods developed thusfar for fully three-dimensional flow with separation from a smooth surface are the vortex-lattice type (e.g. Almosnino & Rom-1973). In general the calculated values of the aerodynamic coefficients (for prescribed separation lines) are in reasonable agreement with experimental data. However, most results are for a relatively low number of vortices, which mostly avoids the chaos inherently connected with the discrete-vortex approximation, but provides insufficient resolution of the pressure distribution.

## 6.4 Methods developed in the present study

The present investigation is aimed at the development and subsequent application of reliable numerical methods for predicting the detailed aerodynamic characteristics of configurations with ordered vortex flow.

From the inventory of existing methods, presented in the present chapter, it will be clear that for this purpose the method has to either "fit" or "capture" the vortical flow regions. In summary, in the present study it is assumed that:

- the flow is incompressible and steady;
- viscosity may be neglected, except as a cause of separation;
- the topology of the vortex flow is ordered and known a priori, e.g. from experiment;
- the rotational flow regions remain compact.

The above assumptions, together with the requirement that the method had to be developed on the by present standards small, mainframe computer available at NLR during the development, have led to choosing the "fitted-vortex" type of approach of potential flow with embedded vortex-sheets and vortex cores. The mathematical model underlying this approach has been described in detail in Part I.

From the inventory given in the previous section it must be concluded that the discrete-vortex/ vortex-lattice methods have quite some flexibility in modeling vortex flow, but also that numerical problems occur due to the highly singular velocity field associated with the approximation. In this thesis vortex flow will be simulated using the vortex-sheet method, i.e. vortex sheets are modeled as continuous surface vorticity distributions, resulting in a more accurate and reliable computational method. However, on the other hand it is less flexible than the discrete-vortex/vortex-lattice method in modeling more complicated vortical-flow patterns with multiple centres of roll-up. The latter often occur in the wake behind aircraft during take-off and landing, and one of our aims is to show that a vortex-sheet method is capable of computing this type of wake in a reliable fashion.

In the remainder of this part we describe the development of a vortex-sheet method for:

- computing vortex sheet motion in two-dimensions, i.e. the two-dimensional time-dependent analogy of three-dimensional (weak-interaction) vortex wakes (chapter 7);
- computing, within the framework of slender-body theory, the strong-interaction vortex flow about more or less arbitrarily shaped slender wings and bodies with vortex sheets emanating from prescribed locations (chapter 8);
- computing the three-dimensional strong-interaction vortex flow about slender thin, delta-like wings with leading-edge vortex flow (chapter 9).

The methods developed will be evaluated by comparison of their results with results of other computational methods, as well as with available experimental results.

# 7 METHOD FOR QUASI TWO-DIMENSIONAL VORTEX-WAKE ROLL-UP

## 7.1 Introduction

In this chapter a computational procedure is described for computing the inviscid roll-up of vortex wakes. It is assumed that the two-dimensional unsteady analogy, derived in section 5.3, may be employed. The main limitation of this analogy is that the interaction of the rolling-up wake with a nearby part of the aircraft configuration cannot be accounted for. Nevertheless, the unsteady analogy is valuable for obtaining a first, qualitative, insight in the topology of the rolling-up wake and also for obtaining a first approximation for the solution of a method that treats the fully three-dimensional nonlinear problem.

The type of geometry considered in the present study is shown in Fig. 7.1. It consists of a vortex sheet subdivided in several segments. Segments may begin or end with a feeding sheet connecting the edge of a segment to a concentrated vortex. Alternatively, a vortex-sheet segment may begin or end in the flow, as long as the doublet distribution is zero at the edge. Also, a vortex sheet segment may be connected to another vortex-sheet segment, in which case it is implied that the doublet distribution and geometry are continuous across the connecting edge. This model of the vortex sheet geometry covers most cases that occur in practice, including cases with port-starboard side symmetry, single and double branched vortex cores, and closed vortex sheets.

In our computational procedure the velocity field is computed employing a second-order accurate panel method. This method will be described in the next section. A second-order panel method requires that the geometry $\bar{X}(t)$ and the doublet distribution $\mu(t)$ are nonsingular in the sense that the second derivative of both quantities is finite. However, at the wing tip the doublet distribution usually behaves like $\mu(t)\sim\sqrt{\varepsilon}$, $\varepsilon$ being the distance from the tip. This implies that the second-order panel method cannot be employed there. In the third section it is described how this difficulty can be circumvented.

Often the doublet distribution and vortex sheet geometry develop large gradients during the computation. In order to obtain a more or less uniform distribution of the discretization error the discretization should be refined in regions of large gradients. Such a solution-adaptive panel scheme is described in the fourth section of this chapter. The fifth section describes in some detail the steps of the computational procedure. In the sixth section the method is applied to a number of test cases. Also, computed results are compared with results of other numerical methods. The final section describes the extension of the method to the case of periodic vortex-sheets. It includes, through a numerical study of the Kelvin-Helmholtz instability, an assessment of the smoothing implied in the present method.

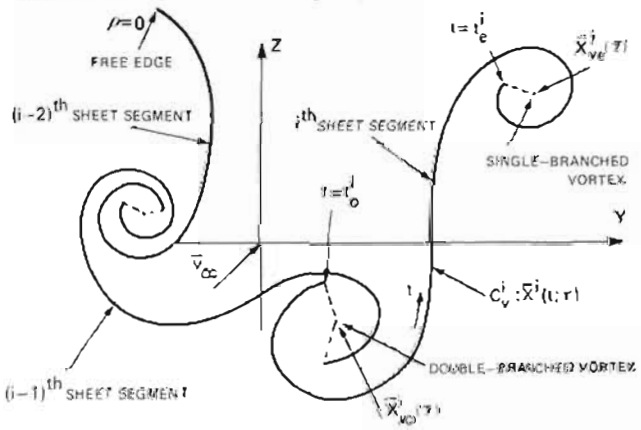


Fig. 7.1 Geometry for 2D time-dependent wake roll-up

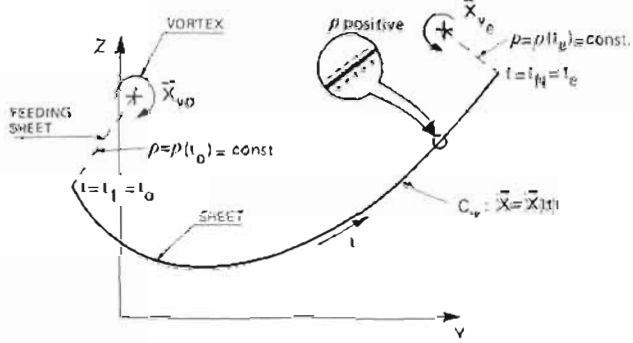


Fig. 7.2 Doublet distribution on 2D vortex-sheet segment at time τ

## 7.2 Two-dimensional second-order panel method

### 7.2.1 General aspects

In this section we develop the panel method employed to compute the velocity in the Trefftz plane. At the point $\bar{X}_o$ in this plane the velocity is the sum of the contribution from the free stream and the velocity induced by the doublet distribution on the vortex-sheet segments, i.e. according to Eq. (5.34):

$$\bar{v}(\bar{X}_o) = \bar{V}_\infty + \sum_k \bar{U}_\mu^k(\bar{X}_o) \tag{7.1a}$$

where $\bar{V}_\infty$ is the component of the free stream parallel to the Trefftz plane, see Eq. 5.21c, and $\bar{U}_\mu^k$ the velocity at time $\tau$ induced at the point $\bar{X}_o$ by the doublet distribution on segment $C_v^k$ (see Fig. 7.2). A segment consists of a continuous vortex sheet given by $\bar{X}^k(t)$, $t\in[t_o^k, t_e^k]$ with $t$ a parameter along $C_v^k$ and two vortices, one vortex at $\bar{X}_{vo}^k$ connected through feeding sheet to $\bar{X}^k(t_o^k)$ and one vortex at $\bar{X}_{ve}^k$ connected through a feeding sheet to $\bar{X}^k(t_e^k)$. Denoting the doublet distribution $\mu^k(t;\tau)$ on segment $C_v^k$ by $\rho^k(t)$ the induced velocity is expressed as, see Eq. (5.34c):

$$\bar{U}_\mu^k(\bar{X}_o) = \frac{\bar{e}_x}{2\pi}\times\left(-\int_{C_v^k}\frac{d}{dt}\rho^k(t)\frac{\bar{R}^k}{|\bar{R}^k|^2}dt + \delta_{ve}^k\left(\frac{\bar{R}_{ve}^k}{|\bar{R}_{ve}^k|^2}\right)\rho_e^k - \delta_{vo}^k\left(\frac{\bar{R}_{vo}^k}{|\bar{R}_{vo}^k|^2}\right)\rho_o^k\right) \tag{7.1b}$$

where $\bar{R}^k = \bar{X}_o - \bar{X}^k(t)$, $\bar{R}_{ve}^k = \bar{X}_o - \bar{X}_{ve}^k$ and $\bar{R}_{vo}^k = \bar{X}_o - \bar{X}_{vo}^k$. In Eq. (7.1b) $\delta_{ve}^k$ and $\delta_{vo}^k$ are 1 in case the corresponding edge is connected to a vortex and $\delta_{ve}^k$ and $\delta_{vo}^k$ are 0 otherwise. Also in case $|\bar{R}_{ve}^k| < \varepsilon$ we take $\delta_{ve}^k = 0$ and similarly $\delta_{vo}^k = 0$ in case $|\bar{R}_{vo}^k| < \varepsilon$, where $\varepsilon$ is a small quantity ($10^{-6}$ here). The first term in Eq. (7.1b) corresponds to $\bar{U}_1^k(\bar{X}_o)$, the contribution in the induced velocity due to the vorticity (of strength $-\bar{e}_x\frac{d\rho^k}{dt}$) on the sheet. The second and third term corresponds to the contribution due to the vortex of strength $\rho_e^k = \rho^k(t_e)$ at $\bar{X}_{ve}^k$ and the one of strength $\rho_o^k = \rho^k(t_o)$ at $\bar{X}_{vo}^k$, respectively.

Discrete vortices will be associated with any jump in the doublet distribution $\rho^k(t)$ on geometry $\bar{X}^k(t)$, see also Appendix A. These discontinuities include the ones due to discretization errors in the doublet distribution and geometry, but we will show later that these contribute terms of higher order which may be omitted.

In the remainder of this section we consider just one particular segment and drop superscript k and the the summation.

In the present study the parameter t along the curve $C_v$ is chosen to be linearly proportional to the arc-length along the curve; i.e. with primes denoting differentiation with respect to t:

$$t = t_o + \frac{1}{b}\int_{t_o}^{t} |\bar{X}'(\xi)|d\xi, \qquad \text{for all } t\in[t_o,t_e] \tag{7.2a}$$

with b as the constant of proportionality. This constant can be chosen arbitrarily. In the present chapter we choose b = 1, i.e. t corresponds to the arc length along the curve. In the next chapter b is chosen to be equal to the total arc length along the segment, i.e. there t is the normalized arc length along the curve. It is implied by Eq. (7.2a) that

$$|\bar{X}'(t)| = b = \text{constant} \qquad \text{for all } t\in[t_o,t_e] \tag{7.2b}$$

The unit tangential vector along the curve then is

$$\bar{e}_t = \bar{X}'(t)/b \tag{7.2c}$$

The unit normal vector, pointing to the left when moving with increasing t along the curve is:

$$\bar{e}_n = \bar{e}_x \times \bar{e}_t \tag{7.2d}$$

It is implied by Eq. (7.2b) that $\bar{X}''(t)$ is a vector perpendicular to $\bar{X}'(t)$, i.e. it can be written as

$$\bar{X}''(t) = k_n b^2 \bar{e}_n \tag{7.2e}$$

where the curvature $k_n(t)$ is defined as

$$k_n(t) = \frac{1}{b^3}\{\bar{X}'(t)\times\bar{X}''(t)\}.\bar{e}_x \tag{7.2f}$$

7.2.2 Small-curvature expansion

The curve $C_v$ is subdivided into NP = N-1 panels, for which $t\in[t_j,t_{j+1}]$, j = 1(1)NP and the integral in Eq. (7.1) is replaced by the sum of integrals over the individual panels. On each panel the functions $\bar{X}(t)$ and $\rho(t)$ are approximated by piecewise quadratic representations, i.e. we expand these functions as:

$$\bar{X}(t) = \bar{X}(t_j^*) + \Delta t\bar{X}'(t_j^*) + \tfrac{1}{2}\Delta t^2\bar{X}''(t_j^*) + O(\delta_j^3) \tag{7.3a}$$

$$\rho(t) = \rho(t_j^*) + \Delta t\rho'(t_j^*) + \tfrac{1}{2}\Delta t^2\rho''(t_j^*) + O(\delta_j^3) \tag{7.3b}$$

where $\Delta t = t-t_j^*$, $t_j^*\in[t_j,t_{j+1}]$ denotes the so-called expansion point and $\delta_j = b(t_{j+1}-t_j)$ denotes the panel width in terms of arc length. In the above expressions it is implied that the higher-order terms are small, i.e. that both $|\bar{X}'''(\xi)|/b^3$ and $|\rho'''(\xi)|/b^3$ are bounded for all $\xi\in[t_j,t_{j+1}]$.

When satisfying the boundary conditions the point $\bar{X}_o$ will be situated at each point of the vortex system, including at points on the vortex sheet $C_v$ itself. The integrand in Eq. (7.1) becomes singular for the point were $\bar{X}_o = \bar{X}(t)$. This implies that the integration cannot be carried out by one of the standard rules for numerical integration. Here we resort to the so-called small-curvature expansion of Hess-1975, to arrive at a second-order accurate expression. In this approach $\bar{R}$ is replaced by (Fig. 7.3):

$$\bar{R} = \bar{R}_f - \tfrac{1}{2}\Delta t^2\bar{X}''(t_j^*) + O(\delta_j^3) \tag{7.4a}$$

where

$$\bar{R}_f = \bar{X}_o - \bar{X}(t_j^*) - \Delta t\bar{X}'(t_j^*) \tag{7.4b}$$

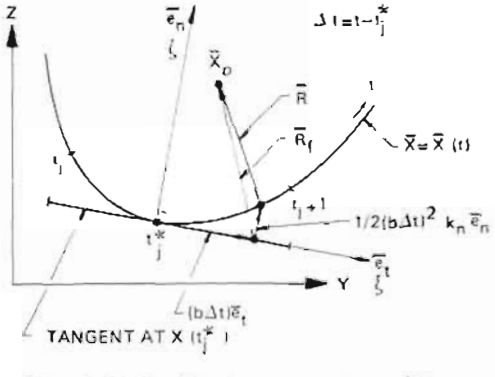


Fig. 7.3 Small-curvature expansion

is the vector pointing from the point on the tangent at $\bar{X}(t_j^*)$ to the point $\bar{X}_o$. Denoting the order of magnitude of $\bar{R}_f$ by D and assuming that $k_n(t_j^*)$, $\rho'(t_j^*)/b$ and $\rho''(t_j^*)/b^2$ are O(1) one obtains, upon summing over all panels of the vortex sheet $C_v$, for the first term in Eq. (7.1b):

$$\bar{U}_Y(\bar{X}_o) = \frac{1}{2\pi}\sum_{j=1}^{NP}\{\rho'(t_j^*)(\bar{E}_o+k_n(t_j^*)\bar{E}_o^c)+\rho''(t_j^*)\bar{E}_1+ O(\delta_j^2\delta_j^2/D^2,\delta_j^2\delta_j^3/D^3,\ldots)\} \tag{7.5a}$$

where

$$\bar{E}_k = -\bar{e}_x \times \int_{t_j}^{t_{j+1}} \Delta t^k \left(\frac{\bar{R}_f}{|\bar{R}_f|^2}\right) dt \tag{7.5b}$$

$$\bar{E}_k^c = \bar{e}_x \times \int_{t_j}^{t_{j+1}} b^2 \Delta t^{k+2} \left(\frac{1}{2}\bar{e}_n - \frac{\bar{R}_f \cdot \bar{e}_n}{|\bar{R}_f|^2}\bar{R}_f\right) \frac{dt}{|\bar{R}_f|^2}$$

$$= \bar{e}_x \times \int_{t_j}^{t_{j+1}} \frac{1}{2} b \Delta t^{k+2} \frac{\partial}{\partial t}\left(\frac{\bar{e}_x \times \bar{R}_f}{|\bar{R}_f|^2}\right) dt \tag{7.5c}$$

The integrals in the expressions for $\bar{E}_k$, and $\bar{E}_k^c$ can be expressed in closed form, see Appendix D for details.

The first term in Eq. (7.5a) is $O(\delta_j/D)$, the second and third term are of $O(\delta_j\delta_i/D)$ and $O(\delta_j\delta_i^2/D^2)$, respectively. For points $\bar{X}_o$ near the influencing panel D will by $\delta_j$ and the local error indicated in Eq.(2.5a) will be $O(\delta^2)$. For points $\bar{X}_o$ not near the influencing panel $\delta_j/D$ will be smaller than 1.
For the simple case of a doublet distribution on a double-infinite flat plate with a uniform paneling it can actually be shown that the composite error associated with the approximation of Eq. (7.5) is $O(\delta^2)$. However, for the general case of a doublet distribution on a arbitrary (but smooth) curve with a non-uniform paneling, it must be postulated that the composite error is $O(\delta^2)$ where $\delta^2$ is a measure of the average panel width.

The discontinuity in both $\rho(t)$ and $\bar{X}(t)$ across the panel edges is, within the framework of the quadratic representation, of order $\delta_j^3$. This implies that the contribution due to the vortices associated with these discretization error discontinuities at the panel edges $t = t_j$, $j = 2(1)NP$ is of the same order as the error in Eq. (7.5a) and may be neglected. At the edges $t = t_1 = t_o$ and $t = t_N = t_e$ the doublet distribution is either zero, continued onto a linking segment or continued as a constant onto the feeding sheet. The vortex due to the discontinuity in $\rho$ at the end of the feeding sheet is accounted for in the last two terms of Eq. (7.1).

For points $\bar{X}_o$ close to panel edges spurious effects may be caused by noncancelling logarithmic singularities due to discontinuities in geometry and doublet distribution and their derivatives. To avoid this as much as possible we have chosen the panel midpoints as the points where the velocity is computed. For the influence of a panel on itself we have to choose the same midpoint as the expansion point, so that then $\bar{X}_o = \bar{X}(t_j^*)$. For points $\bar{X}_o$ not on the panel there is some freedom in the choice of $t_j^*$. Note that for flat panels the choice of $t_j^*$ does not affect the induced velocity at all, while for curved panels there is a small effect as long as the point $\bar{X}_o$ is not in or close to the region where the position of the true panel deviates from the tangent line. In the present study we have chosen for an expansion point that is fixed irrespective of the position of $\bar{X}_o$. The obvious choice is that the expansion point situated at the panel midpoint, i.e. at $t_j^* = \frac{1}{2}(t_j + t_{j+1})$, $j = 1(1)NP$. The latter implies that for the present method the distance between two individual portions of the vortex sheet, or between the vortex sheet and a vortex should always be greater than $(b\Delta t_j)^2 k_n(t_j^*)$.

The velocity induced at a panel midpoint is dominated by the contribution due to the panel itself. With the panel midpoint as expansion point it follows from the expressions given in Appendix D that the influence of panel i at its own midpoint $t = t_i^*$ is

$$\bar{U}_Y^i(\bar{X}(t_i^*)) = \frac{1}{2}\left\{\frac{\rho'(t_i^*)}{b}\right\}\mathrm{sign}(\zeta)\bar{e}_t$$

$$+ \frac{1}{2\pi}\left[-\frac{1}{2}\left\{\frac{\rho'(t_i^*)}{b}\right\}k_n(t_i^*)\bar{e}_t + \left\{\frac{\rho''(t_i^*)}{b^2}\right\}\bar{e}_n\right] b\Delta t_i \tag{7.6}$$

where $\mathrm{sign}(\zeta)$ is the sign of $\zeta$, i.e. $\mathrm{sign}(\zeta) = \pm 1$ for $\zeta = 0^{\pm}$ (see Fig. 7.3). When traveling along the curve in the direction of increasing t, $\zeta = 0^-$ denotes the left-hand side and $\zeta = 0^+$ denotes the right-hand side of the curve.

Across the vortex sheet the velocity experiences a jump of magnitude $\rho'(t_j^*)/b$. The average tangential velocity is proportional to $k_n(t_j^*)\rho'(t_j^*)$, while the normal velocity is proportional to $\rho''(t_j^*)$.

For points $\bar{X}_o$ in the far-field of the panel computing time is saved by using a single-pole expansion rather than the computationally more expensive small-curvature expansion. In terms of the single-pole expansion the contribution of the j-th panel in $\bar{U}_Y(\bar{X}_o)$ is, (see Eq. (7.1)):

$$\frac{-1}{2\pi}\rho'(t_j^*)\bar{e}_x \times \frac{\bar{X}_o - \bar{X}(t_j^*)}{|\bar{X}_o - \bar{X}(t_j^*)|^2}\Delta t_j + O(\delta_j^3) \tag{7.7}$$

where $t_j^*$ is the panel midpoint. The truncation error of order $\Delta t_j^3$ ensures that in the summation over all far-field panels the second-order accuracy is maintained.

In the case $V_\infty \equiv 0$ and the geometry and doublet distribution are symmetric with respect to the plane Y=0, i.e. port side/starboard side symmetry, we need to consider the points on the vortex system for which Y≥0 only. However, the port-side (Y<0) of the system does contribute in the velocity at the point $\bar{X}_o$ on the starboard side ($Y_o \geq 0$). As explained in section 3.7 this contribution is obtained most conveniently by adding to the velocity $\bar{U}_d(\bar{X}_o)$ induced at $\bar{X}_o$ by the segment on the starboard side, i.e. Eq. (7.1) the term $[S]\bar{U}_d([S]\bar{X}_o)$ where [S] is defined in Eq. (3.22a).

7.2.3 Numerical scheme

As discussed above the panel midpoints are chosen as the expansion points and also as the points where the velocity is computed, i.e.

$$t_i^* = \tfrac{1}{2}(t_i + t_{i+1}), \qquad \text{for } i = 1(1)NP \tag{7.8}$$

This choice avoids spurious effects caused by permissible discontinuities in the panelwise representations for the geometry and the doublet distribution.

The description of the second-order panel method is made complete by choosing the manner in which the quantities related to geometry and doublet distribution are expressed in terms of the given quantities. Here we assume that the function values of both $\sigma(t)$ and $\bar{X}(t)$ are specified at the panel-edge points. The function value, first and second derivative at the panel midpoint are obtained from the function value at the panel-edge points as follows. For $t\in[t_j, t_{j+1}]$ the function $f(t)$, denoting either $\bar{X}(t)$ or $\sigma(t)$, is expressed as the quadratic representation

$$\begin{aligned} f(t) &= f_2(t) \\ &= f_3(t_j^*) + (t-t_j^*)f_3'(t_j^*) + \tfrac{1}{2}(t-t_j^*)^2 f_3''(t_j^*) \end{aligned} \tag{7.9a}$$

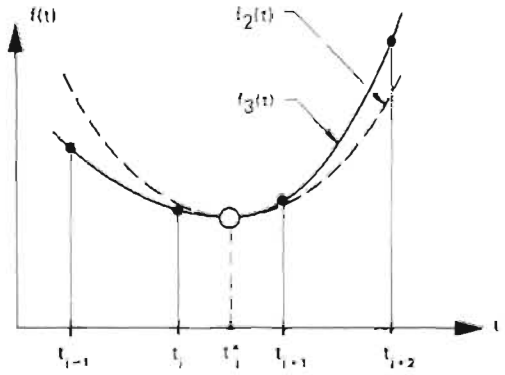


Fig. 7.4 Quadratic representation $f_2(t)$

where $f_3(t)$ is the cubic fitted through the function values at $t=t_{j-1}$, $t_j$, $t_{j+1}$ and $t_{j+2}$ (see Fig. 7.4). This implies that $f_3(t_j^*)$, $f_3'(t_j^*)$ and $f_3''(t_j^*)$ can be written as a linear (finite-difference type of) expression involving $f(t)$ at $t_{j-1}$, $t_j$, $t_{j+1}$ and $t_{j+2}$. These expressions are for a general non-uniform panel scheme:

$$\begin{aligned} f_3(t_j^*) = &-\frac{1}{8}\,\frac{\Delta t_j^2\,(\Delta t_j + 2\Delta t_{j+1})}{\Delta t_{j-1}(\Delta t_{j-1} + \Delta t_j)(\Delta t_{j-1} + \Delta t_j + \Delta t_{j+1})} f(t_{j-1}) \\ &+\frac{1}{8}\,\frac{(\Delta t_j + 2\Delta t_{j+1})(2\Delta t_{j-1} + \Delta t_j)}{\Delta t_{j-1}(\Delta t_j + \Delta t_{j+1})} f(t_j) \\ &+\frac{1}{8}\,\frac{(\Delta t_j + 2\Delta t_{j+1})(2\Delta t_{j-1} + \Delta t_j)}{\Delta t_{j+1}(\Delta t_{j-1} + \Delta t_j)} f(t_{j+1}) \\ &-\frac{1}{8}\,\frac{\Delta t_j^2\,(2\Delta t_{j-1} + \Delta t_j)}{\Delta t_{j+1}(\Delta t_j + \Delta t_{j+1})(\Delta t_{j-1} + \Delta t_j + \Delta t_{j+1})} f(t_{j+2}) \end{aligned} \tag{7.9b}$$

$$\begin{aligned} f_3'(t_j^*) = &\;\frac{1}{4}\,\frac{\Delta t_j^2}{\Delta t_{j-1}(\Delta t_{j-1} + \Delta t_j)(\Delta t_{j-1} + \Delta t_j + \Delta t_{j+1})} f(t_{j-1}) \\ &-\frac{1}{4}\,\frac{\Delta t_j^2 + 4\Delta t_{j-1}(\Delta t_j + \Delta t_{j+1})}{\Delta t_{j-1}\Delta t_j(\Delta t_j + \Delta t_{j+1})} f(t_j) \\ &+\frac{1}{4}\,\frac{\Delta t_j^2 + 4\Delta t_{j+1}(\Delta t_{j-1} + \Delta t_j)}{\Delta t_j\Delta t_{j+1}(\Delta t_{j-1} + \Delta t_j)} f(t_{j+1}) \\ &-\frac{1}{4}\,\frac{\Delta t_j^2}{\Delta t_{j+1}(\Delta t_j + \Delta t_{j+1})(\Delta t_{j-1} + \Delta t_j + \Delta t_{j+1})} f(t_{j+2}) \end{aligned} \tag{7.9c}$$

$$\begin{aligned} f_3''(t_j^*) = &\;\frac{\Delta t_j + 2\Delta t_{j+1}}{\Delta t_{j-1}(\Delta t_{j-1} + \Delta t_j)(\Delta t_{j-1} + \Delta t_j + \Delta t_{j+1})} f(t_{j-1}) \\ &+\frac{2\Delta t_{j-1} - (\Delta t_j + 2\Delta t_{j+1})}{\Delta t_{j-1}\Delta t_j(\Delta t_j + \Delta t_{j+1})} f(t_j) \\ &+\frac{2\Delta t_{j+1} - (2\Delta t_{j-1} + \Delta t_j)}{\Delta t_j\Delta t_{j+1}(\Delta t_{j-1} + \Delta t_j)} f(t_{j+1}) \\ &+\frac{2\Delta t_{j-1} + \Delta t_j}{\Delta t_{j+1}(\Delta t_j + \Delta t_{j+1})(\Delta t_{j-1} + \Delta t_j + \Delta t_{j+1})} f(t_{j+2}) \end{aligned} \tag{7.9d}$$

The panelwise quadratic representation $f_2$ is discontinuous in function value as well as in first and in second derivative across the panel edges. All these discontinuities are small of (appropriate) higher order and may be neglected.

On the first and the last panel, i.e. for j=1 and j=NP respectively, the scheme is reduced to a one-sided 3-point scheme, still second-order accurate. This scheme is conveniently obtained by choosing for j=1 $\Delta t_0 = \infty$ and for j=NP $\Delta t_{NP+1} = \infty$.

It has been verified by numerical experiments that the $f_2$-representation of both $\bar{X}(t)$ and $\rho(t)$ is stable for convecting the vortex sheet with the local velocity vector.

7.3 Treatment of highly rolled-up regions

During the evolution of two-dimensional time-dependent vortex sheets, two types of rolled-up regions occur: single-branched and double-branched spirals (e.g. see Fig. 3.13 and Fig. 3.14, respectively).

7.3.1 Single-branched vortex

The single-branched spiral appears instantaneously at locations where at $\tau=0$ the doublet distribution is singular, such as at a wing tip or side edge, where

$$\rho(t) \sim \sqrt{(2\varepsilon)} \qquad (7.10)$$

$\varepsilon$ being the distance measured in the plane of the wing and normal to the edge. If the second-order panel method is used to compute the velocity field induced by a doublet distribution with such behaviour, large errors appear near the wing tip and an accurate simulation of the roll-up process is precluded. In view of this it seems appropriate to use the self-similar solution of Pullin-1978, for the rolling-up of a semi-infinite vortex sheet, to construct a non-singular initial doublet distribution and corresponding geometry that can be used for the present method. Therefore it is assumed that for times $\tau < \tau_o$ the temporal development at the edge is a purely local phenomenon not influenced by other more remote parts of the sheet.

In the similarity solution one considers a semi-infinite vortex sheet extending from $y=-\infty$ to $y=0$ with doublet distribution $\rho=2a\sqrt{|y|}$ (see Fig. 7.5). The problem solved is formulated as, see Eq. (5.31):

$$\frac{d}{d\tau}\bar{X}(\rho;\tau) = \bar{U}_\mu(\bar{X}(\rho;\tau)) \quad \text{for} \quad 0 < \tau < \tau_o \qquad (7.11a)$$

with initial condition

$$\bar{X}(\rho;0) = -(\rho/2a)^2\,\bar{e}_y \qquad (7.11b)$$

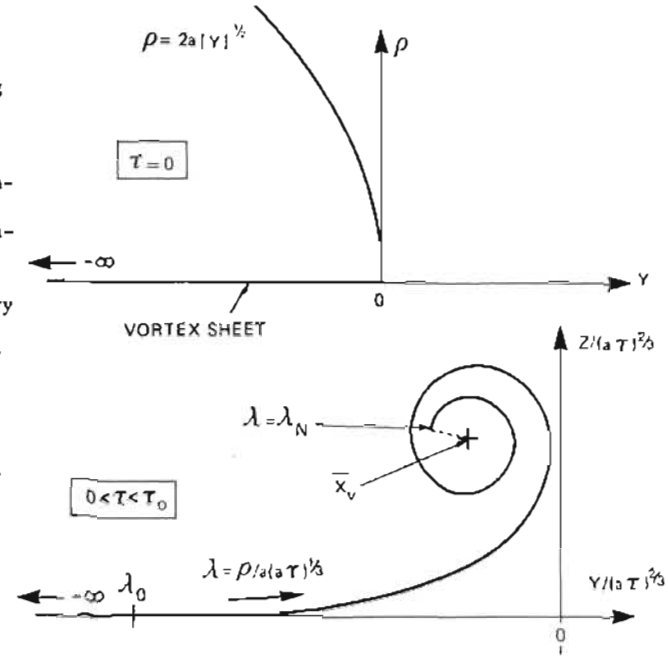


Fig. 7.5 Vortex sheet roll-up at edge

where the arc-length parameter t in Eq. (5.31) is conveniently replaced by the here monotonically varying $\rho$. The velocity induced by the doublet distribution is found from Eq. (7.1) as

$$\bar{U}_\mu(\rho;\tau) = -\frac{\bar{e}_x}{4\pi}\times\left(\int_{-\infty}^{0}\frac{\bar{X}(\rho;\tau)-\bar{X}(\rho';\tau)}{|\bar{X}(\rho;\tau)-\bar{X}(\rho';\tau)|^2}d\rho' - \frac{\bar{X}(\rho;\tau)-\bar{X}_v}{|\bar{X}(\rho;\tau)-\bar{X}_v|^2}\rho_v\right) \qquad (7.11c)$$

where $\rho_v = 0$ for the moment.

Since the dimension of $\rho$ is velocity times length (L), i.e. $L^2/T$, one finds that the dimension of a is $L\sqrt{L}/T$. The similarity solution, which exists because in this problem no length scale is involved, then is obtained in terms of the similarity parameter

$$\lambda = \rho/(a^{4/3}\tau^{1/3}) \qquad (7.12a)$$

for the shape of the vortex sheet expressed as

$$\bar{X}(\rho;\tau) = (a\tau)^{2/3}\,\bar{\zeta}(\lambda) \qquad (7.12b)$$

Substitution of Eq. (7.12) into Eq. (7.11) yields:

$$\frac{1}{3}(2\bar{\zeta}-\lambda\frac{d\bar{\zeta}}{d\lambda}) = -\frac{\bar{e}_x}{2\pi}\times\left(\int_{-\infty}^{0}\frac{\bar{\zeta}(\lambda)-\bar{\zeta}(\lambda')}{|\bar{\zeta}(\lambda)-\bar{\zeta}(\lambda')|^2}d\lambda' - \frac{\bar{\zeta}(\lambda)-\bar{\zeta}_v}{|\bar{\zeta}(\lambda)-\bar{\zeta}_v|^2}\lambda_v\right) \qquad (7.13a)$$

where it follows from the initial condition that

$$\bar{\zeta}(\lambda) \to -(\tfrac{1}{4}\lambda^2)\,\bar{e}_y \quad \text{for} \quad \lambda \to \infty \qquad (7.13b)$$

Pullin-1978 obtains a numerical solution by dividing the vortex sheet in three sections (Fig. 7.5):

(i) For $\lambda\in[\infty, \lambda_o]$ the vortex sheet is far from the rolling-up region and taken as the undisturbed straight sheet, extending from $\bar{\zeta} = -\infty\,\bar{e}_y$ to $\bar{\zeta} = \bar{\zeta}_o = -(\lambda_o^2/4)\bar{e}_y$, where $\lambda_o$ is sufficiently large.

(ii) For $\lambda\in[\lambda_o, \lambda_N]$ the position $\bar{\zeta}_j = \bar{\zeta}(\lambda_j)$ of the vortex sheet at $\lambda = \lambda_j$, j = 1(1)N is determined by satisfying Eq. (7.13a) in discretized form.

(iii) For $\lambda\in[\lambda_N, 0]$, the tightly rolled-up part of the sheet, it is assumed that the velocity induced by this part at points on $\lambda > \lambda_N$ may be approximated by the velocity induced by an isolated vortex of strength $\lambda_N$ positioned at the center of circulation $\bar{\zeta} = \bar{\zeta}_v$ and connected to the sheet by a cut. Eq. (7.13a) then is satisfied in some average sense.

The above subdivision of the vortex sheet implies that in Eq. (7.13a) $\lambda_v = \lambda_N$, while the integration from $\lambda = \infty$ to $\lambda_o$ can be found in closed form, resulting in

$$\frac{1}{3}(2\bar{\zeta}-\lambda\frac{d\bar{\zeta}}{d\lambda}) = -\frac{\bar{e}_x}{2\pi}\times[\bar{G}(\bar{\zeta},\bar{\zeta}_o) + \sum_{j=1}^{N}\{\int_{\lambda_{j-1}}^{\lambda_j}\frac{\bar{\zeta}(\lambda)-\bar{\zeta}(\lambda')}{|\zeta(\lambda)-\bar{\zeta}(\lambda')|^2}d\lambda'\} - \frac{\bar{\zeta}(\lambda)-\bar{\zeta}_v}{|\bar{\zeta}(\lambda)-\bar{\zeta}_v|^2}\lambda_N] \tag{7.14a}$$

where

$$\bar{G}(\bar{\zeta},\bar{\zeta}_o) = \frac{1}{|\bar{\zeta}|^{\frac{1}{2}}}(-f_1\cos\frac{\theta}{2} + f_2\sin\frac{\theta}{2})\bar{e}_y + \frac{1}{|\bar{\zeta}|^{\frac{1}{2}}}(-f_1\sin\frac{\theta}{2} + f_2\cos\frac{\theta}{2})\bar{e}_z \tag{7.14b}$$

with

$$f_1 = \frac{1}{2}\ln\{\frac{|\bar{\zeta}| + 2|\bar{\zeta}|^{\frac{1}{2}}|\bar{\zeta}_o|^{\frac{1}{2}}\cos\frac{\theta}{2} + |\bar{\zeta}_o|}{|\bar{\zeta}| - 2|\bar{\zeta}|^{\frac{1}{2}}|\bar{\zeta}_o|^{\frac{1}{2}}\cos\frac{\theta}{2} + |\bar{\zeta}_o|}\} \tag{7.14c}$$

$$f_2 = -\pi + \tan^{-1}\{\frac{|\bar{\zeta}_o|-|\bar{\zeta}|}{2|\bar{\zeta}|^{\frac{1}{2}}|\bar{\zeta}_o|^{\frac{1}{2}}\sin\frac{\theta}{2}}\} \tag{7.14d}$$

$$\cos\theta = -(\bar{\zeta}.\bar{e}_y)/|\bar{\zeta}|,\ \sin\theta = (\bar{\zeta}.\bar{e}_z)/|\bar{\zeta}| \tag{7.14e}$$

Eq. (7.14a) is imposed at the N midpoints $\lambda_j^* = \frac{1}{2}(\lambda_{j-1} + \lambda_j)$, j=1(1)N, using the trapezoidal integration rule for the integral. This yields 2N nonlinear algebraic equations for the 2N+2 unknowns.
The remaining two equations are obtained from Eq. (7.13a) by integrating the equation from $\lambda$=0 to $\lambda_N$. The left-hand side of Eq. (7.13a) then gives:

$$\lambda_N\{\bar{\zeta}_v - \frac{1}{3}\bar{\zeta}(\lambda_N)\}$$

where we approximated $\int\bar{\zeta}(\lambda)d\lambda$ by $\bar{\zeta}_v\lambda_N$, so that $\bar{\zeta}_v$ is the center of vorticity of the inner spiral. The integral over the right-hand-side is approximated by the value of the integrand at $\bar{\zeta}_v$ times $\lambda_N$, quite similar to the zero-net-force condition applied to the vortex-feeding sheet combination of chapter 3.
This results in:

$$\bar{\zeta}_v - \frac{1}{3}\bar{\zeta}(\lambda_N) = -\frac{\bar{e}_x}{2\pi}\times[\bar{G}(\bar{\zeta}_v,\bar{\zeta}_o) + \sum_{j=1}^{N}\{\int_{\lambda_{j-1}}^{\lambda_j}\frac{\bar{\zeta}_v-\bar{\zeta}(\lambda')}{|\bar{\zeta}_v-\bar{\zeta}(\lambda')|^2}d\lambda'\}] \tag{7.15}$$

VORTEX: $\rho_v = 0.7123\,a(aT)^{1/3}$
$Y_v = -0.308\,(aT)^{2/3}$
$Z_v = 0.498\,(aT)^{2/3}$

In the present investigation we use the numerical solution obtained by Pullin-1978 for $\lambda_o = 3.6$ and $\bar{\zeta}_o = -3.24\,\bar{e}_y$ (Fig. 7.6). In this solution the vortex sheet is represented by 97 panels and loops four times about the vortex of strength $\lambda_{97} = 0.7123$ which is positioned at $\bar{\zeta}_v = -0.308\,\bar{e}_y + 0.498\,\bar{e}_z$. We obtain a nonsingular starting geometry and doublet distribution by matching the value of $\rho(t)$ and $\bar{X}(t)$ at some $t_o$ near the edge to $\lambda_o$ and $\bar{\zeta}_o$ of the self-similar solution. The latter yields the value of $\tau_o$ and a which determine the initial geometry and doublet distribution for $t > t_o$. With the singular behaviour removed the second-order panel method can be applied to accurately simulate the subsequent evolution of the vortex sheet.

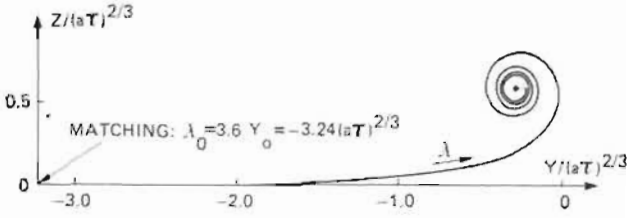


Fig. 7.6 Self-similar solution of Pullin-1978

In some other cases the solution at $\tau = 0$ will already feature a single-branched vortex. An example of this is the wake downstream of a delta wing with a leading-edge vortex where the single-branched (leading-edge) vortex developed upstream of the trailing edge. Here also the vortex core is modeled by the vortex-filament/feeding sheet combination.

7.3.2 Double-branched vortex

The double-branched spiral may appear at locations where the vortex sheet is initially smooth and the doublet distribution nonsingular. Examples of this occur in the wake of delta and ring wings and in the wake behind wings with deployed part-span flaps. Usually the double-branched spiral evolves near positions where the trailing vorticity attains a local extremum. It may also often be regarded as the result of the nonlinear evolution of an instability in the time-dependent development of the vortex sheet.

In the innermost region of the double-branched vortex the sheet is rolling-up tightly, stretching and curving considerably in the process. In order to maintain the overall level of accuracy the number of panels has to increase with the stretching while at the same time the increasing curvature requires smaller panels. This will result in a very rapid increase of the number of panels and correspondingly in the computational effort required to compute the velocity. Furthermore, since the time step allowed in the discretization of Eq. (5.31) in the time-like direction will depend on the length of the smallest panel, the computation will cease to progress significantly in time $\tau$. As before it is argued that the precise details of the innermost region of the spiral are immaterial for the flow outside this region and that the highly rolled-up region may be represented by the vortex filament/feeding sheets model of Fig. 3.14.

In this way a vortex sheet is split-up into two segments, and eventually a vortex system with multiple vortex sheet segments and centers of roll-up evolves quite naturally. Since the insertion of the double-branched vortex model for the double-branched spiralling vortex sheet eliminates the region of highest curvature and the small panels associated with it, the time step allowed is increased and the computation will proceed at a more satisfactory rate in $\tau$.

7.4 Rediscretization

The discretization of the vortex sheet by panels is chosen optimally if the truncation error due to the second-order panel method is uniform along the vortex sheet and remains at the same level as the computation proceeds in time. Such a uniform distribution of the error is obtained by decreasing the panel size in regions of large curvature and regions of large variation of the doublet distribution. Here it is hypothesized that in the absence of solid walls the regions of high curvature and the ones of rapidly changing doublet distribution coincide. This leads to a rediscretization scheme in which the local panel size $\Delta t_j$ depends on the local curvature $k_n(t)$, defined in Eq. (7.2f). In the present study $\Delta t_j$ is computed as (see Fig. 7.7):

$$\Delta t_j = \mathrm{Min}\{\Delta_{max}, \Delta\Theta_{max}/k_n\} \tag{7.16}$$

where $\Delta_{max}$ is the basic panel size and $\Delta\Theta_{max}/k_n$ is the length of the arc spanned by a segment of $\Theta_{max}$ radians of a circle with radius $1/k_n$. The latter is the average radius of curvature of the panel. The basic, maximum, panel size is to be chosen such that the desired degree of accuracy is ensured in regions of relatively small curvature. Its choice is primarily governed by the level of overall accuracy desired for the panelwise representation of the doublet distribution. The second parameter, $\Delta\Theta_{max}$, ensures that at highly curved parts of the sheet the panel size is reduced so that here also the required level of accuracy is obtained. Usually $\Delta\Theta_{max}$ is chosen such that a circle having a radius equal to the local radius of curvature is represented by 12-18 panels.

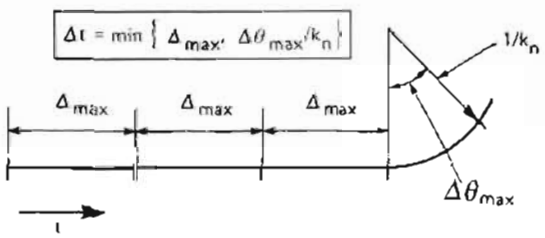


Fig. 7.7 Curvature-dependent panel scheme

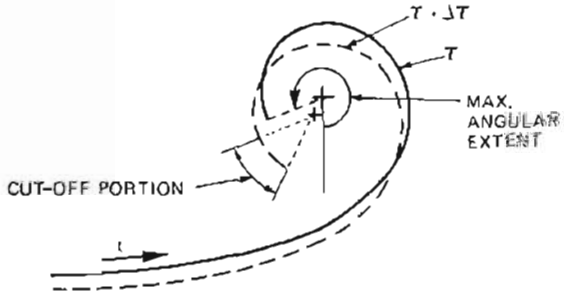


Fig. 7.8 Process of cutting the vortex sheet

During the roll-up the stretching vortex sheet tends to wrap around the vortex cores, resulting in an increasing number of loops as the computation progresses, steadily increasing the number of panels in the process. In order to keep the computational effort manageable the extent of the vortex sheet can be controlled by specifying its maximal arc length or by specifying its maximal angular extent (Fig. 7.8). The latter causes the inclination of the feeding sheets to remain fixed in time $\tau$.
Any part of the vortex sheet that extends beyond the maximal sheet length or angular extent is cut-off. If the sheet is cut, the vorticity contained in the cut-off portion of the sheet is dumped in the vortex, which subsequently is placed at the center of vorticity of the original vortex and the cut-off portion of the sheet. In this manner the vortex cores are allowed to grow in strength in time (i.e. in downstream direction), which also occurs in reality.

7.5 Computational procedure

The computational procedure to compute the motion of the vortex system consists of 6 steps. In the following we describe these 6 steps for the simple case of a single vortex sheet segment, with the first point located in the plane of symmetry and a single-branched vortex connected to the last point of the vortex sheet (Fig. 7.9). The extension of the description to the general case of a multiple-segmented vortex system as depicted in Fig. 7.1 is straightforward.

1. From a given position $\bar{X}(t;\tau)$ and strength $\rho(t)$ of the vortex sheet at time $\tau$, specified by the values $Y_j$, $Z_j$ and $\rho_j$ for $j = 1(1)N$ at discrete points (i.e. the panel edges, see Fig. 7.9), a cubic (B-)spline fit is computed which yields both $\bar{X}$ and $\rho$ as a function of the arc length parameter $t$ along the sheet.

2. In case the vortex sheet has stretched beyond its maximal length or its maximal angular extent it is cut off and the vortex core position and strength are updated such that the circulation and the first moment of the vorticity distribution are conserved (see Fig. 7.8).

3. With the cubic spline representation for $\bar{X}(t;\tau)$ the curvature-dependent panel scheme, see Eq. (7.16), is computed. The cubic spline representation then yields the values $Y_j$, $Z_j$ and $\rho_j$, $j = 1(1)NN$ at the new panel-edge points.

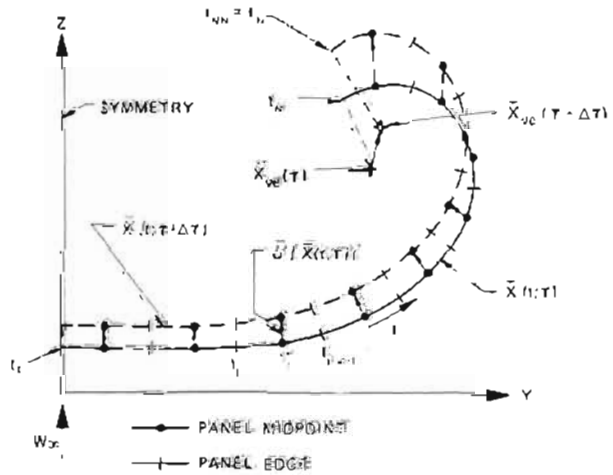


Fig. 7.9 Vortex-sheet arrangement

4. The discrete values of $Y_j$, $Z_j$ and $\rho_j$, $j = 1(1)NN$ are the input for the second-order panel method described in section 7.2. The panel method computes the velocity $\bar{U}_j = (0, V_j, W_j)^T$ at the panel midpoints $t^*_j = (t_j + t_{j+1})/2$ for $j = 1(1)NN-1$, where $\bar{U}_j$ is the sum of the free-stream velocity $\bar{V}_\infty$ and the velocity $\bar{U}^j$ induced at $\bar{X}(t^*_j, \tau)$ by the doublet distribution.

5. The panel midpoints are advanced in time by an Euler scheme with variable time step, i.e.

$$Y(t_j^*;\tau+\Delta\tau) = Y(t_j^*;\tau) + \Delta\tau(V_\infty + V_{\mu j})$$
$$Z(t_j^*;\tau+\Delta\tau) = Z(t_j^*;\tau) + \Delta\tau(W_\infty + W_{\mu j}) \qquad \text{for } j = 1(1)NN-1 \tag{7.17a}$$

where $\Delta\tau$ is chosen such that it does not exceed $\Delta\tau_{max}$ and simultaneously such that each midpoint $\bar{X}(t_j^*;\tau)$ is not displaced more than a specified fraction F of the chord $b\Delta t_j$ of the panel it is situated on, i.e.

$$\Delta\tau = \mathrm{Min}[\mathrm{Min}\{\Delta\tau_{max}, F\ \mathrm{Min}_j(\frac{b\Delta t_j}{|\bar{U}_{\mu j}|})\}, \Delta X_{max}\ \mathrm{Min}_j(\frac{1}{|\bar{U}_{\mu j}|})] \tag{7.17b}$$

where $\Delta\tau_{max}$ and $\Delta X_{max}$ are to be chosen such that the accuracy of the Euler scheme is ensured, maintained in time and is of the same order of magnitude as the error in the spatial discretization. The new position of the end points $t = t_1$ and $t = t_{NN}$ is found by quadratic extrapolation from the new values at the first three and last three midpoints, respectively. Also the position of the vortex core(s) $\bar{X}_{ve}(\tau)$ and $\bar{X}_{vo}(\tau)$ is advanced by the local velocity multiplied by the time step $\Delta\tau$.

6. The new values of Y and Z at $t_j^*$, $j = 1(1)NN-1$ as well as their values at $t_1$ and $t_{NN}$ form the input data for a quadratic (B-)spline procedure which computes the new values of Y and Z at the panel edge points $t_j$, $j = 1(1)NN$. These panel-edge point values of Y and Z at time $\tau + \Delta\tau$, $Y_j$, $Z_j$, $j = 1(1)NN$, together with the conserved value of $\rho$ (computed in step 3), form the new data for step 1.

It should be noted here that in step 1, where function values are specified at nodal points, interpolatory cubic splines are used for reasons of numerical (spline) stability. Because in step 6 the function values are provided at midpoints interpolatory quadratic splines are employed for the same reason. The accuracy of both spline representations is such that the second-order accuracy of the spatial discretization is maintained.

## 7.6 Invariants of the motion

For two-dimensional time-dependent incompressible flow one can derive a number of invariants, i.e. properties that remain constant in time $\tau$. In the applications we employ these invariants to monitor the accumulation of errors in the computation as time proceeds.

The velocity field can be expressed as the sum of the free-stream velocity $\bar{U}_\infty = (0,V_\infty,W_\infty)^T$ and the velocity induced by all vortex sheet segments (see Eq. (7.1) for the velocity induced by a single segment), i.e.

$$\bar{U}(\bar{X}) = \bar{U}_\infty + \bar{U}_\mu(\bar{X}) \tag{7.18a}$$

where

$$\bar{U}_\mu(\bar{X}) = \frac{\bar{e}_x}{2\pi} \times \Sigma_k\{-\int_{C_v^k} \frac{\bar{R}^k}{|\bar{R}^k|^2} \frac{d}{d\tau}\rho^k(\tau')d\tau' + \delta_{ve}^j(\frac{\bar{R}_{ve}^k}{|\bar{R}_{ve}^k|^2})\rho_e^k - \delta_{vo}^k(\frac{\bar{R}_{vo}^k}{|\bar{R}_{vo}^k|^2})\rho_o^k\} \tag{7.18b}$$

with $\bar{R}^k = \bar{X}-\bar{X}^k(\tau';\tau)$, $\bar{R}_{ve}^k = \bar{X}-\bar{X}_{ve}^k(\tau)$ and $\bar{R}_{vo}^k = \bar{X}-\bar{X}_{vo}^k(\tau)$.

In case of symmetry with respect to the Y=0 plane and if $V_\infty=0$ the summation in Eq. (7.18b) is over the vortex sheet segments on the starboard side (Y≥0) only. The contribution due to the portside is then obtained by adding to Eq. (7.18a) the term $[S]\bar{U}_\mu([S]\bar{X})$, where the symmetry matrix [S] is given in Eq. (3.22a).

The two-dimensional time-dependent analogy is based on, see Eq. (5.31)-(5.32):

$$\frac{d}{d\tau}\bar{X}^i(t;\tau) = \bar{U}(\bar{X}^i(t;\tau)) \tag{7.19a}$$

$$\frac{d}{d\tau}\bar{X}_{ve}^i(\tau) = \bar{U}(\bar{X}_{ve}^i(\tau)) \text{ and } \frac{d}{d\tau}\bar{X}_{vo}^i(\tau) = \bar{U}(\bar{X}_{vo}^i(\tau)) \tag{7.19b}$$

Consider now the following expression (see Fig. 7.1):

$$I(F(\bar{X}(\tau))) = \Sigma_i\{-\int_{C_v^i} F(\bar{X}^i(t;\tau))\frac{d}{dt}\rho^i(t)dt + \delta_{ve}^i F(\bar{X}_{ve}^i(\tau))\rho_e^i - \delta_{vo}^i F(\bar{X}_{vo}^i(\tau))\rho_o^i\} \tag{7.20a}$$

where F is to be specified later and where the superscript i refers to the i-th vortex sheet segment and the summation is over all segments. Since the vortex sheet moves with the fluid, such that each point on it can be identified by its doublet strength $\rho$ at the initial time, we obtain:

$$\frac{dI}{d\tau} = \Sigma_i\{-\int_{C_v^i} \frac{d}{d\tau}F(\bar{X}^i(t;\tau))\frac{d}{dt}\rho^i(t)dt + \delta_{ve}^i\frac{d}{d\tau}F(\bar{X}_{ve}^i(\tau))\rho_e^i - \delta_{vo}^i\frac{d}{d\tau}F(\bar{X}_{vo}^i(\tau))\rho_o^i\} \tag{7.20b}$$

In case of symmetry with respect to the Y=0 plane and $V_\infty=0$ the summation in Eq. (7.20) is over the vortex sheet segments on the starboard side only and for the port-side contribution we subtract a second term, equal to the first term but with $\bar{X}^i$, $\bar{X}_{ve}^i$ and $\bar{X}_{vo}^i$ replaced by $[S]\bar{X}^i$, $[S]\bar{X}_{ve}^i$ and $[S]\bar{X}_{vo}^i$, respectively. However, in the following we will also consider the contribution, denoted by $I_s(\tau)$, of the starboard side in isolation.

Next invariants of the motion will be discussed resulting from specific choices of the function F in Eqs. (7.20a and b).

(i) The circulation of the vortex system
Choosing F=1 in Eq. (7.20) results in

$$C(\tau) = \sum_i \{-\int_{C_v^i} \frac{d}{dt}\rho^i(t)dt + \delta^i_{ve}\rho^i_e - \delta^i_{vo}\rho^i_o\} = \text{constant} \tag{7.21}$$

For a situation like the one sketched in Fig. 7.1 the circulation of the vortex system is zero, as follows directly from Eq. (7.21). Also in the case of symmetry with respect to the plane Y=0 the net circulation is zero. However, there are situations in which the circulation is not zero, e.g. a circular vortex sheet of uniform strength $\gamma$ has a circulation of $2\pi R\gamma$. In the latter case the circulation will remain constant in time because of Eqs. (5.31b) and (5.32b). Note that since in an unbounded fluid the kinetic energy due to a vortex system with nonzero net circulation becomes logarithmically infinite, the circulation is bound to be zero in all physically realistic cases.

In the case of symmetry with respect to the Y=0 plane the circulation of the starboard side is constant, i.e.

$$C_s(\tau) = \sum_i \{(1-\delta^i_{vo})\rho^i_o - (1-\delta^i_{ve})\rho^i_e\} = \text{constant} \tag{7.22}$$

where the summation is over all the segments on the starboard side. The circulation of the port side is equal in magnitude but opposite in sign, so that in the symmetric case the net circulation of the complete vortex system is identically zero.

(ii) Linear momentum in Y-direction
Choosing F=Y in Eq. (7.20) results in

$$I_Y(\tau) = \sum_i \{-\int_{C_v^i} Y^i(t;\tau)\frac{d}{dt}\rho^i(t)dt + \delta^i_{ve}Y^i_{ve}(\tau)\rho^i_e - \delta^i_{vo}Y^i_{vo}(\tau)\rho^i_o\} \tag{7.23a}$$

so that, using Eqs. (7.18a, 7.19a and b):

$$\frac{dI_Y}{d\tau} = V_\infty C(\tau)$$

$$+ \sum_i \{-\int_{C_v^i} V_\mu(\bar{X}^i(t;\tau))\frac{d}{dt}\rho^i(t)dt + \delta^i_{ve}V_\mu(\bar{X}^i_{ve}(\tau))\rho^i_e - \delta^i_{vo}V_\mu(\bar{X}^i_{vo}(\tau))\rho^i_o\} \tag{7.23b}$$

It can be shown by substitution of the velocity $V_\mu$ induced by the vortex system itself, Eq. (7.18b), that the second term on the right-hand side of Eq. (7.23b) vanishes because of anti-symmetry, so that

$$\frac{dI_Y}{d\tau} = V_\infty C(\tau) = \text{constant} \tag{7.23c}$$

and with $I_1$ as an arbitrary constant

$$I_Y(\tau) = V_\infty C\tau + I_1 \tag{7.23d}$$

This implies that for cases with $V_\infty=0$ and for cases with zero net circulation $I_Y$ itself will be an invariant of the motion.

In case of symmetry with respect to the Y=0 plane both C and $V_\infty$ are zero and one directly finds from Eq. (7.20a):

$$I_Y = 2I_{sY} = I_1 \tag{7.23e}$$

where $I_{sY}$ is given in Eq. (7.23a) with the summation over the segments on the starboard side only. Eq. (7.23e) indicates that the center of vorticity (COV) of the starboard side

$$Y_{cov_s} = I_{sY}/C_s \tag{7.23f}$$

is invariant in time.

(iii) Linear momentum in Z-direction
Choosing F=Z in Eq. (7.20) results in

$$I_Z(\tau) = \sum_i \{-\int_{C_v^i} Z^i(t;\tau)\frac{d}{dt}\rho^i(t)dt + \delta^i_{ve}Z^i_{ve}(\tau)\rho^i_e - \delta^i_{vo}Z^i_{vo}(\tau)\rho^i_o\} \tag{7.24a}$$

so that, using Eqs. (7.18a, 7.19a and b):

$$\frac{dI_Z}{d\tau} = W_\infty C(\tau)$$

$$+ \sum_i \{-\int_{C_v^i} W_\mu(\bar{X}^i(t;\tau))\frac{d}{dt}\rho^i(t)dt + \delta^i_{ve}W_\mu(\bar{X}^i_{ve}(\tau))\rho^i_e - \delta^i_{vo}W_\mu(\bar{X}^i_{vo}(\tau))\rho^i_o\} \tag{7.24b}$$

Here again the second term on the right-hand side of Eq. (7.24b) vanishes, so that

$$\frac{dI_Z}{d\tau} = W_\infty C(\tau) = \text{constant} \tag{7.24c}$$

and with $i_2$ as an arbitrary constant:

$$I_z = W_\infty C\tau + i_2 \tag{7.24d}$$

This shows that for cases with $W_\infty = 0$ as well as for cases with zero net circulation $I_Z$ itself will be an invariant of the motion.

In the case of symmetry with respect to Y=0 C is zero and one finds directly from Eq. (7.20a):

$$I_Z = I_{sZ} - I_{sZ} \equiv 0 \tag{7.24e}$$

meaning that $I_Z$ is identical zero for this case and that $I_{sZ}$ in general is not an invariant of the motion, nor is the vertical position of the center of vorticity of the starboard side

$$Z_{cov_s} = I_{sZ}/C_s \tag{7.24f}$$

(iv) Dispersion of vorticity

The dispersion of vorticity is the degree in which the vorticity is distributed about the center of vorticity. This quantity is obtained by choosing $F = (Y-Y_{cov})^2 + (Z-Z_{cov})^2$ in Eq. (7.20) and taking the square root of the resulting expression. This leads to

$$DISP(\tau) = [I_2(\tau)/C - \{I_Y(\tau)^2 + I_Z(\tau)^2\}/C^2]^{\frac{1}{2}} \tag{7.25a}$$

where we used $Y_{cov} = I_y/C$ and $Z_{cov} = I_Z/C$ and where

$$I_2(\tau) = \sum_i \{-\int_{C_v^i} |\bar{X}^i(\xi;\tau)|^2 \frac{d}{dt}\rho^i(t)dt + \delta^i_{ve}|\bar{X}^i_{ve}|^2\rho^i_e - \delta^i_{vo}|\bar{X}^i_{vo}|^2\rho^i_o\} \tag{7.25b}$$

Now we obtain from Eq. (7.25a):

$$\frac{d}{d\tau}\{DISP(\tau)\}^2 = \frac{d}{d\tau}I_2(\tau) - 2\{I_y(\tau)\frac{d}{d\tau}I_y(\tau) + I_z(\tau)\frac{d}{d\tau}I_z(\tau)\}/C \tag{7.25c}$$

From Eq. (7.25b) one gets, using Eqs. (7.18a), (7.19a and b):

$$\begin{aligned}\frac{d}{d\tau}I_2(\tau) = {} & 2V_\infty I_y(\tau) + 2W_\infty I_z(\tau) \\ & + 2\sum_i [-\int_{C_v^i} (\bar{X}^i(\xi;\tau).\bar{U}_\mu(\bar{X}^i(\xi;\tau))\}\frac{d}{dt}\rho^i(t)dt \\ & + \delta^i_{ve}\{\bar{X}^i_{ve}(\tau).\bar{U}_\mu(\bar{X}^i_{ve}(\tau))\}\rho^i_e - \delta^i_{vo}\{\bar{X}^i_{vo}(\tau).\bar{U}_\mu(\bar{X}^i_{vo}(\tau))\}\rho^i_o]\end{aligned} \tag{7.25d}$$

Substitution of the expression for the velocity components induced by the doublet distribution, i.e. Eq. (7.18b), into Eq. (7.25d) shows that the summation term in Eq. (7.25d) vanishes. Substitution of the expressions for $I_y$ and $I_z$, Eq. (7.23d) and (7.24d) respectively, yields

$$\frac{d}{d\tau}I_2(\tau) = 2(V_\infty^2+W_\infty^2)C\tau + 2(V_\infty i_1 + W_\infty i_2) \tag{7.25e}$$

Substitution of Eqs. (7.23d), (7.24d) and (7.25e) into Eq. (7.25c) results in

$$\frac{d}{d\tau}\{DISP(\tau)\}^2 = 0 \tag{7.25f}$$

and with $i_3$ an arbitrary constant one gets

$$DISP(\tau) = i_3 \tag{7.25g}$$

In case of symmetry with respect to the Y=0 plane the dispersion of vorticity of just the starboard side becomes

$$DISP_s(\tau) = [I_{sZ}(\tau)/C_s - \{I_{sY}(\tau)^2 + I_{sz}(\tau)^2\}/C_s^2]^{\frac{1}{2}} \tag{7.25h}$$

which, as it turns out, cannot be shown to be an invariant of the motion.

(v) Hamiltonian of the system

In analogy with the hamiltonian for a system of discrete vortices one can for the present vortex system define the Hamiltonian $H(\tau)$ by choosing for F in Eq. (7.20) the following expression:

$$F(\bar{X}) = \frac{1}{2\pi}\sum_j [\int_{C_v^j} h(\bar{X},\bar{X}^j(\xi';\tau))\frac{d\rho^j}{d\xi'}d\xi' - \delta^j_{ve}h(\bar{X},\bar{X}^j_{ve}(\tau))\rho^j_e + \delta^j_{vo}h(\bar{X},\bar{X}^j_{vo}(\tau))\rho^j_o] \tag{7.26a}$$

where

$$h(\bar{X},\bar{Y}) = \ln|\bar{X}-\bar{Y}| \tag{7.26b}$$

so that

$$H = \frac{1}{2\pi}\sum_i\{-\int_{C_v^i}(\sum_j(\int_{C_v^j}h(\bar{X}^i(\tau;\tau),\bar{X}^j(\tau';\tau))\frac{d\rho^j}{d\tau'}d\tau' - \delta^j_{ve}h(\bar{X}^i(\tau;\tau),\bar{X}^j_{ve}(\tau))\rho^j_e + \delta^j_{vo}h(\bar{X}^i(\tau;\tau),\bar{X}^j_{vo}(\tau))\rho^j_o))\frac{d\rho^i}{d\tau}d\tau$$

$$+ \delta^i_{ve}(\sum_j(\int_{C_v^j}h(\bar{X}^i_{ve}(\tau),\bar{X}^j(\tau';\tau))\frac{d\rho^j}{d\tau'}d\tau' - \delta^j_{ve}h(\bar{X}^i_{ve}(\tau),\bar{X}^j_{ve}(\tau))\rho^j_e + \delta^j_{vo}h(\bar{X}^i_{ve}(\tau),\bar{X}^j_{vo}(\tau))\rho^j_o))\rho^i_e$$

$$- \delta^i_{vo}(\sum_j(\int_{C_v^j}h(\bar{X}^i_{vo}(\tau),\bar{X}^j(\tau';\tau))\frac{d\rho^j}{d\tau'}d\tau' - \delta^j_{ve}h(\bar{X}^i_{vo}(\tau),\bar{X}^j_{ve}(\tau))\rho^j_e + \delta^j_{vo}h(\bar{X}^i_{vo}(\tau),\bar{X}^j_{vo}(\tau))\rho^j_o))\rho^i_o\} \qquad (7.26c)$$

Using

$$\frac{\partial h}{\partial\tau} = \frac{1}{|\bar{X}-\bar{X}'|^2}(\bar{X}-\bar{X}').\frac{d}{d\tau}(\bar{X}-\bar{X}') \qquad (7.26d)$$

it follows after some elaborate algebra that

$$\frac{d}{d\tau}H(\tau) = 0 \qquad (7.26e)$$

so that with $i_4$ an arbitrary constant

$$H(\tau) = i_4 \qquad (7.26f)$$

The Hamiltonian of the vortex system is a double sum over the vortex sheet segments. This double sum can be reduced to a single sum over the vortex sheet segments by partial integration in Eq. 7.26c. This leads to

$$H = \sum_i\{-\int_{C_v^i}\rho^i(\tau)\bar{U}_\mu(\bar{X}^i(\tau;\tau)).\bar{e}_x\times\frac{d}{d\tau}\bar{X}^i(\tau;\tau)d\tau$$

$$- \delta^i_{ve}\rho^i_e\int_{C_e^i}\bar{U}_\mu(\bar{X}^i_e(\tau;\tau)).\bar{e}_x\times\frac{d}{d\tau}\bar{X}^i_e(\tau;\tau)d\tau)$$

$$+ \delta^i_{vo}\rho^i_o\int_{C_o^i}\bar{U}_\mu(\bar{X}^i_o(\tau;\tau)).\bar{e}_x\times\frac{d}{d\tau}\bar{X}^i_o(\tau;\tau)d\tau\}] \qquad (7.27a)$$

where $\bar{X}^i_e(\tau;\tau)$ and $\bar{X}^i_o(\tau;\tau)$ denote the geometry of the feeding sheet $C^i_e$ connecting $\bar{X}^i(\tau^i_e;\tau)$ to $\bar{X}^i_{ve}(\tau)$ and the feeding sheet $C^i_o$ connecting $\bar{X}^i(\tau^i_o;\tau)$ to $\bar{X}^i_{vo}(\tau)$, respectively. Here we used that these functions can be expressed as

$$\bar{X}^i_e(\tau;\tau) = (1-\tau)\bar{X}^i(\tau^i_e;\tau) + \tau\bar{X}^i_{ve}(\tau)$$

and

$$\bar{X}^i_o(\tau;\tau) = (1-\tau)\bar{X}^i(\tau^i_o;\tau) + \tau\bar{X}^i_{vo}(\tau) \qquad (7.27b)$$

for $\tau\in[0,1]$.

In the derivation of Eq. (7.27a) the terms with the integral over the feeding sheet appear in integrated form. However, it can be shown that, using Eqs. (7.18b) and (7.27b), that

$$2\pi\int_{C_e^i}\bar{U}_\mu(X^i_e(\tau;\tau)).\bar{e}_x\times\frac{d}{d\tau}\bar{X}^i_e(\tau;\tau)d\tau =$$

$$= -\sum_j\{-\int_{C_v^j}\ln\frac{|\bar{X}^i(\tau^i_e;\tau)-\bar{X}^j(\tau';\tau)|}{|\bar{X}^i_{ve}(\tau)-\bar{X}^j(\tau';\tau)|}\frac{d}{d\tau}\rho^j(\tau')d\tau' + \delta^j_{ve}\rho^j_e\ln(\frac{|\bar{X}^i(\tau^i_e;\tau)-\bar{X}^j_{ve}(\tau)|}{|\bar{X}^i_{ve}(\tau)-\bar{X}^j_{ve}(\tau)|})$$

$$- \delta^j_{vo}\rho^j_o\ln(\frac{|\bar{X}^i(\tau^i_e;\tau)-\bar{X}^j_{vo}(\tau)|}{|\bar{X}^i_{ve}(\tau)-\bar{X}^j_{vo}(\tau)|})\} \qquad (7.27c)$$

and a similar expression for the integral over feeding sheet $C^i_o$ can be derived by replacing in Eq. (7.27c) $\tau^i_e$ by $\tau^i_o$ and $\bar{X}^i_{ve}(\tau)$ by $\bar{X}^i_{vo}(\tau)$.

Further note that Eq. (7.27a) is nothing else than the line integral along the segments of the vortex system of the jump in potential (= doublet strength $\rho$) multiplied by the normal component of the velocity induced at the segment, i.e. the integral found also for the induced drag of the configuration that generated the vortex system.

In the case of symmetry it follows from Eq. (7.27a) that

$$H(\tau) = 2H_s(\tau) = I_4 \tag{7.27d}$$

where $H_s$ is given by Eq. (7.26c) or (7.27a) with the summation over the (portions of the) *segments on the* starboard side only. This shows that the Hamiltonian of just the starboard side is an invariant of the motion as well.

Note that the integral over the vortex sheet, appearing in Eq. (7.20a) is regularly behaved for $F = 1$, $\bar{X}$ and $|\bar{X}|^2$, so that in the numerical evaluation of the corresponding invariant quantities we use the simple rectangular (midpoint) integration rule.
In the case of the Hamiltonian, Eq. (7.27a) is employed where the first term is evaluated using the midpoint integration rule, i.e. it is assumed that both $\rho(t)$ and $\bar{U}_\mu(\bar{X}(t;\tau))$ behave smoothly. The integrals over the feeding sheets are evaluated by replacing the integral by the value of the integrand at the vortex ($t=1$) times the length of the feeding sheet, e.g. the second integral in Eq. (7.27a) becomes:

$$\int_{C_e^i} \bar{U}_\mu(\bar{X}_e^i(t;\tau)).\bar{e}_x \times \frac{d}{dt}\bar{X}_e^i(t;\tau)dt \approx \bar{U}_\mu(\bar{X}_{ve}^i(\tau)).\bar{e}_x \times \{\bar{X}_{ve}^i(\tau) - \bar{X}^i(t_e^i;\tau)\} \tag{7.28}$$

and a similar expression for the integral along feeding sheet $C_o^i$. An alternatively to Eq. (7.28)) to compute the contribution of the feeding sheets in the Hamiltonian is to use Eq. (7.27c). However, it turns out that using this expression, employing the midpoint rule to evaluate the integral, is more expensive and less accurate.

The accuray of evaluating the Hamiltonian using the midpoint rule in Eq. (7.27a) may be questioned. A better procedure might be to substitute for the velocity induced by the doublet distribution the small-curvature expression derived earlier and integrate once more. This results in rather elaborate expressions and has not been pursued in this study.

## 7.7 Examples of application

In this section we describe the application of the present method to four cases, also frequently found in the literature. We will also compare results of the present method with published results of other methods and on one occasion with experimental data. We consider the rolling-up wake downstream of the trailing edge of the following four configurations:

(i) an elliptically loaded wing,
(ii) a ring wing or nacelle,
(iii) a wing with deployed part-span flap,
(iv) a unit-aspect-ratio delta wing with leading-edge vortex separation.

For all four cases it is assumed that the configuration is symmetric with respect to the plane Y=0 and the angle of side slip is zero, so that only the starboard side of the configuration needs to be considered. For the first three cases the incidence is zero, the delta wing is at 20 deg angle of attack.

### 7.7.1 Elliptically loaded wing

The case of the elliptically loaded wing for which at $\tau=0$:

$$\rho(t) = \sqrt{(1-t^2)}\ ,\ \bar{X}(t) = t\bar{e}_y \tag{7.29}$$

for $t\in[0,1]$ is the classical case used to test vortex sheet roll-up procedures. The initial doublet distribution is singular at the tip $t=1$ and a tip vortex is formed instantaneously at $\tau = 0^+$. Here we use Pullin's-1978 self-similar solution, discussed in section 7.3.1 to obtain for $\tau=\tau_o$ a desingularized starting solution. The matching point is chosen at $t=0.95$ so that it follows from section 7.3.1 that, with $a=1/\sqrt{2}$, $\tau_o = (0.05/3.24)^{3/2}/a = .00271$. The self-similar solution corresponding to this choice is shown in Fig. 7.10a. The velocity distribution induced by this composite initial solution is presented in Fig. 7.10b. It shows that over the greater part of the vortex sheet the classical result (e.g. Küchemann-1978) is obtained

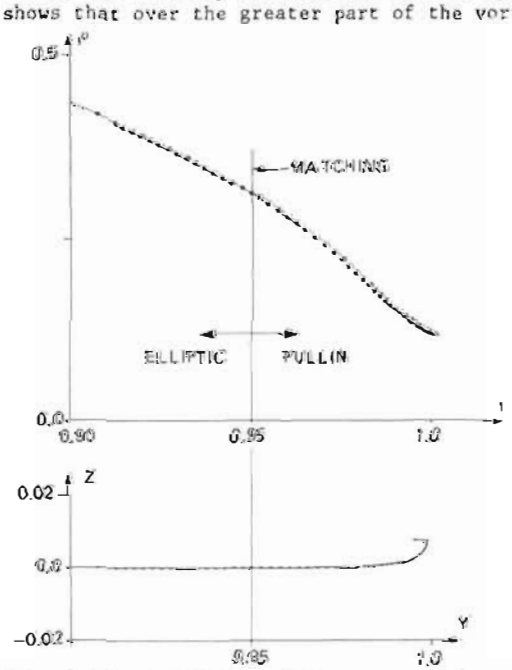


Fig. 7.10a Pullin's solution as used in present applications

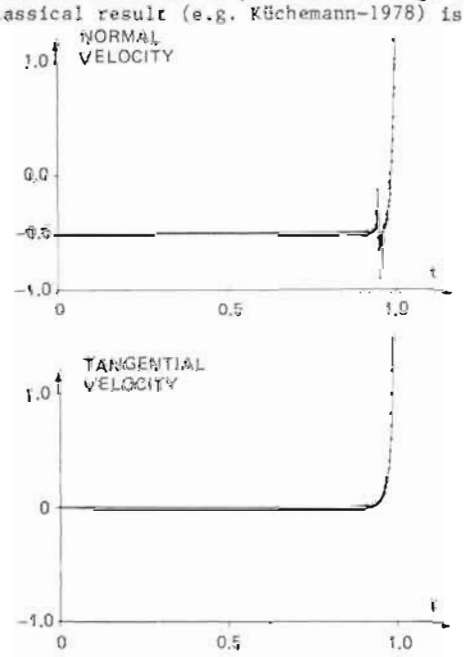


Fig. 7.10b Normal and tangential velocity distribution along vortex sheet at $\tau=\tau_o$

that, with the present non-dimensionalization (see section 5.3.1), the normal velocity is -0.5, while the (average) tangential velocity is zero, i.e. the values they had at $\tau=0$. In the spiral region both components of the velocity attain large values. Note that the matching introduces a disturbance, especially evident in the normal component of the induced velocity.

Pullin's solution involves four complete turns of the sheet (Fig. 7.6), which is judged to be too detailed a solution for the present purpose and only one-quarter turn is used here. Subsequently the evolution of the sheet is computed by letting the sheet roll-up from the position of the cut (feeding sheet) at $\theta \sim \pi/2$ shown in Fig. 7.10a to $\theta = 4\pi$, which is reached at $\tau-\tau_o = 0.00630$. Afterwards the cut is held steady at $\theta = 4\pi$, each time step cutting off the sheet in access of $\theta = 4\pi$ as described in section 7.4 (Fig. 7.7). This implies that the vortex core has a fixed strength up to $\tau-\tau_o = 0.00630$ but increases in strength afterwards. During the initial phase of the computation (up to $\tau-\tau_o = 0.0055$) the panel scheme is held fixed, mainly to avoid spurious effects in the region where at $\tau=\tau_o$ Pullin's solution was matched to the flat sheet (see Fig. 7.10b). In the subsequent phase of the computation the adaptive panel scheme, Eq. (7.16), is used with $\Delta\theta^{max} = 20$ deg, which ensures that each turn of the sheet is represented by approximately 20 panels. The second parameter used in the adaptive scheme, $\Delta_{max}$ the maximum panel width, is adjusted in time, more or less according to the decrease in the magnitude of the gradient of the doublet distribution. During the computation the number of panels varied between 56 and 136. The time step used in the scheme for the integration in time followed from Eq. (7.17b), with F=0.2, $\Delta X^{max} = 0.005$ and $\Delta\tau^{max}_{max}$ at a large value, ensuring that the error in the time discretization remained small. Tabel 7.1 summarizes the most important parameters used in the present computation.

Table 7.1
Characteristics of computation of evolution of wake downstream of elliptically loaded wing

| $\tau-\tau_o$ | Number of time steps | Number of panels | $\Delta_{max}$ |
|---|---|---|---|
| 0 -0.0055 | 200 | 136* | 0.01 |
| 0.0055-0.0515 | 500 | 84-87 | 0.02 |
| 0.0515-0.0807 | 100 | 70 | 0.03 |
| 0.0807-0.1136 | 100 | 62 | 0.04 |
| 0.1136-5.8429 | 1400 | 57-106 | 0.05 |
| 5.8429-10.6401 | 600 | 56-69 | 0.1 |
| | 2900 total | *) Fixed scheme | |

F = 0.2
$\Delta X^{max} = 0.005$
$\Delta\theta^{max} = 20_6$ deg
$\Delta\tau^{max}_{max} = 10^6$

The number of panels used in the adaptive panel scheme as a function of time is shown in Fig. 7.10c. This clearly shows the gradual increase in the number of panels as the computation proceeds, with a jump whenever $\Delta_{max}$ is changed, e.g. at $\tau = 5.8429$ where we increased the basic panel width $\Delta_{max}$ from 0.05 to 0.1. In the present case the number of panels increases only to accommodate the continual stretching of the sheet, the vortex sheet does not develop regions where the curvature increases and no new rolled-up regions evolve.

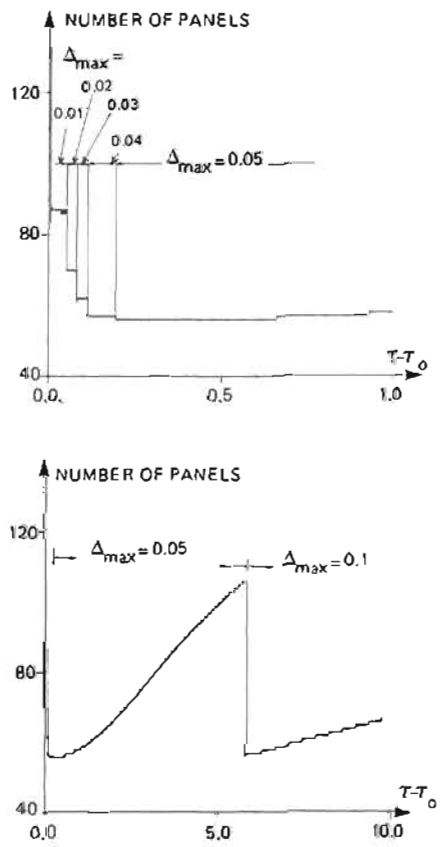


Fig. 7.10c Number of panels used for case of elliptically loaded wing

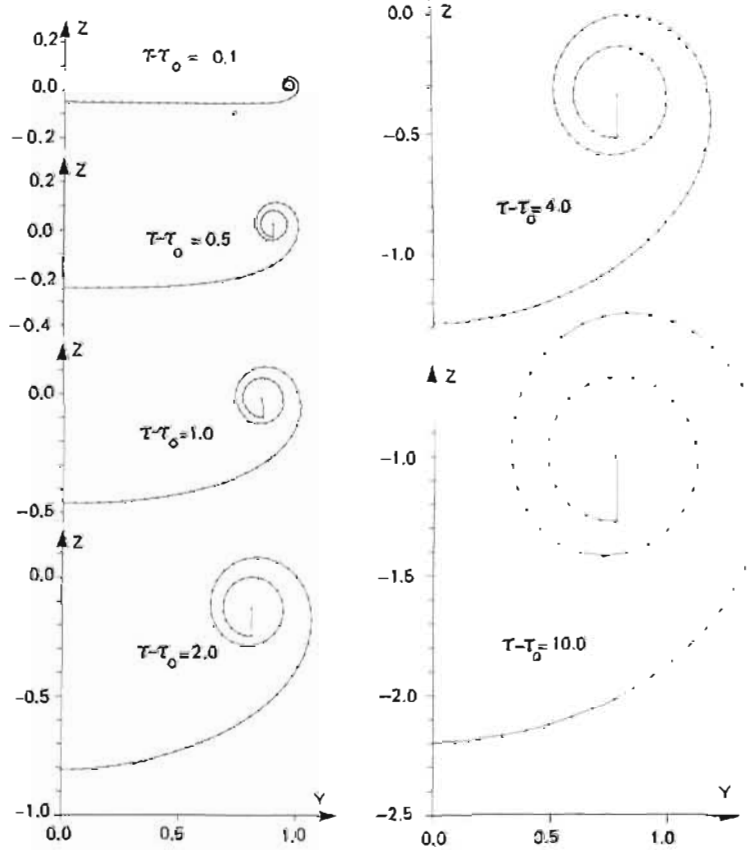


Fig. 7.10d Wake of elliptically loaded wing

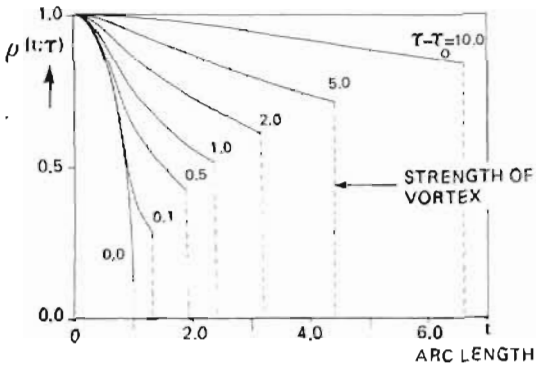


Fig. 7.10e Evolution of doublet distribution

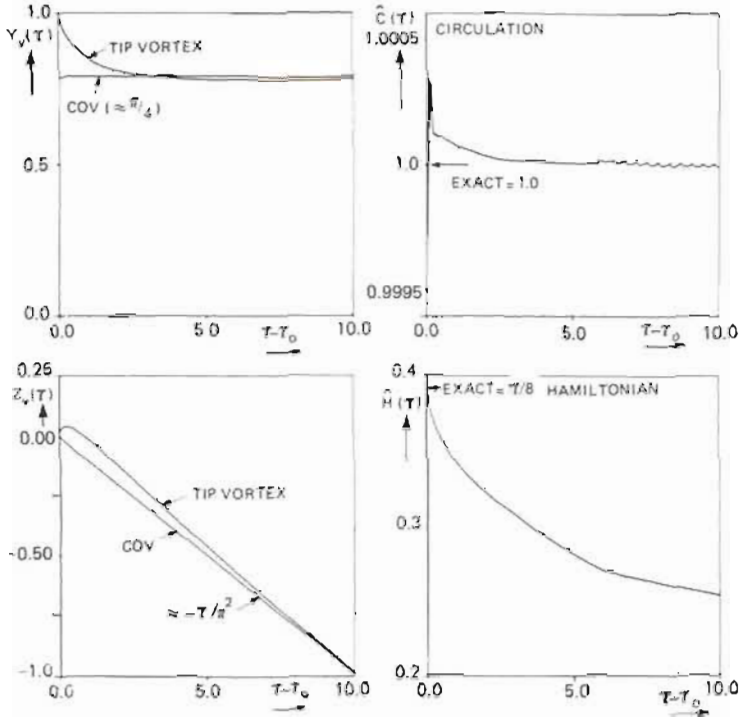


Fig. 7.10f Vortex position, circulation an Hamiltonian versus time

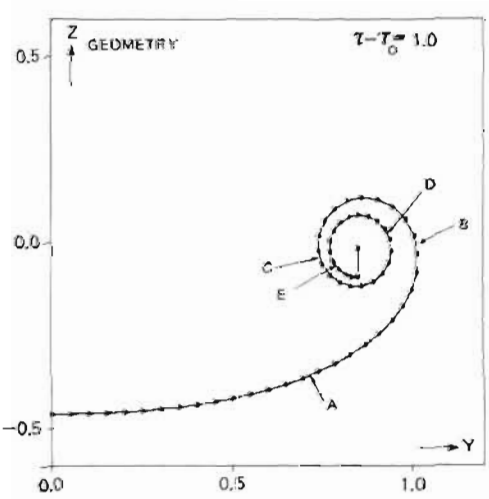


Fig. 7.10g Details of solution at $\tau-\tau_0=1.0$

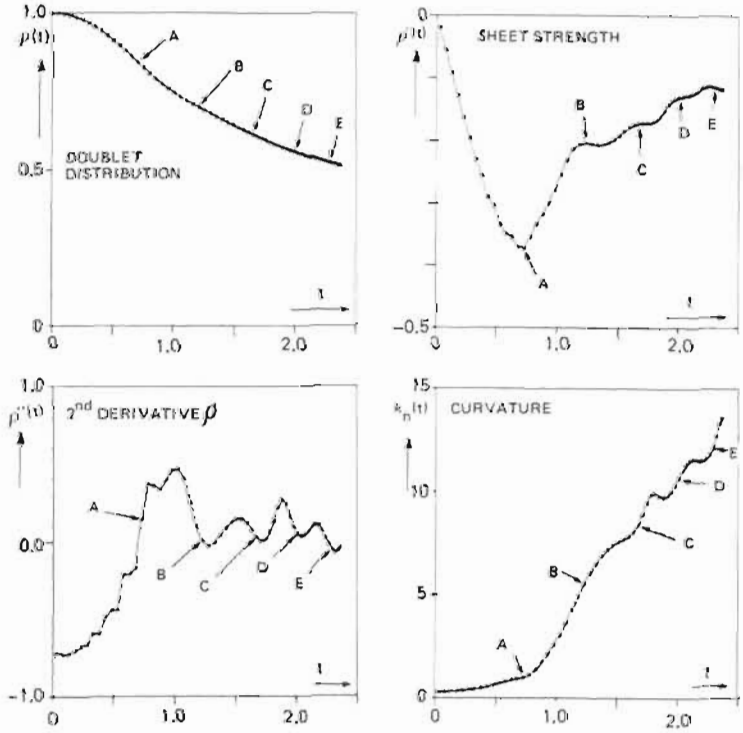


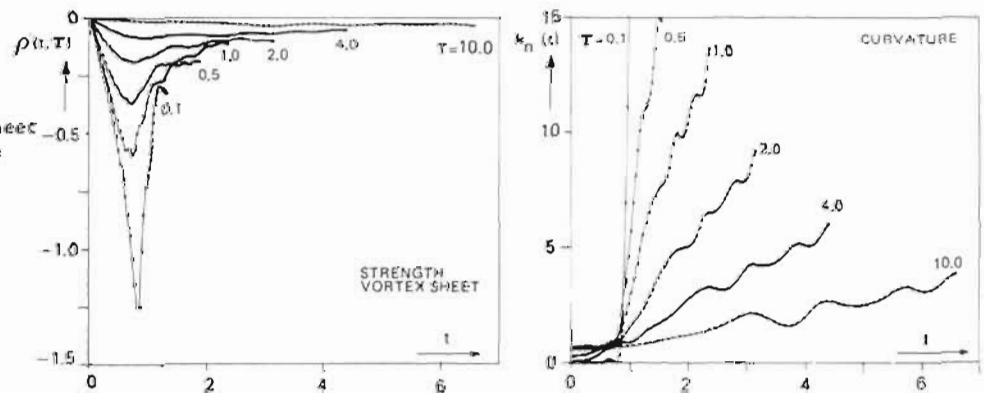


Fig. 7.10h
Evolution of vortex sheet strength and curvature

Fig. 7.10d shows the computed shape of the vortex sheet for $\tau-\tau_o$ =0.1, 0.5, 1.0, 2.0, 4.0 and 10.0, demonstrating that smooth results are obtained by the present computational method. For times up to $\tau-\tau_o \sim 4.0$ the turns of the vortex sheet around the vortex core remain more or less circular in appearance. At later times the turns become more elliptic in shape, due to the mutual influence of starboard and port side vortex sheets. Note that there is no sign of developing instabilities, which, presumably, is related to the circumstance that the sheet is continually stretching everywhere up to $\tau-\tau_o \sim 5.0$ and almost everywhere for larger times. In the latter case the sheet is stretching everywhere, except at local extrema of $\rho''$ where simultaneously the curvature is increasing in magnitude as well. Usually this occurs at points just ahead of local curvature maxima.

In Fig. 7.10e the doublet distribution is plotted vs arc length t for various times $\tau$. It shows the evolution of the doublet distribution from an elliptical distribution with high gradients at small $\tau$ to one with low gradients and 85% of the vorticity contained in the core at large $\tau$. The strength of the vortex core, which corresponds to $\rho(t_o)$, increases very rapidly from its initial value of about 0.1 at $\tau=\tau_o$ to a value of about 0.85 at $\tau-\tau_o = 10.0$.

In Fig. 7.10f the position of the vortex core, i.e. the tip vortex, and the position of the center of vorticity (COV) of the starboard vortex sheet and core are plotted as function of $\tau-\tau_o$. It indicates that initially the tip vortex moves rapidly upward and inboard and that for longer times the vortex (containing an ever-increasing portion of the vorticity) and the COV position closely approach each other, as should be expected.

The theoretical COV lateral position of $\pi/4$, which follows from Eq. (7.23) upon substitution of Eq. (7.29), is one of the invariants and is quite accurately predicted to within an error of 1% at $\tau-\tau_o = 10$. The slope of the vertical position, which theoretically tends to $1/\pi^2$ for large $\tau$, is also quite accurately predicted. It appears that the COV moves downward at an almost constant rate, not only for large $\tau$, but also for small $\tau$.

Fig. 7.10f includes the time-wise variation of the circulation and the "Hamiltonian" of the starboard side of the configuration, both quantities should be invariants of the computation (see section 7.6). It shows that the error in the circulation is small, but that the "Hamiltonian" deviates considerably from its theoretical value of $\pi/8$. The latter indicates that both the amalgamation process, in which the feeding sheet is held steady, and the insertion of the tip vortex do not conserve the "Hamiltonian".

Before comparing our results with results of alternative methods we consider the solution at $\tau-\tau_o$ = 1.0 in somewhat more detail. In Fig. 7.10g are presented the geometry, the doublet distribution $\rho(t)$, the first derivative of $\rho$ (which corresponds to the negative of the sheet strength), the second derivative of $\rho$ and the curvature of the vortex sheet. All these quantities are relatively smooth, with some disturbances in the doublet distribution and its derivatives occurring near the point where the curvature of the vortex sheet starts to increase (the point marked A). This point corresponds to the point where the vortex sheet strength attains its maximum. The other waves in $\rho'$ and $\rho''$ correspond to variations in the curvature as the vortex sheet loops around the vortex core, see the points marked B-E in the figure.

As time progresses the length of the vortex sheet increases, while both the strength and the curvature of the vortex sheet decrease. The latter is demonstrated in Fig. 7.10h which shows $\rho'(t)$ and $k_n(t)$ for the 6 timeframes shown in Fig. 7.10d. The maximum sheet strength drops rapidly, its location moving slightly in inboard direction. This corresponds with the evolution of the curvature $k_n(t)$ with time, its magnitude decreasing constantly in time, at least in the region of roll-up. For the portion of the vortex sheet near the plane of symmetry the curvature first increases (from zero) while for large $\tau$ it starts to decrease again.

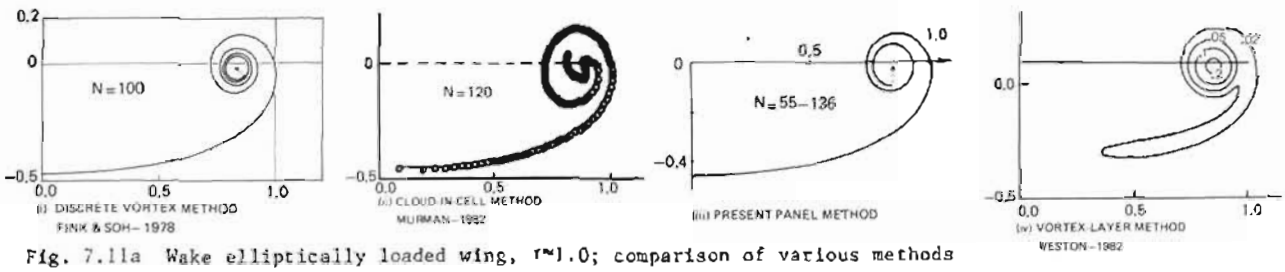


Fig. 7.11a Wake elliptically loaded wing, $\tau \approx 1.0$; comparison of various methods

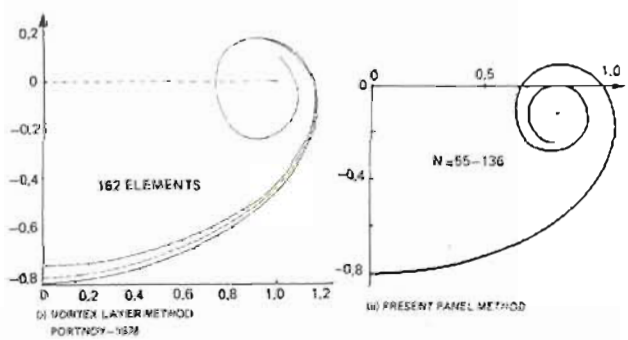


Fig. 7.11b Wake elliptically loaded wing, $\tau \approx 2.0$; comparison of various methods

In Fig. 7.11a, b and c we compare results of the present method with published results of other methods, discussed in Chapter 6. Results are compared at $\tau \approx 1.0$, 2.0 and 4.0. It shows (e.g. Fig. 7.11c) that the discrete-vortex method gives instabilities as the number of vortices is increased, and the discretization becomes rather coarse in regions where the sheet is stretched considerably. The rediscretization technique of Fink & Soh (Fig. 7.11b) solves these problems to some extent, especially if during the roll-up process the number of vortices is increased such that the distance between the equidistant vortices remains the same. The "cloud-in-cell" method results in unrealistic behaviour near the center of the spiral (Fig. 7.11a). The

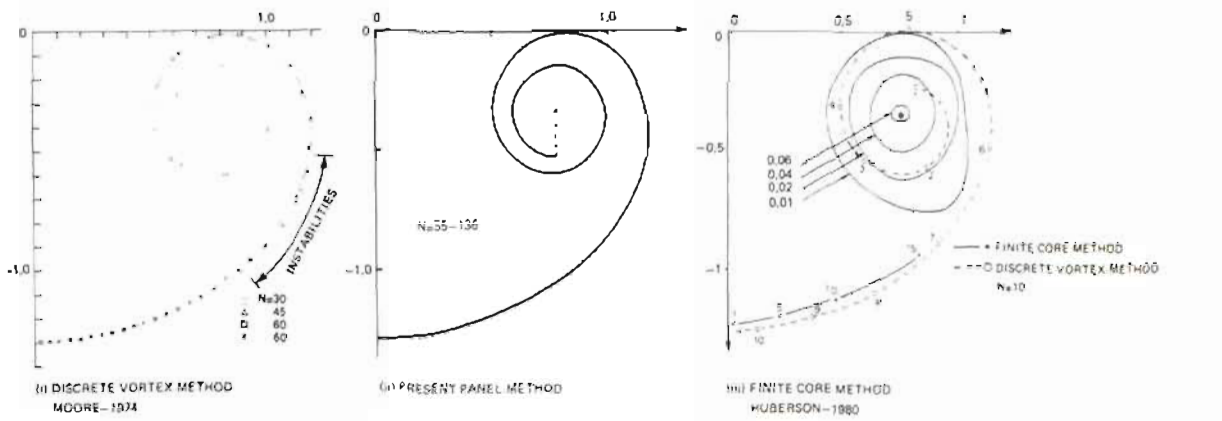


Fig. 7.11c Wake elliptically loaded wing, $\tau \sim 4.0$; comparison of various methods

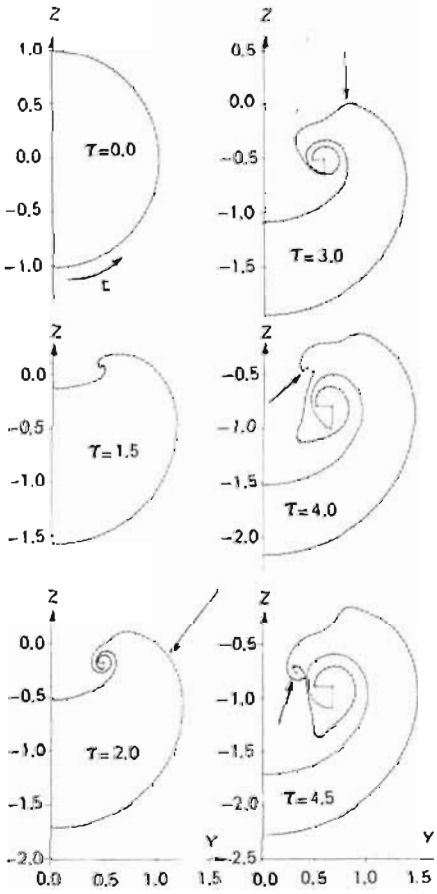


Fig. 7.12a Computed vortex wake of ring wing, $\Delta_{max}=0.05$

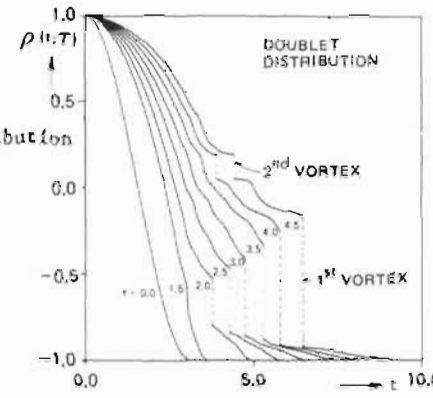


Fig. 7.12b Evolution of doublet distribution

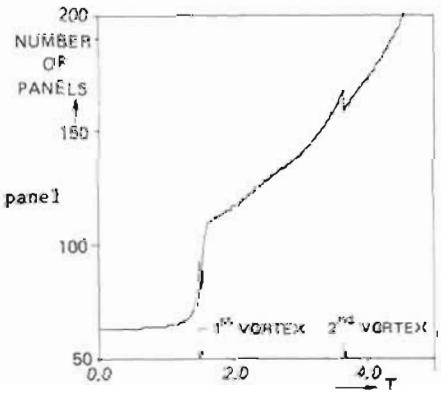


Fig. 7.12c Number of panels used in adaptive panel scheme

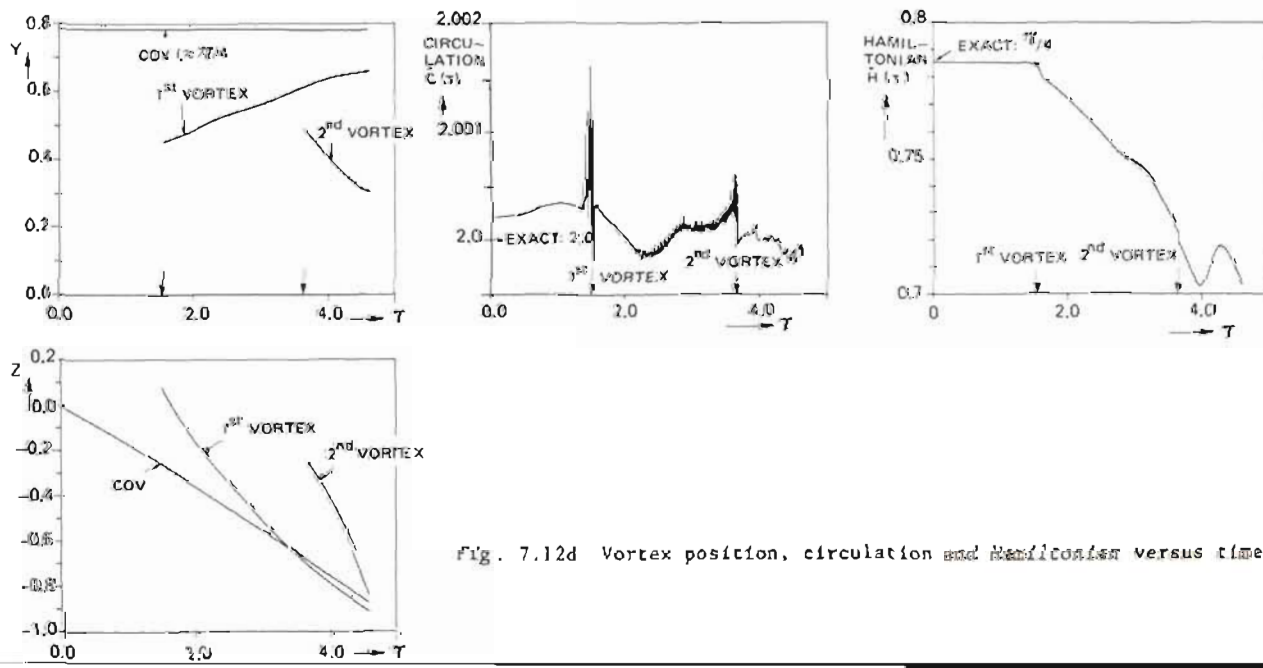


Fig. 7.12d Vortex position, circulation and Hamiltonian versus time

results of the finite-core method and vortex-layer method are quite similar to the vortex sheet method. However, as is clear from Fig. 7.11b the choice of an elliptic cross-section as initial shape in the vortex-layer method of Portnoy does not result into a core region with distributed vorticity as would be expected and as is the case for the method of Huberson and that of Weston & Liu.

We close this section with the correlation of the time-like coordinate $\tau$ with the distance downstream of the trailing edge of a wing of semi-span s and root-circulation $\Gamma_o$, both chosen equal to unity in the results above. For the wing of semi-span s with root-circulation $\Gamma_o$ the induced velocity is $\bar{U}^* = (\Gamma_o/s)\bar{U}$, where $\bar{U}$ is the velocity induced by the "reference" wing. For the "real" wing one has $\bar{X}^*(\tau^* + \Delta\tau^*) = \bar{X}^*(\tau^*) + \Delta\tau^*\bar{U}^*$, where $\bar{X}^*$ denotes a point in the cross-flow plane of the "real" wing and $\tau^*$ the "real" time. For the "reference" wing we had $\bar{X}(\tau + \Delta\tau) = \bar{X}(\tau) + \Delta\tau\bar{U}$, so that with $\bar{X}=\bar{X}^*/s$ one obtains $\tau^* = \tau(s^2/\Gamma_o)$. The distance downstream of the trailing edge of the "real" wing is $x-x_{T.E.} = U_\infty\tau^* = U_\infty\tau s^2/\Gamma_o$. Since $\Gamma_o = \frac{1}{2}c(0)c_\ell(0)$ we obtain

$$(x-x_{T.E.})/c(0) = \frac{2}{c_\ell(0)}\left(\frac{s}{c(0)}\right)^2\tau$$

This shows that for a wing with $c_\ell(0) = 1$ and $2s/c = 10$ the situation at $\tau=1.0$ corresponds with the cross-flow plane 50 chord lengths or 5 spans downstream of the trailing edge. Above relation also shows that as the aspect ratio of the wing is decreased the roll-up of the wake will have progressed further at a given station.

7.7.2 Ring wing

The case of the vortex wake of a ring wing is of interest because initially both the geometry and the doublet distribution are regular. Furthermore this case also gives insight in the behaviour of the wake downstream of a nacelle and to some extent in the development of the cross-sectional shape of a jet in a cross-flow.

At $\tau = 0$ one has

$$\mu(t) = \cos(t), \quad \bar{X}(t) = \bar{e}_y\sin(t) - \bar{e}_z\cos(t) \tag{7.30}$$

for $t\in[0,\pi]$. Substitution of Eq. (7.30) in the expression for the induced velocity, Eq. (7.1) shows that the resulting expression can be integrated exactly (using table 2) to $\bar{U}(\bar{X}(t)) = -\frac{1}{2}(\bar{e}_x\times\bar{X}')\cos(t)$, i.e. at the initial time the velocity is everywhere perpendicular to the vortex sheet.

This case has been treated by Baker-1980 employing Fink & Soh's-1978 method and by Baker-1977 employing the "cloud-in-cell" method. Results of the present method, using the adaptive panel scheme with $\Delta_{max} = 0.05$ and $\Theta_{max} = 20$ deg, obtained in 1170 time steps of the modified Euler time-wise integration scheme are presented in Figs. 7.12a-d. Table 7.2 gives the value of the computational parameters used in the calculation.

TABLE 7.2
Characteristics of computation of evolution of wake downstream of ring wing

| $\tau-\tau_o$ | Number of time steps | Number of segments | number of panels |
|---|---|---|---|
| 0 -1.5020 | 326 | 1 | 63-93 |
| 1.5020-3.6363 | 550 | 2 | 80-167 |
| 3.6363-4.6012 | 202 | 3 | 158-205 |
| | 1078 total | | |

$F = 0.4$
$\Delta X_{max} = 0.005$
$\Delta\tau_{max} = 0.005$
$\Delta\Theta_{max} = 20$ deg
$\Delta_{max} = 0.05$

From Fig. 7.12a it is clear that after some time, here $\tau = 1.502$, a vortex structure evolves which resembles the tip vortex of the preceding case. The appearance of this (double-branched) vortex is the result of the continual steepening of the doublet distribution from the smooth cosine distribution to one with regions with large slope (see Fig. 7.12b). In Fig. 7.12b the length of the dashed lines corresponds to the strength of the vortices. The increase of the magnitude of the gradient of the doublet distribution i.e. the vorticity distribution, is accompanied by an increase in the local curvature of the vortex sheet. This implies that the panels generated in the adaptive panel scheme become increasingly smaller and the number of panels increases rapidly (see Fig. 7.12c). It also results in a corresponding reduction of the time step in the Euler scheme. In this stage of the roll-up process, only the central portion of developing double-branched vortex changes significantly, the greater portion of the sheet remains unaffected.

Upon introduction of the isolated vortex/feeding sheet model, which cuts the sheet into two segments, the computation of the evolution of the now desingularized vortex sheet proceeds again at a faster and more practical rate in time. As evident in Fig. 7.12c, the number of panels following $\tau = 1.502$ first increases rapidly until the final inclination of the feeding sheets ($\Theta = 4_\pi$ and $3_\pi$) is reached whereupon the number of panels increases at a slower rate with increasing arc length.
At $\tau = 3.6363$ a second, but weaker, double-branched vortex appears, apparently as the result of the nonlinear growth of a wave on the vortex sheet.

The position of the vortices and center of vorticity of the starboard vortex system as a function of time are shown in Fig. 7.12d. From this it can be seen that after its "birth" the first vortex moves downward at a faster rate than the COV, but gradually slows to move at the same downward speed as the COV. The lateral position of the COV is theoretically $\pi/4$, which is predicted with an error of less than 0.5%. It is also seen that for large $\tau$ the slope of the vertical position tends to $2/\pi^2$ which would be the sinkage rate for the starboard sheet rolled up into one single vortex.

The lateral position of the COV is one of the invariants of the motion, two other ones, the starboard side circulation and the "Hamiltonian" are also presented in Fig. 7.12d. It again shows that the variations in the circulation are small, less than 0.1% for this case, with largest deviations near the "critical" times, i.e. the time that a new vortex evolves.

The starboard-side "Hamiltonian" has a larger variation, especially after the introduction of the first vortex core and the subsequent continual cutting of the vortex sheet and amalgamation of vorticity into the core.

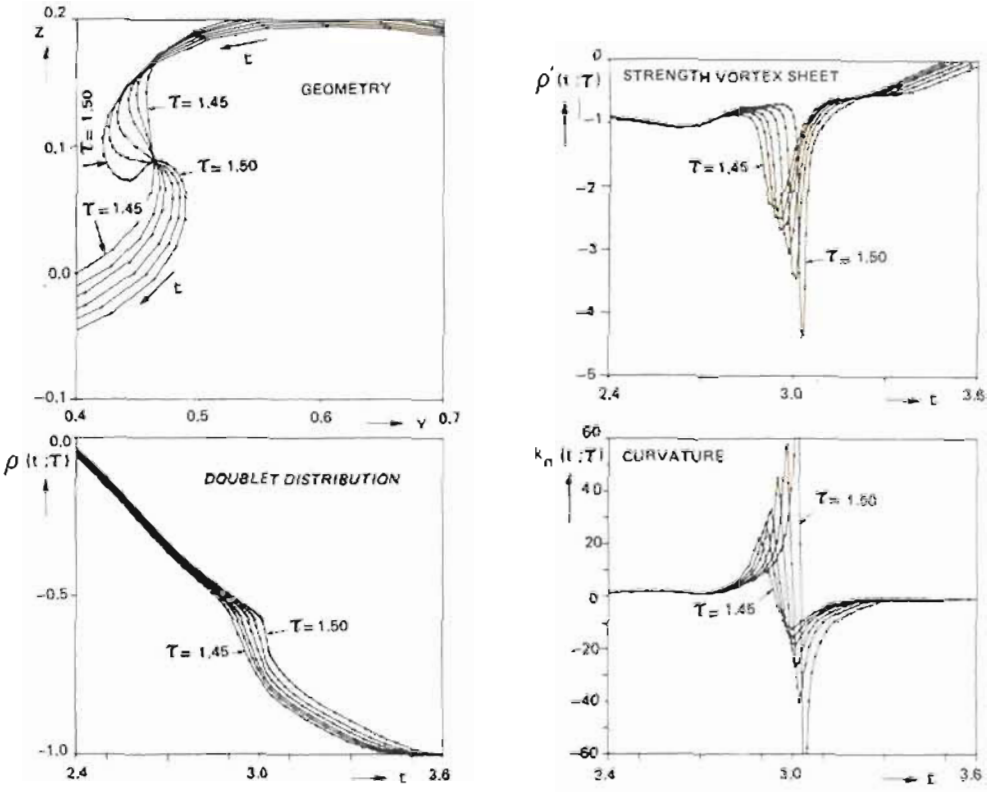


Fig. 7.12e Formation of (first) vortex in wake of ring wing, $\Delta_{max}$=0.05

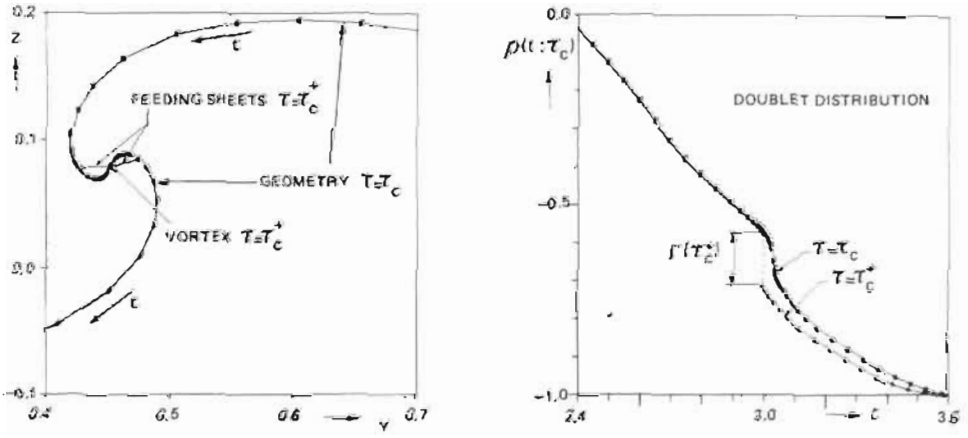


Fig. 7.12f Introduction of vortex-core model at $\tau=\tau_c$

In Figs. 7.12e we illustrate the formation of the first vortex core. It shows the geometry and doublet distribution at a number of times just before the "critical" time $\tau_c$ = 1.5020, namely $\tau$ = 1.45(0.01)1.50. Clearly the geometry deforms very rapidly, forming the double-branched spiral, while at the same time the doublet distribution steepens up quite considerably. Note that the adaptive panel scheme rapidly refines the paneling in the regions of high curvature. In Fig. 7.12e it is also shown how the vortex sheet strength and curvature develop for times leading up to $\tau_c$. It appears that the sheet strength develops a spike and the curvature a double spike.

In Fig. 7.12f it is demonstrated how at $\tau=\tau_c$ the inner part of the spiral is removed and replaced by a discrete vortex (at the COV of the removed part). At the same time this then removes the region with large sheet strength and curvature and the new "desingularized" solution can be progressed to times exceeding the critical time $\tau_c$ as is amply shown in Fig. 7.12a.

The point of the sheet where the vortex forms is the point ("doublet marker") that at $\tau$=0 was at $t*180/\pi$ = 130 deg, the portion of the sheet removed in Fig. 7.12f was at $\tau$=0 located between $t*180/\pi$ is 125 and 135 deg.

No criterion could be found that when applied to a smooth nonsingular initial solution yields the point(s) on the sheet where the roll up would appear eventually.

In examining the results of the computation it becomes clear that vortices do develop in regions near points where the vorticity has an extremum and where the sheet stretches the least or does not stretch at all. Furthermore, because of the implied smoothing of the computational scheme, a vortex structure can develop only if its length scale is larger than a few times $\Delta_{max}$. This is also demonstrated in Fig. 7.12a, where the first bump in the shape of the sheet does not develop into a vortex, while the second one, indicated by the arrow, does.

The consequence of this effect is best checked by repeating the computations for different $\Delta_{max}$. The vortex sheet shapes shown in Fig. 7.13 are computed with $\Delta_{max}$=0.1, It can be seen that the global piccure obtained is the same, but that the bulges apparent in Fig. 7.12a have been eliminated and a smoother shape evolves. The first vortex appears later, namely at $\tau$=1.88. Repeating the computation with a $\Delta_{max}$ of half the value used for the results shown in Fig. 7.12, i.e. $\Delta_{max}$=0.025, shows that now the first vortex appears at $\tau$=1.32 but also that still further small-scale structures develop, This is demonstrated in Fig. 7.14 which shows results for $\tau$=1.77 obtained with $\Delta_{max}$=0.1, 0.05 and 0.025. Depending on $\Delta_{max}$ the first vortex has not yet developed or has developed further. As $\Delta_{max}$ is reduced further more waves appear that eventually will develop into vortices. Generally the global structure is not affected, disturbances with a wave length of less than a few times $\Delta_{max}$ being smoothed. This, more or less fortuitously, resembles reality where it has been observed that in shear layers regular small-scale structures with a length scale less than a few times the shear-layer thickness do not amplify into well-defined rotational cores but are smoothed out. In this sense the results of the present computation may be regarded as results for a large but finite Reynolds number, the value of which is related to $\Delta_{max}$ in an as yet unknown manner. The results also suggest that the (inviscid) initial value problem for the ring-wing vortex sheet is ill-posed, i.e. inherently unstable with singularities developing in finite time.

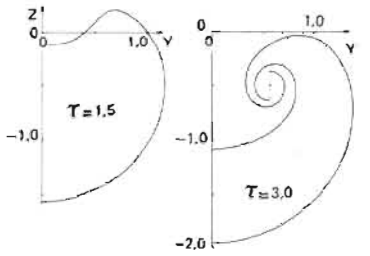


Fig. 7.13 Ring wing, computed vortex sheet shapes $\Delta_{max}$=0.1

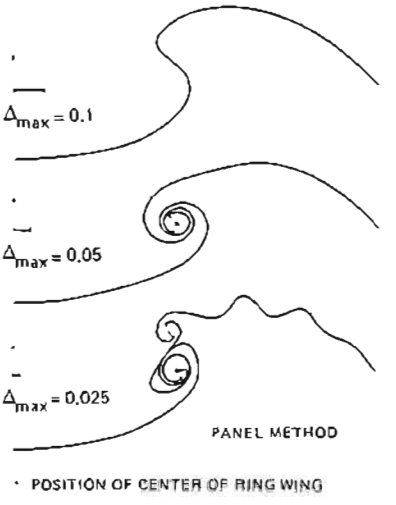


Fig. 7.14 Wake behind ring wing, $\tau$=1.77; influence of $\Delta_{max}$

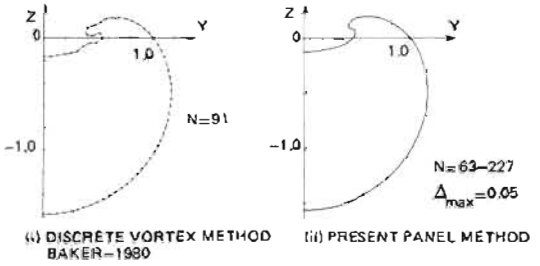


Fig. 7.15a Wake behind ring wing, $\tau$=1.5

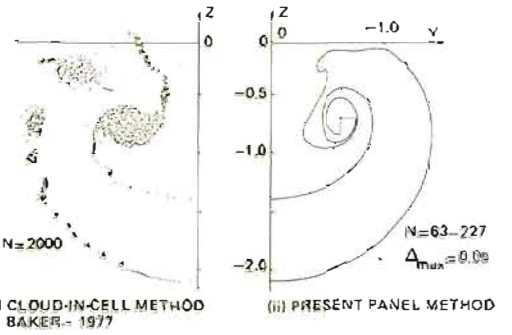


Fig. 7.15b Wake behind ring wing, $\tau$=3.69

In Fig. 7.15 we compare elsewhere published results of other methods with ones obtained using the present method. As has been demonstrated by Baker-1980 the discrete-vortex method of Fink & Soh (Fig. 7.15a) results into instabilities in the region where the first double-branched vortex develops, while the present panel method results in a smooth roll-up behaviour. Results for longer times are shown in Fig. 7.15b. The "cloud-in-cell" method produces a number of (grid dependent) sub-scale structures. In the present panel method results also long-wave (compared to the panel size) instabilities occur, but it appears that they are more regular than the ones in the results of the "cloud-in-cell" method.

7.7.3 Wing with deployed part-span flap

In the two applications discussed above the trailing vorticity $-\rho'(\tau;0)$ was positive everywhere. The next two applications are of interest because the sheet contains vorticity with both positive and negative sign, resulting in counter-rotating vortex cores. First consider the load distribution which schematically represents the case of a wing/fuselage combination with a deployed part-span flap, somewhat characteristic for a jet liner with deployed inboard flaps. This distribution is the same as that used by Baker-1979 for a similar calculation using the "cloud-in-cell" method and it is known from experiment that three vortices will develop. The doublet distribution is shown in Fig. 7.16a. It consists of three parts:

$t\in[0,0.3]$ :
cubic polynomial with $\rho(0) = -1.4, \frac{d\rho}{dt}(0) = 0$

$$\rho(0.3) = -2.0, \frac{d\rho}{dt}(0.3) = 0$$

$t\in[0.3,0.7]$:
cubic polynomial with $\rho(0.3) = -2.0, \frac{d\rho}{dt}(0.3) = 0$ (7.31)

$$\rho(0.7) = -A\ , \frac{d\rho}{dt}(0.7) = 0.7/A$$

$t\in[0.7,1.0]$:
elliptic distribution $\rho(t) = \sqrt{(1-t^2)}$

where $A = \sqrt{(1-0.7^2)}$.

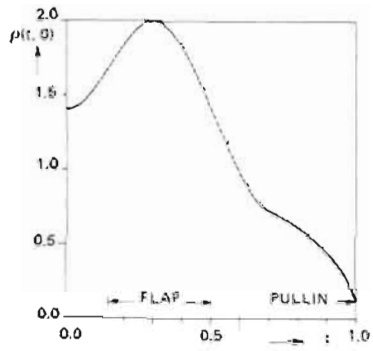


Fig. 7.16a Doublet distribution for wing with deployed part-span flap

As for the case of the elliptically loaded wing, Pullin's-1978 solution with $\tau_0 = 0.00271$ is used to desingularize the solution at the wing tip t=1. Results of the present method, using the adaptive panel scheme, obtained in 2100 time steps of the time-integration procedure and using between 76 and 223 panels are shown in Fig. 7.17b through f(see Table 7.3 for the value of the computational parameters).

Table 7.3
Computational parameters used for wing with deployed part-span flap

| $\tau-\tau_0$ | $\Delta_{max}$ | Number of segments | Number of time steps | Number of panels |
|---|---|---|---|---|
| 0 -0.0069 | 0.01 | 1 | 240 | 136* |
| 0.0069 -0.06697 | 0.02 | 1 | 600 | 88-95 |
| 0.06697-0.12497 | 0.03 | 1 | 200 | 76-113 |
| 0.12497-0.26836 | 0.03 | 2 | 260 | 85-170 |
| 0.26836-0.45943 | 0.03 | 3 | 200 | 140-192 |
| 0.45943-1.33710 | 0.04 | 3 | 400 | 166-223 |
| 1.33710-1.99482 | 0.05 | 3 | 200 | 191-217 |
| | | | 2100 total | |

F = 0.2
$\Delta X_{max} = 0.005$
$\Delta\theta_{max} = 20$ deg
$\Delta\tau_{max} = 10^6$

*) fixed initial panel scheme

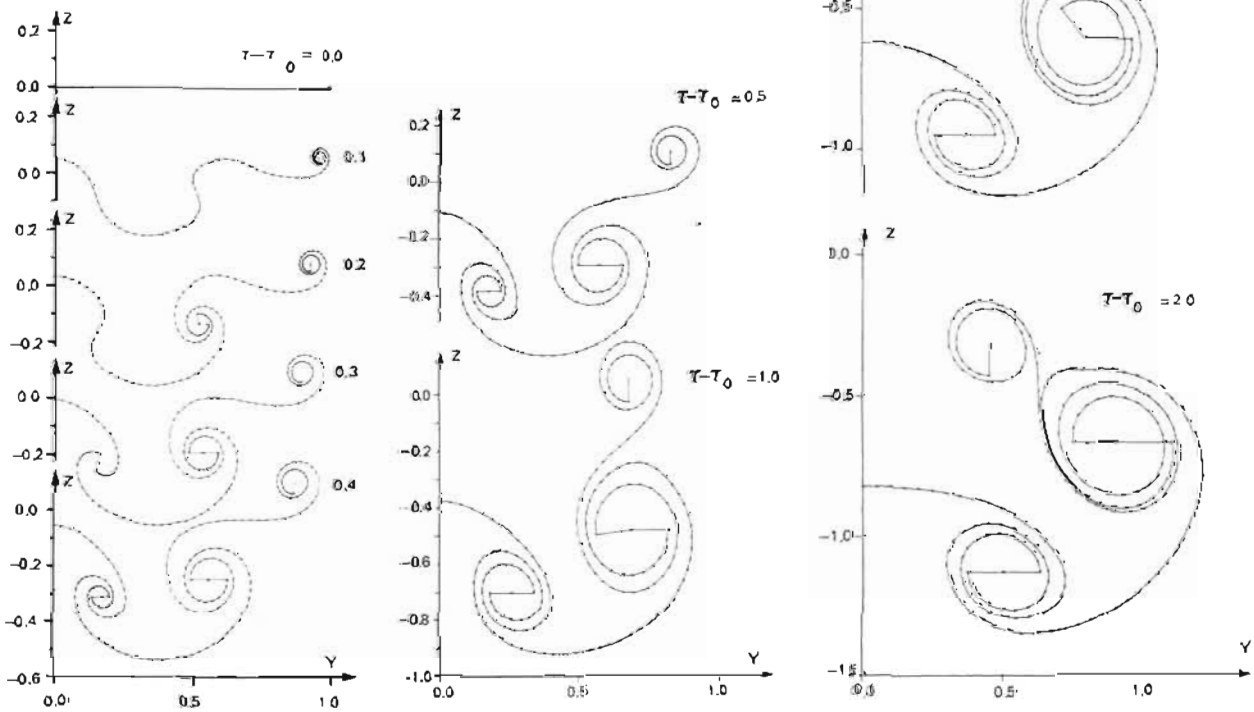


Fig. 7.16b Vortex wake of wing with deployed part-span flap

Fig. 7.16c Vortex wake for large $\tau$

Fig. 7.16b shows the computed geometry of the vortex wake at $\tau-\tau_0 = 0$, 0.1, 0.2, 0.3 and 0.4, while Fig. 7.16c shows the computed vortex wake at larger times, namely at $\tau-\tau_0 = 0.5$, 1.0, 1.5 and 2.0. Indeed, in total three vortices emerge:

- the tip vortex, appearing instantaneously at $\tau = 0^+$, which is already part of the initial data at $\tau=\tau_0$
- the flap-outboard-edge vortex. This double-branched vortex, inserted as representation of a highly rolled-up region, appears at $\tau-\tau_0 = 0.125$. It is sometimes referred to as the "flap vortex".
- the flap-inboard-edge vortex. This double-branched vortex, sometimes referred to as the "fuselage vortex" appears at $\tau-\tau_0 = 0.268$.

After the emergence of the three vortices the computation has been continued up to $\tau-\tau_0 = 2.0$, increasing $\Delta_{max}$ from time to time to lessen the CPU time requirements somewhat.

The inclination of the feeding sheets is held fixed at a position such that the vortex is represented by a sufficient number of loops. As evident from Fig. 7.16c, at times following $\tau = 1.0$, the feeding sheet connecting the outboard flap-edge vortex to the vortex sheet segment which on its turn is connected to the tip vortex, moves again, making one complete revolution before it is steady again. This unintentionally is caused by a flaw (triggered when one vortex of the same segment moves past the lateral position of the other vortex of the segment) in the algorithm that determines the angular extent of the vortex sheet.

The evolution of the doublet distribution, Fig. 7.16d, shows that the flap-outboard-edge vortex is the strongest vortex, it is twice as strong as the tip vortex, while the flap-inboard-edge vortex has about the same amount of circulation (but of opposite sign) as the tip vortex. At the final time of $\tau-\tau_0=2.0$ 87.5% of all vorticity with negative sign has accumulated in the flap-inboard-edge vortex, while 60% and 30% of all vorticity with positive sign has accumulated in the flap-outboard-edge and tip vortex, respectively.

Fig. 7.16e shows the number of panels used in the adaptive panel scheme. In this figure the rapid roll-up is evident as a rapid increase in the number of panels just before the "critical" time, followed by an abrupt drop when the rolled-up region is replaced by a discrete vortex. Also changing the basic panel size $\Delta_{max}$ results in a drop in the number of panels needed to discretize the vortex sheet segments.

Fig. 7.16f shows the position of the three vortices and the center of vorticity (COV). The lateral position of the latter is theoretically at 0.8669, the numerically found position varies within a band of less than 0.5% about this value.

The starboard-side circulation and "Hamiltonian", also shown in Fig. 7.16f, exhibit the same type of behaviour as for the previous two cases, i.e. the circulation is nearly invariant, while the "Hamiltonian" decreases gradually, presumably due to the amalgamation process.

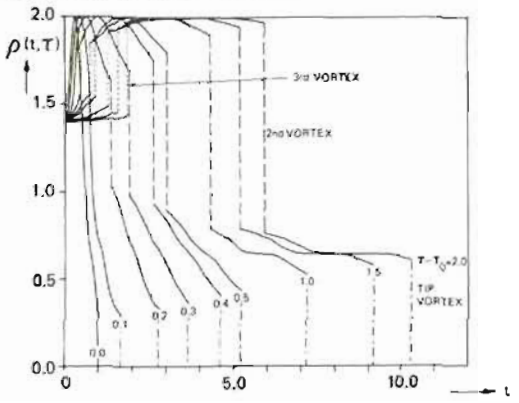


Fig. 7.16d Evolution of doublet distribution panel scheme

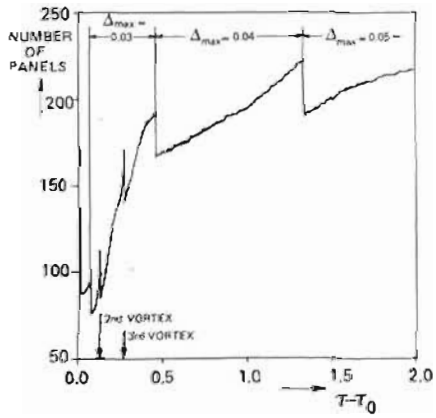


Fig. 7.16e Number of panels used in adaptive

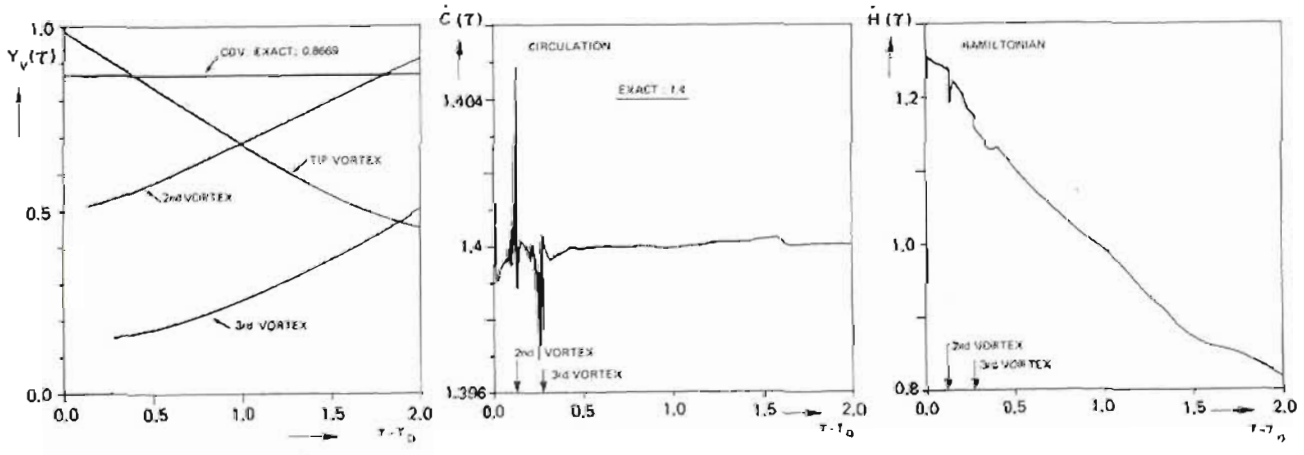


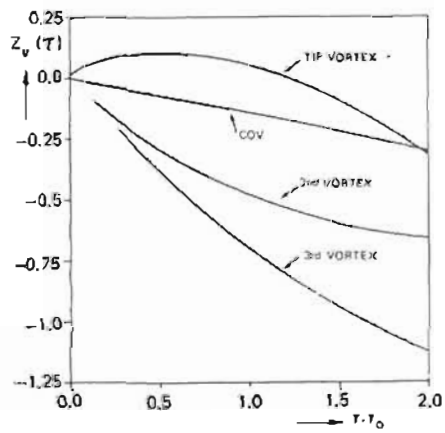


Fig. 7.16f Vortex position, circulation and Hamiltonian versus time

The correlation of the time-like variable $\tau$ with the distance downstream of the trailing edge is similar to the one we derived for the case of the ellipticallly loaded wing, i.e.

$$(x-x_{T.E.})/c(0) \approx \frac{2.8}{c_\ell(0)}\left(\frac{s}{c(0)}\right)^2 \tau$$

This implies that for a wing of aspect ratio 10 and $c_\ell(0) \approx 1.0$ $\tau \approx 0.1$ corresponds with a cross-flow plane 7 chord lengths downstream of the trailing edge, suggesting (Fig. 7.16b) that already near the position of the tail surfaces the wake has deformed considerably.

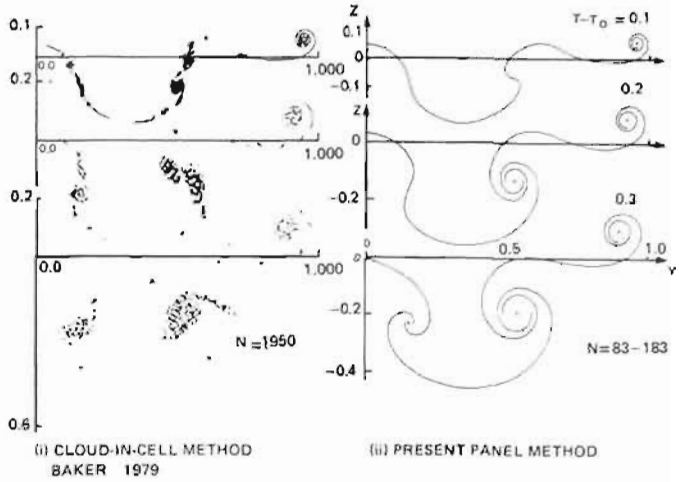


Fig. 7.17 Wing with deployed part-span flap; comparison of different methods

In Fig. 7.17 results are compared of the "cloud-in-cell" method and of the present panel method. Although the many small-scale structures in the results of Baker-1979 make it difficult to identify the sheet, the global structure agrees reasonably well with that of the panel method.

For the present method the computation of the evolution of the vortex sheet was continued for times beyond the ones of Fig. 7.16b, primarily with the objective of comparing the present potential-flow vortex sheet method with the Navier-Stokes method of Weston & Liu-1982. It showed that the method gives smooth results up to long times. The vortices do not gain much in strength after $\tau \approx 1.0$ and the tip vortex and "fuselage" vortex start to orbit around the stronger "flap" vortex. After $\tau \approx 2.0$ the tip and the flap vortex start to interact more strongly and Weston & Liu's Navier-Stokes results indicate a merger of these two vortices. In the present calculation vortex sheet segments 2 and 3, connecting the "fuselage" with the "flap" vortex and the "flap" with the tip vortex respectively, move very close towards each other. As finally, at about $\tau - \tau_0 \approx 2.4$, the two weak vortex sheet segments intersect the computation was stopped. However, without problem the computation could have been continued with shorter vortex sheet segments.

Fig. 7.18 Wing with deployed part-span flap; comparison of different methods

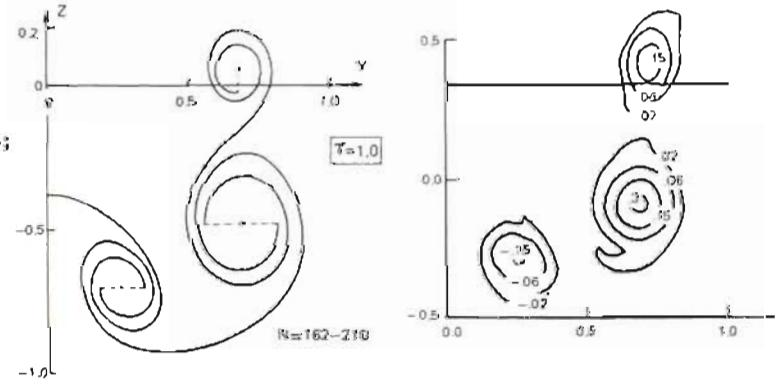


Fig. 7.18 compares at $\tau = 1.0$ the result of the present panel method with that of Weston & Liu's-1982 Navier-Stokes result. In both results the vortex cores have approximately the same elliptical appearance, dimension and position in space, suggesting that vorticity diffusion effects in the Navier-Stokes solution have been small.

*Fig. 7.19a*
Initial shape of wake and corresponding doublet distribution for unit-aspect-ratio delta wing at 20 deg incidence

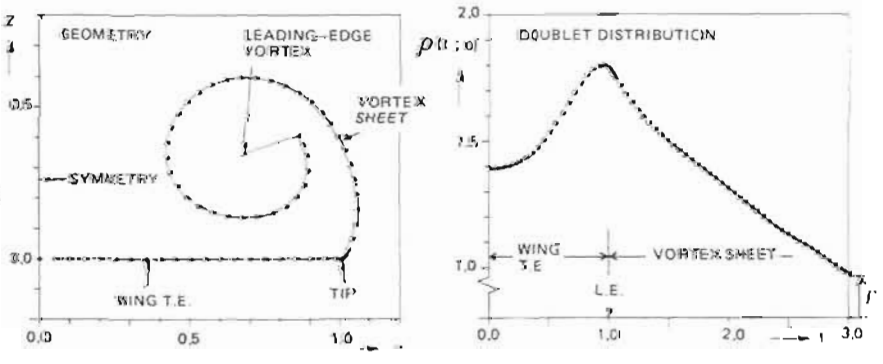

7.7.4 Delta wing with leading-edge vortex separation

The final application concerns the wake downstream of a slender delta wing of unit aspect ratio at 20 deg incidence. At this incidence the flow separates at the leading edge and a leading-edge vortex flow develops above the wing. The doublet distribution on the wing and leading-edge vortex sheet as well as the position of the leading-edge vortex system have been obtained with the method, based on the slender-body approximation, described in the next chapter.

The result of this computation, carried out such that the x-axis lies along the wing upper surface, is shown in Fig. 7.19a. The geometry includes the wing surface as well as the leading-edge vortex sheet and leading-edge vortex. From the doublet distribution one observes that along the trailing edge of the wing the vorticity, $-\bar{e}_x \rho'(t;0)$, is negative, almost up to the tip (i.e. leading edge) and positive on the leading-edge vortex sheet. The total amount of positive vorticity (circulation) is 1.8, that of negative vorticity is 0.4.

The computational parameters used in the present computation are given in Table 7.4.

Table 7.4
Computational parameters used for delta wing with leading-edge vortex sheet

| $\tau$ | Number of segments | Number of time steps | Number of panels |
|---|---|---|---|
| 0. -0.5921 | 1 | 226 | 64-106 |
| 0.5921-1.3421 | 2 | 250 | 87-143 |
| | | 476 total | |

F = 0.4
$\Delta x_{max}$ = 0.005
$\Delta\tau_{max}$ = 0.003
$\Delta\theta_{max}$ = 20 deg
$\Delta_{max}$ = 0.05

The relation between the time-like coordinate $\tau$ and the distance downstream of the trailing edge is:

$$\frac{x-x_{t.e}}{c} = \tau\left(\frac{s}{c}\right)\cos\alpha$$

where c is the root chord of the wing and s is the semi span of the wing, i.e. since s = ½c and $\alpha$=20 deg the factor multiplying $\tau$ becomes 0.235.

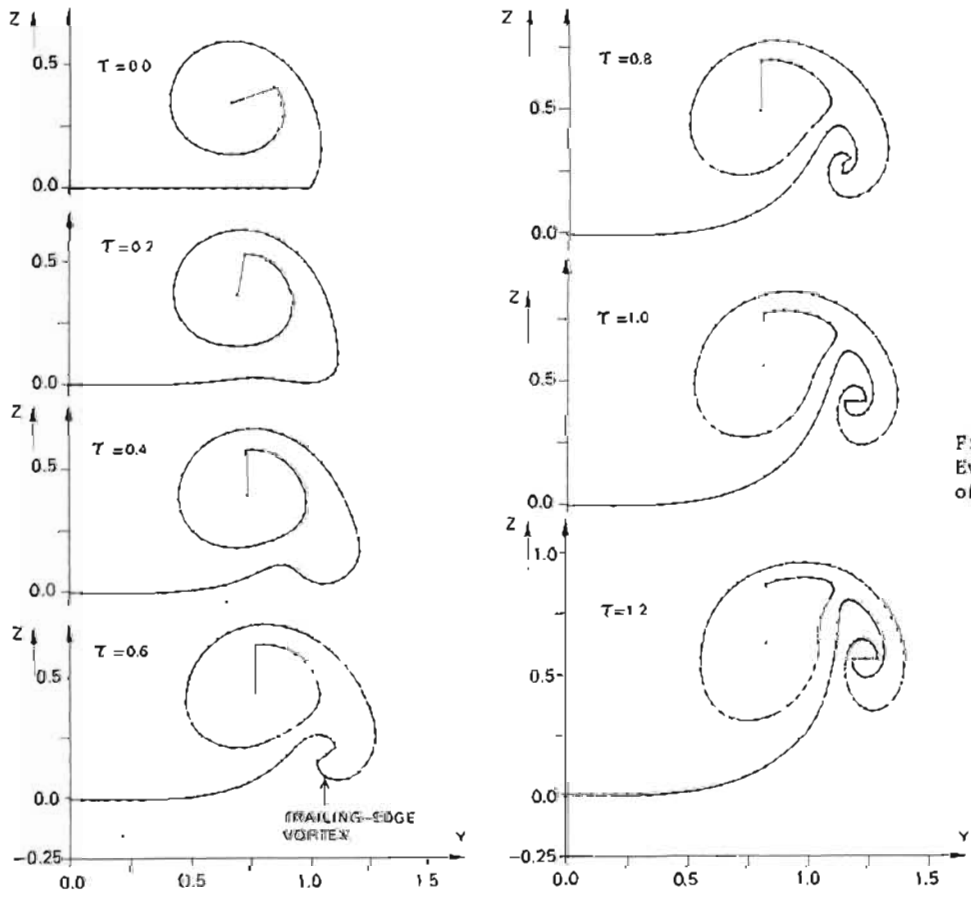


Fig. 7.19b
Evolution of vortex wake of slender delta wing

The computed geometry of the wake (in planes perpendicular to the wing surface) is shown in Fig. 7.19b for $\tau$ = 0.0(0.2)1.2. It clearly shows the development of the (double-branched) trailing-edge vortex, as observed in experiments by Hummel-1979, and the subsequent development of a mushroom shaped vortex wake.

The computation started with the feeding sheet of the leading-edge vortex at about a "2 o'clock" position. During the initial phase this cut was allowed to move to the "12 o'clock" position, reached at $\tau \approx 0.23$, at which time the amalgamation process was started.

In the computation the trailing-edge vortex was introduced at $\tau$ = 0.5921, which corresponds to 14% root chord downstream of the trailing-edge. The vorticity contained within this vortex is of different sign compared with the vorticity contained within the leading-edge vortex, while the origin of its center can be traced back to a location on the trailing edge at about 70% semi-span.

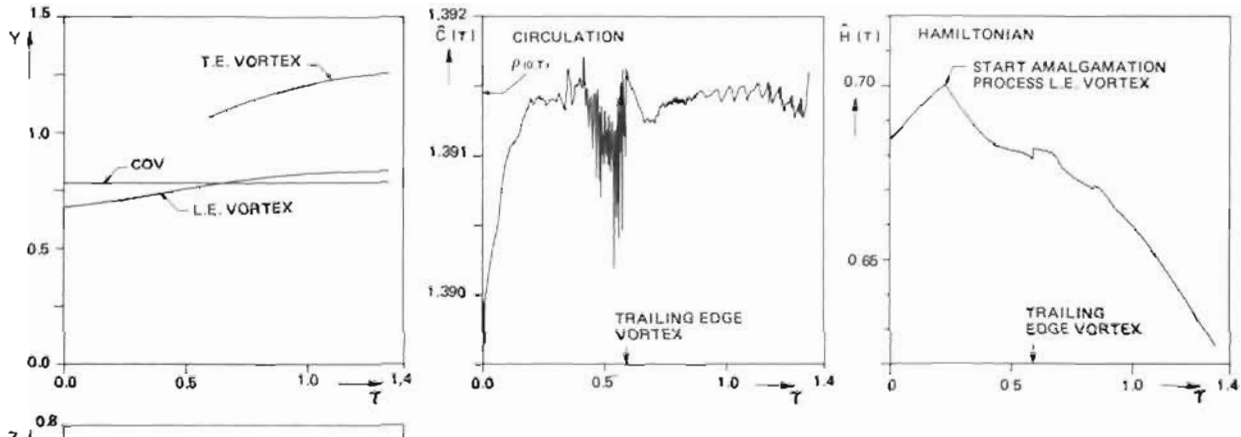


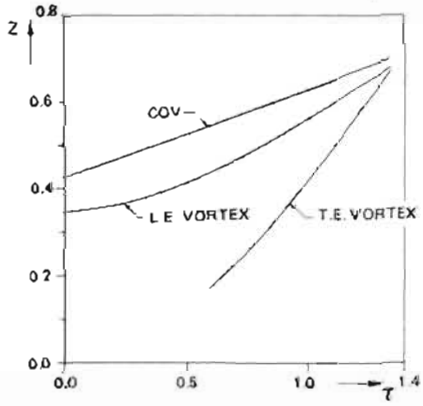


Fig. 7.19f Position of vortex cores, circulation and Hamiltonian of starboard side of vortex wake

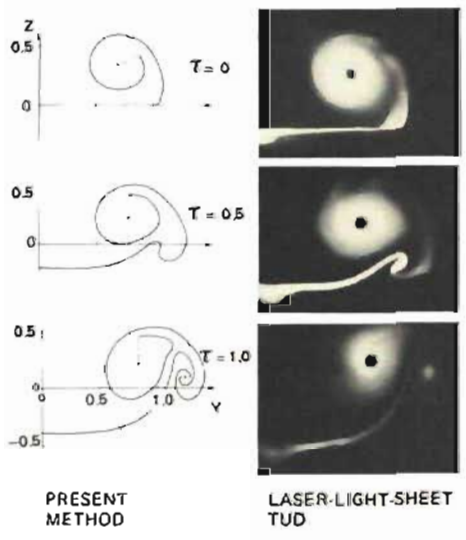


Fig. 7.20
Comparison of computation and experiment in planes perpendicular to the free-stream direction

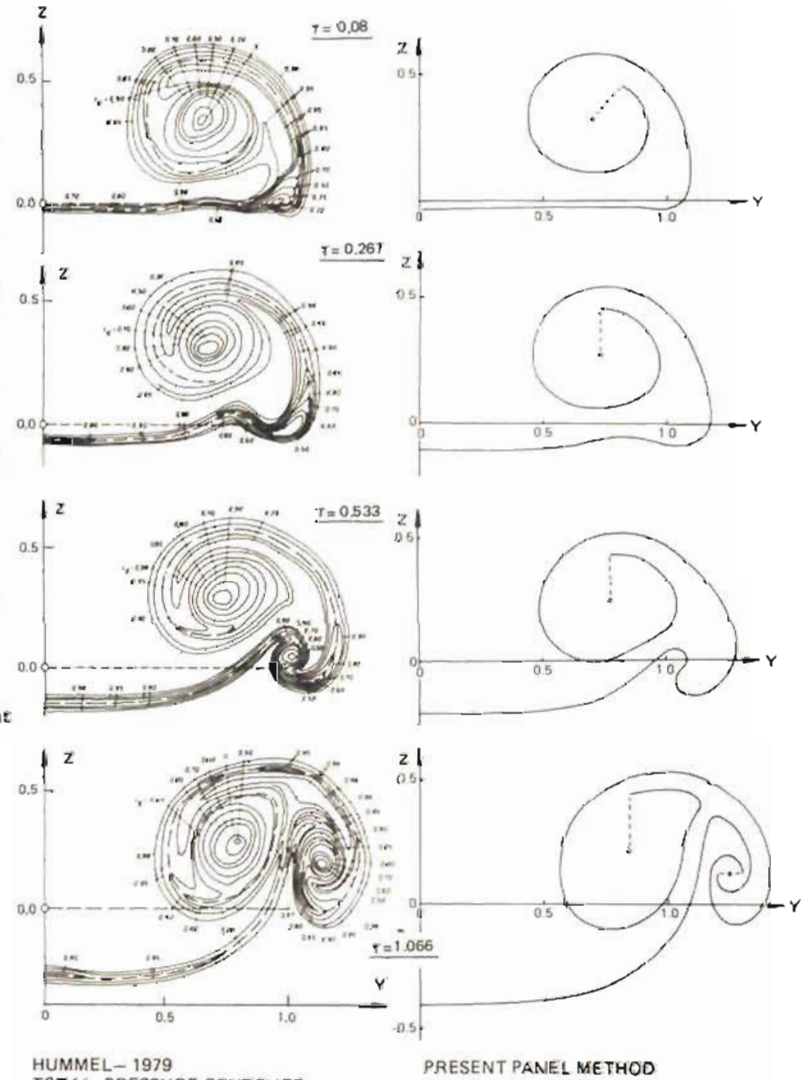


Fig. 7.21 Comparison of computational results with measured total pressure contours in planes perpendicular to the free-stream direction

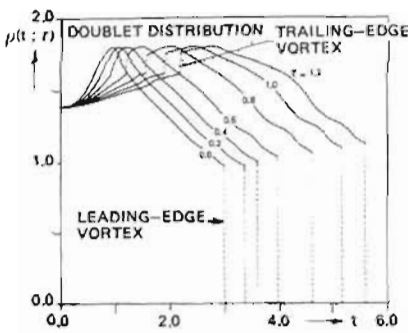


Fig. 7.19c Evolution of the doublet distribution

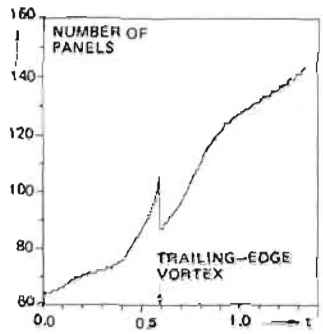


Fig. 7.19d Number of panels used in adaptive panel scheme

*The time-wise development of the doublet distribution is shown in Fig. 7.19c. It shows the increase in* strength of the leading-edge vortex, following the start of the amalgamation, as well as the formation of the much weaker trailing-edge vortex resulting from of the steepening of the doublet distribution. The number of panels increases due to the continual stretching of the vortex sheet as well as due to the formation of the trailing-edge vortex. In Fig. 7.19d the latter is marked by a sharp increase just before of the "critical" time $\tau_c = 0.5921$ is reached.

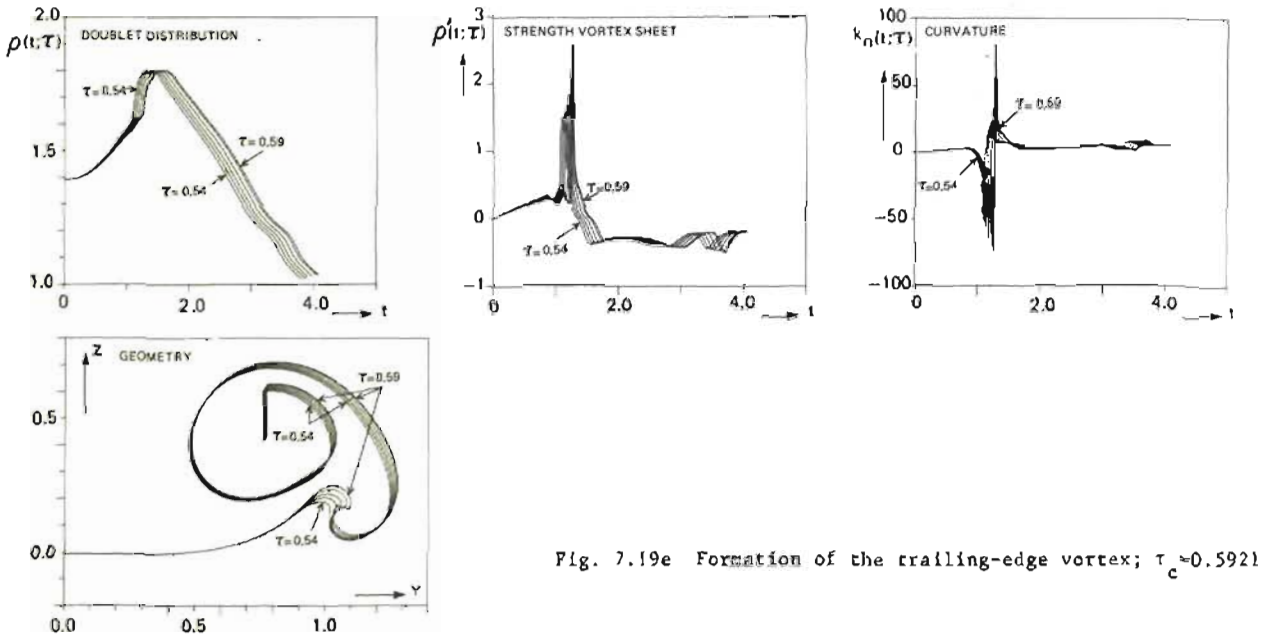


Fig. 7.19e Formation of the trailing-edge vortex; $\tau_c$=0.5921

The formation of the trailing-edge vortex is considered in more detail in Fig. 7.19e. Presented are the geometry, doublet distribution, vortex sheet strength ($= \rho'(t;\tau)$) and curvature for 6 time frames ($\tau$=0.54(0.1)0.59) just ahead of the "critical" time. Quite clearly one observes the formation of the double-branched vortex and associated with it the steepening of the doublet distribution, increase in vortex sheet strength and the double peak in the vortex sheet curvature. Note that the apparent shift in the curves for the doublet distribution its first derivative and the curvature for values of t exceeding 1 is almost solely due to the increase in arc length in the region where the double branched vortex forms.

The position of the vortices and that of the center of vorticity (COV) are shown in Fig. 7.19f. The lateral position of the COV is nearly invariant, while both the leading-edge and trailing-edge vortex turn in the direction of the free stream. The vertical position of the leading-edge vortex indicates, as observed in experiment, that the inclination of the leading-edge vortex increases from about $\alpha/4$ at the trailing-edge (at 100% root chord) to about $\alpha/2$ further downstream (at ± 130% root chord). As in the preceding cases the vertical position of the COV varies almost linear with time, its inclination is slightly more than $\alpha/2$.

Fig. 7.19f also shows the variation in time of the starboard-side circulation and "Hamiltonian". The circulation is not changing very much, but the "Hamiltonian" develops the same type of variation we have seen before. Clearly evident in this figure is the beginning of the amalgamation, as a sudden change of the sign in the slope of the curve.

In most experiments the flow characteristics are measured in planes perpendicular to the tunnel axis, i.e. perpendicular to the direction of the freestream $\bar{U}_\infty$. So above computation was repeated in exactly that framework, i.e. the wing was set at an angle of 20 deg. The solution at $\tau$=0 was also obtained in that same framework.

In Fig. 7.20 the computed shapes at the trailing edge, at 12.5 and at 25% root chord behind the trailing edge ($\tau$=0, 0.5 and 1.0, respectively) are compared with the shapes visualized in the low-speed windtunnel of the Department of Aerospace Engineering of the Technical University Delft using the laser-light-sheet technique. The agreement between the computed vortex sheet shapes and the observed smoke traces is quite good.

Note that in the experiment small-scale structures are clearly recognizable in the shear layer, especially at $\tau$=0. A further comparison with experimental data is provided in Fig. 7.21. Here we compare computational results of the present method with the by now already classical total-pressure-contour results of Hummel-1979, obtained for the unit-aspect-ratio wing now at 20.5 deg incidence.
The numerical result is also in rather close agreement with these experimental data, especially with regard to the formation of the second vortex and its further evolution. Note that compared with Hummel's result there is a difference in the downward displacement of the central part of the wake, possibly attributable to wind-tunnel floor interference.

## 7.8 Assessment of inherent smoothing properties of present method - Periodic vortex sheet

### 7.8.1 Introduction

Some insight into the numerical smoothing properties of the present computational procedure is obtained by considering the linear growth phase of the Kelvin-Helmholtz instability. The Kelvin-Helmholtz instability is the susceptibility of a double-infinite vortex sheet of constant strength to instability, i.e. according to linear stability theory (see Appendix C) disturbances of infinitesimal wave length have an infinite growth rate. This instability is also an important subject in the more general case of the development of waves on the interface between two streams of different density, sometimes including the effects of gravity and interfacial surface tension. In the statically stable case of a lighter fluid on top of a heavier fluid one speaks of the Kelvin-Helmholtz instability in the other case of the Rayleigh-Taylor instability. There is also a correspondence with the case where a spatially growing mixing layer is simulated as a time-developing vortex sheet in a coordinate system that moves with the mean velocity.

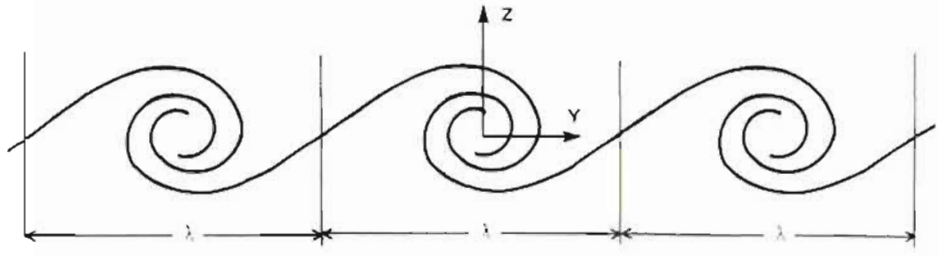


Fig. 7.22 Periodic vortex sheet

In this section we will consider the development in time of a periodic vortex sheet, see Fig. 7.22, with a prescribed initial sinusoidal disturbance of wave length $\lambda$ and of small amplitude $\varepsilon$. The particular form of the perturbation we choose is the so-called normal mode; it follows from the integration of the sinusoidal disturbance found in the linearized approximation of Appendix C. The normal mode is given by:

$$\bar{X}(t;0) = \bar{e}_y\{t/\lambda - \varepsilon\sin(2\pi t/\lambda)\} - \varepsilon\bar{e}_z\sin(2\pi t/\lambda)$$
$$\rho(t) = t/\lambda \qquad (7.32)$$

for $t\in(-\infty,\infty)$.

By comparing the growth rate according to linear stability theory and the one found from the results of the present method we can assess the smoothing properties of the present computational procedure.

### 7.8.2 Computation of the velocity field

The velocity field induced by a specific vortex sheet segment is given by Eq. (7.1). The velocity field induced by an infinite periodic vortex system is obtained by replacing in Eq. (7.1) $\bar{X}(t)$ by $\bar{X}(t) + k\lambda\bar{e}_y$, $\bar{X}_{ve}$ by $\bar{X}_{ve} + k\lambda\bar{e}_y$, $\bar{X}_{vo}$ by $\bar{X}_{vo} + k\lambda\bar{e}_y$ and summing over k from $-\infty$ to $+\infty$. It turns out that this summation can be carried out in closed form (e.g. van de Vooren-1980) resulting in (considering just one vortex sheet segment, $C_v$, the generalisation to multiple segments is quite straightforward):

$$\bar{U}_u(\bar{X}_o) = \frac{-\bar{e}_x}{2\lambda}\times\left\{\int_{C_v}\frac{\bar{R}^p}{R^{p2}}\frac{d}{dt}\rho(t)dt - \delta_{ve}\frac{\bar{R}^p_{ve}}{R^{p2}_{ve}}\rho_e + \delta_{vo}\frac{\bar{R}^p_{vo}}{R^{p2}_{vo}}\rho_o\right\} \qquad (7.33a)$$

with $$\bar{R}^p = \bar{e}_y\sinh\omega(Y_o - Y(t)) + \bar{e}_z\sinh\omega(Z_o - Z(t)) \qquad (7.33b)$$

$$R^{p2} = \cosh\omega(Z_o - Z(t)) - \cos\omega(Y_o - Y(t)) \qquad (7.33c)$$

and similar expressions for $\bar{R}^p_{ve}$, $R^{p2}_{ve}$, $\bar{R}^p_{vo}$ and $R^{p2}_{vo}$. Here we also used the conventional definition of the frequency, i.e. $\omega=2\pi/\lambda$.

It appears that a small-curvature type of expansion of the integral in Eq. (7.33a) does not lead to closed-form expressions. Alternatively one could write the integral in Eq. (7.33a) as

$$\frac{1}{2\lambda}\left[\int_{C_v}\left(\frac{\bar{R}^p}{R^{p2}}\right)\frac{d}{dt}\rho(t)dt\right] = \frac{1}{2\lambda}\left[\int_{C_v}\left(\frac{\bar{R}}{|\bar{R}|^2}\right)\frac{d}{dt}\rho(t)dt\right] + \frac{1}{2\lambda}\left[\int_{C_v}\left(\frac{\bar{R}^p}{R^{p2}} - \frac{\bar{R}}{|\bar{R}|^2}\right)\frac{d}{dt}\rho(t)dt\right], \qquad (7.34)$$

use the small-curvature expression Eq. (7.5) for the first integral on the right-hand side and some conventional numerical integration scheme for the non-singular integral on the right-hand side. However, this still requires special attention in the near field of a panel and requires the frequent evaluation of goniometric and hyperbolic functions. In the present study therefore we adopt the following approach. First, we compute the contribution due to the vortex sheet near the region $Y\in[-\lambda/2,\lambda/2]$, to be considered by summing the contribution due to 2K+1 periods. Second, we add the contribution due to the remaining periods of the vortex sheet by approximating the influence of each of these periods by that of a vortex which strength is equal to its circulation and whose position is its center of vorticity. The latter contribution can be summed in closed form after subtraction of appropriate terms for the 2K+1 "near-field" periods, leading to

$$\bar{U}_u(\bar{X}_o) = \sum_{k=-K}^{K}\left\{\bar{U}^k_u(\bar{X}_o) + \frac{C}{2\pi}\bar{e}_x\times\frac{\bar{R}^k_{cov}}{|\bar{R}^k_{cov}|^2}\right\} - \frac{C}{2\lambda}\bar{e}_x\times\frac{\bar{R}^p_{cov}}{R^{p2}_{cov}} \qquad (7.35a)$$

where

$$\bar{U}_\mu^k(\bar{X}_o) = -\frac{\bar{e}_x}{2\pi}\times\Big[\int_{C_v}\Big(\frac{\bar{R}^k}{|\bar{R}^k|^2}\Big)\frac{d}{dt}p(t)dt - \delta_{ve}\frac{\bar{R}^k_{ve}}{|\bar{R}^k_{ve}|^2}\rho_e + \delta_{vo}\frac{\bar{R}^k_{vo}}{|\bar{R}^k_{vo}|^2}\rho_o\Big] \tag{7.35b}$$

and $$\bar{R}^k = \bar{X}_o-(\bar{X}(t) + k\lambda\bar{e}_y) \tag{7.35c}$$

$$\bar{R}^k_{ve} = \bar{X}_o-(\bar{X}_{ve} + k\lambda\bar{e}_y) \tag{7.35d}$$

$$\bar{R}^k_{vo} = \bar{X}_o-(\bar{X}_{vo} + k\lambda\bar{e}_y) \tag{7.35e}$$

$$\bar{R}^k_{cov} = \bar{X}_o-(\bar{X}_{cov} + k\lambda\bar{e}_y) \tag{7.35f}$$

$$\bar{R}^p_{cov} = \bar{e}_y\sin\omega(Y_o-Y_{cov}) + \bar{e}_z\sinh\omega(Z_o-Z_{cov}) \tag{7.35g}$$

$$R^{2p}_{cov} = \cosh\omega(Z_o-Z_{cov}) - \cos\omega(Y_o-Y_{cov}) \tag{7.35h}$$

and where C is the circulation and $\bar{X}_{cov} = (0,Y_{cov},Z_{cov})^T$ is the position of the center of vorticity of the period for which $Y\in[-\lambda/2,\lambda/2)$.

Note further that

$$\bar{U}^k_\mu(\bar{X}_o) = \bar{U}^o_\mu(\bar{X}_o-k\lambda\bar{e}_y) \tag{7.36}$$

so that we just have to consider the expressions for the integration along the period for which k=0.
The above approach yields for sufficiently large K an accurate result and circumvents the small-curvature expansion for the integral in Eq. (7.33a).
A problem that remains is the one that occurs when the point where the velocity is to be computed coincides with the center of vorticity. The latter problem is resolved by considering in Eq. (7.35a) the last term in combination with the second term of the summation for k=0. Expanding for small values of $Y_o-Y_{cov}$ and $Z_o-Z_{cov}$ yields:

$$\lim_{|\bar{X}_o-\bar{X}_{cov}|\to 0}\Big[\frac{C}{2\pi}\bar{e}_x\times\Big\{\frac{\bar{R}^o_{cov}}{|\bar{R}^o_{cov}|^2} - (\frac{\pi}{\lambda})\frac{\bar{R}^p_{cov}}{R^{p2}_{cov}}\Big\}\Big]$$

$$= \frac{C}{2\pi}\frac{\omega^2}{12}\{(Z_o-Z_{cov})\bar{e}_y + (Y_o-Y_{cov})\bar{e}_z\} \tag{7.37}$$

For the periodic case one can also derive a number of invariants of the motion, e.g. van de Vooren-1980. Referring to section 7.6 invariants are C, $I_y$, $I_z$ and H, defined in Eqs. (7.21), (7.23a), (7.24a) and (7.26), respectively, where in the latter expression h is now defined as

$$h(\bar{X},\bar{X}') = \ln\{\cosh\omega(Z-Z') - \cos\omega(Y-Y')\} \tag{7.38}$$

Finally, it is remarked here that the quadratic and cubic interpolatory splines as employed in the computational procedure, described in section 7.5, have been adapted to the periodic case. This involves the way in which the necessary data (first derivative) at the first or the last point of the segments intersecting the boundaries of the period are considered.

7.8.3 Linear growth of normal mode

In this section we present results of calculations for the periodic vortex sheet representing a normal mode of the linear stability theory. The initial conditions are given in Eq. (7.32) with c=1/100. The vortex sheet is subdivided into panels of equal width and we study the growth of the perturbation as it develops in time. The time integration was carried out with a constant time step of $\Delta\tau$=0.001 for 100 time steps with K=3 and using between 4 and 80 panels. In Fig. 7.23 we present the maximum height of the computed vortex sheet versus time This figure shows that for the present computational procedure phenomena represented by of the order of 20 panels are not restrained to grow while structures represented by less than about 10 panels will smooth out as time progresses.

In the present computational procedure as applied in this chapter the panel width is not constant but is adapted to the local curvature, so that there are 15-20 panels on a circle with radius equal to the local radius of curvature. This implies that when a structure has been formed, or provided as input, to sufficient detail it will evolve further more or less unconstrained.

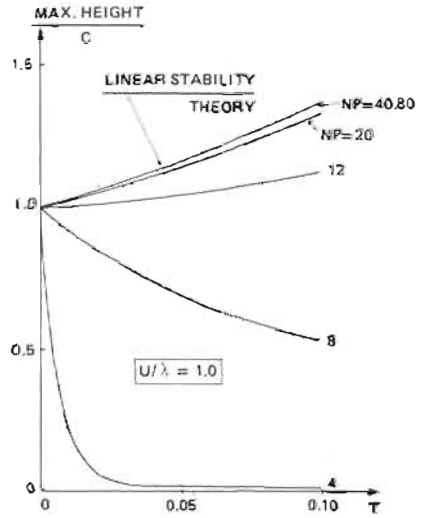


Fig. 7.23 Growth of sinusoidal normal mode, c=0.01; equidistant panel scheme, $\Delta\tau$=0.001

7.8.4 Nonlinear growth of normal mode

The stability theory applies only to the early-time development of the perturbation. At later times nonlinear effects will come into play and affect the development of the vortex sheet and presumably reduce the rate of growth. This is not investigated further in the present study.

# 8 METHOD FOR QUASI TWO-DIMENSIONAL VORTEX FLOW ABOUT SLENDER CONFIGURATIONS

## 8.1 *Introduction*

In this chapter we describe a quasi two-dimensional method for computing the flow about configurations with free vortex sheets, emanating from prescribed separation lines, mostly sharp edges. For these configurations the rolling-up vortex sheet is always in the near proximity of the surface and a strong interaction takes place between the vortex sheet and the flow over the surface. This results in a complicated flow pattern and typically one observes a nonlinear dependence of the lift on angle of attack and a strong dependence of the surface pressure distribution on the location and strength of the rolling-up vortex layers.

In this chapter we will assume that the configuration is sufficiently slender and simultaneously the flow is so slowly changing in streamwise direction that the problem can be treated within the framework of the slender-body approximation. In that case the fully three-dimensional problem can be reduced to a sequence of simpler two-dimensional problems, while the variation in streamwise direction is accounted for via the boundary conditions. The formulation of the problem within the framework of the slender-body approximation has already been derived in section 5.2, which included the special case of (slender) conical flow. In the latter case the geometric dimensions and doublet strength increase linearly in streamwise direction.

The method can advantageously be employed to:

(i) investigate the influence of parameters in the computational method such as sheet length, panel scheme, etc. in greater detail and at less expense than possible for a fully three-dimensional flow method;

(ii) obtain a first insight in the influence of changing, for design purposes, the cross-sectional geometry;

(iii) construct a reasonable initial guess for a fully three-dimensional method, like the one described in the next chapter.

The major drawback of the slender-body approximation is that the effect of the trailing edge is not accounted for. Furthermore the relatively large variations in streamwise direction as for example inevitably occur near the apex and also near abrupt changes in cross-sectional geometry are not allowed in the strict sense of the slender-body formulation.

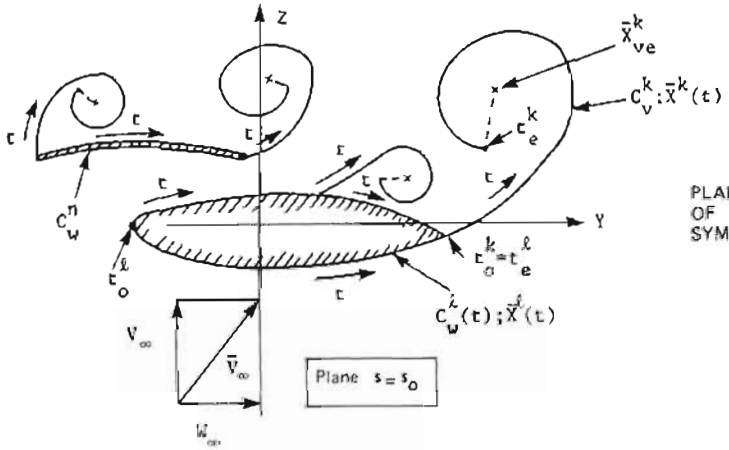


Fig. 8.1 Cross-flow-plane geometry for method based on slender-body approximation

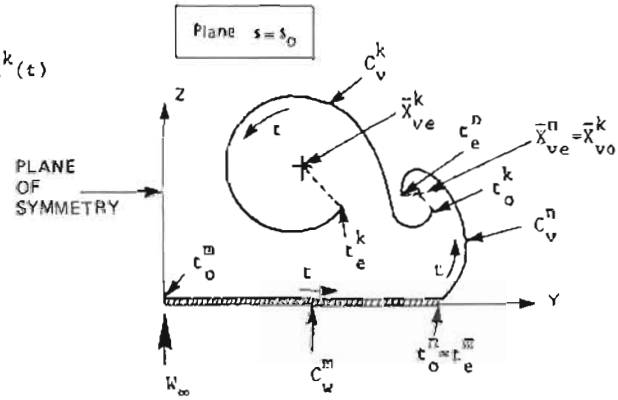


Fig. 8.2 Example cross-flow-plane geometry with geometry with symmetry and single- and double-branched vortex

The geometry considered in the present investigation may be quite general as far as its cross-section is concerned, see Figs. 8.1 and 8.2. The configuration is built up out of so-called segments. There are three types of segments:

(i) "Wing" segments $C_w$ that carry a doublet distribution. These segments represent thin solid parts of the configuration wetted by the flow on both sides, i.e. lifting surfaces like segment n in Fig. 8.1.

(ii) "Wing" segments $C_w$ that carry a composite source/doublet distribution. These segments like segment 2 in Fig. 8.1, constitute the closed contour of parts of the configuration with thickness. The Neumann condition for the external flow field is satisfied through the Dirichlet condition for the fictitious internal flow field (see section 3.7).

(iii) "Vortex-sheet" segments $C_v$ that carry a doublet distribution and represent vortex sheets. It is assumed that the first point $t_o^i$ of this type of segment is attached to another segment ($C_v$ or one or two $C_w$'s), while the last point $t_e^i$, through a feeding sheet, is attached to the vortex filament that represents the rolled-up part of the vortex sheet. Optionally the last point of the segment $C_v$ may be linked, through a double-branched vortex core model, to another vortex sheet segment (see Fig. 8.2).

*In case both the configuration and the flow about it are symmetric with respect to the x-z plane only* the starboard side of the configuration needs to be considered, though of course the influence of the port side is considered in the determination of the starboard side velocity field.

In the second section of this chapter we will describe how the streamwise derivatives in the formulation presented in section 5.2 are discretized. In the third section we will discuss how the second-order accurate panel method developed in section 7.2 is used to compute the velocity as the product of a matrix of influence coefficients and a column vector containing the yet unknown singularity (doublet and source) parameters. In the 4th section the discretization of the boundary conditions is described, which results in a system of non-linear algebraic equations for the unknown singularity and geometric parameters.
In the 5th section the iterative procedure to solve this system is described, together with continuation procedures used to obtain a good initial guess for the solution of a sequence of cases. In the final section of this chapter application of the method to various configurations is discussed. The latter includes comparison with results of other theoretical methods and comparison with experimental data.

8.2 Treatment of streamwise derivatives

The derivatives with respect to the streamwise direction s of the geometry and doublet distribution, that occur in the expression for the velocity and boundary conditions, derived in section 5.2, are approximated by a simple backward difference formula:

$$f_s(t;s_o) = \{f(t;s_o) - f(t;s_o-\Delta s)\}/\Delta s + O(\Delta s^2) \tag{8.1}$$

where $\Delta s$ is the distance between two consecutive cross-flow planes, the one at $s = s_o-\Delta s$ and the one at $s_o$. Note that the above formulation requires that the computational (s,t) plane is rectangular and that in the present and in the preceding cross-flow plane the solution is known at the corresponding values of t. The distance between two consecutive planes is to be chosen such that the error made in Eq. (8.1) is of magnitude comparable to the one in the velocity field due to the slender-body approximation.

In the remainder of this chapter we will denote functions $f(t;s)$ and $g(s)$ in the plane $s = s_o$ by $f(t) = f(t;s_o)$ and $g=g(s_o)$, respectively. Similarly, functions $f(t;s)$ and $g(s)$ in the plane $s = s_o-\Delta s$ are denoted by $f0(t)= f(t;s_o-\Delta s)$ and $g0 = g(s_o-\Delta s)$, respectively.

In case of conical flow, which in the present study is just a special case of the more general slender-body formulation, the geometry and doublet distribution vary linearly in s and Eq. (8.1) is exact. Moreover, for the conical case both geometry $\bar{X}0(t)$ and doublet distribution $\mu o(t)$ are zero, since they represent the apex of the configuration.

8.2.1 Velocity potential

The expressions for the velocity potential, induced at the point $\bar{X}_o$ in the cross-flow plane $s=s_o$, by the singularity distributions have been derived in section 5.2. It follows that to order $s_o\varepsilon^3$ of the slender-body approximation the perturbation velocity potential induced by the singularity distributions can be expressed as

$$\phi(\bar{X}_o) = \frac{1}{4\pi}\sum_k \{\delta_\mu^k\{\phi_\mu^k(\bar{X}_o)+\delta_{ve}^k\phi_Q^k(\bar{X}_o)\} + \delta_q^k\phi_q^k(\bar{X}_o)\} \tag{8.2a}$$

where the summation is over all segments. For a segment $C_w^k$ that is a lifting surface $\delta_\mu^k = 1$, $\delta_{ve}^k = 0$ and $\delta_q^k = 0$; for a segment $C_w^k$ with the Dirichlet boundary condition $\delta_\mu^k=1$, $\delta_{ve}^k=0$ and $\delta_q^k=1$; for a vortex sheet segment $\delta_\mu^k=1$, $\delta_{ve}^k=1$ and $\delta_q^k=0$.
The expressions for the various contributions in Eq. (8.2a) are:

(i) $\phi_\mu^k(\bar{X}_o)$, the contribution in the cross-flow plane due to the doublet distribution on a wing or vortex-sheet segment, which follows from Eqs. (5.13b-d) as:

$$\phi_\mu^k(\bar{X}_o) = \frac{1}{2\pi}\Big[\int_{C_v^k \text{ or } w} \mu^k(t)\bar{e}_x.\{\frac{d}{dt}\bar{X}^k(t)\}\times\frac{\bar{R}^k}{|\bar{R}^k|^2}dt$$

$$-\delta_{ve}^k\mu^k(t_e^k)FS(\bar{X}_o,\bar{X}_{ve}^k,\bar{X}^k(t_e^k)) + \delta_{vo}^k\mu^k(t_o^k)FS(\bar{X}_o,\bar{X}_{vo}^k,\bar{X}^k(t_o^k))\Big] \tag{8.2b}$$

where $\bar{R}^k = \bar{X}_o-\bar{X}^k(t)$. The expression in Eq. (8.2b) applies to all lifting-surface segments $C_w^k$, to all wing segments $C_w^k$ with Dirichlet boundary conditions and to all vortex sheet segments $C_v^k$. Only for the latter $\delta_{ve}^k$ and $\delta_{vo}^k$ are different from zero. If a feeding sheet is attached to $\bar{X}^k(t_e^k)$ $\delta_{ve}^k=1$ and $\delta_{vo}^k=0$ otherwise, similarly if a feeding sheet is attached to $\bar{X}^k(t_o^k)$ $\delta_{vo}^k=1$ and 0 otherwise (see Fig. 8.2). The function FS in the contribution due to the feeding sheets follows from Eqs. (5.13c and d) as:

$$FS(\bar{X}_o,\bar{X}_v,\bar{X}) = \tan^{-1}\frac{(\bar{X}_o-\bar{X}_v).(\bar{X}_v-\bar{X})}{(\bar{X}_o-\bar{X}_v).\bar{e}_x\times(\bar{X}_v-\bar{X})} - \tan^{-1}\frac{(\bar{X}_o-\bar{X}).(\bar{X}_v-\bar{X})}{(\bar{X}_o-\bar{X}).\bar{e}_x\times(\bar{X}_v-\bar{X})} \tag{8.2c}$$

(ii) $\phi_Q^k(\bar{X}_o)$, the contribution in the cross-flow plane due to the source representing the entrainment of the vortex core, follows from Eq. (5.14b) as:

$$\phi_Q^k(\bar{X}_o) = \frac{1}{2\pi}Q_v^k\ln(|\bar{R}_{ve}^k|/s_o)) \tag{8.2d}$$

with $\bar{R}_{ve}^k = \bar{X}_o-\bar{X}_{ve}^k$.

The source strength $Q_v^k$ follows from Eq. (5.14e), to consistent order of approximation:

$$Q_v^k = -\pi R_F^k(R_F^k-R0_F^k)U_\infty\{1 + 2(\Gamma^k/2\pi U_\infty R_F^k)^2\}^{\frac{1}{2}}-1\}/\Delta s \tag{8.2e}$$

where $R_F^k$ and $\Gamma^k$ are the radius and circulation of the vortex core in the cross flow plane $s=s_o$ respectively. $R0_F^k$ is the radius in the cross flow plane $s=s_o-\Delta s$.
For the case of a single-branched vortex core we choose as the effective radius the length of the feeding sheet,

$$R_F^k = |\bar{X}_{ve}^k - \bar{X}^k(t_e^k)|$$

while the circulation of the vortex core is defined by

$$\Gamma^k = \mu^k(t_e^k)$$

For a double-branched vortex core connecting vortex sheet segment $C_v^n$ to vortex sheet segments $C_v^k$, as in Fig. (8.2), a possible choice of $R_F^n$ is:

$$R_F^n = \frac{1}{2}|\bar{X}_{ve}^n - \bar{X}^n(t_e^n)| + \frac{1}{2}|\bar{X}_{vo}^k - \bar{X}^k(t_o^k)|$$

while the strength of the vortex is given by

$$\Gamma^n = \mu^n(t_e^n) - \mu^k(t_o^k)$$

In the latter case one has of course that $\bar{X}_{ve}^n = \bar{X}_{vo}^k$. However, since generally double-branched vortex cores are relatively weak, we will neglect the entrainment effect of these vortex cores altogether.

(iii) $\phi_q^k(\bar{X}_o)$, the contribution in the cross-flow plane due to the source distribution on wing segments $C_w^k$ with the Dirichlet boundary condition, follows from Eq. (5.12c) as:

$$\phi_q^k(\bar{X}_o) = \frac{1}{2\pi}\int_{C_w^k} q^k(t)\{\ln(|\bar{R}^k|/s_o)\}\left|\frac{d}{dt}\bar{X}^k(t)\right|dt \tag{8.2f}$$

where $\bar{R} = \bar{X}_o - \bar{X}^k(t)$. The source distribution follows directly from Eq. (5.23b).

In the case of port-side/starboard-side symmetry the integrals in the above expressions are over the starboard-side segments only. The contribution of the port side segments is accounted for by adding to Eq. (8.2a) the expression $\phi([S]\bar{X}_o)$, see Eq. (3.22a).

Across the singularity distribution the velocity potential is discontinuous, it follows from Eq. (5.20b) that

$$\Delta\phi(\bar{X}^k(t)) = \lim_{\varepsilon\to 0}[\phi(\bar{X}^k(t)+\varepsilon\bar{e}_n) - \phi(\bar{X}^k(t)-\varepsilon\bar{e}_n)]$$

$$= \delta_\mu^k \mu^k(t) \tag{8.2g}$$

8.2.2 Velocity field

The velocity at the point $\bar{X}_o$ in the cross-flow plane s=s$_o$ has been considered in section 5.2. It follows that to order $\varepsilon^2$ of the slender-body approximation the velocity field can be expressed as:

$$\bar{u}(\bar{X}_o) = \bar{e}_x(U_\infty \cos\alpha\cos\beta + \sum_k[\delta_\mu^k u_\mu^k(\bar{X}_o) + \delta_q^k u_q^k(\bar{X}_o)])$$

$$+ \bar{V}_\infty + \sum_k[\delta_\mu^k(\bar{U}_\mu^k(\bar{X}_o)+\delta_{ve}^k \bar{U}_Q^k(\bar{X}_o)) + \delta_q^k \bar{U}_q(\bar{X}_o)] \tag{8.3a}$$

where $\delta_\mu^k$, $\delta_q^k$ and $\delta_{ve}^k$ have the same meaning as before.

The components of the velocity in the cross-flow plane s=s$_o$ are:

(i) The cross-flow-plane component $\bar{V}_\infty$ of the free stream, see Eq. (5.21c).

(ii) $\bar{U}_\mu^k(\bar{X}_o)$, the velocity in the cross-flow plane s=s$_o$ induced by the doublet distribution on a wing or vortex-sheet segment. It follows from Eqs. (5.16c) and (5.17c) as

$$\bar{U}_\mu^k(\bar{X}_o) = \frac{\bar{e}_x}{2\pi}\times\left(-\int_{C_v^k \text{ or } w}\frac{d}{dt}\mu^k(t)\frac{\bar{R}^k}{|\bar{R}^k|^2}dt + \delta_{ve}^k\frac{\bar{R}_{ve}^k}{|\bar{R}_{ve}^k|^2}\mu^k(t_e^k) - \delta_{vo}^k\frac{\bar{R}_{vo}^k}{|\bar{R}_{vo}^k|^2}\mu^k(t_o^k)\right) \tag{8.3b}$$

where $\bar{R}^k = \bar{X}_o - \bar{X}^k(t)$, $\bar{R}_{ve}^k = \bar{X}_o - \bar{X}_{ve}^k$, $\bar{R}_{vo}^k = \bar{X}_o - \bar{X}_{vo}^k$ and the $\delta$'s have the same meaning as before, i.e. $\delta_{ve}^k = \delta_{vo}^k = 0$ in case of a lifting surface segment and in the case the segment is a vortex sheet segment $\delta_{ve}^k = 1$ while $\delta_{vo}^k = 0$ unless the segment has a feeding sheet attached to the point $\bar{X}^k(t_o^k)$.

(iii) $\bar{U}_Q(\bar{X}_o)$, the contribution in the cross-flow-plane velocity due to the source representing the entrainment of the vortex core, follows from Eq. (5.19b) as

$$\bar{U}_Q^k(\bar{X}_o) = \frac{1}{2\pi}Q_v^k\frac{\bar{R}_{ve}^k}{|\bar{R}_{ve}^k|^2} \tag{8.3c}$$

with $\bar{R}_{ve}^k = \bar{X}_o - \bar{X}_{ve}^k$ and $Q_v^k$ specified in Eq. (8.2e).

(iv) $\bar{U}_q^k(\bar{X}_o)$, the contribution in the cross-flow-plane velocity due to the source distribution on wing segments $C_w^k$ with the Dirichlet condition, follows from Eq. (5.15c) as:

$$\bar{U}_q^k(\bar{X}_o) = \frac{1}{2\pi}\int_{C_w^k} q^k(t)\frac{\bar{R}^k}{|\bar{R}^k|^2}\left|\frac{d}{dt}\bar{X}^k(t)\right|dt \tag{8.3d}$$

where $\bar{R}^k = \bar{X}_o - \bar{X}^k(t)$.

(v) $u_\mu^k(\bar{X}_o)$, the component in x-direction induced by the doublet distribution on a wing or vortex sheet segment, follows from Eqs. (5.16c), (5.17d), (5.18a and b) upon substitution of Eq. (8.1) as:

$$u_\mu^k(\bar{X}_o) = \frac{1}{\Delta s}(-\bar{X}_o\cdot\bar{U}_\mu^k(\bar{X}_o) + \psi_\mu^k(\bar{X}_o)) \tag{8.3e}$$

where $\bar{U}_\mu(\bar{X}_o)$ is given in Eq. (8.3b) and $\psi_\mu^k(\bar{X}_o)$ is defined as

$$\psi_\mu^k(\bar{X}_o) = \phi_\mu^k(\bar{X}_o) - \phi_{\mu o}^k(\bar{X}_o) + \hat{\phi}_\mu^k(\bar{X}_o) \tag{8.3f}$$

where $\phi_\mu^k(\bar{X}_o)$ is defined in Eq. (8.2b), $\phi_{\mu o}^k(\bar{X}_o)$ is given by the same expression but with $\mu^k(t)$ replaced by $\mu_o^k(t)$ and the third quantity in Eq. (8.3f) can be expressed as

$$\Phi_\mu^k(\bar{X}_o) = \frac{1}{2\pi}\{-\int_{C_{v \text{ or } w}^k} \frac{d}{dt}\mu^k(t)\bar{X}o^k(t).\frac{\bar{e}_x\times\bar{R}^k}{|\bar{R}^k|^2}dt$$

$$+ \delta_{ve}^k \frac{\bar{e}_x\times\bar{R}_{ve}^k}{|\bar{R}_{ve}^k|^2}.\bar{X}o_{ve}^k\mu^k(t_e^k) - \delta_{vo}^k \frac{\bar{e}_x\times\bar{R}_{vo}^k}{|\bar{R}_{vo}^k|^2}.\bar{X}o_{vo}^k\mu^k(t_o^k)\} \tag{8.3g}$$

Note that Eq. (8.3e) resembles the Euler relation for conical flow ($\varphi = x\varphi_x + y\varphi_y + z\varphi_z$) and indeed reduces to this relation for conical flow. Further note that $\Phi_\mu^k(\bar{X}_o)$ very much resembles the expression for $\bar{U}_\mu^k(\bar{X}_o)$, Eq. (8.3b).

(vi) $u_q^k(\bar{X}_o)$, the component in streamwise direction induced by the source distribution on a wing segment $C_w^k$ with the Dirichlet condition, follows from Eq. (5.15d) upon substitution of Eq. (8.1) as:

$$u_q^k(\bar{X}_o) = \frac{1}{\Delta s}\{-\bar{X}_o.\bar{U}_q^k(\bar{X}_o) + \psi_q^k(\bar{X}_o)\} \tag{8.3h}$$

where $\bar{U}_q^k(\bar{X}_o)$ is defined in Eq. (8.3d) and $\psi_q^k(\bar{X}_o)$ is defined as

$$\psi_q^k(\bar{X}_o) = \frac{1}{2\pi}\int_{C_w^k} q^k(t)\bar{X}o^k(t).\frac{\bar{R}^k}{|\bar{R}^k|^2}|\frac{d}{dt}\bar{X}^k(t)|dt \tag{8.3i}$$

which has a close resemblance to the expression for $\bar{U}_q^k(\bar{X}_o)$.

In case of symmetry with respect to Y=0 the influence of the port-side segments is accounted for in the manner explained at the end of section 3.7, e.g. by adding to Eq. (8.3b) $[s]\bar{U}_\mu^k([s]\bar{X}_o)$.

Across the singularity distribution the velocity is discontinuous. It follows from Eq. (5.20b) that in the present context, using Eq. (8.1), one finds for $t\in[t_o^k,t_e^k]$ and any $C_{v \text{ or } w}^k$:

$$\Delta\bar{u}(\bar{X}^k(t)) = \lim_{\varepsilon\to 0}[\bar{u}(\bar{X}^k(t)+\varepsilon\bar{e}_n) - \bar{u}(\bar{X}^k(t)-\varepsilon\bar{e}_n)]$$

$$= \delta_\mu^k \frac{\frac{d}{dt}\mu^k(t)}{|\frac{d}{dt}\bar{X}^k(t)|}\bar{e}_t + \delta_q^k q^k(t)\bar{e}_n$$

$$+ \frac{\bar{e}_x}{\Delta s}[\delta_\mu^k\{\mu^k(t)-\mu o^k(t) - \frac{\frac{d}{dt}\mu^k(t)}{|\frac{d}{dt}\bar{X}^k(t)|}\bar{e}_t.(\bar{X}^k(t)-\bar{X}o^k(t))\}$$

$$- \delta_q^k q^k(t)\bar{e}_n.(\bar{X}^k(t)-\bar{X}o^k(t))] \tag{8.3j}$$

Note that for the case of conical flow $\mu o^k = 0$, $\bar{X}o^k = 0$ and $\Delta s = s_o$, so that all of above expressions do not change much in character, except for Eq. (8.3f) where the second and third term on the right-hand side are both zero.

8.2.3 Boundary conditions

The boundary conditions, to be imposed in the cross-flow plane $s = s_o$, are given in Eqs. (5.22)-(5.25).

The Neumann boundary condition, to be applied on both lifting surface segments $C_w$ and vortex-sheet segments $C_v$ carrying just a doublet distribution, given in Eq. (5.22a), becomes upon substitution of Eq. (8.1):

$$\bar{U}_{tot}(\bar{X}^i(t)).\bar{e}_n = 0, \text{ for } t\in[t_o^i,t_e^i] \tag{8.4a}$$

where

$$\bar{U}_{tot}(\bar{X}^i(t)) = \bar{V}_\infty + \Sigma_k[\delta_\mu^k\{\bar{U}_\mu^k(\bar{X}^i(t)) + \delta_{ve}^k\bar{U}_Q^k(\bar{X}^i(t))\} + \delta_q^k\bar{U}_q^k(\bar{X}^i(t))] +$$

$$- \frac{1}{\Delta s}U_\infty\cos\alpha\cos\beta(\bar{X}^i(t)-\bar{X}o^i(t)) \tag{8.4b}$$

and $\bar{e}_n = \{\bar{e}_x\times\frac{d}{dt}\bar{X}^i(t))\}/|\frac{d}{dt}\bar{X}^i(t)|$ (8.4c)

The Dirichlet boundary condition to be applied on wing segments $C_w$ representing any closed part of the configuration which carry the composite doublet/source distribution follows from Eq. (5.23a) as

$$-\frac{1}{2}\mu^i(t) + \Sigma_k[\delta_\mu^k\{\Phi_\mu^{kP}(\bar{X}^i(t)) + \delta_{ve}^k\Phi_Q^k(\bar{X}^i(t))\} + \delta_q^k\Phi_q^k(\bar{X}^i(t))] = 0, \tag{8.5a}$$

for $t\in[t_o^i,t_e^i]$

Note that for k=i one has to take the Principal Value of $\Phi_\mu^k$. The magnitude of the source distribution $q^k(t)$ follows from Eq. (5.23b) upon substitution of Eq. (8.1) as

$$q^k(t) = -[\bar{V}_\infty - \frac{1}{\Delta s}U_\infty\cos\alpha\cos\beta\{\bar{X}^k(t)-\bar{X}o^k(t)\}].\bar{e}_n, \text{ for } t\in[t_o^k,t_e^k] \tag{8.5b}$$

The velocity on the segments $C_w^i$ with the Dirichlet boundary condition is obtained, without integral representation, directly from the expression given in Eq. (5.23c). Upon substitution of Eq. (8.1) this becomes:

$$\bar{u}(\bar{X}^k(t)) = \bar{U}_\infty + \bar{e}_n q^k(t) + \bar{e}_t \frac{d}{dt}\mu^k(t)/\left|\frac{d}{dt}\bar{X}^k(t)\right| + \bar{e}_x[\mu^i(t)-\mu_o{}^i(t) - \{\bar{e}_n q^k(t) + \bar{e}_t \frac{d}{dt}\mu^k(t)/\left|\frac{d}{dt}\bar{X}^k(t)\right|\}.\{\bar{X}^i(t)-\bar{X}o^i(t)\}]/\Delta s \tag{8.5c}$$

The pressure difference boundary condition, to be applied on $C_v$, given in Eq. (5.24), becomes upon substitution of Eq. (8.1) and using Eq. (8.4a):

$$\frac{\frac{d}{dt}\mu^i(t)}{\left|\frac{d}{dt}\bar{X}^i(t)\right|}\bar{U}_{tot}(\bar{X}^i(t)).\bar{e}_t + \frac{1}{\Delta s}U_\infty \cos\alpha\cos\beta(\mu^i(t)-\mu_o{}^i(t)) = 0 \quad \text{for } t\in[t_o^i, t_e^i] \tag{8.6a}$$

where

$$\bar{e}_t = \{\frac{d}{dt}\bar{X}^i(t)\}/\left|\frac{d}{dt}\bar{X}^i(t)\right| \tag{8.6b}$$

The tangential velocity component in Eq. (8.6a) is the average value (Cauchy Principal Value) across the vortex sheet $C_v^i$. In the present method the velocity is computed on the "upper side" of the doublet distribution, that is the left hand side when travelling in the direction of increasing t (see Fig. 8.3). This implies that in order to obtain the average value of the tangential component one has to subtract half the tangential component of the velocity jump. The jump in the velocity follows directly from Eq. (8.3j).

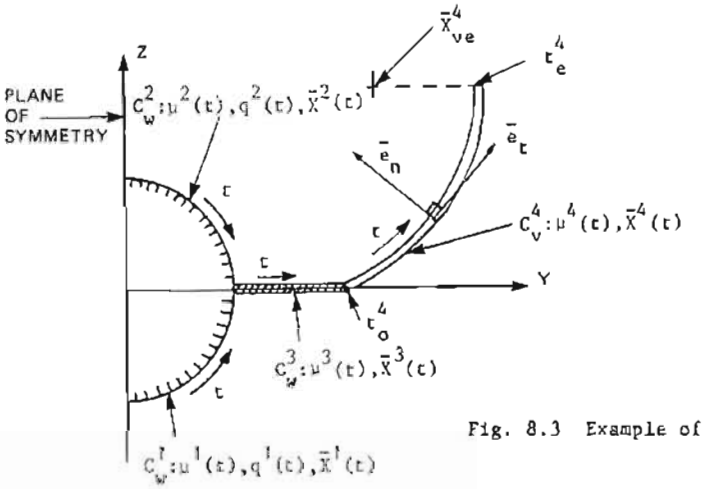


Fig. 8.3 Example of configuration with several segments

The zero-net-force condition, to be applied on the single-branched vortex filament/feeding sheet core model, becomes upon substitution of Eq. (8.1) in Eq. (5.25e) and using Eq. (8.4a):

$$\rho_\infty \bar{e}_x \times[\mu^i(t_e^i)\bar{U}_{tot}(\bar{X}_{ve}^i) - Q_v^i \bar{e}_x \times \bar{U}_{tot}(\bar{X}_{ve}^i) - \frac{1}{\Delta s}U_\infty \cos\alpha\cos\beta\{\mu^i(t_e^i)-\mu_o{}^i(t_e^i)\}(\bar{X}_{ve}^i - \bar{X}^i(t_e^i))] = 0 \tag{8.7a}$$

for all vortex sheet segments $C_v^i$ which end in a single-branched vortex core.
In the case of a double-branched vortex core we assume that $Q_v^i = 0$ and the vortex consists of the filament at $\bar{X}_{ve}^i = \bar{X}_{vo}^j$, the first branch connecting the vortex to $\bar{X}^i(t_e^i)$, the last point of $C_v^i$, while the second branch connects the filament to $\bar{X}^j(t_o^j)$, the first point of $C_v^j$.

The condition on the double-branched vortex then becomes:

$$\rho_\infty \bar{e}_x \times[\{\mu^i(t_e^i)-\mu^j(t_o^j)\}\bar{U}_{tot}(\bar{X}_{ve}^i) - \frac{1}{\Delta s}U_\infty \cos\alpha\cos\beta\{\mu^i(t_e^i)-\mu_o{}^i(t_e^i)\}(\bar{X}_{ve}^i - \bar{X}^i(t_e^i)) + \frac{1}{\Delta s}U_\infty \cos\alpha\cos\beta\{\mu^j(t_o^j)-\mu_o{}^j(t_o^j)\}(\bar{X}_{ve}^i - \bar{X}^j(t_o^j))] = 0 \tag{8.7b}$$

Note that in Eq. (8.7a) we included the force due to $Q_v^i$. Formally speaking the $\bar{U}_{tot}$ used for the second term of Eq. (8.7a) should not contain the term with $1/\Delta s$, since when multiplied with the entrainment $Q_v^i$ it would be a higher-order term. In the present study we retain terms such as these for reasons of practical convenience.

In the present method the computation is started using specified data at the initial station s=0. In case this station is the apex of a pointed configuration both $\bar{X}(t;0)$ and $\mu(t;0)$ are zero and the first problem solved, the one in the plane $s=\Delta s$, is equivalent to a conical flow problem. However, it is also possible to start the computation with other data at s=0, for instance in the case of a low-aspect ratio rectangular wing $\bar{X}(t;0) = \frac{1}{2}bt\bar{e}_y$ and $\mu(t;0)=0$, etc.

Given the data at s=0 the solution at the station $s=\Delta s$ is obtained by satisfying the boundary conditions derived above. This solution is then used to obtain the solution at the next station, etc.

The boundary conditions contain terms related to the streamwise variation of the geometry and singularity distributions and terms with $\bar{U}_\mu$, $\bar{U}_0$ and $\bar{U}_\sigma$ that depend on local cross-flow-plane values only. The streamwise perturbation velocity $u_\mu$ and $u_\sigma$ do not occur in the boundary conditions, but will be required in the expression for the pressure coefficient, Eq. (5.26), but not before the local cross-flow-plane solution has been obtained.

8.3 Two-dimensional second-order panel method

In this section we describe the approach followed to compute the velocity potential, cross-flow-plane components of the velocity and streamwise component of the velocity in the cross-flow plane $s=s_o$. The velocity components will be computed to second-order accuracy in the panel width. A consistent approach then requires that the velocity potential is computed to third order accuracy in the panel width. As in section 7.3 we will employ the small-curvature expansion to derive the expressions for the influence due to the doublet distribution, Eqs. (8.2b), (8.3b) and (8.3e), and the source distribution, Eqs. (8.2f), (8.3d) and (8.3h), on the contour of the segments $C_\mu$ and $C_\nu$. In each case we will derive the expressions for one specific segment and drop the superscript k for convenience.

In the present chapter the parameter t along the contour is chosen as the scaled arc length along the contour. This implies that $t\in[0,1]$. For vortex-sheet segments the total arc length of the sheet, i.e. b in Eq. (7.2a), is a quantity that is given. This means that during the iterative procedure to determine its position and strength the length of the vortex sheet remains b.

The analysis presented in the next sub-sections is based on the subdivision of the contour of the segment into NP panels and the panelwise representation of the singularity distribution and the geometry, i.e. the small-curvature expansion described in section 7.2.2.

8.3.1 Velocity potential due to doublet distribution

Substitution of Eqs. (7.3)-(7.4) in Eq. (8.2b), with $\sigma$ in Eq. (7.3b) replaced by $\mu$, and subsequent expansion results in:

$$\begin{aligned}\phi_\mu(\bar{X}_o) = \frac{1}{2\pi}\Big[\sum_{j=1}^{NP}\Big\{&\mu(t_j^*)(b\bar{E}_o\cdot\bar{e}_t + k_n(t_j^*)b(\bar{E}_o^c\cdot\bar{e}_t+b\bar{E}_1\cdot\bar{e}_n))\\ &+ \mu'(t_j^*)(b\bar{E}_1\cdot\bar{e}_t + k_n(t_j^*)b(\bar{E}_1^c\cdot\bar{e}_t+b\bar{E}_2\cdot\bar{e}_n))\\ &+ \tfrac{1}{2}\mu''(t_j^*)b\bar{E}_2\cdot\bar{e}_t + O(\delta_j^3\delta_j/D,\delta_j^3\delta_j^2/D^2\ \ldots)\Big\}\\ &- \delta_{ve}\mu(t_e)FS(\bar{X}_o,\bar{X}_{ve},\bar{X}(t_e)) + \delta_{vo}\mu(t_o)FS(\bar{X}_o,\bar{X}_{vo},\bar{X}(t_o))\Big]\end{aligned} \tag{8.8a}$$

where the primes denote differentiation with respect to t and $\bar{E}_k$ and $\bar{E}_k^c$ are defined in Eqs. (7.5b-c). All the $\bar{E}_k$'s have been worked out in Appendix D. The local truncation errors in Eq. (8.8a) accumulate to a global error of $O(\delta^3)$ at most, where $\delta$ is the average panel width. Note that in Eq. (8.8a) the terms with $k_n(t_j^*)$ correspond to the expressions given in Eqs. (D.7a and b).

8.3.2 Cross-flow plane velocity due to doublet distribution

The velocity induced in the cross-flow plane by the doublet distribution, Eq. (8.3b), is equivalent to Eq. (7.1b). Its small-curvature expansion is derived in section 7.2. In the present notation we have:

$$\begin{aligned}\bar{U}_\mu(\bar{X}_o) = \frac{1}{2\pi}\Big[\sum_{j=1}^{NP}\Big\{&\mu'(t_j^*)(\bar{E}_o+k_n(t_j^*)\bar{E}_o^c) + \mu''(t_j^*)\bar{E}_1\Big\}\\ &+ \bar{e}_x\times\Big\{\delta_{ve}\frac{\bar{R}_{ve}}{|\bar{R}_{ve}|^2}\mu(t_e) - \delta_{vo}\frac{\bar{R}_{vo}}{|\bar{R}_{vo}|^2}\mu(t_o)\Big\}\Big] + O(\delta^2)\end{aligned} \tag{8.8b}$$

where $\bar{E}_o$, $\bar{E}_1$ and $\bar{E}_o^c$ are given in Appendix D.

For points $\bar{X}_o$ in the far-field of the panel computing time is saved by using a single-pole expansion rather than the above computationally more expensive small-curvature expansion. In terms of the single-pole expansion the contribution in Eq. (8.8a) of the j-th panel in $\bar{U}_\mu(\bar{X}_o)$ is (see Eq. (7.7)):

$$\frac{-1}{2\pi}\mu'(t_j^*)\Big\{\bar{e}_x\times\frac{\bar{X}_o-\bar{X}(t_j^*)}{|\bar{X}_o-\bar{X}(t_j^*)|^2}\delta t_j\Big\} + O(\delta_j^3) \tag{8.8c}$$

where $t_j^*$ is the panel midpoint. The truncation error of order $\delta_j^3$ ensures that in the summation over all far-field panels the second-order accuracy is maintained.

8.3.3 Streamwise velocity due to doublet distribution

The streamwise component of the velocity induced by the doublet distribution follows from the Euler-type of expression given in Eq. (8.3e). The scalar function $\psi_\mu$ that appears in this relation consists of three parts, see Eq. (8.3f). The first term is the velocity potential due to the doublet distribution $\mu(t)$ on the cross-section $C_{v\ or\ w}$ given by $\bar{X}=\bar{X}(t)$. The second term, $\phi_{\mu_o}$, corresponds to the velocity potential induced by a doublet distribution of strength $\mu_o(t)$ on that same cross-section. The small-curvature expansion given in Eq. (8.8a) is used to obtain a $O(\delta^3)$ accurate expression for the first two terms of $\psi_\mu$. The third term in Eq. (8.3f), $\phi_{\bar{\mu}}$, defined in Eq. (8.3g), resembles the expression for $\bar{U}_\mu$ and is expanded by replacing in its small-curvature expansion, Eq. (8.8b), $\mu'(t)$ by $\bar{X}O(t)\mu'(t)$, which results in

$$\begin{aligned}\phi_{\bar{\mu}}(\bar{X}_o) = \frac{1}{2\pi}\Big[\sum_{j=1}^{NP}\Big\{&\mu'(t_j^*)\{\bar{X}O(t_j^*).(\bar{E}_o+k_n(t_j^*)\bar{E}_o^c) + \bar{X}O'(t_j^*).\bar{E}_1\} + \mu''(t_j^*)\bar{X}O(t_j^*).\bar{E}_1\Big\}\\ &+ \delta_{ve}\frac{\bar{e}_x\times\bar{R}_{ve}}{|\bar{R}_{ve}|^2}.\bar{X}O_{ve}\mu(t_e) - \delta_{vo}\frac{\bar{e}_x\times\bar{R}_{vo}}{|\bar{R}_{vo}|^2}.\bar{X}O_{vo}\mu(t_o)\Big] + O(\delta^3)\end{aligned} \tag{8.8d}$$

8.3.4 Velocity potential due to source distribution

Substitution of Eqs. (7.3a) and (7.4) into Eq. (8.2f), yields upon expansion of q(t) in a Taylor series about $t_j^*$:

$$\phi_q(\bar{X}_o) = \frac{b}{2\pi}\Big[\sum_{j=1}^{NP}\{q(t_j^*)(E_o - \tfrac{1}{4}b^2k_n(t_j^*)\bar{e}_t.\bar{E}_2) + q'(t_j^*)E_1 + O(\delta^3\tfrac{\delta}{D}, \ldots)\}\Big] \tag{8.9a}$$

where

$$E_k = \int_{t_j}^{t_{j+1}} \Delta t^k \ln\left(\frac{|\bar{R}_f|}{s_o}\right)dt \tag{8.9b}$$

is worked out in Appendix D. The composite error of Eq. (8.8e) is $O(\delta^3)$, as required to obtain the velocity field to second-order accuracy.

8.3.5 Cross-flow plane velocity due to source distribution

The close correspondence between the expression for the velocity induced by a doublet distribution and the one for the velocity induced by a source distribution, i.e. compare Eqs. (8.3b) and Eq. (8.3d) which shows that $\bar{U}_q = b\bar{e}_x\times\bar{U}_{\mu=q}$, yields

$$\bar{U}_q(\bar{X}_o) = \frac{b}{2\pi}\Big[\sum_{j=1}^{NP}\{q(t_j^*)\bar{e}_x\times(\bar{E}_o + k_n(t_j^*)\bar{E}_o^c) + q'(t_j^*)\bar{e}_x\times\bar{E}_1\}\Big] + O(\delta^2) \tag{8.9c}$$

where we note that if $\bar{A} = (0, A_y, A_z)^T$ then is $\bar{e}_x\times\bar{A} = (0, -A_z, A_y)^T$.
For points $\bar{X}_o$ in the far-field of a panel the contribution due to this panel is obtained from the single-pole expansion, similar to the one used to obtain Eq. (7.7), i.e. for that panel the contribution is computed as

$$\frac{b}{2\pi}q(t_j^*)\left\{\frac{\bar{X}_o - \bar{X}(t_j^*)}{|\bar{X}_o - \bar{X}(t_j^*)|^2}\right\}\Delta t_j \tag{8.9d}$$

8.3.6 Streamwise velocity due to source distribution

The streamwise component of the velocity due to the source distribution follows from the Euler-like relation given in Eq. (8.3h). The function $\psi_q$ that appears in that expression, defined in Eq. (8.3i), is computed employing the small-curvature expansion for the cross-flow component of the velocity due to the source distribution, Eq. (8.9c), resulting in

$$\psi_q(\bar{X}_o) = \frac{b}{2\pi}\sum_{j=1}^{NP}\Big[q(t_j^*)\{\bar{X}O(t_j^*).\bar{e}_x\times(\bar{E}_o + k_n(t_j^*)\bar{E}_o^c) + \bar{X}O'(t_j^*).\bar{e}_x\times\bar{E}_1\}$$

$$+ q'(t_j^*)\bar{X}O(t_j^*).\bar{e}_x\times\bar{E}_1\Big] + O(\delta^2) \tag{8.9e}$$

8.3.7 Influence of a panel on itself

For the study of the stability of the numerical schemes, it is of some importance to know what the influence is of the singularity distribution on a panel at its own expansion point, here always taken as the panel midpoint, i.e. $t_j^* = \frac{1}{2}(t_j + t_{j+1})$. Using Appendix D it follows from Eqs. (8.8) and (8.9) that the self-induced velocity potential at $t = t_i^*$ is:

$$\delta_\mu\Big[\mu(t_i^*)\{\tfrac{1}{2}\mathrm{sign}(\zeta) + \tfrac{1}{2\pi}k_n(t_i^*)\tfrac{b}{2}\Delta t_i\}\Big]$$

$$+ \delta_q\Big[q(t^*)\tfrac{1}{2\pi}\{-1 + \ln(\tfrac{b}{2}\Delta t_i/s_o)\}b\Delta t_i\Big] \tag{8.10a}$$

where sign($\zeta$) is +1 for the upper side and −1 for the lower side of $C_v$. Note that the upper side of the contour is at the left-hand side when moving along the contour in the direction of increasing t.

The self-induced velocity follows from Eqs. (8.8) and (8.9) as

$$\delta_\mu\Big[\tfrac{1}{b}\mu'(t_i^*)\{\tfrac{1}{2}\mathrm{sign}(\zeta) - \tfrac{1}{2\pi}k_n(t_i^*)\tfrac{b}{2}\Delta t_i\}\bar{e}_t + \tfrac{1}{b^2}\mu''(t_i^*)\{\tfrac{1}{2\pi}b\Delta t_i\}\bar{e}_n\Big]$$

$$+ \delta_q\Big[q(t_i^*)\{\tfrac{1}{2}\mathrm{sign}(\zeta) - \tfrac{1}{2\pi}k_n(t_i^*)\tfrac{b}{2}\Delta t_i\}\bar{e}_n - \tfrac{1}{b}q'(t_i^*)\{\tfrac{1}{2\pi}b\Delta t_i\}\bar{e}_t\Big] \tag{8.10b}$$

8.3.8 Numerical scheme - aerodynamic influence coefficients

In the discrete representation of the continuous integral formulation weak logarithmic singularities occur at the panel edges where the panel-wise representations of geometry and singularity distributions abut. To avoid spurious effects of this panel-edge behaviour as much as possible we choose the panel midpoints, $t_j^* = \frac{1}{2}(t_j + t_{j+1})$ for j=1(1)NP, as the expansion points and as the points where the boundary conditions are imposed.

The description of the second-order panel method is completed by specifying the scheme used to express $\bar{X}$, $\bar{X}'$, $\bar{X}''$, $\mu$, $\mu'$, $\mu''$ q and q' at the panel midpoints in terms of the set of parameters to be solved for. In the present method the following schemes are employed.

(i) Wing segment $C_v$ carrying a doublet distribution

In this case the geometry of the (lifting-surface) segment is specified by the value of $\bar{X}$ at the panel corner points, i.e. including the first and the last point of the segment. A cubic spline procedure provides the midpoint values of $\bar{X}(t_j^*)$, $\bar{X}'(t_j^*)$ and $\bar{X}''(t_j^*)$, for j=1(1)NP.

The doublet distribution is to be solved for by imposing the zero-normal-velocity condition, Eq. (8.4), at the NP panel midpoints. The choice of the numerical scheme to express $\mu$, $\mu'$ and $\mu''$ in terms of segment doublet parameters to be solved for is motivated by quadratic spline stability arguments as follows. It follows from Eq. (8.4) and Eq. (8.10b) that the dominating term in the normal component of the velocity induced at $t_j^*$ by the doublet distribution is proportional to $\mu''(t_j^*)$. A quadratic spline-type of representation is stable if one prescribes function value or second derivative at interval midpoints, plus appropriate conditions at the first and last point of the range. This suggested the following 3-point centered, second-order accurate scheme:

$$\mu(t_j^*) = \mu_j \tag{8.11a}$$

$$\begin{aligned}\mu'(t_j^*) = &- \frac{2(\Delta t_j+\Delta t_{j+1})}{(\Delta t_{j-1}+\Delta t_j)(\Delta t_{j-1}+2\Delta t_j+\Delta t_{j+1})}\mu_{j-1} \\ &- \frac{2(\Delta t_{j-1}-\Delta t_{j+1})}{(\Delta t_{j-1}+\Delta t_j)(\Delta t_j+\Delta t_{j+1})}\mu_j \\ &+ \frac{2(\Delta t_{j-1}+\Delta t_j)}{(\Delta t_j+\Delta t_{j+1})(\Delta t_{j-1}+2\Delta t_j+\Delta t_{j+1})}\mu_{j+1}\end{aligned} \tag{8.11b}$$

$$\begin{aligned}\mu''(t_j^*) = &\frac{8}{(\Delta t_{j-1}+\Delta t_j)(\Delta t_{j-1}+2\Delta t_j+\Delta t_{j+1})}\mu_{j-1} \\ &- \frac{8}{(\Delta t_{j-1}+\Delta t_j)(\Delta t_j+\Delta t_{j+1})}\mu_j \\ &+ \frac{8}{(\Delta t_j+\Delta t_{j+1})(\Delta t_{j-1}+2\Delta t_j+\Delta t_{j+1})}\mu_{j+1}\end{aligned} \tag{8.11c}$$

The scheme expresses $\mu(t_j^*)$, $\mu'(t_j^*)$ and $\mu''(t_j^*)$ in terms of the value of the doublet distribution at panel midpoints. This scheme is obtained by fitting a quadratic polynomial through the three midpoints $t_{j+k}^*$, k=-1(1)1 and evaluating the value of the doublet strength, its first and second derivative at $t_j^*$.
For the first midpoint (j=1) of the segment we choose $\mu_o = \mu(t_o)$ and $\Delta_o = 0$. For the last midpoint (j=NP) of the segment we choose $\mu_{NP+1} = \mu(t_e)$ and $\Delta_{NP+1} = 0$, so that also here second-order accuracy is maintained. The total number of unknown doublet parameters on a wing segment amounts now to NP+2 (see Fig. 8.4).

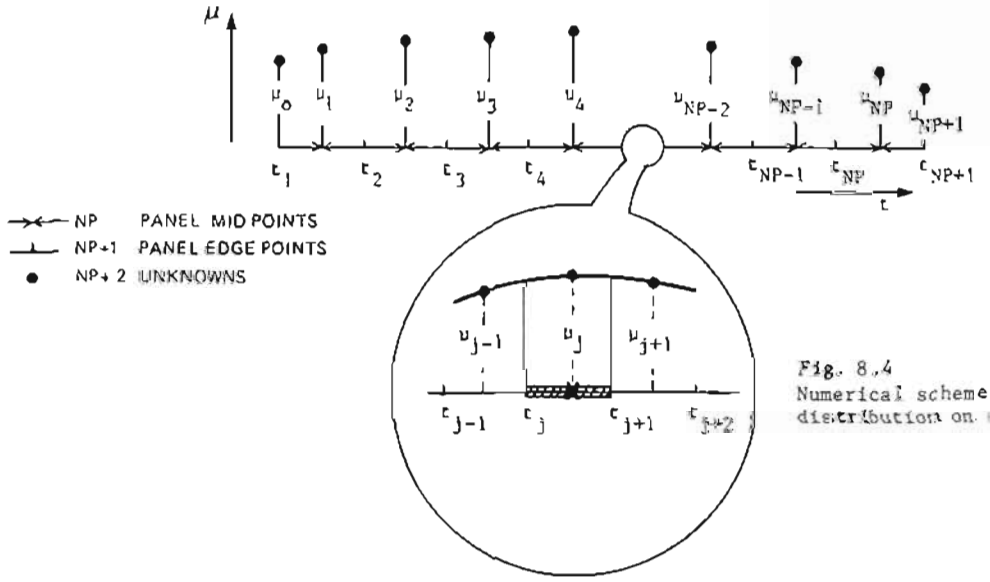


Fig. 8.4
Numerical scheme for singularity distribution on solid geometry $C_\omega$

(ii) Wing segment $C_\omega$ carrying the composite source/doublet distribution
In this case the geometry of the segment is specified by the value of $\bar{X}$ at the panel corner points. The cubic spline procedure is again employed to obtain the midpoint values $\bar{X}(t_j^*)$, $\bar{X}'(t_j^*)$ and $\bar{X}''(t_j^*)$, for j=1(1)NP.

The zero-normal-velocity boundary condition is imposed through the Dirichlet condition, Eq. (8.5a), for the flow inside the closed contour of which segment $C_\omega$ is a part. In this formulation the source distribution follows from Eq. (8.5b), i.e. $q(t_j^*)$ and $q'(t_j^*)$ follow directly from this equation.
The doublet distribution then follows from Eq. (8.5a), which has as leading term the value of the doublet distribution at the panel midpoint, i.e. the collocation point. Quadratic spline-stability arguments suggest the choice of the same centered, second-order accurate scheme as used on lifting surface segments $C_\omega$, i.e. the scheme given in Eqs. (8.11a-c) and depicted in Fig. 8.4. It contributes NP+2 unknown parameters to the problem.

(iii) Vortex sheet segment $C_\omega$ carrying a doublet distribution
In this case both the geometry and the doublet distribution are unknown and two boundary conditions are to be imposed, the normal-velocity boundary condition, Eq. (8.4), and the pressure-jump boundary condition, Eq. (8.6). As far as the doublet distribution is concerned the leading term of the first condition, applied at $t_j^*$, is proportional to $\mu''(t_j^*)$ and that of the second condition is proportional to $\mu''(t_j^*)$. The dependence of the two conditions on the geometric quantities is much more complex, but clearly $\bar{X}'(t_j^*)$ plays an important role in both conditions.

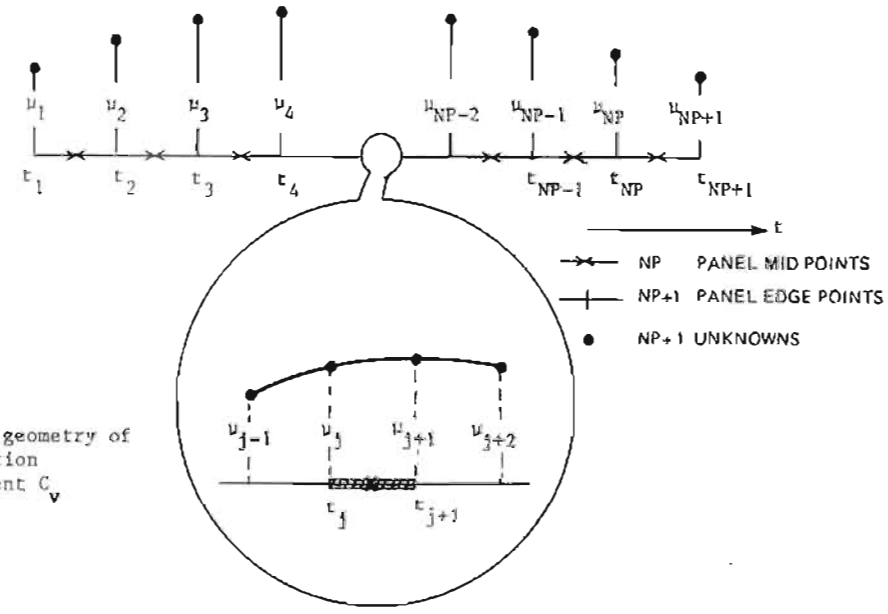


Fig. 8.5
Numerical scheme for geometry of and doublet distribution on vortex sheet segment $C_v$

The choice of a numerical scheme that is stable for both conditions has necessarily been based on some numerical experimentation. The experience gained in the study of the motion of two-dimensional vortex sheets proved to be useful. We take the same scheme as used in that study, i.e. the 4-point centered, second-order accurate scheme defined in Eq. (7.9). This scheme expresses the midpoint quantities $\mu(t_j^*)$, $\mu'(t_j^*)$, $\mu''(t_j^*)$ in terms of the value of $\mu$ at the panel edges and similarly the geometric midpoint quantities $\bar{X}(t_j^*)$, $\bar{X}'(t_j^*)$ and $\bar{X}''(t_j^*)$ are expressed in terms of the value of $\bar{X}$ at the panel edge points (see Fig. 8.5). This implies that a vortex sheet segment contributes NP+1 unknown doublet parameters $\mu_j$ and 2(NP+1) unknown geometric parameters $\bar{X}_j$.
On the first and the last panel, i.e. for j=1 and j=NP respectively, the scheme is reduced to a one-sided 3-point scheme, still second-order accurate. This latter scheme is conveniently obtained by choosing for j=1 $\Delta t_o = \infty$ and for j=NP $\Delta t_{NP+1} = \infty$.

Note that the panel-wise quadratic representations

$$f(t) = f(t_j^*) + (t-t_j^*)f'(t_j^*) + \tfrac{1}{2}(t-t_j^*)^2 f''(t_j^*),\quad t\in[t_j, t_{j+1}] \tag{8.12}$$

implied by the numerical scheme given in Eq. (7.9) as well as Eq. (8.11) are discontinuous in function value, first and second derivative across the panel edges. However, all these discontinuities are small of appropriate higher order and may be neglected.

Substitution of the schemes for $\mu(t_j^*)$, $\mu'(t_j^*)$ and $\mu''(t_j^*)$ in the expression for the induced velocity potential or velocity in the cross-flow plane, Eq. (8.8a) and Eq. (8.8b) respectively, results in

$$\Phi_\mu(\bar{X}_o) = \sum_{j=1}^{NSING} A_j(\bar{X}_o)S_j \tag{8.13a}$$

$$\bar{U}_\mu(\bar{X}_o) = \sum_{j=1}^{NSING} \bar{A}_j(\bar{X}_o)S_j \tag{8.13b}$$

$\Phi_\mu(\bar{X}_o)$ and $\bar{U}_\mu(\bar{X}_o)$ are the cross-flow-plane velocity potential and velocity induced at $\bar{X}_o$ by all segments $C_\mu$ or $C_v$ carrying a doublet distribution; $S_j$ is the j-th, out of a total of NISNG, unknown doublet parameter (or entrainment $Q_v$) and $A_j$ and $\bar{A}_j(\bar{X}_o)$ are the so-called aerodynamic influence coefficients that depend on the known (on $C_w$) or unknown (on $C_v$ and vortex core) position of the collocation point $\bar{X}_o$, on the known (on $C_w$) or unknown (on $C_v$) geometric quantities $\bar{X}(t_k^*)$, $\bar{X}'(t_k^*)$ and $\bar{X}''(t_k^*)$ of the panel (k=j) and the two neighboring panels (k=j-1 and j+1) and on the unknown position of the vortex cores.
In case the configuration is symmetric with respect to the Y=0 plane the $A_j$'s and $\bar{A}_j$'s include the contribution due to the port side of the configuration.

8.4 Application of boundary and auxiliary conditions

In this section the application of the boundary and auxiliary conditions is described. For each of the three types of segment, the wing-doublet, the wing-doublet/source and the sheet-doublet segment, as many equations will be derived as there are unknown parameters in the numerical scheme.

8.4.1 Lifting-surface segment $C_w$

Associated with a lifting-surface segment, subdivided into NP panels, there are NP+2 unknown singularity parameters (see Fig. 8.4). The NP+2 equations required to close the system are the zero-normal-velocity boundary condition, Eq. (8.4), imposed at the NP panel midpoints and two so-called abutment conditions, one for each of the two segment edges. The latter two, auxiliary, conditions are imposed to obtain the correct behaviour of the doublet distribution at the edges of the segment. Note that the unit vector tangential to the edge of the segment can be expressed as:

$$\bar{e}_\tau = \bar{e}_x + \bar{X}_s + O(\varepsilon^2) \tag{8.14a}$$

while the unit vector both tangential to the wing segment and normal to the edge is given by $\bar{n}\times\bar{e}_\tau$, i.e. using Eq. (5.9a), by

$$\bar{e}_c = \bar{e}_t - (\bar{X}_s\cdot\bar{e}_t)\bar{e}_x + O(\varepsilon^2) \tag{8.14b}$$

This then implies that the component of the surface vorticity along and normal to the edge are, see Eq. (5.10):

$$(\bar{\gamma}.\bar{e}_r) = -\frac{1}{b}\mu' + O(\varepsilon^2) \text{ and} \tag{8.14c}$$

$$(\bar{\gamma}.\bar{e}_c) = \mu_s + O(\varepsilon^2) \tag{8.14d}$$

respectively. For the abutment conditions several situations that occur are discussed next.

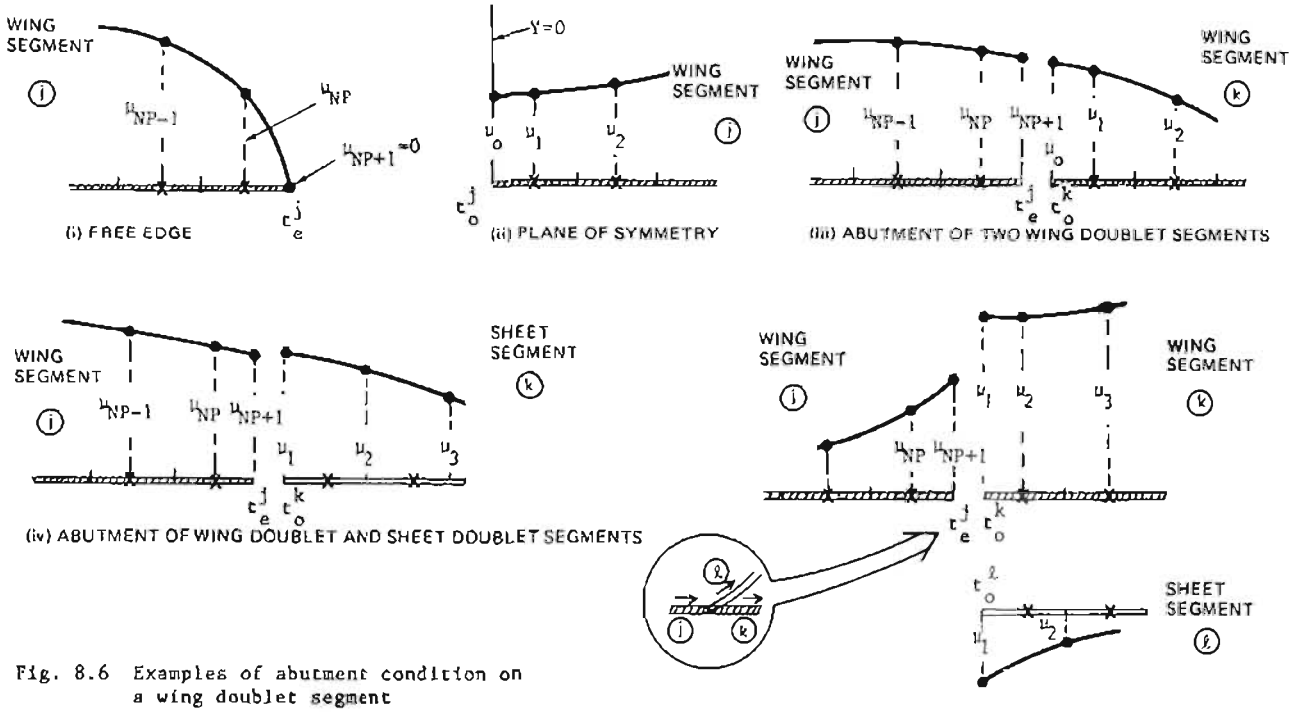


Fig. 8.6 Examples of abutment condition on a wing doublet segment

(i) free edge (Fig. 8.6i)
In this case the edge $t=t_e^j$ of the segment acts as a leading edge with the flow attached to it and the appropriate "abutment" condition is that the doublet distribution vanishes at the edge, i.e.:

$$\mu^j(t_e^j) = 0 \tag{8.15}$$

(ii) plane of symmetry (Fig. (8.6ii)
In the plane of symmetry the vorticity is zero, so that the first derivative of the doublet distribution vanishes here, i.e. according to Eq. (8.14c):

$$\frac{d}{dt}\mu^j(t_o^j) = 0 \tag{8.16}$$

(iii) abutment to another lifting-surface segment (Fig. 8.6iii)
In this case continuity of the doublet distribution is enforced by requiring:

$$\mu^j(t_e^j) - \mu^k(t_o^k) = 0 \tag{8.17a}$$

This condition implies that the component of the surface vorticity normal to the edge is continuous, see Eq. (8.14d). Continuity of the component along the edge requires:

$$\frac{1}{b_j}\frac{d}{dt}\mu^j(t_e^j) - \frac{1}{b_k}\frac{d}{dt}\mu^k(t_o^k) = 0 \tag{8.17b}$$

where $b_j$ and $b_k$ are the total arc length of the j-th and the k-th segment, respectively. In this case Eq. (8.17a) is the auxiliary condition for the j-th segment and Eq. (8.17b) is the auxiliary condition for the k-th segment.

(iv) abutment to vortex sheet segment (Fig. 8.6iv)
Here the requirement that the doublet distribution is continuous across the edge leads for the j-th segment to the condition

$$\mu^j(t_e^j) - \mu^k(t_o^k) = 0 \tag{8.18a}$$

For the k-th segment, i.e. the vortex sheet, one has the following three conditions:

$$\frac{1}{b_k}\frac{d}{dt}\mu^k(t_o^k) - \frac{1}{b_j}\frac{d}{dt}\mu^j(t_e^j) = 0 \tag{8.18b}$$

for the doublet distribution, while for the geometry the conditions

$$Y^k(t_o^k) - Y^j(t_e^j) = 0 \tag{8.18c}$$

$$Z^k(t_o^k) - Z^j(t_e^j) = 0 \tag{8.18d}$$

ensure that the vortex sheet is attached to the leading edge. Note that Eqs. (8.18a and b) guarantee that the surface vorticity vector is continuous across the abutment.

(v) "secondary-separation" abutment (Fig. 8.6v)
In this case three segments are abutted, two lifting-surface (doublet) segments and one vortex sheet-doublet segment. The appropriate abutment conditions for this case are derived from the requirement of continuity of doublet distribution, surface vorticity and geometry. For the j-th segment this results in:

$$\mu^j(t_e^j) - \mu^k(t_o^k) - \mu^\ell(t_o^\ell) = 0 \tag{8.19a}$$

which ensures continuity of the doublet distribution at the separation position.
For the other lifting-surface segment, the k-th segment, situated underneath the "secondary vortex", we apply

$$\frac{1}{b_k}\frac{d}{dt}\mu^k(t_o^k) = 0 \tag{8.19b}$$

i.e. the condition that no vorticity is shed from the downstream side of the separation point.
For the ℓ-th segment, i.e the "secondary vortex sheet" segment, the conditions are identical to the ones used for the leading-edge vortex sheet, i.e.:

$$\frac{1}{b_\ell}\frac{d}{dt}\mu^\ell(t_o^\ell) - \frac{1}{b_j}\frac{d}{dt}\mu^j(t_e^j) = 0 \tag{8.19c}$$

$$Y^\ell(t_o^\ell) - Y^j(t_e^j) = 0 \tag{8.19d}$$

$$Z^\ell(t_o^\ell) - Z^j(t_e^j) = 0 \tag{8.19e}$$

8.4.2 Wing segment $C_w$ with composite source/doublet distribution

Closed contours of the cross-section are modeled by segments carrying a composite source/doublet distribution determined by the Dirichlet condition on the internal flow. This yields the strength of the source distribution directly, see Eq. (8.5b), while the doublet distribution remains to be determined. A segment, subdivided into NP panels, has associated with it NP+2 unknown doublet parameters, see Fig. 8.4. The necessary NP+2 equations are obtained by applying the Dirichlet condition Eq. (8.5a) at the NP panel mid-points (i.e. on the side not wetted by the external flow) and by two abutment conditions, one for each edge of the segment. The two velocity components, one along and one normal to the edge, that we will use follow from Eq. (5.23c) or Eq. (8.5c) and Eqs. (8.14a-b) as:

$$(\bar{u}.\bar{e}_r) = U_\infty\cos\alpha\cos\beta + \mu_s + \bar{V}_\infty.\bar{X}_s + O(\varepsilon^2) \tag{8.20a}$$

$$(\bar{u}.\bar{e}_c) = (\bar{V}_\infty - U_\infty\cos\alpha\cos\beta\bar{X}_s).\bar{e}_t + \frac{1}{b}\mu' + O(\varepsilon^2) \tag{8.20b}$$

In the following we consider some of the situations that may arise.

(i) plane of symmetry (Fig. 8.7i)
At the plane of symmetry the velocity component normal to the Y=0 plane vanishes. It follows from Eq. (8.20b) that

$$\frac{1}{b_j}\frac{d}{dt}\mu^j(t_o^j) + \frac{1}{b_j}\left[\bar{V}_\infty - U_\infty\cos\alpha\cos\beta\{\bar{X}^j(t_o^i) - \bar{X}0^j(t_o^j)\}/\Delta s\right].\frac{d}{dt}\bar{X}^j(t_o^j) = 0 \tag{8.21}$$

In case $\bar{e}_t$ is normal to the plane of symmetry, which is often the case, Eq. (8.21) implies that the first derivative of the doublet distribution is zero at the plane of symmetry.

(ii) abutment to other segment $C_w$ with composite source/doublet distribution (Fig. 8.7ii)
Continuity of the doublet distribution requires that

$$\mu^j(t_e^j) - \mu^k(t_o^k) = 0 \tag{8.22a}$$

which also ensures that the velocity component along the edge is continuous at the edge. The second abutment condition used here is that, in order to let the pressure be continuous, the component of the velocity normal to the edge is continuous, i.e. using that $\bar{X}_s^j(t_e^j) \equiv \bar{X}_s^k(t_o^k)$:

$$\frac{1}{b_j}\frac{d}{dt}\mu^j(t_e^j) - \frac{1}{b_k}\frac{d}{dt}\mu^k(t_o^k)$$

$$+ \left[\bar{V}_\infty - U_\infty\cos\alpha\cos\beta\{\bar{X}^j(t_e^j) - \bar{X}0^j(t_e^j)\}/\Delta s\right].\left(\frac{1}{b_j}\frac{d}{dt}\bar{X}^j(t_e^j) - \frac{1}{b_k}\frac{d}{dt}\bar{X}^k(t_o^k)\right) = 0 \tag{8.22b}$$

In case the slope of the cross section is continuous at the edge Eq. (8.22b) reduces to the condition that the first derivative of μ with respect to t is continuous at the edge.

(iii) junction of body and lifting surface (Fig. 8.7iii)
At the junction of a body and a lifting surface three segments abut, two with a composite source/doublet and one with a doublet distribution. Continuity of doublet strength requires that

$$\mu^j(t_e^j) - \mu^k(t_o^k) - \mu^\ell(t_o^\ell) = 0 \tag{8.23a}$$

which is the abutment condition for segment ℓ.
The other two conditions that apply here are that at the junction the velocity component normal to the junction line vanishes, i.e. from Eq. (8.20b), the abutment condition for segments j and k follows as:

$$\frac{1}{b_j}\frac{d}{dt}\mu^j(\tau_e^j) + \frac{1}{b_j}[\bar{V}_\infty - U_\infty \cos\alpha\cos\beta\{\bar{X}^j(\tau_e^j) - \bar{X}0^j(\tau_e^j)\}/\Delta s].\frac{d}{dt}\bar{X}^j(\tau_e^j) = 0 \qquad (8.23b)$$

$$\frac{1}{b_k}\frac{d}{dt}\mu^k(\tau_o^k) + \frac{1}{b_j}[\bar{V}_\infty - U_\infty \cos\alpha\cos\beta\{\bar{X}^k(\tau_o^k) - \bar{X}0^k(\tau_o^k)\}/\Delta s].\frac{d}{dt}\bar{X}^k(\tau_o^k) = 0 \qquad (8.23c)$$

respectively, which implies that $\frac{d}{dt}\mu^\ell(\tau_o^\ell)$ will be zero as well.
In case segment j and the lifting surface, segment ℓ, abut smoothly, i.e. without a corner, Eq. (8.23b) is replaced by the condition that the tangential velocity is continuous across the junction, i.e.

$$\frac{1}{b_j}\frac{d}{dt}\mu^j(\tau_e^j) - \frac{1}{b_\ell}\frac{d}{dt}\mu^\ell(\tau_o^\ell) + \frac{1}{b_j}[\bar{V}_\infty - U_\infty \cos\alpha\cos\beta\{\bar{X}^j(\tau_e^j) - \bar{X}0^j(\tau_e^j)\}/\Delta s].\frac{d}{dt}\bar{X}^j(\tau_e^j) = 0 \qquad (8.23d)$$

A similar expression replaces Eq. (8.23c) if segments k and ℓ join smoothly.

(iv) abutment to vortex sheet segment

Separation of the flow from the closed contour may take place at any prescribed (fixed) point, which often will coincide with a discontinuity in the slope of the contour. However, also "smooth-body" separation such as separation at a rounded leading edge and secondary separation underneath vortex cores can be treated. Three segments abut, two with a composite source/doublet distribution and one vortex-sheet segment. It is assumed that at the point of separation the vortex-sheet segment is tangential to one of the two closed-contour wing segments. In fact we have a situation like sketched in Fig. 8.6v, with the wing segments now wetted by the flow on their upper side only. Continuity of the doublet strength requires

$$\mu^j(\tau_e^j) - \mu^k(\tau_o^k) - \mu^\ell(\tau_o^\ell) = 0 \qquad (8.24a)$$

which is taken as the abutment condition for the j-th segment.
The component of the velocity normal to the separation line is zero on the downstream side (at the lower side of the vortex sheet), i.e.

$$\frac{1}{b_k}\frac{d}{dt}\mu^k(\tau_o^k) + \frac{1}{b_k}(\bar{V}_\infty - U_\infty \cos\alpha\cos\beta\bar{X}_s).\frac{d}{dt}\bar{X}^k(\tau_o^k) = 0 \qquad (8.24b)$$

which is chosen as the abutment condition for segment k.
The tangential velocity component is continuous at the upstream side, i.e.

$$\frac{1}{b_j}\frac{d}{dt}\mu^j(\tau_e^j) + \frac{1}{b_j}(\bar{V}_\infty - U_\infty \cos\alpha\cos\beta\bar{X}_s).\frac{d}{dt}\bar{X}^j(\tau_e^j) = \frac{1}{b_\ell}\frac{d}{dt}\mu^\ell(\tau_o^\ell) \qquad (8.24c)$$

which is one of the three abutment conditions for the ℓ-th segment.
These conditions Eqs. (8.24a-c) also imply that the component of the velocity along the separation line is continuous when passing from the wing segment j onto the vortex sheet segment ℓ.
The other two abutment conditions for segment ℓ are:

$$Y^\ell(\tau_o^\ell) - Y^j(\tau_e^j) = 0 \qquad (8.24d)$$

$$Z^\ell(\tau_o^\ell) - Z^j(\tau_e^j) = 0 \qquad (8.24e)$$

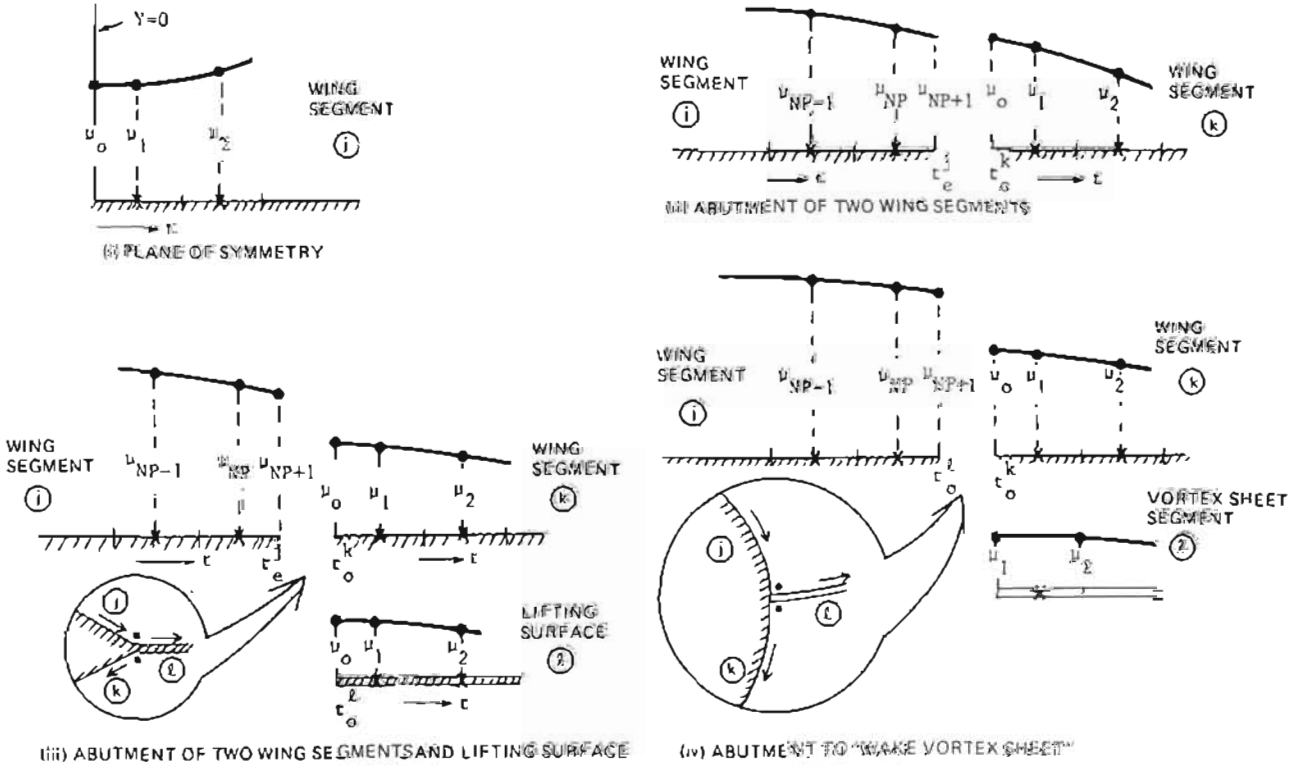


Fig. 8.7 Examples of abutment condition wing source/doublet segment

(v) abutment to wake vortex sheet (Fig. 8.7iv)
Downstream of a trailing edge the wake may be attached to a closed (body or wing) contour. In this case again three segments abut, two wing segments which form part of a closed contour and one vortex sheet segment. In case the closed contour has a discontinuity in the slope the wake will be attached to this point and further vorticity will be fed into the vortex sheet that forms the wake, i.e. this is similar to case (iv) considered above.
In case the contour is smooth the first condition is that the doublet strength is continuous, i.e.

$$\mu^j(\tau_e^j)-\mu^k(\tau_o^k)-\mu^\ell(\tau_o^\ell) = 0 \qquad (8.25a)$$

The second condition is that no further vorticity is shed at the intersection, i.e. that the vortex sheet vorticity component normal to the intersection vanishes, i.e. from Eq. (8.14d) it follows that

$$\mu_s^\ell(\tau_o^\ell) = 0 \qquad (8.25b)$$

Finally there are the two conditions that the velocity should be directed along the intersection. These two conditions are:

$$\frac{1}{b_j}\frac{d}{d\tau}\mu^j(\tau_e^j) + \frac{1}{b_j}(\bar{V}_\infty - U_\infty \cos\alpha\cos\beta\bar{X}_s).\frac{d}{d\tau}\bar{X}^j(\tau_e^j) = 0$$

$$\frac{1}{b_k}\frac{d}{d\tau}\mu^k(\tau_o^k) + \frac{1}{b_k}(\bar{V}_\infty - U_\infty \cos\alpha\cos\beta\bar{X}_s).\frac{d}{d\tau}\bar{X}^k(\tau_o^k) = 0$$

Since the slope of the contour is continuous at the intersection the second term in both conditions is identical, so that it is convenient to replace them by their difference and average. The difference leads to

$$\frac{1}{b_j}\frac{d}{d\tau}\mu^j(\tau_e^j) - \frac{1}{b_k}\frac{d}{d\tau}\mu^k(\tau_o^k) = 0 \qquad (8.25c)$$

which implies that the first derivative of the doublet distribution as well as the surface velocity on $C_\mu$ is continuous across the intersection.

The fourth condition is the average of the two conditions, which using Eq. (8.25c) can be expressed as:

$$\frac{1}{b_j}\frac{d}{d\tau}\mu^j(\tau_e^j) + \frac{1}{b_j}(\bar{V}_\infty - U_\infty \cos\alpha\cos\beta\bar{X}_s).\frac{d}{d\tau}\bar{X}^j(\tau_e^j) = 0 \qquad (8.25d)$$

Now we have four conditions, while for the abutment of the three segments only three unknown doublet parameters are to be determined, that is if we assume that the position of the intersection is fixed. Apparently the formulation that prohibits shedding of vorticity implies that the point of intersection "slides" along the closed contour to the point where all four conditions are satisfied. In the present study we will not consider such a sliding point of intersection and apply equations (8.25a-c) only. A posteriori one could determine the tangential velocity at the intersection and move the assumed intersection in that direction.
For the $\ell$-th segment two further, geometric, abutment conditions apply, i.e.

$$Y^\ell(\tau_o^\ell) - Y^j(\tau_e^j) = 0 \qquad (8.25e)$$

$$Z^\ell(\tau_o^\ell) - Z^j(\tau_e^j) = 0 \qquad (8.25f)$$

8.4.3 Vortex-sheet segment $C_\nu$
The doublet distribution on a vortex sheet, subdivided into NP panels, is defined by NP+1 unknown parameters (see Fig. 8.5).
The geometry of the vortex sheet contributes 2(NP+1) unknown geometric parameters. The edge vortex contributes 2 unknown geometric parameters (its position) and 1 unknown source (entrainment) parameter.

At the NP panel midpoints the following 3 equations are imposed:
- the zero-normal-velocity condition, Eq. (8.4);
- the zero-pressure-jump condition, Eq. (8.6);
- the condition that t is the scaled arc length along the sheet.

In effect the last condition specifies that Y(t) and Z(t) form a curve and are therefore two interrelated functions. In the present method the arc-length equation is derived from Eq. (7.2a) as

$$\frac{1}{b\Delta\tau_i}\int_{\tau_i}^{\tau_{i+1}} \left|\frac{d}{d\tau}\bar{X}(\tau)\right| d\tau - 1 = 0 \quad , \text{ for } i = 1(1)NP \qquad (8.26a)$$

where the sheet length b, is a given quantity.
In Eq. (8.26a) the integral over the panel is approximated by a two-interval trapezoidal rule leading to:

$$\frac{1}{4b}\left\{\left|\bar{X}'(\tau_i^*) - \frac{\Delta\tau_i}{2}\bar{X}''(\tau_i^*)\right| + 2\left|\bar{X}'(\tau_i^*)\right| + \left|\bar{X}'(\tau_i^*) + \frac{\Delta\tau_i}{2}\bar{X}''(\tau_i^*)\right|\right\} - 1 = 0$$

or

$$(1/4b)\left\{\sum_{m=-1}^{1} \Omega_m \left|\bar{X}'(\tau_i^*) + \frac{m}{2}\Delta\tau_i\bar{X}''(\tau_i^*)\right|\right\} - 1 = 0 \qquad (8.26b)$$

where $\Omega_{-1} = \Omega_1 = 1$ and $\Omega_0 = 2$, to be applied for i=1(1)NP. Note that specifying the length b of the sheet results in a problem which can be thought of as finding the shape of an inelastic rope subject to the two boundary conditions. The sheet is prevented from sliding along the stream surface it is situated on by the abutment conditions at the leading edge it is attached to.

For a single-branched vortex the zero-net-force condition, Eq. (8.7a), yields two equations, while the strength of the source due to the entrainment follows from the entrainment relation Eq. (8.2e).

For a double-branched vortex we obtain two equations from Eq. (8.7b), the zero-net-force condition applied to the vortex filament and the two feeding sheets. The third condition is that the entrainment is zero.

Once more, the abutment conditions complete the system of equations. As far as these latter conditions are concerned, there are a number of possibilities that will be considered next (Fig. 8.8). Note that abutment with other type of segments has already been considered in the preceding sections.

(i) free edge (Fig. 8.8i)
A free edge of a sheet-doublet distribution is always associated with a single-branched vortex core. The strength of the vortex, which equals the doublet value at the edge of the sheet, is substituted directly into the equations, so that at the free edge no further condition is required.

(ii) plane of symmetry (Fig. 8.8ii)
At the plane of symmetry the first derivative of μ and Z vanishes while the first derivative of Y becomes b, i.e.:

$$\frac{d}{dt}\mu^j(t_o^j) = 0 \tag{8.27a}$$

$$\frac{1}{b_j}\frac{d}{dt}Y^j(t_o^j) = 1 \tag{8.27b}$$

$$\frac{d}{dt}Z^j(t_o^j) = 0 \tag{8.27c}$$

(iii) abutment with another sheet-doublet segment (Fig. 8.8iii)
In this case continuity of doublet distribution and geometry is enforced by requiring for segment j:

$$\mu^j(t_e^j) - \mu^k(t_o^k) = 0 \tag{8.28a}$$

$$Y^j(t_e^j) - Y^k(t_o^k) = 0 \tag{8.28b}$$

$$Z^j(t_e^j) - Z^k(t_o^k) = 0 \tag{8.28c}$$

and for segment k:

$$\frac{1}{b_j}\frac{d}{dt}\mu^j(t_e^j) - \frac{1}{b_k}\frac{d}{dt}\mu^k(t_o^k) = 0 \tag{8.28d}$$

$$\frac{1}{b_j}\frac{d}{dt}Y^j(t_e^j) - \frac{1}{b_k}\frac{d}{dt}Y^k(t_o^k) = 0 \tag{8.28e}$$

$$\frac{1}{b_j}\frac{d}{dt}Z^j(t_e^j) - \frac{1}{b_k}\frac{d}{dt}Z^k(t_o^k) = 0 \tag{8.28f}$$

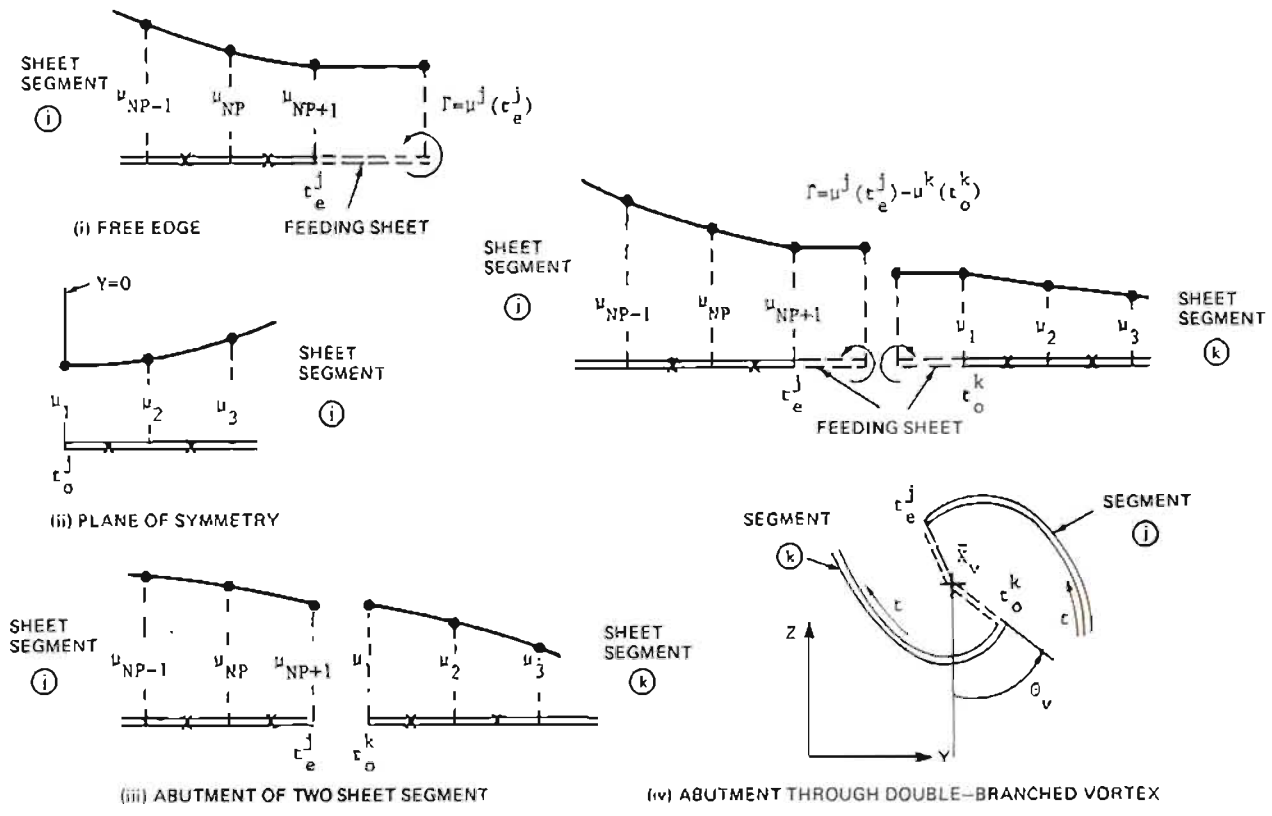


Fig. 8.8 Examples of abutment conditions for a sheet-doublet segment

(iv) abutment through double-branched vortex (Fig. 8.8iv)
In this case we had already 2 equations resulting from the zero-overall force condition on the double-branched vortex core and one from the entrainment relation for a total of 6 unknowns: the source strength, the coordinates (2) of the vortex and the coordinates (2) of the edge point of segment k as well as the value of the doublet distribution at this point. Three conditions are required for the second branch connecting the vortex to $\bar{X}^k(t_o^k)$. The first two equations are the zero-normal-velocity condition and the zero-pressure-jump condition applied at $\bar{X}^k(t_o^k)$.

The velocity at the edge $t_o^k$ required in these conditions is determined by linear extrapolation from the velocity at the first two panel midpoints on segment $C_v^k$. This extrapolation is of consistent order of approximation and avoids the singular behaviour at the edge. The condition that closes the system is the condition that the feeding sheet, connecting the vortex to the edge of segment k, stays at a fixed specified inclination, i.e.

$$(Y^k(t_o^k)-Y_v)\cos\theta_v + (Z^k(t_o^k)-Z_v)\sin\theta_v = 0 \qquad (8.29)$$

where $\theta_v$ is the specified angular extent of the feeding sheet.
The condition as expressed in Eq. (8.29) can be thought of as the condition that prevents the second vortex sheet (see Fig. 8.2), which again can be considered as an inelastic rope of specified length, from sliding along the stream surface it is located on.

The strength of the double-branched vortex, which equals the magnitude of the jump of the doublet distribution across the vortex, is substituted directly into the equations and no separate equation is required for it.

8.4.4 Kutta condition

The Kutta condition is the condition that the flow separates smoothly at the line of separation, here mostly the leading edge. In numerical methods for simulating the flow about wings, the Kutta condition has been implemented in many different ways. Examples are: set at a point just downstream of the trailing edge the velocity component normal to the assumed direction of the wake equal to zero; set upper and lower surface pressure equal at the edge, etc.

In the present formulation the Kutta condition is satisfied implicitly by the abutment conditions at the leading edge, which in effect desingularize the velocity distribution at that point. Furthermore, applying the zero-pressure-jump condition at the discrete collocation points on the free vortex sheet implies, to consistent order of approximation, that the pressure jump across the sheet is zero at all points, including the leading-edge point, of the continuous vortex sheet. So, no explicit Kutta condition is necessary in our present formulation.

8.5 Solution of system of nonlinear equations

8.5.1 System of equations

The equations resulting from applying the boundary conditions, supplemented by the auxiliary (abutment, arc-length) conditions, form a system of mostly nonlinear algebraic equations. In this system of equations the number of equations equals the number of unknowns. The nonlinearity refers in particular to the dependence of the equations on the unknowns due to the vortex sheet geometry. With the exception of the entrainment relation the dependence of the equations on the singularity parameters is linear (normal-velocity condition) or quadratic (pressure-jump, force conditions) at most.

The equations are ordered in the same manner as the parameters describing the singularity distribution and the geometry are ordered, i.e. for each segment we have the following ordering:

i) Abutment condition(s) at edge-1 ($t=t_1$) of the segment, followed by the condition(s) at the NP panel midpoints $t_i^*=(t_i + t_{i+1})/2$, i=1(1)NP, i.e.

iia) Normal-velocity boundary condition implemented directly on lifting-surface segments and formulated as Dirichlet condition on the segments of closed contours of the cross-section;
iib) Zero-pressure-jump condition (only in case of "vortex-sheet" segments);
iic) Arc-length condition (only in case of "vortex-sheet" segments);

iii) Abutment condition(s) at edge-N ($t=t_e$) of the segment;

and in case of a "vortex-sheet" segment the following three equations:

iva) The entrainment relation;
ivb) Zero component of the force normal to the (first branch of the) feeding sheet;
ivc) Zero component of the force along the (first branch of the) feeding sheet;

in case of a double-branched vortex core followed by the conditions:

(ivd) Normal-velocity boundary condition at $t=t_o$ of the segment connected through the second branch of the feeding sheet to the vortex-filament;
(ive) Zero-pressure-jump condition at the same point;
(ivf) Attitude condition on second branch of the feeding sheet.

On "lifting-surface" segments and "Dirichlet" segments the ordering of the unknown parameters is $\mu_j$, j = 0(1)NP+1.
On "vortex-sheet" segments the ordering of the unknown parameters is $(\nu_j, Y_j, Z_j)$, j=1(1)NP+1 and for the vortex core it is $(Q, Y_v, Z_v)$.

8.5.2 Newton's method

The system of nonlinear equations, schematically written as

$$F_i(P_1, \ldots, P_M) = 0, \quad \text{for } i=1(1)M, \tag{8.30a}$$

where M is the total number of unknown parameters, is solved by Newton's iterative solution procedure. In this procedure the solution $P_j^{it+1}$ at iteration it+1 is obtained from the solution $P_j^{it}$ at iteration it (the initial guess for it=1) as

$$P_j^{it+1} = P_j^{it} + \Delta P_j^{it}, \quad \text{for } j=1(1)M \tag{8.30b}$$

where the increment $\Delta P_j^{it}$ is obtained from the system of linear equations

$$\sum_{j=1}^{M} \left[\frac{\partial F_i}{\partial P_j}\right]_{it} \Delta P_j^{it} = - F_i(P_1^{it}, \ldots, P_M^{it}) \ , \text{ for } i = 1(1)M \tag{8.30c}$$

In the "full" Newton procedure used in the present study each element of the so-called Jacobian matrix $\frac{\partial F_i}{\partial P_j}$ is recomputed during each iteration. If then $P^{it}$ is within the "domain of attraction" of (one of) the root(s) of the system of equations the method will converge quadratically in the vicinity of the root. The latter means that the number of accurate digits is doubled during each iteration. The nonlinearity of the equations implies that more than one root may exist, implying also that, as a function of for example angle of attack, the solution may exhibit turning and/or branch points. One often employed method to check for these points is to monitor the sign of the determinant of the Jacobian matrix $\frac{\partial F_i}{\partial P_j}$.

Computing the Jacobian matrix involves taking the derivative with respect to the unknown geometric ($G_\ell$) and singularity ($S_\ell$) parameters of all the boundary and auxiliary conditions. In the present method the Jacobian matrix is computed from the analytically obtained derivatives of the nonlinear equations. In the following we will derive the expressions used for computing the Jacobian matrix. Table 8.0 summarizes the computations that have to be carried out to obtain the "geometric" and "aerodynamic" influence coefficients.

| Collocation point $\bar{X}_o=(0,Y_o,Z_o)$ on: | panel on: $C_w$-DIR | $C_w$-LS | $C_v$ + Vortex core |
|---|---|---|---|
| $C_w$-DIR | $\Phi_{\mu,q}$; $\frac{\partial}{\partial S_\ell}\Phi_\mu$ | $\Phi_\mu$; $\frac{\partial}{\partial S_\ell}\Phi_\mu$ | $\Phi_{\mu,Q}$; $\frac{\partial}{\partial S_\ell}\Phi_{\mu,Q}$, $\frac{\partial}{\partial G_\ell}\Phi_{\mu,Q}$ |
| $C_w$-LS | $\bar{U}_{\mu,q}$; $\frac{\partial}{\partial S_\ell}\bar{U}_\mu$ ; $u_{\mu,q}$ | $\bar{U}_\mu$; $\frac{\partial}{\partial S_\ell}\bar{U}_\mu$ ; $u_\mu$ | $\bar{U}_{\mu,Q}$; $\frac{\partial}{\partial S_\ell}\bar{U}_{\mu,Q}$, $\frac{\partial}{\partial G_\ell}\bar{U}_{\mu,Q}$ ; $u_{\mu,Q}$ |
| $C_v$ + Vortex core | $\bar{U}_{\mu,q}$; $\frac{\partial}{\partial S_\ell}\bar{U}_\mu$ ; $u_{\mu,q}$ | $\bar{U}_\mu$; $\frac{\partial}{\partial S_\ell}\bar{U}_\mu$ ; $u_\mu$ | $\bar{U}_{\mu,Q}$; $\frac{\partial}{\partial S_\ell}\bar{U}_{\mu,Q}$, $\frac{\partial}{\partial G_\ell}\bar{U}_{\mu,Q}$ |
| | $\frac{\partial}{\partial \bar{X}_o}\bar{U}_{\mu,q}$ | $\frac{\partial}{\partial \bar{X}_o}\bar{U}_\mu$ | $\frac{\partial}{\partial \bar{X}_o}\bar{U}_{\mu,Q}$ ; $u_{\mu,Q}$ |
| Field point | $\bar{U}_{\mu,q}$ ; $u_{\mu,q}$ | $\bar{U}_\mu$ ; $u_\mu$ | $\bar{U}_{\mu,Q}$; ; $u_{\mu,Q}$ |

a) Required integral representations for various collocation points and types of segments

| | $\Phi$ | $\bar{U}$ | u | $\frac{\partial\Phi}{\partial S_\ell}$ | $\frac{\partial\Phi}{\partial G_\ell}$ $\frac{\partial\Phi}{\partial \bar{X}_c}$ | $\frac{\partial\bar{U}}{\partial S_\ell}$ | $\frac{\partial\bar{U}}{\partial G_\ell}$ $\frac{\partial\bar{U}}{\partial \bar{X}_o}$ |
|---|---|---|---|---|---|---|---|
| μ | (8.8a) | (8.8b,c) | (8.3e) + (8.8d) | (8.13a) | (8.34b) | (8.13b) | (8.32d) |
| q | (8.9a) | (8.9c,d) | (8.3h) + (8.9e) | - | - | - | - (8.32f) |
| Q | (8.3d) | (8.3c) | - | (8.13a) | (8.34d) | (8.13b) | (8.32e) |

b) Equation number where expression is given

Table 8.0 Quantities to be computed for aerodynamic and geometric influence coefficients

Derivatives of zero-normal-velocity boundary condition, Eq. (8.4)

Denoting the zero-normal-velocity condition at $t_j^{i*}$, the j-th midpoint of the i-th segment, by $F_k$ where k is the accumulated equation number, one obtains from Eq. (8.4):

$$F_k = \bar{U}_{tot}(\bar{X}^i(t_j^{i*})).\bar{e}_n(t_j^{i*}) = 0 \tag{8.31a}$$

where $\bar{U}_{tot}$ and $\bar{e}_n$ are given in Eqs. (8.4b) and (8.4c) respectively. The point $t_j^{i*}$ may be situated on a lifting surface segment or on a free vortex sheet, but $\bar{U}_{tot}$ contains of course the contribution of all segments and vortex cores.

Differentiation of $F_k$ with respect to any singularity distribution parameter $S_\ell$ yields

$$\frac{\partial F_k}{\partial S_\ell} = \{\frac{\partial}{\partial S_\ell}\bar{U}_{tot}(\bar{X}^i(t_j^{i*}))\}.\bar{e}_n(t_j^{i*}) \tag{8.31b}$$

It then follows from Eq. (8.4b) that:

$$\frac{\partial}{\partial S_\ell}\bar{U}_{tot} = \sum_m [\delta^m_\mu\{\frac{\partial}{\partial S_\ell}\bar{U}^m_\mu(\bar{X}^i(t_j^{i*})) + \delta^m_{ve}\frac{\partial}{\partial S_\ell}\bar{U}^m_Q(\bar{X}^i(t_j^{i*}))\}] \tag{8.31c}$$

The derivative with respect to $S_\ell$ of the various contributions in the induced cross-flow-plane velocity follows directly from Eq. (8.8b) for $\bar{U}^m_\mu$, from Eq. (8.3c) for $\bar{U}^m_Q$ while the derivative $\bar{U}^m_q$ is zero. The derivative with respect to $S_\ell$ of $\bar{U}_{tot}$ corresponds to $A_\ell(\bar{X}^i(t_j^{i*}))$, the aerodynamic influence coefficient at collocation point $\bar{X}^i(t_j^{i*})$ of singularity parameter $S_\ell$, e.g. see Eq. (8.13b).

The derivative with respect to the unknown geometric unknown $G_\ell$ of $F_k$ is more complex:

$$\frac{\partial F_k}{\partial G_\ell} = \{\frac{\partial}{\partial G_\ell}\bar{U}_{tot}(\bar{X}^i(t_j^{i*}))\}.\bar{e}_n(t_j^{i*}) + \bar{U}_{tot}(\bar{X}^i(t_j^{i*})).\frac{\partial}{\partial G_\ell}\bar{e}_n(t_j^{i*}) \tag{8.32a}$$

where it follows from Eq. (8.4b) that:

$$\frac{\partial}{\partial G_\ell}\bar{U}_{tot} = \sum_m [\delta^m_\mu\{\frac{\partial}{\partial G_\ell}\bar{U}^m_\mu(\bar{X}^i(t_j^{i*})) + \delta^m_{ve}\frac{\partial}{\partial G_\ell}\bar{U}^m_Q(\bar{X}^i(t_j^{i*}))\} + \delta^m_q\frac{\partial}{\partial G_\ell}\bar{U}^m_q(\bar{X}^i(t_j^{i*}))]$$

$$- \frac{1}{\Delta s}U_\infty \cos\alpha\cos\beta\frac{\partial}{\partial G_\ell}\bar{X}^i(t_j^{i*}) \tag{8.32b}$$

In above expression $\frac{\partial}{\partial G_\ell}\bar{X}^i(t_j^{i*})$ is only nonzero when segment i is the vortex-sheet segment to which $G_\ell$ belongs and the j-th panel at that segment is one of the four panels nearest to the panel-edge point corresponding to geometric parameter $G_\ell$. The latter follows directly from Eq. (7.9) and is illustrated in Fig. 8.9.

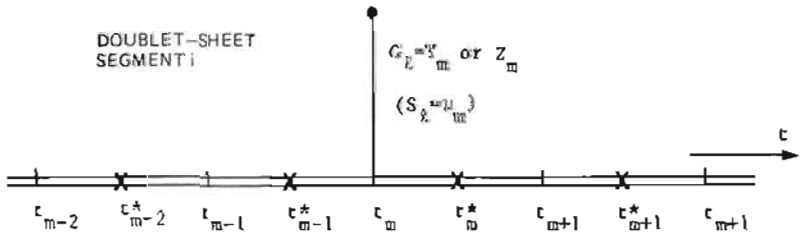


X Panel midpoints where e.g. $Y^i(t^*_j)$, $\frac{dY^i}{dt}(t^*_j)$ and $\frac{d^2Y^i}{dt^2}(t^*_j)$ involve unknown geometric parameter $Y_m$ at panel corner points

Fig. 8.9 Domain of influence of parameters at panel edge $t_m$ of free vortex sheet segment

For the derivative of the normal vector at $t_j^{i*}$ one finds from Eq. (8.4c), using that in the present formulation t is the normalized arc length:

$$\frac{\partial}{\partial G_\ell}\bar{e}_n(t_j^{i*}) = \frac{\bar{e}_x}{b_i} \times \frac{\partial}{\partial G_\ell}\{\frac{d\bar{X}^i}{dt}(t_j^{i*})\} \tag{8.32c}$$

which clearly involves the derivative with respect to the geometric parameter $G_\ell$ of the first derivative with respect to t of $\bar{X}^i(t)$ at $t_j^{i*}$. Here again we only get a contribution in the "region of influence" of $G_\ell$, which is a Y or Z coordinate of one of the vortex sheet segments.

The remaining terms to be considered more closely here, concern the derivative with respect to $G_\ell$ of the induced velocity contributions. For the one induced by the doublet distribution it follows from Eq. (8.8b), that for one specific segment, subdivided into NP panels:

$$\frac{\partial}{\partial G_\ell}\bar{U}_\mu(\bar{X}_o) = \frac{1}{2\pi}\Big[\sum_{j=1}^{NP}\Big\{\mu'(t_j^*)\Big(\frac{\partial \bar{E}_o}{\partial G_\ell} + k_n(t_j^*)\frac{\partial \bar{E}_o^c}{\partial G_\ell} + \frac{\partial k_n}{\partial G_\ell}\bar{E}_o^c\Big) + \mu''(t_j^*)\frac{\partial \bar{E}_1}{\partial G_\ell}\Big\}$$

$$+ \bar{e}_x\times\Big\{\delta_{ve}\frac{\mu(t_e)}{|\bar{R}_{ve}|^2}\Big(\frac{\partial \bar{R}_{ve}}{\partial G_\ell} - 2\frac{\bar{R}_{ve}}{|\bar{R}_{ve}|^2}\Big(\bar{R}_{ve}\cdot\frac{\partial \bar{R}_{ve}}{\partial G_\ell}\Big)\Big)$$

$$-\delta_{vo}\frac{\mu(t_o)}{|\bar{R}_{vo}|^2}\Big(\frac{\partial \bar{R}_{vo}}{\partial G_\ell} - 2\frac{\bar{R}_{vo}}{|\bar{R}_{vo}|^2}\Big(\bar{R}_{vo}\cdot\frac{\partial \bar{R}_{vo}}{\partial G_\ell}\Big)\Big)\Big\}\Big] \qquad (8.32d)$$

In a similar fashion it follows from Eq. (8.3c) that:

$$\frac{\partial}{\partial G_\ell}\bar{U}_Q(\bar{X}_o) = \frac{1}{2\pi}Q_v\Big(\frac{\partial \bar{R}_{ve}}{\partial G_\ell} - 2\frac{\bar{R}_{ve}}{|\bar{R}_{ve}|^2}\Big(\bar{R}_{ve}\cdot\frac{\partial \bar{R}_{ve}}{\partial G_\ell}\Big)\Big)/|\bar{R}_{ve}|^2 \qquad (8.32e)$$

while differentiation of Eq. (8.9c) gives for one specific segment carrying a source distribution:

$$\frac{\partial}{\partial G_\ell}\bar{U}_q(\bar{X}_o) = \frac{b}{2\pi}\sum_{j=1}^{NP}\bar{e}_x\times\Big\{q(t_j^*)\Big(\frac{\partial \bar{E}_o}{\partial G_\ell} + k_n(t_j^*)\frac{\partial \bar{E}_o^c}{\partial G_\ell}\Big) + q'(t_j^*)\frac{\partial \bar{E}_1}{\partial G_\ell}\Big\}\Big] \qquad (8.32f)$$

which, because a source distribution is on a fixed known geometry, is nonzero only if $Y_o$ or $Z_o$ is within the range of influence of $G_\ell$.
The derivative with respect to $G_\ell$ of $\bar{E}_o$, $\bar{E}_1$ and $\bar{E}_o^c$ is worked out in detail in Appendix E. The derivative of the curvature, follows directly from Eq. (7.2g) as:

$$\frac{\partial}{\partial G_\ell}k_n(t_j^{i*}) = \frac{1}{b_i^3}\Big[\Big\{\frac{\partial}{\partial G_\ell}\frac{d\bar{X}^i}{dt}(t_j^{i*})\Big\}\times\Big\{\frac{d^2\bar{X}^i}{dt^2}(t_j^{i*})\Big\} + \Big\{\frac{d\bar{X}^i}{dt}(t_j^{i*})\Big\}\times\Big\{\frac{\partial}{\partial G_\ell}\frac{d^2\bar{X}^i}{dt^2}(t_j^{i*})\Big\}\Big]\cdot\bar{e}_x \qquad (8.32g)$$

The derivative with respect to $G_\ell$ of the first and second derivative with respect to t of $\bar{X}^i(t)$ at $t=t_j^{i*}$ will result in a non-zero contribution only if the panel midpoint $t=t_j^i$ is within the "domain of influence" of $G_\ell$ (Fig. 8.9).

The derivative with respect to $G_\ell$ of $\bar{R}_{ve} = \bar{X}_o - \bar{X}_{ve}$ will result in a nonzero contribution only when the panel midpoint $\bar{X}_o$ at which the velocity is computed is within the "range of influence" of $G_\ell$ or when $G_\ell$ is either $Y_v$ or $Z_v$, and similarly for the geometric derivative of $\bar{R}_{vo}$.

In case the collocation point $\bar{X}_o$ is in the far-field of a panel the contribution due to this panel is computed using the single-pole expansion given in Eq. (8.8c) and (8.9b).
The derivative with respect to the unknown geometric parameter $G_\ell$ of these expressions is:

$$-\frac{1}{2\pi}\mu'(t_j^*)\bar{e}_x\times\Big\{\frac{\partial \bar{R}}{\partial G_\ell} - 2\frac{\bar{R}}{|\bar{R}|^2}\Big(\bar{R}\cdot\frac{\partial \bar{R}}{\partial G_\ell}\Big)\Big\}\Delta t_j \qquad (8.32h)$$

and

$$\frac{b}{2\pi}q(t_j^*)\Big\{\frac{\partial \bar{R}}{\partial G_\ell} - 2\frac{\bar{R}}{|\bar{R}|^2}\Big(\bar{R}\cdot\frac{\partial \bar{R}}{\partial G_\ell}\Big)\Big\}\Delta t_j \qquad (8.32i)$$

respectively, and where $\bar{R} = \bar{X}_o - \bar{X}^i(t_j^{i*})$. Here also the derivative with respect to $G_\ell$ of $\bar{X}_o$ and $\bar{X}(t_j^{i*})$ is nonzero only if it is within the "range of influence" of $G_\ell$.

Derivatives of Dirichlet boundary condition, Eq. (8.5a)

This condition, applied at $t_k^{i*}$, the j-th midpoint of the i-th segment, is denoted by $F_k$. Here the collocation point $t_j^{i*}$ is always on a segment with the composite source/doublet distribution. Differentiation of $F_k$ with respect to any unknown singularity parameter $S_\ell$ yields:

$$\frac{\partial F_k}{\partial S_\ell} = -\frac{1}{2}\frac{\partial}{\partial S_\ell}\mu^i(t_j^{i*}) + \sum_m\Big[\Big\{\delta_\mu^m\frac{\partial}{\partial S_\ell}\phi_\nu^m(\bar{X}^i(t_j^{i*})) + \delta_{ve}^m\phi_Q^m(\bar{X}^i(t_j^{i*}))\Big\}\Big] \qquad (8.33)$$

The derivative of $\mu^i(t_j^{i*})$ with respect to $S_\ell$ is nonzero only if $S_\ell$ is the doublet strength at $t=t_j^{i*}$.
The other terms in Eq. (8.33) follow from Eqs. (8.8a) and (8.2d) for the contribution due to the doublet distribution and vortex-core entrainment respectively. This implies that the derivative with respect to $S_\ell$ of the Dirichlet boundary condition corresponds to $A_{k\ell}(\bar{X}^i(t_j^{i*}))$ the aerodynamic influence coefficient at collocation point $\bar{X}^i(t_j^{i*})$ of singularity parameter $S_\ell$, see Eq. (8.13a).

The derivative with respect to the unknown geometric parameter $G_\ell$ follows from Eq. (8.5a) as

$$\frac{\partial F_k}{\partial S_\ell} = \sum_m\Big[\delta_\mu^m\frac{\partial}{\partial G_\ell}\phi_\mu^m(\bar{X}^i(t_j^{i*})) + \delta_{ve}^m\frac{\partial}{\partial G_\ell}\phi_Q^m(\bar{X}^i(t_j^{i*}))\Big] \qquad (8.34a)$$

The derivative with respect to $G_\ell$ of the contribution due to the doublet distribution on one specific (vortex-sheet) segment with N panels, follows from Eq. (8.8a) as:

8.6.2 Influence of length of vortex sheet

The length of the vortex sheet is an important parameter in the model of the vortex core. A longer vortex sheet will result in an increased number of turns around the vortex filament, yielding a more accurate representation of the flow field in a larger portion of the cross-flow plane. On the other hand a longer sheet will require more panels to discretize leading to a larger computational effort. In addition the initial guess for the Newton iterative solution procedure is more critical, the long sheet becoming easily entangled in itself.

Fig. 8.11 and Table 8.1 compare for the above testcase ($\Lambda$=76, $\alpha$=20 deg) the solution for four different lengths of the vortex sheet: b=0.90, 1.30, 1.65 and 2.0 respectively. The choice of the b's corresponds to solutions with about $\frac{1}{2}$, $\frac{3}{4}$ and $1\frac{1}{4}$ turn of the vortex sheet around the vortex core.

Table 8.1 shows that although the strength of the vortex core varies considerably with the length of the vortex sheet the normal force is almost constant.

Furthermore, it is concluded from Fig. 8.11 that the influence of the sheet length on the wing pressure distribution is quite modest. The height of the suction peak and its position varies somewhat but the remainder of the pressure distribution is not affected.

The length of the vortex sheet has some influence on the calculated position of the vortex core, where it appears that the center of vorticity might not differ that much for the four vortex sheet lengths considered. Also note that the position of the vortex sheet near the leading edge does not change when the length of the sheet is increased.

| NPW | NPV | b | $\Delta t$ | $\Gamma/KxU_\infty$ | $C_Z$ |
|---|---|---|---|---|---|
| 20 | 18 | 0.90 | 0.05 | 1.294 | 0.998 |
| 20 | 26 | 1.30 | 0.05 | 1.145 | 0.994 |
| 20 | 33 | 1.65 | 0.05 | 1.040 | 0.996 |
| 20 | 40 | 2.00 | 0.05 | 0.932 | 0.993 |

$\Lambda$ = 76 deg

$\alpha$ = 20 deg

Table 8.1 Solution for different lengths of the vortex sheet

8.6.3 Convergence of the numerical scheme

To study the convergence characteristics of the numerical scheme we compute the solution for the 76-deg swept delta wing at 20 deg incidence for four discretizations of increasing density, i.e. for 30, 60, 120, and 240 panels keeping the vortex sheet length fixed at b=2.0.

| NPW | NPV | NDF | b | $\Delta t$ | $\Gamma/KxU_\infty$ | $C_Z$ |
|---|---|---|---|---|---|---|
| 10 | 20 | 78 | 2.0 | 0.1 | 0.903 | 0.969 |
| 20 | 40 | 148 | 2.0 | 0.05 | 0.932 | 0.993 |
| 40 | 80 | 288 | 2.0 | 0.025 | 0.945 | 1.005 |
| 80 | 160 | 568 | 2.0 | 0.0125 | 0.950 | 1.011 |

$\Lambda$ = 76 deg

$\alpha$ = 20 deg

NDF = Number of unknown parameters

Table 8.2 Solution for different panel densities

In Fig. 8.12 and Table 8.2 the solutions are compared. The Table shows that the strength $\Gamma$ of the vortex core and the normal force coefficient increases about 4 per cent when the number of panels NPW on the wing is increased from 10 to 80. Fig. 8.12, which shows the computed vortex sheet geometry, doublet distribution and spanwise pressure distribution, also indicates that the solution converges as the paneling is refined.

As the number of panels increases the peak in the spanwise pressure distribution increases slightly in height and moves somewhat in outboard direction. Similarly in the shape of the vortex sheet the regions of large curvature become somewhat more pronounced.

For most purposes a paneling with $\Delta t$ between 0.1 and 0.2 will, for the present case, provide a sufficient degree of accuracy.

8.6.4 Iterative solution procedure

The full Newton method employed to solve the system of nonlinear equations converges quadratically, at least if the initial guess for the solution is close enough to one of the roots of the system. In the present method various continuation procedures can be utilized (see section 8.5.3). Fig. 8.13 shows one of these procedures, the one to use the solution obtained earlier as initial solution for a nearby angle of attack. In this figure the history convergence is given for the cases where the solution for $\alpha$=17.5 deg and $\alpha$=22.5 deg are obtained starting from the solution at 20 deg incidence. It shows that quadratic convergence, once it is obtained, drives the residual to machine accuracy ($\approx 10^{-12}$) within 2 or 3 iterations.

Figure 8.13 further provides insight in the changes that occur in the vortex sheet geometry and spanwise pressure distribution when the incidence is changed by 2.5 deg.

8.6.5 Effect of entrainment on the solution

In the preceding examples of application the entrainment of the inner portion of the vortex core was not accounted for, i.e. $Q_v \equiv 0$. In this section we consider the influence of including in the model the entrainment in the form of a source of strength given in Eq. 8.2e. For the case considered in section 8.6.2, i.e. the 76-deg swept delta wing at 20 deg incidence with four different lengths of the vortex sheet, the solution was computed with the entrainment option on. The results are summarized in Table 8.3:

| NPW | NPV | b | $\Delta t$ | $\Gamma/KxU_\infty$ | $Q_v/KxU_\infty$ | $C_Z$ |
|---|---|---|---|---|---|---|
| 20 | 18 | 0.90 | 0.05 | 1.343 | -0.027 | 1.039 |
| 20 | 26 | 1.30 | 0.05 | 1.191 | -0.022 | 1.027 |
| 20 | 33 | 1.65 | 0.05 | 1.084 | -0.018 | 1.023 |
| 20 | 40 | 2.00 | 0.05 | 0.975 | -0.014 | 1.015 |

$\Lambda$ = 76 deg

$\alpha$ = 20 deg

Table 8.3 Influence length of vortex sheet on solution with entrainment accounted for

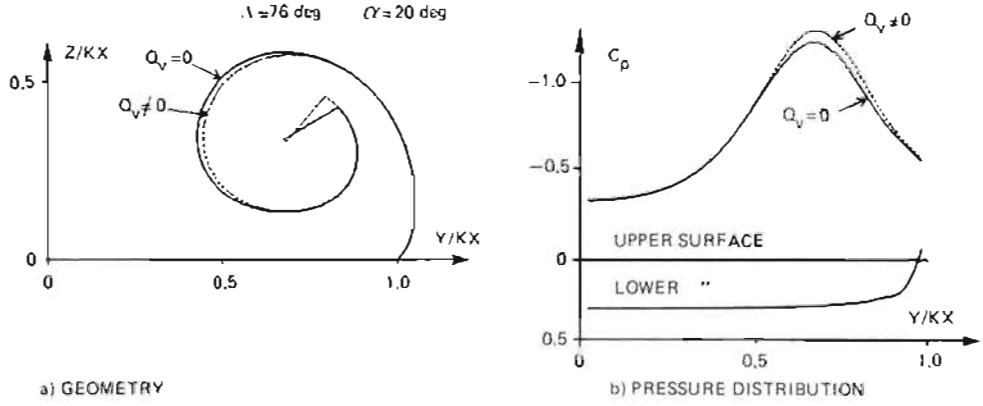


Fig. 8.14 Influence of entrainment modeling on solution

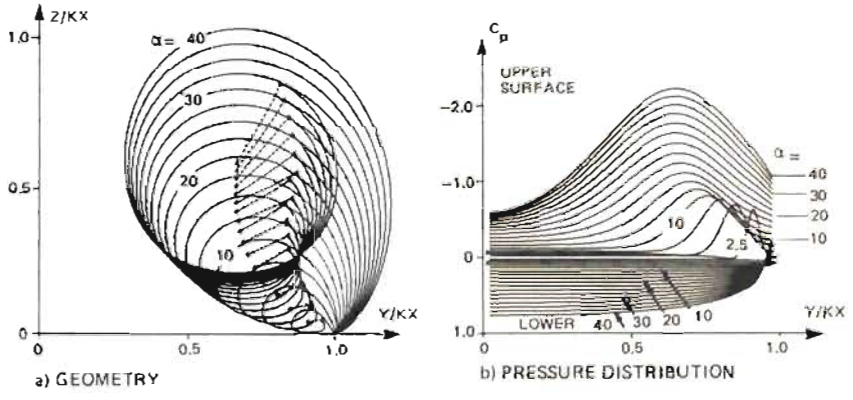


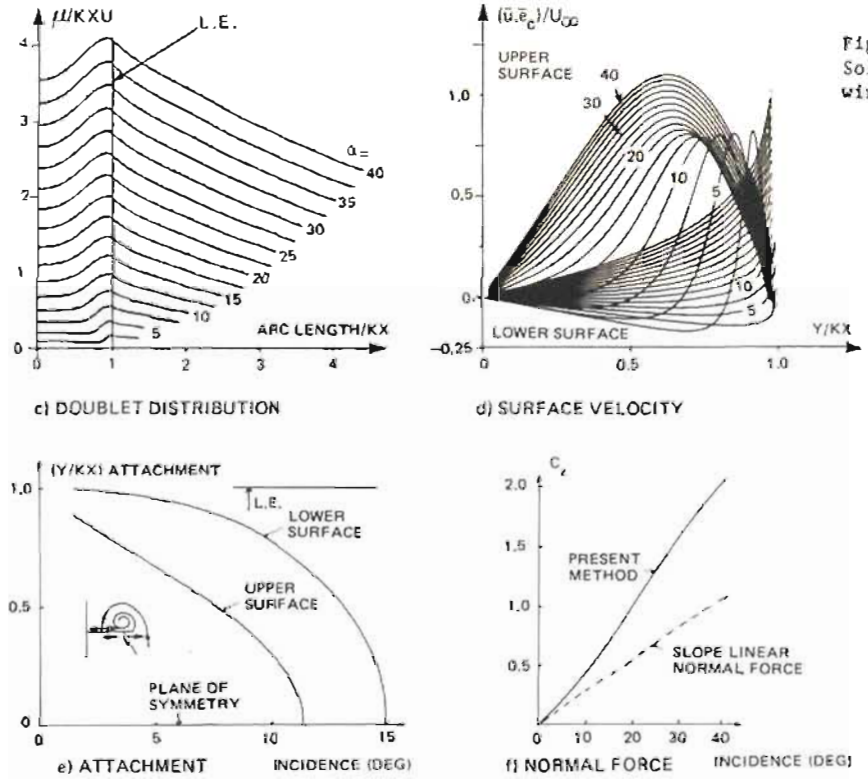


Fig. 8.15
Solution for unit-aspect ratio wing at incidence 2.5(2.5)40 deg




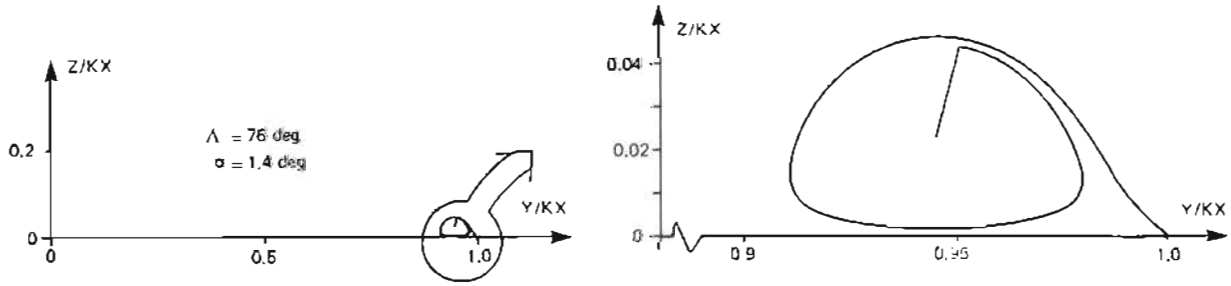


Fig. 8.16 Solution for low incidence

It follows from Table 8.3 that for this present case the entrainment is quite small, smaller than the $O(\varepsilon)\approx O(K)$ we pre-assumed in the analysis of Chapter 4. This is explained by the circumstance that $Q_v/\Gamma$ is proportional to $r_c'$ which in the present case is approximately 0.2 K, also according to Fig. 4.11 yielding the relatively small values of the entrainment. In comparing Tables 8.1 and 8.3 it is seen that both the strength of the vortex and the normal force coefficient increase a few percent when the entrainment is included. For the longer sheet, i.e. the better representation of the vortex core, the sink strength required to model the inflow due to the cut-off part of the spiral vortex core decreases rapidly.
Fig. 8.14 compares for the case of the longest vortex sheet considered here the geometry of the vortex sheet and the wing surface pressure distribution for the solution with and the one without entrainment modeled. The comparison shows that including $Q_v$ results in a shape of the vortex sheet that is more circular, while the height of the upper wing surface pressure peak increases somewhat.
*In the remainder of this chapter we will neglect the entrainment of the inner portion of the core and set* $Q_v \equiv 0$.

8.6.6 Solution for unit-aspect-ratio delta wing for at angles of attack between 2.5 and 40 deg

For the 76-deg swept delta wing the solution has been computed for incidences from 2.5 to 40 deg. Table 8.4 lists the computational parameters used and the global characteristics of the solution.

| α(deg) | NPW | NPV | b | $\mu^2(0)/KXU_\infty$ | $\Gamma/KXU_\infty$ | $C_Z$ |
|---|---|---|---|---|---|---|
| 2.5 | 38* | 29 | 0.3625 | 0.164 | 0.127 | 0.083 |
| 5.0 | 40 | 26 | 0.65 | 0.346 | 0.239 | 0.182 |
| 7.5 | 40 | 37 | 0.925 | 0.548 | 0.347 | 0.298 |
| 10.0 | 20 | 23 | 1.25 | 0.748 | 0.446 | 0.417 |
| 12.5 | 20 | 28 | 1.4 | 0.973 | 0.552 | 0.553 |
| 15.0 | 20 | 32 | 1.6 | 1.211 | 0.672 | 0.696 |
| 17.5 | 20 | 36 | 1.8 | 1.461 | 0.798 | 0.843 |
| 20.0 | 20 | 40 | 2.0 | 1.721 | 0.932 | 0.993 |
| 22.5 | 20 | 43 | 2.15 | 1.992 | 1.087 | 1.144 |
| 25.0 | 20 | 47 | 2.35 | 2.271 | 1.237 | 1.293 |
| 27.5 | 20 | 50 | 2.5 | 2.558 | 1.409 | 1.440 |
| 30.0 | 20 | 54 | 2.7 | 2.852 | 1.574 | 1.583 |
| 32.5 | 20 | 58 | 2.9 | 3.152 | 1.747 | 1.720 |
| 35.0 | 20 | 62 | 3.1 | 3.457 | 1.929 | 1.850 |
| 37.5 | 20 | 66 | 3.3 | 3.768 | 2.118 | 1.970 |
| 40.0 | 20 | 70 | 3.5 | 4.082 | 2.317 | 2.080 |

Λ = 76 deg

* non-uniform

Table 8.4 Solution AR=1 wing for α=2.5(2.5)40 deg

Further details of the solutions are depicted in Fig. 8.15. *In the computations* the length of the vortex sheet b is chosen such that the attitude of the feeding sheet stays about the same. For the lower incidences the paneling of the wing and of the vortex sheet were refined, this to account for the locally larger gradients.

Fig. 8.15a indicates that the vortex system increases very considerably with increasing incidence as is its footprint, the suction peak on the upper wing surface. At low incidences the vortex is close to the leading edge and induces a small but steep suction peak. At high angle of attack the whole semispan experiences the influence of the vortex. Actually for incidences exceeding 35 deg the vortex core starts to move in outboard direction, due to the so-called crowding effect, i.e. the port-side vortex system pushing the starboard system in outboard direction and vice versa.
It follows from Table 8.4 and Fig. 8.15c that the total circulation of the vortex system, $\mu^2(\xi^2=0)$, and the strength of the vortex, $\Gamma=\mu^2(\xi_c^2)$, increase slightly more rapid than linear. The circulation of the vortex varies from 77 per cent of the total at α=2.5 deg to about 55 per cent at α=15 deg keeping that value up to high incidences. The evolution of the doublet distribution with increasing incidence is shown in Fig. 8.15c. It indicates that the slope of μ on the vortex sheet, a measure for the magnitude of the axial component of the vorticity, increases with rising α. Although the doublet distribution evolves quite gradually with incidence the solution on the wing upper *and* lower surface changes character during pitch-up. This is illustrated in Fig. 8.15d where the spanwise distribution of the conical cross-flow component $\underline{u}.\underline{e}_c$, with $\underline{e}_c$ given in Eq. (8.14b), of the surface velocity is plotted and in Fig. 8.15e which shows the location the cross-flow plane attachment points. At low incidences the flow attaches on the lower wing surface close to the leading edge, separates at the edge, curves around the vortex system and re-attaches on the upper wing surface. At intermediate values of the incidence the upper wing surface (secondary) attachment point moves to the plane of symmetry which is reached at about 11.5 deg. Simultaneously, the lower wing surface (primary) attachment point moves from the leading edge towards the plane of symmetry which is reached at about 15 deg incidence.

The normal force coefficient is depicted in Fig. 8.15f. For reference purposes the line indicating the slope of the normal force without leading-edge vortex flow is included. The normal force increases at first very rapidly, reaching at about 25 deg a value twice as large as attainable in linear theory. Above 30 deg incidence the "crowding" effect is responsible for the diminishing slope of the normal force coefficient.

It must be realized that the present approximate method will overpredict the normal force coefficient, due to the effect of the trailing-edge Kutta condition not accounted for in the method. Furthermore, above 35 deg angle of attack another 3D flow phenomenon, i.e vortex breakdown will become an important factor limiting the further increase in normal force. As may be clear from Figs. 8.15b and d at the lower incidences the sharp pressure rise on the downstream side of the upper wing surface suction peak will provoke large secondary separation effects.

8.6.7 Solution at very low incidence

To further demonstrate the ability of the present method, the solution at α=2.5 deg was continued, though with small steps in α, to the one at α=1.4 deg. The shape of the vortex sheet for this case is shown in Fig. 8.16. The wing was discretized using 51 panels in a non-uniform distribution with a maximum panel width of 0.05 near the plane of symmetry and a minimum panel width of 0.005 near the leading edge. The vortex sheet of length equal to 1 semi-span consisted of 50 panels also of 0.005 width.
*The vortex system is very small in extent, it is confined to the last 10 percent semi-span and the vortex* sheet approaches the wing surface very closely. At finite Reynolds number a solution at such low incidence presumably will be affected to a large extent by viscous effects. The real flow will probably exhibit a viscous flow character dominated by a leading-edge separation bubble.

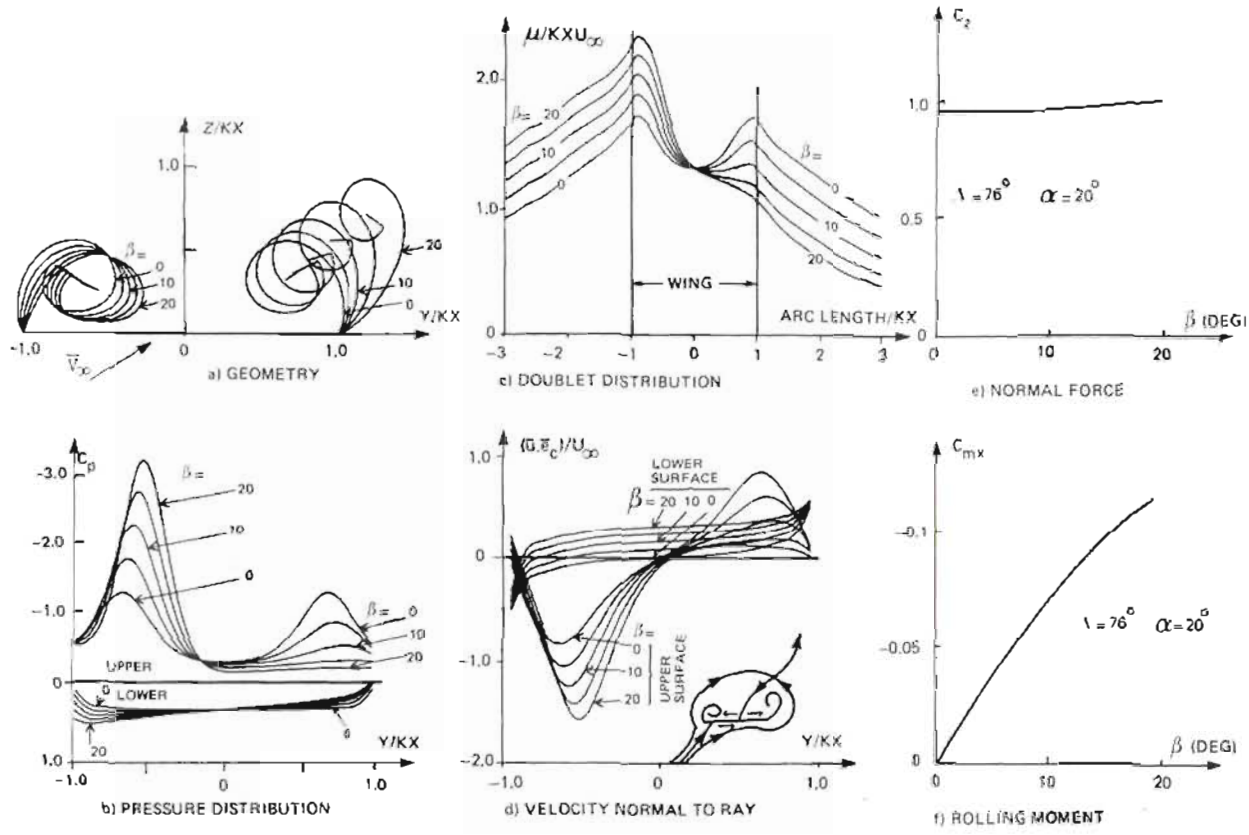


Fig. 8.17 Solution for side-slipping Λ=76 deg delta wing at 20 deg incidence

8.6.8 Side-slipping delta wing

In the previous examples both the geometry and the flow were symmetric with respect to the Y=0 plane. In the present example we study the flow about the 76-deg delta wing in side slip at a constant incidence of 20 deg. The characteristics of the solution for angles of side slip up to 20 deg are presented in Fig. 8.17.

The wing is represented by 20 panels, the port-side and starboard-side vortex sheet by 20 panels each. The length of both vortex sheets was kept fixed at 2 (=1 span). The solutions were obtained for β=0,2.5,5,6(1)20 deg where the solution obtained at each β is used as starting solution for the next β. For β=0 the starboard-side solution described in section 8.6.1 was used to construct an initial solution for the full-span case.

Fig. 8.17a shows that as the angle of side slip is increased the vortex system attached to the attacking edge does not change very much, while the vortex system attached to the retreating edge is swept off the wing surface. Note that at α=14 deg the starboard-side leading edge becomes a trailing edge. The spanwise pressure distribution, see Fig. 8.17b, changes from a symmetric distribution with two upper wing surface suction peaks to one with just one suction peak on the port-side of the wing at the highest angle of side slip.

At the latter flow condition the pressure distribution is quite similar to a pressure distribution on an airfoil section in two-dimensional flow.

The doublet distribution shown in Fig. 8.17c indicates that the circulation of the starboard-side vortex system decreases and the circulation of the port-side vortex system increases with increasing β. The latter explains that for β increasing the suction peak on the port side while staying at nearly the same position in space increases in height because of the port-side vortex system growing in strength.

From Fig. 8.17d the cross-flow plane streamline pattern can be constructed. The lower wing surface (primary) attachment point moves from the plane of symmetry at β=0 quite rapidly in the direction of the attacking leading edge. In contrast the upper-wing surface re-attachment point stays very close to the plane of symmetry.

As has also been found in experimental investigations the normal force does not vary very much with side slip (Fig. 8.17e). However, due to the asymmetry in the solution the wing experiences a rolling moment. The variation of the rolling moment with β is approximately linear up to 10 deg side slip. For higher values of β the slope of the curve decreases due to the rapidly diminishing influence of the starboard side vortex system.

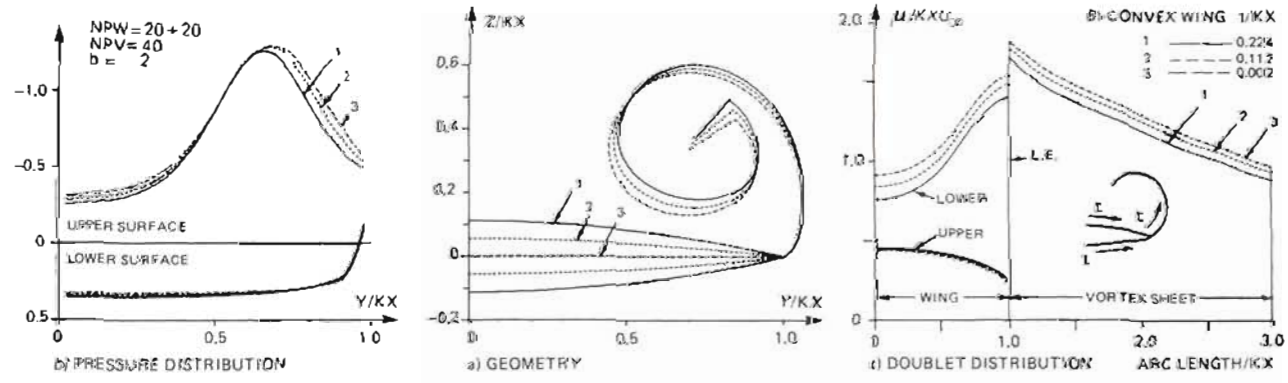


Fig. 8.18 Solution for wing with thickness Λ=76 deg, α=20 deg

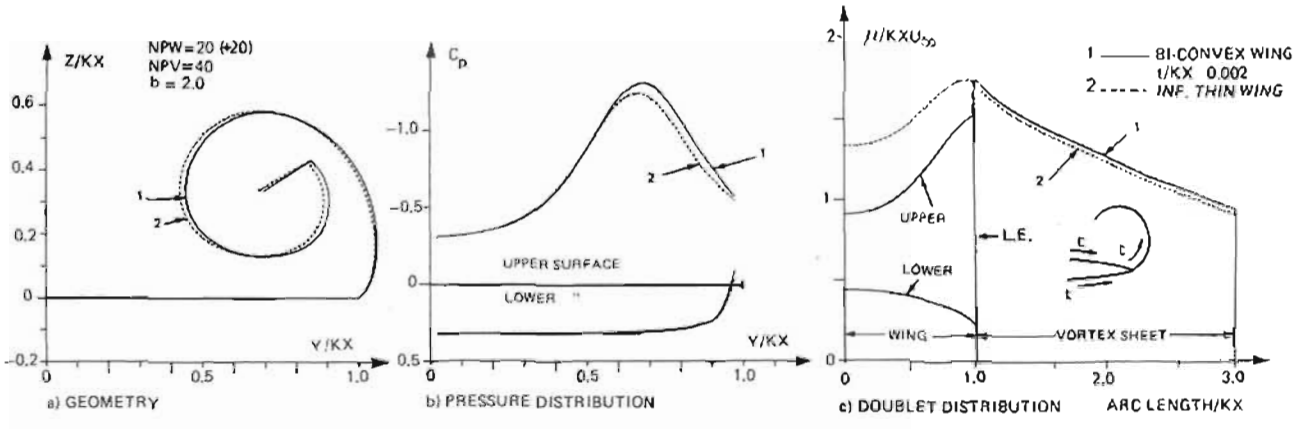


Fig. 8.19 Comparison of solution for thin bi-convex wing with solution for *infinitesimally thin* wing $\Lambda$=76 deg, $\alpha$=20 deg

8.6.9 Bi-convex delta wing

The delta wing considered in the preceding sections has zero thickness. In Fig. 8.18 the solution for three bi-convex delta wings of unit aspect ratio is compared. The solution was obtained at 20 deg incidence using the Dirichlet boundary condition on the interior of the wing cross-section. The three conical wings have a thickness of 22.4, 11.2 and 0.2 per cent semi-span. The effect of the thickness on the geometry of the vortex system is as expected, increasing the thickness pushes the vortex system upward and outboard (Fig. 8.18a) keeping the distance between vortex system and upper wing surface about the same. The effect in the spanwise pressure distribution is more difficult to explain. However, the doublet distribution on the two wing surfaces and leading-edge vortex sheet reveals that the circulation of the vortex system decreases with increasing thickness so that the thinnest wing has the highest upper wing surface suction peak. The lower wing surface pressure distribution is almost identical for the three wings, as is the lower wing surface doublet distribution.

To validate the formulation with the Dirichlet condition we compare in Fig. 8.19 the solution for the bi-convex wing of 0.2 per cent thickness with the solution for the infinitesimally thin wing with Neumann condition. The comparison indicates that there are slight differences in the shape of the vortex sheet, the spanwise pressure distribution and in the doublet distribution on the vortex sheet. The explanation of the differences is most probably the differences in the formulation at the leading edge.

8.6.10 Investigation of the vortex core

In this section the vortex core, as modeled by a large number of turns of the vortex sheet around the vortex filament representing its innermost part, is studied in more detail. The solution considered is the basic test case ($\Lambda$=76 deg, $\alpha$=20 deg, $\beta$=0), with a vortex sheet of length 5 times the semi-span. The solution, presented in Fig. 8.20, has 20 wing panels and 112 panels on the vortex sheet. The panel scheme of the wing was uniform, that on the vortex sheet non-uniform, the panel width decreasing with increasing curvature. As shown in Fig. 8.20a the vortex sheet loops 5 times around the vortex filament, with the last turns becoming nearly circular. The circulation contained in the vortex sheet amounts to 77.5 per cent of the total circulation in the vortex system. The strength of the vortex sheet (Fig. 8.20d), largest at the leading edge, decreases gradually along the vortex sheet. The local extrema in $\gamma$ coincide with the local extrema in the curvature.

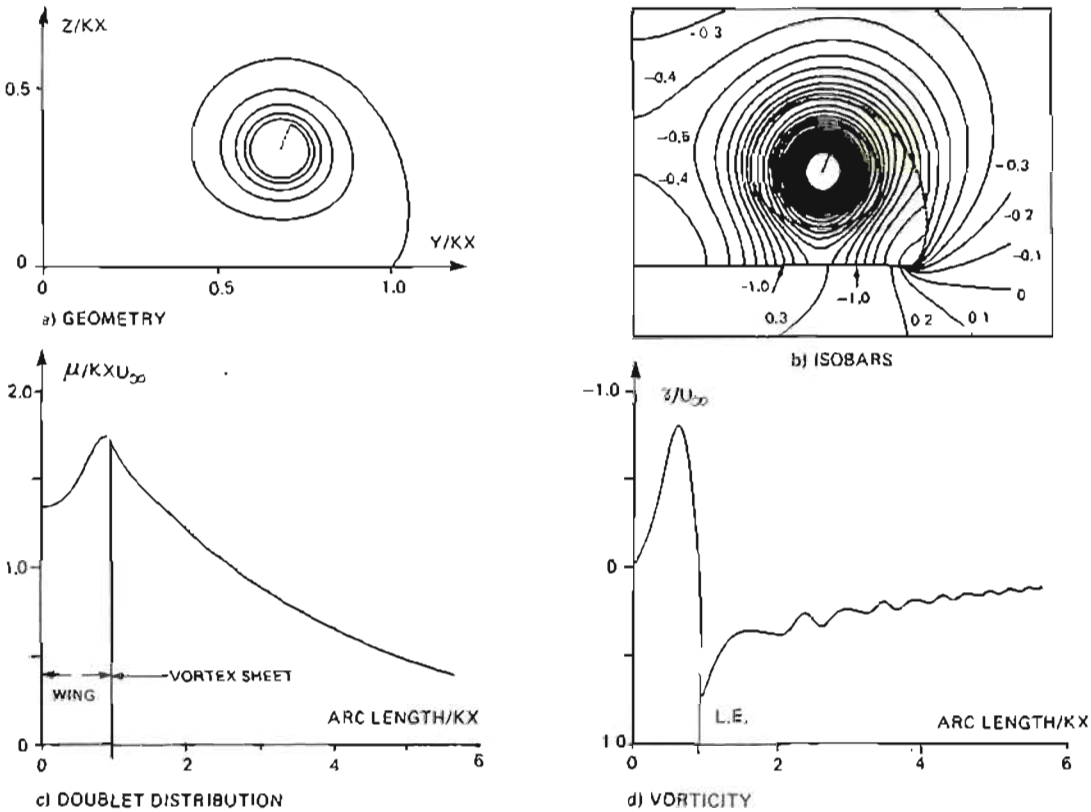


Fig. 8.20 Solution for long vortex sheet ($\Lambda$=76 deg, $\alpha$=20 deg)

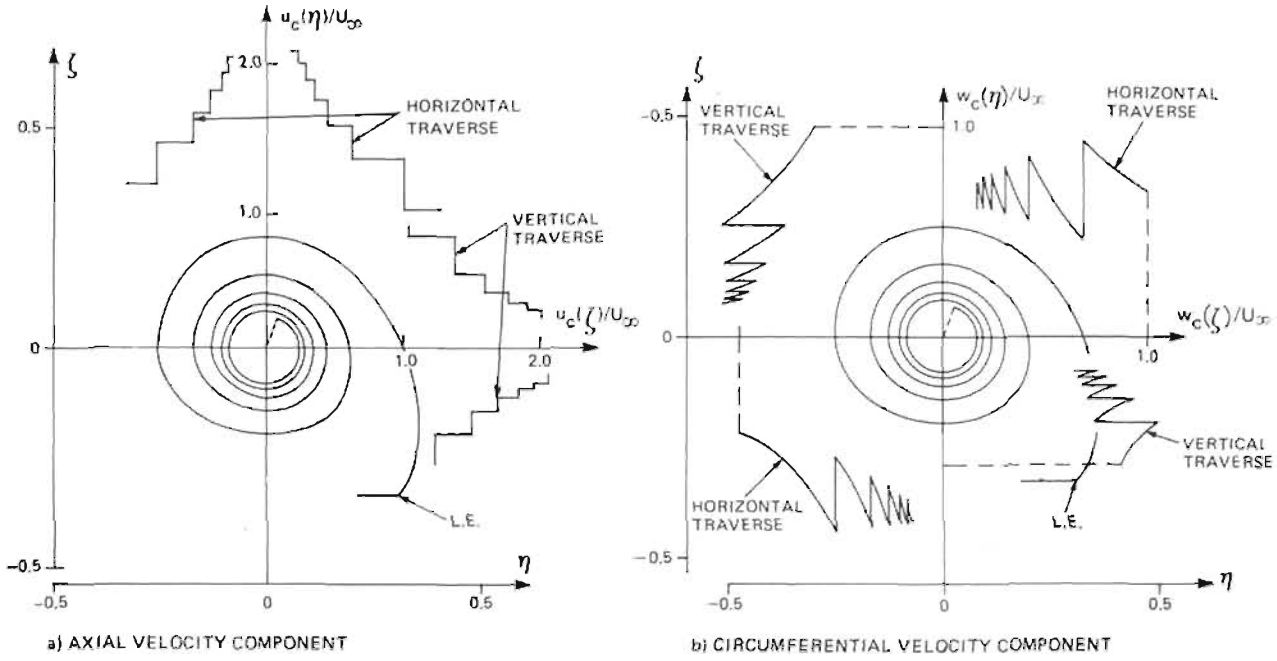


a) AXIAL VELOCITY COMPONENT

b) CIRCUMFERENTIAL VELOCITY COMPONENT

Fig. 8.21 Velocity components in vortex-core axis coordinate system ($\Lambda$=76 deg, $\alpha$=20 deg)

For the present solution the velocity and pressure coefficient were computed at a large number of points (2250) on a grid above and below the delta wing. Iso-contours of the static pressure coefficient are given in Fig. 8.20b. It shows the rapid variation of the pressure near the leading edge and the rapid drop in the pressure as the center of the core is approached. Also note that across the vortex sheet (the dashed curve) the pressure is continuous in function value, one of the conditions imposed on the vortex sheet, but discontinuous in slope. In Fig. 8.20b this discontinuity is not always exactly at the position of vortex sheet because of the grid resolution. At the plane of symmetry at the position where the vertical component of the velocity changes sign (the "re-attachment" point) the pressure coefficient has a local maximum.

To investigate the flow field near the vortex in further detail and to try to correlate the results of the present method with the results of the asymptotic isolated vortex core models of Chapter 4 the velocity field was determined on traverses through the center of the vortex core. Two traverses were taken in a vortex-core axis coordinate system with the axes:

$$\bar{e}_{1c} = \bar{e}_x + \bar{X}_v \tag{8.39a}$$

$$\bar{e}_{2c} = \bar{e}_{3c} \times \bar{e}_{1c} \tag{8.39b}$$

$$\bar{e}_{3c} = (\bar{e}_{1c} \times \bar{e}_y)/|\bar{e}_{1c} \times \bar{e}_y| \tag{8.39c}$$

Two traverses are considered, the "horizontal" one along $\bar{e}_{2c}$ and the "vertical" one along $\bar{e}_{3c}$. The axial velocity component ($\bar{u}.\bar{e}_{1c}$) and the circumferential velocity component ($\bar{u}.\bar{e}_{3c}$ for the horizontal and $\bar{u}.\bar{e}_{2c}$ for the vertical traverse) are presented in Fig. 8.21a and b, respectively.

Both the axial and the circumferential component show the pattern we derived in Chapter 4 for isolated vortex cores. Towards the center of the vortex core the axial component increases stepwise in magnitude, reaching a value of about 2 times the free-stream velocity. Each step corresponds with a passage through the vortex sheet. The circumferential component has the same type of saw-tooth like distribution that followed from the isolated vortex sheet core model, the jumps in the velocity becoming smaller as the center of the core is approached.

Any attempt to match the solution as presented here with the isolated vortex core solution of Chapter 4 will have to take into account the non-uniform "cross-flow" caused by the presence of the wing, the presence of the mirror-imaged vortex system on the other side of the plane of symmetry and the finite extent of the vortex sheet.

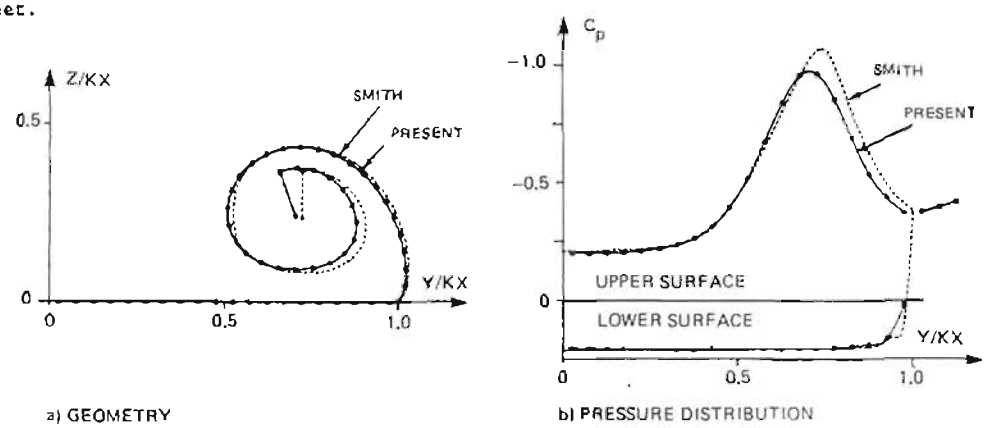


a) GEOMETRY

b) PRESSURE DISTRIBUTION

Fig. 8.22 Comparison of present solution with Smith's conformal mapping method ($\Lambda$=76 deg, $\alpha$=20 deg)

8.6.11 Comparison with Smith's solution

Smith-1966 computes the solution for the case of unit conical flow parameter (approximated as $\alpha/K$). For the 76-deg swept delta wing that corresponds to $\alpha$=14.285 deg.
In Fig. 8.22 the solution obtained with the present physical-plane panel method is compared with the solution of Smith's procedure of conformal mapping plus paneling of the vortex sheet in the transformed plane. The present solution has 20 panels on the wing and 35 panels on the vortex sheet (b=1.75 Kx), see Fig. 8.22. In Smith's method the vortex sheet was discretized by 21 elements.
The geometry of the vortex sheet differs somewhat as does the upper wing surface pressure distribution. However, taking into account the differences in the formulation, e.g. the implementation of the Kutta condition at the leading edge, a satisfactory agreement between the two results is obtained.

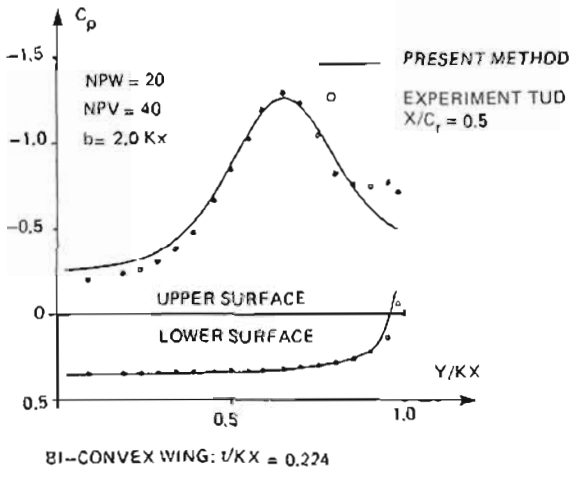


Fig. 8.23 Comparison with experiment
$\Lambda$=76 deg, $\alpha$=20 deg

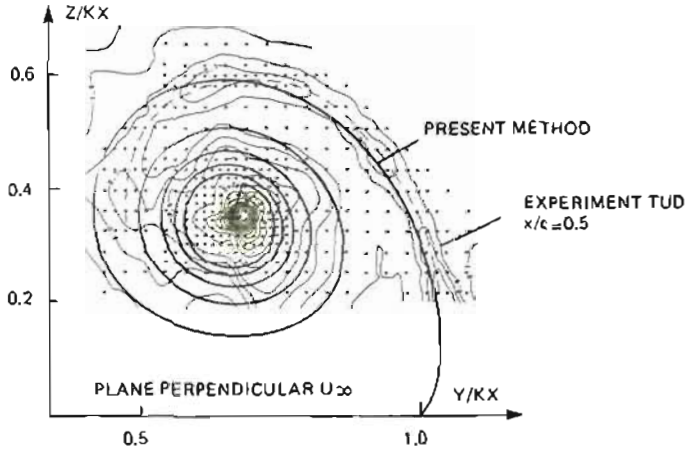


Fig. 8.24 Comparison of computed vortex sheet geometry and measured total-pressure contours
($\Lambda$=76 deg, $\alpha$=20 deg)

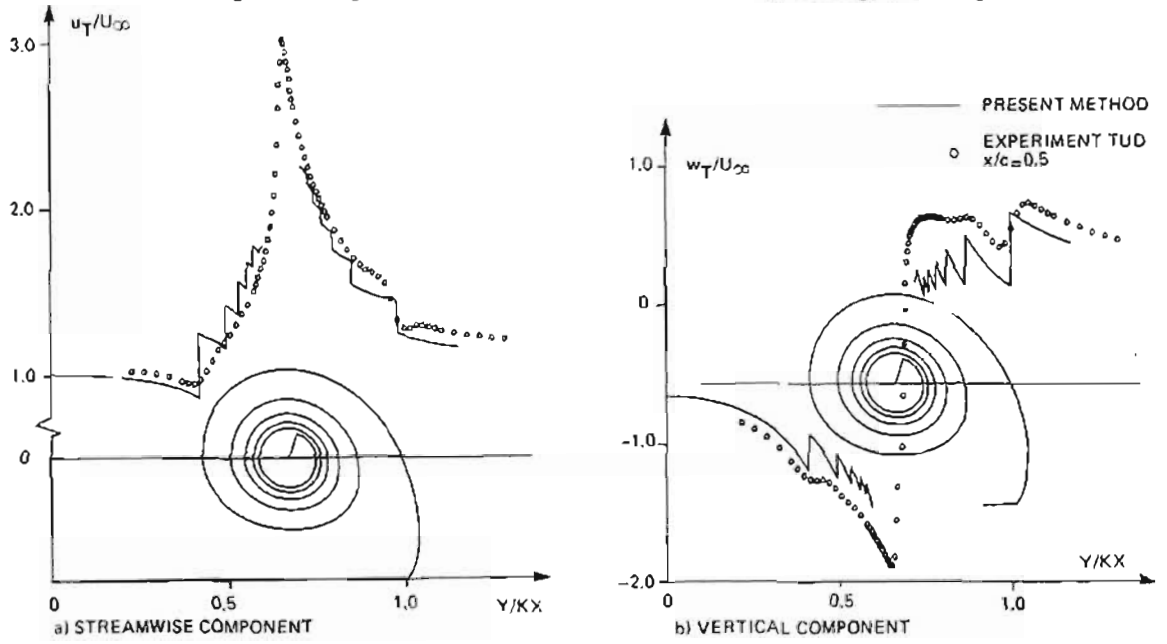


Fig. 8.25 Comparison of computed and measured velocity components on horizontal traverse through vortex axis ($\Lambda$=76 deg, $\alpha$=20 deg)

8.6.12 Comparison with experimental data

In this section results of the present method are compared with experimental data. Usually the computed spanwise pressure distribution correlates reasonably with experimental data on the central part of the wing, i.e. away from the apex and away from the trailing edge. This is demonstrated in Fig. 8.23 for the case of the 76-deg swept delta wing at 20 deg incidence. The agreement at mid-chord between theory and experiment is excellent. In this particular case the upper wing surface boundary layer appeared to be turbulent and the secondary separation occurred not before the 80 per cent local semi-span location.

Fig. 8.24 compares the computed shape of the vortex sheet with the total pressure contours obtained by Verhaagen & Kruisbrink-1984 at the Technical University Delft. It demonstrates that the location of the free shear layer and that of the computed vortex sheet agree quite well, while also the position of the vortex core is predicted satisfactorily.

In Fig. 8.25 we return to the case with the long vortex sheet. Compared are, for a horizontal traverse through the vortex core, the computed and the measured (5-hole probe) component of the velocity along $U_\infty$ (the tunnel axis) and the component of the velocity in vertical direction. For the streamwise velocity component the agreement between computed and measured distribution is remarkably good. For the vertical component theory and experiment still correlate qualitatively, but theory appears to underpredict the measured values of the circumferential velocity. Reasons for the discrepancy could be wind-tunnel wall interference which for this relatively large half-model are known to result in an effective incidence larger than the value of 20 deg used for the computations. Note that the first two full turns of the leading-edge vortex sheet can be recognized in the experimental data, the remainder of the core may be considered as a region of distributed vorticity.

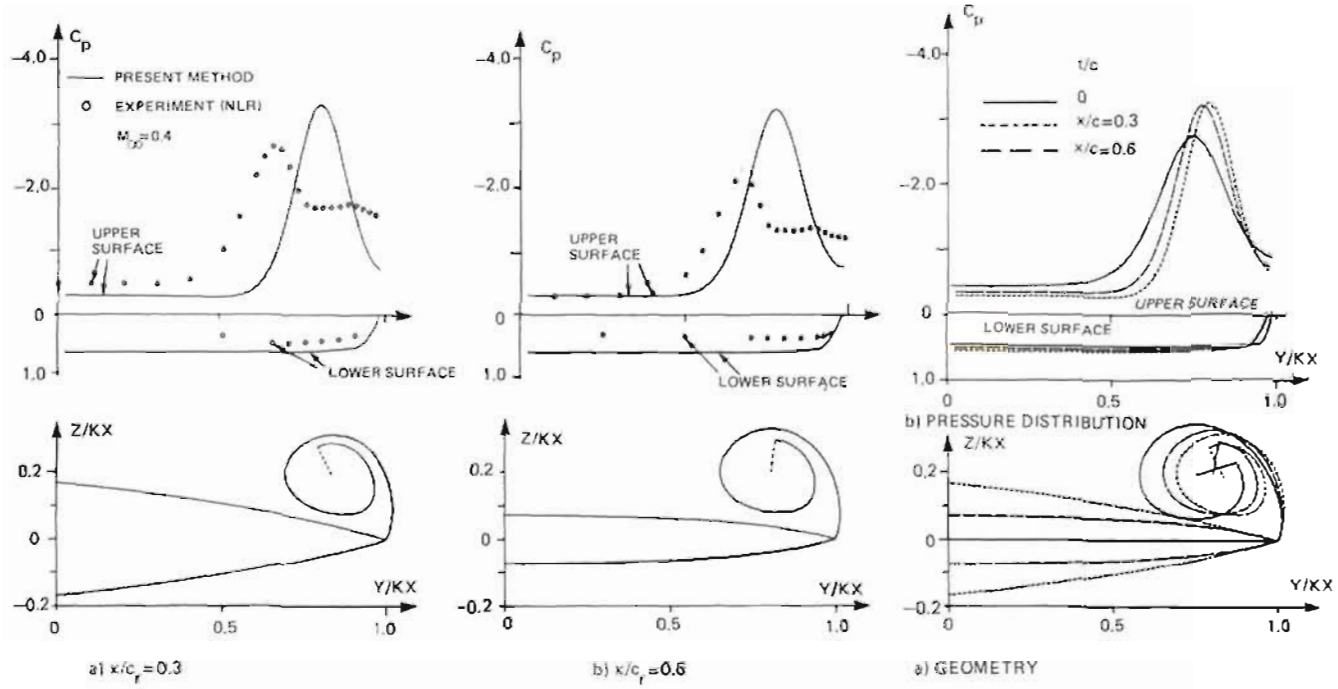


Fig. 8.26 Comparison of computed and measured pressure distribution on thick wing configuration ($\Lambda$=65 deg, $\alpha$=20°)

Fig. 8.27 Comparison of solution for cross-section at $x/c_r$=0.3 and 0.6 and ($\Lambda$=65 deg, $\alpha$=20°)

In Fig. 8.26 results of the present method for a 65-deg swept sharp-edged delta wing with thickness at 20 deg incidence are compared with experimental data obtained at NLR during the so-called International Vortex Flow Experiment. The model used in this experiment has a constant airfoil section in planes parallel to the plane of symmetry, i.e. it is not conical. The computed results shown in Figs. 8.26a and b are for a conical wing with a cross-section identical to the cross-section of the model at $x/c_r$=0.3 and 0.6, respectively. The figure shows that the upper wing surface suction peak for this 65-deg swept delta wing is much higher than for the 76-deg swept delta's considered above. This is explained as follows: the conical similarity dictates that if for two wings $A=\tan\alpha/\cot\Lambda$ is the same $C_p/\cot^2\Lambda$ will be the same. This means that for the present case of $\Lambda$=65 deg the curves in Fig. 8.15b have to be scaled by the factor $(\cot 65/\cot 76)^2=3.5$. Note the case $\Lambda$=65, $\alpha$=20 deg and the case $\Lambda$=76, $\alpha$=11 deg have the same conical similarity parameter. The steep suction peak will trigger a secondary separation that will push the primary vortex core inboard and upward and the suction peak will be lower and at a more inboard position. If this is taken into account and the probably small effects of compressibility the computed and the measured spanwise pressure distributions correlate quite reasonably. This is especially the case for $x/c_r$=0.6. For $x/c_r$=0.3 the agreement is not as satisfactory, the computed vortex being too far outboard. This is attributable to three-dimensional flow effects and to this wing geometry being least conical at the apex. Actually, in cross-flow planes the wing becomes increasingly thicker when the apex is approached.

The effects of the thickness of the 65-deg wing is considered in Fig. 8.27, which compares the two conical flow solutions discussed above with the solution for the wing without thickness. It appears that although in general for a thicker wing the vortex is weaker the vortex is closer to the wing upper surface resulting in a higher and steeper suction peak.

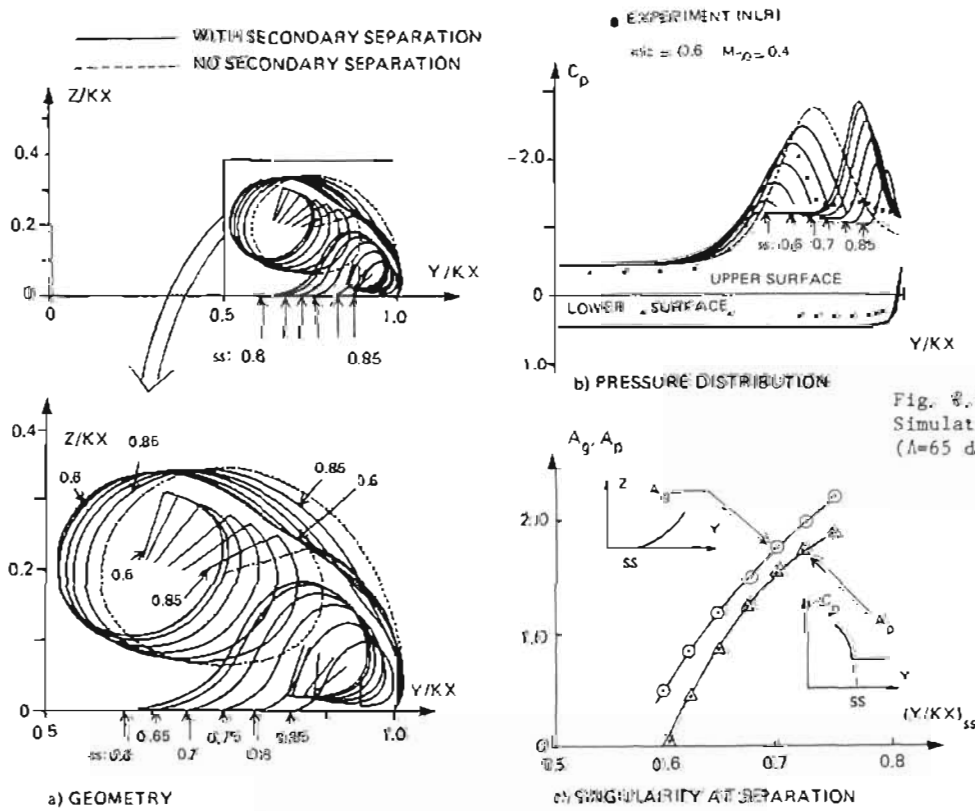


Fig. 8.28
Simulation of secondary separation ($\Lambda$=65 deg, $\alpha$=20 deg)

8.6.13 An attempt to model secondary separation

As demonstrated above secondary separation can have a large effect on the upper wing surface pressure distribution. The position of secondary separation is determined by viscous-flow phenomenona.
In this section we study the effect on the inviscid solution of modeling the region of vortical flow due to the secondary separation by a vortex sheet that starts at some prescribed location on the upper wing surface and rolls up into a vortex core.

The testcase chosen is the 65-deg delta wing at 20 deg incidence discussed in the preceding section. For reasons of keeping the study as simple as possible just the infinitesimally thin wing was considered. The results of the investigation are shown in Fig. 8.28. The cases considered where no secondary separation and secondary separation (SS) at 60(5)85 per cent semi span. In the case shown in Fig. 8.26 secondary separation was turbulent and took place at about 77.5 per cent semi span. In the case of laminar flow on the wing surface the separation will be more inboard.
Fig. 8.28 shows that inclusion of the second vortex system has the qualitatively correct effect on the position of the primary vortex core, it moves inboard and upward. Furthermore, inspection showed that as the point of secondary separation moves outboard the amount of circulation within the primary vortex system and that within the secondary system both decrease, while the normal force is almost constant. The effect on the upper wing surface pressure distribution is that the height of the suction peak is reduced while its location is slightly more inboard. Just like in the experimental data a plateau of about constant pressure is formed just outboard of the secondary separation point. However, between this plateau and the leading edge the present computational model predicts a second suction peak. This suction peak, right underneath the vortex filament of the secondary vortex system, is much more pronounced than the one found in experiments, e.g. Fig. 8.26. In the numerical results the height of the secondary suction peak is directly associated with the presence of the vortex filament, representing the concentrated vorticity of the secondary vortex, in the near proximity of the wing surface. Including tertiary separation would probably reduce the height of the peak, but it may also be argued that in the real flow viscous effects will have a relatively large effect on the relatively weak secondary vortex, preventing the formation of a concentrated vortex core. Note that apart from the second suction peak the agreement of computed and measured pressure distribution (with secondary separation at 77.5 per cent semi span) is quite remarkable.

Considering the details of the computed vortex sheet geometry it is hard to envision that the classical picture of the topology applies. In the classical picture the secondary attachment line is located on the upper wing surface between the secondary separation point and the leading edge. Indeed, computing the surface velocity components along and normal to rays from the apex revealed a different topology, the one sketched in Fig. 8.29. The most striking observation is that the attachment point associated with secondary separation is situated on the primary vortex sheet, forming a half saddle point. Note that although on the primary vortex sheet the mean cross-flow velocity is directed from the leading edge towards the primary vortex core, on the inner side of the vortex sheet between $A_3$ and the leading edge the flow is towards the leading edge. No attempt has been made here to assess whether this is a topologically consistent solution, but it is certainly an interesting outcome of the present study.

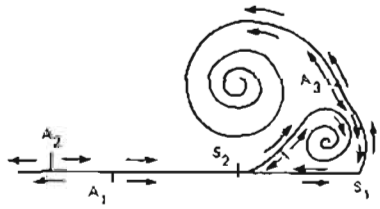


Fig. 8.29 Sketch of details of solution with secondary vortex

In an attempt to predict the secondary separation position it has been tried to match the assumed separation point with the separation point as follows from a boundary-layer calculation with the inviscid pressure distribution obtained with a primary and a secondary vortex system, the latter emanating from the assumed secondary separation point (see de Bruin & Hoeijmakers-1986). This attempt was not successful, the laminar boundary layer always separated just downstream (outboard) of the primary suction peak, always upstream (inboard) of the assumed point of separation. This appears to be due to the singular behaviour of the inviscid solution at the assumed point of separation. This is demonstrated in Fig. 8.28c where two quantities are plotted:

- $A_g$, the parameter in the expansion for the position of the secondary vortex sheet near the point of secondary separation $y_{ss}$, i.e.

$$z/Kx = A_g((y-y_{ss})/Kx)^{3/2} + \ldots \qquad (8.40a)$$

indicative for the magnitude of the singular behaviour in the curvature of the vortex sheet at $y_{ss}$, see F.T. Smith-1978.
- $A_p$, the parameter in the expansion for the pressure upstream of $y_{ss}$, i.e.

$$C_p = (C_p)_{ss} - A_p((y-y_{ss})/Kx)^{1/2} \qquad (8.40b)$$

indicative for the singularity ($\partial C_p/\partial y \to \infty$) in the pressure distribution at $y_{ss}$.

The case of so-called "smooth separation" corresponds to the case of $A_g$ (and $A_p$) becoming zero. Due to inaccuracies in determining $A_g$ and $A_p$ from a discrete solution they do not become zero at the same $y_{ss}$. For the present case smooth separation occurs at about 60 per cent semi span. Only in that case the singularity has disappeared and the boundary layer calculation could proceed up to $y_{ss}$. However, the so found location is much too far inboard when compared with experimental data.
The way to proceed is to allow for a strong interaction between the boundary layer and the inviscid flow field. In such an interaction the influence of the singularity due to the inviscid separation is spread in upstream direction which is not allowed in the classical boundary layer theory. This then induces a displacement effect of the boundary layer which weakens the adverse pressure gradient and enables the boundary layer to reach the assumed line of separation. For the case of separation from a slender cone Fiddes-1980 used the triple-deck formulation of Sychev and F.T. Smith as extended to some special 3D flow cases by F.T. Smith-1978, an asymptotic theory for large Reynolds numbers, to derive the permissable value of $A_g$ as a function of the Reynolds number. The resulting expression involves aside from the Reynolds number certain boundary-layer quantities for the case of "smooth-separation".

In the present study we follow the same procedure. It follows directly from Eq. (5.2) in Smith-1978 that the permissable $A_g$ can be expressed as:

$$A_g = \frac{2}{3}C\left[\frac{\partial(V/V_e)}{\partial(\zeta')}\right]^{9/8}_{z=0}(U_e/KV_e)^{5/8}(Re_x)^{-1/16} \qquad (8.41a)$$

where $C = 0.44$ and $Re_x$ the Reynolds number $U_e x/\nu$. U and V are the velocity components along and normal to the separation line, respectively while the subscript e denotes the external, inviscid, value. The term inside the square brackets is related to the skin friction, $\zeta' = (\sqrt{Re_x})z/Kx$ and $K = \cot\Lambda$. The displacement thickness $\delta^*$ can be expressed as

$$\delta^*/c_r = D(x/c_r)^{\frac{1}{2}}/(U_\infty c_r/\nu)^{\frac{1}{2}} \qquad (8.41b)$$

where D is a constant and $c_r$ the root chord. Employing Eq. (8.41b) and assuming that $U_e = U_\infty$ one finds for the term within the square bracket:

$$[\ ]_{z=0} = (K/D)\left\{\frac{\partial(V/V_e)}{\partial(Z/\delta^*)}\right\}_{z=0} \qquad (8.41c)$$

From a 3D boundary-layer computation the term within the curly brackets was found to be 0.7521, while $\delta^*/c_r$ was $0.1046\times10^{-3}$. For a Reynolds number (based on the root chord) of 9 million then one finds that at mid chord D = 0.4438 and the square bracket becomes 0.7902. From the inviscid solution it follows that $V_e/U_e = 0.7062$, resulting in:

$$A_g = 0.4506(Re_x)^{-1/16} \qquad (8.41d)$$

The permissible singularity in the curvature is quite small, shifting the position of the secondary separation by at most 2.5 per cent semi-span, see Fig. 8.28c. This shift is small, presumably in line with the asymptotic theory used to derive Eq. (8.41a), but does not help much to arrive at a computed separation position that agrees more satisfactorily with experimental data.
This finding contrasts with the result in Fiddes-1980 where for the case of the separation from a 5-deg cone a large shift was found and correlation with experiment was remarkably good. Unfortunately subsequent inspection of the Fiddes' analysis revealed that a factor 4 is missing, reducing the shift by this same factor and destroying the earlier found excellent correlation with experiment, but bringing the result in Fiddes-1980 in line with the one for the present case.

*In case of turbulent flow the "weak-interaction" model does not result in a satisfactory match between* predicted and assumed locations of secondary separation either, see de Bruin & Hoeijmakers-1986. For the case of turbulent flow an asymptotic formulation has not been developed.

So in conclusion, predicting secondary separation location will require more elaborate models of the viscous-inviscid interaction than employed here.

8.6.14 Separated flow from a slender circular cone

In this section we turn to another interesting feature of the present nonlinear flow problem: the possibility of multiple solutions.

We study the flow about a slender circular cone, with prescribed separation lines. The specific case chosen is the cone with semi-vertex angle of 10 deg at 30 deg incidence with prescribed separation at $\theta$=120 and $\theta$=220 deg, where $\theta$=0 denotes the bottom of the cone. Geometrically this configuration is symmetric with

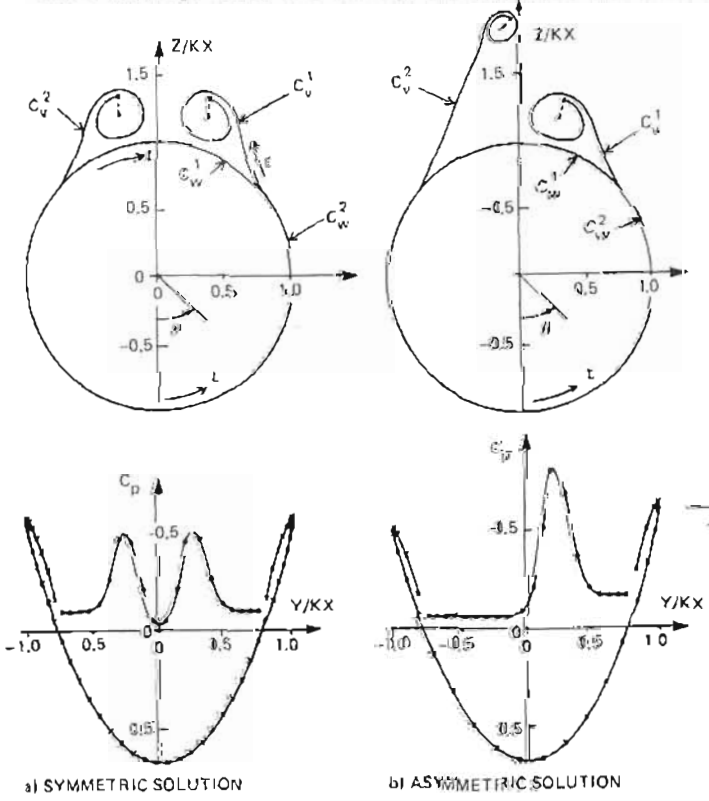


Fig. 8.30a Solutions for 10-deg cone at 30 deg incidence

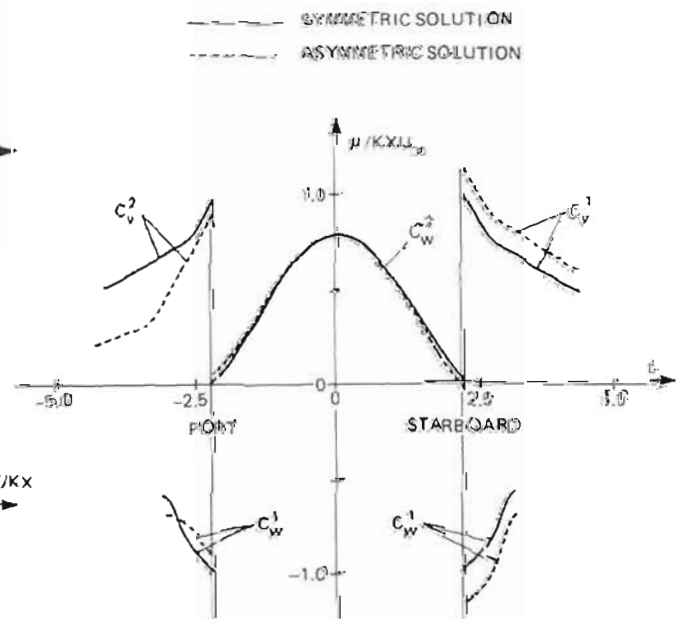


Fig. 8.30b Doublet distribution for 10 deg cone at 30 deg incidence

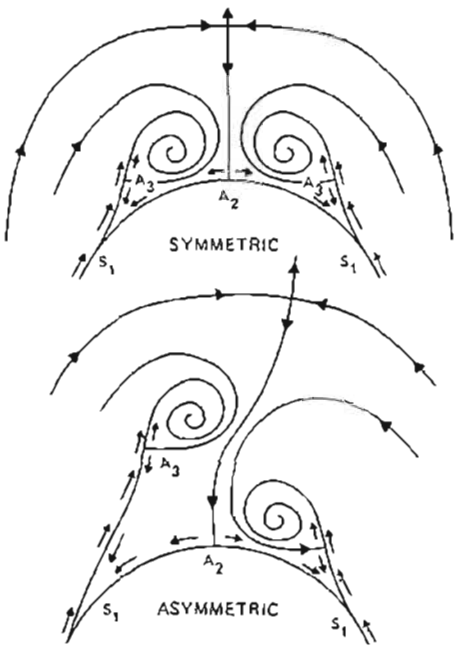


Fig. 8.30c Sketch of possible flow topology flow about slender cone

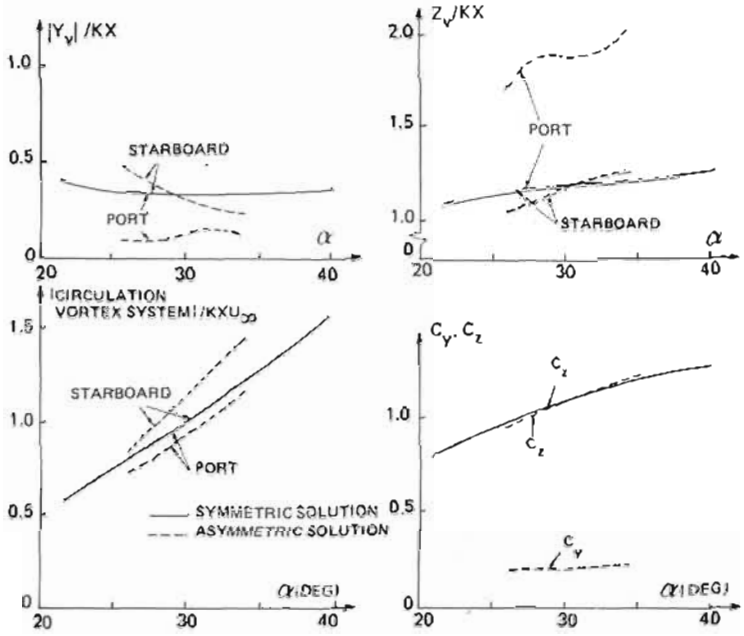


Fig. 8.30d Solutions for flow about slender cone at high angle of attack

respect to the y=0 plane. However, since we will search for asymmetric solutions no symmetry was assumed in the present computations and both starboard and portside were panelled.

Fig. 8.30a shows the solutions found for 30 deg incidence, one symmetric and one asymmetric solution. The mirror-image of the latter solution is of course also a valid solution.

The cone is subdivided into 2 segments, $C_w^1$ is the upper part between the two separation points spanning 80 deg, $C_w^2$ is the lower part of the cone spanning 280 deg. These two segments with the composite singularity distribution and the Dirichlet boundary condition are subdivided into panels as indicated in Table 8.5.

| | SYMMETRIC | | | | ASYMMETRIC | | | |
|---|---|---|---|---|---|---|---|---|
| | PANELS | b | $y_v$ | $z_v$ | PANELS | b | $y_v$ | $z_v$ |
| $C_w^1$ | 20 | 1.745 | - | - | 20 | 1.745 | - | - |
| $C_w^2$ | 52 | 4.538 | - | - | 26 | 4.538 | - | - |
| $C_v^1$ | 20 | 2.0 | 0.334 | 1.181 | 30 | 2.0 | 0.299 | 1.175 |
| $C_v^2$ | 20 | 2.0 | -0.334 | 1.181 | 45 | 2.25 | -0.111 | 1.850 |
| | $C_y$=0.0 , $C_z$ = 1.088 | | | | $C_y$=0.194 , $C_z$ = 1.098 | | | |

Table 8.5 Multiple solutions for 10 deg cone at 30 deg incidence

The symmetric solution was obtained by starting with short sheets and extending them panel by panel using one of the continuation procedures described before. The asymmetric solution gave more problems. The solution for short sheets was easily obtained by choosing the position of the vortex filament in a rather asymmetric manner. However, extending the port-side sheet to a length such that it loops around the filament using the standard procedure of panel by panel extension was not successful: the last one or two panels of the vortex sheet had a strong tendency to curve inwards, i.e. to roll-up before winding around the vortex core. The procedure that did work very nicely is the one in which the solution for $b=b_1$, and NPV vortex sheet panels is taken as initial solution for the case for which $b=b_1+\Delta b$ and NPV+1 vortex sheet panels. Once the end of the port-side vortex sheet was close to the position of the vortex filament and started to loop around it the automatic procedure of panel by panel extension could be used again.

Fig. 30a and b show the final result of the computation. There is a large difference between the two solutions, especially in the geometry and the doublet distribution of the port-side vortex sheet, as well as the doublet and pressure distribution on $C_w^1$, the upper surface. The doublet and pressure distribution on $C_w^2$, the lower surface is not much different for the symmetric and asymmetric case. Although the pressure distribution on the cone is so different the normal force is about the same, in the asymmetric case almost entirely produced by the starboard vortex. Comparison of the symmetric and asymmetric solution (see Fig. 30b) shows that the vortex sheet that moves away from the cone becomes weaker, while the one that stays near the cone becomes stronger. In Fig. 8.30c a sketch is presented of a possible flow topology for the two cases, as derived from the computed conical cross-flow plane component of the velocity on $C_w$ and $C_v$. Clearly the topology becomes rather complex.

The problems we encountered for the asymmetric solution with the port-side vortex sheet appear to be associated with the circumstance that the relatively long first part of this vorrex sheet is almost straight (Fig. 8.30a) and of uniform strength (Fig. 8.30b) which makes it susceptable to the Kelvin-Helmholtz instability. It also suggests that still another solution is possible, one in which a third (double-branched) vortex core is embedded within the port-side vortex sheet.

The variation with incidence of the position of the vortices, the circulation of the vortex systems and the normal and lateral forces are shown in Fig. 8.30d. Symmetric solutions have been obtained for incidences from 21.5 to 40 deg. Asymmetric solutions for incidences from 26 to 34 deg. In the present study it was not attempted to explore branching points or other interesting features of the space of possible solutions.

For the case of the 10 deg cone at 30 deg incidence the symmetric and asymmetric solutions obtained here using the panel method in the physical plane are quite similar to the solutions obtained by Fiddes & Smith-1982 using a succession of several conformal transformations followed by a panel-method type of approach to solve for the position and strength of the vortex sheets within the transformed plane.

8.6.15 Double-delta wing

Each of the preceding applications is a case of conical flow, the following two applications concern the flow about non-conical configurations. In this section a relatively slender double-delta is considered. The sweep of the leading edge is 84.3 deg and 68.2 deg for the forward and aft half of the wing respectively. The root chord is taken as 20 so that at the kink in the leading edge the semi span is 1.0 and at the trailing edge the semi span equals 5.0. The incidence is chosen as 10.3 deg.

The solution for this case was obtained by first computing the solution at the mid-chord position, i.e. at x=10.0. At this station the wing was discretized in 20 panels and the vortex sheet, which had a length of 2.5 times the local semi span, in 50 panels. Subsequently the solution was marched in downstream direction, keeping the discretization the same and adjusting the sheet length such that the feeding sheet has about the same attitude at each station. A total of 21 stations (x=10.0, 10.0625, 10.125, 10.25, 10.5(0.5)13.5, 13.75(0.25)14.5, 15.0(1.0)20.0) was considered. Near the kink small steps in x-direction were necessary for convergence, further downstream larger steps could be taken.

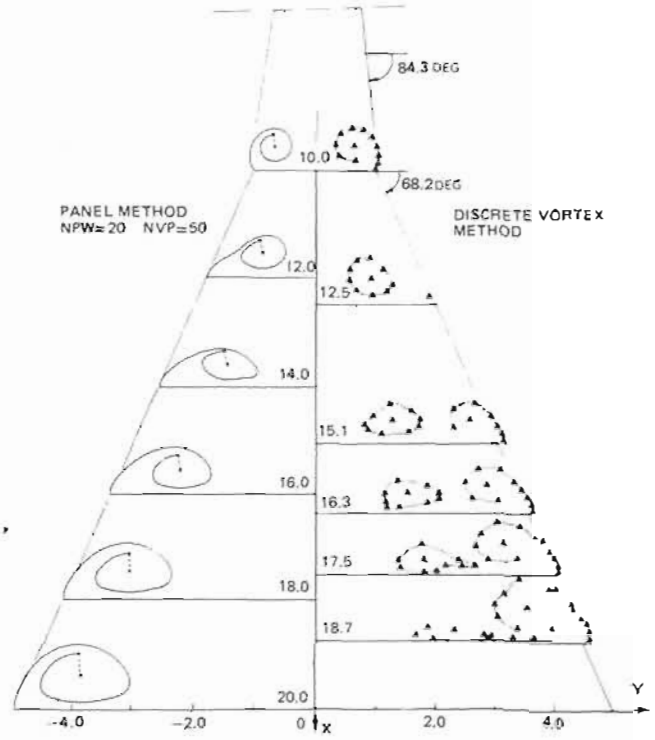


Fig. 8.31 Computed vortex sheet geometry for double-delta wing. Comparison of present panel method and discrete vortex method of Peace-1983, $\alpha$=10.3 deg

*In Fig. 8.31 the present solution is compared* with the discrete-vortex method of Peace-1983. In Peace's solution two distinct centers of roll up evolve and instabilities set in before the trailing edge is reached. In the present panel method solution the kink in the leading edge results in a dent (portion of the vortex sheet with curvature of opposite sign) travelling along the vortex sheet towards the vortex core. The dent, designated here as the "kink vortex", is most easily identified as that point $t_{KV}$ on the vortex sheet where the doublet strength equals the value of the doublet distribution at the kink, i.e. for which $\mu^2(t^2_{KV};x) = \mu^2(t^2;x=10)$.
Just downstream of x=16 the "kink vortex" reaches the feeding sheet and is amalgamated into the primary vortex. A similar process occurs in reality on slender double-delta wings like the present one (see Chapter 2), where at the kink a double-branched vortex forms within the shear layer emanating from the leading edge. The double-branched vortex also travels along the layer to finally merge with the primary core.

It appears that Peace's double vortex system is caused by the numerical procedure used, specifically immediately downstream of the kink the shedding of new vortices had to be halted for some distance because of numerical reasons.

The present solution is considered in some more detail in Figs. 8.32a-b. *In Fig. 8.32a the cross-sections of the vortex sheet at the 21 stations computed have been combined into one plot. Also the 21 span-*wise pressure distributions are combined into one figure. The streamwise development of the solution visualized in this way shows the transition from the high-sweep solution at the kink, where the vortex system is relatively large and effects most of the flow across the span, to the lower-sweep solution further downstream where the spatial extent of the vortex system is relatively smaller but the suction peak higher.

Fig. 8.32b depicts the vertical and horizontal coordinates of the leading-edge and the kink vortex, the total circulation of the vortex system $\mu^2(t^2_0;x)$ and the strength $\mu^2(t^2_e;x)$ of the vortex filament, all as a function of x.
The figure shows that the primary effect of the kink on the vortex core is that it bends downward relatively abruptly while at the same time it slowly drifts in outboard direction. Further downstream the primary vortex core is on a trajectory that is almost parallel to the leading edge and at an angle of about $\alpha/3$ in the vertical plane. Immediately downstream of the kink the growth rate of the circulation increases sharply, corresponding to the higher shedding rate of vorticity at a wing of lower sweep. However, it takes some time before the primary vortex core which grows in strength due to amalgamation starts to grow in strength at a faster rate.

Finally note that the computation has not proceeded to a station sufficiently downstream to see whether the solution is expected to become conical, refined to some fictitious apex, again.

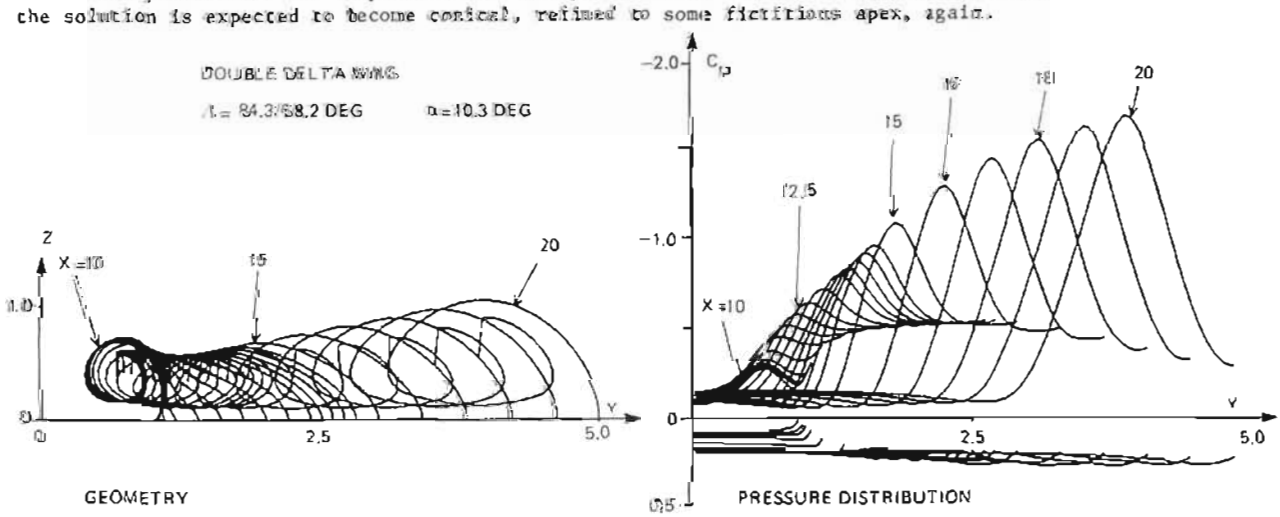


Fig. 8.32a Solution for 84.3/68.2 double delta wing, $\alpha$=10.3 deg

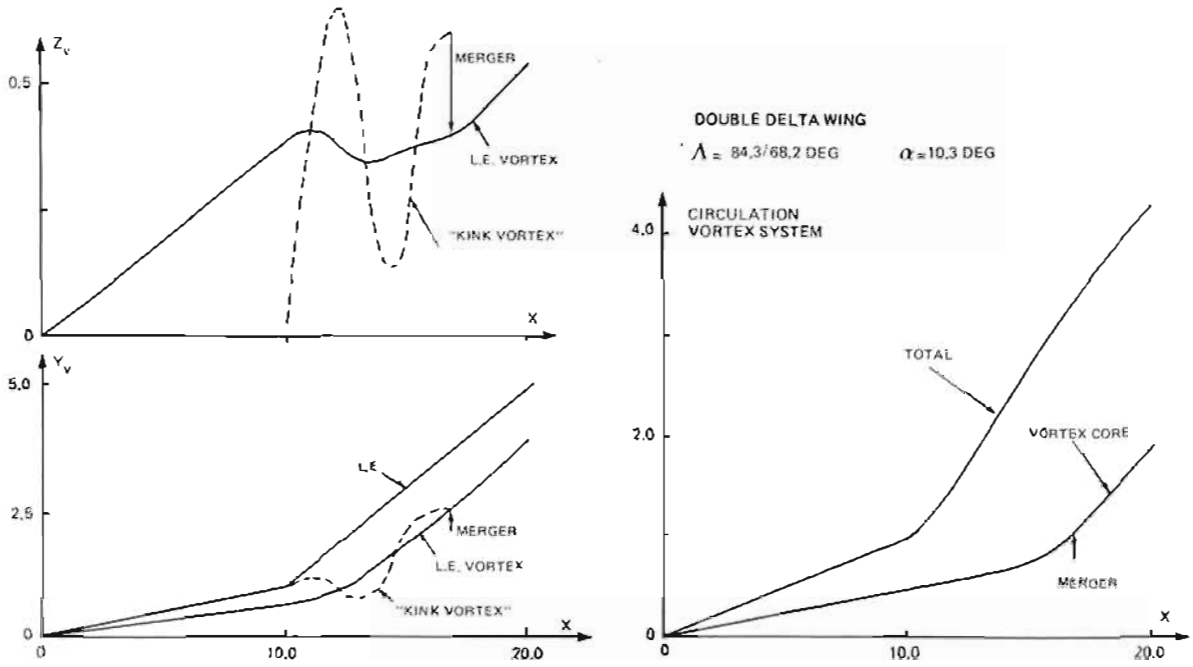


Fig. 8.32b Streamwise development of solution on double delta wing

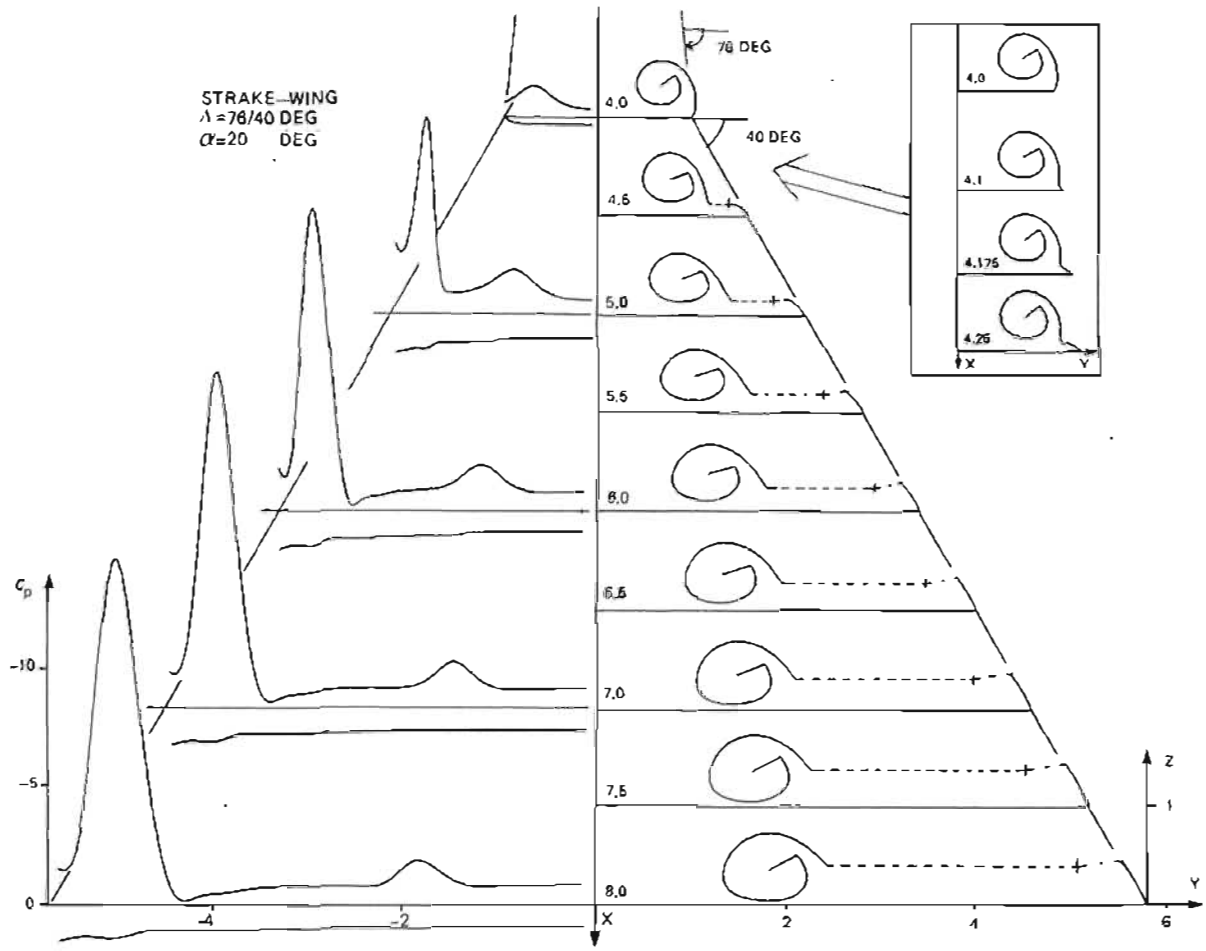


Fig. 8.33a Solution for 76/40 strake-wing configuration at 20 deg incidence

8.6.16 Strake-wing configuration

In case the discontinuity in the sweep of the leading edge is relatively large and the angle of attack is not too large the vortex originating at the kink will not merge with the vortex originating at the apex of the double-delta wing. In general this is the case for strake-wing configurations for which the sweep of the wing usually does not exceed 50 to 55 deg. In this section we consider the case in which the strake has a sweep of 76 deg and the wing a sweep of 40 deg. The junction of the strake and the wing is at 50 per cent root chord which was taken as 8.0. The incidence chosen is 20 deg, which is assumed to be sufficiently high to provoke flow separation from the leading edge of both the strake and the wing.

The solution is started at the 50 per cent chord station x=4.0 with the conical solution of the unit-aspect ratio wing at 20 deg incidence, the solution discussed extensively in a number of preceding sub-sections. This solution, obtained with 20 panels on the wing and 40 panels on the leading-edge vortex sheet (b=2.0), was then employed to march in downstream direction. In this process the panelling was kept the same but the length of the vortex sheet was increased such that the attitude of the feeding sheet did not change very much.

The stations considered were x=4.0, 4.025, 4.05, 4.1, 4.15, 4.175, 4.20 and 4.25. At these 8 stations the solution could be obtained without much difficulty. For the underlined stations the computed geometry of the vortex sheet is included in Fig. 8.33a. It shows that the vortex sheet becomes severely indented, evidence of the "kink" vortex, here designated as "wing vortex". Attempts to march the solution further downstream employing one vortex sheet segment to model the vortex system failed.
Hereupon the leading-edge vortex sheet segment at x=4.25 of length 2.25 was split into two segments linked together through the double-branched wing vortex. The first segment has a length of 0.2 and is discretized by 4 panels, the second segment of length 2.0 is subdivided into 40 panels, while the double-branched vortex is positioned at the center of vorticity of the cut-off part with the second branch at about -90 deg.

Using this solution at x=4.25 as initial solution the solution could be obtained without much difficulty at x=4.3, 4.4, 4.5, 4.75, 5.0(0.5)8.0. The resulting shape of the leading-edge vortex system is included in Fig. 8.33a. Note that at each station the length of the vortex sheet was chosen such that the attitude of the (first branch of the) vortex core stayed about same.

Fig. 8.33 shows that downstream of 50 per cent root chord the "strake vortex" continues its path on a trajectory close to the upper wing surface. The "wing vortex" which builds up in strength very rapidly, is relatively close to the leading-edge and the upper wing surface, so that strake and wing vortex move apart quickly and merging of the two vortex systems is not very likely.

In Fig. 8.33a the geometry of the leading-edge vortex system and the spanwise pressure distribution are shown. The pressure distribution on the upper wing surface develops a double suction peak. The first suction peak, induced by the strake vortex, moves with the vortex in outboard direction while its height remains approximately constant at a value near 2.0. The second suction peak is due to the double-branched wing vortex, and moves with this vortex in outboard direction. The height of this second suction peak increases very rapidly to values of $c_p$ of the order of -15. It may be expected that here secondary separation will have a tremendous effect on the solution.
Fig. 8.33b gives some of the global characteristics of the solution as the trajectory of the vortices and the circulation of the vortex system. The latter shows that downstream of the discontinuity in the sweep angle of the leading edge the circulation of the vortex system grows very rapidly, specifically the strength of the wing vortex. The strength of the strake vortex continues to grow at a much slower rate, it only being fed by the vorticity contained within the vortex sheet between the wing vortex core and the strake vortex core. As an example, at x=4.0, i.e. at the kink, about 55 per cent of the circulation resides in the strake vortex core and 45 per cent in the vortex sheet. At x=6.0 the vortex sheet connected to the leading edge, the wing vortex, the vortex sheet connecting wing and strake vortex and the strake vortex core account for about 7.5, 62.5, 6 and 24 per cent of the total circulation, respectively. This shows the enormous increase in the circulation due to shedding of vorticity from the wing leading edge and the amalgamation of vorticity into the strake vortex core. At x=8.0 the breakdown into the four contributions in the circulation is 7, 74.5, 1 and 17.5 per cent, respectively.

The latter indicates that the vortex sheet connecting wing and strake vortex has become very weak and viscous effects may have a large effect. Furthermore, in the real 3D flow the very strong vortex will be subject to a large adverse pressure gradient near the trailing edge and be perceptive to vortex breakdown, as experimental data Verhaagen-1983 indicates.

Finally it must be remarked that the correctness of the topology of the vortex system as chosen here is debatable. In the computational results discussed above the attitude of the second branch of the feeding sheet of the wing vortex was held fixed at the -90 deg position, resulting on a rather long feeding sheet. No attempt has been undertaken to improve the model by choosing for example an attitude of 0 deg (the "six o'clock position"), but it may be expected that the resulting (weak) vortex sheet will be very close to the wing surface which probably invalidates the inviscid vortex sheet model. Perhaps that, at least on the aft portion of the wing, a topology with disjoint strake and wing vortex systems, as briefly discussed in Chapter 2, is to be preferred.

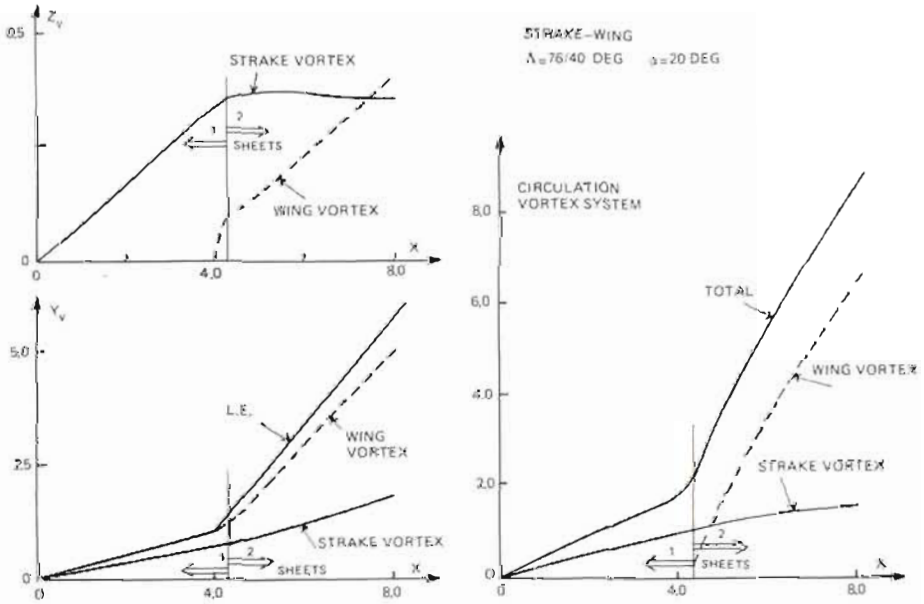


Fig. 8.33b Streamwise development of solution on strake wing

# 9 METHOD FOR THREE-DIMENSIONAL LEADING-EDGE VORTEX FLOW ABOUT THIN WINGS

## 9.1 Introduction

In this chapter we describe a method for computing the three-dimensional flow about wings with leading-edge vortex sheets. The mathematical model of the flow is the potential flow model derived in chapter 3, see Fig. 9.1. The general formulation of the solution has been discussed in section 5.1.

The method is aimed at computing the flow about thin pointed delta-like wings of symmetric planform in symmetric flow. Both the leading and the trailing edge of the wing may be curved, the side edge of the wing should form a smooth continuation of the leading edge. It is assumed that the flow separates along the entire length of the leading edge and of course along the trailing edge.
The geometry consists of the thin wing, the leading-edge vortex sheet with the vortex-filament/feeding-sheet vortex core model, the "near-wake" vortex sheet immediately downstream of the trailing edge and the "far-wake" vortex sheet. The latter forms the continuation to downstream infinity of the near wake.

The wing and the vortex sheets are modeled by a doublet distribution, the strength of which is zero at the apex, constant in the plane x=constant on the feeding-sheet and constant in x-direction on the far wake.

The problem is solved on a rectangular computational domain in which the wing, leading-edge, near-wake and far-wake vortex sheets correspond to rectangular sub-domains. The transformation from the physical space to the computational domain is described in section 9.2. In the third section of this chapter we describe the second-order panel method used to compute the velocity field. The discrete form of boundary conditions and the auxiliary conditions are discussed in section 9.4. The resulting system of nonlinear equations is solved using a quasi-Newton iterative procedure which is discussed in section 9.5.
In the final section of this chapter the application of for the method to a number of wings is discussed.

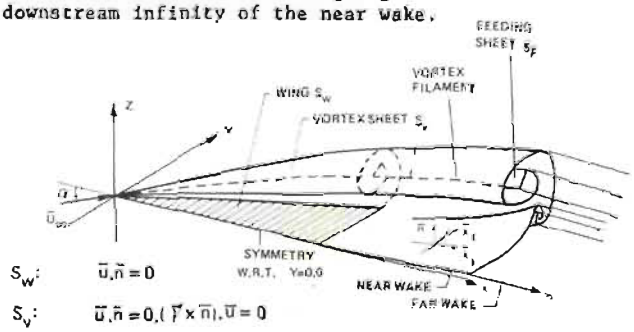


$S_W$: $\bar{u}.\bar{n} = 0$

$S_v$: $\bar{u}.\bar{n} = 0, (\bar{l} \times \bar{n}).\bar{u} = 0$

$\partial S_W$: KUTTA CONDITION

CORE: FORCE FREE $\quad \Phi_{xx} + \Phi_{yy} + \Phi_{zz} \neq 0$

$x \to -\infty$: $\bar{u} \to \bar{U}_\infty$

Fig. 9.1 Three-dimensional potential flow model flow about delta-like wings in symmetric flow

## 9.2 Transformation to a rectangular computational domain

In a higher-order panel method the variation of the geometry of and singularity distribution on a panel involves information from neighboring panels. This can be accounted for in physical space by using local (panel by panel) transformations and least-squares type of fits of coordinates and singularity strength, all in terms of the local surface coordinates. However, in the present method we choose to express the three-dimensional surface formed by wing, leading-edge and near-wake vortex sheets in terms of (s,t) surface co-ordinates first. This transforms the problem to a rectangular computational domain. Upon subdivision of the rectangular domain into rectangular panels the panel-wise variation, in terms of the now globally defined surface coordinates, of the geometry and doublet distribution can be found from relatively simple finite-difference type of expressions.

The transformation of the three-dimensional surface in physical space to the rectangular computational domain hinges on the description of two curves: the projection onto the z=0 plane of the leading and of the trailing edge and their continuation onto the leading-edge and near-wake vortex sheet, see Fig. 9.2.

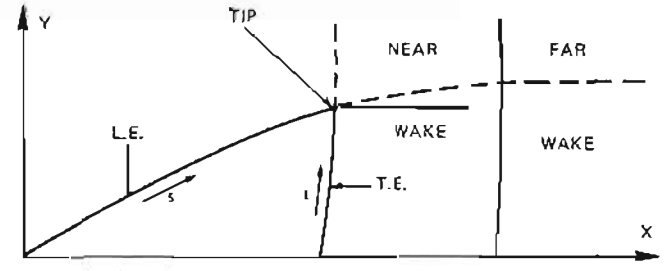


a) Projection of leading and trailing edge onto x-y plane

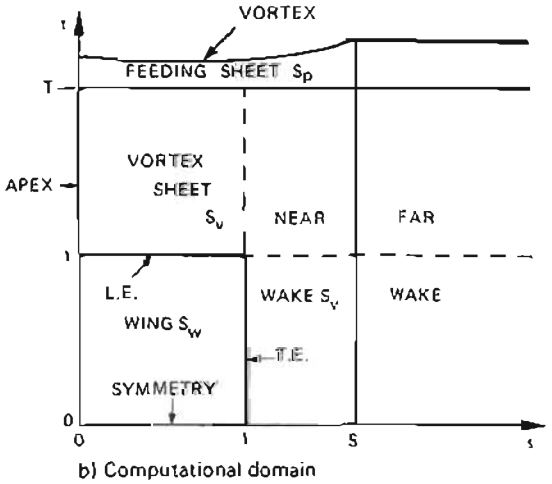


b) Computational domain

Fig. 9.2 Construction of computational domain

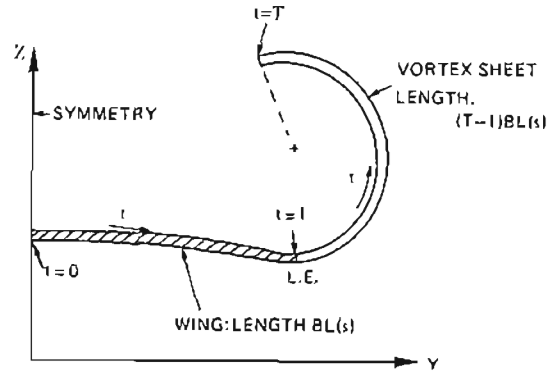


a) Wing and leading-edge vortex sheet (s < 1)

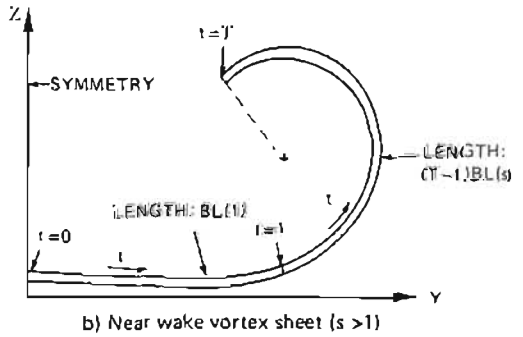


b) Near wake vortex sheet (s >1)

Fig. 9.3 The (3D) curve s=constant

The leading-edge and its continuation are represented parametrically by

$$\bar{x} = \bar{x}_L(s) = \begin{pmatrix} x_L(s) \\ y_L(s) \\ z_L(s) \end{pmatrix} \tag{9.1}$$

where s is a parameter along the leading edge, here taken as the normalized arc length, i.e. the arc length non-dimensionalized with the arc length from the apex to the trailing edge.

Similarly, the trailing edge and its continuation are represented parametrically as

$$\bar{x} = \bar{x}_T(t) = \begin{pmatrix} x_T(t) \\ y_T(t) \\ z_T(t) \end{pmatrix} \tag{9.2}$$

where t is a parameter along the trailing edge, here again taken as the normalized arc length, i.e. the arc length non-dimensionalized with the arc length from the plane of symmetry to the wing tip.

In general the position of the points located on a three-dimensional surface can be expressed as

$$\bar{x} = \bar{x}(s,t) = \begin{pmatrix} x(s,t) \\ y(s,t) \\ z(s,t) \end{pmatrix} \tag{9.3}$$

where s and t are curvi-linear surface coordinates. This representation is made complete by specification of two relations, i.e. the definition of s and t. Next we discuss the representation in terms of surface co-ordinates of the surface of the wing, leading-edge and near-wake vortex sheets.

For the geometric representation of the wing surface $S_w$ it is here assumed that it can be written as z=z(x,y), where z is a single-valued function of x and y. This implies that we may choose both x(s,t) and y(s,t) which then yields the unique value of z(s,t). On the wing we use:

$$\bar{x} = \bar{x}(s,t) = \begin{pmatrix} x_L(s)x_T(t)/c \\ y_L(s)y_T(t)/\frac{b}{2} \\ z(s,t) \end{pmatrix}, \quad (s,t)\in([0,1],[0,1]) \tag{9.4}$$

where $c=x_L(1) = x_T(1)$ and $\frac{b}{2} = y_L(1) = y_T(1)$. Here s and t are the parameters used in the description of the leading and trailing edge, respectively.

For the geometric representation of the vortex sheet $S_v$ we choose $\bar{x}(s,t)$ and the explicit definition of the parameter t, the parameter along the contour in the "cross-flow" plane. This results in:

$$\bar{x}=\bar{x}(s,t) = \begin{pmatrix} x_L(s)x_T(t)/c \\ y(s,t) \\ z(s,t) \end{pmatrix}, \tag{9.5}$$

where for the leading-edge vortex sheet $s\in[0,1]$ and $t\in[0,1]$ while for the near-wake vortex sheet $s\in[1,S]$ and $t\in[0,T]$. Here s is the parameter used to describe the leading edge and t is the normalized arc length in the "cross flow plane" s=constant, and well such that along the curve s=constant

$$\left|\frac{\partial}{\partial t}\bar{x}(s,t)\right| = b\ell(s) \tag{9.6}$$

where $b\ell(s)$ may be any given function of s. In the present method we choose $b\ell(s)$ for $s \leq 1$ as the total arc length along the curve s=constant on the wing surface and for $s > 1$ as $b\ell(1)$, see Fig. 9.3. The present description of the geometry implies that along s=constant the length of the vortex sheet is held fixed, while its shape will be free to adjust to the shape required to satisfy the boundary conditions.

The far-wake vortex sheet is defined by the contour $\bar{x}=\bar{x}(S,t)$ of the "trailing-edge" of the near wake and lines in planes y=constant, extending from $\bar{x}(S,t)$ to infinity downstream, along the direction of the near wake at s=S in the plane of symmetry (t=0).

$$\bar{x}=\bar{x}(s,t) = \begin{pmatrix} x(S,t) + (s-S)\cos\theta_S \\ y(S,t) \\ z(S,t) + (s-S)\sin\theta_S \end{pmatrix}, \quad \text{for } (s,t)\in([S,\infty],[0,T]) \tag{9.7}$$

where $\tan\theta_S = (\bar{e}_z.\bar{x}_s(S,0))/(\bar{e}_y.\bar{x}_s(S,0))$. This choice for the direction of the far wake appears to result in fewer problems near the junction of the near-wake and the far-wake than choosing $\theta_S$ equal to 0 or equal to $\alpha$.

The position of the vortex core is given by

$$\bar{x}=\bar{x}_v(s) = \begin{pmatrix} x_L(s)x_T(T)/c \\ y_v(s) \\ z_v(s) \end{pmatrix}, \quad \text{for } s\in[0,S] \tag{9.8a}$$

while for $s\in[S,\infty]$ the position of the vortex core in the far-wake region is defined by

$$\bar{x}=\bar{x}_v(s) = \begin{pmatrix} x_v(S) + (s-S)\cos\theta_S \\ y_v(S) \\ z_v(S) + (s-S)\sin\theta_S \end{pmatrix}, \quad s\in[S,\infty] \tag{9.8b}$$

The description of the geometry of the feeding sheet, given in Eq. (5.4c), follows directly from above expressions for $\bar{x}(s,t=T)$ of the vortex sheet and $\bar{x}_v(s)$ of the vortex core:

$$\bar{x}(s,t) = (1-t)\bar{x}(s,T) + t\bar{x}_v(s), \quad \text{for } (s,t)\in([0,\infty],[0,1]) \tag{9.9}$$

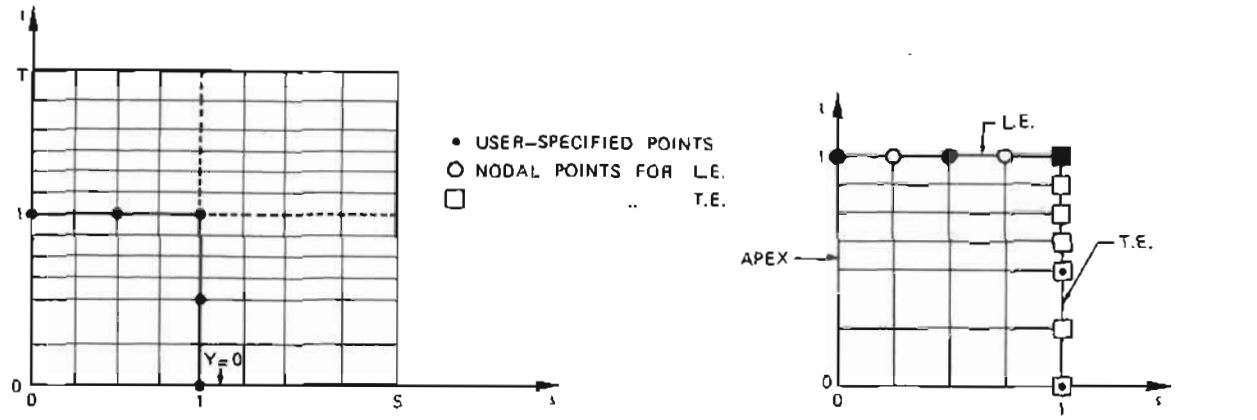


a) SUBDIVISION GEOMETRIC NETWORK TOTAL SURFACE

b) SUBDIVISION GEOMETRIC NETWORK WING SURFACE

Fig. 9.4 The geometric network

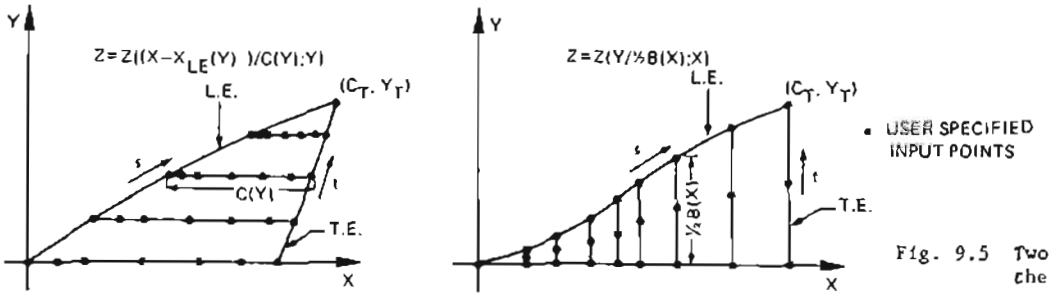


Fig. 9.5 Two ways to specify the wing surface

In the surface representations described above $x_L(s)$ and $y_L(s)$ for $s\in[0,S]$, i.e the projection of the leading-edge and its continuation on the x-y plane, are determined from the point-wise specification of the leading edge. The continuation is chosen as a straight line with specified slope. Similarly the functions $x_T(t)$ and $y_T(t)$ for $t\in[0,T]$ follow from the point-wise specification of the trailing edge and its continuation, here the straight line $x=c_T$.
Both the leading and the trailing edge are fitted by a cubic Hermite polynomial (H.P.) representation on the so-called geometric network (Fig. 9.4).

This geometric network is also used to express the wing surface as $z=z(s,t)$ in terms of a bi-cubic Hermite-polynomial representation (Fig. 9.4b). To this aim the wing surface is specified as a set of curves y=constant, each curve given as the value of z at the same set of percent-chord positions (Fig. 9.5), i.e. as:

$$z=z\{(x-x_L(y))/c(y);y\} \tag{9.10a}$$

which is also described in terms of bi-cubic Hermite polynomials. The bi-cubic representation of z in terms of s and t, which requires the value of $\frac{\partial z}{\partial s}$, $\frac{\partial z}{\partial t}$ and $\frac{\partial^2 z}{\partial s \partial t}$ at the nodal points of the geometric network, is then readily obtained.

In case the trailing edge is straight and unswept the wing surface may optionally be specified as a set of curves x=constant, each curve given as the value of z at the same set of local semi-span percentage positions (Fig. 9.5), i.e. as

$$z=z(y/\tfrac{b}{2}(x);x) \tag{9.10b}$$

also described in terms of bi-cubic Hermite polynomials.

The initial guess for the geometry of the leading-edge vortex sheet and the position of the vortex, i.e. the functions $y(s,t)$ and $z(s,t)$ for $s\in[0,1]$ in Eq. (9.5), is obtained from one given cross-section, scaled such that it fits the wing at all s-lines of the geometric network. Usually the coordinates used to specify the cross-section are derived from the solution obtained in the framework of the slender-body approximation (Chapter 8).

The initial guess for the geometry of the near-wake vortex sheet and vortex core is either obtained as the extrapolation of the wing surface and leading-edge vortex sheet or from a set of curves corresponding to the s-lines of the geometric network. The data required for the latter option is usually derived from the solution obtained within the framework of the time-dependent 2D analogy (Chapter 7).

The description (i.e definition) of the wing geometry and the initial guess of the leading-edge and near-wake vortex sheet geometry in terms of bi-cubic Hermite polynomials on the geometric network is now complete.

The potential flow problem, nonlinear in terms of the boundary conditions, is solved on a different network, the so-called aerodynamic network (Fig. 9.6). This network, obtained by subdividing the computational domain of Fig. 9.2 into rectangular panels, should be chosen such that both the doublet distribution $\mu(s,t)$ and the geometry $\underline{x}(s,t)$ are represented with an accuracy that is as uniform as possible over the whole computational domain. On the aerodynamic network the wing is subdivided into NUPW and NVPW panels in s- and t-direction respectively. The whole network consists of NUP and NVP panels in s-direction and t-direction, respectively. In addition we have: the far wake consisting of NVP semi-infinite panels; the feeding sheet with NUP (non-rectangular) elements and a semi-infinite far-wake extension; the vortex core built up out of NUP elements and its semi-infinite far-wake extension.

In the next section the second-order panel method used to compute the velocity field induced by the doublet distribution discretized on the aerodynamic network is described in detail.

## 9.3 Second-order panel method

### 9.3.1 Preliminaries

In this section we describe the second-order panel method used to compute the three-dimensional velocity field induced by the doublet distribution, i.e. see Eqs. (5.2c), (3.15b) and (9.9):

$$\bar{u}^{s}_{\mu}(\bar{x}_o) = \frac{1}{4\pi}\Big\{\int_{s=0}^{S}\Big\{\int_{t=0}^{T}(-\bar{x}_s\mu_t+\bar{x}_t\mu_s)\times\frac{\bar{r}}{|\bar{r}|^3}dt\Big\}ds\Big\}-\frac{1}{4\pi}\Big[\int_{s=S}^{\infty}\Big\{\int_{t=0}^{T}\bar{x}_s\mu_t(S,t)\times\frac{\bar{r}}{|\bar{r}|^3}dt\Big\}ds\Big]$$

$$+\frac{1}{4\pi}\Big[\int_{s=0}^{S}\Big\{\int_{t=0}^{1}\mu_s(s,T)(\bar{x}_v(s)-\bar{x}(s,T))\times\frac{\bar{r}_{FS}}{|\bar{r}_{FS}|^3}dt\Big\}ds\Big]$$

$$-\frac{1}{4\pi}\Big[\int_{s=0}^{S}\mu(s,T)\frac{\bar{r}_v}{|\bar{r}_v|^3}\times\bar{x}_{v_s}\,ds\Big]-\frac{1}{4\pi}\mu(S,T)\int_{s=S}^{\infty}\Big(\frac{\bar{r}_v}{|\bar{r}_v|^3}\times\bar{x}_{v_s}\Big)ds \qquad (9.11a)$$

where $\bar{r}=\bar{x}_o-\bar{x}(s,t)$, $\bar{r}_{FS}=\bar{x}_o-(1-t)\bar{x}(s,T)-t\bar{x}_v(s)$ and $\bar{r}_v=\bar{x}_o-\bar{x}_v(s)$. The above expression corresponds to the velocity induced at $\bar{x}_o$ by the doublet distribution on the starboard-side of configuration, the velocity induced by the port-side doublet distribution is simply, see Eq. (3.22b):

$$\bar{u}^{p}_{\mu}(\bar{x}_o) = [S]\bar{u}^{s}_{\mu}([S]\bar{x}_o) \qquad (9.11b)$$

where $[S]$ is the symmetry matrix defined in Eq. (3.22a). Here we will only discuss the discretization of Eq. (9.11a), the discretization of Eq. (9.11b) follows along identical lines.

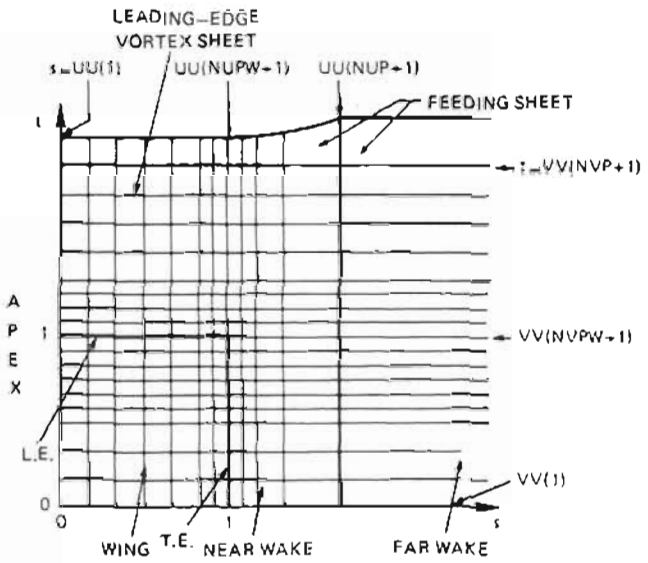


Fig. 9.6 The aerodynamic network

The first term in Eq. (9.11a) is the contribution due to the doublet distribution on the wing, leading-edge and near-wake vortex sheet. The second term is the contribution due to the far-wake vortex sheet. The third term is the one due to the doublet distribution, constant in t-direction, on the feeding sheet. The last two terms correspond to the contribution due to the vortex core.
In Eq. (9.11a) the integration with respect to $s$ is split into the integration from 0 to S and the integration over the far wake, i.e. $s=S$ to $\infty$. The latter integration can be carried out in closed form.

For the second integral in Eq. (9.11a) this results in

$$\frac{-1}{4\pi}\Big\{\int_{t=0}^{T}\mu_t(S,t)\frac{\bar{e}_{fw}\times(\bar{x}_o-\bar{x}(S,t))}{|\bar{e}_{fw}\times(\bar{x}_o-\bar{x}(S,t))|^2}\Big(1-\bar{e}_{fw}\cdot\frac{\bar{x}_o-\bar{x}(S,t)}{|\bar{x}_o-\bar{x}(S,t)|}\Big)dt\Big\} \qquad (9.11c)$$

where $\bar{e}_{fw}$ is the direction of the far wake, defined as $\bar{e}_x\cos\theta_s+\bar{e}_z\sin\theta_s$, as follows from Eq. (9.7).

The far-wake contribution of the feeding sheet is zero because $\mu_s\neq 0$ on the far wake, and was already omitted from Eq. (9.11a).

The far-wake part in the velocity induced by the vortex core, the last term in Eq. (9.11a), is upon carrying out the integration found to be:

$$\frac{-1}{4\pi}\mu(S,T)\frac{\bar{e}_{fw}\times(\bar{x}_o-\bar{x}_v(S))}{|\bar{e}_{fw}\times(\bar{x}_o-\bar{x}_v(S))|^2}\Big(1-\bar{e}_{fw}\cdot\frac{\bar{x}_o-\bar{x}_v(S)}{|\bar{x}_o-\bar{x}_v(S)|}\Big) \qquad (9.11d)$$

In the contribution due to the doublet distribution on the feeding sheet, i.e. the third term in Eq. (9.11a), the integration with respect to $t$ can be carried out in closed form, resulting in

$$\frac{-1}{4\pi}\int_{s=0}^{S}\mu_s(s,T)\frac{(\bar{x}_o-\bar{x}_v(s))\times(\bar{x}_o-\bar{x}(s,T))}{|(\bar{x}_o-\bar{x}_v(s))\times(\bar{x}_o-\bar{x}(s,T))|^2}(\bar{x}_v(s)-\bar{x}(s,T))\cdot\Big\{\frac{\bar{x}_o-\bar{x}(s,T)}{|\bar{x}_o-\bar{x}(s,T)|}-\frac{\bar{x}_o-\bar{x}_v(s)}{|\bar{x}_o-\bar{x}_v(s)|}\Big\}ds \qquad (9.11e)$$

The remaining integrals over the interval $s\in[0,S]$ in Eq. (9.11) are replaced by the sum of the integrals over the intervals $s\in[s_j,s_{j+1}]$, $j=1(1)NWP$. Similarly, the integrals over the interval $t\in[0,T]$ in Eq. (9.11) are replaced by the sum of the integrals over the intervals $t\in[t_j,t_{j+1}]$, $j=1(1)NWP$. This leads to the final 5-term expression:

$$\bar{u}^{s}_{\mu}(\bar{x}_o) = \frac{1}{4\pi}\sum_{i=1}^{NUP}\int_{s_i}^{s_{i+1}}\Big\{\sum_{j=1}^{NVP}\int_{t_j}^{t_{j+1}}(-\bar{x}_s\mu_t+\bar{x}_t\mu_s)\times\frac{\bar{x}_o-\bar{x}(s,t)}{|\bar{x}_o-\bar{x}(s,t)|^3}dt\Big)ds$$

$$-\frac{1}{4\pi}\sum_{j=1}^{NVP}\int_{t_j}^{t_{j+1}}\mu_t(S,t)\frac{\bar{e}_{fw}\times(\bar{x}_o-\bar{x}(S,t))}{|\bar{e}_{fw}\times(\bar{x}_o-\bar{x}(S,t))|^2}\Big(1-\bar{e}_{fw}\cdot\frac{\bar{x}_o-\bar{x}(S,t)}{|\bar{x}_o-\bar{x}(S,t)|}\Big)dt$$

$$-\frac{1}{4\pi}\sum_{i=1}^{NUP}\int_{s_i}^{s_{i+1}}\mu_s(s,T)\frac{(\bar{x}_o-\bar{x}_v(s))\times(\bar{x}_o-\bar{x}(s,T))}{|(\bar{x}_o-\bar{x}_v(s))\times(\bar{x}_o-\bar{x}(s,T))|^2}(\bar{x}_v(s)-\bar{x}(s,T))\cdot\Big\{\frac{\bar{x}_o-\bar{x}(s,T)}{|\bar{x}_o-\bar{x}(s,T)|}-\frac{\bar{x}_o-\bar{x}_v(s)}{|\bar{x}_o-\bar{x}_v(s)|}\Big\}ds$$

$$-\frac{1}{4\pi}\sum_{i=1}^{NUP}\int_{s_i}^{s_{i+1}}\mu(s,T)\frac{\bar{x}_o-\bar{x}_v(s)}{|\bar{x}_o-\bar{x}_v(s)|^3}\times\bar{x}_{v_s}(s)ds$$

$$+\frac{1}{4\pi}\mu(S,T)\frac{\bar{e}_{fw}\times(\bar{x}_o-\bar{x}_v(S))}{|\bar{e}_{fw}\times(\bar{x}_o-\bar{x}_v(S))|^2}\Big(1-\bar{e}_{fw}\cdot\frac{\bar{x}_o-\bar{x}_v(S)}{|\bar{x}_o-\bar{x}_v(S)|}\Big) \qquad (9.12)$$

9.3.2 Small-curvature expansion for the surface integrals

The integrals that appear in Eq. (9.12) are singular and require special care for points $\bar{x}_o$ near the distribution. Here we use, once more, the small-curvature expansion to arrive at integrals that can be determined analytically and possess the correct behaviour, especially with respect to discontinuities, for points $\bar{x}_o$ near or on the distribtuion.

For $s\in[s_i,s_{i+1}]$ and $t\in[t_j,t_{j+1}]$, the position vector on the surface, the position vector of the vortex and the doublet distribution are expanded as

$$\bar{x}(s,t) = \bar{x}^* + \Delta s\bar{x}^*_s + \Delta t\bar{x}^*_t + \tfrac{1}{2}\Delta s^2\bar{x}^*_{ss} + \Delta s\Delta t\bar{x}^*_{st} + \tfrac{1}{2}\Delta t^2\bar{x}^*_{tt} + O(\delta^3) \qquad (9.13a)$$

$$\bar{x}_v(s) = \bar{x}^*_v + \Delta s\bar{x}^*_{v_s} + \tfrac{1}{2}\Delta s^2\bar{x}^*_{v_{ss}} + O(\delta^3) \qquad (9.13b)$$

$$\mu(s,t) = \mu^* + \Delta s\mu^*_s + \Delta t\mu^*_t + \tfrac{1}{2}\Delta s^2\mu^*_{ss} + \Delta s\Delta t\mu^*_{st} + \tfrac{1}{2}\Delta t^2\mu^*_{tt} + O(\delta^3) \qquad (9.13c)$$

with $\Delta s=s-s^*_i$, $\Delta t=t-t^*_j$ (9.13d)

where $s^*_i=\frac{1}{2}(s_i+s_{i+1})$, for i=1(1)NUP and $t^*_j=\frac{1}{2}(t_j+t_{j+1})$, for j=1(1)NVP, while $\bar{x}^*,\bar{x}^*_s,\bar{x}^*_t,\bar{x}^*_{ss},\bar{x}^*_{st}$ and $\bar{x}^*_{tt}$ denote the value of $\bar{x},\bar{x}_s,\bar{x}_t,\bar{x}_{ss},\bar{x}_{st}$ and $\bar{x}_{tt}$ at the panel midpoint $(s^*_i,t^*_j)$, respectively. Similarly $\mu^*$, $\mu^*_s$, etc. denote the value of $\mu$, $\mu_s$ etc. at the panel midpoint, while $\bar{x}^*_v$, $\bar{x}^*_{v_s}$ and $\bar{x}^*_{v_{ss}}$ denote the value of $\bar{x}_v(s^*_i)$, $\bar{x}_{v_s}(s^*_i)$ and $\bar{x}_{v_{ss}}(s^*_i)$ respectively.

Now we can write the distance vector $\bar{r}$ as (Fig. 9.7):

$$\bar{r} = \bar{r}_f - \bar{r}_2 + O(\delta^3) \qquad (9.14a)$$

where

$$\bar{r}_f=\bar{x}_o-\bar{x}^* - \Delta s\bar{x}^*_s-\Delta t\bar{x}^*_t \qquad (9.14b)$$

$$\bar{r}_2=\tfrac{1}{2}\Delta s^2\bar{x}^*_{ss} + \Delta s\Delta t\bar{x}^*_{st} + \tfrac{1}{2}\Delta t^2\bar{x}^*_{tt} \qquad (9.14c)$$

In Eq. (9.14) $\bar{r}_f$ denotes the vector from $\bar{x}_o$ to the tangent plane defined by the vector $\bar{x}^*_s$ along the curve $t=t^*_j$ and the vector $\bar{x}^*_t$ along the curve $s=s^*_i$. The vector $\bar{r}_2$, assumed to be of order $\delta^2$, contains the curvature and twist of the panel, in general it is not perpendicular to the tangent plane. Substitution of Eqs. (9.13a and c) and (9.14) into the first term of Eq. (9.12) results in

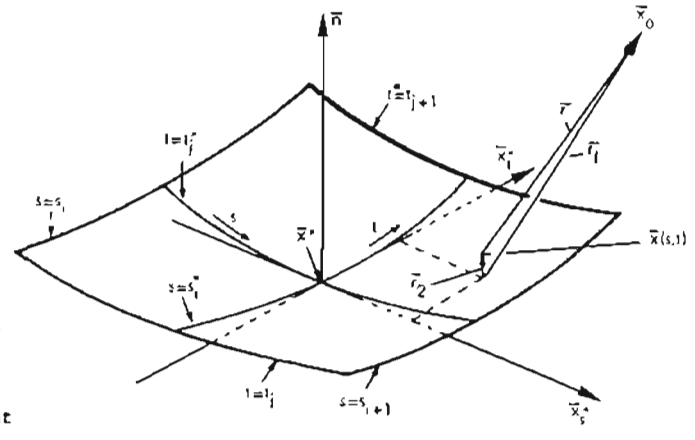


Fig. 9.7 Small-curvature expansion for surface panel

$$\bar{u}^{(1)}_{\mu}(\bar{x}_o) = \frac{1}{4\pi}\sum_{i=1}^{NUP}\sum_{j=1}^{NVP}\Big[\Delta s\mu^*_s(\bar{E}_{10}+\bar{E}^c_{10}) + \mu^*_t(\bar{E}_{01}+\bar{E}^c_{01}) + \mu^*_{ss}\bar{E}_{20}+\mu^*_{st}\bar{E}_{11}+\mu^*_{tt}\bar{E}_{02} + O\Big(\delta^2\frac{\delta^2}{D^2}\Big)\Big)\Big] \qquad (9.15a)$$

where

$$\bar{E}_{10} = \bar{x}_t^* \times \bar{I}_{00} \tag{9.15b}$$

$$\bar{E}_{10}^c = \bar{x}_{st}^* \times \bar{I}_{10} + \bar{x}_{tt}^* \times \bar{I}_{01} - \bar{x}_t^* \times \bar{I}_c \tag{9.15c}$$

$$\bar{E}_{01} = -\bar{x}_s^* \times \bar{I}_{00} \tag{9.15d}$$

$$\bar{E}_{01}^c = -\bar{x}_{ss}^* \times \bar{I}_{10} - \bar{x}_{st}^* \times \bar{I}_{01} + \bar{x}_s^* \times \bar{I}_c \tag{9.15e}$$

$$\bar{E}_{20} = \bar{x}_t^* \times \bar{I}_{10} \tag{9.15f}$$

$$\bar{E}_{11} = -\bar{x}_s^* \times \bar{I}_{10} + \bar{x}_t^* \times \bar{I}_{01} \tag{9.15g}$$

$$\bar{E}_{02} = -\bar{x}_s^* \times \bar{I}_{01} \tag{9.15h}$$

and

$$\bar{I}_{k\ell} = \int_{s_i}^{s_{i+1}} \int_{t_j}^{t_{j+1}} (\Delta s^k \Delta t^\ell) \frac{\bar{r}_f}{|\bar{r}_f|^3} ds dt; \quad k\ell = 00,\ 10 \text{ or } 01 \tag{9.15i}$$

$$\bar{I}_c = \int_{s_i}^{s_{i+1}} \int_{t_j}^{t_{j+1}} [\frac{\bar{r}_2}{|\bar{r}_f|^3} - 3(\bar{r}_2 \cdot \bar{r}_f) \frac{\bar{r}_f}{|\bar{r}_f|^5}] ds dt \tag{9.15j}$$

Here $\delta$ is a measure of the average panel width and D is $\delta$ in the near field and the order of $|\bar{x} - \bar{x}^*|$ otherwise. This implies that the composite error in Eq. (9.15a) will be of order $\delta^2$. In Eq. (9.15) $\bar{E}_{10}$ and $\bar{E}_{01}$ are both of order $\delta^2/D^2$, i.e. of order 1, all further terms are of order $\delta\delta^2/D^2$, where $\bar{E}_{10}^c$ and $\bar{E}_{01}^c$ involve the second derivatives with respect to s and t of $\bar{x}(s,t)$. The integrals appearing in Eqs. (9.15i-j) can be determined in closed form, see Appendix F, sections 1 and 2, for the details.

From Appendix F, third section, it follows that the velocity induced by a panel at its own midpoint, which is also the main contribution to the summation in Eq. (9.15a), can be written as

$$\bar{u}_{\mu_{ij}}^{(1)}(\bar{x}^*) = \frac{1}{2}\{\frac{\mu_s^* \bar{x}_t^* - \mu_t^* \bar{x}_s^*}{|\bar{x}_s^*||\bar{x}_t^*|} \times \bar{e}_n\} \text{sign}(\zeta)$$

$$- \frac{1}{4\pi} \frac{|\bar{x}_s^* \times \bar{x}_t^*|}{|\bar{x}_s^*||\bar{x}_t^*|} \{\frac{\mu_{ss}^*}{|\bar{x}_s^*|^2} h_2 - \frac{\mu_{st}^*}{|\bar{x}_s^*||\bar{x}_t^*|}(h_2 + h_4) + \frac{\mu_{tt}^*}{|\bar{x}_t^*|^2} h_3\} \bar{e}_n \tag{9.15k}$$

where all * quantities are to be evaluated at $(s_i^*, t_j^*)$, and we left out the curvature terms. Eq. (9.15k) shows that the first derivatives of $\mu$ contribute to the first term, which is tangential to the panel and changes sign across the panel. We used the latter property already earlier in the general formulation. The second term in Eq. (9.15k), of order $\delta$, is in normal direction and involves the second derivatives of the doublet distribution.

9.3.3 Small-curvature expansion for the far-wake integrals

The second term in Eq. (9.12) constitutes the contribution due to the far wake. Its expansion for small curvature is obtained as a special case of Eq. (9.15), i.e. because $\mu(s,t) = \mu(S,t_j^*) + \Delta t \mu_t(S,t_j^*) + \frac{1}{2}\Delta t^2 \mu_{tt}(S,t_j^*) + O(\delta^3)$:

$$\bar{u}_\mu^{(2)}(\bar{x}_o) = \frac{1}{4\pi} \sum_{j=1}^{NVP} \{\mu_t(S,t_j^*)(\bar{E}_{01w} + \bar{E}_{01w}^c) + \mu_{tt}(S,t_j^*)\bar{E}_{02w}\} + O(\delta^2) \tag{9.16a}$$

where $\bar{E}_{01w}$, $\bar{E}_{01w}^c$ and $\bar{E}_{02w}$ follow from $\bar{E}_{01}$, $\bar{E}_{01}^c$ and $\bar{E}_{02}$ defined in Eq. (9.15) and worked out in Appendix F where:

$$s_1 = s_1^* = S, \quad s_{i+1} = \infty \tag{9.16b}$$

$$\bar{e}_s = \bar{x}_s^* = \bar{e}_{fw} \tag{9.16c}$$

$$\bar{x}_{ss}^* = \bar{x}_{st}^* = 0 \tag{9.16d}$$

The further details of this limiting case are considered in the 4th section of Appendix F.

The value of $\mu_t$ and that of $\mu_{tt}$ at $(s,t) = (S,t_j^*)$ follow from the quantities at $(s,t) = (s_{NUP}^*, t_j^*)$, to consistent order of approximation, as:

$$\mu_t(S,t_j^*) = \mu_{t_{NUP,j}}^* + \frac{1}{2}\Delta s_{NUP} \mu_{st_{NUP,j}}^* \tag{9.17a}$$

$$\mu_{tt}(S,t_j^*) = \mu_{tt_{NUP,j}}^* \tag{9.17b}$$

Upon substitution of Eqs. (9.17a and b) in Eq. (9.16a) we get the contribution of the far wake as terms adding in Eq. (9.15a) to $\mu_{t_{ij}}^*$, $\mu_{st_{ij}}^*$ and $\mu_{tt_{ij}}^*$ for i=NUP.

9.3.4 Small-curvature expansion for the feeding-sheet integrals

The third term in Eq. (9.12) represents the contribution due to the feeding sheet. Its expansion for small curvature is also obtained as a special case of Eq. (9.15), i.e. since $\mu(s,t) = \mu(s_i^*,T) + \Delta s\mu_s(s_i^*,T) + \frac{1}{2}\Delta s^2\mu_{ss}(s_i^*,T) + O(\delta^3)$:

$$\bar{u}_\mu^{(3)}(\bar{x}_o) = \frac{1}{4\pi}\sum_{i=1}^{NUP}\{\mu_s(s_i^*,T)(\bar{E}_{10f}+\bar{E}^c_{10f}) + \mu_{ss}(s_i^*,T)\bar{E}_{20f}) + O(\delta^2) \tag{9.18a}$$

where $\bar{E}_{10f}$, $\bar{E}^c_{10f}$ and $\bar{E}_{20f}$ follow from $\bar{E}_{10}$, $\bar{E}^c_{10}$ and $\bar{E}_{20}$ as worked out in Appendix F, where the expansion point is at $t=1$, i.e.:

$$\bar{x}^*_s = \bar{x}_{v_s}(s_i^*) \tag{9.18b}$$

$$\bar{x}^*_t = \bar{x}_v(s_i^*) - \bar{x}(s_i^*,T) \tag{9.18c}$$

$$\bar{x}^*_{ss} = \bar{x}_{ss}(s_i^*) \tag{9.18d}$$

$$\bar{x}^*_{st} = \bar{x}_{v_s}(s_i^*) - \bar{x}_s(s_i^*,T) \tag{9.18e}$$

$$\bar{x}^*_{tt} = 0 \tag{9.18f}$$

The further details of this case are considered in the 5th section of Appendix F.

The value of $\mu_s$ and that of $\mu_{ss}$ at $(s,t)=(s_i^*,T)$ follow from the quantities at $(s,t) = (s_i^*,t^*_{NVP})$, to consistent order of approximation as

$$\mu_s(s_i^*,T) = \mu^*_{s_{i,NVP}} + \tfrac{1}{2}\Delta t_{NVP}\mu^*_{st_{i,NVP}} \tag{9.19a}$$

$$\mu_{ss}(s_i^*,T) = \mu^*_{ss_{i,NVP}} \tag{9.19b}$$

Upon substitution of Eqs. (9.19a and b) in Eq. (9.18a) one gets the contribution of the feeding sheet as terms adding in Eq. (9.15a) to $\mu^*_{s_{ij}}$, $\mu^*_{st_{ij}}$ and $\mu^*_{ss_{ij}}$ with $j$=NVP.

9.3.5 Small-curvature expansion contribution of vortex

The fourth term in Eq. (9.12) is the contribution due to the isolated vortex filament. Using the expansion given in Eq. (9.13b) we write (see Fig. 9.8):

$$\bar{r}_v = \bar{r}_{vf} - \bar{r}_{v2} + O(\delta^3) \tag{9.20a}$$

where

$$\bar{r}_{vf} = \bar{x}_o - \bar{x}^*_v - \Delta s\bar{x}^*_{v_s} \tag{9.20b}$$

$$\bar{r}_{v2} = \tfrac{1}{2}\Delta s^2\bar{x}^*_{v_{ss}} \tag{9.20c}$$

In Eq. (9.20) $\bar{r}_{vf}$ denotes the vector from $\bar{x}_o$ to the tangent to the vortex core $\bar{x} = \bar{x}_v(s)$ at $s=s_i^*$. The vector $\bar{r}_{v2}$, assumed to be order $\delta^2$, is related to the curvature and torsion of the curve. Substitution of Eqs. (9.20) and (9.13c) into the fourth term of Eq. (9.12) gives

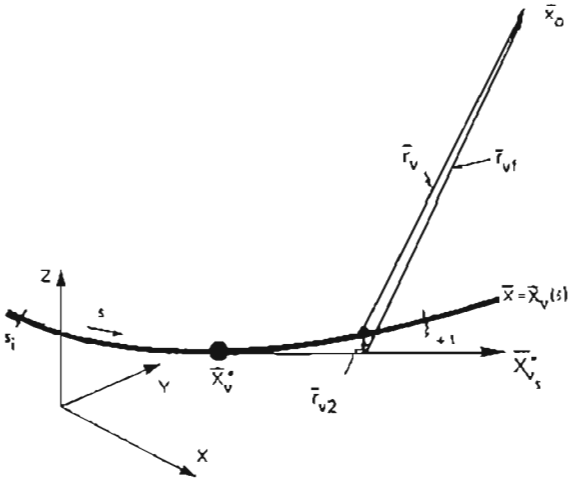


Fig. 9.8 Small curvature expansion for vortex core

$$\bar{u}_\mu^{(4)}(\bar{x}_o) = \frac{1}{4\pi}\sum_{i=1}^{NUP}\{\mu(s_i^*,T)(\bar{E}_{ov}+\bar{E}^c_{ov})+\mu_s(s_i^*,T)(\bar{E}_{1v}+\bar{E}^c_{1v})+\mu_{ss}(s_i^*,T)\bar{E}_{2v}+O(\delta^2\tfrac{\ell^2}{D^2})\} \tag{9.21a}$$

where

$$\bar{E}_{ov} = \bar{x}^*_{v_s}\times\bar{I}_{vo} \tag{9.21b}$$

$$\bar{E}^c_{ov} = \bar{x}^*_{v_{ss}}\times\bar{I}_{v1} + \bar{x}^*_{v_s}\times\bar{I}^c_{vo} \tag{9.21c}$$

$$\bar{E}_{1v} = \bar{x}^*_{v_s}\times\bar{I}_{v1} \tag{9.21d}$$

$$\bar{E}^c_{1v} = \bar{x}^*_{v_{ss}}\times\bar{I}_{v2} + \bar{x}^*_{v_s}\times\bar{I}^c_{v1} \tag{9.21e}$$

$$\bar{E}_{2v} = \tfrac{1}{2}\bar{x}^*_{v_s}\times\bar{I}_{v2} \tag{9.21f}$$

and

$$\bar{I}_{vk} = \int_{s_i}^{s_{i+1}} f(\Delta s^k)\frac{\bar{r}_{vf}}{|\bar{r}_{vf}|^3}ds \ , \qquad k = 0,\ 1 \text{ and } 2 \tag{9.21g}$$

$$\bar{I}^c_{vk} = -\int_{s_i}^{s_{i+1}} f(\Delta s^k)\left(\frac{\bar{r}_{v2}}{|\bar{r}_{vf}|^3} - 3(\bar{r}_{v2}.\bar{r}_{vf})\frac{\bar{r}_{vf}}{|\bar{r}_{vf}|^5}\right)ds \ , \ k = 0 \text{ and } 1 \tag{9.21h}$$

Here $\delta$ is a measure of the panel width in s-direction and D is $\delta$ in the near field and larger otherwise. Note that the above error estimate is not valid for points very close to the vortex core where both $\bar{E}_{ov}$ and $\bar{E}^c_{ov}$ become singular. The integrals appearing in Eqs. (9.21g-h) can be found in closed form, see Appendix F, section 6, for the details. It follows directly from the expressions derived in this Appendix that for the point $\bar{x}_o$ approaching $\bar{x}_v(s_i^*)$ one has that the contribution of the i-th segment becomes, see also section 3.4.2:

$$\bar{u}^{(4)}_{\mu}(\bar{x}_o\to\bar{x}_v(s_i^*)) = \frac{\mu(s_i^*,T)}{2\pi}\left(\frac{\bar{x}^*_{v_s}\times\bar{\varepsilon}}{|\bar{x}^*_{v_s}|\varepsilon^2}\right)$$

$$+ \frac{\mu(s_i^*,T)}{4\pi}\left(\frac{\bar{x}^*_{v_{ss}}\times\bar{x}^*_{v_s}}{|\bar{x}^*_{v_s}|^3}\ln\left(\frac{\varepsilon}{|\bar{x}^*_{v_s}|\Delta s_i}\right)\right.$$

$$\left. - \frac{\bar{x}^*_{v_s}}{|\bar{x}^*_{v_s}|^3}\times\left(\bar{x}^*_{v_{ss}} - (\bar{x}^*_{v_{ss}}.\bar{\varepsilon})\frac{\bar{\varepsilon}}{\varepsilon^2}\right)\right) + O(\varepsilon\ln\varepsilon,\varepsilon^2) \tag{9.22}$$

The first term is the familiar 1/c term, which also occurs in two-dimensional flow, associated with the singular velocity field induced by a straight vortex segment. At the axis of the core itself this term is to be omitted. The next term is the term due to the curvature of the vortex core. It contains a logarithmic singularity as well as a term of order unity. In the present study the vortex filament was introduced as a model of a finite-area vortex core, while it is also assumed that the curvature of the core is small. This leads to the model in which the velocity induced by the vortex filament at its own collocation point (mid-point) is taken equal to zero.

7.3.6 Numerical integration

The small-curvature expansion of the integrals in Eq. (9.12) results in complex, though closed-form, expressions. These expressions are to be used in case the point $\bar{x}_o$ lies on the panel (i,j) itself, i.e. $\bar{x}_o = \bar{x}(s_i^*,t_j^*)$, or in case the point $\bar{x}_o$ is very close to the panel. For points $\bar{x}_o$ far away from the panel, or the curve segment in case of the line-integrals, we use far-field expressions, which are computationally cheaper to evaluate, but as accurate.

For the surface integral, the first term in Eq. (9.12), the contribution due to panel (ij) is for

$$|\bar{x}_o-\bar{x}(s_i^*,t_j^*)| < C(|\bar{x}_s(s_i^*,t_j^*)|^2\Delta s_i^2 + |\bar{x}_t(s_i^*,t_j^*)|^2\Delta t_j^2)^{\frac{1}{2}} \tag{9.23a}$$

expressed as

$$\bar{u}^{(1)}_{\mu}(\bar{x}_o) = \frac{1}{4\pi}\bar{I}^{(1)}(s_i^*,t_j^*)\Delta s_i\Delta t_j \tag{9.23b}$$

where

$$\bar{I}^{(1)}(s,t) = \mu_s(s,t)\frac{\bar{x}_t(s,t)\times(\bar{x}_o-\bar{x}(s,t))}{|\bar{x}_o-\bar{x}(s,t)|^3} - \mu_t(s,t)\frac{\bar{x}_s(s,t)\times(\bar{x}_o-\bar{x}(s,t))}{|\bar{x}_o-\bar{x}(s,t)|^3} \tag{9.23c}$$

is the integrand of the surface integral in Eq. (9.12). The truncation error of $O(\delta^4)$ implied in Eq. (9.23) will result in $O(\delta^2)$ overall accuracy. The simple mid-point rule used to obtain Eq. (9.23) is not very well suited for panels that have a large aspect ratio. Such panels occur for instance at the apex of the delta-wing. In the present study we employ an extended mid-point rule in which the in s-direction elongated panel is subdivided into ie subpanels. This leads to

$$\bar{u}^{(1)}_{\mu}(\bar{x}_o) = \frac{1}{4\pi}\sum_{k=1}^{ie}\{\bar{I}^{(1)}(\hat{s}_k,t_j^*)\}\frac{\Delta s_i\Delta t_j}{ie} \tag{9.24a}$$

which for the same accuracy allows us to use a smaller C in Eq. (9.23a), thereby saving computing time.

In Eq. (9.24a) the midpoints of the subpanels follow from

$$\hat{s}_k = s_i^* + \frac{2k-ie-1}{2ie}\Delta s_i \tag{9.24b}$$

and $f(\hat{s}_k,t_j^*)$, etc. are expanded as (see Eq. (9.13)):

$$f(\hat{s}_k,t_j^*) = f(s_i^*,t_j^*) + (\hat{s}_k-s_i^*)f_s(s_i^*,t_j^*) + \tfrac{1}{2}(\hat{s}_k-s_i^*)^2f_{ss}(s_j^*,t_j^*) + O(\Delta^3) \tag{9.24c}$$

$$f_s(\hat{s}_k,t_j^*) = f_s(s_i^*,t_j^*) + (\hat{s}_k-s_i^*)f_{ss}(s_i^*,t_j^*) + O(\Delta^2) \tag{9.24d}$$

$$f_t(\hat{s}_k,t_j^*) = f_t(s_i^*,t_j^*) + (\hat{s}_k-s_i^*)f_{st}(s_i^*,t_j^*) + O(\Delta^2) \tag{9.24e}$$

In Eq. (9.24) one finds the number of subpanels ie from

$$ie = \text{Max}[1,\text{Min}(ie_{max},\text{Int}(\frac{|\bar{x}_s(s_i^*,t_j^*)|\Delta s_i}{|\bar{x}_t(s_i^*,t_j^*)|\Delta t_j} + \frac{1}{2}))] \tag{9.24f}$$

where $ie_{max}$ is some upper limit and Int indicates the truncated integer value. Above relation only involves the geometry of the panel and not the location of the point $\bar{x}_o$ with respect to the panel midpoint. Clearly the subdivision is not required for points $\bar{x}_o$ far from the panel. Therefore Eq. (9.24f) is applied whenever, in addition to Eq. (9.23a):

$$|\bar{x}_o-\bar{x}(s_i^*,t_j^*)|<F^*\text{Max}(|\bar{x}_s(s_i^*,t_j^*)|\Delta s_i,\ |\bar{x}_t(s_i^*,t_j^*)|\Delta t_j)$$

while ie = 1 otherwise. The latter then reduces Eq. (9.24) to the conventional mid-point rule of Eq. (9.23). In most of the present applications we chose F to be equal to 2.0. For the points $\bar{x}_o$ satisfying Eq. (9.24g) choosing ie as given by Eq. (9.24f) results in the panel being subdivided into approximately square subpanels (see Fig. 9.9).

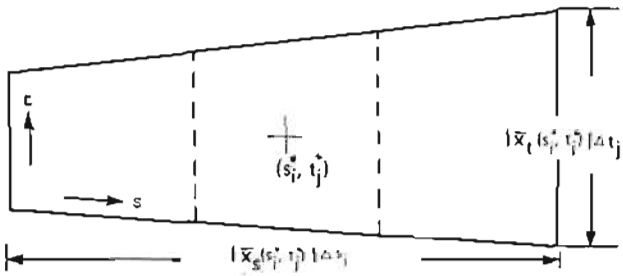


Fig. 9.9 Subdivision of panel into subpanels

For points $\bar{x}_o$ much closer to the panel (i,j) considered, i.e. for points $\bar{x}_o$ not satisfying Eq. (9.23a), the 3-point Gaussian integration rule is applied, again after subdividing the panel into ie subpanels according to Eq. (9.24f). This results in

$$\bar{u}_\mu^{(1)}(\bar{x}_o) = \frac{1}{4\pi}[\sum_{k=1}^{ie}\{\sum_{m=1}^{3} w_m(\sum_{n=1}^{3} w_n \bar{I}^{(1)}(\tilde{s}_{km},\tilde{t}_n))\}\frac{\Delta s_i \Delta t_j}{ie}] \tag{9.25a}$$

where

$$\tilde{s}_{km} = \hat{s}_k + (m-2)C\frac{\Delta s_i}{ie} \tag{9.25b}$$

$$\tilde{t}_n = t_j^* + (n-2)C\Delta t_j \tag{9.25c}$$

and where $w_g$ are the weights ($w_1=w_3=5/18$, $w_2=4/9$) while $C=\frac{1}{2}(0.6)^{\frac{1}{2}}$ is the constant appearing in the location of the Gaussian integration points. The value of quantities at $(\tilde{s}_{km},\tilde{t}_n)$ are found from the Taylor series expansion given in Eqs. (9.13). In case in Eq. (9.25a) the point $\bar{x}_o$ and the midpoint $(\hat{s}_k,t_j^*)$ of a specific subpanel are farther apart than the far-field criterion Eq. (9.23a), i.e. for

$$|\bar{x}_o-\bar{x}(\hat{s}_k,t_j^*)|>G\{|\bar{x}_s(\hat{s}_k,t_j^*)|^2(\frac{\Delta s_i}{ie})^2 + |\bar{x}_t(\hat{s}_k,t_j^*)|^2\Delta c_j^2\}^{\frac{1}{2}} \tag{9.25d}$$

the expression in Eq. (9.25a) within { } is replaced by $\bar{I}^{(1)}(\hat{s}_k,t_j^*)$; for that subpanel the integration reduces to the mid-point rule.

The line integrals in Eq. (9.12) are, for points not near the interval itself, also evaluated using the modified mid-point and the Gaussian integration rule.

The second term in Eq. (9.12), i.e. the one due to the contribution of the far wake, is approximated as

$$\bar{u}_\mu^{(2)}(\bar{x}_o) = \frac{1}{4\pi}\bar{I}^{(2)}(S,t_j^*)\Delta t_j \tag{9.26a}$$

for $|\bar{x}_o-\bar{x}(S,t_j^*)|>G|\bar{x}_t(S,t_j^*)|\Delta t_j$

and as

$$\bar{u}_\mu^{(2)}(\bar{x}_o) = \frac{1}{4\pi}[\sum_{n=1}^{3} w_n \bar{I}^{(2)}(S,\tilde{t}_n)\Delta t_j] + O(\delta^3) \tag{9.26b}$$

for $|\bar{x}_o-\bar{x}(S,t_j^*)|<G|\bar{x}_t(S,t_j^*)|\Delta t_j$. In Eq. (9.26) $\bar{I}^{(2)}(S,t)$ follows directly from the second term in Eq. (9.12). Again the truncation error implied results in a globally second-order accuracy.

The third term in Eq. (9.12), the one due to the feeding sheet, is for points $\bar{x}_o$ for which

$$(\frac{1}{2}(|\bar{x}_o-\bar{x}_v(s_i^*)|^2+|\bar{x}_o-\bar{x}(s_i^*,T)|^2))^{\frac{1}{2}}>G\{|\bar{x}_v(s_i^*)-\bar{x}(s_i^*,T)|^2+|\bar{x}_{v_s}(s_i^*)|^2\Delta s_i^2\}^{\frac{1}{2}} \tag{9.27a}$$

approximated as

$$\bar{u}_\mu^{(3)}(\bar{x}_o) = \frac{1}{4\pi}[\sum_{k=1}^{ie}\{\bar{I}^{(3)}(\hat{s}_k,T)\}\frac{\Delta s_i}{ie}] \tag{9.27b}$$

where the number of subpanels follows from

$$ie = \text{Max}[1,\text{Min}(ie_{max},\text{Int}(\frac{|\bar{x}_{v_s}(s_i^*)|\Delta s_i}{|\bar{x}_v(s_i^*)-\bar{x}(s_i^*,T)|} + \frac{1}{2}))] \tag{9.27c}$$

but for points $\bar{x}_o$ satisfying both Eq. (9.27a) and

$$\text{Min}\{|\bar{x}_o-\bar{x}_v(s_i^*)|,|\bar{x}_o-\bar{x}(s_i^*,T)|\}>F*\text{Max}\{|\bar{x}_{v_s}(s_i^*)|\Delta s_i,|\bar{x}_v(s_i^*)-\bar{x}(s_i^*,T)|\} \tag{9.27d}$$

we restrict ie to 1, which reduces Eq. (9.27b) to the conventional midpoint integration scheme.

For points $\bar{x}_o$ closer to the feeding sheet than according to relation (9.27a) we use the 3-point Gaussian integration scheme. This results in

$$\bar{u}_\mu^{(3)}(\bar{x}_o) = \frac{1}{4\pi}\Big[\sum_{k=1}^{ie}\Big\{\sum_{m=1}^{3}(w_m\bar{I}^{(3)}(\tilde{s}_{km},T))\Big\}\frac{\Delta s_i}{ie}\Big] \tag{9.27e}$$

where $\tilde{s}_{km}$ follows from Eq. (9.25b). Here again the expression within { } is replaced by $\bar{I}^{(3)}(\hat{s}_k,T)$ whenever relation (9.27a) with $s_i^*$ and $\Delta s_i$ replaced by $\hat{s}_k$ and $\Delta s_i/ie$, respectively, is satisfied. The expression for $\bar{I}^{(3)}(s,T)$ used above follows directly from the third term in Eq. (9.12).

The fourth term in Eq. (9.12) is the contribution due to the vortex core. As indicated in the preceding section we omit the influence of a segment of the vortex filament at its own midpoint. For points far away from the segment, i.e. for

$$|\bar{x}_o-\bar{x}_v(s_i^*)|>G|\bar{x}_v(s_i^*)-\bar{x}(s_i^*,T)| \tag{9.28a}$$

we employ

$$\bar{u}_\mu^{(4)}(\bar{x}_o) = \frac{1}{4\pi}\Big[\sum_{k=1}^{ie}\{\bar{I}^{(4)}(\hat{s}_k)\}\frac{\Delta s_i}{ie}\Big] \tag{9.28b}$$

where the number of subpanels ie follows from Eqs. (9.27c and d).

For points $\bar{x}_o$ closer to the vortex segment than given in Eq. (9.28a) the 3-point Gaussian integration rule is used once more; resulting in

$$\bar{u}_\mu^{(4)}(\bar{x}_o) = \frac{1}{4\pi}\Big[\sum_{k=1}^{ie}\Big\{\sum_{m=1}^{3}(w_m\bar{I}^{(4)}(\tilde{s}_{km}))\Big\}\frac{\Delta s_i}{ie}\Big] \tag{9.28c}$$

where $\tilde{s}_{km}$ follows from Eq. (9.25b). In case relation (9.28a) with $s_i^*$ replaced by $\hat{s}_k$ is satisfied in Eq. (9.28b) the expression inside { } is replaced by $\bar{I}^{(4)}(\hat{s}_k)$.
The expression for $\bar{I}^{(4)}(s)$ used in Eq. (9.28) follows directly from the fourth term of Eq. (9.12).

The final point to be considered is in what region to apply the small- curvature type of expressions and where the much simpler numerical integration formula's. Numerical experimentation, though admittedly of limited scope, has suggested that, for the configurations considered here, with relatively short vortex sheets not closely approaching each other or the wing surface, numerical integration can be applied in a fairly large region. As a matter of experience the small-curvature expressions are only used for computing the influence a panel exerts at its own midpoint.

9.3.7 Numerical scheme - doublet distribution

The boundary conditions are imposed at the panel midpoints, which is also the expansion point (s*,t*) used for the approximate evaluation of the integral representation of the velocity field.

The description of the panel method is made complete by specifying the schemes used to express the function value, first and second derivatives of the unknown $\bar{x}(s,t)$ and $\mu(s,t)$, all at the panel midpoints, in terms of the set of parameters to be solved for. In this section we consider the scheme used for the doublet distribution on the aerodynamic network (see Fig. 9.6) comprising wing, leading-edge vortex sheet and near wake. In the subsequent section we consider the scheme used for the geometry of leading-edge vortex sheet, near wake and vortex core.

As a consequence of the Kutta condition the doublet distribution and its first derivatives will be continuous as well as finite across both the leading and the trailing edge. This suggests to choose just one scheme for the whole computational domain, i.e. a scheme which does not discriminate between wing and vortex sheet and requires no special measures at leading or trailing edge. To find a simple scheme that is stable for the mixed type (analysis/design) and nonlinear boundary conditions proved to be hard. In the present method stability is achieved by choosing a mixed type of scheme, based on the following heuristic spline-stability type of arguments.
It follows from Eq. (9.15k) that the normal-velocity boundary condition imposed at $(s_i^*,t_j^*)$ has as leading term the second derivatives of $\mu$ at $(s_i^*,t_j^*)$. This implies that for quadratic representations with the parameters at the midpoints a central difference scheme is required for stability, since these schemes allow function value or second derivatives to be prescribed at the midpoints.
The zero-pressure jump condition on the vortex sheet is the condition that the tangential component of the average velocity across the vortex sheet, $\bar{u}_2(\bar{x}(s_i^*,t_j^*))$, be parallel to the surface vorticity vector $\bar{\gamma}(\bar{x}(s_i^*,t_j^*))$. It follows from Eq. (9.15k) and Appendix F that the average tangential velocity induced by a vortex sheet panel on itself is of order 5 and proportional to the panel curvature and the first derivatives of the doublet distribution. Therefore since the free-stream component dominates in the average tangential velocity it is concluded that the dominant term in the zero-pressure jump condition involves $\gamma$, i.e. the first derivatives of $\mu$ at $(s_i^*,t_j^*)$. This provokes a stability problem for the central quadratic schemes which are unstable for prescribing first derivatives at the midpoints. It has led us to an in upstream direction biased scheme to be used for the first derivatives of $\mu$, involving the parameters at the midpoints $(s_k^*,t_j^*)$, $k=(i-2)1(i)$ for $\mu_s(s_i^*,t_j^*)$ and at the midpoints $(s_i^*,t_\ell^*)$, $\ell=(j-2)1(j)$ for $\mu_t(s_i^*,t_j^*)$.

The scheme used is depicted in Fig. 9.10. Denoting the parameters, the value of the doublet distribution at the panel midpoints, by $\mu_k$ and ordering them in strips s=constant, the scheme can be written as

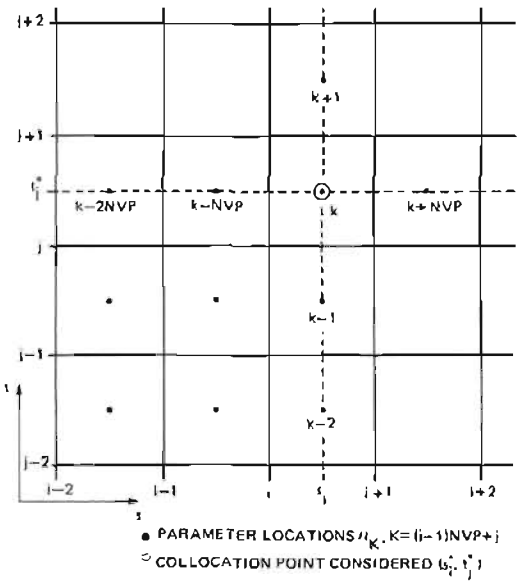


Fig. 9.10 Numerical scheme for the doublet distribution

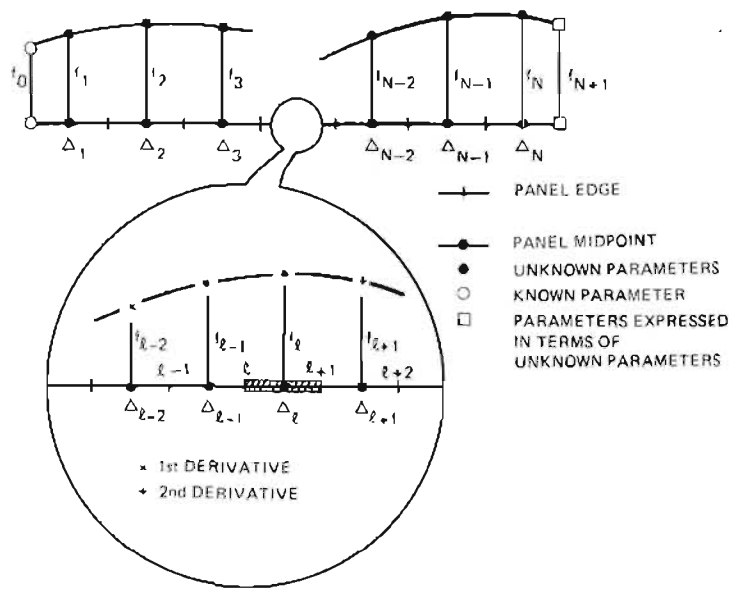


Fig. 9.11 One-dimensional basic scheme

$$\mu(s_i^*,t_j^*) = \mu_k \tag{9.29a}$$

$$\mu_s(s_i^*,t_j^*) = du1_1^i \mu_{k-2NVP} + du1_2^i \mu_{k-NVP} + du1_3^i \mu_k \tag{9.29b}$$

$$\mu_t(s_i^*,t_j^*) = dv1_1^j \mu_{k-2} + dv1_2^j \mu_{k-1} + dv1_3^j \mu_k \tag{9.29c}$$

$$\mu_{ss}(s_i^*,t_j^*) = du2_2^i \mu_{k-NVP} + du2_3^i \mu_k + du2_4^i \mu_{k+NVP} \tag{9.29d}$$

$$\mu_{tt}(s_i^*,t_j^*) = dv2_2^j \mu_{k-1} + dv2_3^j \mu_k + dv2_4^j \mu_{k+1} \tag{9.29e}$$

where k=(i-1)NVP+j. The cross-derivative $\mu_{st}(s_i^*,t_j^*)$ is found by taking the tensor product of $du1^i$ with $dv1^j$. The coefficients in Eq. (9.29) follow from one-dimensional finite-difference expressions as

$$du1_m^i = d1_m^i \ , \ m=1(1)3 \tag{9.30a}$$

$$dv1_m^j = d1_m^j \ , \ m=1(1)3 \tag{9.30b}$$

$$du2_m^i = d2_m^i \ , \ m=2(1)4 \tag{9.30c}$$

$$dv2_m^j = d2_m^j \ , \ m=2(1)4 \tag{9.30d}$$

where the one-dimensional coefficients follow from (Fig. 9.11)

$$f'_\ell = d1_1^\ell f_{\ell-2} + d1_2^\ell f_{\ell-1} + d1_3^\ell f_\ell + d1_4^\ell f_{\ell+1} \tag{9.31a}$$

$$f''_\ell = d2_1^\ell f_{\ell-2} + d2_2^\ell f_{\ell-1} + d2_3^\ell f_\ell + d2_4^\ell f_{\ell+1} \tag{9.31b}$$

with

$$d1_m^\ell = \bar{d}1_m^{\ell-1} + \tfrac{1}{2}(\Delta_{\ell-1} + \Delta_\ell)\, \bar{d}2_m^{\ell-1} \ , \ m=1(1)3; \ d1_4^\ell = 0 \tag{9.31c}$$

$$d2_m^\ell = \bar{d}2_{m-1}^\ell \ , \ m=2(1)4; \ d2_1^\ell = 0 \tag{9.31d}$$

where $\bar{d}1_n^k$ and $\bar{d}2_n^k$, n=1(1)3 are the usual central difference coefficients

$$\bar{d}1_1^k = \frac{2(\Delta_k + \Delta_{k+1})}{(\Delta_{k-1} + \Delta_k)(\Delta_{k-1} + 2\Delta_k + \Delta_{k+1})} \tag{9.31e}$$

$$\bar{d}1_2^k = \frac{2(\Delta_{k+1} - \Delta_{k-1})}{(\Delta_{k-1} + \Delta_k)(\Delta_k + \Delta_{k+1})} \tag{9.31f}$$

$$\bar{d}1_3^k = \frac{2(\Delta_{k-1} + \Delta_k)}{(\Delta_k + \Delta_{k+1})(\Delta_{k-1} + 2\Delta_k + \Delta_{k+1})} \tag{9.31g}$$

$$\bar{d}2_1^k = \frac{8}{(\Delta_{k-1} + \Delta_k)(\Delta_{k-1} + 2\Delta_k + \Delta_{k-1})} \tag{9.31h}$$

$$\bar{d}2_2^k = \frac{-8}{(\Delta_{k-1} + \Delta_k)(\Delta_k + \Delta_{k+1})} \tag{9.31i}$$

$$\bar{d}2_3^k = \frac{8}{(\Delta_k + \Delta_{k+1})(\Delta_{k-1} + 2\Delta_k + \Delta_{k-1})} \tag{9.31j}$$

we used earlier as well, see Eq. (8.11).

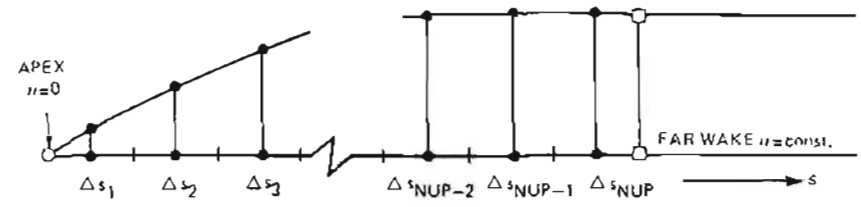


Fig. 9.12 Panels widths to be used in finite-difference expressions for doublet distribution derivatives in s-direction

| | i=1 *) | i=2 | i=NUP |
|---|---|---|---|
| $\Delta_{j-2}$ | 0 | 0 | $\Delta s_{NUP-2}$ |
| $\Delta_{j-1}$ | 0 | $\Delta s_1$ | $\Delta s_{NUP-1}$ |
| $\Delta_j$ | $\Delta s_1$ | $\Delta s_2$ | $\Delta s_{NUP}$ |
| $\Delta_{j+1}$ | $\Delta s_2$ | $\Delta s_3$ | 0 |

*) First derivative by central scheme

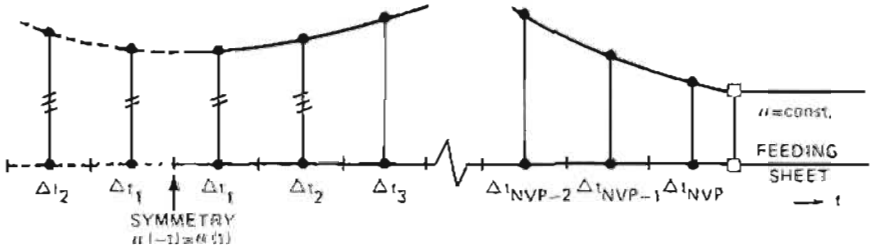


Fig. 9.13 Panel widths to be used in finite-difference expressions for doublet distribution derivatives in t-direction

| | j=1 | j=2 | j=NVP |
|---|---|---|---|
| $\Delta_{j-2}$ | $\Delta t_2$ | $\Delta t_1$ | $\Delta t_{NVP-2}$ |
| $\Delta_{j-1}$ | $\Delta t_1$ | $\Delta t_1$ | $\Delta t_{NVP-1}$ |
| $\Delta_j$ | $\Delta t_1$ | $\Delta t_2$ | $\Delta t_{NVP}$ |
| $\Delta_{j+1}$ | $\Delta t_2$ | $\Delta t_3$ | 0 |

The boundaries of the computational domain required special measures. Here the following is implemented at the first point:

(a) In case $f_0$ is known we choose $\Delta_{-1}=\Delta_0=0$ and in addition for $\underline{\ell=1}$ the upstream biased scheme for the first derivative is changed to the central scheme, i.e.

$$d1^1_m = d1^1_{m-1}\ ,\ m=2(1)4;\ d1^1_1=0 \tag{9.31k}$$

(b) In case of symmetry with respect to the first point the mirror-imaged values of f are used with ($\Delta_{-1}=\Delta_2$, $f_{-1}=f_2$) and ($\Delta_0=\Delta_1$, $f_0=f_1$). Note that in Fig. 9.11 $f_0$ is now moved over a distance of $\frac{1}{2}\Delta_1$ to the left. So now we have instead of Eqs. (9.31a-b)

$\underline{\text{for } \ell=1}$:

$$f'_1 = (d1^1_2 + d1^1_3)f_1 + (d1^1_1 + d1^1_4)f_2 \tag{9.31l}$$

and a similar expression for $f''_1$.

$\underline{\text{for } \ell=2}$:

$$f'_2 = (d1^2_1 + d1^2_2)f_1 + d1^2_3 f_2 + d1^2_4 f_3 \tag{9.31m}$$

At the last point $\Delta_{N+1}=0$ while $f_{N+1}$, which only occurs in the expression for $f''_N$, is expressed in terms of $f_{N-2}$, $f_{N-1}$ and $f_N$ as follows. From the quadratic representation on interval N one finds:

$$f_{N+1} = f_N + \tfrac{1}{2}\Delta_N f'_N + \tfrac{1}{2}(\tfrac{1}{2}\Delta_N)^2 f''_N$$

substitution of Eqs. (9.31a and b) and with $d1^N_4=d2^N_1=0$ one then finds for $f_{N+1}$

$$f_{N+1} = (\tfrac{1}{2}\Delta_N d1^N_1 f_{N-2}$$

$$+ (\tfrac{1}{2}\Delta_N d1^N_2 + \tfrac{1}{2}(\tfrac{1}{2}\Delta_N)^2 d2^N_2) f_{N-1}$$

$$+ (1 + \tfrac{1}{2}\Delta_N d1^N_3 + \tfrac{1}{2}(\tfrac{1}{2}\Delta_N)^2 d2^N_3) f_N)/(1 - \tfrac{1}{2}(\tfrac{1}{2}\Delta_N)^2 d2^N_4) \tag{9.31n}$$

This expression is for $\ell=N$ substituted into Eq. (9.31b), so that for this value of $\ell$ there is a nonzero contribution from $f_{j-2}$.

Returning now to the doublet distribution on the aerodynamic network, we consider the schemes for the derivative with respect to s. At the boundary s=0 the doublet distribution $\mu(0,t)$ is zero for $t\in[0,T]$. The choices of the interval lengths implied by this are listed in Fig. 9.12.

In the t-direction the boundary t=0 is the plane of symmetry, i.e. $\mu(s,-t)=\mu(s,t)$ for $s\in[0,S]$. The choices to be made for the $\Delta_j$'s implied by this boundary are listed in Fig. 9.13.

Across panel edges the panelwise quadratic doublet distribution is discontinuous, both in function value and in its first derivatives with respect to s and t. However, because these discontinuities are small of higher order they are neglected altogether.

9.3.8 Numerical scheme - geometry

(i) Geometry of the wing

The geometry of the wing surface $\underline{x}(s,t)$ for $(s,t)\in([0,1],[0,1])$, see Fig. (9.4) is known and described in section 9.2. The value of $\underline{x}$, $\underline{x}_s$, $\underline{x}_t$, $\underline{x}_{st}$, $\underline{x}_{ss}$ and $\underline{x}_{tt}$ at the panel midpoints of the aerodynamic network are obtained directly from the description of the wing geometry, in terms of bi-cubic Hermite Polynomials, on the geometric network (section 9.2).

(ii) Geometry of the leading-edge and near-wake vortex sheets

The geometry of the leading-edge and near-wake vortex sheets, $\underline{x}(s,t)$ for $(s,t)\in([0,1],[1,T])$ and $(s,t)\in([1,S],[0,T])$, respectively is given in Eq. (9.5). The x-component of this description is known in terms of the description of the leading and trailing edge. The y- and z-component of $\underline{x}(s,t)$ have to be determined as part of the solution.

The three conditions to be applied at the midpoints of the panels on the vortex sheets are highly non-linear in terms of $\bar{x}$, $\bar{x}_s$ and $\bar{x}_t$. Different schemes were tried, but it turned out that stability could best be achieved using the same mixed type of scheme as used for the doublet distribution. So in the present method on the vortex sheet the y- and z-components of $\bar{x}(s_i^*,t_j^*)$, $\bar{x}_s(s_i^*,t_j^*)$, $\bar{x}_t(s_i^*,t_j^*)$, $\bar{x}_{ss}(s_i^*,t_j^*)$, $\bar{x}_{st}(s_i^*,t_j^*)$ and $\bar{x}_{tt}(s_i^*,t_j^*)$ are expressed in terms of the parameters $\bar{x}_k$ at the panel midpoints by the scheme given in Eqs. (9.29-9.31).

The part of the aerodynamic network comprising the near-wake vortex sheet is split by the line t=1 into two subdomains, mainly to avoid complex logic near the wing tip (Fig. 9.14).

Application of the finite-difference scheme in s-direction is now fairly easy. In subdomain I we can apply the scheme shown in Fig. 9.12, while at the apex (s=0) also y and z are zero and on the far wake (s>S) y is constant but z is linearly varying.
In subdomain II the situation is slightly different in the sense that now the first and second point are at i=NUPW+1 and i=NUPW+2, respectively. Furthermore, y and z at the edge are now not zero but are known, actually they are computed from the known quantities at $s=s^*_{NUPW}$. The complete situation for the schemes used for the geometric derivatives is depicted in Fig. 9.15.

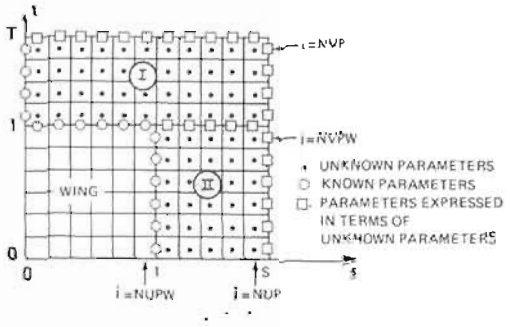


Fig. 9.14 Split-up of computational domain

Application of finite-difference scheme in t-direction is for subdomain II quite similar to the situation in Fig. 9.13. However, at t=0 the symmetry condition, which is the same for μ and z, is actually an asymmetry condition for y. Furthermore the last point is now at j=NVPW.
For subdomain I the first point is either on the leading edge (i≤NUPW) or on the extension of the leading edge beyond s=1 (i>NUPW). In the latter case this value of y and z is expressed in terms of the unknown parameters at j=NVPW-2, NVPW-1 and NVPW. In the former case the value on the leading edge is computed from the known geometric quantities at $t=t^*_{NVPW}$. Fig. 9.16 summarizes the choices made for the scheme in t-direction.

(iii) Geometry of the leading-edge vortex core
The equation for the leading-edge vortex $\bar{x}_v(s)$ for $s\in[0,S]$ is given in Eq. (9.8a). The x-component of $\bar{x}_v(s)$ is given in terms of the description of leading and trailing edge. The y- and z-component are determined as part of the solution. For the first and second derivative with respect to s of $\bar{x}_v(s)$, which occur in the expressions for the velocity field induced by the vortex, the same mixed type of scheme is used once more. The specific choices of panel widths correspond with the choices made for domain I, i.e. as depicted in Fig. 9.15. Here at the apex both $y_v$ and $z_v$ are zero as well.

For an initial guess, or for the values obtained during a previous iteration, of the geometric parameters $y_k$, $z_k$, k=(i-1)NVP+j with (i,j) within subdomain I or II, and $y_{v_i}$, $z_{v_i}$, i=1(1)NUP, all geometric quantities appearing in the expressions derived for the various contributions to the induced velocity can be evaluated. Upon substituting the numerical scheme for the derivatives of the doublet distribution, i.e. Eq. (9.29), the velocity induced at $\bar{x}_o$ by the doublet distribution on both starboard and portside can be expressed as

$$\bar{u}_\mu(\bar{x}_o) = \frac{1}{4\pi}\Big[\sum_{i=1}^{NUP}\sum_{j=1}^{NVP}\{\mu_k \bar{a}_k(\bar{x}_o,\bar{x}^*_{ij},\bar{x}^*_{s_{ij}},\bar{x}^*_{t_{ij}},\bar{x}^*_{ss_{ij}},\bar{x}^*_{st_{ij}},\bar{x}^*_{tt_{ij}},\bar{x}^*_{v_i},\bar{x}^*_{vs_i},\bar{x}^*_{vss_i})\}\Big] \qquad (9.32)$$

where k=(i-1)NVP+j. The coefficient $\bar{a}_k$, the so-called aerodynamic influence coefficient, is a function of geometric quantities which on their turn depend on the unknown geometric parameters $(y_\ell,z_\ell)$ and $(y_m,z_m)$ through the schemes described above.

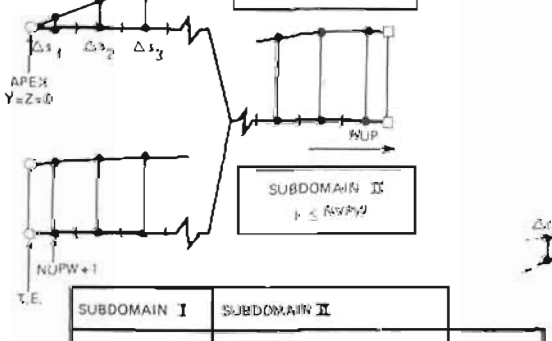


| | SUBDOMAIN I | | SUBDOMAIN II | | |
|---|---|---|---|---|---|
| | i=1*) | i=2 | i=NUPW+1*) | i=NUPW+2 | i=NUP |
| $\Delta_{i-2}$ | 0 | 0 | 0 | 0 | $\Delta s_{NUP-2}$ |
| $\Delta_{i-1}$ | 0 | $\Delta s_1$ | 0 | $\Delta s_{NUPW+1}$ | $\Delta s_{NUP-1}$ |
| $\Delta_i$ | $\Delta s_1$ | $\Delta s_2$ | $\Delta s_{NUPW+1}$ | $\Delta s_{NUPW+2}$ | $\Delta s_{NUP}$ |
| $\Delta_{i+1}$ | $\Delta s_2$ | $\Delta s_3$ | $\Delta s_{NUPW+2}$ | $\Delta s_{NUPW+3}$ | 0 |

*) First derivative by central scheme

Fig. 9.15 Panel widths to be used in finite difference expressions for geometric derivatives in s-direction

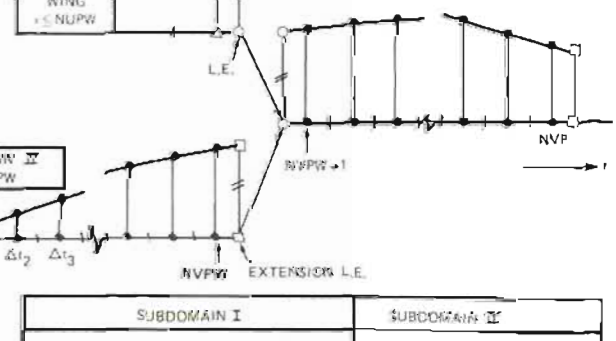


| | SUBDOMAIN I | | | SUBDOMAIN II | | |
|---|---|---|---|---|---|---|
| | j=NVPW+1*) | j=NVPW+2 | j=NVP | j=1 | j=2 | j=NVPW |
| $\Delta_{j-2}$ | 0 | 0 | $\Delta t_{NVP-1}$ | $\Delta t_2$ | $\Delta t_1$ | $\Delta t_{NVPW-2}$ |
| $\Delta_{j-1}$ | 0 | $\Delta t_{NVPW+1}$ | $\Delta t_{NVP-1}$ | $\Delta t_1$ | $\Delta t_1$ | $\Delta t_{NVPW-1}$ |
| $\Delta_j$ | $\Delta t_{NVPW+1}$ | $\Delta t_{NVPW+2}$ | $\Delta t_{NVP}$ | $\Delta t_1$ | $\Delta t_2$ | $\Delta t_{NVPW}$ |
| $\Delta_{j+1}$ | $\Delta t_{NVPW+2}$ | $\Delta t_{NVPW+3}$ | 0 | $\Delta t_2$ | $\Delta t_3$ | 0 |

*) First derivative by central scheme

Fig. 9.16 Panel widths to be used in finite difference expressions for geometric derivatives in t-direction

9.4 Implementation of boundary and auxiliary conditions

In this section we consider the way in which the boundary and other conditions are implemented. The unknown parameters of the problem are arranged in a strip by strip fashion, where a strip is defined as that part of the aerodynamic network for which $s \in [s_i, s_{i+1}]$. The conditions to be imposed are arranged accordingly. On a specific strip, sub-divided in NVP panels, two types of panel may be encountered: wing panels and vortex-sheet panels. Furthermore, associated with each strip is a segment of the vortex core.
Next we consider the boundary conditions (summarized in section 5.1.3) and other conditions to be applied at wing-panel midpoints, vortex sheet-panel midpoints and vortex-core-segment midpoints. Also we discuss the conditions that are imposed implicitly in the present computational model.

9.4.1 Conditions on wing panel

Any wing panel contributes one unknown parameter, namely a doublet parameter. At the midpoint of a wing panel the normal component of the velocity is set equal to zero, i.e. with Eq. (9.32):

$$(\bar{U}_\infty . \bar{e}_n)_{mn} + \sum_{i=1}^{NUP} \{ \sum_{j=1}^{NVP} \mu_k \bar{a}_k (\bar{x}^*_{mn}, \bar{x}^*_{ij}, \text{ etc.}) . (\bar{e}_n)_{mn} \} = 0 \tag{9.33a}$$

where mn denotes the midpoint at $(s^*_m, t^*_n)$, while $(m,n) \in ([1,NUPW],[1,NVPW])$. The unit normal vector at this midpoint, i.e.

$$\bar{e}_n = \frac{\bar{x}^*_s \times \bar{x}^*_t}{|\bar{x}^*_s \times \bar{x}^*_t|} \tag{9.33b}$$

does not depend on any unknown geometric parameter.

9.4.2 Conditions on vortex-sheet panel

Every vortex-sheet panel contributes three unknown parameters, one doublet parameter $\mu_k$ and two geometric parameters, $y_k$ and $z_k$.
At the midpoint of a vortex-sheet panel two boundary conditions and one geometric condition are imposed, in the following order:

(i) The normal component of the velocity vanishes. This equation is identical to Eq. (9.33) with (m,n) either in subdomain I or II of Fig. 9.14. However, now the normal vector defined in Eq. (9.33b) does depend on unknown geometric parameters.

(ii) The pressure is continuous across the vortex sheet (Eq. 5.6b). At the midpoint of panel (m,n) we then obtain, using the expression for $\bar{\gamma}$ given in Eq. (3.15d):

$$\left\{ \frac{(-\bar{x}^*_s \mu^*_t + \bar{x}^*_t \mu^*_s) \times \bar{e}_n}{|\bar{x}^*_s \times \bar{x}^*_t|} \right\}_{mn} \cdot \{ \bar{U}_\infty + \sum_{i=1}^{NUP} \sum_{j=1}^{NVP} \mu_k \bar{a}_k (\bar{x}^*_{mn}, \bar{x}^*_{ij}, \text{ etc.}) \} = 0 \tag{9.34}$$

where mn denotes the panel midpoint at $(s^*,t^*)$, situated in subdomain I or II. The vectors $\bar{x}^*_s$, $\bar{x}^*_t$ and $\bar{e}_n$ depend on the unknown geometric parameters, while $\mu^*_s$ and $\mu^*_t$ depend on the unknown doublet parameters.

(iii) The third condition to be imposed on a vortex sheet panel is a geometric condition. It is the equation that defines the parameter t along the curve s=constant on the vortex sheet. This relation, which prescribes that y and z are not independent quantities but are the coordinates of a point on a curve, is given in Eq. (9.6). In the present method this equation is discretized as:

$$\frac{1}{b\,\ell(s^*_m)} \left( \frac{1}{4} |\bar{x}^*_t - \tfrac{1}{2}\Delta t_n \bar{x}^*_{tt}| + \frac{1}{2} |\bar{x}^*_t| + \frac{1}{4} |\bar{x}^*_t + \tfrac{1}{2}\Delta t_n \bar{x}^*_{tt}| \right)_{mn} - 1 = 0 \tag{9.35}$$

which follows from applying the trapezoidal rule to Eq. (9.6) integrated in t-direction over the panel width. For the purpose of this numerical integration the panel is subdivided into two equal intervals. Note that Eq. (9.35) depends only on the unknown geometric parameters $(y_{k-2}, z_{k-2})$, $(y_{k-1}, z_{k-1})$ and $(y_{k+1}, z_{k+1})$, with $k=(m-1)NVP+n$.

9.4.3 Conditions on vortex-core segment

A vortex-core segment has associated with it two unknowns, namely the y- and z-component of its position, denoted by $y_{v_i}$ and $z_{v_i}$, respectively.
The condition applied is the condition that the resultant force on the vortex/ feeding-sheet combination be zero. Using the equation for the description of the feeding sheet Eq. (9.9) and with $\mu = \mu(s,T)$ the integral in Eq. (3.20c) is approximated by the value of the integrand at $\bar{x}_v(s)$ times the length of the integration interval (=1). Combining Eqs. (3.20a and c) then yields for the resultant force on the i-th segment of the vortex-core model:

$$d\bar{F} = \rho_\infty \Delta s_i \{ \bar{U}_\infty + \bar{u}_v(x_v(s^*_i)) \} \times \{ \mu(s^*_i,T) \bar{x}_{v_s}(s^*_i) + \mu_s(s^*_i,T) (\bar{x}_v(s^*_i) - \bar{x}(s^*_i,T)) \} = 0 \tag{9.36}$$

This force can be decomposed in three mutually perpendicular components along the unit vectors

$$\bar{e}_1 = \frac{\bar{x}_{v_s}(s^*_i) \times (\bar{x}_v(s^*_i) - \bar{x}(s^*_i,T))}{|\bar{x}_{v_s}(s^*_i) \times (\bar{x}_v(s^*_i) - \bar{x}(s^*_i,T))|} \tag{9.37a}$$

$$\bar{e}_2 = \bar{e}_3 \times \bar{e}_1 \tag{9.37b}$$

$$\bar{e}_3 = \frac{\bar{x}_{v_s}(s^*_i)}{|\bar{x}_{v_s}(s^*_i)|} \tag{9.37c}$$

where $\bar{e}_3$ is along the vortex, $\bar{e}_1$ perpendicular to both the vortex and the feeding sheet and $\bar{e}_2$ is perpendicular to the vortex and is tangential to the feeding sheet. The three components of the force on the vortex core model Eq. (9.36) are:

$$\rho_\infty \Delta s_i \{\bar{U}_\infty + \bar{u}_\mu(\bar{x}_v(s_i^*))\}.[\{\mu(s_i^*,T)\bar{x}_{v_s}(s_i^*) + \mu_s(s_i^*,T)(\bar{x}_v(s_i^*) - \bar{x}(s_i^*,T))\} \times \bar{e}_1] = 0 \qquad (9.38a)$$

$$\rho_\infty \Delta s_i [\{\bar{U}_\infty + \bar{u}_\mu(\bar{x}_v(s_i^*))\}.\bar{e}_1]\{\mu(s_i^*,T)|\bar{x}_{v_s}(s_i^*)| + \mu_s(s_i^*,T)\frac{\bar{x}_{v_s}(s_i^*).(\bar{x}_v(s_i^*) - \bar{x}(s_i^*,T))}{|\bar{x}_{v_s}(s_i^*)|}\} = 0 \qquad (9.38b)$$

$$\rho_\infty \Delta s_i [\{\bar{U}_\infty + \bar{u}_\mu(\bar{x}_v(s_i^*))\}.\bar{e}_1]\{\mu(s_i^*,T)\frac{|\bar{x}_{v_s}(s_i^*) \times (\bar{x}_v(s_i^*) - \bar{x}(s_i^*,T))|}{|\bar{x}_{v_s}(s_i^*)|}\} = 0 \qquad (9.38c)$$

It follows from Eq. (9.38) that we get a zero resultant force on the model of the vortex core by satisfying the following two conditions:

$$\{\bar{U}_\infty + \bar{u}_\mu(\bar{x}_v(s_i^*))\}.[\{\mu(s_i^*,T)\bar{x}_{v_s}(s_i^*) + \mu_s(s_i^*,T)(\bar{x}_v(s_i^*) - \bar{x}(s_i^*,T))\} \times \bar{e}_1]/|\bar{x}_{v_s}(s_i^*)| = 0 \qquad (9.39a)$$

$$[\{\bar{U}_\infty + \bar{u}_\mu(\bar{x}_v(s_i^*))\}.\bar{e}_i]\mu(s_i^*,T) = 0 \qquad (9.39b)$$

where both equations have the same dimension. The second equation has been multiplied by the strength of the vortex to obtain a suitable structure of the Jacobian of the system of nonlinear equations. Note that the second equation forces the total velocity vector to be situated in the plane formed by the vectors $\bar{x}_{v_s}(s_i^*)$ and $\bar{x}_v(s_i^*) - \bar{x}(s_i^*,T)$, i.e. to be tangential to the feeding sheet (see Fig. 9.17). In aforementioned plane the velocity vector is neither parallel to the vortex nor to the vortex lines on the feeding sheet. However, the force exerted on the vortex and the one exerted on the feeding sheet, both of which are normal to the feeding sheet, cancel when Eq. (9.39a) is satisfied.

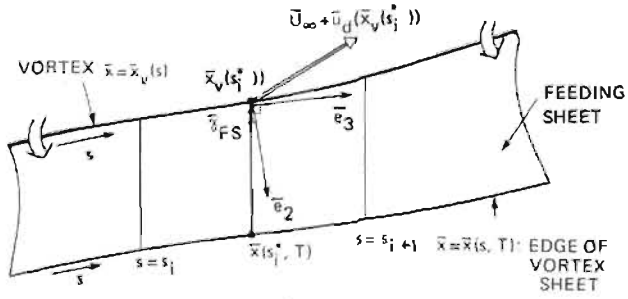


Fig. 9.17 Segment of vortex core

The two equations that apply to the vortex core are nonlinear both in terms of the unknown doublet parameters and (very highly) in terms of the unknown geometric parameters.

### 9.4.4 Implied conditions

The equations given above are the explicitly imposed conditions. There are other conditions that are assumed to be satisfied implicitly in the present computational model, namely

(i) Kutta condition
The doublet distribution is continuously differentiable ($C^1$) across both the leading and the trailing edge. This together with the two boundary conditions on the vortex sheet imply that the Kutta condition at these edges is satisfied to the order of the approximation of the formulation.

(ii) Condition at the apex
At the apex the doublet distribution $\mu(o,t)$, the position of the vortex sheet $\bar{x}(0,t)$ and vortex $\bar{x}_v(0)$ is set equal to zero. The behaviour of the solution at the apex is not known, but in subsonic flow some type of a singular behaviour may be expected. In the present method it is assumed that both function value and first derivatives of $\mu(s,t)$, $\bar{x}(s,t)$ and $\bar{x}_v(s,t)$ remain bounded for $s \to 0$.

(iii) Far-wake condition
No boundary conditions are applied on the far wake ($s>S$). The far wake is used to carry the doublet distribution from the near wake to infinity downstream. Since the far wake is a cylindrical surface, the lines t=constant being the generators along which the doublet distribution is constant, it follows that the vortex lines are parallel lines running from $s=S$ to $s=\infty$. In first approximation the pressure jump condition Eq. (9.34) then is satisfied. Similarly, assuming that the far-wake vortex lines are more or less parallel to the free-stream direction, it follows that the stream-surface condition Eq. (9.33) is satisfied to sufficient order of approximation. In the latter it is implied that the above far-wake model has little effect on the solution on the wing. Note that similar arguments as used here for the far wake are used in classical wing theory to model the whole wake as a cylindrical surface carrying the doublet distribution from the wing to downstream infinity.

(iv) Symmetry
The plane y=0 is the plane of symmetry for both the geometry and the doublet distribution. This implied symmetry is utilized in the finitedifference expressions for the derivatives of the doublet distribution and geometry. In the present study we do not consider possibly multiple nonsymmetric solutions.

## 9.5 Solution of system of nonlinear equations

The system of nonlinear equations that results from application of the boundary conditions has as many equations as unknowns. The equations are ordered in a strip by strip manner, the equations due to one strip form one block in the system. In each of the NUP blocks the equations applying to one specific panel are grouped together in the order discussed in the previous section, i.e. Eq. (9.33a) for a vortex sheet panel followed by Eqs. (9.34) and (9.35). The last two equations in a block are the two vortex core conditions Eqs. (9.39a and b).

The unknowns are grouped similarly, all the unknowns of one strip form a sub-vector. In this sub-vector the unknowns belonging to one panel are grouped as $\mu_k$, $y_k$, $z_k$, the latter two of course only for vortex sheet panels. The last two unknowns of the sub-vector are the y- and z-coordinate of the vortex position.

In the NUPW blocks due to the "wing strips" there are NVPW+3(NVP-NVPW)+2 equations, the NUP-NUPW blocks due to the "wake strips" contain 3NVP+2 equations. For a case with a more or less typical standard paneling of 10 "wing strips" of 10 wing and 10 vortex sheet panels in t-direction and 3 "wake strips" the number of unknowns amounts to 612. The "full" Newton method employed in the preceding chapter would become rather costly for cases with refined paneling, so that a more rapid iteration procedure had to be developed. This procedure is described next, followed by a description of how to get a reasonable initial guess for the solution of the system of nonlinear equations.

9.5.1 Quasi-Newton method

The system of nonlinear equations is solved using a quasi-Newton method. In this method the Jacobian matrix is stripped such that it contains the most dominant elements only. This saves computing time not only because only part of the matrix is to be computed, but also because we take care that the resulting system of linear equations for the corrections can be solved rapidly.

In the procedure the system of equations and the column vector with the unknown parameters are subdivided into blocks as described above, i.e. the system of equations is written as

$$\{fb_i(\{pb_1\},\{pb_2\},\ldots,\{pb_{NUP}\})\} = 0,\ i=1(1)NUP \tag{9.40}$$

where $\{fb_i\}$ denotes the sub-vector with the equations applied at the collocation points of the i-th strip and the sub-vector $\{pb_j\}$ contains the unknown parameters of strip j. Here the first NUPW column vectors have NVPW+3(NVP-NVPW)+2 entries, the remaining NUP-NUPW column vectors have dimension 3NVP+2. The total number of equations/unknowns is therefore M = NUPW*NVPW+3(NUP*NVP-NUPW*NVPW)+2NUP.

In the present quasi-Newton method the solution at the it-th iteration is obtained from the (it-1)-th solution as

$$\{pb_j\}^{it} = \{pb_j\}^{it-1} + \{\Delta pb_j\},\ j=1(1)NUP \tag{9.41a}$$

where the correction $\{\Delta pb_j\}$ follows from

$$[AA_i]\{\Delta pb_{i-2}\} + [A_i]\{\Delta pb_{i-1}\} + [B_i]\{\Delta pb_i\} + [C_i]\{\Delta pb_{i+1}\} = -\{F_i\}^{it-1} \tag{9.41b}$$

for i=1(1)NUP, with

$$[AA_i] = \frac{\partial fb_i}{\partial pb_{i-2}},\quad [A_i] = \frac{\partial fb_i}{\partial pb_{i-1}},\quad [B_i] = \frac{\partial fb_i}{\partial pb_i},\quad [C_i] = \frac{\partial fb_i}{\partial pb_{i+1}} \tag{9.41c}$$

where the (it-1)-th solution $\{pb_j\}^{it-1}$, j=1(1)NUP is used to evaluate these four blocks of the stripped Jacobian. The residual vector $\{F_i\}^{it-1}$ used in Eq. (9.41b) follows from

$$\{F_i\}^{it-1} = \{fb_i(\{pb_1\}^{it-1}, \{pb_2\}^{it-1},\ldots,\{pb_{NUP}\}^{it-1})\} \tag{9.41d}$$

It follows from Eq. (9.41b) that we retained a four-diagonal-block structure of the original full Jacobian (Fig. 9.18). It contains the derivatives with respect to the unknown parameters of the (i-2)-th, (i-1)-th, i-th and (i+1)-th strip. The motivation for this particular choice is that it has the same structure as the finite-difference scheme used in s-direction, while it still can be solved very efficiently (see Appendix G) in $O(M^3/NUP^2)$ operations.

9.5.2 Derivation of Jacobian matrix

At each iteration step all still required derivatives with respect to the unknown parameters are computed from the expressions obtained from taking, analytically, the derivative of the discretized boundary conditions, Eqs. (9.33), (9.34), (9.35) and (9.39).

Next consider the derivatives of the stream-surface condition Eq. (9.33), here written as

$$f^1_\ell = \{(\bar{U}_\infty + \bar{u}_\mu).\bar{e}_n\}_\ell,\ \ell=(m-1)NVP+n \tag{9.42a}$$

where $\bar{u}_\mu$, the velocity induced at $\bar{x}(s^*_m,t^*_n)$ by the doublet distribution, is expressed in terms of aerodynamic influence coefficients, see Eq. (9.32).

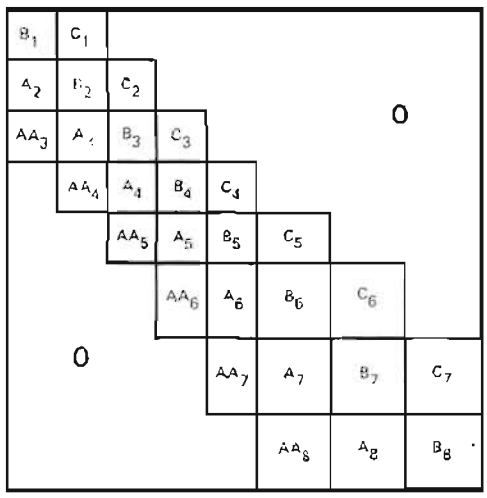


Fig. 9.18 Stripped 4-diagonal-block Jacobian matrix

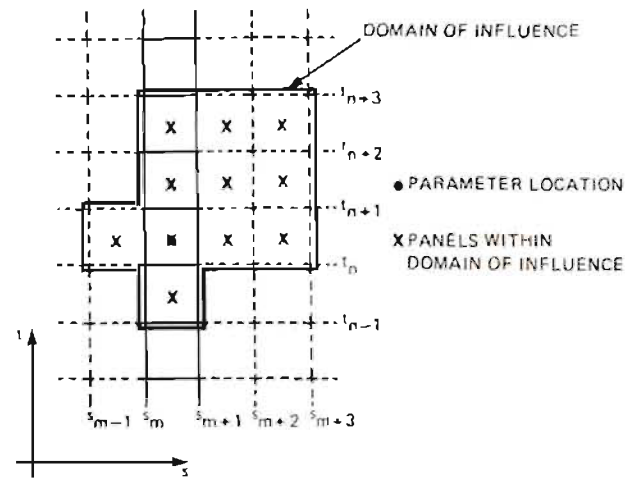


Fig. 9.19 Domain of influence of parameter at $(s^*_m,t^*_n)$

The derivative with respect to $\mu_k$ of $f^1_\ell$ then is straightforward, i.e.

$$\frac{\partial f^1_\ell}{\partial \mu_k} = \bar{a}_k(\bar{x}^*_{mn}, \bar{x}^*_{ij}, \text{etc.}).(\bar{e}_n)_\ell, \quad k=(i-1)NVP+j \tag{9.42b}$$

The derivative with respect to a geometric unknown like for example $y_k$ is

$$\frac{\partial f^1_\ell}{\partial y_k} = (\bar{U}_\infty + \bar{u}_\mu)_\ell . \frac{\partial}{\partial y_k}(\bar{e}_n)_\ell + \frac{\partial \bar{u}_\mu}{\partial y_k}.(\bar{e}_n)_\ell \tag{9.42c}$$

Since everything is expressed in terms of $\bar{x}$, $\bar{x}_s$, $\bar{x}_t$, $\bar{x}_{ss}$, $\bar{x}_{st}$ and $\bar{x}_{tt}$ all evaluated at panel midpoints, the derivative with respect to for example $y_k$ is most conveniently expressed as:

$$\begin{aligned}\frac{\partial}{\partial y_k} = \sum_{ii}\Big[\sum_{jj}\Big\{&\Big(\frac{\partial}{\partial y_k} y^*_{ijj}\Big)\frac{\partial}{\partial y^*_{ijj}} \\ &+ \Big(\frac{\partial}{\partial y_k} y^*_{s_{ijj}}\Big)\frac{\partial}{\partial y^*_{s_{ijj}}} + \Big(\frac{\partial}{\partial y_k} y^*_{t_{ijj}}\Big)\frac{\partial}{\partial y^*_{t_{ijj}}} \\ &+ \Big(\frac{\partial}{\partial y_k} y^*_{ss_{ijj}}\Big)\frac{\partial}{\partial y^*_{ss_{ijj}}} + \Big(\frac{\partial}{\partial y_k} y^*_{st_{ijj}}\Big)\frac{\partial}{\partial y^*_{st_{ijj}}} + \Big(\frac{\partial}{\partial y_k} y^*_{tt_{ijj}}\Big)\frac{\partial}{\partial y^*_{tt_{ijj}}}\Big\} + \\ &+ \Big(\frac{\partial}{\partial y_k} y^*_{v_{ii}}\Big)\frac{\partial}{\partial y^*_{v_{ii}}} + \Big(\frac{\partial}{\partial y_k} y^*_{v_{s_{ii}}}\Big)\frac{\partial}{\partial y^*_{v_{s_{ii}}}} + \Big(\frac{\partial}{\partial y_k} y^*_{v_{ss_{ii}}}\Big)\frac{\partial}{\partial y^*_{v_{ss_{ii}}}}\Big]\end{aligned} \tag{9.42d}$$

where the terms inside () follow from the finite-difference expressions discussed earlier.

Returning to Eq. (9.42d) one observes that the derivative of $\bar{e}_n$ is easily obtained from its definition in Eq. (9.33b), i.e. the only nonzero derivatives, to be substituted in Eq. (9.42d) are:

$$\frac{\partial \bar{e}_n}{\partial y^*_s} = \frac{\bar{e}_y \times \bar{x}^*_t}{|\bar{x}^*_s \times \bar{x}^*_t|} - \bar{e}_n\Big(\frac{\bar{e}_n.(\bar{e}_y \times \bar{x}^*_t)}{|\bar{x}^*_s \times \bar{x}^*_t|}\Big) \tag{9.42e}$$

$$\frac{\partial \bar{e}_n}{\partial y^*_t} = \frac{\bar{x}^*_s \times \bar{e}_y}{|\bar{x}^*_s \times \bar{x}^*_t|} - \bar{e}_n\Big(\frac{\bar{e}_n.(\bar{x}^*_s \times \bar{e}_y)}{|\bar{x}^*_s \times \bar{x}^*_t|}\Big) \tag{9.42f}$$

for ii=m and jj=n.

The derivatives with respect to the geometric unknowns of the induced velocity $\bar{u}_\mu$, the "geometric influence coefficients" involve all terms in Eq. (9.42d), at least as long as panel midpoint (ii,jj) is within the "domain of influence" of $y_k$ (see Fig. 9.19). The derivative with respect to the panel midpoint quantities of the induced velocity involves taking the derivative of the expressions derived in section 9.3. This straightforward, but rather elaborate, analytic differentiation has been carried out in full detail, but the resulting expressions are not given here.

The pressure-jump condition, Eq. (9.34), is here written as

$$f^2_\ell = (\bar{U}_\infty + \bar{u}_\mu)_\ell . (\bar{\gamma} \times \bar{e}_n)_\ell, \quad \ell = (m-1)NVP+n \tag{9.43a}$$

where $\bar{\gamma}$ is the surface vorticity vector. The derivative with respect to $\mu_k$ of $f^2_\ell$ then follows as

$$\frac{\partial f^2_\ell}{\partial \mu_k} = \bar{a}_k(\bar{x}^*_{mn}, \bar{x}^*_{ij}, \text{etc.}).(\bar{\gamma} \times \bar{e}_n)_\ell + (\bar{U}_\infty + \bar{u}_\mu)_\ell . (\frac{\partial \bar{\gamma}}{\partial \mu_k} \times \bar{e}_n)_\ell \tag{9.43b}$$

where

$$\frac{\partial}{\partial \mu_k}\bar{\gamma}_\ell = \Big(\frac{-\bar{x}^*_s}{|\bar{x}^*_s \times \bar{x}^*_t|}\Big)_{mn} \frac{\partial}{\partial \mu_k} \mu_t(s^*_m, t^*_n) + \Big(\frac{\bar{x}^*_t}{|\bar{x}^*_s \times \bar{x}^*_t|}\Big)_{mn} \frac{\partial}{\partial \mu_k} \mu_s(s^*_m, t^*_n) \tag{9.43c}$$

So for this equation one requires the "aerodynamic influence coefficients" and the finite-difference scheme for $\mu^*_s$ and $\mu^*_t$.

The derivative with respect to geometric parameters, like $y_k$, becomes:

$$\frac{\partial f^2_\ell}{\partial y_k} = (\bar{U}_\infty + \bar{u}_\mu)_\ell . (\frac{\partial \bar{\gamma}}{\partial y_k} \times \bar{e}_n + \bar{\gamma} \times \frac{\partial \bar{e}_n}{\partial y_k})_\ell + \frac{\partial \bar{u}_\mu}{\partial y_k}.(\bar{\gamma} \times \bar{e}_n)_\ell \tag{9.43d}$$

where the derivative of $\bar{u}_\mu$ is again the "geometric influence coefficient". The derivative of $\bar{e}_n$ follows from Eqs. (9.42d-f), while the derivative of $\bar{\gamma}$ follows from Eq. (9.42d) with as only nonzero entries:

$$\frac{\partial \bar{\gamma}}{\partial y^*_s} = -\mu^*_t \frac{\bar{e}_y}{|\bar{x}^*_s \times \bar{x}^*_t|} - \bar{\gamma}\left(\frac{\bar{e}_n \cdot (\bar{e}_y \times \bar{x}^*_t)}{|\bar{x}^*_s \times \bar{x}^*_t|}\right) \tag{9.43e}$$

$$\frac{\partial \bar{\gamma}}{\partial y^*_t} = \mu^*_s \frac{\bar{e}_y}{|\bar{x}^*_s \times \bar{x}^*_t|} - \bar{\gamma}\left(\frac{\bar{e}_n \cdot (\bar{x}^*_s \times \bar{e}_y)}{|\bar{x}^*_s \times \bar{x}^*_t|}\right) \tag{9.43f}$$

for ii=m and jj=n.

The arc-length equation, Eq. (9.35), is here written as

$$f^3_\ell = \frac{1}{b\ell(s^*_m)}\left(\frac{1}{4}|\bar{x}^-_t| + \frac{1}{2}|\bar{x}^*_t| + \frac{1}{4}|\bar{x}^+_t|\right)_\ell - 1 \tag{9.44a}$$

where $\bar{x}^\pm_t = \bar{x}^*_t \pm \frac{1}{2}\Delta t_n \bar{x}^*_{tt}$.

Clearly the derivative with respect to $\mu_k$ is zero, while the derivative with respect to for example $y_k$ becomes:

$$\begin{aligned}\frac{\partial f^3_\ell}{\partial y_k} = \frac{1}{b\ell(s^*_m)}\Bigg(&\frac{1}{4}\frac{\bar{x}^-_t}{|\bar{x}^-_t|} \cdot \left(\frac{\partial \bar{x}^*_t}{\partial y_k} - \frac{1}{2}\Delta t_n \frac{\partial \bar{x}^*_{tt}}{\partial y_k}\right) \\ &+ \frac{1}{2}\frac{\bar{x}^*_t}{|\bar{x}^*_t|} \cdot \left(\frac{\partial \bar{x}^*_t}{\partial y_k}\right) \\ &+ \frac{1}{4}\frac{\bar{x}^+_t}{|\bar{x}^+_t|} \cdot \left(\frac{\partial \bar{x}^*_t}{\partial y_k} + \frac{1}{2}\Delta t_n \frac{\partial \bar{x}^*_{tt}}{\partial y_k}\right)\Bigg)_\ell\end{aligned} \tag{9.44b}$$

The remaining derivatives follow directly from the finite-difference schemes for $\bar{x}^*_t$ and $\bar{x}^*_{tt}$.

Finally consider the two conditions on the vortex core. The first condition, Eq. (9.39a), is that there is no resultant force normal to the feeding sheet. It is written as:

$$g^1_m = (\bar{U}_\infty + \bar{u}_\mu)_m \cdot (\bar{g}_\nu \times \bar{e}_1)_m \tag{9.45a}$$

where $\bar{u}_\mu = \bar{u}_\mu(\bar{x}_\nu(s^*_m))$ and the "vorticity vector" $\bar{g}_\nu$ follows from Eq. (9.39a) as

$$\bar{g}_\nu = \{\mu(s^*_m,T)\bar{x}_{\nu_s}(s^*_m) + \mu_s(s^*_m,T)(\bar{x}_\nu(s^*_m) - \bar{x}(s^*_m,T))\}/|\bar{x}_{\nu_s}(s^*_m)| \tag{9.45b}$$

The derivative with respect to $\mu_k$ of $g^1_m$ then follows as

$$\frac{\partial g^1_m}{\partial \mu_k} = \bar{a}_k(\bar{x}_\nu(s^*_m), \bar{x}^*_{ij}, \text{etc.}) \cdot (\bar{g}_\nu \times \bar{e}_1)_m + (\bar{U}_\infty + \bar{u}_\mu)_m \cdot \left(\frac{\partial \bar{g}_\nu}{\partial \mu_k} \times \bar{e}_1\right)_m \tag{9.45c}$$

with

$$\begin{aligned}\frac{\partial \bar{g}_\nu}{\partial \mu_k} = {}& \bar{x}_{\nu_s}(s^*)\frac{\partial}{\partial \mu_k}\{\mu(s^*_m,t^*_n) + \tfrac{1}{2}\Delta t_n \mu_t(s^*_m,t^*_n) + \tfrac{1}{4}(\tfrac{1}{2}\Delta t_n)^2 \mu_{tt}(s^*_m,t^*_n)\}_{n=NVP} + \\ &\{\bar{x}_\nu(s^*_m) - \bar{x}(s^*_m,T)\}\frac{\partial}{\partial \mu_k}\{\mu_s(s^*_m,t^*_n) + \tfrac{1}{2}\Delta t_n \mu_{st}(s^*_m,t^*_n)\}_{n=NVP}\}/|\bar{x}_{\nu_s}(s^*_m)|\end{aligned} \tag{9.45d}$$

So to get the derivative with respect to $\mu_k$ we need both the aerodynamic influence coefficients and the finite-difference schemes for $\mu^*$, $\mu^*_s$, $\mu^*_t$, $\mu^*_{st}$ and $\mu^*_{tt}$.

*The derivative with respect to geometric parameters like $y_k$ can be found from*

$$\frac{\partial g^1_m}{\partial y_k} = (\bar{U}_\infty + \bar{u}_\mu)_m \cdot \left(\frac{\partial \bar{g}_\nu}{\partial y_k} \times \bar{e}_1 + \bar{g}_\nu \times \frac{\partial \bar{e}_1}{\partial y_k}\right)_m + \frac{\partial \bar{u}_\mu}{\partial y_k} \cdot (\bar{g}_\nu \times \bar{e}_1)_m \tag{9.45e}$$

where, once more, the derivative of $\bar{u}_\mu$ is the "geometric influence coefficient". The derivative of $\bar{g}_\nu$ follows from Eq. (9.42d) with as nonzero entries:

$$\frac{\partial \bar{g}_\nu}{\partial y^*} = -\mu_s(s^*_m,T)\frac{\bar{e}_y}{|\bar{x}^*_{\nu_s}|} \tag{9.45f}$$

$$\frac{\partial \bar{g}_\nu}{\partial y^*_t} = \tfrac{1}{2}\Delta t_{NVP}\frac{\partial \bar{g}_\nu}{\partial y^*}, \qquad \frac{\partial \bar{g}_\nu}{\partial y^*_{tt}} = \tfrac{1}{4}(\Delta t_{NVP})^2\left(\frac{\partial \bar{g}_\nu}{\partial y^*}\right) \tag{9.45g}$$

$$\frac{\partial \bar{g}_v}{\partial y^*_{v_s}} = \mu_s(s^*_m,T)\frac{\bar{e}_y}{|\bar{x}^*_{v_s}|} \tag{9.45h}$$

$$\frac{\partial \bar{g}_v}{\partial y^*_{v_s}} = \mu(s^*_m,T)\frac{\bar{e}_y}{|\bar{x}^*_{v_s}|} - \bar{g}_v\left(\frac{\bar{x}^*_{v_s}\cdot\bar{e}_y}{|\bar{x}^*_{v_s}|^2}\right) \tag{9.45i}$$

for ii=m and jj=NVP. The derivative of $\bar{e}_l$, defined in Eq. (9.39a) also follows from Eq. (9.42d) with as non-zero entries:

$$\frac{\partial \bar{e}_l}{\partial y^*} = -\frac{\partial \bar{e}_l}{\partial y^*_v} \tag{9.45j}$$

$$\frac{\partial \bar{e}_l}{\partial y^*_c} = \tfrac{1}{2}\Delta t_{NVP}\frac{\partial \bar{e}_l}{\partial y^*}\,, \quad \frac{\partial \bar{e}_l}{\partial y^*_{tt}} = \tfrac{1}{2}(\tfrac{1}{2}\Delta t_{NVP})^2\left(\frac{\partial \bar{e}_l}{\partial y^*}\right) \tag{9.45k}$$

$$\frac{\partial \bar{e}_l}{\partial y^*_{v_s}} = \frac{\bar{x}^*_{v_s}\times\bar{e}_y}{|\bar{x}^*_{v_s}\times(\bar{x}^*_v-\bar{x}(s^*_m,T))|} - \bar{e}_l\left(\frac{\bar{e}_l\cdot\bar{x}^*_{v_s}\times\bar{e}_l}{|\bar{x}^*_{v_s}\times(\bar{x}^*_v-\bar{x}(s^*_m,T))|}\right) \tag{9.45l}$$

$$\frac{\partial \bar{e}_l}{\partial y^*_{v_s}} = \frac{\bar{e}_y\times(\bar{x}^*_v-\bar{x}(s^*_m,T))}{|\bar{x}^*_{v_s}\times(\bar{x}^*_v-\bar{x}(s^*_m,T))|} - \bar{e}_l\left(\frac{\bar{e}_l\cdot\bar{e}_y\times(\bar{x}^*_v-\bar{x}(s^*_m,T))}{|\bar{x}^*_{v_s}\times(\bar{x}^*_v-\bar{x}(s^*_m,T))|}\right) \tag{9.45m}$$

also for ii=m and jj=NVP.

The second condition applied at the vortex core is that the velocity vector is parallel to the feeding sheet, Eq. (9.39b). It is written as

$$g^2_m = \{(\bar{U}_\infty + \bar{u}_\mu).\bar{e}_l\}_m\mu(s^*_m,T) \tag{9.46a}$$

The derivative with respect to $\nu_k$ of $g^2_m$ is:

$$\frac{\partial g^2_m}{\partial \nu_k} = \bar{a}_k(\bar{x}_v(s^*_m),\ \bar{x}^*_{1j},\text{etc.}).(\bar{e}_l)_m\mu(s^*_m,T)$$

$$+ \{(\bar{U}_\infty+\bar{u}_\mu).\bar{e}_l\}_m\frac{\partial}{\partial \nu_k}\{\mu(s^*_m,t^*_n)+\tfrac{1}{2}\Delta t_n\mu_t(s^*_m,t^*_n)+(\tfrac{1}{2}\Delta t_n)^2\mu_{tt}(s^*_m,t^*_n)\}_{n=NVP} \tag{9.46b}$$

So also here we need both the "aerodynamic influence coefficients" and the finite-difference schemes for $\mu^*$, $\mu^*_t$ and $\mu^*_{tt}$.

The derivative with respect to geometric parameters like $y_k$ can be found from

$$\frac{\partial g^2_m}{\partial y_k} = \{(\bar{U}_\infty + \bar{u}_\mu).\frac{\partial \bar{e}_l}{\partial y_k} + \frac{\partial \bar{u}_\mu}{\partial y_k}.\bar{e}_l\}_m\mu(s^*_m,T) \tag{9.46c}$$

where the derivative of $\bar{e}_l$ is given in Eqs. (9.45j-m) and we use, once more, the "geometric influence coefficients", i.e. the derivative with respect to $y_k$ of $\bar{u}_\mu$.

In considering the derivatives with respect to the unknown geometric parameters we only considered derivatives with respect to $y_k$, $y^*$, $y^*_s$, etc. To obtain the derivative with respect to $z_k$, $z^*$, $z^*_s$, etc. one just replaces y by z, and also $\bar{e}_y$ by $\bar{e}_z$.

9.5.3 Initial guess for iteration procedure

The present quasi-Newton procedure does not require step-size control. The norm of the residual vector decreases by an order of magnitude per iteration. However, as with a any Newton method the iteration has to start with an initial guess for the solution that is within the "domain of attraction" of the final solution.

The starting solution for a specific case can be obtained in several ways. The easiest way is to use one of the solutions obtained previously as the initial guess for the (slightly different) new case. The following "continuation" procedures can be used:

(i) Use the solution obtained at a nearby incidence as initial guess for the present incidence.
(ii) Use the solution obtained for a certain panel distribution as starting solution for the case with a refined or redistributed panel scheme.
(iii) Extend a solution computed earlier to one with a longer leading-edge vortex sheet or near wake and use this as initial guess.
(iv) Implant the solution obtained for one wing geometry onto the computational domain of a new slightly different wing geometry.

For a completely new case results of the slender-body method and of the 2D-time-dependent analogy described in previous chapters can be used to obtain an initial guess. For a given geometry of wing, leading-edge vortex sheet, and near wake an improved initial doublet distribution is obtained by imposing the stream surface condition, Eq. (9.33), on the wing and the pressure-jump condition on the leading-edge vortex sheet and the near-wake. These equations are at most quadratic in $\nu_k$ and are solved by the full Newton method. The initial guess for this pre-iteration procedure is found by solving for the doublet distribution applying the stream-surface everywhere, i.e. on the wing, leading-edge vortex sheet and near wake.

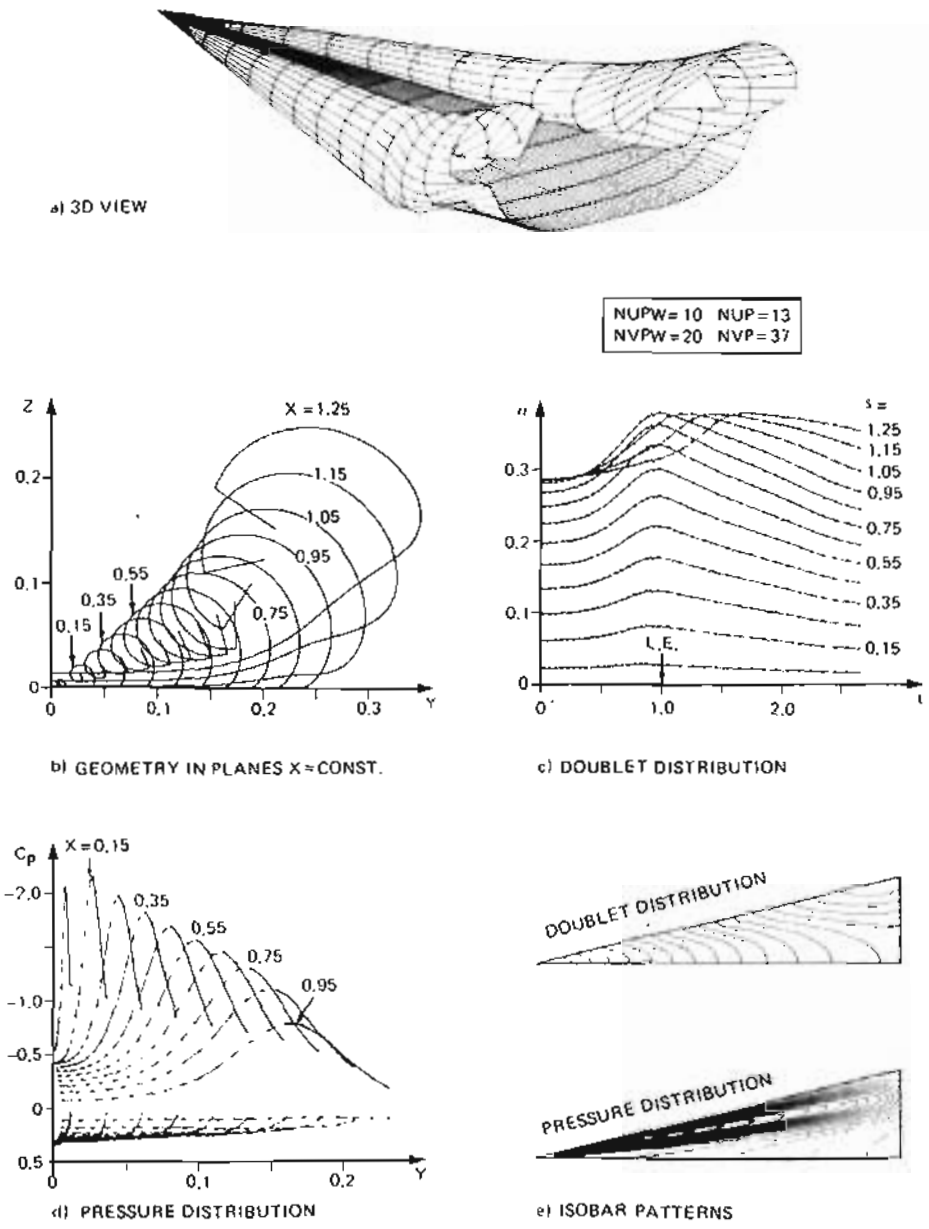


Fig. 9.20 Solution for unit-aspect-ratio wing at 20 deg incidence

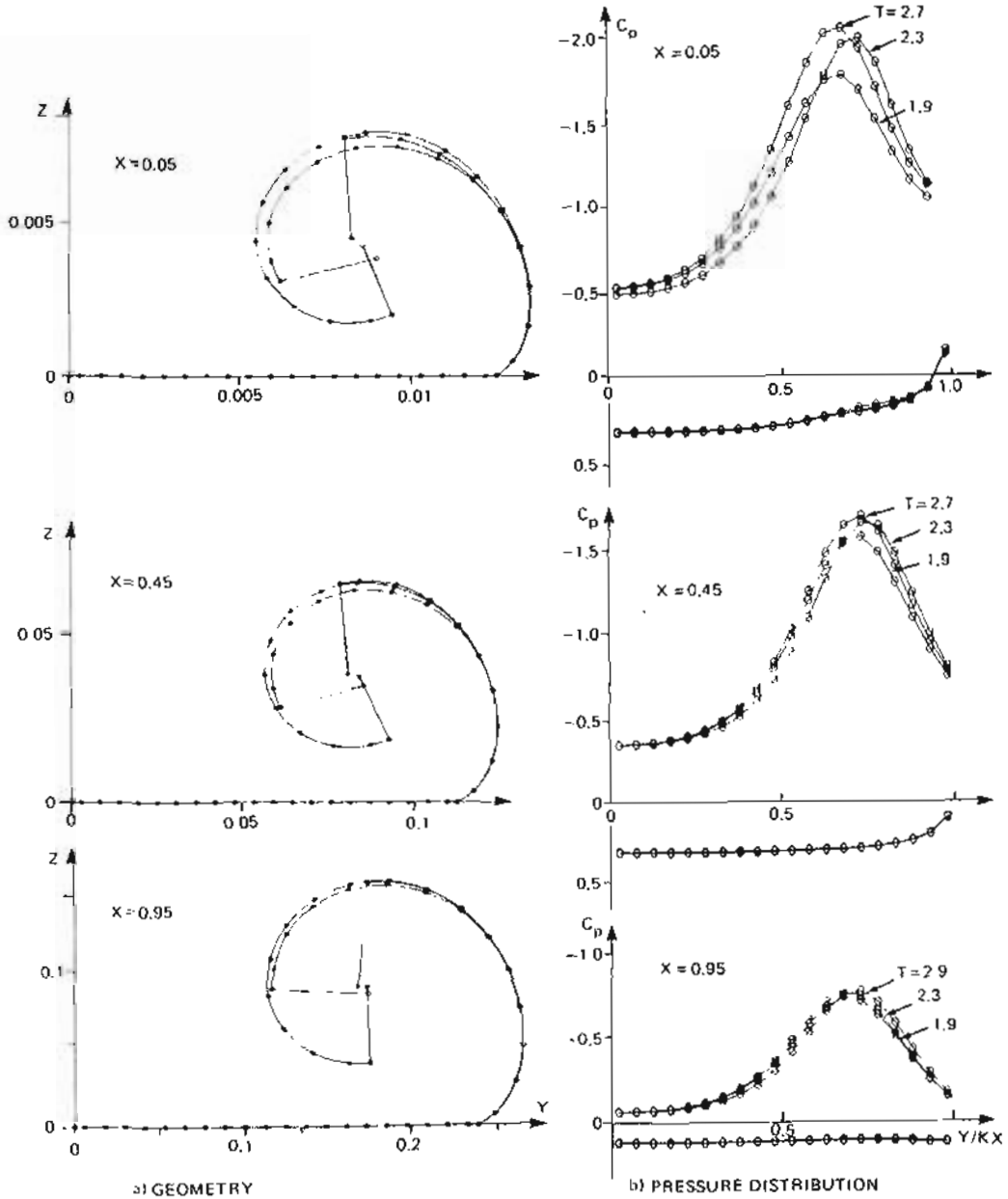


Fig. 9.21 Solution for various lengths of leading-edge vortex sheet ($\Lambda$=76 deg, $\alpha$= 20 deg)

9.6 Examples of application

In this section we apply the three-dimensional flow method to a number of cases. We will consider some computational aspects, such as convergence of the iteration procedure, convergence of the solution for increasing number of panels, behaviour of the solution near the apex, influence of leading-edge vortex sheet cut-off parameter T and near-wake cut-off parameter S, etc.
Furthermore, we compare results of the present method with results of other computational methods as well as with experimental data.

9.6.1 Basic test case: Unit-aspect-ratio delta wing at 20 deg incidence

This case is more or less a standard test case for computational vortex flow methods and we used it earlier as an example in chapters 7 and 8.

It is a good test case, the geometry is simple and the leading-edge vortex has a dominant effect on the flow. The sweep of the leading-edge of this delta wing is 76 deg.

Fig. 9.20 provides an overview of the solution for this case, obtained for a wake cut-off parameter S=1.3, vortex sheet cut-off parameter T=2.7, a uniform paneling in s-direction (NUPW=10, NUP=13) as well as in t-direction, where we used 20 panels with $\Delta t=0.05$ and 17 (sheet) panels with $\Delta t=0.1$. The figure includes:

(a) 3D view of the (starboard and portside of the) geometry of the wing, the leading-edge vortex sheet and the near wake. The far wake, which is attached to the "trailing edge" of the near wake, is not drawn. In the present method the trailing-edge vortex is not modeled explicitly, however, it does show up as a wrinkling in the near wake vortex sheet.

b) Cross-sections of the geometry of the vortex sheet. Both from the 3D view and the cross-sections one observes that the leading-edge vortex sheet has a conical appearance almost up to the trailing edge of the wing. In the crosssections of the near wake the dent corresponding to the trailing-edge vortex is clearly evident. It represents the smoothed-out representation of the double-branched trailing-edge vortex that forms there.

(c) Doublet distribution, shown as $\mu(t;s)$ has a conical appearance in the sense that its shape is similar for all the cross-flow planes that intersect the wing. However, its variation in streamwise (s-)direction deviates rather soon from the linear variation assumed in conical flow. At the trailing edge the doublet distribution reaches its maximum. On the near wake the doublet strength is constant along streamlines. Observe that on the near wake the point where the doublet distribution has its maximum slope, which corresponds with the position of the center of vorticity of the trailing-edge vortex, shifts in spanwise direction. The figure with the iso-doublet contours (the curves of which correspond with vortex lines), Fig. 9.20e, on the wing also indicates the three-dimensional character of the solution. The latter figure shows further that the vortex lines leave the wing almost perpendicular to the leading edge turning sharply in the process. Whence on the leading-edge vortex sheet the vortex lines turn sharply again, now in streamwise direction.

(d) Pressure distribution, Fig. 9.20d. It shows that on the upper wing surface the pressure distribution is not conical (i.e. constant along y/x=constant) at all: in streamwise direction it increases monotonically from a region near the apex to the trailing edge. This is also evident from the isobar plot, which for conical flow would have consisted of a fan of rays emanating from the apex.

In the next few sections the influence of several parameters of the computational model are investigated, all for the above basic test case.

9.6.2 Influence of the length of the leading-edge vortex sheet

The computational effort strongly depends on the number of panels on the leading-edge vortex sheet and near wake; each of these panels contributing 3 unknowns to the problem. Therefore it is important to know what the influence on the solution is of the length of the leading-edge vortex sheet. The results of three cases are compared, the solution of Fig. 9.20 with T=2.7 and the feeding sheet at approximately the "six-o'clock" position, a solution with T=2.3 (feeding sheet at "nine o'clock") and one with T=1.9 (feeding sheet at "twelve o'clock"). All other computational parameters are identical, i.e. S=1.3, $\Delta s=0.1$, $\Delta t=0.05$ on the wing and 0.1 on the leading-edge vortex sheet, see Table 9.1.

| | NUPW | NVPW | NUP | NVP | S | T | $\Delta s$ | $\Delta t$ wing/sheet | $C_z$ | $C_m$ |
|---|---|---|---|---|---|---|---|---|---|---|
| 12h | 10 | 20 | 13 | 29 | 1.3 | 1.9 | 0.1 | 0.05/0.1 | 0.861 | -0.512 |
| 9h | " | " | " | 33 | " | 2.3 | " | " | 0.870 | -0.518 |
| 6h | " | " | " | 37 | " | 2.7 | " | " | 0.898 | -0.533 |

$\Lambda$=76 deg, $\alpha$=20 deg

Table 9.1 Solution for three different T

The table includes the value of the normal force $C_z$ and the pitching moment $C_m$ (with the apex as point of reference). It shows that both the normal force and the pitching moment increase slightly (of the order of 5%) in magnitude with increasing T. Fig. 9.21 shows the effect of T on the geometry of the vortex system and on the pressure distribution. It demonstrates that the position of both the outer part of the vortex sheet and of the vortex core is affected. The pressure distribution is only affected on the wing upper surface, where the height of the suction peak increases slightly with increasing T and its lateral position varies as well. The change in the lateral position of the suction peak more or less corresponds with the change in the lateral position of the vortex core. The height of the suction peak probably depends on both the circulation of the leading-edge vortex system and its center if vorticity. With just three values of T investigated and the observation that for a given s the circulation varies non-monotonically with T, it is hard to conjecture what precisely causes the height of the suction peak to increase when T increases from T=1.9 to 2.3 and further to 2.7. However, the longest sheet employed here obviously represents a better model of the rolled-up-vortex-sheet/wing interaction than the shortest sheet.

The effect of the length of the leading-edge vortex sheet is, relatively, largest near the apex. However, because of the small absolute dimensions of the wing near the apex the effect on overall normal force and pitching moment is much smaller.

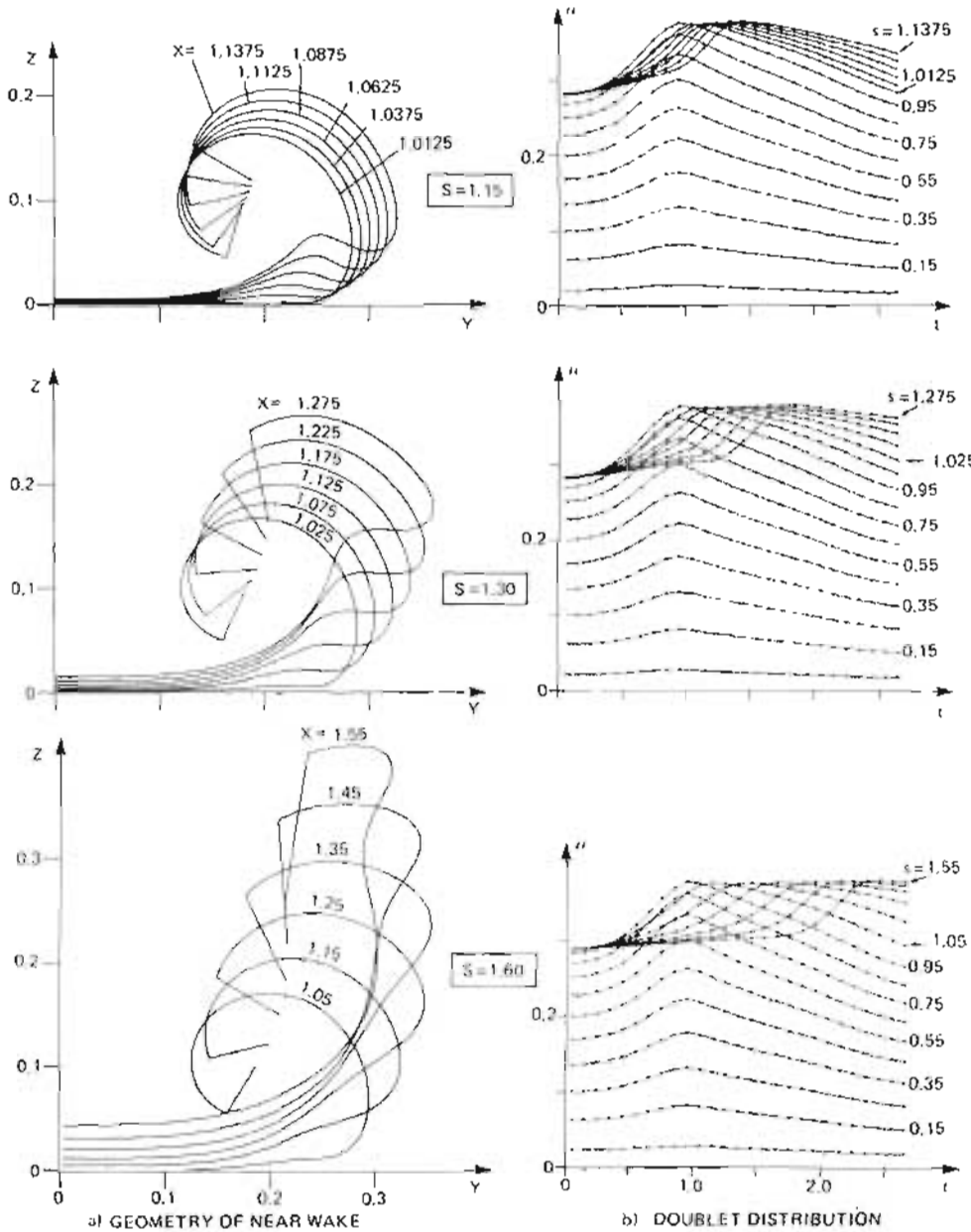


Fig. 9.22 Solution for various length S of near wake (Λ=76 deg, α=20 deg)

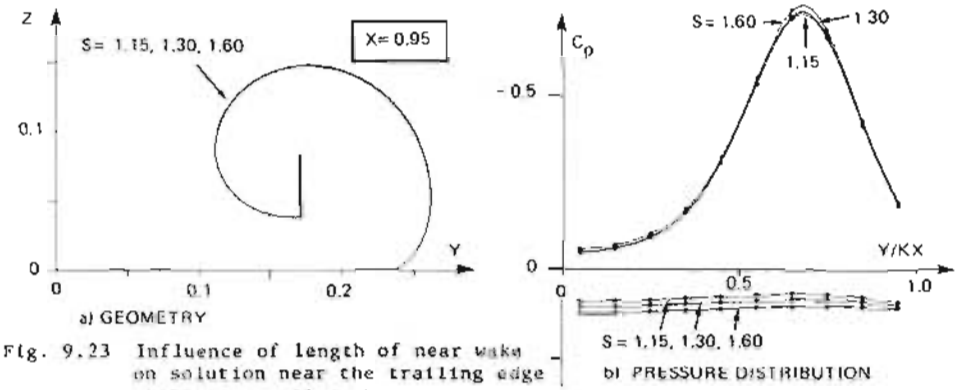


Fig. 9.23 Influence of length of near wake on solution near the trailing edge (Λ=76 deg, α=20 deg)

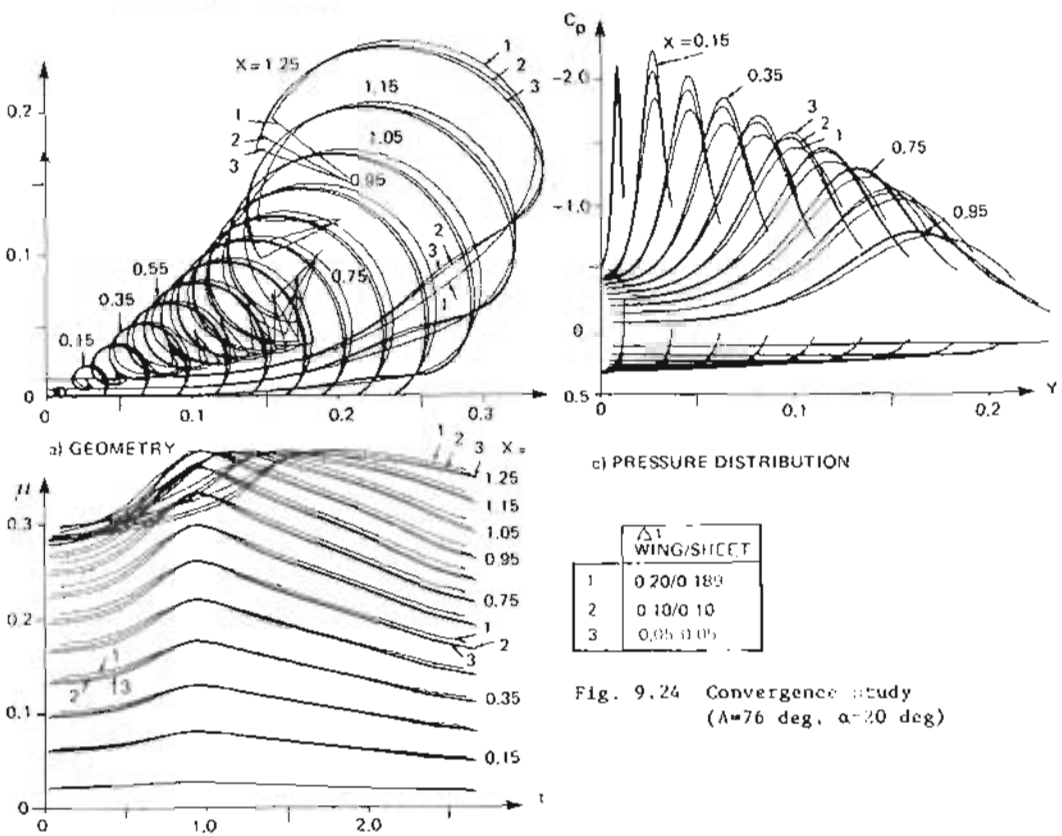


| | Δt WING/SHEET |
|---|---|
| 1 | 0.20/0.189 |
| 2 | 0.10/0.10 |
| 3 | 0.05/0.05 |

Fig. 9.24 Convergence study (Λ=76 deg, α=20 deg)

9.6.3 Influence of the length of the near wake

In the present method the near wake takes on the shape required to satisfy both the zero-normal-velocity boundary condition and the (not linearized) zero pressure-difference boundary condition, the same conditions that are imposed on the leading-edge vortex sheet. There is no special measure taken to model the trailing-edge vortex, however it is evident as a dent in the cross-sectional shape of the near wake. This shows up quite clearly in the 3D-view presented earlier in Fig. 9.20a. For that computation we used 3 near-wake strips, each of width $\Delta s=0.1$.

It is to be expected that more details of this second center of roll-up will be revealed by increasing the number of panels in t-direction, while its downstream development will be accelerated by refining the paneling in s-direction. The latter effect is investigated in Fig. 9.22.

Presented are three solutions, all for an identical panel scheme but with a different length of the near-wake, namely for a near-wake cut-off parameter S of 1.15, 1.30 and 1.60, respectively (see Table 9.2).

| NUPW | NVPW | NUP | NVP | S | T | $\Delta s$ wing/sheet | $\Delta t$ | $C_z$ | $C_m$ |
|---|---|---|---|---|---|---|---|---|---|
| 10 | 10 | 16 | 27 | 1.15 | 2.7 | 0.1/0.025 | 0.1 | 0.873 | -0.513 |
| " | " | " | " | 1.30 | " | 0.1/0.05 | " | 0.875 | -0.515 |
| " | " | " | " | 1.60 | " | 0.1/0.1 | " | 0.886 | -0.525 |

$\Lambda$=76 deg, $\alpha$=20 deg

Table 9.2 Solution for three different S

The results shown in Fig. 9.22 indicate that the details of the trailing-edge vortex are better resolved for smaller values of $\Delta s$ on the near-wake, but also that even for the coarsest scheme the trajectory of the vortex (i.e. the point of inflection in the cross-sectional shape) can be followed up to the last near-wake strip.

The doublet distributions for the three cases, also shown in Fig. 9.22 show a progressively further developed near wake. For the shortest one much vorticity still resides in the vortex sheet, while for the longest one almost all vorticity has been swept into the leading-edge vortex or has become concentrated in the region around the dent, i.e. the here not explicitly resolved but "stretched-out" trailing-edge vortex.

For the same value of S the effect on the near wake of halving $\Delta s$ (i.e. doubling the number of near wake strips) can be inferred from comparison of Figs. 9.20b and c and the middle part of Fig. 9.22a, showing an increased amount of "roll-up".

Although the choice of S has a large effect on the computed shape of the near wake, its effect on the flow on the wing itself is quite small. This is evident from the computed normal force and pitching moment, also listed in table 9.2, as well as from a comparison of the shape of the leading-edge vortex sheet, the wing doublet distribution and the wing pressure distribution. Naturally the largest influence is felt on the wing strip immediately upstream of the trailing edge, see Fig. 9.23. For the three values of S the cross-sectional shapes of the leading-edge vortex sheet are within plotting accuracy. The comparison of the pressure distribution shows that there are slight differences in the height of the upper-wing-surface suction peak and in the level of the lower-wing-surface pressure distribution.

It will be clear from the above study that the normal force, pitching moment, shape of leading-edge vortex sheet and the wing pressure distribution are relative insensitive to the length of the near wake (S-1) and its discretization. All the cases discussed in the sequel therefore have just 3 near-wake strips of width comparable to that of the wing strips.

9.6.4 Convergence of the numerical scheme

To investigate the convergence of the numerical scheme three cases are compared, each with identical length of the leading-edge vortex sheet, length of the near wake and discretization in s-direction but with decreasing panel size in t-direction (see Table 9.3).

| | NUPW | NVPW | NUP | NVP | S | T | $\Delta s$ | $\Delta t$ wing/sheet | $C_z$ | $C_m$ |
|---|---|---|---|---|---|---|---|---|---|---|
| 1 | 10 | 5 | 13 | 14 | 1.3 | 2.7 | 0.1 | 0.2/0.189 | 0.883 | -0.525 |
| 2 | " | 10 | " | 27 | " | " | " | 0.1/0.1 | 0.888 | -0.526 |
| 3 | " | 20 | " | 54 | " | " | " | 0.05/0.05 | 0.892 | -0.529 |

$\Lambda$=76 deg, $\alpha$=20 deg

Table 9.3 Solution for different panel densities

Table 9.3 shows that the normal force and pitching moment increase slightly in magnitude as the panel scheme is refined. Fig. 9.24 shows for the three cases the geometry, doublet distribution and pressure distribution. It indicates that as the panel scheme is refined the regions with higher curvature, e.g. on the leading-edge vortex sheet near the leading edge and at the "9-o'clock" position and on the near wake near the "trailing-edge vortex", are better resolved.

A similar observation is made for the doublet distribution where regions with larger slopes become more pronounced for the finer panel schemes. Note that it appears that, relatively, on the wing the doublet distribution at the leading edge (t=1.0) does not change very much with increasing panel density.

The pressure distribution presented in Fig. 9.24c shows that the results of the two finest panel schemes approach each other closely, with the smallest differences on the rearward part on the wing. As was the case for the influence of the length of the leading-edge vortex sheet discussed earlier, it is observed that the lower wing surface pressure distribution is only slightly affected by the panel density.

For the cross-flow planes x=0.45 and 0.95 Fig. 9.25 provides a more detailed comparison of the three solutions. Clearly this demonstrates again that the results for the two finest panel schemes are quite close to each other. For these two discretizations the paneling is fine enough to resolve the high curvature regions of the vortex sheet as well as the upper wing surface suction peak to a sufficient degree. On the other hand the solution for the coarsest panel scheme, only 5 wing panels and 8 vortex sheet panels in t-direction, already resolves the main characteristics of the final solution to a great extent.

From the present, limited, convergence study as well as from associated studies where the panel scheme on the wing and leading-edge vortex sheet was varied separately, it is concluded that in most cases panel schemes with $\Delta t$ of the order of 0.1 will give results that are sufficiently accurate.

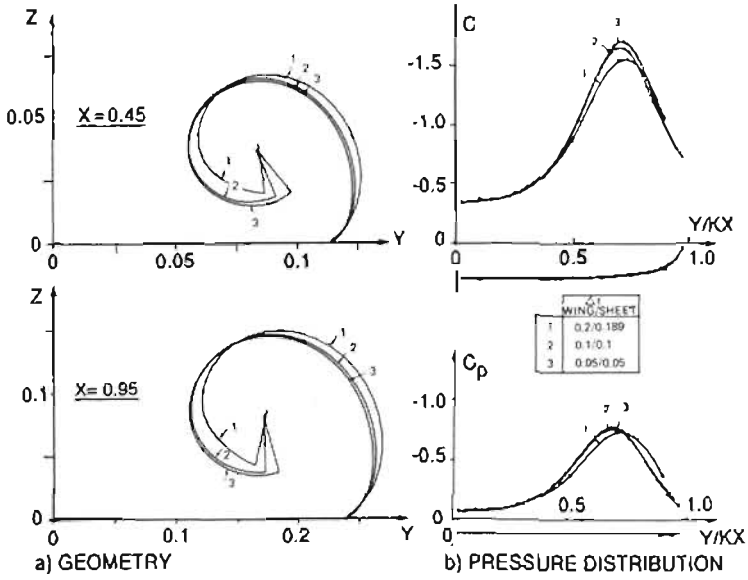


Fig. 9.25 Convergence study ($\Lambda$=76 deg, $\alpha$=20 deg)

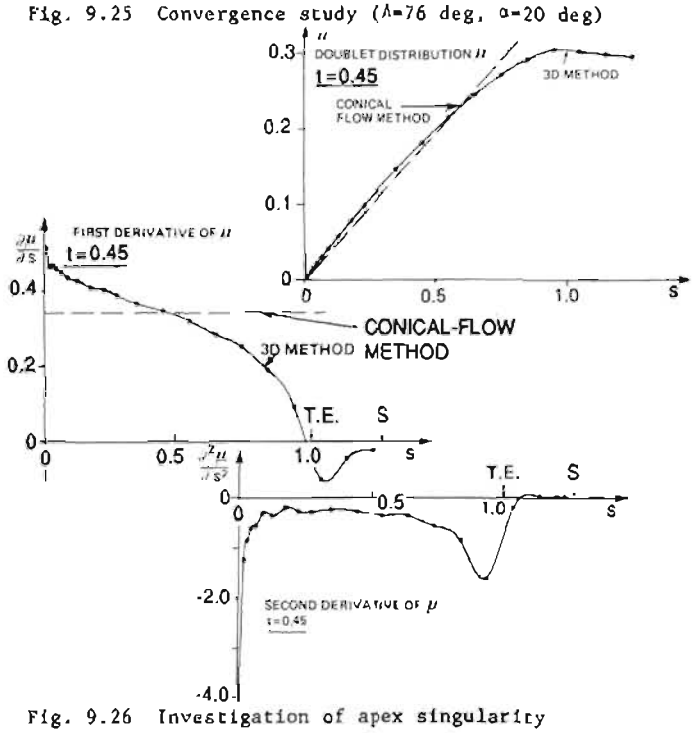


Fig. 9.26 Investigation of apex singularity

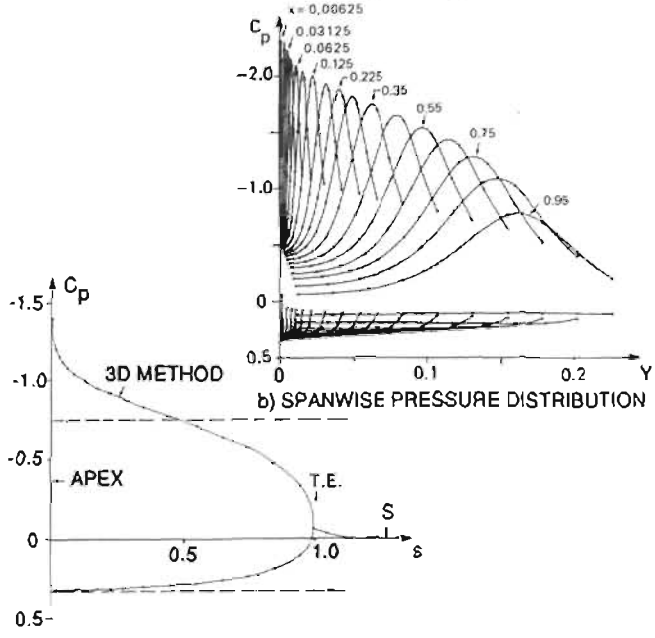


Fig. 9.27 3D character of the pressure distribution

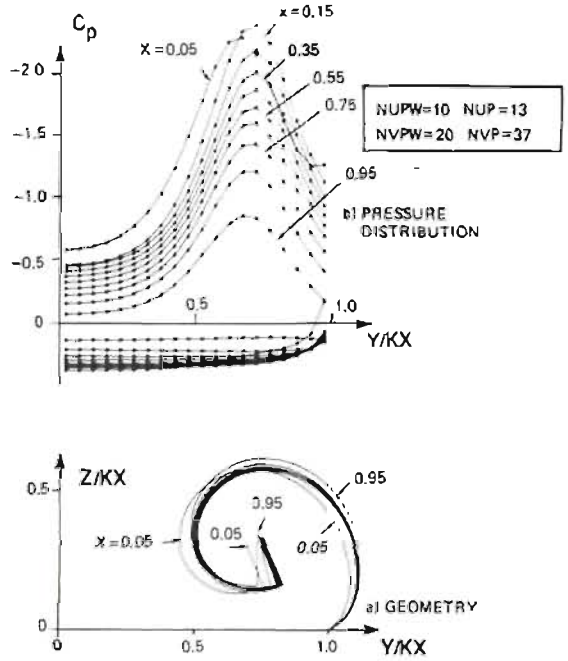


Fig. 9.28 Conicity of 3D solution ($\Lambda$=76 deg, $\alpha$=20 deg)

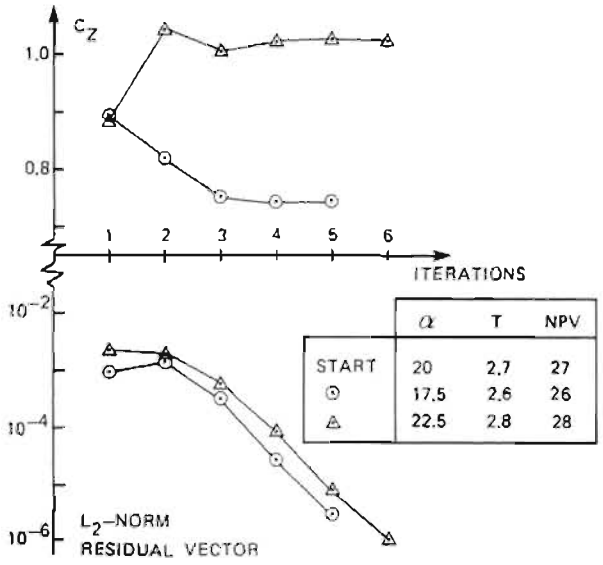


Fig. 9.29 Convergence iterative procedure

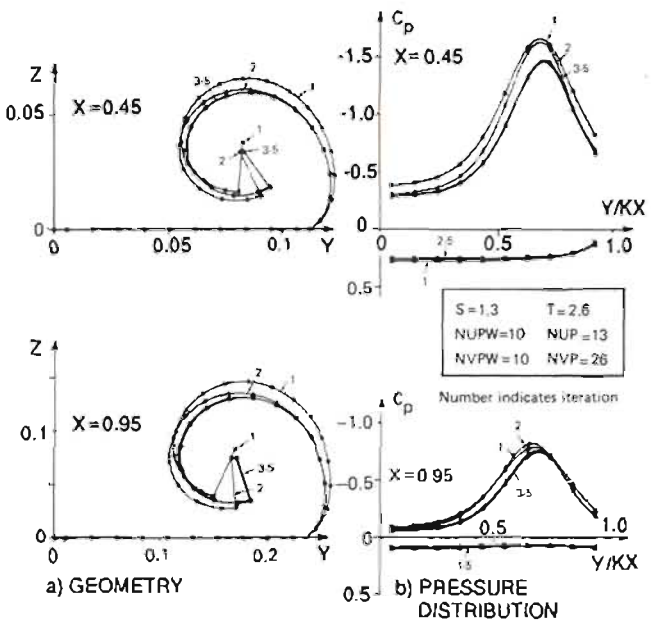


Fig. 9.30 Convergence history for case $\Lambda$=76 deg, $\alpha$=17.5 deg, with initial guess from solution for case $\Lambda$=76 deg, $\alpha$=20 deg

9.6.5 Three-dimensional character of the solution

In comparison with the quasi-conical solutions considered in Chapter 8 the fully three-dimensional solution considered here will deviate most from this approximate solution near the apex as well as near the trailing edge of the wing, the regions where the assumptions underlying the slender-body approximation are not valid.

At the apex it is to expected that the potential flow solution is singular. It has been shown by Germain-1955 that for the case of a flat-plate delta wing of semi-infinite extent with attached flow Laplace's equation has eigensolutions of the form

$$\varphi_m = r^{\nu_m} f_m\left(\frac{y}{r}, \frac{z}{r}\right) \qquad (9.47)$$

where r is the distance from the apex and $\nu_m$ depends on the sweep angle $\Lambda$. The first eigenvalue $\nu_1$ has a value between 0 and 1, with as special cases:

$\nu_1 =$ 1 for the case of a "needle", i.e. $\Lambda$=90 deg.

½ for the case of the unswept (2D) wing of infinite extent, i.e. $\Lambda$=0 deg. This corresponds with the familiar square-root singularity, in the velocity, of lifting-surface theory.

0 for the limiting case of a wing that covers the whole x-y plane, i.e. $\Lambda$=-90 deg.

For the case with leading-edge vortex sheets the eigensolutions are unknown. It will be hard to obtain these solutions, particularly because they would have to include the shape of the vortex sheet as well. However, with vortex sheets attached to the leading edge the singularity at the edge is weakened and the pressure remains finite (e.g. Figs. 9.20d, 9.21b, 9.23b, 9.25b). In exactly what way the solution behaves as we approach the apex along the leading edge is subject to speculation, but it may be expected that the singularity at the apex is weakened correspondingly. This then suggests that the first eigenvalue would have a value between 1 and 2. To check on this numerically, a case is considered with increased panel density near the apex. The panel scheme chosen in NUP=20, NVP=27, NUPW=17 and NVPW=10, equidistant in t direction ($\Delta t$=0.1) and with $s_i$=0(0.0125)0.05; 0.05(0.025)0.1; 0.1(0.05)0.3; 0.3(0.1)1.3 so that there are 4 strips on the first 5% of the wing.

Fig. 9.26 shows the doublet distribution (=$\Delta\phi$ across the surface) and its first and second derivative with respect to s, along t=constant=0.45. This figure indicates that as the apex is approached (s↓0) along t=constant $\mu$ tends to zero with both the magnitude of $\frac{\partial \mu}{\partial s}$ and of $\frac{\partial^2 \mu}{\partial s^2}$ rapidly increasing.

It also indicates that the region in which the singular behaviour is felt is small, much smaller than 5% of the root chord. It is hard to extract the exact form of the singular behaviour from the numerical results, recall that the method assumes a panelwise polynomial type of behaviour, but the above mentioned conjecture that $\nu_1 \in [1,2]$ appears to be confirmed. On the other hand, the rather sharp rise in the first and second derivative might suggest a ($x^2 \log x$)-type of behaviour as an alternative possibility.

At the trailing edge the pressure on the upper and lower wing surface equalize. Therefore the pressure increases from the apex towards the trailing edge, as shown in earlier figures and also in Fig. 9.27a which presents the spanwise pressure distributions for the case with the refined paneling near the apex discussed above. The figure clearly shows the behaviour near the apex and the steady increase of the pressure towards the trailing edge. The behaviour of the pressure distribution near the trailing edge is more clearly illustrated in Fig. 9.27b, where for t=0.45 $C_p$ is plotted versus s.

Near the trailing edge the doublet distribution (see Fig. 9.26) no longer increases in magnitude with increasing s, its slope gradually decreases towards zero, the value it has on the far wake.

In Figs. 9.26 and 9.27 we included the result of the slender-body method discussed in Chapter 8. It clearly shows the shortcomings of the (slender) conical-flow assumption near apex and trailing edge. However, note that on the central part of the wing the results of the conical flow method are in good quantitative agreement with the results of the 3D method.

The conicalness of the results of the latter method are assessed further in Fig. 9.28. Here the cross-sections of the geometry as well as the pressure distribution of the basic test case (Fig. 9.20) are plotted in "conical" terms, i.e. scaling the cross-flow plane coordinates with Kx, where K=cot$\Lambda$. This figure illustrates that geometrically the solution is almost conical indeed, with the exception of the cross-section nearest to the apex and the one nearest to the trailing edge. On the other hand, the pressure distribution is far from conical, which of course can be explained by the elliptic nature of this subsonic flow problem. Evidently in subsonic flow a conical geometry (wing and free vortex sheets) does not imply a conical flow. In this respect one wonders what, if any, geometry will generate subsonic conical flow.

9.6.6 Convergence history of iterative solution procedure

The four-diagonal-block approximate Jacobian matrix used in the quasi-Newton iteration procedure is recomputed at each iteration. The iteration procedure converges fairly rapidly, provided the initial guess is not too far removed from the solution sought. The extent of the "domain of attraction" depends upon the shape of the wing and angle of attack and may be quite small for "critical" cases as wings at a low angle of attack, wings with a small sweep and cases with a relatively long leading-edge vortex sheet.

As an example consider the situation encountered when carrying out an "angle-of-attack sweep". In such a sweep one uses the solution obtained at one incidence as initial guess for the solution to be obtained at a neighboring incidence. In Fig. 9.29 we consider migrating the solution for $\Lambda$=76 deg, $\alpha$=20 deg with panel scheme (NUP=13, NVP=27, NUPW=10, NVPW=10) and S=1.3, T=2.7 to $\alpha$=17.5 deg with the vortex sheet shortened by one panel (NPV=26, T=2.6) and to $\alpha$=22.5 deg with the vortex sheet extended by one panel (NPV=28, T=2.8). The reduction/extension of the leading-edge vortex sheet is introduced to obtain solutions with the feeding sheet at about the same ("six-o'clock") inclination. The figure shows that after the first 2 iterations the $L_2$-norm of the residual vector decreases nearly linearly by a factor of 10 per iteration. Also only 3 or 4 iterations are required to get the normal force accurate up to the third digit. It should be noted that above example is not very critical, at lower incidences considerably smaller decrement/increments in angle of attack are necessary for convergence.

For the migration from $\alpha$=20 to $\alpha$=17.5 deg Fig. 9.30 shows for two spanwise stations the shape of the leading-edge vortex sheet as well as the wing pressure distribution for the subsequent iterations. It again demonstrates the rapid convergence towards the final solution. It also shows clearly how the vortex sheet adjusts to the decrease in incidence, i.e. rolling-up in a tighter spiral, indeed positioning the feeding sheet at about the same attitude it had at the higher incidence with the longer vortex sheet.

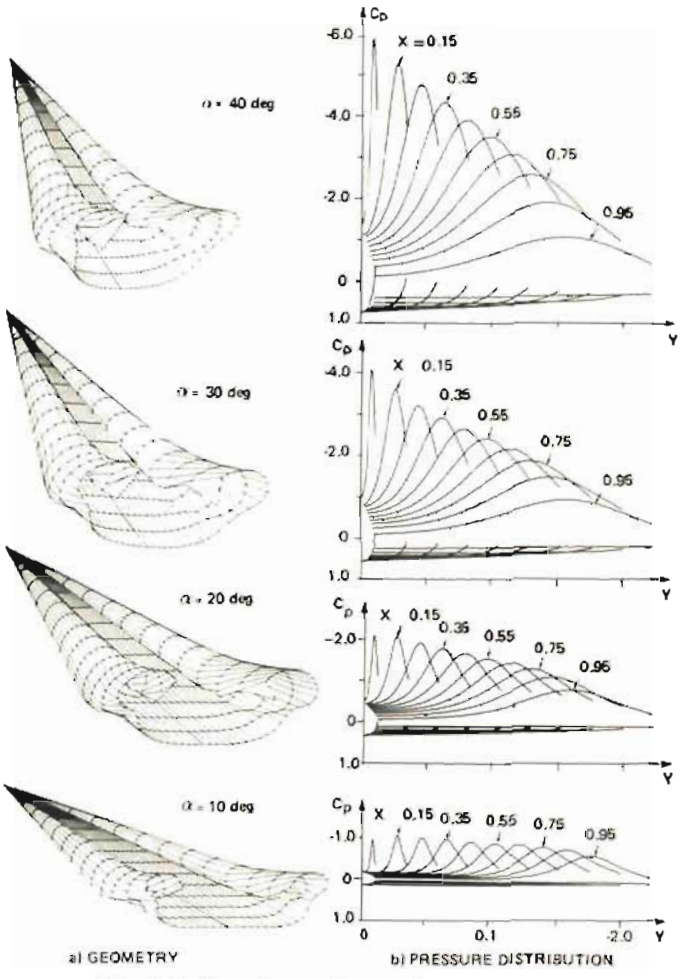


Fig. 9.31 Solution for unit-aspect-ratio wing at various angles of attack

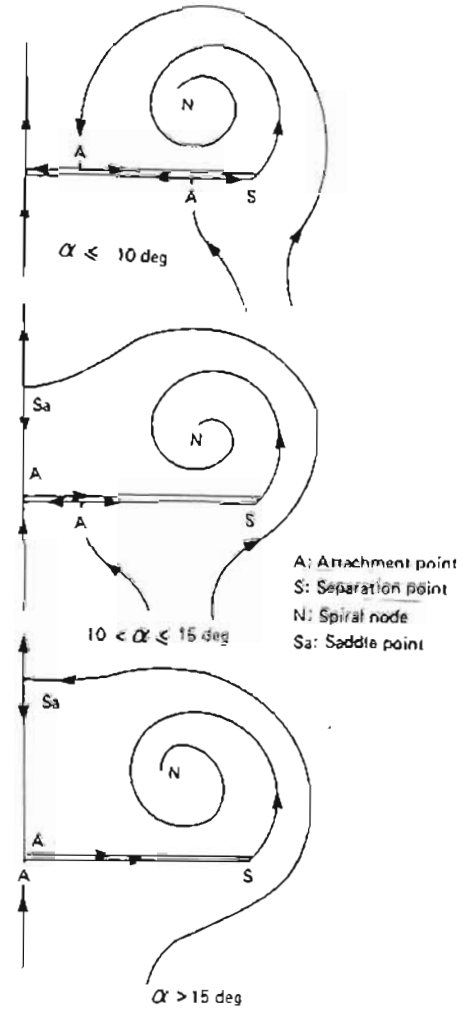


Fig. 9.33 Cross-flow plane flow topology $\Lambda$=76 deg delta wing (sketch)

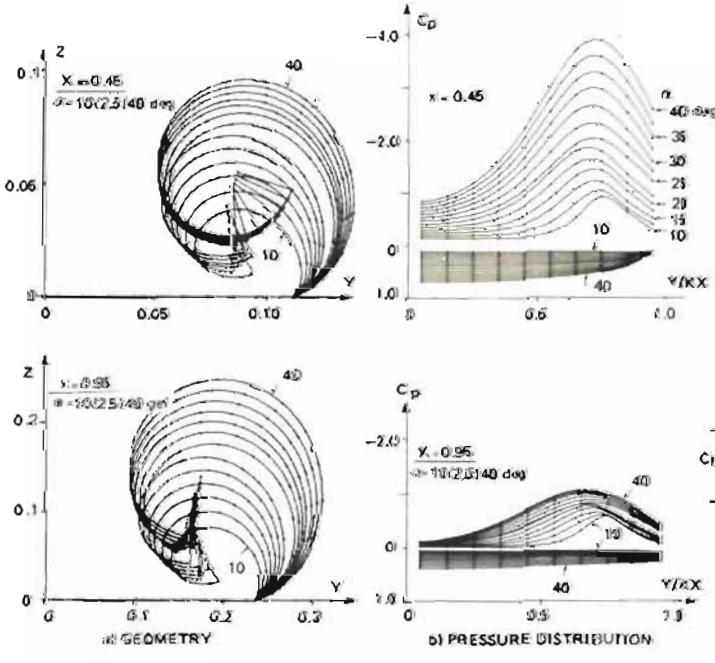


Fig. 9.32 Solution for unit-aspect-ratio wing at α=10(2.5)40 deg

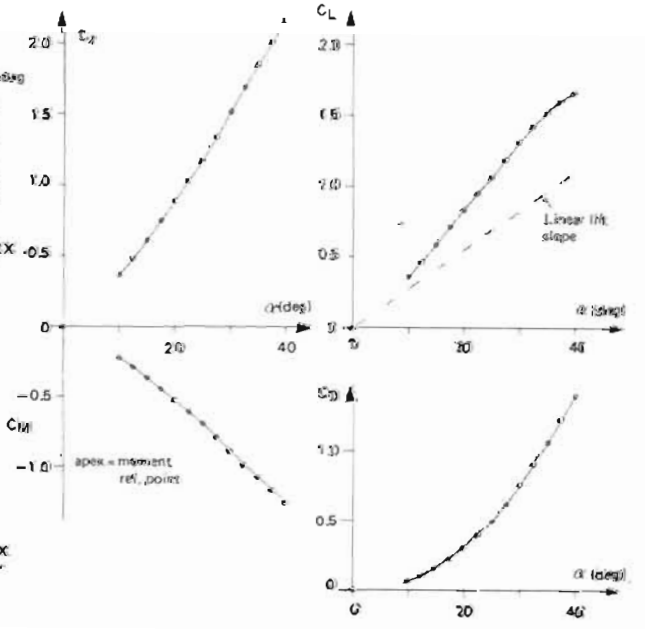


Fig. 9.34 Normal force, pitching moment, lift and drag vs incidence for unit-aspect-ratio wing

9.6.7 Solution for the 76-deg swept delta wing for angles of attack between 10 and 40 deg

For the unit-aspect-ratio delta wing ($\Lambda$=76 deg) we carried out an alpha sweep, marching the solution from 10 to 40 deg incidence. The computational parameters, normal force and pitching moment are listed below.

| $\alpha$(deg) | NUPW | NVPW | NUP | NVP | S | T | $\Delta$s | $\Delta$t wing/sheet | $C_z$ | $C_m$ |
|---|---|---|---|---|---|---|---|---|---|---|
| 10.0 | 10 | 10 | 13 | 22 | 1.3 | 2.1 | 0.1 | 0.1/0.0917 | 0.365 | -0.221 |
| 12.5 | " | " | " | 22 | " | 2.2 | " | " /0.1 | 0.478 | -0.288 |
| 15.0 | " | " | " | 24 | " | 2.4 | " | " /0.1 | 0.608 | -0.364 |
| 17.5 | " | " | " | 26 | " | 2.6 | " | " /0.1 | 0.749 | -0.446 |
| 20.0 | " | " | " | 27 | " | 2.7 | " | " /0.1 | 0.888 | -0.526 |
| 22.5 | " | " | " | 28 | " | 2.8 | " | " /0.1 | 1.032 | -0.609 |
| 25.0 | " | " | " | 20 | " | 2.9 | " | " /0.19 | 1.175 | -0.694 |
| 27.5 | " | " | " | 21 | " | 3.05 | " | " /0.186 | 1.341 | -0.787 |
| 30.0 | " | " | " | 23 | " | 3.2 | " | " /0.169 | 1.519 | -0.886 |
| 32.5 | " | " | " | 25 | " | 3.35 | " | " /0.157 | 1.692 | -0.985 |
| 35.0 | " | " | " | " | " | 3.45 | " | " /0.163 | 1.856 | -1.077 |
| 37.5 | " | " | " | " | " | 3.55 | " | " /0.17 | 2.015 | -1.168 |
| 40.0 | " | " | " | " | " | 3.65 | " | " /0.177 | 2.170 | -1.256 |

$\Lambda$=76 deg

Table 9.4 Alpha sweep unit-aspect-ratio delta wing

Note that the length of the vortex sheet, chosen such that the feeding sheet is at about the "six o'clock" position for all incidences, increases considerably when pitching up from 10 to 40 deg. On the leading-edge vortex sheet the panel width in t-direction is not the same for each $\alpha$, for $\alpha$'s in excess of 22.5 deg the panel width is chosen larger. This is allowed because the curvature of the vortex sheet decreases with increasing $\alpha$, as does the distance of the vortex sheet to the wing upper surface.

The geometry and spanwise pressure distribution for $\alpha$=10(10)40 deg are presented in Fig. 9.31. The figure demonstrates that with increasing angle of attack the vortex system increases in size quite a bit, affecting the upper wing surface pressure distribution over a region that increases in area. Also the height of the suction peak increases dramatically, especially near the apex. It appears that the "trailing-edge vortex" causes the largest distortion in the geometry of the near wake at the lower incidences. This can be explained by considering the ultimate strength of this vortex in comparison with the ultimate strength of the leading-edge vortex. The ultimate strength of the "trailing-edge vortex" will be

$$\Gamma_{t.e.} = \max_t\{u(1,t)\}-u(1,0) \tag{9.48a}$$

and that of the leading-edge vortex

$$\Gamma_{l.e.} = \max_t\{u(1,t)\} \tag{9.48b}$$

It turns out that $\Gamma_{t.e.}/\Gamma_{l.e.}$ decreases from 0.35 at $\alpha$=10 deg to 0.17 at $\alpha$=35 deg and increases again for larger incidences.

Further note that the shape of the leading-edge vortex sheet preserves its conical appearance up to high $\alpha$, although the trailing edge affects the solution more at the higher incidences. In the latter case the wake has to turn over a larger angle from the direction along the wing into a direction more along the free stream. For the cross-flow planes $x$=0.45 and $x$=0.95 the solutions are considered in more detail in Fig. 9.32. It shows that the vortex sheet gradually expands as the incidence is increased and correspondingly the area on the upper wing surface affected by the leading-edge vortex system. The figure also provides insight into the path that the vortex core follows as $\alpha$ is increased. At small incidence (up to 10 deg) the vortex core moves from a position very near to the leading edge rapidly inboard and upward, for $\alpha$'s between 20 and 30 deg the trajectory becomes vertical (at ≈ 75% semispan) and at still higher incidences the vortex core starts to move outboard again. The latter movement in outboard direction is thought to be the effect of the port-side and starboard-side vortices pushing each other aside.

The seemingly not completely gradual expansion of the vortex system between 22.5 and 25 deg is caused by the sudden increase in panel width (see table 9.4), which in retrospect should have been chosen more gradual.

The cross-flow plane flow topology (Fig. 9.33) that underlies the cases for $\alpha$>15 deg is one in which the flow attaches to the wing lower surface at the plane of symmetry ($y$=0), flows towards the leading edge and separates there. There is a dividing streamline turning around the leading-edge vortex, hitting the plane of symmetry above the wing in a saddle point. This saddle point is connected to a half-saddle (attachment) point on the intersection of the plane of symmetry and the wing upper surface.

At lower incidences, $\alpha\in[10,15]$ deg the lower wing surface attachment point moves away from the plane of symmetry (at $\alpha$=12.5 deg it is at $y/Kx$≈0.475). At still smaller incidences $\alpha\leq$10 deg the flow attaches to the wing upper surface, somewhat inboard of the lateral position of the leading-edge vortex (it is at $y/Kx$≈0.175 at $\alpha$=10 deg). In the meantime the lower-wing-surface attachment point has moved further outboard (it is at $y/Kx$≈0.85 at $\alpha$=10 deg).

The normal force, pitching moment, lift and drag coefficients as functions of the incidence are depicted in Fig. 9.34. The normal force and pitching moment vary nonlinearly with incidence, especially for $\alpha$<25 deg. For higher incidences the curves become nearly linear, partly caused by the "crowding" effect of the port-side and starboard-side vortices.

The lift coefficient varies also nonlinearly with incidence, clearly starting to fall off for incidences above 35 deg. This is not caused by vortex breakdown, because that is not modeled at all here, but again by the crowding effect. For the present wing the flow separates all along the leading edge, which implies that the velocity and consequently also the pressure is finite there. It furthermore implies that there is no suction force acting on the leading edge, so that the resulting force is perpendicular to the wing, i.e. $C_x$≡0. This then leads to

$$C_L = C_z\cos\alpha \tag{9.49a}$$

$$C_D = C_z\sin\alpha \tag{9.49b}$$

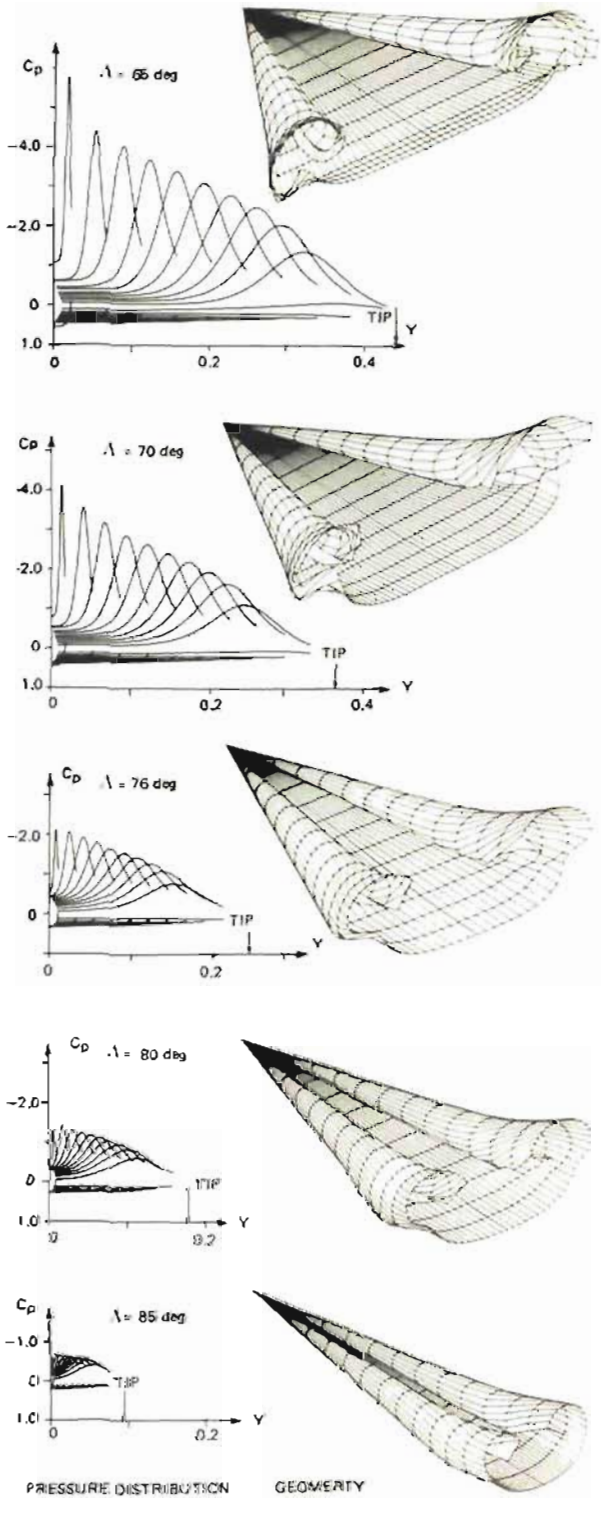


Fig. 9.35 20-deg incidence solution for delta wings of different sweep

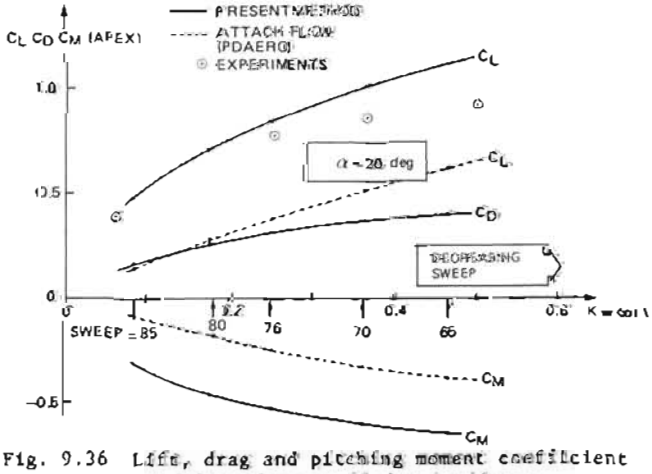


Fig. 9.36 Lift, drag and pitching moment coefficient on delta wings at 20 deg incidence

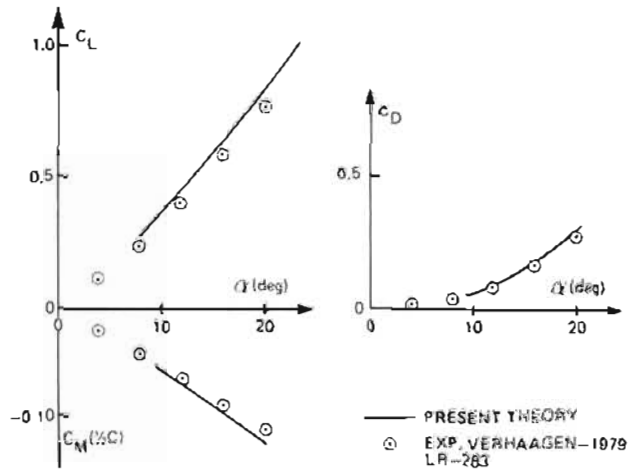


Fig. 9.37 Comparison of theory and experiment, unit-aspect-ratio wing

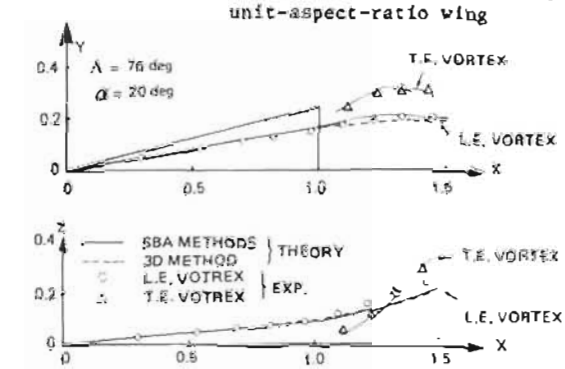


Fig. 9.38 Vortex core positions

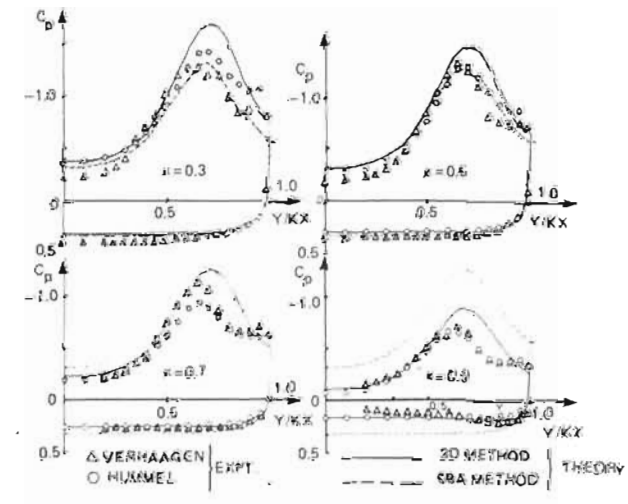


Fig. 9.39 Comparison with turbulent flow data

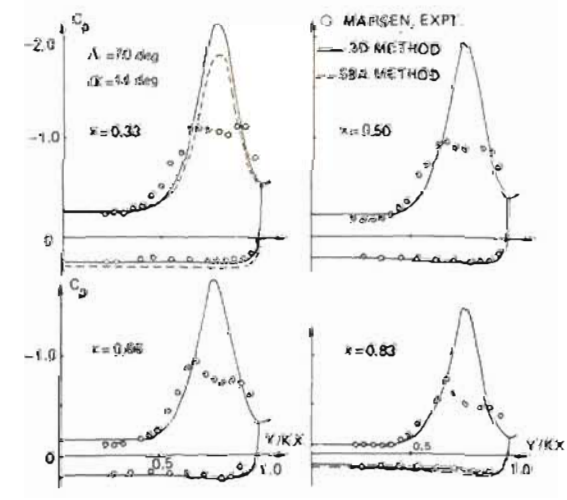


Fig. 9.40 Comparison with laminar flow data

The last equation indicates that the generation of the nonlinear lift has a penalty: a large drag due to the loss of the leading-edge suction.

Included in Fig. 9.34 is the line that indicates the slope of the lift of this unit aspect-ratio-wing in attached flow: $\frac{\partial C_L}{\partial \alpha} = \frac{\pi}{2}$. This indicates the amount of nonlinear lift generated by the leading-edge vortex system and it confirms that the nonlinear lift curve tends to the linear one as $\alpha \downarrow 0$.

9.6.8 Solution for delta wings of different angles of sweep

In this section we consider the solution for a series of flat delta wings of different sweep all inclined at an angle of 20 deg with respect to the oncoming flow. The solutions considered range from $\Lambda$=65 to $\Lambda$=85 deg, see Table 9.5.

| $\Lambda$(deg) | NUPW | NVPW | NUP | NVP | S | T | $\Delta s$ wing/near wake | $\Delta t$ wing/sheet | $C_L$ | $C_D$ | $C_M$ |
|---|---|---|---|---|---|---|---|---|---|---|---|
| 65 | 10 | 20 | 13 | 32 | 1.1 | 2.2 | 0.1/0.033 | 0.05/0.1 | 1.100 | 0.400 | -0.657 |
| 70 | " | 20 | " | 34 | 1.3 | 2.4 | 0.1/0.1 | 0.05/0.1 | 1.011 | 0.368 | -0.620 |
| 76 | " | 10 | " | 27 | 1.3 | 2.7 | 0.1/0.1 | 0.1/0.1 | 0.834 | 0.304 | -0.526 |
| 80 | " | 10 | " | 32 | 1.3 | 3.2 | 0.1/0.1 | 0.1/0.1 | 0.712 | 0.259 | -0.462 |
| 85 | " | 10 | " | 25 | 1.3 | 4.0 | 0.1/0.1 | 0.1/0.2 | 0.498 | 0.181 | -0.337 |

Table 9.5 Solution for delta wings at $\alpha$=20 deg

Starting from the earlier obtained solution for $\Lambda$=76 deg the wing planform was gradually changed to planforms with increasing and also decreasing sweep angle, using the last obtained solution as initial guess for the new planform (not all cases computed are included in Table 9.5).

The geometry and the pressure distribution for the 5 delta wings considered are presented in Fig. 9.35. It clearly demonstrates that for increasing sweep the vortex system increases in magnitude relative to the wing semi span.
Note that at $\Lambda$=85 deg the starboard-side vortex system almost touches the one on the port side.
At the lower leading-edge sweeps the disturbances due to the presence of the (larger) wing are largest, resulting in the highest levels of suction on the upper surface of the wing. On the other hand, at the higher sweep angles the influence of the vorex is felt on a larger part of the span of the wing.
Another interesting feature is that at the lower sweep angles the relative amount of vorticity of negative sign is greater than at the higher sweep angles, resulting in a stronger and more pronounced trailing-edge vortex at the lower sweeps. The next table gives the ultimate strength of the trailing-edge vortex in fractions of the ultimate strength of the leading-edge vortex.

| $\Lambda$(deg) | $\Gamma_{t.e.}/\Gamma_{l.e.}$ |
|---|---|
| 65 | 0.38 |
| 70 | 0.32 |
| 76 | 0.24 |
| 80 | 0.18 |
| 85 | 0.09 |

Table 9.6 Relative strength of trailing edge vortex of delta wings at 20 deg incidence

This explains why at $\Lambda$=85 deg the trailing-edge vortex is not resolved, it is just too weak to become visible on the panel scheme employed.

The lift, drag and pitching moment as a function of K=cot$\Lambda$ are plotted in Fig. 9.36. It shows that as the wing sweep decreases the lift increases, just like in attached flow*). The relative amount of nonlinear lift decreases with decreasing sweep angle, as comparison with results of attached flow theory learns. Comparison with experimental data shows further that at the lower sweep angles the present method tends to overpredict the lift. This is due to the neglected secondary separation effects, which for the lower sweeps, with their sharp upper surface suction peaks, are more severe than for the more slender wings with their broader upper-wing-surface regions with low pressures.

9.6.9 Comparison with experiment

Comparison of the computational results with experimental data demonstrates that the present 3D method is capable of predicting the characteristics of vortex flow. Fig. 9.37 compares, for the unit-aspect-ratio delta wing, computed and measured lift, drag and pitching moment.

The agreement of theory and experiment is quite satisfactory, the theory indeed predicting the correct nonlinear variation of forces and moment with incidence.

Fig. 9.38 compares for the same wing, at 20 deg incidence, computed and measured position of leading and trailing-edge vortex. The two quasi-3D methods quite accurately predict the vortex core positions. Also the fully 3D method provides a good prediction, both for the leading-edge vortex and for the trailing-edge vortex taken as the point of inflection in Figs. 9.20b and 9.22a.

In Fig. 9.39 the computed pressure distribution is compared with experimental data of Verhaagen and of Hummel. Although agreement of computed and measured pressure distributions is quite satisfactory, it also demonstrates one of the main difficulties of comparing computed (inviscid) and real-life vortex flow results, namely the secondary separation discussed earlier. In Hummel's experiment the boundary layer was fully turbulent (trip wire), while in Verhaagen's experiment (natural) transition from laminar to turbulent flow took place at about 60% root chord. This corresponds with the effects of secondary separation being more pronounced in the latter experiment when compared with Hummel's test.

*) The attached flow (PDAERO) results do not include the contribution due to the leading-edge suction, a term in $C_L$ of order $\sin^3\alpha$.

Further note that the 3D method predicts correctly the increase of the pressure coefficient from apex towards trailing edge. It also appears that the conical flow method provides a good prediction around 50% root chord. However, on the aft portion of the wing the upstream effect of the trailing edge becomes rapidly larger, invalidating the assumptions underlying the slender-body approximation.

The effects of secondary separation become larger for lower incidence and lower sweep (more peaky upper-wing-surface pressure distributions) and are more severe for laminar flow compared to turbulent flow. This explains why for the case of the 70-deg swept wing at 14 deg incidence the correlation of theoretical and experimental results is not as good. The upper wing surface suction peaks, predicted by the 3D-flow method, are not attained in the laminar flow experiment of Marsden (Fig. 9.40).

9.6.10 Comparison with results of an Euler code

In Fig. 9.41 results of the present potential-flow method, are compared with results of Rizzi's incompressible-flow Euler method (Rizzi-1984), for the flow about a 70-deg swept delta wing at 20 deg incidence. The potential flow result has been obtained employing 13 spanwise strips of 36 panels each, 468 panels in total. The wing surface is represented by 10 strips of 20 panels each, providing sufficient resolution of the suction peak. The length of the leading-edge vortex sheet was T=2.4, the length of the near wake corresponds with S=1.3.

The spatial grid used for solving Euler's equations is of the so-called O-O type with 80 cells around half-span, 40 in chordwise and 24 cells in normal direction, a total of 76800 cells.
In Fig. 9.41 the computed shape of the vortex sheet is super-imposed on the vorticity contours resulting from the Euler method. Due to the artificial dissipation implied in the numerical scheme used to solve Euler's equations, in the results of the Euler code the vortex sheet is spread over a number of cells. This means that in general the vortical flow region as computed by the Euler code occupies a larger region than that enclosed by the vortex sheet that is computed by the present potential flow method. Taking this into account it can be concluded from Fig. 9.41 that the two solutions agree quite well, except near the apex where the vortical flow region computed by the Euler method is somewhat larger and more inboard than indicated by the vortex sheet solution.
In the vortex sheet solution the (surface) vorticity is largest near the leading edge where the vortex sheet is most curved. In the results of the Euler code a similar behaviour is observed, i.e. highest magnitude of the (spatial) vorticity occurs near the sharp leading edge.

Fig. 9.41 also compares the spanwise pressure distribution at three stations x=constant. The upper-wing surface suction peaks predicted by the two methods agree quite satisfactorily. At the most upstream station shown the slight discrepancy in the position of the suction peak appears to correspond with the differences in the vortical flow pattern. However, in general the height of the suction peak, its position and its width as predicted by both methods are in close agreement. On the lower wing surface the two pressure distributions are virtually identical.
It must be noted here that the earlier results of the Euler code on a coarser and less well-tuned spatial mesh substantially underpredicted the pressure peaks in the potential flow results, indicating a large influence of the details of the spatial mesh. On the other hand, the results presented in Fig. 9.41 are in much closer agreement than had been achieved before, see Rizzi & Hoeijmakers-1984 for further comparisons.

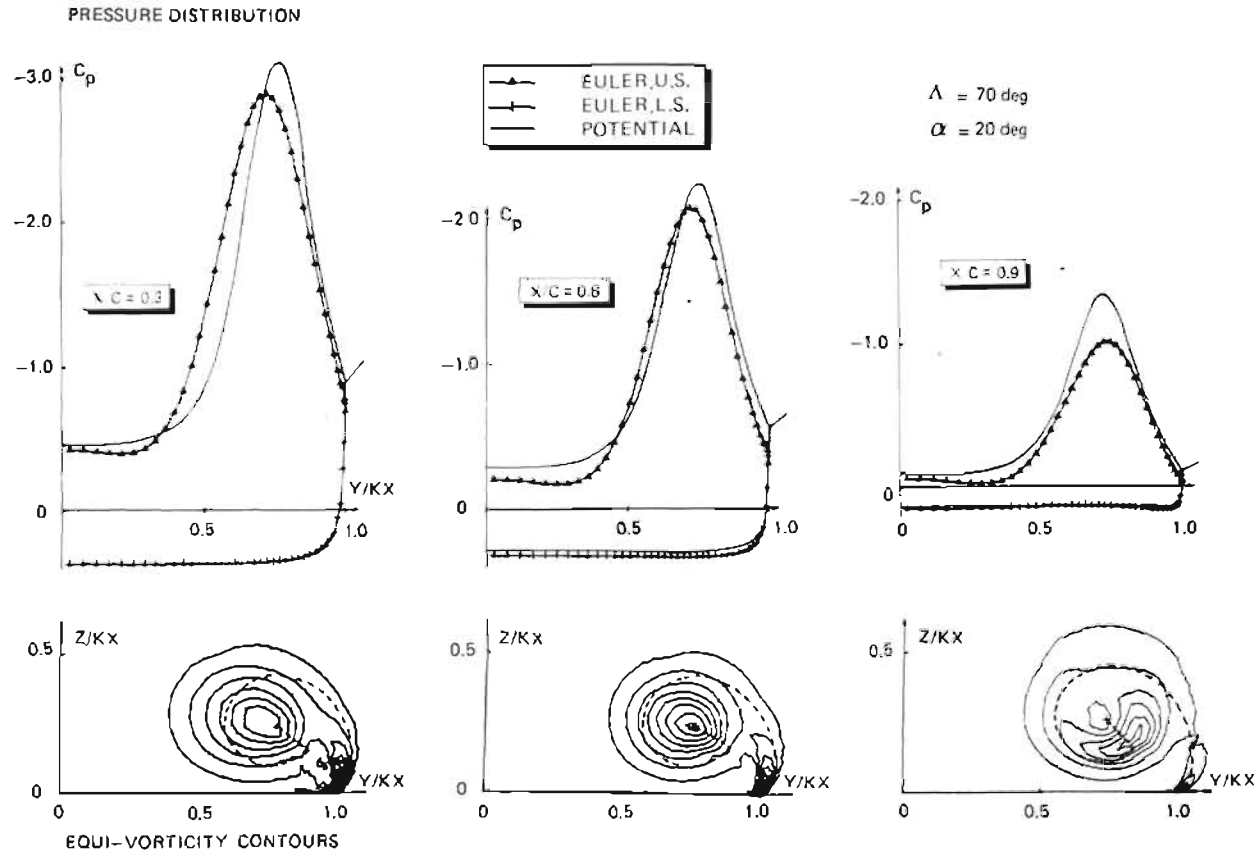


Fig. 9.41 Comparison of present potential flow solution with results Rizzi's Euler code. 70-deg swept delta wing at 20 deg incidence.

## 10 CONCLUDING REMARKS

The panel methods developed in this thesis explicitly employ vortex sheets in modeling vortex flow. Vortex cores appear as highly rolled-up regions of the vortex sheets and can also be treated explicitly. This implies that accurate results can be obtained for cases with a well-defined vortical flow pattern of which the topology must be known in advance. For cases of ordered vortex flow for which a priori the precise topology is not known the application of a free-vortex-sheet method is still possible but may require several adaptations of the initially assumed structure of the vortex system before a satisfatory result is achieved.

For cases with a complex vortical flow pattern a computational method that captures the rotational flow automatically, like one that solves the Euler equations, will be more practical. However, the quality of the numerical simulation obtained with such a method will depend on the detail with which the vortex layers and vortex cores are resolved.

The computational method for quasi two-dimensional vortex wakes presented in this thesis enables the development of a vortex wake to be followed in a reliable and smooth manner up to large distances downstream of the configuration that generated the wake. Results of the method provide clues for the topology of the three-dimensional vortex wake.
Besides the second-order panel method used for the accurate computation of the velocity field, the basic elements of the computational procedure are the adaptive curvature-dependent panel scheme for the rediscretization of the vortex sheets and the amalgamation of vorticity in single and double-branched vortex cores.
In applications of the present method some evidence has been found of vortex-sheet instabilities of the Kelvin-Helmholtz type.
In view of the interest in aerodynamics for the evolution of inherently more stable (thin) shear layers with features of scale large compared with their thickness, the significance of results computed with the method may be the circumstance that the numerical smoothing implied in it effectively turns the vortex sheet into a thin shear layer. However, the correlation of the smoothing with an effective thickness has not been pursued.

The computational method for quasi two-dimensional vortex flow about slender configurations, developed in this thesis, enables the calculation of the flow with free vortex sheets and vortex cores about configurations of more or less arbitrary cross-sections. The methods' basic elements are a second- order panel method, a Newton iterative procedure to solve the system of nonlinear equations resulting from application of the boundary conditions and continuation procedures to easily obtain sequences of solutions. Free vortex sheets, single and double-branched vortex cores can be employed to model vortex systems of quite general structure.
Application of the method leads to the following observations:
Comparison of computed spanwise pressure distributions and measured ones amply demonstrate that modeling of secondary separation underneath the primary vortex core is a prerequisite for obtaining a good correlation. The attempt to model the secondary separation by a vortex sheet emanating from a prescribed separation line and rolling up in a second vortex core has the desired effect on the upper wing surface suction peak. However, it also introduces a suction peak underneath the vortex core of the secondary vortex core which is much more pronounced than found in experiment.
It appears that the prediction of the location of the secondary separation line, as well as the primary separation line on smooth bodies, will require a strongly coupled viscous-inviscid interaction procedure at least.
It has been demonstrated that symmetric and asymmetric solutions can be simulated for slender cones at high angle of attack. Although some effort has been invested in a search for asymmetric solutions for a flat-plate slender delta wing no such solution was found thusfar. A more extensive search starting from an asymmetric solution for a cone and using a geometry deformation process might yield more conclusive evidence on the existence of asymmetric thin-delta-wing solutions.
Further investigation should be undertaken in alternative topologies for the vortex flow about the strake-wing configuration.

The computational method for the three-dimensional flow about thin wings with leading edge vortices described in this thesis shows that a 3D potential flow method with a strong interaction between rolling up vortex sheets and the flow about the wing is feasible. The main elements of the method are the second-order panel method and the quasi Newton four-block diagonal iterative solution procedure for the system of non-linear equations.

Application of the method shows that geometrically the three-dimensional solution has a conical appearance. However, in incompressible flow the velocity and pressure distribution is highly threedimensional due to the upstream influence of the trailing edge but also due to the three-dimensional (non-conical) flow effects at the apex.

Comparison of computed results with experimental data re-emphasizes the importance of including some kind of model that accounts for secondary separation effects.
Comparison of the present potential flow method fitting the vortical flow regions with results of an Euler code capturing the vortical flow demonstrates that these two inviscid flow methods can yield results of comparable quality.

The computing times required for the two quasi two-dimensional flow methods are quite modest. The ones for the three-dimensional flow method becomes quite substantial for the cases with the finer panel schemes, but are still rather modest when compared to the computing times required for methods based on the Euler or Navier-Stokes equations.

REFERENCES


Almosnino, D., Rom, J.(1983): Calculation of Symmetric Vortex Separation Affecting Subsonic Bodies at High Incidence. AIAA J. Vol. 21, No. 3, pp. 398-406.

Angelucci, S.B.(1971): A Multi-vortex Method for Axisymmetric Bodies at Angle of Attack. J. of Aircraft, Vol.8, no. 12, pp. 959-966.

Baker, G.R.(1977): Studies in Vortex Motion. PhD Thesis California Institute of Technology.

Baker, G.R.(1979): The "Cloud in Cell" Technique Applied to the Roll-Up of Vortex Sheets. J. of Comp. Physics, Vol. 31, pp. 76-95.

Baker, G.R.(1980): A Test of the Method of Fink & Soh for Following Vortex-Sheet Motion. JFM, Vol. 100, pp. 209-220.

Batchelor, G.K.(1970): An Introduction to Fluid Dynamics. Cambridge University Press.

Belotserkovskii, S.M.(1968): Calculation of the Flow about Wings of Arbitrary Planform at a Wide Range of Angles of Attack. RAE Lib. Transl. 1433.

Bilanin, A.J., Teske, M.E., Donaldson, C.duP., Williamson, G.G. (1977): Vortex Interactions and Decay in Aircraft Wakes. NASA CR-2870.

Bollay, W.(1939): A Non-linear Wing Theory and its Application to Rectangular Wings of Small Aspect Ratio. ZAMM, Vol. 19, pp. 21-35.

Botnan, J.I.(1981): Aerodynamics of Cones at High Angles of Attack in Low Subsonic Flow. NDRE Publ. 81/1004.

Brennenstuhl, U., Hummel, D.(1982): Vortex Formation over Double-Delta Wings. ICAS Paper 82-6.6.3.

Brown, C.E., Michael, W.H.(1954): Effect of Leading-Edge Separation on the Lift of a Delta Wing. J. of Aeron. Sciences, Vol. 21, pp. 690-694.

Bruin, A.C. de, Hoeijmakers, H.W.M.(1986): Computation of Three-Dimensional Boundary Layer Transition and Separation on a 65 Deg Swept Delta Wing at 20 Deg Angle of Attack. NLR MP 86075 U.

Bryson, A.E.(1959): Symmetric Vortex Separation on Circular Cylinders and Cones. J. of Appl. Mech.(ASME), Vol. 26, pp. 643-646.

Butter, D.J., Hancock, G.J.(1971): A Numerical Method for Calculating the Trailing Vortex System Behind a Swept Wing at Low Speed. The Aeron. J. of the Roy. Aeron. Soc., Vol. 75, pp. 564-568.

Chattot, J.J., Boschiero, M., Koeck, Ch.(1982): Méthodes Numérique de Prédiction de L'Aerodynamique des Missiles. AGARD CP-336.

Clark, R.W.(1976): Non-Conical Flow past Slender Wings with Leading-Edge Vortex Sheets. RAE TR 76037.

Deffenbaugh, F.D., Koerner, W.G.(1977): Asymmetric Vortex Wake Development on Missiles at High Angles of Attack. J. of Spacecraft Vol. 14, No. 3, pp. 155-162.

Dyer, D.E., Fiddes, S.P., Smith, J.H.B.(1981): Asymmetric Vortex Formation from Cones at Incidence - A Simple Inviscid Model. Aeron. Quarterly, Vol. 33, pp. 293-312.

Earnshaw, P.B.(1962): An Experimental Investigation of the Structure of a Leading-Edge Vortex. ARC R&M No. 3281.

Erickson, G.E.(1982): Water-Tunnel Studies of Leading-Edge Vortices. J. of Aircraft, vol. 19, No. 6, pp. 442-448.

Ericsson, L.E., Reding, J.P.(1981): Steady and Unsteady Vortex-Induced Asymmetric Loads on Slender Vehicles. J. of Spacecraft, Vol. 18, pp. 97-109.

Eriksson, L.E., Rizzi, A.(1981): Computation of Vortex Flow Around Wings Using the Euler Equations. Proc. 4th GAMM Conf. on Num. Meth. in Fl. Mech., Ed. H. Viviand, Vieweg Verlag, pp. 87-105.

Fiddes, S.P.(1980): A Theory for the Separated Flow Past a Slender Elliptic Cone at Incidence. AGARD CP-291, Paper 30.

Fiddes, S.P., Smith, J.H.B.(1982): Calculations of Asymmetric Separated Flow Past Circular Cones at Large Angles of Incidence. AGARD CP-336, Paper 14.

Fink, P.T., Taylor, J.(1967): Some Early Experiments on Vortex Separation. ARC R.&M. No. 3489.

Fink, P.T., Soh, W.K.(1978): A New Approach to Roll-up Calculations of Vortex Sheets. Proc. Roy. Soc. Lond., Vol. A 362, pp. 195-209.

Fujii, K., Kutler, P.(1983): Numerical Simulation of the Leading-Edge Separation Vortex for a Wing and Strake-Wing Configuration. AIAA Paper 83-1908; see also AIAA Paper 84-1550.

Gad-el-Hak, M., Blackwelder, R.F.(1985): The Discrete Vortices From a Delta Wing. AIAA J., Vol. 23, No. 6, pp. 961-962.

Germain, P.(1955): Sur L'écoulement Subsonique au Voisinage de la Pointe Avant d'Une Aile Delta. La Rech. Aéron., No. 4, pp. 3-8.

Gersten, K.(1961): Nichtlineare Tragflächentheorie insbesondere für Tragflügel mit kleinem Seitenverhältnis. Ing. Archv, Vol.30, pp. 431-452; see also AGARD Report 342.

Guiraud, J.P., Zeytounian, R.Kh.(1977): A Double-Scale Investigation of the Asymptotic Structure of Rolled-Up Vortex Sheets. JFM, Vol. 79, pp. 93-112.

Guiraud, J.P., Zeytounian, R.Kh.(1979): A Note on the Viscous Diffusion of Rolled Vortex Sheets. JFM, Vol. 90, pp. 197-201.

Hall, M.G.(1961): A Theory for the Core of a Leading-Edge Vortex. JFM, Vol. 11, pp. 209-227.

Hall, M.G.(1972): Vortex Breakdown. An. Rev. of Fl. Dyn., Vol. 4, pp. 195-218.

Hedman, S.G.(1973): Computation of Vortex Models for Wings at High Angle of Attack in Incompressible Flow. FFA TN AU-653.

Helmholtz, H. von: Various publications, e.g. see Batchelor-1970.

Hess, J.L.(1975): Consistent Velocity and Potential Expansions for Higher-Order Surface Singularity Methods. Rept. MDC J6911L.

Hitzel, S.M., Schmidt, W.(1984): Slender Wings with Leading-Edge Vortex Separation: A Challenge for Panel Methods and Euler Solvers. J. of Aircraft, Vol. 21, No. 10, pp. 751-759.

Hoeijmakers, H.W.M., Bennekers, B.(1979): A Computational Model for the Calculation of the Flow About Wings with Leading-Edge Vortices. AGARD CP-247, Paper 25.

Hoeijmakers, H.W.M., Vaatstra, W.(1981): A Higher-Order Panel Method for the Computation of the Flow about Slender Delta Wings with Leading-Edge Vortex Separation. Proc. 4th GAMM Conf. on Num. Meth. in Fl. Mech., Ed. H. Viviand, Vieweg Verlag, pp. 137-149; see also NLR MP 81053 U.

Hoeijmakers, H.W.M.(1983): Computational Vortex Flow Aerodynamics. AGARD CP-342, Paper 18; see also NLR MP 83017 U.

Hoeijmakers, H.W.M., Vaatstra, W.(1983): Higher-Order Panel Method Applied to Vortex Sheet Roll-Up. AIAA J. Vol. 21, No. 4, pp. 516-523; see also AIAA Paper 82-0096.

Hoeijmakers, H.W.M., Vaatstra, W., Verhaagen, N.G.(1983): On the Vortex Flow over Delta and Double-Delta Wings. J. of Aircraft, Vol. 20, No. 9, pp. 825-832; see also AIAA Paper 82-0949.

Hoeijmakers, H.W.M.(1984): Numerical Computation of Vortical Flow About Wings. VKI-LS "Computational Fluid Dynamics"; see also NLR MP 83073 U.

Hoeijmakers, H.W.M., Rizzi, A.(1984): Vortex-Fitted Potential Solution Compared with Vortex-Captured Euler Solution for Delta Wing with Leading-Edge Vortex Separation. AIAA Paper 84-2144; see also AIAA J. Vol. 23, No. 12, 1985, pp. 1983-1985.

Hoeijmakers, H.W.M., Verhaagen, N.G.(1985): Theoretical and Expimental Investigations into Vortex Flow. NLR MP 85085 U.

Hoeijmakers, H.W.M.(1986): Numerical Simulation of Vortical Flow. VKI-LS "Introduction to Vortex Dynamics"; see also NLR MP 86032 U.

Hoeijmakers, H.W.M.(1987): Methods for Numerical Simulation of Leading-Edge Vortex Flow. In: "Studies of Vortex Dominated Flows", Ed. M.Y. Hussaini and M.D. Salas, Springer Verlag, pp. 221-269; see also NLR MP 85052.

Holst, T.L., Slooff, J.W., Yoshihara, H., Ballhaus, Jr. W.F.(1982): Applied Computational Transonic Aerodynamics. AGARDograph 266.

Huberson, S.(1980): Numerical Computation of Flows with Rolled-Up Vortex Sheets. Rech. Aérosp. No. 1980-3, Engl. Ed., pp. 57-63.

Hummel, D.(1979): On the Vortex Formation Over a Slender Wing at Large Incidence. AGARD CP-247, Paper 15.

Jepps, S.A.(1978): The Computation of Vortex Flows by Panel Methods. VKI Lecture Series 1978-4.

Johnson, F.T., Tinoco, E.N., Lu, P., Epton, M.A.(1980): Three-Dimensional Flow over Wings with Leading-Edge Vortex Separation. AIAA J., Vol. 18, No. 4, pp. 367-380; see also AIAA Paper 79-0282.

Kaden, H.(1931): Aufwicklung einer Unstabilen Unstetigkeitsfläche. Ing. Archiv, Vol. 2, pp. 140-168.

Kandil, O.A., Mook, D.T., Nayfeh, A.H.(1976): Nonlinear Prediction of Aerodynamic Loads on Lifting Surfaces. J. of Aircraft, Vol. 13, No. 1, pp.22-28.

Krause, F., Shi, X.G., Hartwich, P.M.(1983): Computation of Leading-Edge Vortices. AIAA Paper 83-1907.

Küchemann, D.(1978): The Aerodynamic Design of Aircraft. Pergamon Press.

Labrujère, Th.E., de Vries, O.(1974): Evaluation of a Potential Theoretical Model of the Wake behind a Wing via Comparison of Measurement and Calculations. NLR TR 74063 U.

Lamar, J.E., Luckring, J.M.(1979): Recent Theoretical Developments and Experimental Studies Pertinent to Vortex Flow Aerodynamics - With a View Towards Design. AGARD CP-247, Paper 24.

Lamar, J.E.(1980): Analysis and Design of Strake-Wing Configurations. J. of Aircraft, Vol. 17, No. 1, pp. 20-27.

Legendre, R.(1952): Ecoulement au Voisinage de la Pointe Avant d'une Aile à Forte Flèche aux Incidences Moyennes. La Rech. Aéron. Vol. 30, pp. 3-8; Vol. 31, pp. 3-6; Vol. 35, pp. 7-8.

Leonard, A.(1980): Vortex Methods for Flow Simulation. Review Article. J. of Comp. Physics, Vol. 37, pp. 289-335.

Leonard, A.(1985): Computing Three-Dimensional Incompressible Flows With Vortex Elements. Ann. Rev. of Fl. Mech., No. 17, pp. 523-559.

Luckring, J.M.(1979): Aerodynamics of Strake-Wing Interactions. J. of Aircraft, Vol. 16, No. 11, pp. 756-762.

Luckring, J.M.(1986): Comment on "Convergence Characteristics of a Vortex-Lattice Method for Nonlinear Configuration Aerodynamics". J. of Aircraft, Vol. 23, No. 10, pp. 798-799.

Maltby, R.L.(1962): Flow Visualization in Wind Tunnels Using Indicators. AGARDograph No. 70.

Mangler, K.W., Smith, J.H.B.(1959): A Theory of the Flow Past a Slender Delta Wing with Leading-Edge Separation. Proc. Roy. Soc. A, Vol. 251, pp. 200-217.

Mangler, K.W., Weber, J.(1967): The Flow Field near the Centre of a Rolled-Up Vortex Sheet. JFM, Vol. 30, pp. 177-196.

Marsden, D.J, Simpson, R.W., Rainbird, W.J.(1957): The Flow over Delta Wings at Low Speeds with Leading-Edge Separation. Cranfield College of Aeronautics Rep. No. 114.

Maskell, E.C.(1962): Some Recent Developments in the Study of Edge Vortices. In: Proc. 3rd ICAS Congress, Stockholm.

Maskew, B.(1973): The Calculation of Potential Flow Aerodynamic Characteristics of Combined Lifting Surfaces with Relaxed Wakes. Hawker Sidely Aviation Limited Note No. YAD 3192.

Miller, D.S., Wood, R.M.(1983): An Investigation of Wing Leading-Edge Vortices at Supersonic Speeds. AIAA Paper 83-1816; see also J. of Aircraft, Vol. 21, No. 9, 1984, pp. 680-686 and NASA TP 2430, 1985.

Moore, D.W.(1974): A Numerical Study of the Roll-up of a Finite Vortex Sheet. JFM, Vol. 63, pp. 225-235.

Moore, D.W.(1979): The Spontaneous Appearance of a Singularity in the Shape of an Evolving Vortex Sheet. Proc. Roy. Soc. Lond., Vol. A 365, pp. 105-119.

Morchoisne, Y.(1986): Calcul D'écoulements Instationaires par la Méthode des Tourbillons Ponctuels. Paper presented at AGARD-FDP-RTD, Aix-en-Provence, France, April 10, 1986.

Murman, E.M., Stremel, P.M.(1982): A Vortex Wake Capturing Method for Potential Flow Calculations. AIAA Paper 82-0947.

Nangia, R.K., Hancock, G.J.(1970): A Theoretical Investigation for Delta Wings with Leading-Edge Vortex Separation at Low Speeds. ARC C.P. No. 1086.

Newsome, R.W.(1985): A Comparison of Euler and Navier-Stokes Solu-tions for Supersonic Flow over a Conical Delta Wing. AIAA Paper 85-0111.

Payne, F.M., Ng, T.T., Nelson, R.C., Schiff, L.B.(1986): Visualization and Flow Surveys of the Leading-Edge Vortex Structure on Delta-Wing Planforms. AIAA Paper 86-0330.

Peake, D.J., Tobak, M.(1980): Three-dimensional Interactions and Vortical Flows with Emphasis on High Speeds. NASA TM 81169; see also AGARDograph 252.

Peace, A.J.(1983): A Multi-Vortex Model of Leading-Edge Vortex Flows. Int. J. Num. Meth. in Fluids, Vol. 3, pp. 543-565.

Polhamus, E.C.(1966): A Concept of the Vortex Lift of Sharp-Edge Delta Wings Based on a Leading-Edge Suction Analogy. NASA TN D-3767.

Portnoy, H.(1977): Thick, Two-Dimensional Wake Roll-Up Behind a Wing of Finite Span - Extended Calculations. Aeron. J. Oct. 1977, pp. 460-463.

Prandtl, L.(1922): Über die Enstehung von Wirbeln in der Idealen Flüssigkeit, mit Anwendung auf die Tragflügeltheorie und Andere Aufgaben. In: "Vortrage aus dem Gebiete der Hydro- und Aerodynamik", Ed. Th. von Kármán and T. Levi-Civita, Springer, 1924.

Pullin, D.I.(1978): The Large-Scale Structure of Unsteady Self- Similar Rolled-Up Vortex Sheets. JFM, Vol. 88, pp. 401-430.

Pullin, D.I., Phillips, W.R.C.(1981): On a Generalization of Kaden's Problem, JFM, Vol. 104, pp. 45-53.

Raj, P.(1984): Computational Simulation of Free Vortex Flows Using an Euler Code. ICAS Paper 84-1.3.1.

Rao, B.M., Maskew, B.(1982): Flows with Leading-Edge Vortex Separation. NASA CR-165858.

Rayleigh, J.W.S. Lord (1896): The Theory of Sound. Dover Publications, New York, 2nd edition, Vol. II, 1945, pp. 392-394.

Rehbach, C.(1971): Etude Numérique de L'influence de la Forme de L'éxtrémité d'une Aile sur L'enroulement de la Nappe Tourbillonnaire. La Rech. Aérosp. No. 1971-6, pp. 367-368.

Rehbach, C.(1973): Calcul D'écoulements autour D'ailes sans Épaisseur avec Nappes Tourbillonnaires Évolutives. La Rech. Aérosp. No. 1973-2, pp. 53-61.
Rehbach, C.(1978): Numerical Calculation of Three-Dimensional Unsteady Flow with Vortex Sheets. AIAA Paper 78-111.
Rizzi, A.(1982): Damped Euler-Equation Method to Compute Transonic Flow Around Wing-Body Combinations. AIAA J., Vol. 20, No. 10, pp.1321-1328.
Rizzi, A.(1984): Euler Solutions of Transonic Flows Around the Dillner Wing - Compared and Analyzed. AIAA Paper 84-2142.
Rizzi, A.(1985): Computation of Inviscid Incompressible Flow with Rotation. JFM, Vol. 153, pp. 275-312.
Rosenhead, L.(1931): The Formation of Vortices from a Surface of Discontinuity. Proc. Roy. Soc. Lond., Vol. 134, pp. 170-192.
Rusak, Z., Wasserstrom, E., Seginer, A.(1983): Numerical Calculation of Nonlinear Aerodynamics of Wing-Body Configurations. AIAA Journal, Vol. 21, No. 7, pp. 929-936.
Sacks, A.H., Lundberg, R.E., Hanson, Ch.W.(1967): A Theoretical Investigation of the Aerodynamics of Slender Wing-Body Combinations Exhibiting Leading-Edge Separation. NASA CR-719.
Saffman, P.G., Baker, G.R.(1979): Vortex Interactions. Ann. Rev. of Fl. Dyn. No. 11, pp. 95-122.
Schröder, W.(1978): Berechnung der Nichtlinearen Beiwerte von Flügeln mit Kleinem und Mittlerem Seitenverhältnis nach dem Wirbelleiterverfahren in Inkompressibler Strömung. DFVLR FB 78-26.
Skow, A.M., Erickson, G.E.(1982): Modern Fighter Aircraft Design for High-Angle-of-Attack Maneuvring. AGARD LSP-121.
Smith, F.T.(1978): Three-Dimensional Viscous and Inviscid Separation of a Vortex Sheet from a Smooth Non-slender Body. RAE TR 78095.
Smith, J.H.B.(1959): A Theory of the Separated Flow from the Curved Leading Edge of a Slender Wing. ARC R.& M. No. 3116.
Smith, J.H.B.(1968): Improved Calculations of Leading-Edge Separation from Slender, Thin, Delta Wings. Proc. Roy. Soc. London, Vol. A 306, pp. 67-90; see also RAE TR 66070.
Smith, J.H.B.(1980): Vortical Flows and Their Computation. VKI LS-1980-5; see also RAE TM Aero 1866.
Smith, J.H.B.(1983): Theoretical Modelling of Three-dimensional Vortex Flows in Aerodynamics. AGARD CP-342, Paper 17.
Stanbrook, A., Squire, L.C.(1964): Possible Types of Flow at Swept Leading Edges. Aeron. Quarterly, Vol. 15, pp. 72-82.
Steger, J.L., Kutler, P.(1977): Implicit Finite-Difference Procedures for the Computation of Vortex Wakes. AIAA J., Vol. 15, No. 4, pp. 581-590.
Stewartson, K., Hall, M.G.(1963): The Inner Viscous Solution for the Core of a Leading-Edge Vortex. JFM, Vol. 15, pp. 306-318.
Syrsma, H.A., Hewitt, B.L., Rubbert, P.E.(1979) : A Comparison of Panel Methods for Subsonic Flow Computation. AGARD AG-241.
Thompson, D.H.(1985): A Visualization Study of the Vortex Flow Around Double-Delta Wings. ARL-AERO-R-165.
Verhaagen, N.G. (1979): Some Low-Speed Wind-Tunnel Experiments on a Sharp-Edged Delta Wing of Aspect Ratio 1 with and without Yaw. Rep. LR-283, Fac. Aerosp. Eng., Technical University Delft.
Verhaagen, N.G.(1979): Measurement of the Pressure Distribution on a Biconvex Delta Wing of Aspect Ratio 1. Unpubl. Rep. Fac. Aerosp. Eng., Technical University Delft.
Verhaagen, N.G.(1983): An Experimental Investigation of the Vortex Flow over Delta and Double-Delta Wings at Low Speeds. AGARD CP-342, Paper 7.
Verhaagen, N.G., Kruisbrink, A.C.H.(1985): The Entrainment Effect of a Leading-Edge Vortex. AIAA Paper 85-1584; see also AIAA J. J., Vol. 25, No. 8, 1987, pp. 1025-1032.
Verhaagen, N.G., Naarding, S.H.J.(1988): Experimental and Numerical Investigation of the Vortex Flow over a Yawed Delta Wing. AIAA Paper 88-2563.
Verhaagen, N.G., Manen, R. van(1987): A Laser-Light-Sheet Investigation of the Leading-Edge Vortex Layer. Unpubl. Work, Fac. Aerosp. Eng., Technical University Delft.
Vooren, A.I. van der(1980) A Numerical Investigation of the Rolling-Up of Vortex Sheets. Proc. Roy. Soc. London, Vol. A 373, pp. 67-91.
Ward, G.N.(1955): Linearized Theory of Steady High-Speed Flow. Cambridge University Press.
Wardlaw, A.B.(1974): Prediction of Yawing Force at High Angle of Attack. AIAA J. Vol. 12, pp. 1142-1144.
Wentz, W.H., McMahon, M.C.(1966): An Experimental Investigation of the Flow Fields about Delta and Double-Delta Wings at Low Speeds. NASA CR 521.
Weston, R.P., Liu, C.H.(1982): Approximate Boundary Condition Procedure for the Two-Dimensional Numerical Solution of Vortex Wakes. AIAA Paper 82-0951.
Westwater, F.L.(1935): Rolling-up of the Surface of Discountinuity Behind an Aerofoil of Finite Span. ARC R.&M. No. 1962.
Zabusky, N.J., Overman II, E.A.(1983): Regularization of Contour Dynamical Algorithms, I. Tangential Regularization. J. of Comp. Phys., Vol. 52, pp. 351-373.

LIST OF SYMBOLS

Symbols used locally only are defined in the text

| | |
|---|---|
| AR | aspect ratio, $(\text{span})^2/\text{area}$ |
| b | wing span, or arc length of wing or vortex sheet segment (Chpts. 7-8) |
| $b_\ell$ | arc length of wing in cross-flow plane (Chpt. 9) |
| c | chord |
| $C(\tau)$, $C(\tau)$ | circulation of vortex system, circulation of starboard side of symmetric vortex system |
| $C_L$ | lift coefficient |
| $C_m$ | pitching moment coefficient |
| $C_p$ | pressure coefficient |
| $C_y$ | lateral force coefficient |
| $C_z$ | normal force coefficient |
| $\bar{e}_n$ | unit vector normal to contour in 2D or in cross-flow plane |
| $\bar{e}_t$ | unit vector tangent to contour in 2D or in cross-flow plane |
| $\bar{e}_x, \bar{e}_y, \bar{e}_z$ | unit vectors in x,y and z direction |
| H | enthalpy |
| $H(\tau)$, $H(\tau)$ | hamiltonian of vortex system, hamiltonian of starboard side of symmetric vortex system |
| $k_n$ | curvature of contour in cross-flow plane |
| K | $\cot\Lambda$ |
| $M_\infty$ | freestream Mach number |
| $\bar{n}$ | unit vector normal to three-dimensional surface |
| NP | number of panels in cross-flow plane |
| NPV | number of panels on vortex sheet(s) in cross-flow plane |
| NPW | number of panels on wing segments in cross-flow plane |
| NUP | total number of panels in s-direction |
| NUPW | number of panels on wing in s-direction |
| NVP | total number of panels in t-direction |
| NVPW | number of panels on wing in t-direction |
| p | static pressure coefficient |
| $q(s,t)$ | surface source distribution |
| $Q(t)$ | line source distribution |
| $Q_v$ | source distribution on vortex filament |
| $\bar{r}, \bar{R}$ | distance vector in 3D, distance vector in 2D |
| $r_e$ | radius of edge of vortex core |
| Re | Reynolds number |
| s,t | surface coordinate system; often s in streamwise direction, t along the contour |
| S | near-wake vortex sheet cut-off parameter |
| T | leading-edge vortex sheet cut-off parameter |
| $\bar{u}=(u,v,w)$ | velocity vector, components in Cartesian coordinate system |
| $\bar{U}=(0,V,W)$ | velocity vector in 2D or in cross-flow plane |
| $U_e, V_e$ | axial and circumferential velocity component at edge of vortex core |
| $\bar{U}_\infty=(U_\infty, V_\infty, W_\infty)$ | free-stream velocity vector |
| $\bar{V}_\infty=(0, V_\infty, W_\infty)$ | free-stream velocity vector in cross-flow plane |
| $\bar{x}=(x,y,z)$ | position vector in Cartesian coordinate system |
| $\bar{X}=(0,Y,Z)$ | position vector in 2D or in cross-flow plane |
| $\bar{x}_v$ | vortex position vector |
| $\bar{X}_v=(0,Y_v,Z_v)$ | vortex position vector in 2D or in cross-flow plane |
| $\alpha$ | angle of attack |
| $\beta$ | angle of side slip |
| $\bar{\gamma}$ | surface vorticity vector |
| $\Gamma$ | circulation of vortex filament |
| $\Lambda$ | sweep angle of leading edge |
| $\mu$ | doublet distribution |
| $\nu$ | kinematic viscosity |
| $\rho$ | density, or doublet distribution on contour in cross-flow plane (Chpt. 7) |
| $\tau$ | time |
| $\phi, \varphi$ | velocity potential |
| $\Phi$ | velocity potential in 2D or in the cross-flow plane |
| $\psi$ | stream function |
| $\bar{\omega}$ | vorticity vector |

ABBREVIATIONS

| | |
|---|---|
| COV | center of vorticity |
| LE | leading edge |
| SS | secondary separation |
| TE | trailing edge |

TABLES 1-3
List of various integrals employed in present study

1. Integration over interval $x\in[-\infty, +\infty]$, 3D → 2D

1.1 $$\lim_{x_\infty\to\infty}\left[\int_{x=-x_\infty}^{x_\infty}\frac{dx}{[(x_o-x)^2+R^2]^{1/2}}\right] = -\lim_{x_\infty\to\infty}[\ln(R^2/4x_\infty^2)]$$

1.2 $$\lim_{x_\infty\to\infty}\left[\int_{x=-x_\infty}^{x_\infty}\frac{dx}{[(x_o-x)^2+R^2]^{3/2}}\right] = \frac{2}{R^2}$$

1.3 $$\lim_{x_\infty\to\infty}\left[\int_{x=-x_\infty}^{x_\infty}\frac{(x_o-x)dx}{[(x_o-x)^2+R^2]^{3/2}}\right] = 0$$

2. Integration in circumferential direction

2.1 $$\int_0^{2\pi}\frac{d\delta}{R_o^2+R^2-2R_oR\cos\delta} = 2\pi/|R_o^2-R^2|$$

2.2 $$\int_0^{2\pi}\frac{\cos\delta d\delta}{R_o^2+R^2-2R_oR\cos\delta} = \pi\{-1+(R_o^2+R^2)/|R_o^2-R^2|\}/RR_o$$

2.3 $$\int_0^{2\pi}\frac{\cos^2\delta d\delta}{R_o^2+R^2-2R_oR\cos\delta} = \pi\{-1+(R_o^2+R^2)/|R_o^2-R^2|\}(R_o^2+R^2)/2R_o^2R^2$$

2.4 $$\int_0^{2\pi}\frac{\sin\delta d\delta}{R_o^2+R^2-2R_oR\cos\delta} = 0$$

2.5 $$\int_0^{2\pi}\frac{\sin^2\delta d\delta}{R_o^2+R^2-2R_oR\cos\delta} = \pi\{R_o^2+R^2-|R_o^2-R^2|\}/2R^2R_o^2$$

2.6 $$\int_0^{2\pi}\frac{\sin\delta\cos\delta d\delta}{R_o^2+R^2-2R_oR\cos\delta} = 0$$

2.7 $$\int_0^{2\pi}\ln\left(\frac{R_o^2+R^2-2RR_o\cos\delta}{R_o^2}\right)d\delta = 2\pi\ln\left(\frac{R_o^2+R^2+|R_o^2-R^2|}{2R_o^2}\right)$$

2.8 $$\int_0^{2\pi}\cos\delta\ln\left(\frac{R_o^2+R^2-2RR_o\cos\delta}{R_o^2}\right)d\delta = -\pi\{R_o^2+R^2-|R_o^2-R^2|\}/RR_o$$

2.9 $$\int_0^{2\pi}\sin\delta\ln\left(\frac{R_o^2+R^2-2RR_o\cos\delta}{R_o^2}\right)d\delta = 0$$

3. Integration on interval $x\in[0,\infty]$ 3D → Q2D

Consider $I_k^{\ell} = \lim_{x_\infty\to\infty}\left[\int_{x=0}^{x_\infty} \frac{(x_o-x)^k dx}{|\bar{R} + (x_o-x)(\bar{e}_x+\bar{S})|^{\ell+1}}\right]$

where $\bar{e}_x.\bar{R}\equiv 0$, $\bar{e}_x.\bar{S}\equiv 0$, $\bar{R}=O(\varepsilon x_o)$, $\bar{S}=O(\varepsilon)$

Define: $a = 1 + |\bar{S}|^2$

$b = \bar{S}.\bar{R}$

$c = |\bar{R}|^2$

so that $ac-b^2 = |\bar{R}|^2 + |\bar{S}\times\bar{R}|^2$

3.1 $I_o^o = \frac{-1}{a^{\frac{1}{2}}}\left[\lim_{x_\infty\to\infty}\{\ln\frac{ac-b^2}{a(x_\infty-x_o)}\} - \ln 2\{a^{\frac{1}{2}}(ax_o^2+2bx_o+c)^{\frac{1}{2}} + ax_o+b\}\right]$

$= -\ln(\frac{|\bar{R}|^2}{x_o}) + \lim_{x_\infty\to\infty}\{\ln(4x_\infty/x_o)\} + O(\varepsilon^2)$

3.2 $I_1^o = \frac{1}{a}\left[a^{\frac{1}{2}}\lim_{x_\infty\to\infty}\{x_o-x_\infty\} + \frac{b}{a^{\frac{1}{2}}} + (ax_o^2+2bx_o+c)^{\frac{1}{2}}\right] - \frac{b}{a}I_o^o$

$= [1 + O(\varepsilon^2)]\lim_{x_\infty\to\infty}\{2x_o-x_\infty\} + O(x_o\varepsilon^2\ln\varepsilon)$

3.3 $I_2^o = \frac{1}{2a^2}\left[\lim_{x_\infty\to\infty}\{a^{3/2}(x_o-x_\infty)^2 - 2a^{\frac{1}{2}}b(x_o-x_\infty)\} + \frac{ac-7b^2}{2a^{\frac{1}{2}}} + (ax_o-3b)(ax_o^2+2bx_o+c)^{\frac{1}{2}}\right] + \frac{3b^2-ac}{2a^2}I_o^o$

$= [1 + O(\varepsilon^2)]\lim_{x_\infty\to\infty}\{\frac{1}{2}(x_o-x_\infty)^2\} + [O(\varepsilon^2)]\lim_{x_\infty\to\infty}\{x_o-x_\infty\} + \frac{1}{2}x_o^2 + O(x_o^2\varepsilon^2\ln\varepsilon)$

3.4 $I_o^1 = \frac{1}{ac-b^2}\{a^{\frac{1}{2}} + \frac{ax_o+b}{(ax_o^2+2bx_o+c)^{\frac{1}{2}}}\}$

$= \frac{2}{|\bar{R}|^2}[1 + O(\varepsilon^2)]$

3.5 $I_1^1 = \frac{-1}{ac-b^2}\{\frac{b}{a^{\frac{1}{2}}} + \frac{bx_o+c}{(ax_o^2+2bx_o+c)^{\frac{1}{2}}}\}$

$= -(2\frac{\bar{S}.\bar{R}}{|\bar{R}|^2} + \frac{1}{x_o})[1 + O(\varepsilon^2)]$

3.6 $I_2^1 = \frac{1}{a(ac-b^2)}\{\frac{2b^2-ac}{a^{\frac{1}{2}}} + \frac{(2b^2-ac)x_o+bc}{(ax_o^2+2bx_o+c)^{\frac{1}{2}}}\} + \frac{1}{a}I_o^o$

$= -\ln(\frac{|\bar{R}|^2}{x_o}) + \lim_{x_\infty\to\infty}\{\ln(4\frac{x_\infty}{x_o})\} - 2 + O(\varepsilon^2)$

APPENDIX A

Equivalence between the velocity induced by a doublet distribution and that induced by a surface vorticity distribution

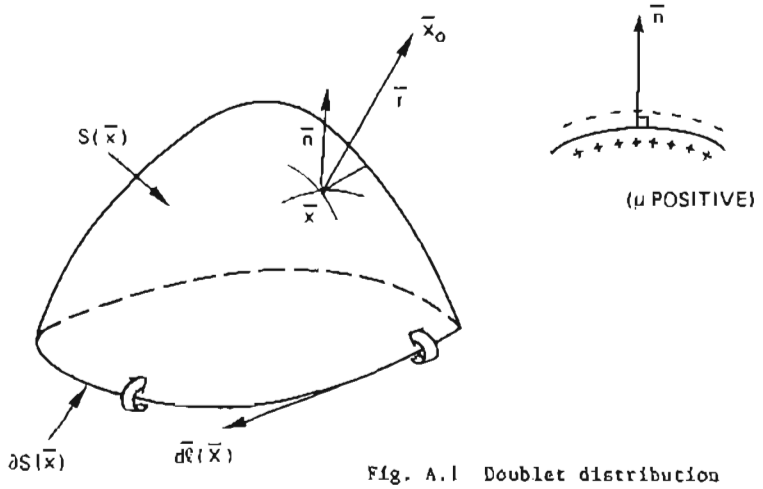


Fig. A.1 Doublet distribution

The velocity potential induced at $\bar{x}_o$ by a doublet distribution $\mu(\bar{x})$ on a surface $S(\bar{x})$ is

$$\varphi(\bar{x}_o) = \frac{1}{4\pi}\iint_S \mu(\bar{x})\bar{n}.\bar{\nabla}_x(\frac{1}{r})dS(\bar{x}) \tag{A.1}$$

where $r = |\bar{r}| = |\bar{x}_o - \bar{x}|$, $\bar{n}$ is the unit normal directed as indicated in Fig. A.1 and $\bar{\nabla}_x$ is the gradient with respect to $\bar{x}$. The velocity induced at $\bar{x}_o$ is obtained by taking the gradient with respect to $\bar{x}_o$:

$$\bar{u}(x_o) = \frac{1}{4\pi}\iint_S \mu(\bar{x})\bar{\nabla}_{x_o}\{\bar{n}.\bar{\nabla}_x(\frac{1}{r})\}dS(\bar{x}) \tag{A.2}$$

Using the identities for $\bar{\nabla}(\bar{a}.\bar{b})$ and $\bar{\nabla}\times(\bar{a}\times\bar{b})$ it is easily shown that

$$\bar{\nabla}_{x_o}\{\bar{n}.\bar{\nabla}_x(\frac{1}{r})\} = (\bar{n}.\bar{\nabla}_{x_o})\bar{\nabla}_x(\frac{1}{r})$$

$$= \bar{\nabla}_{x_o}\times\{\bar{\nabla}_x(\frac{1}{r})\times\bar{n}\} \tag{A.3}$$

leading to

$$\bar{u}(\bar{x}_o) = \frac{1}{4\pi}\bar{\nabla}_{x_o}\times\iint_S \mu(\bar{x})\{\bar{\nabla}_x(\frac{1}{r})\times\bar{n}\}dS(\bar{x}) \tag{A.4}$$

Bringing $\mu(\bar{x})$ under the gradient results in

$$\bar{u}(\bar{x}_o) = \frac{1}{4\pi}\bar{\nabla}_{x_o}\times\{\iint_S \bar{\nabla}_x(\frac{\mu(\bar{x})}{r})\times\bar{n}dS(\bar{x}) - \iint_S \frac{1}{r}\{\bar{\nabla}_x(\mu)\times\bar{n}\}dS(\bar{x})\} \tag{A.5}$$

The first integral in Eq. (A.5) can be reduced to a line integral by employing the appropriate integral theorem. This results in

$$\bar{u}(\bar{x}_o) = \frac{1}{4\pi}\bar{\nabla}_{x_o}\times\{\int_{\partial S}\mu(\bar{x})\frac{d\bar{\ell}(\bar{x})}{r} - \iint_S \frac{1}{r}\{\bar{\nabla}_x(\mu)\times\bar{n}\}dS(\bar{x})\} \tag{A.6}$$

Finally using the identity for $\bar{\nabla}\times(f\bar{a})$ and re-arranging results in

$$\bar{u}(\bar{x}_o) = \frac{1}{4\pi}\iint_S \bar{\gamma}(\bar{x})\times\frac{\bar{r}}{r^3}dS(\bar{x}) - \frac{1}{4\pi}\int_{\partial S}\mu(\bar{x})\frac{\bar{r}\times d\bar{\ell}(\bar{x})}{r^3} \tag{A.7a}$$

where $\bar{\gamma}(\bar{x}) = \bar{n}\times\bar{\nabla}_x(\mu)$ (A.7b)

The first term in Eq. (A.7a) is recognized as the velocity induced by a surface vorticity distribution $\bar{\gamma}(\bar{x})$. The second term in Eq. (A.7a) is the velocity induced by a line vortex of strength $\mu(\bar{x})$, $\bar{x}\in\partial S$ along the boundary $\partial S$ of S. In case the doublet distribution vanishes all along $\partial S$ this term is identical zero. Note that in Eqs. (A.6) and (A.7a) the direction of $d\bar{\ell}$ is chosen such that the sense of the rotation corresponds with the positive direction of the line vortex (see Fig. A.1). Similarly, the definition of $\mu$ as indicated in Fig. (A.1) is chosen such that its value is positive for the case of a wing at positive incidence. In the main text the sign of $d\bar{\ell}$ is reversed, i.e. there it corresponds to the sign of the normal to the surface.

Employing Eq. (A.7a) for the velocity induced by a vorticity distribution and expressing the vorticity distribution in terms of $\mu$ as in Eq. (A.7b) automatically ensures that Kelvin's vortex laws are satisfied, i.e. that vortex lines are closed, i.e. do not end in the flow field.

## APPENDIX B
## Solution of Euler equations for slender axi-symmetric vortex core

The govering equations are Eqs. (4.3)-(4.4c), here written as

$$-\Theta\frac{\partial F}{\partial\Theta} + \frac{2}{\Theta}u_r = 0 \tag{B.1a}$$

$$-\Theta F\frac{\partial}{\partial\Theta}u_x - r_e'\frac{\Theta}{\rho}\frac{\partial p}{\partial\Theta} = 0 \tag{B.1b}$$

$$-\Theta F\frac{\partial}{\partial\Theta}u_r - \frac{1}{\Theta}u_\varphi^2 + \frac{1}{\rho}\frac{\partial p}{\partial\Theta} = 0 \tag{B.1c}$$

$$-\Theta F\frac{\partial}{\partial\Theta}u_\varphi + \frac{1}{\Theta}u_r u_\varphi = 0 \tag{B.1d}$$

where

$$F = r_e'u_x - \frac{1}{\Theta}u_r. \tag{B.1e}$$

subject to the boundary conditions given in Eqs. (4.5a-b):

$$\Theta = 0 : u_r = 0 \tag{B.1f}$$

$$\Theta = 1 : u_x = U_e(x),\ u_\varphi = V_e(x),\ p = P_e(x) \tag{B.1g}$$

Eliminating $u_r$ from Eqs. (B.1a) and (B.1d) yields:

$$u_\varphi\Theta F\frac{\partial}{\partial\Theta}\{\ln(\frac{F^{\frac{1}{2}}}{u_\varphi})\} = 0$$

so that

$$u_\varphi = CF^{\frac{1}{2}} \tag{B.2}$$

with C an arbitrary constant.

Elimination of $\frac{\partial p}{\partial\Theta}$ from Eqs. (B.1b and c) results in

$$-\Theta F(\frac{\partial}{\partial\Theta}u_x + \Theta r_e'\frac{\partial}{\partial\Theta}u_r) - r_e'v_\varphi^2 = 0$$

with Eq. (B.2) substituted one finds

$$-\Theta(\frac{\partial}{\partial\Theta}u_x + \Theta r_e'\frac{\partial}{\partial\Theta}u_r) - C^2r_e' = 0$$

Substituting of F into Eq. (B.1a) yields:

$$\Theta r_e'(\frac{\partial}{\partial\Theta}u_x) = \frac{1}{\Theta}u_r + \frac{\partial}{\partial\Theta}u_r \tag{B.3}$$

so that we find the following equation for $u_r$:

$$\{1 - (\Theta r_e')^2\}\frac{\partial}{\partial\Theta}u_r + \frac{1}{\Theta}u_r + (Cr_e')^2 = 0$$

The solution is:

$$u_r = \frac{C^2}{\Theta} + \frac{D}{\Theta r_e'}[1 + (\Theta r_e')^2]^{\frac{1}{2}}$$

with D a second arbitrary constant. Using the boundary condition Eq. (B.1f) at the center of the core $\Theta = 0$ one finds:

$$u_r = -C^2r_e'G(\Theta) \tag{B.4a}$$

$$\text{where } G(\Theta) = \frac{[1 + (\Theta r_e')^2]^{\frac{1}{2}} - 1}{\Theta r_e'} \tag{B.4b}$$

Substitution of Eq. (B.4) into Eq. (B.3) yields:

$$\Theta r_e'(\frac{\partial}{\partial\Theta}u_x) = -\frac{C^2}{\Theta}\frac{(r_e')^2}{[1 + (\Theta r_e')^2]^{\frac{1}{2}}}$$

and integration with respect to $\Theta$ leads to

$$u_x = -C^2r_e'\ln G(\Theta) + E$$

with E a third arbitrary constant. Using the boundary condition, Eq. B.1g, at the edge of the core it follows that

$$u_x = U_e - C^2 r'_e \ln\left(\frac{G(\theta)}{G(1)}\right) \tag{B.5}$$

The pressure is obtained from Eq. (B.1c) . Substitution of Eqs. (B.4) and (B.5) gives

$$\frac{1}{\rho}\frac{\partial p}{\partial \theta} = \frac{C^2 F}{\theta\{1 + (\theta r'_e)^2\}^{\frac{1}{2}}}$$

F is found from Eq. (B.1c) upon substitution of $u_\varphi$ and $u_x$ as expressed in Eq. (B.4) and (B.5), respectively. Integration with respect to $\theta$ and satisfying the boundary condition at $\theta = 1$ then results in

$$\frac{p}{\rho} = \frac{p_e}{\rho} + C^2 r'_e\left(U_e + \tfrac{1}{2}C^2 r'_e\right)\ln\left(\frac{G(\theta)}{G(1)}\right) - \tfrac{1}{2}\{C^2 r'_e \ln\left(\frac{G(\theta)}{G(1)}\right)\}^2 + \tfrac{1}{2}C^4\left[\frac{G(\theta)}{\theta r'_e} - \frac{G(1)}{r'_e}\right\} \tag{B.6}$$

Substitution of Eqs. (B.4a) and (B.5) and imposing the boundary condition $u_\varphi = V_e$ at $\theta = 1$ then yields the following expression for the constant C:

$$C^2 = \frac{U_e}{r'_e \alpha} \quad \text{with } \alpha = \left[\{1 + 4\,(V_e/U_e)^2 G(1) r'_e\}^{\frac{1}{2}} - 1\right]/\left[2G(1)/r'_e\right] \tag{B.7}$$

Substitution of $C^2$ in the expression for $u_x$, $u_r$, $u_\varphi$ and p and some re-arranging finally results in

$$u_x = U_e\{1 - \alpha \ln\left(\frac{G(\theta)}{G(1)}\right)\} \tag{B.8a}$$

$$u_r = -U_e \alpha G(\theta) \tag{B.8b}$$

$$u_\varphi = V_e\left[1 + (U_e\alpha/V_e)^2\left[\frac{G(\theta)}{\theta r'_e} - \frac{G(1)}{r'_e} - \ln\left(\frac{G(\theta)}{G(1)}\right)\right]\right]^{\frac{1}{2}} \tag{B.8c}$$

$$\frac{p}{\rho} = \frac{p_e}{\rho} + V_e^2\left[\ln\left(\frac{G(\theta)}{G(1)}\right) + \tfrac{1}{2}(U_e\alpha/V_e)^2\left(\frac{G(\theta)}{\theta r'_e} - \frac{G(1)}{r'_e} + G(1)^2 \ln\left(\frac{G(\theta)}{G(1)}\right) - \left[\ln\frac{G(\theta)}{G(1)}\right]^2\right)\right] \tag{B.8d}$$

APPENDIX C
Linear analysis of Kelvin-Helmholtz instability

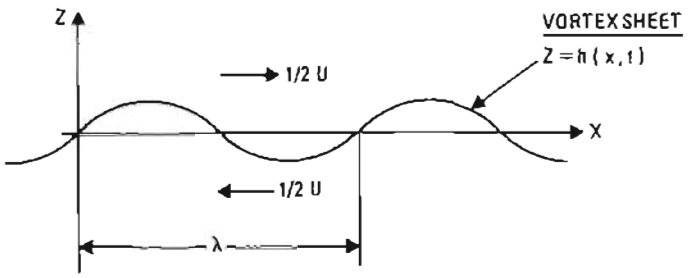


The potential problem involving the perturbed uniform vortex sheet of strength $\gamma=U$ is solved by introducing the perturbation potential $\phi_1$ for $z>h$ and $\phi_2$ for $z<h$, i.e.

$$\phi = \frac{1}{2}Ux + \phi_1(x,z,t) \quad \text{for } z>h$$

$$\phi = -\frac{1}{2}Ux + \phi_2(x,z,t) \quad \text{for } z<h$$

Assuming that $h<<1$, the kinematic condition that the vortex sheet moves with the local flow, $\frac{dh}{dt} = w$, in first approximation is written as

$$\frac{\partial h}{\partial t} + \frac{1}{2}U\frac{\partial h}{\partial x} = \frac{\partial \phi_1}{\partial z}$$

both for $z = 0$

$$\frac{\partial h}{\partial t} - \frac{1}{2}U\frac{\partial h}{\partial x} = \frac{\partial \phi_2}{\partial z}$$

The condition that the pressure is continuous across the sheet can be linearized to

$$\frac{\partial \phi_1}{\partial t} + \frac{1}{2}U\frac{\partial \phi_1}{\partial x} = \frac{\partial \phi_2}{\partial t} - \frac{1}{2}U\frac{\partial \phi_2}{\partial x} \quad \text{for } z = 0$$

Assuming that $h(x,t)$ is periodic in $x$, we write

$$h(x,t) = H(t)\sin(2\pi\frac{x}{\lambda})$$

It can be verified that

$$\phi_1(x,z,t) = \{A_1(t)\sin(2\pi\frac{x}{\lambda}) + B_1(t)\cos(2\pi\frac{x}{\lambda})\}e^{-2\pi\frac{z}{\lambda}}$$

$$\phi_2(x,z,t) = \{A_1(t)\sin(2\pi\frac{x}{\lambda}) + B_2(t)\cos(2\pi\frac{x}{\lambda})\}e^{+2\pi\frac{z}{\lambda}}$$

satisfy LaPlace's equation and the conditions at $z = \pm\infty$. Substitution into the kinematic condition results into

$$\phi_1(x,z,t) = -\{\frac{\lambda}{2\pi}\frac{dH}{dt}\sin(2\pi\frac{x}{\lambda}) + \frac{1}{2}UH\cos(2\pi\frac{x}{\lambda})\}e^{-2\pi\frac{z}{\lambda}}$$

$$\phi_2(x,z,t) = \{\frac{\lambda}{2\pi}\frac{dH}{dt}\sin(2\pi\frac{x}{\lambda}) - \frac{1}{2}UH\cos(2\pi\frac{x}{\lambda})\}e^{+2\pi\frac{z}{\lambda}}$$

Substitution in the pressure condition yields

$$\frac{d^2H}{dt^2} - (\frac{\pi U}{\lambda})^2 H = 0$$

The exponential growing i.e. unstable solution is

$$H(t) = Ce^{\frac{\pi U}{\lambda}t}$$

so that the linear growth rate of the Kelvin-Helmholtz instability is $\pi\gamma/\lambda$.

It is easily shown that at the mean position of the sheet, i.e. $z = 0$, the average velocity in $x$ direction equals the average velocity in $z$-direction. The disturbance which perturbes a point from the mean line under an angle of 45 deg is called a "normal mode".

## APPENDIX D
## Derivation of $\bar{E}_k$, $\bar{E}_k^c$ and $E_k$

In the uniformly valid expression for the third-order accurate potential and second-order accurate velocity induced by a doublet distribution two quantities, Eqs. (7.5b-c) were introduced. The closed-form analytic expression for these quantities is derived in this appendix.

Write $\bar{R}_f$, the vector from the point on the tangent to the collocation point, see Eq. (7.4b), as

$$\bar{R}_f = \xi\bar{e}_t + \zeta\bar{e}_n \tag{D.1a}$$

where

$$\xi = \bar{R}_f.\bar{e}_t = \xi_o - b\Delta t \tag{D.1b}$$

$$\xi_o = (\bar{X}_o - \bar{X}(t_j^*)).\bar{e}_t \tag{D.1c}$$

$$\zeta = \bar{R}_f.\bar{e}_n = (\bar{X}_o - \bar{X}(t_j^*)).\bar{e}_n \tag{D.1d}$$

In Eq. (D.1) $\bar{e}_t$ and $\bar{e}_n$ are the unit tangential and unit normal vector, respectively (see Fig. 7.2) while $b = |\bar{X}'(t_j^*)|$ as follows from Eq. (7.2). Substitution of Eq. (D.1) in Eq. (7.5b-c) yields

$$\bar{E}_o = \{-\zeta J_o\bar{e}_t + J_1\bar{e}_n\}/b \tag{D.2a}$$

$$\bar{E}_1 = \{-\zeta(\xi_o J_o - J_1)\bar{e}_t + (\xi_o J_1 - J_2)\bar{e}_n\}/b^2 \tag{D.2b}$$

$$\bar{E}_2 = \{-\zeta(\xi_o^2 J_o - 2\xi_o J_1 + J_2)\bar{e}_t + (\xi_o^2 J_1 - 2\xi_o J_2 + J_3)\}/b^3 \tag{D.2c}$$

$$\bar{E}_o^c = -\tfrac{1}{2}b\Delta t^2 \frac{\xi\bar{e}_t + \zeta\bar{e}_n}{\xi^2 + \zeta^2}\Bigg|_{t_j}^{t_{j+1}} + b\bar{e}_x \times \bar{E}_1 \tag{D.2d}$$

$$\bar{E}_1^c = -\tfrac{1}{2}b\Delta t^3 \frac{\xi\bar{e}_t + \zeta\bar{e}_n}{\xi^2 + \zeta^2}\Bigg|_{t_j}^{t_{j+1}} + \tfrac{3}{2}b\bar{e}_x \times \bar{E}_2 \tag{D.2e}$$

where

$$J_k = \int_{\xi_j}^{\xi_{j+1}} \frac{\xi^k d\xi}{\xi^2 + \zeta^2} \tag{D.2f}$$

The integrals $J_k$ can be found in closed form. The indefinite form is:

$$J_o = \hat{F}_1 \tag{D.3a}$$

$$J_1 = \hat{F}_2 \tag{D.3b}$$

$$J_2 = \xi - \zeta\hat{F}_1 \tag{D.3c}$$

$$J_3 = \tfrac{1}{2}\xi^2 - \zeta^2\hat{F}_2 \tag{D.3d}$$

where $\hat{F}_1 = \tan^{-1}\frac{\xi}{\zeta}$ (D.3e)

$$\hat{F}_2 = \tfrac{1}{2}\ln(\xi^2 + \zeta^2) \tag{D.3f}$$

Substitution of Eqs. (D.3a-f) into Eqs. (D.2a-c) results in:

$$\bar{E}_o = \{-\bar{e}_t F_1 + \bar{e}_n F_2\}/b \tag{D.4a}$$

$$\bar{E}_1 = \{-\bar{e}_t(\xi_o F_1 - \zeta F_2) + \bar{e}_n(\zeta F_1 + \xi_o F_2 + b\Delta t_j)\}/b^2 \tag{D.4b}$$

$$\bar{E}_2 = [\bar{e}_t\{-(\xi_o^2 - \zeta^2)F_1 + 2\xi_o\zeta F_2 + b\zeta\Delta t_j\} + \bar{e}_n\{2\xi_o\zeta F_1 + (\xi_o^2 - \zeta^2)F_2 + (\xi_o - b(t_j^* - \tfrac{1}{2}(t_j + t_{j+1})))b\Delta t_j\}]/b^3 \tag{D.4c}$$

$$\bar{E}_o^c = [-\bar{e}_t[\zeta F_1+\xi_o F_2+b\Delta t_j+\tfrac{1}{4}b^2((t_{j+1}-t_j^*)^2F_3^{j+1}-(t_j-t_j^*)^2F_3^j)]$$

$$-\bar{e}_n[\xi_o F_1-\zeta F_2 \quad +\tfrac{1}{4}b^2((t_{j+1}-t_j^*)^2F_4^{j+1}-(t_j-t_j^*)^2F_4^j)]]/b \tag{D.4d}$$

$$\bar{E}_1^c = [\bar{e}_t[-3\xi_o\zeta F_1-\tfrac{3}{2}(\xi_o^2-\zeta^2)F_2-\tfrac{3}{2}(\xi_o-b(t_j^*-\tfrac{1}{4}(t_j+t_{j+1})))b\Delta t_j-\tfrac{1}{4}b^3((t_{j+1}-t_j^*)^3F_3^{j+1}-(t_j-t_j^*)^3F_3^j)]$$

$$+\bar{e}_n[-\tfrac{3}{2}(\xi_o^2-\zeta^2)F_1+3\xi_o\zeta F_2+\tfrac{3}{2}b\zeta\Delta t_j-\tfrac{1}{4}b^3((t_{j+1}-t_j^*)^3F_4^{j+1}-(t_j-t_j^*)^3F_4^j)]]/b^2 \tag{D.4e}$$

where $F_1 = \tan^{-1}(\xi_{j+1}/\zeta) - \tan^{-1}(\xi_j/\zeta)$ (D.5a)

$F_2 = \tfrac{1}{2}\ell n[(\xi_{j+1}^2+\zeta^2)/(\xi_j^2+\zeta^2)]$ (D.5b)

$F_2^k = \ell n[(\xi_k^2+\zeta^2)^{\frac{1}{2}}/s_o]$ (D.5c)

$F_3^k = \xi_k/(\xi_k^2+\zeta^2)$ (D.5d)

$F_4^k = \zeta/(\xi_k^2+\zeta^2)$ (D.5e)

and $\xi_j = \bar{R}_f(t_j).\bar{e}_t$ (D.6a)

$\xi_{j+1} = \bar{R}_f(t_{j+1}).\bar{e}_t$ (D.6b)

$\xi_o = \bar{R}_f(t_j^*).\bar{e}_t$ (D.6c)

$\zeta = \bar{R}_f(t_j^*).\bar{e}_n$ (D.6d)

$b = |\bar{X}'(t_j^*)|$ (D.6e)

$\Delta t_j = t_{j+1} - t_j$ (D.6f)

In Eq. (8.8a) two particular combinations of $\bar{E}_k$'s form that reduce to relatively simple expressions:

$$b(\bar{E}_o^c.\bar{e}_t+b\bar{E}_1.\bar{e}_n) = -\tfrac{1}{4}b^2[(t_{j+1}-t_j^*)^2F_3^{j+1}-(t_j-t_j^*)^2F_3^j] \tag{D.7a}$$

$$b(\bar{E}_1^c.\bar{e}_t+b\bar{E}_2.\bar{e}_n) = -\tfrac{1}{4}b^2[(t_{j+1}-t_j^*)^3F_3^{j+1}-(t_j-t_j^*)^3F_3^j]-\tfrac{1}{4}b^2\bar{E}_2.\bar{e}_n \tag{D.7b}$$

In the expression for the third-order accurate potential induced by a source distribution the scalar $E_k$ is introduced, see Eq. (8.9b). Substitution of Eqs. (D.1a-d) yields the indefinite form:

$$E_o = [-\xi\ell n(\frac{(\xi^2+\zeta^2)^{\frac{1}{2}}}{s_o})+J_2]/b \tag{D.8a}$$

$$E_1 = [\tfrac{1}{2}(\xi_o-\xi)^2\ell n(\frac{(\xi^2+\zeta^2)^{\frac{1}{2}}}{s})-\tfrac{1}{2}(\xi_o^2J_1-2\xi_oJ_2+J_3)]/b^2 \tag{D.8b}$$

which upon substitution of Eqs. (D.3b-d) results in:

$$E_o = [-\zeta F_1-\xi_o F_2-b\Delta t_j+b[(t_{j+1}-t_j^*)F_2^{j+1}-(t_j-t_j^*)F_2^j]]/b \tag{D.9a}$$

$$E_1 = [-\xi_o\zeta F_1-\tfrac{1}{2}(\xi_o^2-\zeta^2)F_2-\tfrac{1}{2}\xi_o b\Delta t_j+\tfrac{1}{4}b^2\Delta t_j(t_j^*-\tfrac{1}{4}(t_j+t_{j+1}))+\tfrac{1}{4}b^2[(t_{j+1}-t_j^*)^2F_2^{j+1}-(t_j-t_j^*)^2F_2^j]]/b^2 \tag{D.9b}$$

## APPENDIX E
## Derivative with respect to geometric parameters of $\bar{E}_k$, and $\bar{E}^c_k$

The small-curvature expression for the cross-flow plane velocity potential and velocity induced by a singularity distribution involves the functions $\bar{E}_k$ and $\bar{E}^c_k$, considered in Appendix D. Here we consider the derivative with respect to the unknown geometric parameter $G_\ell$ of these expressions.

The expressions for $\bar{E}_k$ k=0(1)2 and $\bar{E}^c_k$, k=0(1)), see Eqs. (D.2a-e), depend on $Y_o$, $Y(t^*_j)$, $Y'(t^*_j)$, $Z_o$, $Z(t^*_j)$ and $Z'(t^*_j)$ of vortex sheet segments. This leads to:

$$\frac{\partial \bar{E}_k}{\partial G_\ell} = \frac{\partial \bar{E}_k}{\partial Y_o}\frac{\partial Y_o}{\partial G_\ell} + \frac{\partial \bar{E}_k}{\partial Y_j}\frac{\partial Y_j}{\partial G_\ell} + \frac{\partial \bar{E}_k}{\partial Y'_j}\frac{\partial Y'_j}{\partial G_\ell}$$

$$+ \frac{\partial \bar{E}_k}{\partial Z_o}\frac{\partial Z_o}{\partial G_\ell} + \frac{\partial \bar{E}_k}{\partial Z_j}\frac{\partial Z_j}{\partial G_\ell} + \frac{\partial \bar{E}_k}{\partial Z'_j}\frac{\partial Z'_j}{\partial G_\ell} \qquad (E.1)$$

and a similar expression for the derivative of $\bar{E}^c_k$. In Eq. (E.1) we used the notation $Y_j=Y(t^*_j)$, $Y'_j=Y'(t^*_j)$, etc. The derivative with respect to $G_\ell$ of $Y_o$, $Y_j$, $Y'_j$, $Z_o$, $Z_j$ and $Z'_j$ are found from the finite-difference type of expressions for these quantities given in Eq. (7.9).

Here we derive the expressions for the derivative with respect to $Y_o$, $Y_j$, $Y'_j$, $Z_o$, $Z_j$ and $Z'_j$.

Note that $Y_o$ and $Y_j$ always appear in the combination $Y_o-Y_j$. Similarly $Z_o$ and $Z_j$ always appear in the combination $Z_o-Z_j$. This results in:

$$\frac{\partial \bar{E}_k}{\partial Y_o} = -\frac{\partial \bar{E}_k}{\partial Y_j} \qquad (E.2a)$$

$$\frac{\partial \bar{E}_k}{\partial Z_o} = -\frac{\partial \bar{E}_k}{\partial Z_j} \qquad (E.2b)$$

The remaining four derivatives are considered next. First we will consider the derivatives of $\bar{E}_o$, $\bar{E}_1$ and $\bar{E}^c_o$, the terms appearing in the expression for the velocity induced by a doublet and by a source distribution.

Derivatives of $\bar{E}_o$

From Eq. (D.4a) it follows:

$$\frac{\partial \bar{E}_o}{\partial Y_j} = (-\bar{e}_t\frac{\partial F_1}{\partial Y_j} + \bar{e}_n\frac{\partial F_2}{\partial Y_j})/b \qquad (E.3a)$$

$$\frac{\partial \bar{E}_o}{\partial Y'_j} = (-\bar{e}_t\frac{\partial F_1}{\partial Y'_j} + \bar{e}_n\frac{\partial F_2}{\partial Y'_j} - F_1\frac{\partial \bar{e}_t}{\partial Y'_j} + F_2\frac{\partial \bar{e}_n}{\partial Y'_j})/b \qquad (E.3b)$$

Derivatives of $\bar{E}_1$

From Eq. (D.4b) it follows:

$$\frac{\partial \bar{E}_1}{\partial Y_j} = [-\bar{e}_t(\xi_o\frac{\partial F_1}{\partial Y_j} + F_1\frac{\partial \xi_o}{\partial Y_j} - \zeta\frac{\partial F_2}{\partial Y_j} - F_2\frac{\partial \zeta}{\partial Y_j})$$

$$+ \bar{e}_n(\zeta\frac{\partial F_1}{\partial Y_j} + F_1\frac{\partial \zeta}{\partial Y_j} + \xi_o\frac{\partial F_2}{\partial Y_j} + F_2\frac{\partial \xi_o}{\partial Y_j})]/b^2 \qquad (E.4a)$$

$$\frac{\partial \bar{E}_1}{\partial Y'_j} = [-\bar{e}_t(\xi_o\frac{\partial F_1}{\partial Y'_j} + F_1\frac{\partial \xi_o}{\partial Y'_j} - \zeta\frac{\partial F_2}{\partial Y'_j} - F_2\frac{\partial \zeta}{\partial Y'_j}) - (\xi_oF_1-\zeta F_2)\frac{\partial \bar{e}_t}{\partial Y'_j}$$

$$+ \bar{e}_n(\zeta\frac{\partial F_1}{\partial Y'_j} + F_1\frac{\partial \zeta}{\partial Y'_j} + \xi_o\frac{\partial F_2}{\partial Y'_j} + F_2\frac{\partial \xi_o}{\partial Y'_j}) + (\zeta F_1+\xi_oF_2+b\Delta t_j)\frac{\partial \bar{e}_n}{\partial Y'_j}]/b^2 \qquad (E.4b)$$

Again the derivative with respect to $Z_j$ and $Z'_j$ are found by replacing Y by Z.

Derivatives of $\bar{E}^c_o$

From Eq. (D.4d) it follows, using $t^*_j = \frac{1}{2}(t_j+t_{j+1})$:

$$\frac{\partial \bar{E}^c_o}{\partial Y_j} = [-\bar{e}_t(\zeta\frac{\partial F_1}{\partial Y_j} + F_1\frac{\partial \zeta}{\partial Y_j} + \xi_o\frac{\partial F_2}{\partial Y_j} + F_2\frac{\partial \xi_o}{\partial Y_j} + \tfrac{1}{2}(\tfrac{1}{2}b\Delta t_j)^2\frac{\partial F_3}{\partial Y_j})$$

$$-\bar{e}_n(\xi_o\frac{\partial F_1}{\partial Y_j} + F_1\frac{\partial \xi_o}{\partial Y_j} - \zeta\frac{\partial F_2}{\partial Y_j} - F_2\frac{\partial \zeta}{\partial Y_j} + \tfrac{1}{2}(\tfrac{1}{2}b\Delta t_j)^2\frac{\partial F_4}{\partial Y_j})]/b \qquad (E.5a)$$

$$\frac{\partial \bar{E}_o^c}{\partial Y_j'} = \{-\bar{e}_t(\zeta \frac{\partial F_1}{\partial Y_j'} + F_1 \frac{\partial \zeta}{\partial Y_j'} + \xi_o \frac{\partial F_2}{\partial Y_j'} + F_2 \frac{\partial \xi_o}{\partial Y_j'} + \tfrac{1}{2}(\tfrac{1}{2}b\Delta t_j)^2 \frac{\partial F_3}{\partial Y_j'})$$

$$-\bar{e}_n(\xi_o \frac{\partial F_1}{\partial Y_j'} + F_1 \frac{\partial \xi_o}{\partial Y_j'} - \zeta \frac{\partial F_2}{\partial Y_j'} - F_2 \frac{\partial \zeta}{\partial Y_j'} + \tfrac{1}{2}(\tfrac{1}{2}b\Delta t_j)^2 \frac{\partial F_4}{\partial Y_j'})$$

$$- (\zeta F_1 + \xi_o F_2 + b\Delta t_j + \tfrac{1}{2}(\tfrac{1}{2}b\Delta t_j)^2 F_3) \frac{\partial \bar{e}_t}{\partial Y_j'}$$

$$- (\xi_o F_1 - \zeta F_2 + \tfrac{1}{2}(\tfrac{1}{2}b\Delta t_j)^2 F_4) \frac{\partial \bar{e}_n}{\partial Y_j'}\}/b \qquad \text{(E.5b)}$$

where $F_3 = F_3^{j+1} - F_3^j$ and $F_4 = F_4^{j+1} - F_4^j$.
The derivative with respect to $Z_j$ and the one with respect to $Z_j'$ follow from Eqs. (E.5a and b) by replacing Y by Z.

The derivatives of $\bar{e}_n$ and $\bar{e}_t$ are given in Eq. (8.32c) and (8.35c), respectively. In the following we consider the derivative with respect to geometric quantities of $F_k$, k=1(1)4.
$F_1$, $F_2$, $F_3$ and $F_4$ are functions of $\xi_j$, $\xi_{j+1}$ and $\zeta$. This implies that the derivatives of $F_k$, k=1(1)4 are found from

$$\frac{\partial F_k}{\partial P} = \frac{\partial F_k}{\partial \xi_j}\frac{\partial \xi_j}{\partial P} + \frac{\partial F_k}{\partial \xi_{j+1}}\frac{\partial \xi_{j+1}}{\partial P} + \frac{\partial F_k}{\partial \zeta}\frac{\partial \zeta}{\partial P} \qquad \text{(E.6)}$$

where P is $Y_j$, $Y_j'$, $Z_j$ or $Z_j'$. Now it follows directly from Eq. (D.5a) that

$$\frac{\partial F_1}{\partial \xi_j} = -\frac{\zeta}{\xi_j^2 + \zeta^2} \qquad \text{(E.7a)}$$

$$\frac{\partial F_1}{\partial \xi_{j+1}} = \frac{\zeta}{\xi_{j+1}^2 + \zeta^2} \qquad \text{(E.7b)}$$

$$\frac{\partial F_1}{\partial \zeta} = \frac{-\xi_{j+1}}{\xi_{j+1}^2 + \zeta^2} + \frac{\xi_j}{\xi_j^2 + \zeta^2} \qquad \text{(E.7c)}$$

While we obtain from Eq. (D.5b):

$$\frac{\partial F_2}{\partial \xi_j} = -\frac{\xi_j}{\xi_j^2 + \zeta^2} \qquad \text{(E.8a)}$$

$$\frac{\partial F_2}{\partial \xi_{j+1}} = \frac{\xi_{j+1}}{\xi_{j+1}^2 + \zeta^2} \qquad \text{(E.8b)}$$

$$\frac{\partial F_2}{\partial \zeta} = \frac{\zeta}{\xi_{j+1}^2 + \zeta^2} - \frac{\zeta}{\xi_j^2 + \zeta^2} \qquad \text{(E.8c)}$$

From Eq. (D.5c) we obtain with $F_3 = F_3^{j+1} - F_3^j$:

$$\frac{\partial F_3}{\partial \xi_j} = \frac{-1}{\xi_j^2 + \zeta^2} + \frac{2\xi_j^2}{(\xi_j^2 + \zeta^2)^2} \qquad \text{(E.9a)}$$

$$\frac{\partial F_3}{\partial \xi_{j+1}} = \frac{1}{\xi_{j+1}^2 + \zeta^2} - \frac{2\xi_{j+1}^2}{(\xi_{j+1}^2 + \zeta^2)^2} \qquad \text{(E.9b)}$$

$$\frac{\partial F_3}{\partial \zeta} = \frac{-2\zeta\xi_{j+1}}{(\xi_{j+1}^2 + \zeta^2)^2} + \frac{2\zeta\xi_j}{(\xi_j^2 + \zeta^2)^2} \qquad \text{(E.9c)}$$

Similarly from Eq. (D.5d) we find with $F_4 = F_4^{j+1} - F_4^j$:

$$\frac{\partial F_4}{\partial \xi_j} = \frac{2\zeta\xi_j}{(\xi_j^2 + \zeta^2)^2} \qquad \text{(E.10a)}$$

$$\frac{\partial F_4}{\partial \xi_{j+1}} = \frac{-2\zeta\xi_{j+1}}{(\xi_{j+1}^2 + \zeta^2)^2} \qquad \text{(E.10b)}$$

$$\frac{\partial F_4}{\partial \zeta} = \frac{1}{\xi_{j+1}^2 + \zeta^2} - \frac{2\zeta^2}{(\xi_{j+1}^2 + \zeta^2)^2} - \frac{1}{\xi_j^2 + \zeta^2} + \frac{2\zeta^2}{(\xi_j^2 + \zeta^2)^2} \qquad \text{(E.10c)}$$

Finally we have to consider the derivative with respect to $Y_j$, $Y'_j$, $Z_j$ and $Z'_j$ of $\xi_o$, $\xi_j$, $\xi_{j+1}$ and $\zeta$.

It follows from Eq. (D.6a):

$$\xi_j = \frac{1}{b}[(Y_o-Y_j)Y'_j + (Z_o-Z_j)Z'_j + \tfrac{1}{2}\Delta t_j(Y'^2_j+Z'^2_j)] \tag{E.11a}$$

$$\frac{\partial \xi_j}{\partial Y_j} = -\frac{1}{b}Y'_j \tag{E.11b}$$

$$\frac{\partial \xi_j}{\partial Y'_j} = \frac{1}{b}(Y_o-Y_j + \Delta t_j Y'_j) \tag{E.11c}$$

$$\frac{\partial \xi_j}{\partial Z_j} = -\frac{1}{b}Z'_j \tag{E.11d}$$

$$\frac{\partial \xi_j}{\partial Z'_j} = \frac{1}{b}(Z_o-Z_j + \Delta t_j Z'_j) \tag{E.11e}$$

and similarly from Eq. (D.6b):

$$\xi_{j+1} = \frac{1}{b}[(Y_o-Y_j)Y'_j + (Z_o-Z_j)Z'_j - \tfrac{1}{2}\Delta t_j(Y'^2_j+Z'^2_j)] \tag{E.12a}$$

$$\frac{\partial \xi_{j+1}}{\partial Y_j} = -\frac{1}{b}Y'_j \tag{E.12b}$$

$$\frac{\partial \xi_{j+1}}{\partial Y'_j} = \frac{1}{b}(Y_o-Y_j - \Delta t_j Y'_j) \tag{E.12c}$$

$$\frac{\partial \xi_{j+1}}{\partial Z_j} = -\frac{1}{b}Z'_j \tag{E.12d}$$

$$\frac{\partial \xi_{j+1}}{\partial Z'_j} = \frac{1}{b}(Z_o-Z_j - \Delta t_j Z'_j) \tag{E.12e}$$

while from Eq. (D.6c):

$$\xi_o = \frac{1}{b}[(Y_o-Y_j)Y'_j + (Z_o-Z_j)Z'_j] \tag{E.13a}$$

$$\frac{\partial \xi_o}{\partial Y_j} = -\frac{1}{b}Y'_j \tag{E.13b}$$

$$\frac{\partial \xi_o}{\partial Y'_j} = \frac{1}{b}(Y_o-Y_j) \tag{E.13c}$$

$$\frac{\partial \xi_o}{\partial Z_j} = -\frac{1}{b}Z'_j \tag{E.13d}$$

$$\frac{\partial \xi_o}{\partial Z'_j} = \frac{1}{b}(Z_o-Z_j) \tag{E.13e}$$

and finally from Eq. (D.6d):

$$\zeta = \frac{1}{b}[-(Y_o-Y_j)Z'_j + (Z_o-Z_j)Y'_j] \tag{E.14a}$$

$$\frac{\partial \zeta}{\partial Y_j} = \frac{1}{b}Z'_j \tag{E.14b}$$

$$\frac{\partial \zeta}{\partial Y'_j} = \frac{1}{b}(Z_o-Z_j) \tag{E.14c}$$

$$\frac{\partial \zeta}{\partial Z_j} = -\frac{1}{b}Y'_j \tag{E.14d}$$

$$\frac{\partial \zeta}{\partial Z'_j} = -\frac{1}{b}(Y_o-Y_j) \tag{E.14e}$$

Derivatives of $\bar{e}_t$

With $\bar{e}_t=(Y'_j,Z'_j)/b$ we find

$$\frac{\partial \bar{e}_t}{\partial Y'_j} = \frac{1}{b}\bar{e}_y \tag{E.15a}$$

$$\frac{\partial \bar{e}_t}{\partial Z'_j} = \frac{1}{b}\bar{e}_z \tag{E.15b}$$

Derivatives of $\bar{e}_n$

With $\bar{e}_n=(-Z'_j,Y'_j)/b$ we find

$$\frac{\partial \bar{e}_n}{\partial Y'_j} = \frac{1}{b}\bar{e}_z \tag{E.16a}$$

$$\frac{\partial \bar{e}_n}{\partial Z'_j} = \frac{-1}{b}\bar{e}_y \tag{E.16b}$$

In the expression for the velocity potential induced by a doublet distribution two types of terms appear: $(b\bar{E}_k.\bar{e}_t)$, k=0(1)2 and $b(\bar{E}^c_k.\bar{e}_t + b\bar{E}_{k+1}.\bar{e}_n)$, k=0(1)1.
It follows from Eqs. (E.3a and b) that

$$\frac{\partial}{\partial Y_j}(b\bar{E}_0.\bar{e}_t) = -\frac{\partial F_1}{\partial Y_j} \tag{E.17a}$$

$$\frac{\partial}{\partial Y'_j}(b\bar{E}_0.\bar{e}_t) = -\frac{\partial F_1}{\partial Y'_j} \tag{E.17b}$$

and from Eqs. (E.4a and b) that

$$\frac{\partial}{\partial Y_j}(b\bar{E}_1.\bar{e}_t) = -(\xi_o \frac{\partial F_1}{\partial Y_j} + F_1 \frac{\partial \xi_o}{\partial Y_j} - \zeta \frac{\partial F_2}{\partial Y_j} - F_2 \frac{\partial \zeta}{\partial Y_j}) \tag{E.18a}$$

$$\frac{\partial}{\partial Y'_j}(b\bar{E}_1.\bar{e}_t) = -(\xi_o \frac{\partial F_1}{\partial Y'_j} + F_1 \frac{\partial \xi_o}{\partial Y'_j} - \zeta \frac{\partial F_2}{\partial Y'_j} - F_2 \frac{\partial \zeta}{\partial Y'_j}) \tag{E.18b}$$

From Eq. (D.4c) it follows that

$$\frac{\partial}{\partial Y_j}(b\bar{E}_2.\bar{e}_t) = -(\xi_o^2-\zeta^2)\frac{\partial F_1}{\partial Y_j} - 2F_1(\xi_o \frac{\partial \xi_o}{\partial Y_j} - \zeta\frac{\partial \zeta}{\partial Y_j}) + 2\xi_o\zeta\frac{\partial F_2}{\partial Y_j} + 2F_2(\zeta\frac{\partial \xi_o}{\partial Y_j} + \xi_o\frac{\partial \zeta}{\partial Y_j}) + b\Delta t_j \frac{\partial \zeta}{\partial Y_j} \tag{E.19a}$$

$$\frac{\partial}{\partial Y'_j}(b\bar{E}_2.\bar{e}_t) = -(\xi_o^2-\zeta^2)\frac{\partial F_1}{\partial Y'_j} - 2F_1(\xi_o \frac{\partial \xi_o}{\partial Y'_j} - \zeta\frac{\partial \zeta}{\partial Y'_j}) + 2\xi_o\zeta\frac{\partial F_2}{\partial Y'_j} + 2F_2(\zeta\frac{\partial \xi_o}{\partial Y'_j} + \xi_o\frac{\partial \zeta}{\partial Y'_j}) + b\Delta t_j \frac{\partial \zeta}{\partial Y'_j} \tag{E.19b}$$

It follows from Eq. (D.7a), with $t^*_j = \frac{1}{2}(t_j + t_{j+1})$:

$$\frac{\partial}{\partial Y_j}[b(\bar{E}^c_0.\bar{e}_t + b\bar{E}_1.\bar{e}_n)] = -\frac{1}{2}(\frac{1}{2}b\Delta t_j)^2 \frac{\partial F_3}{\partial Y_j} \tag{E.19c}$$

$$\frac{\partial}{\partial Y'_j}[b(\bar{E}^c_0.\bar{e}_t + b\bar{E}_1.\bar{e}_n)] = -\frac{1}{2}(\frac{1}{2}b\Delta t_j)^2 \frac{\partial F_3}{\partial Y'_j} \tag{E.19d}$$

From Eq. (D.7b) it follows:

$$\begin{aligned}\frac{\partial}{\partial Y_j}[b(\bar{E}^c_1.\bar{e}_t + b\bar{E}_2.\bar{e}_n)] = &-\frac{1}{2b}(\frac{1}{2}b\Delta t_j)^3(\frac{\partial F_3^{j+1}}{\partial Y_j} + \frac{\partial F_3^{j}}{\partial Y_j}) \\ &- \frac{1}{2b}[2\xi_o\zeta\frac{\partial F_1}{\partial Y_j} + 2F_1(\zeta\frac{\partial \xi_o}{\partial Y_j} + \xi_o\frac{\partial \zeta}{\partial Y_j}) + \\ &+(\xi_o^2-\zeta^2)\frac{\partial F_2}{\partial Y_j} + 2(\xi_o\frac{\partial \xi_o}{\partial Y_j} - \zeta\frac{\partial \zeta}{\partial Y_j})F_2 + \frac{\partial \xi_o}{\partial t_j}\end{aligned} \tag{E.20a}$$

$$\frac{\partial}{\partial Y'_j}[b(\bar{E}_1^c.\bar{e}_t + b\bar{E}_2.\bar{e}_n)] = -\frac{1}{2b}(\tfrac{1}{2}b\Delta t_j)^3\{\frac{\partial F_3^{j+1}}{\partial Y'_j} + \frac{\partial F_3^j}{\partial Y'_j}\}$$

$$-\frac{1}{2b}\{2\xi_o\zeta\frac{\partial F_1}{\partial Y'_j} + 2F_1(\zeta\frac{\partial \xi_o}{\partial Y'_j} + \xi_o\frac{\partial \zeta}{\partial Y'_j}) +$$

$$+(\xi_o^2-\zeta^2)\frac{\partial F_2}{\partial Y'_j} + 2(\xi_o\frac{\partial \xi_o}{\partial Y'_j} - \zeta\frac{\partial \zeta}{\partial Y'_j})F_2 + \frac{\partial \xi_o}{\partial Y'_j}\} \qquad \text{(E.20b)}$$

where the derivatives of $F_3^{j+1}$ and $F_3^j$ follow from Eq. (E.6) with

$$\frac{\partial F_3^{j+1}}{\partial \xi_j} = 0 \qquad \frac{\partial F_3^j}{\partial \xi_j} = \frac{1}{\xi_j^2 + \zeta^2} - \frac{2\xi_j^2}{(\xi_j^2 + \zeta^2)} \qquad \text{(E.21a)}$$

$$\frac{\partial F_3^{j+1}}{\partial \xi_{j+1}} = \frac{1}{\xi_{j+1}^2+\zeta^2} - \frac{2\xi_{j+1}^2}{(\xi_{j+1}^2+\zeta^2)^2} \qquad \frac{\partial F_3^j}{\partial \xi_{j+1}} = 0 \qquad \text{(E.21b)}$$

$$\frac{\partial F_3^{j+1}}{\partial \zeta} = \frac{-2\xi_{j+1}\zeta}{(\xi_{j+1}^2+\zeta^2)^2} \qquad \frac{\partial F_3^j}{\partial \zeta} = \frac{-2\xi_j\zeta}{(\xi_j^2+\zeta^2)^2} \qquad \text{(E.21c)}$$

## APPENDIX F
## Computation of $\bar{E}_{10}$, $\bar{E}^c_{10}$, $\bar{E}_{01}$, $\bar{E}^c_{01}$, $\bar{E}_{20}$, $\bar{E}_{11}$ and $\bar{E}_{02}$

1. Basic expressions

The small-curvature expansion for the velocity induced by a doublet distribution on the three-dimensional surface of a panel is expressed in terms of the 4 surface integrals defined in Eq. (9.15i-j). In this appendix we consider these expression in detail.

Write the distance vector $\bar{r}_f$, defined in Eq. (9.14b), as

$$\bar{r}_f = (\xi_o-\xi)\bar{e}_s + (\eta_o-\eta)\bar{e}_t + \zeta\bar{e}_n \tag{F.1a}$$

where $\bar{e}_s$ and $\bar{e}_t$ are the unit vectors in s- and t-direction, respectively, while $\bar{e}_n$ is the unit normal, i.e.

$$\bar{e}_s = \bar{x}^*_s/|\bar{x}^*_s| \tag{F.1b}$$

$$\bar{e}_t = \bar{x}^*_t/|\bar{x}^*_t| \tag{F.1c}$$

$$\bar{e}_n = (\bar{e}_s \times \bar{e}_t)/|\bar{e}_s \times \bar{e}_t| \tag{F.1d}$$

Note that in general $\bar{e}_s$ and $\bar{e}_t$ are nonorthogonal. The $(\xi,\zeta,\eta)$ coordinates follow from Eq. (9.14b), with $\bar{r}_o = \bar{x}_o-\bar{x}^*$, as

$$\xi = \Delta s|\bar{x}^*_s| \tag{F.2a}$$

$$\eta = \Delta t|\bar{x}^*_t| \tag{F.2b}$$

$$\xi_o = \frac{|\bar{x}^*_s||\bar{x}^*_t|}{|\bar{x}^*_s\times\bar{x}^*_t|}\,\bar{e}_n.(\bar{r}_o \times \bar{e}_t) \tag{F.2c}$$

$$\eta_o = -\frac{|\bar{x}^*_s||\bar{x}^*_t|}{|\bar{x}^*_s\times\bar{x}^*_t|}\,\bar{e}_n.(\bar{r}_o \times \bar{e}_s) \tag{F.2d}$$

$$\zeta = \bar{r}_o.\bar{e}_n \tag{F.2e}$$

where $\Delta s = s-s^*_i$ and $\Delta t = t-t^*_j$.
Since in general $\bar{e}_s$ and $\bar{e}_t$ are nonorthogonal one finds that

$$b = \bar{e}_s.\bar{e}_t = \frac{\bar{x}^*_s.\bar{x}^*_t}{|\bar{x}^*_s||\bar{x}^*_t|} \tag{F.3}$$

is nonzero.

Now we consider the expressions defined in Eq. (9.15i) in more detail. Upon substitution of Eqs. (F.1)-(F.2) one finds:

$$\bar{I}_{00} = (\bar{e}_s J_{10} + \bar{e}_t J_{01} + \bar{e}_n \zeta J_{00})/|\bar{x}^*_s||\bar{x}^*_t| \tag{F.4a}$$

$$\bar{I}_{10} = \{\xi_o \bar{I}_{00} - \frac{1}{|\bar{x}^*_s||\bar{x}^*_t|}(\bar{e}_s J_{20}+\bar{e}_t J_{11}+\bar{e}_n \zeta J_{10})\}/|\bar{x}^*_s| \tag{F.4b}$$

$$\bar{I}_{01} = \{\eta_o \bar{I}_{00} - \frac{1}{|\bar{x}^*_s||\bar{x}^*_t|}(\bar{e}_s J_{11}+\bar{e}_t J_{02}+\bar{e}_n \zeta J_{01})\}/|\bar{x}^*_t| \tag{F.4c}$$

are expressed in terms of the basic integrals:

$$J_{k\ell} = \int_{x_i}^{x_{i+1}}\int_{y_j}^{y_{j+1}} x^k y^\ell \frac{dxdy}{(x^2+2bxy+y^2+z^2)^{3/2}} \tag{F.5a}$$

where $x=\xi_o-\xi$, $y=\eta_o-\eta$ and $z=\zeta$.
In Eq. (F.5a) the upper and lower limits of integration are, with $(s^*_i,t^*_j)$ as the panel midpoint:

$$x_i = \xi_o + \tfrac{1}{2}|\bar{x}^*_s|\Delta s_i \qquad x_{i+1} = \xi_o - \tfrac{1}{2}|\bar{x}^*_s|\Delta s_i$$
$$y_j = \eta_o + \tfrac{1}{2}|\bar{x}^*_t|\Delta t_j \qquad y_{j+1} = \eta_o - \tfrac{1}{2}|\bar{x}^*_t|\Delta t_j \tag{F.5b}$$

where $\Delta s_i = s_{i+1}-s_i$ and $\Delta t_j = t_{j+1}-t_j$.
In the second section of this appendix closed-form expressions for the basic integrals $J_{k\ell}$ are listed.

Consider now the remaining curvature term $\bar{I}_c$, defined in Eq. (9.15j) as:

$$\bar{I}_c = \int_{s_i}^{s_{i+1}}\int_{t_j}^{t_{j+1}} \{\frac{\bar{r}_2}{|\bar{r}_f|^3} - 3(\bar{r}_2.\bar{r}_f)\frac{\bar{r}_f}{|\bar{r}_f|^5}\}dsdt \tag{F.6a}$$

It can be shown that the integrand of this expression can be expressed as:

$$\bar{e}_s\{\frac{1}{1-b^2}(\frac{\partial}{\partial\xi_o}-b\frac{\partial}{\partial\eta_o})+\bar{e}_t\frac{1}{1-b^2}(-b\frac{\partial}{\partial\xi_o}+\frac{\partial}{\partial\eta_o})+\bar{e}_n\frac{\partial}{\partial\zeta}\}(\frac{\bar{r}_2\cdot\bar{r}_f}{|\bar{r}_f|^3}) \qquad (F.6b)$$

where the term between { } is the $\bar{\nabla}$ with respect to $\bar{x}_o$, denoted here by $\bar{\nabla}_{x_o}$. In case $\bar{r}_2$ is normal to the tangent plane Eq. (F.6) resembles closely the integral expressing the velocity induced by a doublet distribution of strength $\bar{r}_2\cdot\bar{e}_n$ and could be reduced further along the lines indicated in Appendix A. However, $\bar{r}_2$ has also components in the tangent plane and we express $\bar{I}_c$ as

$$\bar{I}_c=\bar{\nabla}_{x_o}(\tfrac{1}{2}\bar{x}^*_{ss}\cdot\bar{I}_{20}+\bar{x}^*_{st}\cdot\bar{I}_{11}+\tfrac{1}{2}\bar{x}^*_{tt}\cdot\bar{I}_{02}) \qquad (F.6c)$$

where, upon substitution of Eqs. (F.1)-(F.2):

$$\bar{I}_{20}=\{-\xi_o^2\bar{I}_{00}+2\xi_o\bar{I}_{10}+\frac{1}{|\bar{x}^*_s||\bar{x}^*_t|}(\bar{e}_sJ_{30}+\bar{e}_tJ_{21}+\bar{e}_n\zeta J_{20})\}/|\bar{x}^*_s|^2 \qquad (F.7a)$$

$$\bar{I}_{11}=\{-\xi_o\eta_o\bar{I}_{00}+\xi_o\bar{I}_{01}+\eta_o\bar{I}_{10}+\frac{1}{|\bar{x}^*_s||\bar{x}^*_t|}(\bar{e}_sJ_{21}+\bar{e}_tJ_{12}+\bar{e}_n\zeta J_{11})\}|\bar{x}^*_s||\bar{x}^*_t| \qquad (F.7b)$$

$$\bar{I}_{02}=\{-\eta_o^2\bar{I}_{00}+2\eta_o\bar{I}_{01}+\frac{1}{|\bar{x}^*_s||\bar{x}^*_t|}(\bar{e}_sJ_{12}+\bar{e}_tJ_{03}+\bar{e}_n\zeta J_{02})\}|\bar{x}^*_t|^2 \qquad (F.7c)$$

Denoting the three derivatives in Eq. (F.6b) as

$$\frac{\partial F}{\partial p_1}=\frac{1}{1-b^2}(\frac{\partial F}{\partial\xi_o}-b\frac{\partial F}{\partial\eta_o})\equiv F^1 \qquad (F.8a)$$

$$\frac{\partial F}{\partial p_2}=\frac{1}{1-b^2}(-b\frac{\partial F}{\partial\xi_o}+\frac{\partial F}{\partial\eta_o})\equiv F^2 \qquad (F.8b)$$

$$\frac{\partial F}{\partial p_3}=\frac{\partial F}{\partial\zeta}\equiv F^3 \qquad (F.8c)$$

one can write Eq. (F.6c) as

$$\begin{aligned}\bar{I}_c=&\bar{e}_s(\tfrac{1}{2}\bar{x}^*_{ss}\cdot\bar{I}^1_{20}+\bar{x}^*_{st}\cdot\bar{I}^1_{11}+\tfrac{1}{2}\bar{x}^*_{tt}\cdot\bar{I}^1_{02})\\&+\bar{e}_t(\tfrac{1}{2}\bar{x}^*_{ss}\cdot\bar{I}^2_{20}+\bar{x}^*_{st}\cdot\bar{I}^2_{11}+\tfrac{1}{2}\bar{x}^*_{tt}\cdot\bar{I}^2_{02})\\&+\bar{e}_n(\tfrac{1}{2}\bar{x}^*_{ss}\cdot\bar{I}^3_{20}+\bar{x}^*_{st}\cdot\bar{I}^3_{11}+\tfrac{1}{2}\bar{x}^*_{tt}\cdot\bar{I}^3_{02})\end{aligned} \qquad (F.9)$$

The derivative with respect to $p_1$, $p_2$ and $p_3$ of $\bar{I}_{20}$, $\bar{I}_{11}$ and $\bar{I}_{01}$ is readily obtained from their definition given in Eq. (F.7). It involves the derivative with respect to $p_1$, $p_2$ and $p_3$ of the basic integrals $J_{k\ell}$ listed in the next section of this appendix.

2. The basic integrals $J_{k\ell}$

The basic integrals $J_{k\ell}$, defined in Eq. (F.5a), are to be evaluated for k=0(1)3 and ℓ=0(1)3. It turns out that all these integrals can be found in closed form. The indefinite form of the integrals is:

$$zJ_{00}=\frac{1}{(1-b^2)^{1/2}}F_1 \qquad (F.10a)$$

$$J_{10}=\frac{1}{1-b^2}(bF_2-F_3) \qquad (F.10b)$$

$$J_{01}=\frac{-1}{1-b^2}(F_2-bF_3) \qquad (F.10c)$$

$$J_{20}=\frac{-z}{(1-b^2)^{3/2}}F_1+yF_2+\frac{b}{1-b^2}F_4 \qquad (F.10d)$$

$$J_{11}=\frac{-bz}{(1-b^2)^{3/2}}F_1-\frac{1}{1-b^2}F_4 \qquad (F.10e)$$

$$J_{02}=\frac{-z}{(1-b^2)^{3/2}}F_1+xF_3+\frac{b}{1-b^2}F_4 \qquad (F.10f)$$

$$J_{30} = -(\frac{3}{2}y^2 + \frac{1}{2}\frac{z^2}{1-b^2})bF_2 - \frac{z^2}{(1-b^2)^2}(bF_2-F_3)+(y + \frac{b(x-by)}{2(1-b^2)})F_4 \quad (F.10g)$$

$$J_{21} = -(\frac{1}{2}y^2 + \frac{1}{2}\frac{z^2}{1-b^2})F_2 + \frac{bz^2}{(1-b^2)^2}(bF_2-F_3) - \frac{x-by}{2(1-b^2)}F_4 \quad (F.10h)$$

$$J_{12} = (\frac{1}{2}x^2 + \frac{1}{2}\frac{z^2}{1-b^2})F_3 - \frac{bz^2}{(1-b^2)^2}(F_2-bF_3) + \frac{bx-y}{2(1-b^2)}F_4 \quad (F.10i)$$

$$J_{03} = -(\frac{3}{2}x^2 + \frac{1}{2}\frac{z^2}{1-b^2})bF_3 + \frac{z^2}{(1-b^2)^2}(F_2-bF_3)+(x + \frac{b(y-bx)}{2(1-b^2)})F_4 \quad (F.10j)$$

where the $F_k$'s are a function of the limits of integration x and y, as well as the constants b and z:

$$F_1(x,y) = \tan^{-1}\frac{(1-b^2)xy-bz^2}{z(1-b^2)^{\frac{1}{2}}(x^2+2bxy+y^2+z^2)^{\frac{1}{2}}} \quad (F.11a)$$

$$F_2(x,y) = \sinh^{-1}\frac{x+by}{((1-b^2)y^2+z^2)^{\frac{1}{2}}} = \ell n\frac{(x+by)+(x^2+2bxy+y^2+z^2)^{\frac{1}{2}}}{((1-b^2)y^2+z^2)^{\frac{1}{2}}} \quad (F.11b)$$

$$F_3(x,y) = \sinh^{-1}\frac{bx+y}{((1-b^2)x^2+z^2)^{\frac{1}{2}}} = \ell n\frac{(bx+y)+(x^2+2bxy+y^2+z^2)^{\frac{1}{2}}}{((1-b^2)x^2+z^2)^{\frac{1}{2}}} \quad (F.11c)$$

$$F_4(x,y) = (x^2+2bxy+y^2+z^2)^{\frac{1}{2}} \quad (F.11d)$$

To compute $\bar{I}_c$ requires the derivative with respect to $p_1$, $p_2$ and $p_3$ of the basic integrals and thus of above four functions. These derivatives can be expressed as:

$$F_1^1 = \frac{z}{(1-b^2)^{\frac{1}{2}}}(-bF_5+F_6) \; ; \; F_1^2 = \frac{z}{(1-b^2)^{\frac{1}{2}}}(F_5-bF_6); \; F_1^3 = -(1-b^2)^{\frac{1}{2}}(yF_5+xF_6) \quad (F.12a)$$

$$F_2^1 = \frac{1}{F_4} + byF_5 \; ; \; F_2^2 = -yF_5 \; ; \; F_2^3 = -zF_5 \quad (F.12b)$$

$$F_3^1 = -xF_6 \; ; \; F_3^2 = \frac{1}{F_4} + bxF_6 \; ; \; F_3^3 = -zF_6 \quad (F.12c)$$

$$F_4^1 = \frac{x}{F_4} \; ; \; F_4^2 = \frac{y}{F_4} \; ; \; F_4^3 = \frac{z}{F_4} \quad (F.12d)$$

where

$$F_5(x,y) = \frac{x+by}{((1-b^2)y^2+z^2)F_4} \quad (F.12e)$$

$$F_6(x,y) = \frac{bx+y}{((1-b^2)x^2+z^2)F_4} \quad (F.12f)$$

3. Influence of a panel at its own midpoint

In case the collocation point is located on the panel itself, $\bar{x}_o = \bar{x}^*$ and it follows from Eq. (F.2) that

$$\xi_o = 0, \; \eta_o = 0, \; \zeta = z = 0^{\pm} \quad (F.13a)$$

while it follows from Eq. (F.5b) that

$$x_i = \tfrac{1}{2}|\bar{x}_s^*|\Delta s_i = -x_{i+1} \quad (F.13b)$$

$$y_j = \tfrac{1}{2}|\bar{x}_t^*|\Delta t_j = -y_{j+1} \quad (F.13c)$$

Since now upon substitution of the limits of integration some of the terms vanish, the expressions for $\bar{I}_{00}$, $\bar{I}_{10}$ and $\bar{I}_{01}$, defined in Eqs. (F.4a-c) become much simpler:

$$\bar{I}_{00} = \frac{1}{|\bar{x}_s^*||\bar{x}_t^*|} h_1\bar{e}_n \quad (F.14a)$$

$$\bar{I}_{10} = \frac{-1}{|\bar{x}_s^*|^2|\bar{x}_t^*|}(h_2\bar{e}_s - h_3\bar{e}_t) \quad (F.14b)$$

$$\bar{I}_{01} = \frac{-1}{|\bar{x}_s^*||\bar{x}_t^*|^2}(-h_3\bar{e}_s + h_4\bar{e}_t) \quad (F.14c)$$

where

$$h_1 = 2\pi \text{sign}(\zeta) \tag{F.15a}$$

$$h_2 = 2y_j \ln\left(\frac{(x_i+by_j)+r_{ij}}{(-x_i+by_j)+\hat{r}_{ij}}\right) + bh_3 \tag{F.15b}$$

$$h_3 = \frac{2}{1-b^2}(r_{ij}-\hat{r}_{ij}) \tag{F.15c}$$

$$h_4 = 2x_i \ln\left(\frac{(bx_i+y_j)+r_{ij}}{(bx_i-y_j)+\hat{r}_{ij}}\right) + bh_3 \tag{F.15d}$$

with $r_{ij}=(x_i^2+2bx_iy_j+y_j^2)^{\frac{1}{2}}$ and $\hat{r}_{ij}=(x_i^2-2bx_iy_j+y_j^2)^{\frac{1}{2}}$.

The curvature term, defined in Eq. (F.9), involves the derivatives with respect to $p_1$, $p_2$ and $p_3$ of $\bar{I}_{20}$, $\bar{I}_{11}$ and $\bar{I}_{02}$. It turns out that these derivatives can best be expressed in terms of the following three vectors:

$$\bar{c}_1 = \bar{e}_t \times (\bar{e}_s \times \bar{e}_t)/(1-b^2) \tag{F.16a}$$

$$\bar{c}_2 = -\bar{e}_s \times (\bar{e}_s \times \bar{e}_t)/(1-b^2) \tag{F.16b}$$

$$\bar{c}_3 = \bar{e}_n \tag{F.16c}$$

so that

$$\bar{e}_s = \bar{c}_1 + b\bar{c}_2 \tag{F.16d}$$

$$\bar{e}_t = b\bar{c}_1 + \bar{c}_2 \tag{F.16e}$$

while also $(\bar{c}_1,\bar{c}_2,\bar{c}_3).\bar{e}_s = (1,0,0)$, $(\bar{c}_1,\bar{c}_2,\bar{c}_3).\bar{e}_t = (0,1,0)$ and $(\bar{c}_1,\bar{c}_2,\bar{c}_3).\bar{e}_n=(0,0,1)$.
It then follows that

$$\bar{I}_{20}^1 = \frac{1}{|\bar{x}_s^*|^3|\bar{x}_t^*|}\{(-2h_2 + h_5)\bar{c}_1 + (-3bh_2 + 2h_3 + 2bh_5 - h_6)\bar{c}_2\} \tag{F.17a}$$

$$\bar{I}_{20}^2 = \frac{1}{|\bar{x}_s^*|^3|\bar{x}_t^*|}\{(h_3 + h_7)\bar{c}_1 + (h_2 - h_5)\bar{c}_2\} \tag{F.17b}$$

$$\bar{I}_{20}^3 = \frac{1}{|\bar{x}_s^*|^3|\bar{x}_t^*|}\{h_2\bar{c}_3\} \tag{F.17c}$$

$$\bar{I}_{11}^1 = \frac{1}{|\bar{x}_s^*|^2|\bar{x}_t^*|^2}\{(h_3 - h_6)\bar{c}_1 - h_5\bar{c}_2\} \tag{F.17d}$$

$$\bar{I}_{11}^2 = \frac{1}{|\bar{x}_s^*|^2|\bar{x}_t^*|^2}\{-h_8\bar{c}_1 + (h_3 - h_7)\bar{c}_2\} \tag{F.17e}$$

$$\bar{I}_{11}^3 = \frac{1}{|\bar{x}_s^*|^2|\bar{x}_t^*|^2}\{-h_3\bar{c}_3\} \tag{F.17f}$$

$$\bar{I}_{02}^1 = \frac{1}{|\bar{x}_s^*||\bar{x}_t^*|^3}\{(h_4 - h_8)\bar{c}_1 + (h_3 + h_6)\bar{c}_2\} \tag{F.17g}$$

$$\bar{I}_{02}^2 = \frac{1}{|\bar{x}_s^*||\bar{x}_t^*|^3}\{(-3bh_4 + 2h_3 - h_7 + 2bh_8)\bar{c}_1 + (-2h_4 + h_8)\bar{c}_2\} \tag{F.17h}$$

$$\bar{I}_{02}^3 = \frac{1}{|\bar{x}_s^*||\bar{x}_t^*|^3}\{h_4\bar{c}_3\} \tag{F.17i}$$

where

$$h_5 = \frac{2x_i}{1-b^2}\left(\frac{bx_i+y_j}{r_{ij}} - \frac{bx_i-y_j}{\hat{r}_{ij}}\right) \tag{F.18a}$$

$$h_6 = \frac{2x_i}{1-b^2}\left(\frac{x_i+by_j}{r_{ij}} - \frac{x_i-by_j}{\hat{r}_{ij}}\right) \tag{F.18b}$$

$$h_7 = \frac{2y_j}{1-b^2}\left(\frac{bx_i+y_j}{r_{ij}} + \frac{bx_i-y_j}{\hat{r}_{ij}}\right) = h_3 - h_6 \tag{F.18c}$$

$$h_8 = \frac{2y_j}{1-b^2}\left(\frac{x_i+by_j}{r_{ij}} + \frac{x_i-by_j}{\hat{r}_{ij}}\right) \tag{F.18d}$$

4. Expressions for a far-wake panel

For a far-wake panel, see section 9.3.3, one requires $\bar{E}_{01w}$, $\bar{E}^c_{01w}$ and $\bar{E}_{02w}$, which follow from Eqs. (F.3c), (F.3d) and (F.3g) as:

$$\bar{E}_{01w} = -\bar{e}_{fw} \times \bar{I}_{00w} \tag{F.19a}$$

$$\bar{E}^c_{01w} = \bar{e}_{fw} \times \bar{I}_{cw} \tag{F.19b}$$

$$\bar{E}_{02w} = -\bar{e}_{fw} \times \bar{I}_{01w} \tag{F.19c}$$

respectively, where it follows from Eqs. (F.4a), (F.4c) and (F.9) that

$$\bar{I}_{00w} = (\bar{e}_{fw}J_{10w}+\bar{e}_t J_{01w}+\bar{e}_n\zeta J_{00w})/|\bar{x}^*_t| \tag{F.20a}$$

$$\bar{I}_{01w} = \{\eta_o\bar{I}_{00w} - \frac{1}{|\bar{x}^*_t|}(\bar{e}_{fw}J_{11w}+\bar{e}_t J_{02w}+\bar{e}_n\zeta J_{01w})\}/|\bar{x}^*_t| \tag{F.20b}$$

$$\bar{I}_{cw} = \bar{e}_{fw}(\tfrac{1}{2}\bar{x}^*_{tt}.\bar{I}^1_{02w}) + \bar{e}_t(\tfrac{1}{2}\bar{x}^*_{tt}.\bar{I}^2_{02w}) + \bar{e}_n(\tfrac{1}{2}\bar{x}^*_{tt}.\bar{I}^3_{02w}) \tag{F.20c}$$

with, using Eq. (F.7c):

$$\bar{I}_{02w} = \{-\eta_o^2\bar{I}_{00w} + 2\eta_o\bar{I}_{01w} + \frac{1}{|\bar{x}^*_t|}(\bar{e}_{fw}J_{12w} + \bar{e}_t J_{03w} + \bar{e}_n\zeta J_{02w})\}/|\bar{x}^*_t|^2 \tag{F.20d}$$

Note that because of the form of Eq. (F.19a-c) the $\bar{e}_{fw}$-terms in Eqs. (F.20a-c) drop out immediately, but must be retained when evaluating Eq. (F.20d).

In above expressions the basic integrals $J_{k\ell w}$ are defined as, see Eq. (F.5):

$$J_{k\ell w} = \int_{\xi_o}^{x_\infty}\int_{y_j}^{y_{j+1}} x^k y^\ell \frac{dxdy}{(x^2+2bxy+y^2+z^2)^{3/2}} \tag{F.21a}$$

where $x_\infty = \lim_{s_\infty\to\infty}(\xi_o+S-s_\infty)$. The expressions for the basic integrals $J_{k\ell}$, listed in the second section of this appendix, are also the expressions for the corresponding integrals $J_{k\ell w}$, but substitution of the limits integration requires some attention. Defining

$$\Box F_k = F_k(x_i,y_j) - F_k(x_i,y_{j+1}) - F_k(x_{i+1},y_j) + F_k(x_{i+1},y_{j+1}) \tag{F.21b}$$

one finds, upon substitution of $x_{i+1}=x_\infty$ and taking the limit, for the basic functions and their combinations with powers of x and y:

$$\Box F_1 = F_1(\xi_o,y_j) - F_1(\xi_o,y_{j+1}) + (\tan^{-1}\frac{(1-b^2)^{\frac{1}{2}}y_j}{z} - \tan^{-1}\frac{(1-b^2)^{\frac{1}{2}}y_{j+1}}{z}) \tag{F.22a}$$

$$\Box F_2 = F_2(\xi_o,y_j) - F_2(\xi_o,y_{j+1}) - \ln(\frac{(1-b^2)y_j^2+z^2}{(1-b^2)y_{j+1}^2+z^2}) \tag{F.22b}$$

$$\Box F_3 = F_3(\xi_o,y_j) - F_3(\xi_o,y_{j+1}) \tag{F.22c}$$

$$\Box F_4 = F_4(\xi_o,y_j) - F_4(\xi_o,y_{j+1}) - b(y_{j+1}-y_j) \tag{F.22d}$$

$$\Box(xF_3) = \xi_o F_3(\xi_o,y_j) - \xi_o F_3(\xi_o,y_{j+1}) - (y_{j+1}-y_j) \tag{F.22e}$$

$$\Box(\frac{1}{F_4}) = \frac{1}{F_4(\xi_o,y_j)} - \frac{1}{F_4(\xi_o,y_{j+1})} \tag{F.22f}$$

$$\Box(\frac{x}{F_4}) = \frac{\xi_o}{F_4(\xi_o,y_j)} - \frac{\xi_o}{F_4(\xi_o,y_{j+1})} \tag{F.22g}$$

$$\Box(\frac{y}{F_4}) = \frac{y_j}{F_4(\xi_o,y_j)} - \frac{y_{j+1}}{F_4(\xi_o,y_{j+1})} \tag{F.22h}$$

$$\Box(\frac{x^2}{F_4}) = \frac{\xi_o^2}{F_4(\xi_o,y_j)} - \frac{\xi_o^2}{F_4(\xi_o,y_{j+1})} + b(y_{j+1}-y_j) \tag{F.22i}$$

$$\Box(\frac{xy}{F_4}) = \frac{\xi_o y_j}{F_4(\xi_o,y_j)} - \frac{\xi_o y_{j+1}}{F_4(\xi_o,y_{j+1})} - (y_{j+1}-y_j) \tag{F.22j}$$

$$\Box(\frac{y^2}{F_4}) = \frac{y_j^2}{F_4(\xi_o,y_j)} - \frac{y_{j+1}^2}{F_4(\xi_o,y_{j+1})} \tag{F.22k}$$

$$\square F_5 = F_5(\xi_o,y_j) - F_5(\xi_o,y_{j+1}) + \frac{1}{(1-b^2)y_j^2+z^2} - \frac{1}{(1-b^2)y_{j+1}^2+z^2} \tag{F.22l}$$

$$\square(yF_5) = y_jF_5(\xi_o,y_j) - y_{j+1}F_5(\xi_o,y_{j+1}) + \frac{y_j}{(1-b^2)y_j^2+z^2} - \frac{y_{j+1}}{(1-b^2)y_{j+1}^2+z^2} \tag{F.22m}$$

$$\square F_6 = F_6(\xi_o,y_j) - F_6(\xi_o,y_{j+1}) \tag{F.22n}$$

$$\square(xF_6) = \xi_oF_6(\xi_o,y_j) - \xi_oF_6(\xi_o,y_{j+1}) \tag{F.22o}$$

The influence of the semi-infinite far-wake panel at the collocation points just upstream of the panel is obtained by assuming that $\xi_o = -\frac{1}{2}\Delta s_{NUP}|\bar{x}^*_{s_{NUP},j}|$, $\eta_o = 0$ and $\zeta = 0$.
It then follows that

$$\bar{I}_{00w} = -\frac{\bar{e}_t}{1-b^2}(\hat{n}_1 - b\hat{n}_2)/|\bar{x}^*_t| \tag{F.23a}$$

$$\bar{I}_{01w} = -\bar{e}_t(\hat{n}_3 + b\hat{n}_4)/|\bar{x}^*_t|^2 \tag{F.23b}$$

$$\bar{I}^2_{02w} = (\bar{e}_1(-3b(\hat{n}_3 + b\hat{n}_4) + 2\hat{n}_4 + 2b\hat{n}_5 - \hat{n}_6) + \bar{e}_2(-2(\hat{n}_3 + b\hat{n}_4) + \hat{n}_5))/|\bar{x}^*_t|^3 \tag{F.23c}$$

$$\bar{I}^3_{02w} = \bar{e}_n(\hat{n}_3 + b\hat{n}_4)/|\bar{x}^*_t|^3 \tag{F.23d}$$

where with $x_i = \xi_o$, $y_j = -y_{j+1} = \frac{1}{2}\Delta t_j|\bar{x}^*_t|$

$$\hat{n}_1 = \ell n\left(\frac{(x_i+by_j) + r_{ij}}{(x_i-by_j) + \hat{r}_{ij}}\right) \tag{F.23e}$$

$$\hat{n}_2 = \ell n\left(\frac{(bx_i+y_j) + r_{ij}}{(bx_i-y_j) + \hat{r}_{ij}}\right) \tag{F.23f}$$

$$\hat{n}_3 = x_i\hat{n}_2 + 2y_j \tag{F.23g}$$

$$\hat{n}_4 = (r_{ij} - \hat{r}_{ij} + 2by_j)/(1-b^2) \tag{F.23h}$$

$$\hat{n}_5 = \frac{y_j}{1-b^2}\left(2 + \frac{x_i + by_j}{r_{ij}} + \frac{x_i - by_j}{\hat{r}_{ij}}\right) \tag{F.23i}$$

$$\hat{n}_6 = \frac{y_j}{1-b^2}\left(2b + \frac{bx_i + y_j}{r_{ij}} + \frac{bx_i - y_j}{\hat{r}_{ij}}\right) \tag{F.23j}$$

where $r_{ij} = (x_i^2 + 2bx_iy_j + y_j^2)^{\frac{1}{2}}$ and $\hat{r}_{ij} = (x_i^2 - 2bx_iy_j + y_j^2)^{\frac{1}{2}}$.

5. Expressions for feeding-sheet panel

For a panel of the feeding sheet, see section 9.3.4, one requires expressions for $\bar{E}_{10f}$, $\bar{E}^c_{10f}$ and $\bar{E}_{20f}$, which follow from Eqs. (F.3a), (F.3b) and (F.3e) as

$$\bar{E}_{10f} = (\bar{e}_t \times \bar{I}_{00f})|\bar{x}^*_t| \tag{F.24a}$$

$$\bar{E}^c_{10f} = \bar{x}^*_{st} \times \bar{I}_{10f} - (\bar{e}_c \times \bar{I}_{cf})|\bar{x}^*_t| \tag{F.24b}$$

$$\bar{E}_{20f} = (\bar{e}_t \times \bar{I}_{10f})|\bar{x}^*_t| \tag{F.24c}$$

respectively, where it follows from Eqs. (F.4a), (F.4b) and (F.9) that

$$\bar{I}_{00f} = (\bar{e}_sJ_{10f} + \bar{e}_tJ_{01f} + \bar{e}_n\zeta J_{00f})/|\bar{x}^*_s||\bar{x}^*_t| \tag{F.25a}$$

$$\bar{I}_{10f} = (\xi_o\bar{I}_{00f} - \frac{1}{|\bar{x}^*_s||\bar{x}^*_t|}(\bar{e}_sJ_{20f} + \bar{e}_tJ_{11f} + \bar{e}_n\zeta J_{10f}))/|\bar{x}^*_s| \tag{F.25b}$$

$$\bar{I}_{cf} = \bar{e}_s(\tfrac{1}{2}\bar{x}^*_{ss}.\bar{I}^1_{20f} + \bar{x}^*_{st}.\bar{I}^1_{11}) + \bar{e}_t(\tfrac{1}{2}\bar{x}^*_{ss}.\bar{I}^2_{20f} + \bar{x}^*_{st}.\bar{I}^2_{11}) + \bar{e}_n(\tfrac{1}{2}\bar{x}^*_{ss}.\bar{I}^3_{20f} + \bar{x}^*_{st}.\bar{I}^3_{11}) \tag{F.25c}$$

with, using Eqs. (F.7a and b):

$$\bar{I}_{20f} = \{-\xi_o^2\bar{I}_{00f}+2\xi_o\bar{I}_{10f}+\frac{1}{|\bar{x}_s^*||\bar{x}_t^*|}(\bar{e}_s J_{20f}+\bar{e}_t J_{21f}+\bar{e}_n\zeta J_{20f})\}/|\bar{x}_s^*|^2 \tag{F.25d}$$

$$\bar{I}_{11f} = \{-\xi_o\eta_o\bar{I}_{00f}+\xi_o\bar{I}_{01f}+\eta_o\bar{I}_{10f}+\frac{1}{|\bar{x}_s^*||\bar{x}_t^*|}(\bar{e}_s J_{21f}+\bar{e}_t J_{12f}+\bar{e}_n\zeta J_{11f})\}/|\bar{x}_s^*||\bar{x}_t^*| \tag{F.25e}$$

In the above expressions the basic integrals $J_{k\ell f}$ are defined as, see Eq. (F.5):

$$J_{k\ell f} = \int_{x_i}^{x_{i+1}}\int_{y_j}^{y_{j+1}} (x^k y^\ell)\frac{dxdy}{(x^2+2bxy+y^2+z^2)^{3/2}} \tag{F.26}$$

with $y_j = \eta_o + |\bar{x}_t^*|$ and $y_{j+1} = \eta_o$, while $x_i$ and $x_{i+1}$ are defined as in Eq. (F.5b). The expressions for above basic integrals $J_{k\ell f}$ are again given by the corresponding integrals $J_{k\ell}$ defined in the second section of this Appendix. However, substitution of the limits of integration requires some care for the case the point $\bar{x}_o$ approaches the expansion point $\bar{x}_v(s_i^*)$. In this case it is assumed that $\xi_o = \eta_o = \zeta = 0$, $x_i = \frac{1}{2}\Delta s_i|\bar{x}_s^*| = -x_{i+1}$, $y_j = |\bar{x}_t^*|$, while $y_{j+1} = \epsilon \to 0^+$ with $\epsilon > 0$, i.e. we reset the collocation point to a point on the feeding sheet, a small distance away from the edge $\bar{x}_v(s)$.
Defining $\Box F_k$ as in Eq. (F.21b) we now find:

$$\Box F_1 = 2\pi \mathrm{sign}(\zeta)/(1-b^2)^{\frac{1}{2}} \tag{F.27a}$$

$$\Box F_2 = \ln\left(\frac{x_i + by_j + r_{ij}}{-x_i + by_j + \hat{r}_{ij}}\right) - \ln\left(\frac{4x_i^2}{(1-b^2)\zeta^2}\right) \tag{F.27b}$$

$$\Box F_3 = \ln\left(\frac{bx_i + y_j + r_{ij}}{-bx_i + y_j + \hat{r}_{ij}}\right) + \ln\left(\frac{1-b}{1+b}\right) \tag{F.27c}$$

$$\Box F_4 = r_{ij} - \hat{r}_{ij} \tag{F.27d}$$

$$\Box yF_2 = y_j\ F_2 \tag{F.27e}$$

$$\Box\frac{1}{F_4} = \frac{1}{r_{ij}} - \frac{1}{\hat{r}_{ij}} \tag{F.27f}$$

$$\Box\frac{x^2}{F_4} = \frac{x_i^2}{r_{ij}} - \frac{x_i^2}{\hat{r}_{ij}} \tag{F.27g}$$

$$\Box\frac{xy}{F_4} = \frac{x_i y_j}{r_{ij}} + \frac{x_i y_j}{\hat{r}_{ij}} \tag{F.27h}$$

$$\Box\frac{y^2}{F_4} = \frac{y_j^2}{r_{ij}} - \frac{y_j^2}{\hat{r}_{ij}} \tag{F.27i}$$

with $r_{ij} = (x_i^2 + 2bx_iy_j + y_j^2)^{\frac{1}{2}}$ and $\hat{r}_{ij} = (x_i^2 - 2bx_iy_j + y_j^2)^{\frac{1}{2}}$.
The expression for $\Box F_2$ contains a logarithmic singularity, caused by the circumstance that the vortex lines on the feeding sheet are not exactly perpendicular to the line vortex at $\bar{x}=\bar{x}_v(s)$.
In the present formulation we ignore this weak singularity, i.e. it is assumed that the curvature is vanishingly small.

6. Expressions for the influence due to a vortex core segment

The small-curvature expansion for the velocity induced by a vortex core is expressed in terms of the five integrals defined in Eqs. (9.21g and h).
Writing the distance vector $\bar{r}_{vf}$, defined in Eq. (9.20b) as

$$\bar{r}_{vf} = (\xi_o-\xi)\bar{e}_v + \bar{d} \tag{F.28a}$$

where $\bar{e}_v$ is the unit vector along the vortex core and $\bar{d}$ the component of $\bar{r}_{vf}$ normal to the vortex core, i.e.

$$\bar{e}_v = \bar{x}_{v_s}^* / |\bar{x}_{v_s}^*| \tag{F.28b}$$

$$\bar{d} = \bar{e}_v \times ((\bar{x}_o-\bar{x}_v^*)\times\bar{e}_v) \tag{F.28c}$$

The $\xi$ coordinate then follows from Eq. (9.20b) as

$$\xi = \Delta s|\bar{x}_{v_s}^*| \tag{F.29a}$$

$$\xi_o = \bar{e}_v\cdot(\bar{x}_o-\bar{x}_v^*) \tag{F.29b}$$

Substitution of Eq. (F.28a) in Eq. (9.21g) gives

$$\bar{I}_{\nu o} = -(\bar{e}_\nu J_{\nu 1} + \bar{d} J_{\nu o})/|\bar{x}^*_{\nu_s}| \tag{F.30a}$$

$$\bar{I}_{\nu 1} = (\xi_o \bar{I}_{\nu o} + (\bar{e}_\nu J_{\nu 2} + \bar{d} J_{\nu 1})/|\bar{x}^*_{\nu_s}|)/|\bar{x}^*_{\nu_s}| \tag{F.30b}$$

$$\bar{I}_{\nu 2} = -(\xi_o^2 \bar{I}_{\nu o} - 2\xi_o \bar{I}_{\nu 1} + (\bar{e}_\nu J_{\nu 3} + \bar{d} J_{\nu 2})/|\bar{x}^*_{\nu_s}|)|\bar{x}^*_{\nu_s}|^2 \tag{F.30c}$$

where

$$J_{\nu k} = \int_{x_i}^{x_{i+1}} x^k \frac{dx}{(x^2 + d^2)^{3/2}}, \quad k = 0(1)3 \tag{F.30d}$$

with $x = \xi_o - \xi$ and $d^2 = |\bar{d}|^2$. The upper and lower limit of integration are, with $s^*_i = \frac{1}{2}(s_i + s_{i+1})$:

$$x_i = \xi_o + \tfrac{1}{2}|\bar{x}^*_{\nu_s}|\Delta s_i \tag{F.30e}$$

$$x_{i+1} = \xi_o - \tfrac{1}{2}|\bar{x}^*_{\nu_s}|\Delta s_i \tag{F.30f}$$

The closed-form expressions for $J_{\nu k}$ are easily obtained as

$$J_{\nu o} = \frac{1}{d^2} f_3 \tag{F.31a}$$

$$J_{\nu 1} = -f_2 \tag{F.31b}$$

$$J_{\nu 2} = f_1 - f_3 \tag{F.31c}$$

$$J_{\nu 3} = f_o + d^2 f_2 \tag{F.31d}$$

where

$$f_o = (x_{i+1}^2 + d^2)^{\frac{1}{2}} - (x_i^2 + d^2)^{\frac{1}{2}} \tag{F.31e}$$

$$f_1 = \ln\left(\frac{x_{i+1} + (x_{i+1}^2 + d^2)^{\frac{1}{2}}}{x_i + (x_i^2 + d^2)^{\frac{1}{2}}}\right) \tag{F.31f}$$

$$f_2 = \frac{1}{(x_{i+1}^2 + d^2)^{\frac{1}{2}}} - \frac{1}{(x_i^2 + d^2)^{\frac{1}{2}}} \tag{F.31g}$$

$$f_3 = \frac{x_{i+1}}{(x_{i+1}^2 + d^2)^{\frac{1}{2}}} - \frac{x_i}{(x_i^2 + d^2)^{\frac{1}{2}}} \tag{F.31h}$$

Consider now the term due to the curvature, Eq. (9.21h). Substitution of Eq. (F.28a) in Eq. (9.21h) yields

$$\begin{aligned}\bar{I}^c_{\nu o} = \tfrac{1}{2}\{&\bar{x}^*_{\nu_{ss}}(\xi_o^2 J_{\nu o} - 2\xi_o J_{\nu 1} + J_{\nu 2}) \\ &-3\bar{e}_\nu\{(\bar{x}^*_{\nu_{ss}}\cdot\bar{e}_\nu)(\xi_o^2 K_{\nu 2} - 2\xi_o K_{\nu 3} + K_{\nu 4}) \\ &\quad + (\bar{x}^*_{\nu_{ss}}\cdot\bar{d})(\xi_o^2 K_{\nu 1} - 2\xi_o K_{\nu 2} + K_{\nu 3})\} \\ &-3\bar{d}\{(\bar{x}^*_{\nu_{ss}}\cdot\bar{e}_\nu)(\xi_o^2 K_{\nu 1} - 2\xi_o K_{\nu 2} + K_{\nu 3}) \\ &\quad + (\bar{x}^*_{\nu_{ss}}\cdot\bar{d})(\xi_o^2 K_{\nu o} - 2\xi_o K_{\nu 1} + K_{\nu 2})\}\}/|\bar{x}^*_{\nu_s}|^2\end{aligned} \tag{F.32a}$$

$$\begin{aligned}\bar{I}^c_{\nu 1} = \tfrac{1}{2}\{&\bar{x}^*_{\nu_{ss}}(\xi_o^3 J_{\nu o} - 3\xi_o^2 J_{\nu 1} + 3\xi_o J_{\nu 2} - J_{\nu 3}) \\ &- 3\bar{e}_\nu\{(\bar{x}^*_{\nu_{ss}}\cdot\bar{e}_\nu)(\xi_o^3 K_{\nu 2} - 3\xi_o^2 K_{\nu 3} + 3\xi_o K_{\nu 4} - K_{\nu 5}) \\ &\quad + (\bar{x}^*_{\nu_{ss}}\cdot\bar{d})(\xi_o^3 K_{\nu 1} - 3\xi_o^2 K_{\nu 2} + 3\xi_o K_{\nu 3} - K_{\nu 4})\} \\ &- 3\bar{d}\{(\bar{x}^*_{\nu_{ss}}\cdot\bar{e}_\nu)(\xi_o^3 K_{\nu 1} - 3\xi_o^2 K_{\nu 2} + 3\xi_o K_{\nu 3} - K_{\nu 4}) \\ &\quad + (\bar{x}^*_{\nu_{ss}}\cdot\bar{d})(\xi_o^3 K_{\nu o} - 3\xi_o^2 K_{\nu 1} + 3\xi_o K_{\nu 2} - K_{\nu 3})\}\}/|\bar{x}^*_{\nu_s}|^4\end{aligned} \tag{F.32b}$$

where $J_{vk}$ is defined in Eqs. (F.30d)-(F.31d) and $K_{vk}$ is defined as

$$K_{vk} = \int_{x_i}^{x_{i+1}} x^k \frac{dx}{(x^2 + d^2)^{5/2}} \quad , \quad k = 0(1)5 \tag{F.32c}$$

The closed-form expressions for the $K_{vk}$-s required (k=0(1)4) are obtained as

$$K_{v0} = \frac{2}{3d^4} f_3 + \frac{1}{3d^2} f_5 \tag{F.33a}$$

$$K_{v1} = -\frac{1}{3} f_4 \tag{F.33b}$$

$$K_{v2} = \frac{1}{3d^2} f_3 + \frac{1}{3} f_5 \tag{F.33c}$$

$$K_{v3} = -f_2 + \frac{d^2}{3} f_4 \tag{F.33d}$$

$$K_{v4} = -\frac{4}{3} f_3 + \frac{d^2}{3} f_5 + f_1 \tag{F.33e}$$

with $f_1$, $f_2$ and $f_3$ defined in Eqs. (F.31f-h) and

$$f_4 = \frac{1}{(x_{i+1}^2 + d^2)^{3/2}} - \frac{1}{(x_i^2 + d^2)^{3/2}} \tag{F.33f}$$

$$f_5 = \frac{x_{i+1}}{(x_{i+1}^2 + d^2)^{3/2}} - \frac{x_i}{(x_i^2 + d^2)^{3/2}} \tag{F.33g}$$

## APPENDIX G

### Solution of a four-diagonal-block matrix equation

The system of equations

$$AA_i x_{i-2} + A_i x_{i-1} + B_i x_i + C_i x_{i+1} = f_i, \quad i=1(1)m \tag{G.1}$$

where $AA_i$, $A_i$, $B_i$ and $C_i$ are sub-matrices of dimension $n_i \times n_{i-2}$, $n_i \times n_{i-1}$, $n_i \times n_i$ and $n_i \times n_{i+1}$, respectively. Both $x_i$ and $f_i$ are sub-column vectors of dimension $n_j$ containing the solution and right-hand side for the j-th sub-system.

The LU-decomposition of the four-diagonal-block matrix is

$$\begin{pmatrix} \tilde{B}_1 & & & & & \\ \tilde{A}_2 & \tilde{B}_2 & & 0 & & \\ AA_3 & \tilde{A}_3 & \tilde{B}_3 & & & \\ & AA_4 & \tilde{A}_4 & \tilde{B}_4 & & \\ & 0 & & & & \\ & & & AA_m & \tilde{A}_m & \tilde{B}_m \end{pmatrix} \begin{pmatrix} 1 & C_1 & & & & \\ & 1 & C_2 & & 0 & \\ & & 1 & C_3 & & \\ & & & & & \\ & 0 & & & & \\ & & & & & 1 \end{pmatrix} \tag{G.2}$$

which is easily obtained from the following relations:

$$\tilde{B}_1 = B_1 \tag{G.3a}$$

$$\tilde{B}_1 \times C_1 = C_1 \tag{G.3b}$$

$$\tilde{A}_2 = A_2 \tag{G.4a}$$

$$\tilde{B}_2 = B_2 - \tilde{A}_2 \times C_1 \tag{G.4b}$$

$$\tilde{B}_2 \times C_2 = C_2 \tag{G.4c}$$

while for i=3(1)m

$$\tilde{A}_i = A_i - AA_i \times C_{i-2} \tag{G.5a}$$

$$\tilde{B}_i = B_i - \tilde{A}_i \times C_{i-1} \tag{G.5b}$$

$$\tilde{B}_i \times C_i = C_i \qquad (i=m) \tag{G.5c}$$

The elements of matrix $C_i$ are obtained from a standard LU decomposition procedure for solving the $n_i \times n_i$ matrix equation $\tilde{B}_i y_j = g_j$ for the $n_{i+1}$ column vectors $y_j$, $j=1(1)n_{i+1}$ of $C_i$ with $g_j$, $j=1(1)n_{i+1}$ the corresponding column vector of $C_i$ as right-hand side.

The solution of Eq. (G.1) is now obtained by carrying out the "downward sweep"

$$\tilde{B}_1 z_1 = f_1 \tag{G.6a}$$

$$\tilde{B}_2 z_2 = f_2 - \tilde{A}_2 z_1 \tag{G.6b}$$

$$\tilde{B}_i z_i = f_i - \tilde{A}_i z_{i-1} - AA_i z_{i-2}, \text{ for } i=3(1)m \tag{G.6c}$$

which is straightforward, especially since the LU-decomposition of the submatrices $\tilde{B}_j$, $j=1(1)m$ has already been computed during execution of Eqs. (G.3b), (G.4c) and (G.5c).
The "downward sweep" is followed by the "upward sweep" during which one obtains the solution $x_j$, $j=1(1)m$:

$$x_m = z_m \tag{G.7a}$$

$$x_i = z_i - C_i x_{i+1}, \text{ for } i=m-1(1)1 \tag{G.7b}$$

The major computational cost involved is that due to the LU-decomposition of the m diagonal blocks of dimension $n_i$, $i=1(1)m$ ($\Sigma n_i^3$) and that due to the 3 matrix-matrix multiplications implied in Eqs. (G.3)-(G.5) ($\Sigma(n_i n_{i-2}^2 + n_i n_{i-1}^2 + n_{i+1} n_i^2)$), so in first approximation of the order of $(mn)^3/m^2$ where n is the average block size.

## CURRICULUM VITAE

Hendrik Willem Marie Hoeijmakers was born in Sevenum (L), The Netherlands, on January 23, 1948. In 1966 he obtained the "HBS-B"-diploma at the Blariacum College in Venlo-Blerick and in September of the same year started his study in aeronautical engineering at the Delft University of Technology. In October 1971 he graduated cum laude on the subject of supersonic lifting surfaces with subsonic leading edges under the guidance of Prof.dr.ir. J.A. Steketee and Dr.ir. R. Coene.

After a year of post-graduate research work at the Department of Aerospace Engineering of the Delft University of Technology the author obtained in September 1972 a NASA International University Fellowship for further study at the Department of Aeronautics of the California Institute of Technology in Pasadena, California, USA.

In June 1974 he obtained the Degree of Aeronautical Engineer at this institute on the thesis "Effects of Planform Curvature in Supersonic Wings", supervised by Prof. H.J. Stewart.

Since November 1974 the author is employed at the National Aerospace Laboratory (NLR) in Amsterdam, The Netherlands. At NLR he worked mainly on the development of computational methods for linearized sub- and supersonic flow about complex three-dimensional configurations and on the development of computational methods for configurations with vortex flow. The present thesis results from the work on the latter subject.

SAMENVATTING

AERODYNAMICA VAN GEORDENDE WERVELSTROMINGEN; ONDERZOCHT MET BEHULP VAN REKENMETHODEN

Wervellagen en wervelkernen spelen een belangrijke rol in de stroming om vliegtuigconfiguraties. Wervellagen ontstaan als de stroming het oppervlak verlaat ter plaatse van een scherpe rand, bijvoorbeeld de vleugelachterrand, of ten gevolge van grenslaagloslating op een glad deel van het oppervlak. In het algemeen hebben vrije wervellagen de neiging op te rollen tot geconcentreerde wervelkernen. Vaak is het resulterende stromingspatroon geordend, stationair en persistent.

In dit proefschrift wordt onderscheid gemaakt tussen wervelstromingen met een zwakke en die met een sterke interactie tussen de wervellagen en kernen aan de ene kant en de stroming op het oppervlak van de configuratie aan de andere kant. De stroming om de vleugel met grote slankheid van een verkeersvliegtuig in kruisvlucht is een voorbeeld van een zwakke interactie wervelstroming. De stroming laat los ter plaatse van de achterrand, de wervellaag (het zog) rolt op in meestal twee sterke en persistente (tip)wervels waarbij de precieze vorm en het oprollen van het zog een geringe invloed hebben op de stroming op het vleugeloppervlak. Dit in tegenstelling met de stroming om vleugels met kleinere slankheid, zoals bij jachtvliegtuigen, waar de stroming loslaat ter plaatse van de zijrand of de sterk gepijlde voorrand. De resulterende wervellagen en wervelkernen liggen nu relatief dicht bij het vleugeloppervlak en hebben een groot, vaak gunstig, effect op de stroming op het vleugeloppervlak. De stroming om slanke lichamen bij hoge invalshoek is een ander voorbeeld van een sterke interactie wervelstroming. Typerend voor gevallen met een sterke interactie is dat de lift niet lineair toeneemt met de invalshoek, wat leidt tot een aanzienlijke toename in lift en dat vaak tot hoge invalshoek. Bij hogere invalshoeken treedt "vortex burst" op en verliest het wervelpatroon zijn geordende structuur.

Het doel van het onderzoek beschreven in dit proefschrift is bij te dragen tot de kennis, en uiteindelijk de toepassing in de praktijk, van geordende en beheersbare wervelstromingen. Hiertoe wordt een aantal rekenmethoden ontwikkeld voor het numeriek simuleren van de stroming om configuraties met zwakke en die met sterke interactie wervelstroming. De validatie van de methoden vindt plaats door verkregen resultaten te vergelijken met resultaten van andere rekenmethoden en met experimentele gegevens. Het onderzoek beperkt zich tot stationaire sub-kritieke stromingen bij hoge Reynolds getallen.

Het proefschrift is onderverdeeld in twee delen.
In het eerste deel, dat de hoofdstukken 1-5 omvat, wordt een beschrijving gegeven van de fysica van geordende wervelstromingen en de mathematische modellering hiervan. Na het inleidende eerste hoofdstuk worden in het tweede hoofdstuk van een aantal bekende zwakke en sterke interactie gevallen de meest karakteristieke stromingsverschijnselen beschreven. In hoofdstuk 3 wordt ingegaan op verschillende aspecten van de mathematische modellering van dit type stromingen. Uiteindelijk wordt gekozen voor een potentiaal-stromings model met ingebedde gebieden met rotatie, namelijk wervelvlakken en wervelkernen welke laatsten ook als sterk opgerolde wervelvlakken beschouwd kunnen worden. Een wervelvlak vormt een discontinuiteits-oppervlak in de verder rotatie-vrije stroming. Het effect van een wervelkern op de stroming buiten de kern zelf wordt benaderd door een relatief eenvoudig model van een werveldraad met "feeding sheets". Deze laatsten maken het mogelijk dat wervelsterkte kan worden toegevoegd aan de werveldraad. In hoofdstuk 4 wordt er in meer detail gekeken naar eigenschappen van wervelkernen en hun modellering, in het bijzonder voor het vereenvoudigde geval van een slanke wervelkern in een verder ongestoorde stroming. De analyse beschouwt de componenten van de wervelsterkte vector in de wervelkern en het snelheidsveld binnen en buiten de wervelkern. Er wordt aangetoond dat in de wervelkern de omtrekssnelheids component wordt omgezet in een axiale snelheidscomponent. Dit resulteert in een stroming met spiraalvormige stroomlijnen, met instroming bij de rand van de wervelkern en met een grote axiale snelheid (straal) nabij de as van de wervelkern.
In het vijfde en laatste hoofdstuk van het eerste deel wordt het gekozen mathematische model voor de driedimensionale stroming samengevat. Ook wordt de oplosmethode, middels singulariteitenbeleggingen op het oppervlak van de configuratie en op de wervelvlakken, beschreven. Het oplossen van het volledige drie-dimensionale probleem, niet-lineair vanwege de randvoorwaarden op de wervelvlakken, is geen eenvoudige taak. Echter, in dit hoofdstuk wordt ook beschreven dat benaderende formuleringen die leiden tot een eenvoudiger probleem mogelijk zijn. Voor zoggen achter vliegtuigconfiguraties (een zwakke-interactie wervelstroming) leidt de aanname dat de veranderingen in stroomafwaartse richting veel geleidelijker plaatsvinden dan die in dwarsrichting tot een quasi twee-dimensionaal probleem. Door de afstand achter de configuratie te relateren aan een tijdsvariable kan dit probleem geformuleerd worden als een beginwaarde probleem. In deze zogenaamde twee-dimensionale tijdsafhankelijke analogie wordt uitsluitend bekeken hoe, in afwezigheid van vaste oppervlakken, een twee-dimensionaal wervelvlak of systeem van wervelvlakken zich ontwikkelt in de tijd.
Voor in langsrichting langgerekte (zogenaamde slanke) configuraties kan met behulp van dezelfde aanname als boven het drie-dimensionale sterke-interactie wervelstromings probleem bij benadering berekend worden door het oplossen van een serie van opeenvolgende twee-dimensionale, niet-lineaire, problemen in vlakken loodrecht op de lengterichting van de configuratie. In deze "slender-body" approximatie komt de drie-dimensionaliteit van het probleem tot uiting in de randvoorwaarden voor elk van de twee-dimensionale "cross-flow-plane" problemen.

Het tweede deel, de hoofdstukken 6-10, beschrijft rekenmethoden voor de bepaling van de geordende wervelstroming om vliegtuigconfiguraties. In hoofdstuk 6 wordt een samenvatting gepresenteerd van bestaande methoden, met hun zwakke en sterke punten. De bijdrage van het voorliggende onderzoek is voornamelijk gelegen in de ontwikkeling en toepassing van panelenmethoden voor het oplossen van het (niet-lineaire) probleem van potentiaalstromingen met vrije wervelvlakken en wervelkernen.
In de volgende drie hoofdstukken wordt de ontwikkeling en toepassing van de rekenmethoden beschreven, in de volgorde van toenemende complexiteit, beginnend met de methode voor de twee-dimensionale tijdsafhankelijke analogie. In hoofdstuk 10 worden de bevindingen van het onderzoek samengevat.

De methode voor het berekenen van de ontwikkeling in de tijd van twee-dimensionale wervelvlakken wordt besproken in hoofdstuk 7. Het snelheidsveld wordt berekend door middel van een tweede-orde nauwkeurige panelenmethode. Op elk tijdstip vindt de discretisatie van de wervelvlakken plaats met een schema dat de lokale paneelgrootte aanpast aan de lokale kromming. Dit maakt het mogelijk het oprolproces tot in detail te volgen. In de methode kan op min of meer natuurgetrouwe wijze wervelsterkte in wervelkernen geaccumuleerd worden. De rekenmethode wordt toegepast om de ontwikkeling van het zog te bepalen achter: een vleugel met een elliptische draagprachtverdeling, een vleugel met een uitgeslagen landingsklep, een doorstroomgondel met een cirkelvormige doorsnijding en een delta vleugel met een voorrand wervelvlak. Resultaten van de huidige methode worden vergeleken met resultaten van andere rekenmethoden en met experimentele gegevens.

Aangetoond wordt dat de ontwikkelde rekenmethode in staat is de stroomafwaartse ontwikkeling van zoggen op een betrouwbare manier te bepalen tot grote afstanden achter de configuratie. De verkregen resultaten geven belangrijke aanwijzingen voor de te verwachten topologie van het drie-dimensionale zog.

In hoofdstuk 8 wordt in detail de methode besproken voor de sterke interactie wervelstroming om slanke configuraties, in de quasi twee-dimensionale formulering die het resultaat is van de "slender-body" approximatie. Het snelheidsveld wordt berekend met de tweede-orde panelenmethode ontwikkeld in hoofdstuk 7. De configuratie mag bestaan uit dragende vlakken en of delen met dikte. Voor de laatste delen wordt voldaan aan de normaalsnelheidsrandvoorwaarden via een equivalente Dirichlet randvoorwaarde. Deze formulering resulteert in een fictieve stroming binnen de gesloten contour. Ook hiervoor is een tweede-orde nauwkeurige panelenmethode ontwikkeld. Wervelvlakken modelleren loslating van voorgeschreven posities, hetzij scherpe randen, hetzij locaties op gladde delen van de contour waar loslating verwacht wordt. Het systeem van niet-lineaire vergelijkingen wordt opgelost met het Newton iteratieve oplosproces, waarbij een aantal continueringsprocedures gevolgd kunnen worden voor het construeren van een beginschatting uit een eerder verkregen naburige oplossing.

Aan de hand van een basis testgeval, de vlakke-plaat delta vleugel met slankheid ) bij 20 graden invalshoek, wordt onderzocht wat de invloed is op de oplossing van de lengte van het wervelvlak, de fijnheid van het discretisatie schema en het in hoofdstuk 4 beschreven verbeterde model van de wervelkern. Vervolgens wordt de oplossing berekend en geanalyseerd voor dezelfde vleugel over een groot traject van invalshoeken en sliphoeken. Ook het effect van dikte op de oplossing wordt bestudeerd. Vergelijking van de rekenresultaten met experimentele gegevens toont aan dat de modellering van secundaire loslating in veel gevallen een voorwaarde is voor een goede correlatie. Hiertoe wordt een poging gedaan door ook de secundaire loslating te modelleren als een wervelvlak-wervelkern combinatie. Dit heeft het gewenste effect op de zuigpiek in de drukverdeling op de bovenzijde van de vleugel ten gevolge van de primaire wervel, maar lijkt het effect van de secundaire wervel zelf te overschatten. Verder blijkt dat voor de voorspelling van de secundaire loslaatpositie meer vereist is dan de zwakke koppeling van het huidige niet-viskeuze model met een grenslaag methode.

Als aansluiting op hoofdstuk 4 wordt onderzocht in hoeverre een wervelkern bestaande uit een combinatie van een relatief lang opgerold wervelvlak en een werveldraad de stroming in het gebied buiten de omgeving van de as van de wervelkern simuleert. Voor het basis testgeval levert dit een verrassende goede correlatie op van berekende en gemeten snelheidsverdelingen in het beschouwde deel van de wervelkern.

Toepassing van de rekenmethode op een slanke kegel bij hoge invalshoek bevestigt het vermoeden dat het onderhavige niet-lineaire probleem meer dan één oplossing kan hebben. Tenslotte wordt de methode toegepast op twee niet-conische configuraties, een dubbel-delta vleugel en een "strake"-vleugel combinatie. In het laatste geval wordt de kern van de zogenaamde vleugelwervel gemodelleerd als een werveldraad met twee "feeding sheets".

In hoofdstuk 9 wordt de methode beschreven voor het berekenen van de drie-dimensionale symmetrische stroming om symmetrische delta-achtige draagvlakken met loslating langs de gehele voorrand. Het snelheidsveld wordt ook hier berekend met een tweede-orde nauwkeurige panelenmethode. Het systeem van niet-lineaire vergelijkingen wordt opgelost met een quasi-Newton iteratieve methode. De methode wordt toegepast op het boven omschreven basis testgeval, mede met het doel de invloed van wervelvlak lengte, paneelschema etc. te onderzoeken. Verder wordt de methode toegepast op deltavleugels met een pijlstelling die varieert van 65° tot 85°. De toepassingen laten zien dat geometrisch gesproken de oplossing over een groot deel van de vleugel conisch is, maar tevens dat de snelheids en drukverdeling een sterk drie-dimensionaal karakter hebben. Dit laatste wordt veroorzaakt door het effect van de aanwezigheid van de achterrand en ook door de invloed van het singuliere gedrag van de oplossing ter plaatse van de voorste punt.

De berekende drukverdelingen zijn in redelijke overeenstemming met gemeten waarden, alhoewel de invloed van de secundaire loslating opnieuw belangrijk is. Tenslotte laat de correlatie van resultaten van de huidige potentiaal-stromings methode met resultaten van een methode gebaseerd op de Euler vergelijkingen zien dat voor incompressibele stromingen deze beide niet-viskeuze methoden predicties van vergelijkbare kwaliteit kunnen leveren. Hierbij zijn de rekentijden voor de potentiaal methode bescheiden vergeleken met die benodigd voor de Euler methode.

## APPENDIX F
## Computation of $\bar{E}_{10}$, $\bar{E}^c_{10}$, $\bar{E}_{01}$, $\bar{E}^c_{01}$, $\bar{E}_{20}$, $\bar{E}_{11}$ and $\bar{E}_{02}$

1. Basic expressions

The small-curvature expansion for the velocity induced by a doublet distribution on the three-dimensional surface of a panel is expressed in terms of the 4 surface integrals defined in Eq. (9.15i-j). In this appendix we consider these expression in detail.

Write the distance vector $\bar{r}_f$, defined in Eq. (9.14b), as

$$\bar{r}_f = (\xi_o-\xi)\bar{e}_s + (\eta_o-\eta)\bar{e}_t + \zeta\bar{e}_n \tag{F.1a}$$

where $\bar{e}_s$ and $\bar{e}_t$ are the unit vectors in s- and t-direction, respectively, while $\bar{e}_n$ is the unit normal, i.e.

$$\bar{e}_s = \bar{x}^*_s/|\bar{x}^*_s| \tag{F.1b}$$

$$\bar{e}_t = \bar{x}^*_t/|\bar{x}^*_t| \tag{F.1c}$$

$$\bar{e}_n = (\bar{e}_s \times \bar{e}_t)/|\bar{e}_s \times \bar{e}_t| \tag{F.1d}$$

Note that in general $\bar{e}_s$ and $\bar{e}_t$ are nonorthogonal. The $(\xi,\zeta,\eta)$ coordinates follow from Eq. (9.14b), with $\bar{r}_o = \bar{x}_o-\bar{x}^*$, as

$$\xi = \Delta s|\bar{x}^*_s| \tag{F.2a}$$

$$\eta = \Delta t|\bar{x}^*_t| \tag{F.2b}$$

$$\xi_o = \frac{|\bar{x}^*_s||\bar{x}^*_t|}{|\bar{x}^*_s\times\bar{x}^*_t|}\,\bar{e}_n\cdot(\bar{r}_o \times \bar{e}_t) \tag{F.2c}$$

$$\eta_o = -\frac{|\bar{x}^*_s||\bar{x}^*_t|}{|\bar{x}^*_s\times\bar{x}^*_t|}\,\bar{e}_n\cdot(\bar{r}_o \times \bar{e}_s) \tag{F.2d}$$

$$\zeta = \bar{r}_o\cdot\bar{e}_n \tag{F.2e}$$

where $\Delta s = s-s^*_i$ and $\Delta t = t-t^*_j$.
Since in general $\bar{e}_s$ and $\bar{e}_t$ are nonorthogonal one finds that

$$b = \bar{e}_s\cdot\bar{e}_t = \frac{\bar{x}^*_s\cdot\bar{x}^*_t}{|\bar{x}^*_s||\bar{x}^*_t|} \tag{F.3}$$

is nonzero.

Now we consider the expressions defined in Eq. (9.15i) in more detail. Upon substitution of Eqs. (F.1)-(F.2) one finds:

$$\bar{I}_{00} = (\bar{e}_s J_{10} + \bar{e}_t J_{01} + \bar{e}_n\zeta J_{00})/|\bar{x}^*_s||\bar{x}^*_t| \tag{F.4a}$$

$$\bar{I}_{10} = (\xi_o\bar{I}_{00} - \frac{1}{|\bar{x}^*_s||\bar{x}^*_t|}(\bar{e}_s J_{20}+\bar{e}_t J_{11}+\bar{e}_n\zeta J_{10}))/|\bar{x}^*_s| \tag{F.4b}$$

$$\bar{I}_{01} = (\eta_o\bar{I}_{00} - \frac{1}{|\bar{x}^*_s||\bar{x}^*_t|}(\bar{e}_s J_{11}+\bar{e}_t J_{02}+\bar{e}_n\zeta J_{01}))/|\bar{x}^*_t| \tag{F.4c}$$

are expressed in terms of the basic integrals:

$$J_{k\ell} = \int_{x_i}^{x_{i+1}}\int_{y_j}^{y_{j+1}} x^k y^\ell \,\frac{dxdy}{(x^2+2bxy+y^2+z^2)^{3/2}} \tag{F.5a}$$

where $x=\xi_o-\xi$, $y=\eta_o-\eta$ and $z=\zeta$.
In Eq. (F.5a) the upper and lower limits of integration are, with $(s^*_i,t^*_j)$ as the panel midpoint:

$$x_i = \xi_o + \tfrac{1}{2}|\bar{x}^*_s|\Delta s_i \qquad x_{i+1} = \xi_o - \tfrac{1}{2}|\bar{x}^*_s|\Delta s_i$$
$$y_j = \eta_o + \tfrac{1}{2}|\bar{x}^*_t|\Delta t_j \qquad y_{j+1} = \eta_o - \tfrac{1}{2}|\bar{x}^*_t|\Delta t_j \tag{F.5b}$$

where $\Delta s_i = s_{i+1}-s_i$ and $\Delta t_j = t_{j+1}-t_j$.
In the second section of this appendix closed-form expressions for the basic integrals $J_{k\ell}$ are listed.

Consider now the remaining curvature term $\bar{I}_c$, defined in Eq. (9.15j) as:

$$\bar{I}_c = \int_{s_i}^{s_{i+1}}\int_{t_j}^{t_{j+1}} \left(\frac{\bar{r}_2}{|\bar{r}_f|^3} - 3(\bar{r}_2\cdot\bar{r}_f)\frac{\bar{r}_f}{|\bar{r}_f|^5}\right)dsdt \tag{F.6a}$$

It can be shown that the integrand of this expression can be expressed as:

$$(\frac{\bar{e}_s}{1-b^2}(\frac{\partial}{\partial\xi_o} - b\frac{\partial}{\partial\eta_o}) + \frac{\bar{e}_t}{1-b^2}(-b\frac{\partial}{\partial\xi_o} + \frac{\partial}{\partial\eta_o}) + \bar{e}_n\frac{\partial}{\partial\zeta})(\frac{\bar{r}_2\cdot\bar{r}_f}{|\bar{r}_f|^3}) \qquad (F.6b)$$

where the term between {} is the $\bar{\nabla}$ with respect to $\bar{x}_o$, denoted here by $\bar{\nabla}_{x_o}$. In case $\bar{r}_2$ is normal to the tangent plane Eq. (F.6) resembles closely the integral expressing the velocity induced by a doublet distribution of strength $\bar{r}_2\cdot\bar{e}_n$ and could be reduced further along the lines indicated in Appendix A. However, $\bar{r}_2$ has also components in the tangent plane and we express $\bar{I}_c$ as

$$\bar{I}_c = \bar{\nabla}_{x_o}(\tfrac{1}{2}\bar{x}^*_{ss}\cdot\bar{I}_{20} + \bar{x}^*_{st}\cdot\bar{I}_{11} + \tfrac{1}{2}\bar{x}^*_{tt}\cdot\bar{I}_{02}) \qquad (F.6c)$$

where, upon substitution of Eqs. (F.1)-(F.2):

$$\bar{I}_{20} = \{-\xi_o^2\bar{I}_{00} + 2\xi_o\bar{I}_{10} + \frac{1}{|\bar{x}^*_s||\bar{x}^*_t|}(\bar{e}_sJ_{30}+\bar{e}_tJ_{21}+\bar{e}_n\zeta J_{20})\}/|\bar{x}^*_s|^2 \qquad (F.7a)$$

$$\bar{I}_{11} = \{-\xi_o\eta_o\bar{I}_{00} + \xi_o\bar{I}_{01} + \eta_o\bar{I}_{10} + \frac{1}{|\bar{x}^*_s||\bar{x}^*_t|}(\bar{e}_sJ_{21}+\bar{e}_tJ_{12}+\bar{e}_n\zeta J_{11})\}|\bar{x}^*_s||\bar{x}^*_t| \qquad (F.7b)$$

$$\bar{I}_{02} = \{-\eta_o^2\bar{I}_{00} + 2\eta_o\bar{I}_{01} + \frac{1}{|\bar{x}^*_s||\bar{x}^*_t|}(\bar{e}_sJ_{12}+\bar{e}_tJ_{03}+\bar{e}_n\zeta J_{02})\}|\bar{x}^*_t|^2 \qquad (F.7c)$$

Denoting the three derivatives in Eq. (F.6b) as

$$\frac{\partial F}{\partial p_1} = \frac{1}{1-b^2}(\frac{\partial F}{\partial\xi_o} - b\frac{\partial F}{\partial\eta_o}) = F^1 \qquad (F.8a)$$

$$\frac{\partial F}{\partial p_2} = \frac{1}{1-b^2}(-b\frac{\partial F}{\partial\xi_o} + \frac{\partial F}{\partial\eta_o}) = F^2 \qquad (F.8b)$$

$$\frac{\partial F}{\partial p_3} = \frac{\partial F}{\partial\zeta} = F^3 \qquad (F.8c)$$

one can write Eq. (F.6c) as

$$\begin{aligned}\bar{I}_c = {} & \bar{e}_s(\tfrac{1}{2}\bar{x}^*_{ss}\cdot\bar{I}^1_{20} + \bar{x}^*_{st}\cdot\bar{I}^1_{11} + \tfrac{1}{2}\bar{x}^*_{tt}\cdot\bar{I}^1_{02}) \\ & + \bar{e}_t(\tfrac{1}{2}\bar{x}^*_{ss}\cdot\bar{I}^2_{20} + \bar{x}^*_{st}\cdot\bar{I}^2_{11} + \tfrac{1}{2}\bar{x}^*_{tt}\cdot\bar{I}^2_{02}) \\ & + \bar{e}_n(\tfrac{1}{2}\bar{x}^*_{ss}\cdot\bar{I}^3_{20} + \bar{x}^*_{st}\cdot\bar{I}^3_{11} + \tfrac{1}{2}\bar{x}^*_{tt}\cdot\bar{I}^3_{02})\end{aligned} \qquad (F.9)$$

The derivative with respect to $p_1$, $p_2$ and $p_3$ of $\bar{I}_{20}$, $\bar{I}_{11}$ and $\bar{I}_{01}$ is readily obtained from their definition given in Eq. (F.7). It involves the derivative with respect to $p_1$, $p_2$ and $p_3$ of the basic integrals $J_{k\ell}$ listed in the next section of this appendix.

2. The basic integrals $J_{k\ell}$

The basic integrals $J_{k\ell}$, defined in Eq. (F.5a), are to be evaluated for k=0(1)3 and $\ell$=0(1)3. It turns out that all these integrals can be found in closed form. The indefinite form of the integrals is:

$$zJ_{00} = \frac{1}{(1-b^2)^{1/2}}F_1 \qquad (F.10a)$$

$$J_{10} = \frac{1}{1-b^2}(bF_2-F_3) \qquad (F.10b)$$

$$J_{01} = \frac{-1}{1-b^2}(F_2-bF_3) \qquad (F.10c)$$

$$J_{20} = \frac{-z}{(1-b^2)^{3/2}}F_1 + yF_2 + \frac{b}{1-b^2}F_4 \qquad (F.10d)$$

$$J_{11} = \frac{bz}{(1-b^2)^{3/2}}F_1 - \frac{1}{1-b^2}F_4 \qquad (F.10e)$$

$$J_{02} = \frac{-z}{(1-b^2)^{3/2}}F_1 + xF_3 + \frac{b}{1-b^2}F_4 \qquad (F.10f)$$

$$J_{30} = -(\frac{3}{2}y^2 + \frac{1}{2}\frac{z^2}{1-b^2})bF_2 - \frac{z^2}{(1-b^2)^2}(bF_2-F_3)+(y + \frac{b(x-by)}{2(1-b^2)})F_4 \quad (F.10g)$$

$$J_{21} = -(\frac{1}{2}y^2 + \frac{1}{2}\frac{z^2}{1-b^2})F_2 + \frac{bz^2}{(1-b^2)^2}(bF_2-F_3) - \frac{x-by}{2(1-b^2)}F_4 \quad (F.10h)$$

$$J_{12} = (\frac{1}{2}x^2 + \frac{1}{2}\frac{z^2}{1-b^2})F_3 - \frac{bz^2}{(1-b^2)^2}(F_2-bF_3) + \frac{bx-y}{2(1-b^2)}F_4 \quad (F.10i)$$

$$J_{03} = -(\frac{3}{2}x^2 + \frac{1}{2}\frac{z^2}{1-b^2})bF_3 + \frac{z^2}{(1-b^2)^2}(F_2-bF_3)+(x + \frac{b(y-bx)}{2(1-b^2)})F_4 \quad (F.10j)$$

where the $F_k$'s are a function of the limits of integration x and y, as well as the constants b and z:

$$F_1(x,y) = \tan^{-1}\frac{(1-b^2)xy-bz^2}{z(1-b^2)^{\frac{1}{2}}(x^2+2bxy+y^2+z^2)^{\frac{1}{2}}} \quad (F.11a)$$

$$F_2(x,y) = \sinh^{-1}\frac{x+by}{((1-b^2)y^2+z^2)^{\frac{1}{2}}} = \ln\frac{(x+by)+(x^2+2bxy+y^2+z^2)^{\frac{1}{2}}}{((1-b^2)y^2+z^2)^{\frac{1}{2}}} \quad (F.11b)$$

$$F_3(x,y) = \sinh^{-1}\frac{bx+y}{((1-b^2)x^2+z^2)^{\frac{1}{2}}} = \ln\frac{(bx+y)+(x^2+2bxy+y^2+z^2)^{\frac{1}{2}}}{((1-b^2)x^2+z^2)^{\frac{1}{2}}} \quad (F.11c)$$

$$F_4(x,y) = (x^2+2bxy+y^2+z^2)^{\frac{1}{2}} \quad (F.11d)$$

To compute $\bar{I}_c$ requires the derivative with respect to $p_1$, $p_2$ and $p_3$ of the basic integrals and thus of above four functions. These derivatives can be expressed as:

$$F_1^1 = \frac{z}{(1-b^2)^{\frac{1}{2}}}(-bF_5+F_6) \; ; \; F_1^2 = \frac{z}{(1-b^2)^{\frac{1}{2}}}(F_5-bF_6); \; F_1^3 = -(1-b^2)^{\frac{1}{2}}(yF_5+xF_6) \quad (F.12a)$$

$$F_2^1 = \frac{1}{F_4} + byF_5 \; ; \; F_2^2 = -yF_5 \; ; \; F_2^3 = -zF_5 \quad (F.12b)$$

$$F_3^1 = -xF_6 \; ; \; F_3^2 = \frac{1}{F_4} + bxF_6 \; ; \; F_3^3 = -zF_6 \quad (F.12c)$$

$$F_4^1 = \frac{x}{F_4} \; ; \; F_4^2 = \frac{y}{F_4} \; ; \; F_4^3 = \frac{z}{F_4} \quad (F.12d)$$

where

$$F_5(x,y) = \frac{x+by}{((1-b^2)y^2+z^2)F_4} \quad (F.12e)$$

$$F_6(x,y) = \frac{bx+y}{((1-b^2)x^2+z^2)F_4} \quad (F.12f)$$

3. Influence of a panel at its own midpoint

In case the collocation point is located on the panel itself, $\bar{x}_o = \bar{x}^*$ and it follows from Eq. (F.2) that

$$\xi_o = 0, \; \eta_o = 0, \; \zeta = z = 0^+ \quad (F.13a)$$

while it follows from Eq. (F.5b) that

$$x_i = \frac{1}{2}|\bar{x}_s^*|\Delta s_i = -x_{i+1} \quad (F.13b)$$

$$y_j = \frac{1}{2}|\bar{x}_t^*|\Delta t_j = -y_{j+1} \quad (F.13c)$$

Since now upon substitution of the limits of integration some of the terms vanish, the expressions for $\bar{I}_{00}$, $\bar{I}_{10}$ and $\bar{I}_{01}$, defined in Eqs. (F.4a-c) become much simpler:

$$\bar{I}_{00} = \frac{1}{|\bar{x}_s^*||\bar{x}_t^*|} h_1\bar{e}_n \quad (F.14a)$$

$$\bar{I}_{10} = \frac{-1}{|\bar{x}_s^*|^2|\bar{x}_t^*|}(h_2\bar{e}_s - h_3\bar{e}_t) \quad (F.14b)$$

$$\bar{I}_{01} = \frac{-1}{|\bar{x}_s^*||\bar{x}_t^*|^2}(-h_3\bar{e}_s + h_4\bar{e}_t) \quad (F.14c)$$

where

$$h_1 = 2\nu s\,\mathrm{sign}(\zeta) \tag{F.15a}$$

$$h_2 = 2y_j \ln\left(\frac{(x_i+by_j)+r_{ij}}{(-x_i+by_j)+\hat{r}_{ij}}\right) + bh_3 \tag{F.15b}$$

$$h_3 = \frac{2}{1-b^2}(r_{ij}-\hat{r}_{ij}) \tag{F.15c}$$

$$h_4 = 2x_i \ln\left(\frac{(bx_i+y_j)+r_{ij}}{(bx_i-y_j)+\hat{r}_{ij}}\right) + bh_3 \tag{F.15d}$$

with $r_{ij}=(x_i^2+2bx_iy_j+y_j^2)^{\frac{1}{2}}$ and $\hat{r}_{ij}=(x_i^2-2bx_iy_j+y_j^2)^{\frac{1}{2}}$.

The curvature term, defined in Eq. (F.9), involves the derivatives with respect to $p_1$, $p_2$ and $p_3$ of $\bar{I}_{20}$, $\bar{I}_{11}$ and $\bar{I}_{02}$. It turns out that these derivatives can best be expressed in terms of the following three vectors:

$$\bar{\varepsilon}_1 = \bar{e}_t \times (\bar{e}_s \times \bar{e}_t)/(1-b^2) \tag{F.16a}$$

$$\bar{\varepsilon}_2 = -\bar{e}_s \times (\bar{e}_s \times \bar{e}_t)/(1-b^2) \tag{F.16b}$$

$$\bar{\varepsilon}_3 = \bar{e}_n \tag{F.16c}$$

so that

$$\bar{e}_s = \bar{\varepsilon}_1 + b\bar{\varepsilon}_2 \tag{F.16d}$$

$$\bar{e}_t = b\bar{\varepsilon}_1 + \bar{\varepsilon}_2 \tag{F.16e}$$

while also $(\bar{\varepsilon}_1,\bar{\varepsilon}_2,\bar{\varepsilon}_3).\bar{e}_s = (1,0,0)$, $(\bar{\varepsilon}_1,\bar{\varepsilon}_2,\bar{\varepsilon}_3).\bar{e}_t = (0,1,0)$ and $(\bar{\varepsilon}_1,\bar{\varepsilon}_2,\bar{\varepsilon}_3).\bar{e}_n=(0,0,1)$.
It then follows that

$$\bar{I}^1_{20} = \frac{1}{|\bar{x}^*_s|^3|\bar{x}^*_t|}\{(-2h_2 + h_5)\bar{\varepsilon}_1 + (-3bh_2 + 2h_3 + 2bh_5 - h_6)\bar{\varepsilon}_2\} \tag{F.17a}$$

$$\bar{I}^2_{20} = \frac{1}{|\bar{x}^*_s|^3|\bar{x}^*_t|}\{(h_3 + h_7)\bar{\varepsilon}_1 + (h_2 - h_5)\bar{\varepsilon}_2\} \tag{F.17b}$$

$$\bar{I}^3_{20} = \frac{1}{|\bar{x}^*_s|^3|\bar{x}^*_t|}\{h_2\bar{\varepsilon}_3\} \tag{F.17c}$$

$$\bar{I}^1_{11} = \frac{1}{|\bar{x}^*_s|^2|\bar{x}^*_t|^2}\{(h_3 - h_6)\bar{\varepsilon}_1 - h_5\bar{\varepsilon}_2\} \tag{F.17d}$$

$$\bar{I}^2_{11} = \frac{1}{|\bar{x}^*_s|^2|\bar{x}^*_t|^2}\{-h_8\bar{\varepsilon}_1 + (h_3 - h_7)\bar{\varepsilon}_2\} \tag{F.17e}$$

$$\bar{I}^3_{11} = \frac{1}{|\bar{x}^*_s|^2|\bar{x}^*_t|^2}\{-h_3\bar{\varepsilon}_3\} \tag{F.17f}$$

$$\bar{I}^1_{02} = \frac{1}{|\bar{x}^*_s||\bar{x}^*_t|^3}\{(h_4 - h_8)\bar{\varepsilon}_1 + (h_3 + h_6)\bar{\varepsilon}_2\} \tag{F.17g}$$

$$\bar{I}^2_{02} = \frac{1}{|\bar{x}^*_s||\bar{x}^*_t|^3}\{(-3bh_4 + 2h_3 - h_7 + 2bh_8)\bar{\varepsilon}_1 + (-2h_4 + h_8)\bar{\varepsilon}_2\} \tag{F.17h}$$

$$\bar{I}^3_{02} = \frac{1}{|\bar{x}^*_s||\bar{x}^*_t|^3}\{h_4\bar{\varepsilon}_3\} \tag{F.17i}$$

where

$$h_5 = \frac{2x_i}{1-b^2}\left(\frac{bx_i+y_j}{r_{ij}} - \frac{bx_i-y_j}{\hat{r}_{ij}}\right) \tag{F.18a}$$

$$h_6 = \frac{2x_i}{1-b^2}\left(\frac{x_i+by_j}{r_{ij}} - \frac{x_i-by_j}{\hat{r}_{ij}}\right) \tag{F.18b}$$

$$h_7 = \frac{2y_j}{1-b^2}\left(\frac{bx_i+y_j}{r_{ij}} + \frac{bx_i-y_j}{\hat{r}_{ij}}\right) = h_3 - h_6 \tag{F.18c}$$

$$h_8 = \frac{2y_j}{1-b^2}\left(\frac{x_i+by_j}{r_{ij}} + \frac{x_i-by_j}{\hat{r}_{ij}}\right) \tag{F.18d}$$

4. Expressions for a far-wake panel

For a far-wake panel, see section 9.3.3, one requires $\bar{E}_{01w}$, $\bar{E}^c_{01w}$ and $\bar{E}_{02w}$, which follow from Eqs. (F.3c), (F.3d) and (F.3g) as:

$$\bar{E}_{01w} = -\bar{e}_{fw} \times \bar{I}_{00w} \tag{F.19a}$$

$$\bar{E}^c_{01w} = \bar{e}_{fw} \times \bar{I}_{cw} \tag{F.19b}$$

$$\bar{E}_{02w} = -\bar{e}_{fw} \times \bar{I}_{01w} \tag{F.19c}$$

respectively, where it follows from Eqs. (F.4a), (F.4c) and (F.9) that

$$\bar{I}_{00w} = (\bar{e}_{fw}J_{10w}+\bar{e}_t J_{01w}+\bar{e}_n\zeta J_{00w})/|\bar{x}^*_t| \tag{F.20a}$$

$$\bar{I}_{01w} = \{\eta_o \bar{I}_{00w} - \frac{1}{|\bar{x}^*_t|}(\bar{e}_{fw}J_{11w}+\bar{e}_t J_{02w}+\bar{e}_n\zeta J_{01w})\}/|\bar{x}^*_t| \tag{F.20b}$$

$$\bar{I}_{cw} = \bar{e}_{fw}(\tfrac{1}{2}\bar{x}^*_{tt}.\bar{I}^1_{02w}) + \bar{e}_t(\tfrac{1}{2}\bar{x}^*_{tt}.\bar{I}^2_{02w}) + \bar{e}_n(\tfrac{1}{2}\bar{x}^*_{tt}.\bar{I}^3_{02w}) \tag{F.20c}$$

with, using Eq. (F.7c):

$$\bar{I}_{02w} = \{-\eta_o^2\bar{I}_{00w} + 2\eta_o\bar{I}_{01w} + \frac{1}{|\bar{x}^*_t|}(\bar{e}_{fw}J_{12w} + \bar{e}_t J_{03w} + \bar{e}_n\zeta J_{02w})\}/|\bar{x}^*_t|^2 \tag{F.20d}$$

Note that because of the form of Eq. (F.19a-c) the $\bar{e}_{fw}$-terms in Eqs. (F.20a-c) drop out immediately, but must be retained when evaluating Eq. (F.20d).

In above expressions the basic integrals $J_{k\ell w}$ are defined as, see Eq. (F.5):

$$J_{k\ell w} = \int_{\xi_o}^{x_\infty}\int_{y_j}^{y_{j+1}} x^k y^\ell \frac{dxdy}{(x^2+2bxy+y^2+z^2)^{3/2}} \tag{F.21a}$$

where $x_\infty = \lim_{s_\infty\to\infty}(\xi_o+S-s_\infty)$. The expressions for the basic integrals $J_{k\ell}$, listed in the second section of this appendix, are also the expressions for the corresponding integrals $J_{k\ell w}$, but substitution of the limits integration requires some attention. Defining

$$\square F_k = F_k(x_i,y_j) - F_k(x_i,y_{j+1}) - F_k(x_{i+1},y_j) + F_k(x_{i+1},y_{j+1}) \tag{F.21b}$$

one finds, upon substitution of $x_{i+1}=x_\infty$ and taking the limit, for the basic functions and their combinations with powers of x and y:

$$\square F_1 = F_1(\xi_o,y_j) - F_1(\xi_o,y_{j+1}) + (\tan^{-1}\frac{(1-b^2)^{\frac{1}{2}}y_j}{z} - \tan^{-1}\frac{(1-b^2)^{\frac{1}{2}}y_{j+1}}{z}) \tag{F.22a}$$

$$\square F_2 = F_2(\xi_o,y_j) - F_2(\xi_o,y_{j+1}) - \ln(\frac{(1-b^2)y_j^2+z^2}{(1-b^2)y_{j+1}^2+z^2}) \tag{F.22b}$$

$$\square F_3 = F_3(\xi_o,y_j) - F_3(\xi_o,y_{j+1}) \tag{F.22c}$$

$$\square F_4 = F_4(\xi_o,y_j) - F_4(\xi_o,y_{j+1}) - b(y_{j+1}-y_j) \tag{F.22d}$$

$$\square(xF_3) = \xi_o F_3(\xi_o,y_j) - \xi_o F_3(\xi_o,y_{j+1}) - (y_{j+1}-y_j) \tag{F.22e}$$

$$\square(\frac{1}{F_4}) = \frac{1}{F_4(\xi_o,y_j)} - \frac{1}{F_4(\xi_o,y_{j+1})} \tag{F.22f}$$

$$\square(\frac{x}{F_4}) = \frac{\xi_o}{F_4(\xi_o,y_j)} - \frac{\xi_o}{F_4(\xi_o,y_{j+1})} \tag{F.22g}$$

$$\square(\frac{y}{F_4}) = \frac{y_j}{F_4(\xi_o,y_j)} - \frac{y_{j+1}}{F_4(\xi_o,y_{j+1})} \tag{F.22h}$$

$$\square(\frac{x^2}{F_4}) = \frac{\xi_o^2}{F_4(\xi_o,y_j)} - \frac{\xi_o^2}{F_4(\xi_o,y_{j+1})} + b(y_{j+1}-y_j) \tag{F.22i}$$

$$\square(\frac{xy}{F_4}) = \frac{\xi_o y_j}{F_4(\xi_o,y_j)} - \frac{\xi_o y_{j+1}}{F_4(\xi_o,y_{j+1})} - (y_{j+1}-y_j) \tag{F.22j}$$

$$\square(\frac{y^2}{F_4}) = \frac{y_j^2}{F_4(\xi_o,y_j)} - \frac{y_{j+1}^2}{F_4(\xi_o,y_{j+1})} \tag{F.22k}$$

$$\Box F_5 = F_5(\xi_o,y_j) - F_5(\xi_o,y_{j+1}) + \frac{1}{(1-b^2)y_j^2+z^2} - \frac{1}{(1-b^2)y_{j+1}^2+z^2} \tag{F.22l}$$

$$\Box(yF_5) = y_j F_5(\xi_o,y_j) - y_{j+1}F_5(\xi_o,y_{j+1}) + \frac{y_j}{(1-b^2)y_j^2+z^2} - \frac{y_{j+1}}{(1-b^2)y_{j+1}^2+z^2} \tag{F.22m}$$

$$\Box F_6 = F_6(\xi_o,y_j) - F_6(\xi_o,y_{j+1}) \tag{F.22n}$$

$$\Box(xF_6) = \xi_o F_6(\xi_o,y_j) - \xi_o F_6(\xi_o,y_{j+1}) \tag{F.22o}$$

The influence of the semi-infinite far-wake panel at the collocation points just upstream of the panel is obtained by assuming that $\xi_o = -\frac{1}{2}\Delta s_{NUP}|\bar{x}^*_{s_{NUP,j}}|$, $\eta_o = 0$ and $\zeta = 0$.
It then follows that

$$\bar{I}_{00w} = -\frac{\bar{e}_\zeta}{1-b^2}(\hat{n}_1 - b\hat{n}_2)/|\bar{x}^*_t| \tag{F.23a}$$

$$\bar{I}_{01w} = -\bar{e}_\zeta(\hat{n}_3 + b\hat{n}_4)/|\bar{x}^*_t|^2 \tag{F.23b}$$

$$\bar{I}^2_{02w} = \{\bar{e}_1(-3b(\hat{n}_3 + b\hat{n}_4) + 2\hat{n}_4 + 2b\hat{n}_5 - \hat{n}_6) + \bar{e}_2(-2(\hat{n}_3 + b\hat{n}_4) + \hat{n}_5)\}/|\bar{x}^*_t|^3 \tag{F.23c}$$

$$\bar{I}^3_{02w} = \bar{e}_n(\hat{n}_3 + b\hat{n}_4)/|\bar{x}^*_t|^3 \tag{F.23d}$$

where with $x_i = \xi_o$, $y_j = -y_{j+1} = \frac{1}{2}\Delta t_j|\bar{x}^*_t|$

$$\hat{n}_1 = \ln\left(\frac{(x_i+by_j) + r_{ij}}{(x_i-by_j) + \hat{r}_{ij}}\right) \tag{F.23e}$$

$$\hat{n}_2 = \ln\left(\frac{(bx_i+y_j) + r_{ij}}{(bx_i-y_j) + \hat{r}_{ij}}\right) \tag{F.23f}$$

$$\hat{n}_3 = x_i\hat{n}_2 + 2y_j \tag{F.23g}$$

$$\hat{n}_4 = (r_{ij} - \hat{r}_{ij} + 2by_j)/(1-b^2) \tag{F.23h}$$

$$\hat{n}_5 = \frac{y_j}{1-b^2}\left(2 + \frac{x_i + by_j}{r_{ij}} + \frac{x_i - by_j}{\hat{r}_{ij}}\right) \tag{F.23i}$$

$$\hat{n}_6 = \frac{y_j}{1-b^2}\left(2b + \frac{bx_i + y_j}{r_{ij}} + \frac{bx_i - y_j}{\hat{r}_{ij}}\right) \tag{F.23j}$$

where $r_{ij} = (x_i^2 + 2bx_iy_j + y_j^2)^{\frac{1}{2}}$ and $\hat{r}_{ij} = (x_i^2 - 2bx_iy_j + y_j^2)^{\frac{1}{2}}$.

5. Expressions for feeding-sheet panel

For a panel of the feeding sheet, see section 9.3.4, one requires expressions for $\bar{E}_{10f}$, $\bar{E}^c_{10f}$ and $\bar{E}_{20f}$, which follow from Eqs. (F.3a), (F.3b) and (F.3e) as

$$\bar{E}_{10f} = (\bar{e}_t \times \bar{I}_{00f})|\bar{x}^*_t| \tag{F.24a}$$

$$\bar{E}^c_{10f} = \bar{x}^*_{st} \times \bar{I}_{10f} - (\bar{e}_t \times \bar{I}_{cf})|\bar{x}^*_t| \tag{F.24b}$$

$$\bar{E}_{20f} = (\bar{e}_t \times \bar{I}_{10f})|\bar{x}^*_t| \tag{F.24c}$$

respectively, where it follows from Eqs. (F.4a), (F.4b) and (F.9) that

$$\bar{I}_{00f} = (\bar{e}_s J_{10f} + \bar{e}_t J_{01f} + \bar{e}_n \zeta J_{00f})/|\bar{x}^*_s||\bar{x}^*_t| \tag{F.25a}$$

$$\bar{I}_{10f} = \{\xi_o \bar{I}_{00f} - \frac{1}{|\bar{x}^*_s||\bar{x}^*_t|}(\bar{e}_s J_{20f} + \bar{e}_t J_{11f} + \bar{e}_n \zeta J_{10f})\}/|\bar{x}^*_s| \tag{F.25b}$$

$$\bar{I}_{cf} = \bar{e}_s(\tfrac{1}{2}\bar{x}^*_{ss}.\bar{I}^1_{20f} + \bar{x}^*_{st}.\bar{I}^1_{11}) + \bar{e}_t(\tfrac{1}{2}\bar{x}^*_{ss}.\bar{I}^2_{20f} + \bar{x}^*_{st}.\bar{I}^2_{11}) + \bar{e}_n(\tfrac{1}{2}\bar{x}^*_{ss}.\bar{I}^3_{20f} + \bar{x}^*_{st}.\bar{I}^3_{11}) \tag{F.25c}$$

with, using Eqs. (F.7a and b):

$$\bar{I}_{20f} = \{-\xi_o^2\bar{I}_{00f}+2\xi_o\bar{I}_{10f}+\frac{1}{|\bar{x}_s^*||\bar{x}_t^*|}(\bar{e}_s J_{20f}+\bar{e}_t J_{21f}+\bar{e}_n\zeta J_{20f})\}/|\bar{x}_s^*|^2 \tag{F.25d}$$

$$\bar{I}_{11f} = \{-\xi_o\eta_o\bar{I}_{00f}+\xi_o\bar{I}_{01f}+\eta_o\bar{I}_{10f}+\frac{1}{|\bar{x}_s^*||\bar{x}_t^*|}(\bar{e}_s J_{21f}+\bar{e}_t J_{12f}+\bar{e}_n\zeta J_{11f})\}/|\bar{x}_s^*||\bar{x}_t^*| \tag{F.25e}$$

In the above expressions the basic integrals $J_{k\ell f}$ are defined as, see Eq. (F.5):

$$J_{k\ell f} = \int_{x_i}^{x_{i+1}}\int_{y_j}^{y_{j+1}} (x^k y^\ell)\frac{dxdy}{(x^2+2bxy+y^2+z^2)^{3/2}} \tag{F.26}$$

with $y_j = \eta_o + |\bar{x}_t^*|$ and $y_{j+1} = \eta_o$, while $x_i$ and $x_{i+1}$ are defined as in Eq. (F.5b). The expressions for above basic integrals $J_{k\ell f}$ are again given by the corresponding integrals $J_{k\ell}$ defined in the second section of this Appendix. However, substitution of the limits of integration requires some care for the case the point $\bar{x}_o$ approaches the expansion point $\bar{x}_v(s_i^*)$. In this case it is assumed that $\xi_o = \eta_o = \zeta = 0$, $x_i = \frac{1}{2}\Delta s_i|\bar{x}_s^*| = -x_{i+1}$, $y_j = |\bar{x}_t^*|$, while $y_{j+1} = \varepsilon+0^+$ with $\varepsilon>0$, i.e. we reset the collocation point to a point on the feeding sheet, a small distance away from the edge $\bar{x}_v(s)$.
Defining $\Box F_k$ as in Eq. (F.21h) we now find:

$$\Box F_1 = 2\pi\,\mathrm{sign}(\zeta)/(1-b^2)^{\frac{1}{2}} \tag{F.27a}$$

$$\Box F_2 = \ln\left(\frac{x_i + by_j + r_{ij}}{-x_i + by_j + \hat{r}_{ij}}\right) - \ln\left(\frac{4x_i^2}{(1-b^2)\varepsilon^2}\right) \tag{F.27b}$$

$$\Box F_3 = \ln\left(\frac{bx_i + y_j + r_{ij}}{-bx_i + y_j + \hat{r}_{ij}}\right) + \ln\left(\frac{1-b}{1+b}\right) \tag{F.27c}$$

$$\Box F_4 = r_{ij} - \hat{r}_{ij} \tag{F.27d}$$

$$\Box yF_2 = y_j\ F_2 \tag{F.27e}$$

$$\Box\frac{1}{F_4} = \frac{1}{r_{ij}} - \frac{1}{\hat{r}_{ij}} \tag{F.27f}$$

$$\Box\frac{x^2}{F_4} = \frac{x_i^2}{r_{ij}} - \frac{x_i^2}{\hat{r}_{ij}} \tag{F.27g}$$

$$\Box\frac{xy}{F_4} = \frac{x_i y_j}{r_{ij}} + \frac{x_i y_j}{\hat{r}_{ij}} \tag{F.27h}$$

$$\Box\frac{y^2}{F_4} = \frac{y_j^2}{r_{ij}} - \frac{y_j^2}{\hat{r}_{ij}} \tag{F.27i}$$

with $r_{ij} = (x_i^2 + 2bx_iy_j + y_j^2)^{\frac{1}{2}}$ and $\hat{r}_{ij} = (x_i^2 - 2bx_iy_j + y_j^2)^{\frac{1}{2}}$.
The expression for $\Box F_2$ contains a logarithmic singularity, caused by the circumstance that the vortex lines on the feeding sheet are not exactly perpendicular to the line vortex at $\bar{x}=\bar{x}_v(s)$.
In the present formulation we ignore this weak singularity, i.e. it is assumed that the curvature is vanishingly small.

6. Expressions for the influence due to a vortex core segment

The small-curvature expansion for the velocity induced by a vortex core is expressed in terms of the five integrals defined in Eqs. (9.21g and h).
Writing the distance vector $\bar{r}_{vf}$, defined in Eq. (9.20b) as

$$\bar{r}_{vf} = (\xi_o-\xi)\bar{e}_v + \bar{d} \tag{F.28a}$$

where $\bar{e}_v$ is the unit vector along the vortex core and $\bar{d}$ the component of $\bar{r}_{vf}$ normal to the vortex core, i.e.

$$\bar{e}_v = \bar{x}_{v_s}^* / |\bar{x}_{v_s}^*| \tag{F.28b}$$

$$\bar{d} = \bar{e}_v\times((\bar{x}_o-\bar{x}_v^*)\times\bar{e}_v) \tag{F.28c}$$

The $\xi$ coordinate then follows from Eq. (9.20b) as

$$\xi = \Delta s\,|\bar{x}_{v_s}^*| \tag{F.29a}$$

$$\xi_o = \bar{e}_v\cdot(\bar{x}_o-\bar{x}_v^*) \tag{F.29b}$$

Substitution of Eq. (F.28a) in Eq. (9.21g) gives

$$\bar{I}_{vo} = -(\bar{e}_v J_{v1} + \bar{d} J_{vo})/|\bar{x}^*_{v_s}| \tag{F.30a}$$

$$\bar{I}_{v1} = (\xi_o \bar{I}_{vo} + (\bar{e}_v J_{v2} + \bar{d} J_{v1})/|\bar{x}^*_{v_s}|)/|\bar{x}^*_{v_s}| \tag{F.30b}$$

$$\bar{I}_{v2} = -(\xi_o^2 \bar{I}_{vo} - 2\xi_o \bar{I}_{v1} + (\bar{e}_v J_{v3} + \bar{d} J_{v2})/|\bar{x}^*_{v_s}|)|\bar{x}^*_{v_s}|^2 \tag{F.30c}$$

where

$$J_{vk} = \int_{x_i}^{x_{i+1}} x^k \frac{dx}{(x^2 + d^2)^{3/2}}, \quad k = 0(1)3 \tag{F.30d}$$

with $x = \xi_o - \xi$ and $d^2 = |\bar{d}|^2$. The upper and lower limit of integration are, with $s_i^* = \frac{1}{2}(s_i + s_{i+1})$:

$$x_i = \xi_o + \tfrac{1}{2}|\bar{x}^*_{v_s}|\Delta s_i \tag{F.30e}$$

$$x_{i+1} = \xi_o - \tfrac{1}{2}|\bar{x}^*_{v_s}|\Delta s_i \tag{F.30f}$$

The closed-form expressions for $J_{vk}$ are easily obtained as

$$J_{vo} = \frac{1}{d^2} f_3 \tag{F.31a}$$

$$J_{v1} = -f_2 \tag{F.31b}$$

$$J_{v2} = f_1 - f_3 \tag{F.31c}$$

$$J_{v3} = f_o + d^2 f_2 \tag{F.31d}$$

where

$$f_o = (x_{i+1}^2 + d^2)^{\frac{1}{2}} - (x_i^2 + d^2)^{\frac{1}{2}} \tag{F.31e}$$

$$f_1 = \ln\left(\frac{x_{i+1} + (x_{i+1}^2 + d^2)^{\frac{1}{2}}}{x_i + (x_i^2 + d^2)^{\frac{1}{2}}}\right) \tag{F.31f}$$

$$f_2 = \frac{1}{(x_{i+1}^2 + d^2)^{\frac{1}{2}}} - \frac{1}{(x_i^2 + d^2)^{\frac{1}{2}}} \tag{F.31g}$$

$$f_3 = \frac{x_{i+1}}{(x_{i+1}^2 + d^2)^{\frac{1}{2}}} - \frac{x_i}{(x_i^2 + d^2)^{\frac{1}{2}}} \tag{F.31h}$$

Consider now the term due to the curvature, Eq. (9.21h). Substitution of Eq. (F.28a) in Eq. (9.21h) yields

$$\begin{aligned}\bar{I}^c_{vo} = \tfrac{1}{2}\{&\bar{x}^*_{v_{ss}}(\xi_o^2 J_{vo} - 2\xi_o J_{v1} + J_{v2}) \\ &- 3\bar{e}_v\{(\bar{x}^*_{v_{ss}}\cdot\bar{e}_v)(\xi_o^2 K_{v2} - 2\xi_o K_{v3} + K_{v4}) \\ &\quad + (\bar{x}^*_{v_{ss}}\cdot\bar{d})(\xi_o^2 K_{v1} - 2\xi_o K_{v2} + K_{v3})\} \\ &- 3\bar{d}\{(\bar{x}^*_{v_{ss}}\cdot\bar{e}_v)(\xi_o^2 K_{v1} - 2\xi_o K_{v2} + K_{v3}) \\ &\quad + (\bar{x}^*_{v_{ss}}\cdot\bar{d})(\xi_o^2 K_{vo} - 2\xi_o K_{v1} + K_{v2})\}\}/|\bar{x}^*_{v_s}|^2\end{aligned} \tag{F.32a}$$

$$\begin{aligned}\bar{I}^c_{v1} = \tfrac{1}{2}\{&\bar{x}^*_{v_{ss}}(\xi_o^3 J_{vo} - 3\xi_o^2 J_{v1} + 3\xi_o J_{v2} - J_{v3}) \\ &- 3\bar{e}_v\{(\bar{x}^*_{v_{ss}}\cdot\bar{e}_v)(\xi_o^3 K_{v2} - 3\xi_o^2 K_{v3} + 3\xi_o K_{v4} - K_{v5}) \\ &\quad + (\bar{x}^*_{v_{ss}}\cdot\bar{d})(\xi_o^3 K_{v1} - 3\xi_o^2 K_{v2} + 3\xi_o K_{v3} - K_{v4})\} \\ &- 3\bar{d}\{(\bar{x}^*_{v_{ss}}\cdot\bar{e}_v)(\xi_o^3 K_{v1} - 3\xi_o^2 K_{v2} + 3\xi_o K_{v3} - K_{v4}) \\ &\quad + (\bar{x}^*_{v_{ss}}\cdot\bar{d})(\xi_o^3 K_{vo} - 3\xi_o^2 K_{v1} + 3\xi_o K_{v2} - K_{v3})\}\}/|\bar{x}^*_{v_s}|^4\end{aligned} \tag{F.32b}$$

where $J_{vk}$ is defined in Eqs. (F.30d)-(F.31d) and $K_{vk}$ is defined as

$$K_{vk} = \int_{x_i}^{x_{i+1}} x^k \frac{dx}{(x^2 + d^2)^{5/2}} \quad , \quad k = 0(1)5 \tag{F.32c}$$

The closed-form expressions for the $K_{vk}$-s required (k=0(1)4) are obtained as

$$K_{v0} = \frac{2}{3d^4} f_3 + \frac{1}{3d^2} f_5 \tag{F.33a}$$

$$K_{v1} = -\frac{1}{3} f_4 \tag{F.33b}$$

$$K_{v2} = \frac{1}{3d^2} f_3 + \frac{1}{3} f_5 \tag{F.33c}$$

$$K_{v3} = -f_2 + \frac{d^2}{3} f_4 \tag{F.33d}$$

$$K_{v4} = -\frac{4}{3} f_3 + \frac{d^2}{3} f_5 + f_1 \tag{F.33e}$$

with $f_1$, $f_2$ and $f_3$ defined in Eqs. (F.31f-h) and

$$f_4 = \frac{1}{(x_{i+1}^2 + d^2)^{3/2}} - \frac{1}{(x_i^2 + d^2)^{3/2}} \tag{F.33f}$$

$$f_5 = \frac{x_{i+1}}{(x_{i+1}^2 + d^2)^{3/2}} - \frac{x_i}{(x_i^2 + d^2)^{3/2}} \tag{F.33g}$$

## APPENDIX G

### Solution of a four-diagonal-block matrix equation

The system of equations

$$AA_i x_{i-2} + A_i x_{i-1} + B_i x_i + C_i x_{i+1} = f_i, \quad i=1(1)m \tag{G.1}$$

where $AA_i$, $A_i$, $B_i$ and $C_i$ are sub-matrices of dimension $n_i \times n_{i-2}$, $n_i \times n_{i-1}$, $n_i \times n_i$ and $n_i \times n_{i+1}$, respectively. Both $x_i$ and $f_i$ are sub-column vectors of dimension $n_i$ containing the solution and right-hand side for the $i$-th sub-system.

The LU-decomposition of the four-diagonal-block matrix is

$$\begin{pmatrix} \beta_1 & & & & & \\ \alpha_2 & \beta_2 & & 0 & & \\ AA_3 & \alpha_3 & \beta_3 & & & \\ & AA_4 & \alpha_4 & \beta_4 & & \\ & 0 & & & & \\ & & & AA_m & \alpha_m & \beta_m \end{pmatrix} \begin{pmatrix} 1 & \gamma_1 & & & & \\ & 1 & \gamma_2 & & 0 & \\ & & 1 & \gamma_3 & & \\ & & & & & \\ & 0 & & & & \\ & & & & & 1 \end{pmatrix} \tag{G.2}$$

which is easily obtained from the following relations:

$$\beta_1 = B_1 \tag{G.3a}$$

$$\beta_1 \times \gamma_1 = C_1 \tag{G.3b}$$

$$\alpha_2 = A_2 \tag{G.4a}$$

$$\beta_2 = B_2 - \alpha_2 \times \gamma_1 \tag{G.4b}$$

$$\beta_2 \times \gamma_2 = C_2 \tag{G.4c}$$

while for i=3(1)m

$$\alpha_i = A_i - AA_i \times \gamma_{i-2} \tag{G.5a}$$

$$\beta_i = B_i - \alpha_i \times \gamma_{i-1} \tag{G.5b}$$

$$\beta_i \times \gamma_i = C_i \qquad (i \neq m) \tag{G.5c}$$

The elements of matrix $\gamma_i$ are obtained from a standard LU decomposition procedure for solving the $n_i \times n_i$ matrix equation $\beta_i y_j = g_j$ for the $n_{i+1}$ column vectors $y_j$, $j=1(1)n_{i+1}$ of $\gamma_i$ with $g_j$, $j=1(1)n_{i+1}$ the corresponding column vector of $C_i$ as right-hand side.

The solution of Eq. (G.1) is now obtained by carrying out the "downward sweep"

$$\beta_1 z_1 = f_1 \tag{G.6a}$$

$$\beta_2 z_2 = f_2 - \alpha_2 z_1 \tag{G.6b}$$

$$\beta_i z_i = f_i - \alpha_i z_{i-1} - AA_i z_{i-2}, \text{ for } i=3(1)m \tag{G.6c}$$

which is straightforward, especially since the LU-decomposition of the submatrices $\beta_j$, $j=1(1)m$ has already been computed during execution of Eqs. (G.3b), (G.4c) and (G.5c).
The "downward sweep" is followed by the "upward sweep" during which one obtains the solution $x_j$, $j=1(1)m$:

$$x_m = z_m \tag{G.7a}$$

$$x_i = z_i - \gamma_i x_{i+1}, \text{ for } i=m-1(1)1 \tag{G.7b}$$

The major computational cost involved is that due to the LU-decomposition of the m diagonal blocks of dimension $n_i$, $i=1(1)m$ ($\Sigma n_i^3$) and that due to the 3 matrix-matrix multiplications implied in Eqs. (G.3)-(G.5) ($\Sigma(n_i n_{i-2}^2 + n_i n_{i-1}^2 + n_{i+1} n_i^2)$), so in first approximation of the order of $(mn)^3/m^2$ where n is the average block size.

## CURRICULUM VITAE

Hendrik Willem Marie Hoeijmakers was born in Sevenum (L), The Netherlands, on January 23, 1948. In 1966 he obtained the "HBS-B"-diploma at the Blariacum College in Venlo-Blerick and in September of the same year started his study in aeronautical engineering at the Delft University of Technology. In October 1971 he graduated cum laude on the subject of supersonic lifting surfaces with subsonic leading edges under the guidance of Prof.dr.ir. J.A. Steketee and Dr.ir. R. Coene.

After a year of post-graduate research work at the Department of Aerospace Engineering of the Delft University of Technology the author obtained in September 1972 a NASA International University Fellowship for further study at the Department of Aeronautics of the California Institute of Technology in Pasadena, California, USA.

In June 1974 he obtained the Degree of Aeronautical Engineer at this institute on the thesis "Effects of Planform Curvature in Supersonic Wings", supervised by Prof. H.J. Stewart.

Since November 1974 the author is employed at the National Aerospace Laboratory (NLR) in Amsterdam, The Netherlands. At NLR he worked mainly on the development of computational methods for linearized sub- and supersonic flow about complex three-dimensional configurations and on the development of computational methods for configurations with vortex flow. The present thesis results from the work on the latter subject.

SAMENVATTING

AERODYNAMICA VAN GEORDENDE WERVELSTROMINGEN; ONDERZOCHT MET BEHULP VAN REKENMETHODEN

Wervellagen en wervelkernen spelen een belangrijke rol in de stroming om vliegtuigconfiguraties. Wervellagen ontstaan als de stroming het oppervlak verlaat ter plaatse van een scherpe rand, bijvoorbeeld de vleugelachterrand, of ten gevolge van grenslaagloslating op een glad deel van het oppervlak. In het algemeen hebben vrije wervellagen de neiging op te rollen tot geconcentreerde wervelkernen. Vaak is het resulterende stromingspatroon geordend, stationair en persistent.

In dit proefschrift wordt onderscheid gemaakt tussen wervelstromingen met een zwakke en die met een sterke interactie tussen de wervellagen en kernen aan de ene kant en de stroming op het oppervlak van de configuratie aan de andere kant. De stroming om de vleugel met grote slankheid van een verkeersvliegtuig in kruisvlucht is een voorbeeld van een zwakke interactie wervelstroming. De stroming laat los ter plaatse van de achterrand, de wervellaag (het zog) rolt op in meestal twee sterke en persistente (tip)wervels waarbij de precieze vorm en het oprollen van het zog een geringe invloed hebben op de stroming op het vleugeloppervlak. Dit in tegenstelling met de stroming om vleugels met kleinere slankheid, zoals bij jachtvliegtuigen, waar de stroming loslaat ter plaatse van de zijrand of de sterk gepijlde voorrand. De resulterende wervellagen en wervelkernen liggen nu relatief dicht bij het vleugeloppervlak en hebben een groot, vaak gunstig, effect op de stroming op het vleugeloppervlak. De stroming om slanke lichamen bij hoge invalshoek is een ander voorbeeld van een sterke interactie wervelstroming. Typerend voor gevallen met een sterke interactie is dat de lift niet lineair toeneemt met de invalshoek, wat leidt tot een aanzienlijke toename in lift en dat vaak tot hoge invalshoek. Bij hogere invalshoeken treedt "vortex burst" op en verliest het wervelpatroon zijn geordende structuur.

Het doel van het onderzoek beschreven in dit proefschrift is bij te dragen tot de kennis, en uiteindelijk de toepassing in de praktijk, van geordende en beheersbare wervelstromingen. Hiertoe wordt een aantal rekenmethoden ontwikkeld voor het numeriek simuleren van de stroming om configuraties met zwakke en die met sterke interactie wervelstroming. De validatie van de methoden vindt plaats door verkregen resultaten te vergelijken met resultaten van andere rekenmethoden en met experimentele gegevens. Het onderzoek beperkt zich tot stationaire sub-kritieke stromingen bij hoge Reynolds getallen.

Het proefschrift is onderverdeeld in twee delen.
In het eerste deel, dat de hoofdstukken 1-5 omvat, wordt een beschrijving gegeven van de fysica van geordende wervelstromingen en de mathematische modellering hiervan. Na het inleidende eerste hoofdstuk worden in het tweede hoofdstuk van een aantal bekende zwakke en sterke interactie gevallen de meest karakteristieke stromingsverschijnselen beschreven. In hoofdstuk 3 wordt ingegaan op verschillende aspecten van de mathematische modellering van dit type stromingen. Uiteindelijk wordt gekozen voor een potentiaal-stromings model met ingebedde gebieden met rotatie, namelijk wervelvlakken en wervelkernen welke laatsten ook als sterk opgerolde wervelvlakken beschouwd kunnen worden. Een wervelvlak vormt een discontinuiteits-oppervlak in de verder rotatie-vrije stroming. Het effect van een wervelkern op de stroming buiten de kern zelf wordt benaderd door een relatief eenvoudig model van een werveldraad met "feeding sheets". Deze laatsten maken het mogelijk dat wervelsterkte kan worden toegevoegd aan de werveldraad. In hoofdstuk 4 wordt er in meer detail gekeken naar eigenschappen van wervelkernen en hun modellering, in het bijzonder voor het vereenvoudigde geval van een slanke wervelkern in een verder ongestoorde stroming. De analyse beschouwt de componenten van de wervelsterkte vector in de wervelkern en het snelheidsveld binnen en buiten de wervelkern. Er wordt aangetoond dat in de wervelkern de omtrekssnelheids component wordt omgezet in een axiale snelheidscomponent. Dit resulteert in een stroming met spiraalvormige stroomlijnen, met instroming bij de rand van de wervelkern en met een grote axiale snelheid (straal) nabij de as van de wervelkern.
In het vijfde en laatste hoofdstuk van het eerste deel wordt het gekozen mathematische model voor de drie-dimensionale stroming samengevat. Ook wordt de oplosmethode, middels singulariteitenbeleggingen op het oppervlak van de configuratie en op de wervelvlakken, beschreven. Het oplossen van het volledige drie-dimensionale probleem, niet-lineair vanwege de randvoorwaarden op de wervelvlakken, is geen eenvoudige taak. Echter, in dit hoofdstuk wordt ook beschreven dat benaderende formuleringen die leiden tot een eenvoudiger probleem mogelijk zijn. Voor zoggen achter vliegtuigconfiguraties (een zwakke-interactie wervelstroming) leidt de aanname dat de veranderingen in stroomafwaartse richting veel geleidelijker plaatsvinden dan die in dwarsrichting tot een quasi twee-dimensionaal probleem. Door de afstand achter de configuratie te relateren aan een tijdsvariable kan dit probleem geformuleerd worden als een beginwaarde probleem. In deze zogenaamde twee-dimensionale tijdsafhankelijke analogie wordt uitsluitend bekeken hoe, in afwezigheid van vaste oppervlakken, een twee-dimensionaal wervelvlak of systeem van wervelvlakken zich ontwikkelt in de tijd.
Voor in langsrichting langgerekte (zogenaamde slanke) configuraties kan met behulp van dezelfde aanname als boven het drie-dimensionale sterke-interactie wervelstromings probleem bij benadering berekend worden door het oplossen van een serie van opeenvolgende twee-dimensionale, niet-lineaire, problemen in vlakken loodrecht op de lengterichting van de configuratie. In deze "slender-body" approximatie komt de drie-dimensionaliteit van het probleem tot uiting in de randvoorwaarden voor elk van de twee-dimensionale "cross-flow-plane" problemen.

Het tweede deel, de hoofdstukken 6-10, beschrijft rekenmethoden voor de bepaling van de geordende wervelstroming om vliegtuigconfiguraties. In hoofdstuk 6 wordt een samenvatting gepresenteerd van bestaande methoden, met hun zwakke en sterke punten. De bijdrage van het voorliggende onderzoek is voornamelijk gelegen in de ontwikkeling en toepassing van panelenmethoden voor het oplossen van het (niet-lineaire) probleem van potentiaalstromingen met vrije wervelvlakken en wervelkernen.
In de volgende drie hoofdstukken wordt de ontwikkeling en toepassing van de rekenmethoden beschreven, in de volgorde van toenemende complexiteit, beginnend met de methode voor de twee-dimensionale tijdsafhankelijke analogie. In hoofdstuk 10 worden de bevindingen van het onderzoek samengevat.

De methode voor het berekenen van de ontwikkeling in de tijd van twee-dimensionale wervelvlakken wordt besproken in hoofdstuk 7. Het snelheidsveld wordt berekend door middel van een tweede-orde nauwkeurige panelenmethode. Op elk tijdstip vindt de discretisatie van de wervelvlakken plaats met een schema dat de lokale paneelgrootte aanpast aan de lokale kromming. Dit maakt het mogelijk het oprolproces tot in detail te volgen. In de methode kan op min of meer natuurgetrouwe wijze wervelsterkte in wervelkernen geaccumuleerd worden. De rekenmethode wordt toegepast om de ontwikkeling van het zog te bepalen achter: een vleugel met een elliptische draagprachtverdeling, een vleugel met een uitgeslagen landingsklep, een doorstroomgondel met een cirkelvormige doorsnijding en een delta vleugel met een voorrand wervelvlak. Resultaten van de huidige methode worden vergeleken met resultaten van andere rekenmethoden en met experimentele gegevens.

Aangetoond wordt dat de ontwikkelde rekenmethode in staat is de stroomafwaartse ontwikkeling van zoggen op een betrouwbare manier te bepalen tot grote afstanden achter de configuratie. De verkregen resultaten geven belangrijke aanwijzingen voor de te verwachten topologie van het drie-dimensionale zog.

In hoofdstuk 8 wordt in detail de methode besproken voor de sterke interactie wervelstroming om slanke configuraties, in de quasi twee-dimensionale formulering die het resultaat is van de "slender-body" approximatie. Het snelheidsveld wordt berekend met de tweede-orde panelenmethode ontwikkeld in hoofdstuk 7. De configuratie mag bestaan uit dragende vlakken en of delen met dikte. Voor de laatste delen wordt voldaan aan de normaalsnelheidsrandvoorwaarden via een equivalente Dirichlet randvoorwaarde. Deze formulering resulteert in een fictieve stroming binnen de gesloten contour. Ook hiervoor is een tweede-orde nauwkeurige panelenmethode ontwikkeld. Wervelvlakken modelleren loslating van voorgeschreven posities, hetzij scherpe randen, hetzij locaties op gladde delen van de contour waar loslating verwacht wordt. Het systeem van niet-lineaire vergelijkingen wordt opgelost met het Newton iteratieve oplosproces, waarbij een aantal continueringsprocedures gevolgd kunnen worden voor het construeren van een beginschatting uit een eerder verkregen naburige oplossing.

Aan de hand van een basis testgeval, de vlakke-plaat delta vleugel met slankheid 1 bij 20 graden invalshoek, wordt onderzocht wat de invloed is op de oplossing van de lengte van het wervelvlak, de fijnheid van het discretisatie schema en het in hoofdstuk 4 beschreven verbeterde model van de wervelkern. Vervolgens wordt de oplossing berekend en geanalyseerd voor dezelfde vleugel over een groot traject van invalshoeken en sliphoeken. Ook het effect van dikte op de oplossing wordt bestudeerd. Vergelijking van de rekenresultaten met experimentele gegevens toont aan dat de modellering van secundaire loslating in veel gevallen een voorwaarde is voor een goede correlatie. Hiertoe wordt een poging gedaan door ook de secundaire loslating te modelleren als een wervelvlak-wervelkern combinatie. Dit heeft het gewenste effect op de zuigpiek in de drukverdeling op de bovenzijde van de vleugel ten gevolge van de primaire wervel, maar lijkt het effect van de secundaire wervel zelf te overschatten. Verder blijkt dat voor de voorspelling van de secundaire loslaatpositie meer vereist is dan de zwakke koppeling van het huidige niet-viskeuze model met een grenslaag methode.

Als aansluiting op hoofdstuk 4 wordt onderzocht in hoeverre een wervelkern bestaande uit een combinatie van een relatief lang opgerold wervelvlak en een werveldraad de stroming in het gebied buiten de omgeving van de as van de wervelkern simuleert. Voor het basis testgeval levert dit een verrassende goede correlatie op van berekende en gemeten snelheidsverdelingen in het beschouwde deel van de wervelkern.

Toepassing van de rekenmethode op een slanke kegel bij hoge invalshoek bevestigt het vermoeden dat het onderhavige niet-lineaire probleem meer dan één oplossing kan hebben. Tenslotte wordt de methode toegepast op twee niet-conische configuraties, een dubbel-delta vleugel en een "strake"-vleugel combinatie. In het laatste geval wordt de kern van de zogenaamde vleugelwervel gemodelleerd als een werveldraad met twee "feeding sheets".

In hoofdstuk 9 wordt de methode beschreven voor het berekenen van de drie-dimensionale symmetrische stroming om symmetrische delta-achtige draagvlakken met loslating langs de gehele voorrand. Het snelheidsveld wordt ook hier berekend met een tweede-orde nauwkeurige panelenmethode. Het systeem van niet-lineaire vergelijkingen wordt opgelost met een quasi-Newton iteratieve methode. De methode wordt toegepast op het boven omschreven basis testgeval, mede met het doel de invloed van wervelvlak lengte, paneelschema etc. te onderzoeken. Verder wordt de methode toegepast op deltavleugels met een pijlstelling die varieert van 65° tot 85°. De toepassingen laten zien dat geometrisch gesproken de oplossing over een groot deel van de vleugel conisch is, maar tevens dat de snelheids en drukverdeling een sterk drie-dimensionaal karakter hebben. Dit laatste wordt veroorzaakt door het effect van de aanwezigheid van de achterrand en ook door de invloed van het singuliere gedrag van de oplossing ter plaatse van de voorste punt.

De berekende drukverdelingen zijn in redelijke overeenstemming met gemeten waarden, alhoewel de invloed van de secundaire loslating opnieuw belangrijk is. Tenslotte laat de correlatie van resultaten van de huidige potentiaal-stromings methode met resultaten van een methode gebaseerd op de Euler vergelijkingen zien dat voor incompressibele stromingen deze beide niet-viskeuze methoden predicties van vergelijkbare kwaliteit kunnen leveren. Hierbij zijn de rekentijden voor de potentiaal methode bescheiden vergeleken met die benodigd voor de Euler methode.